Julius-Maximilians-
UNIVERSITÄT
WÜRZBURG

Fakultät für
Physik und Astronomie

A Correlation Study of Radio Giant Pulses and Very High Energy Photons from the Crab Pulsar

DISSERTATION
zur Erlangung des naturwissenschaftlichen Doktorgrades der
Julius-Maximilians-Universität Würzburg

VORGELEGT VON
Natalia Ewelina Lewandowska
AUS Toruń IN Polen

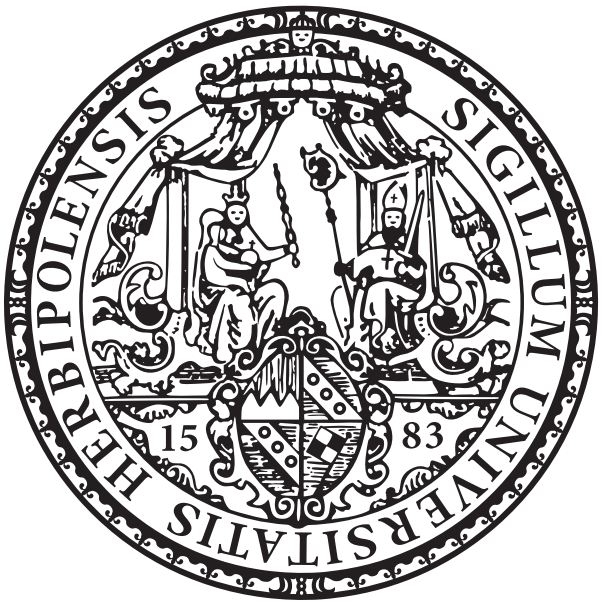

Würzburg 2015

Eingereicht am: .....
bei der Fakultät für Physik und Astronomie

1. Gutachter: .....
2. Gutachter: .....
3. Gutachter: .....
der Dissertation.

Vorsitzende(r): .....

1. Prüfer: .....
2. Prüfer: .....
3. Prüfer: .....
im Promotionskolloquium.

Tag des Promotionskolloquiums: .....

Doktorurkunde ausgehändigt am: .....

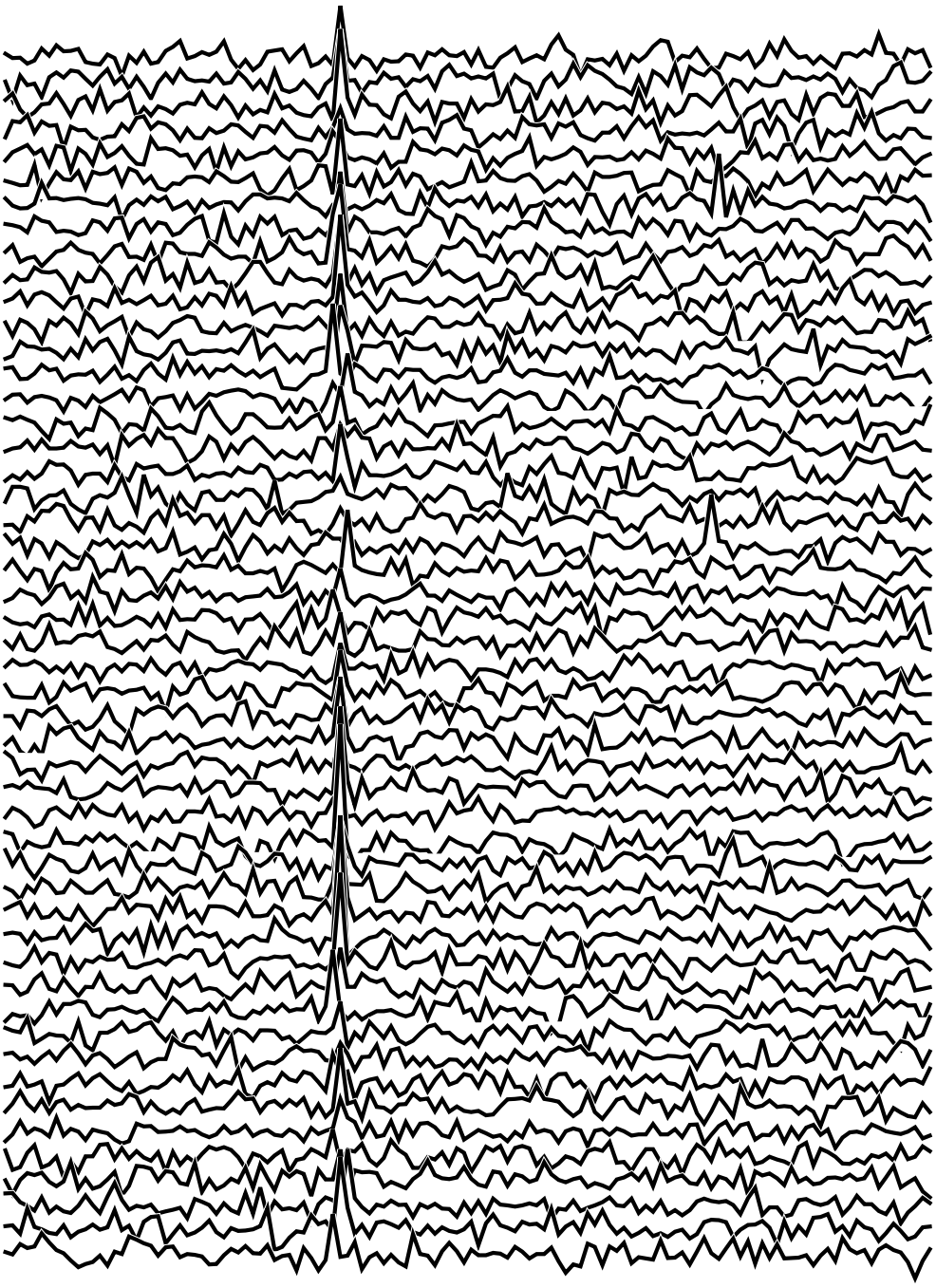

"We were wanderers from the beginning." C. Sagan

Abstract

Pulsars (in short for ***Puls**ating St**ars***) are magnetized, fast rotating neutron stars. The basic picture of a pulsar describes it as a neutron star which has a rotation axis that is not aligned with its magnetic field axis. The emission is assumed to be generated near the magnetic poles of the neutron star and emitted along the open magnetic field lines. Consequently, the corresponding beam of photons is emitted along the magnetic field line axis. The non-alignment of both, the rotation and the magnetic field axis, results in the effect that the emission of the pulsar is only seen if its beam points towards the observer. The emission from a pulsar is therefore perceived as being pulsed although its generation is not. This rather simple geometrical model is commonly referred to as *Lighthouse Model* and has been widely accepted. However, it does not deliver an explanation of the precise mechanisms behind the emission from pulsars (see below for more details).

Nowadays more than 2000 pulsars are known. They are observed at various wavelengths. Multiwavelength studies have shown that some pulsars are visible only at certain wavelengths while the emission from others can be observed throughout large parts of the electromagnetic spectrum. An example of the latter case is the Crab pulsar which is also the main object of interest in this thesis. Originating from a supernova explosion observed in 1054 A.D. and discovered in 1968, the Crab pulsar has been the central subject of numerous studies. Its pulsed emission is visible throughout the whole electromagnetic spectrum which makes it a key figure in understanding the possible mechanisms of multiwavelength emission from pulsars.

The Crab pulsar is also well known for its radio emission strongly varying on long as well as on short time scales. While long time scale behaviour from a pulsar is usually examined through the use of its average profile (a profile resulting from averaging of a large number of individual pulses resulting from single rotations), short time scale behaviour is examined via its single pulses. The short time scale anomalous behaviour of its radio emission is commonly referred to as *Giant Pulses* and represents the central topic of this thesis.

While current theoretical approaches place the origin of the radio emission from a pulsar like the Crab near its magnetic poles (*Polar Cap Model*) as already indicated by the Lighthouse model, its emission at higher frequencies, especially its γ-ray emission, is assumed to originate further away in the geometrical region surrounding a pulsar which is commonly referred to as a pulsar magnetosphere (*Outer Gap Model*). Consequently, the respective emission regions are usually assumed not to be connected. However, past observational results from the Crab pulsar represent a contradiction to this assumption. Radio giant pulses from the Crab pulsar have been observed to emit large amounts of energy on very short time scales implying small emission regions on the surface of the pulsar. Such energetic events might also leave a trace in the γ-ray emission of the Crab pulsar. The aim of this thesis is to search for this connection in the form of a correlation study between radio giant pulses and γ-photons from the Crab pulsar. To make such a study possible, a multiwavelength observational campaign was organized for which radio observations were independently applied for, coordinated and carried out with the Effelsberg radio telescope and the Westerbork Synthesis Radio Telescope and γ-ray observations with the Major Atmospheric Imaging Cherenkov telescopes. The corresponding radio and

γ-ray data sets were reduced and the correlation analysis thereafter consisted of three different approaches:

1) The search for a clustering in the differences of the times of arrival of radio giant pulses and γ-photons;

2) The search for a linear correlation between radio giant pulses and γ-photons using the Pearson correlation approach;

3) A search for an increase of the γ-ray flux around occurring radio giant pulses.

In the last part of the correlation study an increase of the number of γ-photons centered on a radio giant pulse by about 17 % (in contrast with the number of γ-photons when no radio giant pulse occurs in the same time window) was discovered. This finding suggests that a new theoretical approach for the emission of young pulsars like the Crab pulsar, is necessary.

Zusammenfassung

Pulsare (Kurzform von ***Puls**ating **Star**s*) sind stark magnetisierte, rotierende Neutronensterne. Nach dem Standardmodell ist ein Pulsar ein Neutronenstern mit einer Rotationsachse, die nicht entlang der Achse seines Magnetfelds ausgerichtet ist. Es wird angenommen, dass die Pulsarstrahlung in der Nähe der Pole des Neutronensterns an offenen Magnetfeldlinien entsteht. Der dadurch entstehende Photonenstrahl wird entlang der Magnetfeldachse emittiert. Die unterschiedlichen Ausrichtungen der Rotations- und Magnetfeldachse führen dazu, dass die Strahlung des Pulsars von einem Beobachter nur wahrgenommen wird, wenn der Photonenstrahl die Sichtlinie des Beobachters überstreicht. Durch diesen Effekt wird beim Beobachter der Anschein erweckt die Pulsarstrahlung sei gepulst, obwohl sie kontinuerlich produziert wird. Dieses vereinfachte geometrische Model, in der Literatur oftmals als *Leuchtturm Modell* bezeichnet, ist heutzutage weitestgehend akzeptiert. Es liefert dennoch keine Erklärung für die genaue Entstehung der Pulsarstrahlung (siehe weiter unten).
Heutzutage sind mehr als 2000 Pulsare bekannt und werden mittlerweile nicht nur bei Radiowellenlängen untersucht. Multiwellenlängenstudien haben zu der Entdeckung geführt, dass einige Pulsar nur in bestimmten Wellenlängenbereichen sichtbar sind, während die Strahlung von anderen Pulsaren in weiten Teilen des elektromagnetischen Spektrums nachgewiesen werden kann. Ein Beispiel für letzteren Fall ist der Crab Pulsar, das Objekt das die vorliegende Arbeit hauptsächlich betrachtet. Entstanden in einer Supernova, die im Jahre 1054 n.Chr. beobachtet wurde, wurde er 1968 als stellarer Überrest dieser Explosion entdeckt und seitdem im Rahmen zahlreicher Studien untersucht. Seine gepulste Strahlung kann im gesamten elektromagnetischen Spektrum nachgewiesen werden. Diese Eigenschaft macht ihn zu einem Schlüsselobjekt für die Erforschung möglicher Emissionsmechanismen der Strahlung von Pulsaren.
Eine weitere Besonderheit des Crab Pulsars liegt auch in dem anomalen Verhalten seiner Radiostrahlung auf kurzen Zeitskalen. Während das Langzeitverhalten eines Pulsars mittels seines mittleren Pulsprofiles (eines Profils resultierend aus der Mittelung vieler Einzelpulse aus einzelnen Rotationen) untersucht wird, wird das Kurzzeitverhalten mittels einzelner Pulse untersucht. Als anomales Verhalten der Radiostrahlung des Crab Pulsars auf diesen kurzen Zeitskalen sind die sogenannten Riesenpulse (*Giant Pulses*) von Interesse. Einzelpulse dieser Art sind der zentrale zu untersuchende Aspekt der vorliegenden Arbeit.
Gängige theoretische Modelle gehen davon aus, dass die Radiostrahlung eines Pulsars in der Nähe der Pole entsteht (*Polar Cap Model*), wie zuvor vom Leuchtturm Model impliziert wurde, während die hochfrequente Strahlung, wie z.B. die γ-Strahlung, weiter außen in der Magnetosphäre, die den Pulsar umgibt, entsteht (*Outer Gap Model*). Ausgehend von diesen beiden theoretischen Ansätzen, wird angenommen, dass die entsprechenden Entstehungsregionen nicht miteinander verbunden sind. Die bisherigen Beobachtungen des Crab Pulsars widersprechen jedoch dieser Annahme. Untersuchungen der Riesenpulse des Crab Pulsars im Radiobereich haben ergeben, dass diese Einzelpulse große Energiemengen binnen sehr kurzen Zeitskalen freisetzen. Dieses Phänomen deutet auf sehr kleine Emissionsregionen auf der Oberfläche des Pulsars hin. Eine Freisetzung dieser Energiemengen könnte auch Spuren im Bereich der hochenergetischen γ-Strahlung hinterlassen. Das Ziel der vorliegenden Arbeit ist daher eine Un-

tersuchung einer möglichen Verbindung zwischen den Radiopulsen des Crab Pulsars im Radiobereich und seiner γ-Strahlung in der Form einer Korrelationsstudie. Um eine solche Studie zu ermöglichen, wurde eine Multiwellenlängen Beobachtungskampagne organisiert. Im Rahmen dieser Kampagne wurden selbstständig Radiobeobachtungen am Effelsberger Radioteleskop und am Westerbork Synthesis Radio Telescope und γ-Beobachtungen an den Major Atmospheric Imaging Cherenkov Teleskopen erfolgreich beantragt, koordiniert und (teilweise selbstständig vor Ort) ausgeführt. Die daraus entstehenden Datensätze wurden entsprechend bearbeitet und in der resultierenden Korrelationsanalyse wurden die folgenden Aspekte untersucht:

1) Eine Anhäufung in den Ankunftszeiten von Riesenpulsen und γ-Photonen;

2) Eine Suche nach einer lineare Korrelation zwischen Riesenpulsen und γ-Photonen mittels der Pearson Korrelation;

3) Eine Suche nach einer Erhöhung des Flusses von γ-Photonen in der zeitlichen Umgebung eines Riesenpulses im Radiobereich.

Im letzten Teil der Analyse konnte eine Erhöhung der Anzahl von γ-Photonen, die zeitlich auf einem Riesenpuls zentriert sind, von ungefähr 17 % (im Vergleich zu der entsprechenden Anzahl im gleichen Zeitfenster, wenn kein Riesenpuls vorhanden ist) nachgewiesen werden. Dieses Ergebnis gibt einen wichtigen Impuls für die Überarbeitung der bereits vorhandenen Emissionsmodelle von jungen Pulsaren wie dem Crab Pulsar.

Contents

List of Figures

List of Tables

Abbreviations

AGILE	Astro-rivelatore Gamma ad Immagini LEggero
AMC	Active Mirror Control
ADC	Analog to Digital Converter
ASTRON	ASTRonomisch Onderzoek in Nederland (Astronomy institute Netherlands Institute for Radio Astronomy)
ATNF	Australia Telescope National Facility
AP	Average Profile
AXP	Anomalous X-ray Pulsar
BAT	Barycentric Arrival Time
CoG	Center of Gravity
CDF	Cumulative Distribution Function
DAQ	Data Acquisition System
DSPSR	Digital Signal Processing for Pulsars
EGRET	Energetic Gamma-Ray Experiment Telescope
FoV	Field of View
HE	High Energy
HFC	High Frequency Component
GBT	Green Bank Telescope
GMRT	Giant Metre-Wave Telescope
GPS	Global Positioning System
GRB	γ-ray Burst
GPs	Giant Pulses
GW	Gravitational Wave
HFIP	High Frequency Interpulse
HMXB	High-Mass X-Ray Binary

IACT	Imaging Air Cherenkov Telescope
IMXB	Intermediate-Mass X-Ray Binary
ISM	Interstellar Medium
IC	Inverse Compton
IVC	IF to Video Frequency Converter
JVLA	Jansky Very Large Array
JBO	Jodrell Bank Observatory
LAT	Large Area Telescope
LMC	Large Magellanic Cloud
LEE	Look-Elsewhere-Effect
LMXB	Low-Mass X-Ray Binary
LFC	Low Frequency Component
LFIP	Low Frequency Interpulse
M1	Messier catalogue number of the Crab Nebula
MAGIC	Major Atmospheric Imaging Cherenkov telescopes
MCMC	Markov Chain Monte Carlo
MC	Monte Carlo Simulations
MPIfR	Max-Planck Institute for Radioastronomy
NASA	National Aeronautics and Space Administration
NSB	Night Sky Background
NOT	Nordic Optical Telescope
P1	Main Pulse
P2	Interpulse
PSF	Point Spread Function
PMT	Photomultiplier Tube
PSR	Pulsating Source of Radio emission
PuMA	Pulsar Machine
QPO	Quasi-Periodic Oscillations
RFI	Radio Frequency Interference

RMS Root Mean Square

RPP Rotation-Powered Pulsar

RRAT Rotating Radio Transient

SAT Topocentric Arrival Time

SGR Soft γ-ray Repeater

SNR Supernova Remnant

SSB Solar System Barycenter

TOA Time of Arrival

VERITAS Very Energetic Radiation Imaging Telescope Array System

WSRT Westerbork Synthesis Radio Telescope

1. Introduction

1.1. The Discovery of Neutron Stars

Neutron stars are one possible form of a stellar supernova remnant and represent a final stage in the stellar evolution. Discussing the estimated and observed number of discovered supernova remnants in the Milky Way, the Andromeda galaxy and Messier 101, Baade and Zwicky [1934] suggested in 1934 for the first time the existence of a different form of stellar remnant called the neutron star. The authors nevertheless commented that their suggestion needed to be regarded with caution.
At a time when the possible sources for the energy of stars were highly debated and mostly equation of states were chosen according to mathematical convencience, the question arose if a condensed neutron star could result out of stars with a sufficiently high mass (Landau [1938]). It was also picked up and discussed extensively by Oppenheimer and Volkoff [1939] who examined how high the mass of the progenitor star could be. According to their investigations no progenitor star with a mass less than 1.5 $M_{\odot}$ would be able to be converted into a neutron star (confirming earlier results of Landau [1938]), but they were unable to find an upper limit for this mass with their approach. The consideration of neutron stars as a possible step in stellar evolution was consequently taken much earlier into account than the actual detection.
The question how such a neutron star can emit its energy into the interstellar space was examined by Pacini [1967] who suggested the description of an oblique rotator (a magnetic dipole with a non-aligned dipole and angular momentum axis) as a model. His discussion of possible energy releases culminates in two scenarios: 1) Precession of the rotation axis of a neutron star, under the assumption that the total angular momentum is constant, will lead to the dissipation of energy in order to bring both axes into alignment and thus form an equilibrium state. 2) The emission of low frequency electromagnetic waves at a gas density low enough to let them pass which is not possible immediately after the supernova explosion. Pacini [1967] comments that in the case of an emission of electromagnetic waves the latter are propagating into the supernova remnant and power it this way. He suggested that this could be the way the Crab Nebula is being powered from the inside, that is by a neutron star in its central region. At the time when this work was published it was not clear how the emission mechanisms inside the Crab Nebula work. With the work of Pacini [1967] it was stated that a neutron star (which is an oblique rotator) is actually able to emit electromagnetic waves which also can be detected from Earth.
Soon afterwards and more than 30 years after the suggestion made by Baade and Zwicky [1934], Jocelyn Bell and Anthony Hewish discovered the first rotating, magnetized neutron star named CP 1919 in July 1967 (Figure 1.1) which marked the beginning of a new era of scientific studies (Hewish et al. [1968]). The discovery was a product of chance since the original aim of the respective research was to examine interstellar scintillation (see Chapter 1.4.3). The goal of these measurements was to examine quasars which have small angular diameters and therefore provide suitable objects for the verification of scintillation. Different from the usual technical equipment for scintillation studies at that time, a short time receiver was used and the ob-

servations were repeated once per day in the form of a sky survey with an receiving antenna operating at a wavelength of 3.7 m (further details about this research can be found in Hewish [1975]). Not expecting the detection of short time signals, the original signal from CP 1919 was regarded at first as interference of unknown origin (upper part of Figure 1.1). On the contrary to interference the signal re-appeared in the observations. Examining it further with a chart recorder of higher speed, a periodicity of about 1.3 s could be verified in the case of this signal (lower part of Figure 1.1).

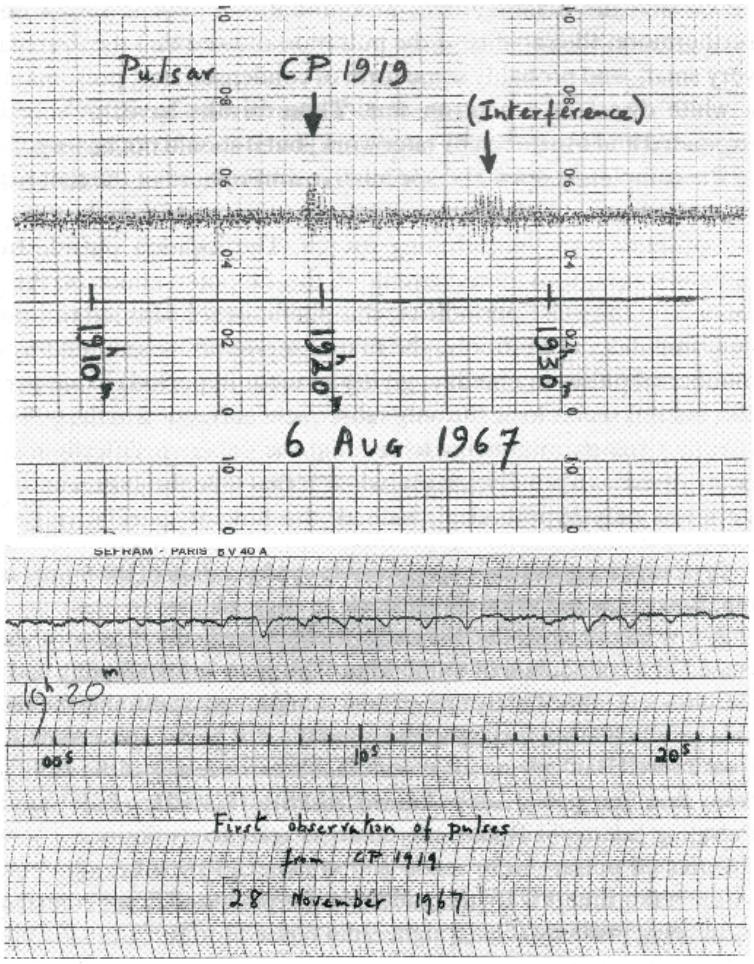

Figure 1.1.: Radio observations recorded on paper chart which led to the discovery of the first pulsar known as PSR B1919+21. Upper plot: The first recording of a radio signal from PSR B1919+21 (at the time of detection referred to as CP 1919, the designation CP standing for "Cambridge Pulsar") as carried out during scintillation studies. Lower plot: Recording of the signal from PSR B1919+21 using higher time resolution. It reveals individual pulses shown as downward deflexions.
Both figures were adopted from Lyne and Graham-Smith [1990].

Detections of further sources of this kind followed quickly (Pilkington et al. [1968], or in the case of the Vela pulsar by Large et al. [1968]).The first discovered pulsars (before the detection

of the Crab and the Vela pulsar) have all long rotation periods, ranging from 0.25 s (CP 0950, Pilkington et al. [1968]) to 1.33 s (CP 1919, Hewish et al. [1968], Pilkington et al. [1968]).
At this time it was not clear if the pulsating signals originated from neutron stars, or white dwarf stars. Although the first published suggestion of this kind was expressed by Hewish et al. [1968], the characteristics of pulsations from white dwarf stars were extensively examined by Faulkner and Gribbin [1968] and Skilling [1968]. Faulkner and Gribbin [1968] investigated white dwarf models, originally constructed by Hamada and Salpeter [1961]. According to their calcuations the vibration periods of white dwarf stars have a lower limit of approximately 1.5 s and could be consequently assigned to the sources of the pulses found by Hewish et al. [1968] and Pilkington et al. [1968]. In another later approach Skilling [1968] determined radial oscillation periods for the modes of white dwarfs at zero degrees temperature with the equation of state, determined by Salpeter (Salpeter [1961]) and dynamics resulting from general relativity. It needs to be noted at this point that earlier approaches by other authors made use of Newtonian dynamics not taking the large gravitational fields of the pulsating sources into account. From his calculations Skilling [1968] determined that white dwarf models in which general relativity effects are included, cannot have oscillation periods of less than 2 s.
In his discussion of rotating neutron stars as the probable origin of the observed radio pulses, Gold [1968] referred to several facts why the latter were not likely originating from white dwarf stars, or changing plasma configurations. The shortness of the pulses with which they were observed (forming about 1/30 of the time of a rotation period), were unlikely to be produced by any other astronomical object than a rotating neutron star. Their precision of their rotation led to the aspect that they could not originate from configurations of plasma, but rather from massive objects like neutron stars. A fine pulse structure among the regular occurring pulses was found in the case of the second pulsar discovered in the constellation Vulpecula (Drake [1968]) paving the way for later studies of marching subpulses (see Chapter 1.4.4). According to Gold [1968] they could be directional beams which rotate like the light rays from a lighthouse. As predicted by such a lighthouse model (and as already observed at that time) the time variations of their intensity had no influence on their phase of occurrence during one rotation period. The generation mechanism of the radio emission was largely unexplored at that time. Taken the rotational energy of the neutron star as the only energy source, Gold [1968] suggested the existence of a co-rotating region, called magnetosphere, around the pulsar (the necessity of a co-rotating magnetosphere around a rotating neutron star in vacuum was already lined out by Deutsch [1955]). In this region relativistic effects give rise to the observed radio emission from pulsars (at the time when the work of Gold [1968] was published, pulsars had been only detected at radio wavelengths. The detection of optical pulses happened later in the case of the Crab pulsar (see Chapter 2.2.3)). Gold [1968] schematically pointed out that this region could only co-rotate up to a certain distance at which its tangential velocity would be equal to the speed of light. The properties and mechanisms which take place in the magnetosphere of a pulsar were (and still are) not clearly understood. From the known distribution of the amplitutes of the observed pulses Gold [1968] concluded that pulsar emission is of narrow-band nature (taken into account that a change of 1 MHz in the observational bandwidth results in a different amplitude of the pulse) and that its mechanism is indicated to be coherent. The latter characteristic was confirmed in later studies, also in the case of the Crab pulsar among others (Chapter 3).
With his considerations Gold [1968] made the first actual suggestion and schematic outline of a pulsar as the source of the observed radio pulses stating that if his theory was right, then the existence of pulsars with shorter rotation periods could be expected and a slow down of the

rotation periods could be observed. This turned out to be the case when the Crab pulsar was discovered a short time later (Staelin and Reifenstein [1968], Lovelace et al. [1968], Comella et al. [1969]).
With this discovery the dispute what kind of object was able to emit the periodically detected radio pulses finally came to an end. Its rotation period of about 33 ms was too short to be associated with oscillations from white dwarf stars as no available model could explain such a small rotation period.
The detection of both, the Crab (Staelin and Reifenstein [1968]) and the Vela pulsar (Large et al. [1968]) led to the association of supernova remnants with neutron stars (see Figure 1.2 and Figure 2.1) confirming the once expressed suggestion by Baade and Zwicky [1934].

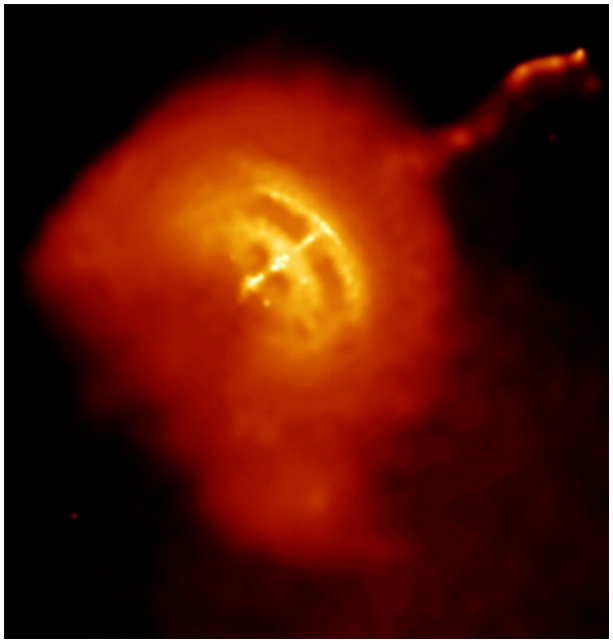

Figure 1.2.: A combined X-ray image of the Vela supernova remnant taken with the Chandra X-ray Observatory. The Vela pulsar is located as the point source in the center of the image. The picture was adopted from the websites of the observatory[1].
Image Credit: NASA/CXC/PSU/G.Pavlov et al.

Since these first steps in the timeline of the discovery of neutron stars, numerous other stellar objects of this kind have been discovered. Not all of them are pulsars and not all discovered pulsars have been detected at radio wavelengths. The different kinds and populations of pulsars are discussed further in Chapter 1.3.

[1] http://chandra.harvard.edu/photo/2003/vela_pulsar/more.html

1.2. The Formation of Neutron Stars

Since the detection of the Crab pulsar and the Vela pulsar which both are still located in their supernova remnants, proof was given that pulsars are born in supernova explosions and were consequently the last stage of stellar evolution. This is the assumed scenario for solitary pulsars (Figure 1.6). The evolution theory for binary pulsars is different (see review by Lorimer [2008]). In this chapter the assumed evolution of a solitary pulsar like the Crab pulsar will be explained shortly.

Stellar Nucleosynthesis
A star is a luminescent sphere consisting of plasma. It is held together by its own gravity. Different types of stars and evolution stages are currently known. A way to describe a star is by measuring its surface temperature and absolute magnitude and assign it thus to a certain spectral class. These quantities of all currently known stars are summarized in the Hertzsprung-Russel diagram (Figure 1.3).

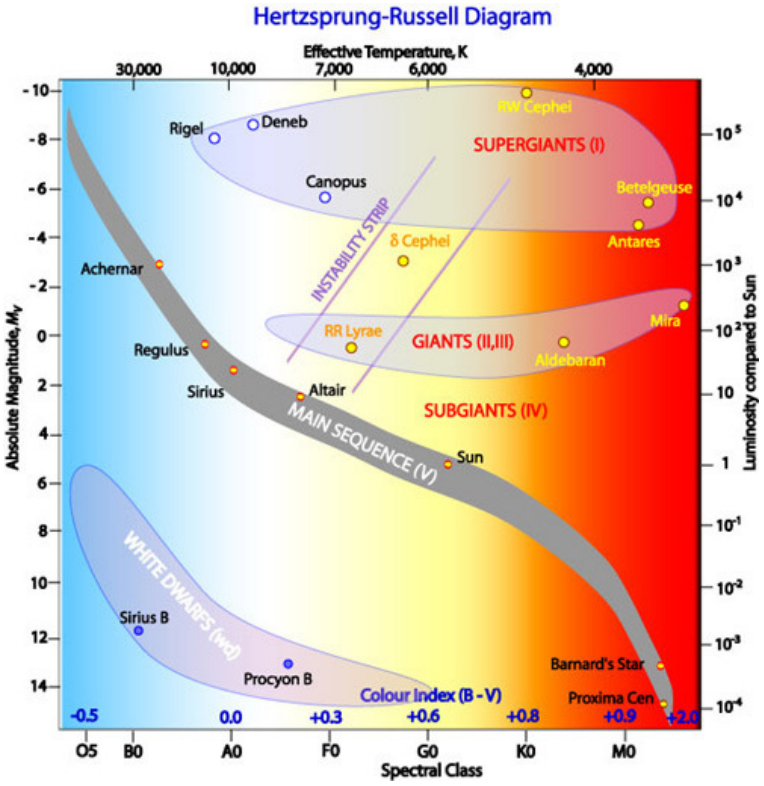

Figure 1.3.: The Hertzsprung-Russel diagram showing the relationship between the absolute magnitudes and the effective temperatures of stars at various stages of their nuclear burning (Image Credit: ATNF[2]).

The emission of a star is built up by the process of thermonuclear fusion, which in other words is the conversion of lighter nucleii into heavier ones. The energetically most prominent

[2]http://www.atnf.csiro.au/outreach/education/senior/astrophysics/stellarevolution_hrintro.html

one is known as hydrogen fusion, or hydrogen burning:

$$4\,{}^{1}\mathrm{H} \longrightarrow {}^{4}\mathrm{He} + 2\,\nu \tag{1.1}$$

The quantity ν stands for an electron neutrino (Cowan et al. [1956]). Only this designation will be used for the electron neutrino in this chapter.
There are two main reaction sequences for the hydrogen fusion. One is known as the "Proton-Proton Chain" (pp-chain) during which hydrogen is converted into deuterium by three main reactions:

$${}^{1}\mathrm{H} \; + {}^{1}\mathrm{H} \; \longrightarrow {}^{2}\mathrm{D} + \mathrm{e}^{+} + \nu + \gamma \tag{1.2}$$

$${}^{2}\mathrm{D} \; + {}^{1}\mathrm{H} \; \longrightarrow {}^{3}\mathrm{He} + \gamma \tag{1.3}$$

$${}^{3}\mathrm{He} + {}^{3}\mathrm{He} \longrightarrow {}^{4}\mathrm{He} + 2\,{}^{1}\mathrm{H} \tag{1.4}$$

The quantity γ stands for the released energy in the corresponding reaction. The process contains two stages (expressed by Equation 1.2 and Equation 1.3) which run through twice and result in Equation 1.4. This process is dominant at stellar conditions and temperatures ranging from about $5 \times 10^{6}\,\mathrm{K}$ to $15 \times 10^{6}\,\mathrm{K}$ and releases the highest amount of energy per mass unit ($6 \times 10^{14}\,\mathrm{J\,kg^{-1}}$, Weigert and Wendker [1996]). At higher temperatures ranging from $1.5 \times 10^{9}\,\mathrm{K}$ to $3 \times 10^{9}\,\mathrm{K}$ a different mechanism is dominant known as "CNO Cycle". It is called like that since it follows a specific reaction sequence in which carbon, nitrogen and oxygen are produced:

$${}^{12}\mathrm{C} + {}^{1}\mathrm{H} \longrightarrow {}^{13}\mathrm{N} + \gamma \tag{1.5}$$

$${}^{13}\mathrm{N} \longrightarrow {}^{13}\mathrm{C} + \mathrm{e}^{+} + \nu \tag{1.6}$$

$${}^{13}\mathrm{C} + {}^{1}\mathrm{H} \longrightarrow {}^{14}\mathrm{N} + \gamma \tag{1.7}$$

$${}^{14}\mathrm{N} + {}^{1}\mathrm{H} \longrightarrow {}^{15}\mathrm{O} + \gamma \tag{1.8}$$

$${}^{15}\mathrm{O} \longrightarrow {}^{15}\mathrm{N} + \mathrm{e}^{+} + \nu \tag{1.9}$$

$${}^{15}\mathrm{N} + {}^{1}\mathrm{H} \longrightarrow {}^{12}\mathrm{C} + {}^{4}\mathrm{He} \tag{1.10}$$

Hydrogen is explicitly converted in Equation 1.5, Equation 1.7, Equation 1.8 and Equation 1.10. The part of this reaction chainm which is the slowest, is expressed by Equation 1.8. It determines the speed of the whole CNO cycle. These two processes, the pp-chain and the CNO cycle

are responsible for the fusion of hydrogen in the central region of a star. Depending upon the temperature, the dominance varies between the pp-chain and the CNO cycle. The reason for this interchange lies in the Coloumb forces which exist between charged particles like protons, or electrons. It is therefore usually only possible to get two protons to interact with each other when they are accelerated appropriately. In the cores of stars such accelerations are caused by the existing high temperatures. The more complex an atom is constructed (meaning built up of more protons, neutrons and electrons), the higher the necessary temperatures are which can cause sufficient accelerations for an interaction (it needs to be noted that even at this temperatures the particles do not have enough kinetic energy to overcome the Coloumb barrier, requiring the quantum mechanical effect of tunneling, Gamow [1928]). This is the reason why the pp-chain is active at lower temperatures than the CNO cycle and why the primary nuclear burning is the fusion of hydrogen. It is the primary energy supply of all main sequence stars (Figure 1.3). Since the process of hydrogen burning is in general understood as slow, stars remain located on the main sequence branch for a longer time, depending upon their mass before this stage of nuclear burning arises.
At some point when the hydrogen in the central region of the star is exhausted, the nuclear burning stops since the temperatures are not high enough for the fusion of heavier elements. Without fusion the thermal pressure of the star becomes smaller than the pressure formed by its own gravity. Consequently the core of the star starts to contract without the previously existing equilibrium between radiation and gravitational pressure. During this contraction the core of the star becomes denser and its temperature increases. The increasing temperature in the core of the star gives rise to the nuclear fusion of heavier elements than hydrogen. Besides it is the reason for the amount of still remaining hydrogen to go into the stage of nuclear fusion in a shell like region around the core where the temperature is still high enough. Due to the reinstated hydrogen fusion, the radiation pressure is increased again and causes the star to increase its radius. A main sequence star then becomes a red giant star moving further to the right in the Hertzsprung-Russel diagram to the giant star branch and thus eventually leaving the main sequence branch. When the hydrogen is finally used up, the nuclear burning of the available helium in the core of the star begins with an appearance known as “Helium Flash“. The corresponding temperature needs to be high enough for this process to start ($\sim 10^8\,\mathrm{K}$ according to Weigert and Wendker [1996]). This is only possible when the core of the star has contracted appropriately, thus increasing the kinetic energy of its particles. The nuclear burning stages of helium are as follows:

$$^4\mathrm{He} + {}^4\mathrm{He} \longleftrightarrow {}^8\mathrm{Be} \tag{1.11}$$

$$^8\mathrm{Be} + {}^4\mathrm{He} \longrightarrow {}^{12}\mathrm{C} + \gamma \tag{1.12}$$

$$^{12}\mathrm{C} + {}^4\mathrm{He} \longrightarrow {}^{16}\mathrm{O} + \gamma \tag{1.13}$$

Equation 1.11 indicates that the resulting Beryllium is not stable and decays after approximately $10^{-16}\,\mathrm{s}$ (Weigert and Wendker [1996]). If it combines with helium before it decays, carbon is produced which is the element which will go through the process of nuclear fusion next. The oxygen which is produced also during helium burning (Equation 1.13) is the second

product apart from carbon. The process expressed by Equation 1.11 and Equation 1.12 is commonly known as "Triple Alpha Process". The released energy during this stage of nuclear burning amounts to $6 \times 10^{13}\,\mathrm{J}$ per 1 kg of $^{4}\mathrm{He}$ (Weigert and Wendker [1996]) which is already less than was released during the fusion of hydrogen.
The exhaustion of helium in the core of the star leads to the same process which happened after the exhaustion of hydrogen. The nuclear fusion stops at first which causes again the loss of the equilibrium between radiation pressure and gravitational pressure. The core of the star contracts again which leads to a higher temperature and thus kinetic energy of the particles. The latter is the reason for the fusion of the remaining helium in a shell like form around the remaining core which consists entirely of carbon. After this process and due to the higher temperature in the star (between $5 \times 10^{8}\,\mathrm{K}$ and $1 \times 10^{9}\,\mathrm{K}$, Weigert and Wendker [1996]), the nuclear fusion of carbon begins after the remaining helium is used up. There is a variety of possible reaction chains via which the fusion of carbon can take place:

$$^{12}\mathrm{C} + {}^{12}\mathrm{C} \longrightarrow {}^{24}\mathrm{Mg} + \gamma \tag{1.14}$$

$$^{12}\mathrm{C} + {}^{12}\mathrm{C} \longrightarrow {}^{23}\mathrm{Mg} + {}^{1}\mathrm{n} \tag{1.15}$$

$$^{12}\mathrm{C} + {}^{12}\mathrm{C} \longrightarrow {}^{23}\mathrm{Na} + {}^{1}\mathrm{H} \tag{1.16}$$

When the process of carbon fusion begins, the radiation pressure becomes higher and leads to a further extension of the star which becomes a red super giant. At this stage the star moves further to the right in the Hertzsprung-Russel diagram to the supergiant branch.
In the next stage the oxygen goes through the nuclear fusion process:

$$^{16}\mathrm{O} + {}^{16}\mathrm{O} \longrightarrow {}^{32}\mathrm{S} + \gamma \tag{1.17}$$

$$^{16}\mathrm{O} + {}^{16}\mathrm{O} \longrightarrow {}^{31}\mathrm{S} + {}^{1}\mathrm{n} \tag{1.18}$$

$$^{16}\mathrm{O} + {}^{16}\mathrm{O} \longrightarrow {}^{31}\mathrm{P} + {}^{1}\mathrm{H} \tag{1.19}$$

$$^{16}\mathrm{O} + {}^{16}\mathrm{O} \longrightarrow {}^{28}\mathrm{Si} + {}^{4}\mathrm{He} \tag{1.20}$$

At this point the temperature of the star has already risen up to about $1.4 \times 10^{9}\,\mathrm{K}$ (Weigert and Wendker [1996]). The nuclear fusion chain comes to an end with the burning of silicon:

$$^{28}\mathrm{Si} + {}^{28}\mathrm{Si} \longrightarrow {}^{56}\mathrm{Fe} + 2\,\nu \tag{1.21}$$

It leads to the production of iron (Equation 1.1), the heaviest element that can be produced through fusion while gaining energy. The process of nuclear fusion stops at this point since

further reactions of this kind do not release energy thus making the star a luminescent object, but spend this energy.
When the nuclear burning of silicon stops, the non-equilibrium between the gravitational and thermal pressure of the star becomes unstable again. Consequently the core of the star starts to contract again. Since the core only consists of the remaining ^{56}Fe which has the highest binding energy between its nucleons and is therefore the most stable isotope of iron, the core cannot contract further and collapses under its gravitation (see next chapter).
Summarising all the explained burning stages, the star can be regarded like a sphere consisting of several shells which successively go through the process of nuclear burning (Figure 1.4). During each of the shell burning stages, the core of the star contracts and its shell is expanded. Due to this expansion the star cools down with each stage of nuclear burning moving towards lower temperatures in the Hertzsprung-Russel diagram (Figure 1.3).
The here generally described process of stellar nucleosynthesis depends upon the mass of a star and proceeds therefore differently for different star types. Regarding main type sequence stars the following homology relations are valid:

$$\frac{M}{R} \sim R^2 \cdot \bar{\rho} \tag{1.22}$$

$$\frac{\bar{P}}{R} \sim \frac{M}{R^2} \cdot \bar{\rho} \tag{1.23}$$

$$\frac{L}{R} \sim R^2 \cdot \bar{\rho^2} \cdot \bar{T}^{\nu} \tag{1.24}$$

$$\frac{\bar{T}}{R} \sim \frac{\bar{\rho} \cdot L}{\bar{T}^3 \cdot R^2} \tag{1.25}$$

The symbol M stands for the mass of the star, R for its radius, $\bar{\rho}$ for its average density, L for its luminosity, $\bar{T}$ its average temperature and $\bar{P}$ for its average pressure. The average indicated by the bar over the quantities, is the volume average over the stellar interior. A detailed derivation of Equation 1.22, to Equation 1.25 is given in Chapter 6 of Weigert and Wendker [1996]. Resulting from these relations (Equation 1.22 and Equation 1.23 including the relations $\rho \sim \frac{P}{T}$) are the following proportionalities:

$$\bar{\rho} \sim \frac{M}{R^3} \tag{1.26}$$

$$\bar{T} \sim \frac{M}{R} \tag{1.27}$$

Taking Equation 1.25, Equation 1.26 and Equation 1.27 into account, result in the following relation for the luminosity of a main sequence star:

$$\mathrm{L} \sim \mathrm{M}^3 \tag{1.28}$$

It was mentioned earlier in this chapter that the process of hydrogen fusion takes a long time which is the reason why many stars accumulate on the main sequence of the Hertzsprung-Russel diagram. The duration of this fusion stage can be determined as:

$$\tau_H = \frac{E_H}{L} \tag{1.29}$$

Due to the long duration of this part of thermal nucleosynthesis, the energy released by this process (E_H), can be taken as proportional to the mass of hydrogen. The latter is proportional to the mass of the star which results in:

$$E_H \sim M_H \sim M \tag{1.30}$$

Accordingly to these considerations the duration of hydrogen fusion for a main sequence star can be determined as:

$$\tau_H = \frac{E_H}{L} \sim \frac{M}{M^{3.5}} = M^{-2.5} \tag{1.31}$$

It needs to be noted that the mass-luminosity relation as expressed in Equation 1.28 was not used for the determination of Equation 1.31. Numerical simulations have shown that different indices of the mass in Equation 1.28 are valid for stars with different masses (see Chapter 5.7 in Salaris and Cassisi [2005]). The common index for main sequence stars is 3.5 which was also used for the calculation of Equation 1.31.
Equation 1.31 indicates that the duration of hydrogen fusion lasts longer for stars with smaller masses. Hence massive stars leave the main sequence earlier and move depending upon their mass to other parts of the Hertzsprung-Russel diagram like the giant, or supergiant branch (Figure 1.3).
The higher the mass of the star at the beginning of the hydrogen fusion process, the more nuclear fusion stages can be passed through by it. The reason for this lies in the higher temperatures which are needed with each stage to start the fusion of the next element. Stars with lower masses are subject to a smaller gravitational pressure than higher massive stars. Consequently the core cannot contract enough to produce the necessary temperatures for the next nuclear fusion stage. In stars which have low masses ($< 2\ M_\odot$, Weigert and Wendker [1996]), nuclear fusion ends with the exhaustion of hydrogen as no higher temperatures for the fusion of helium can be produced. Due to the contracting core the electrons go into the state of a degenerate gas (see next chapter) and build up a pressure which is the counterpart to the gravitational pressure the star experiences keeping the latter stable.
Massive stars ($M > 8\ M_\odot$, Weigert and Wendker [1996]) pass the stages of nuclear burning as described in this chapter and eventually go through the process of a core-collapse supernova explosion (see next chapter). An example of the evolution of a star with $15\ M_\odot$ and the duration of its nuclear burning stages are described in Table 1 in Woosley and Janka [2005] together with a description of the process of nuclear burning for very massive stars described in more detail. Possible death scenarios of very massive stars are discussed in Heger et al. [2003].

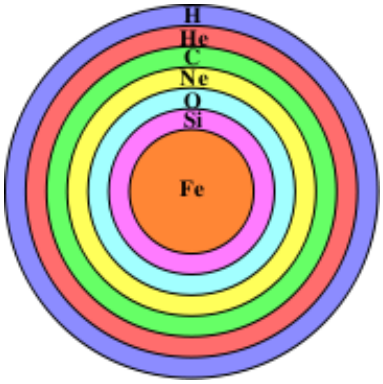

Figure 1.4.: Schematic model of the shell like layers of a massive star which goes through the stages of nuclear fusion.

Core-collapse Supernova

Supernovae are subdivided into different types based on the amount of hydrogen in their optical spectra. Supernova remnants with no hydrogen lines in their spectra, are referred to as type I whereas the ones with hydrogen lines are called type II. Further subdivisions are made between type I supernovae (type Ia, Ib and Ic) depending upon the occurrence of silicon absorption lines. The latter are not a subject of this thesis and will not be discussed further. Supernovae of type II on the other hand result from core-collapses of massive stars and can thus result in the birth of a compact stellar object like a neutron star.

As described in the previous chapter, the stages of nuclear fusion in the core of a star depend upon its mass. When it comes to the fusion of silicon, which results in a core of ^{56}Fe, no further fusion stages from which energy can be gained are left. Therefore the gravitational pressure on the star becomes dominant and leads to the degeneration of the available electrons (in the shells of the available atoms, or moving around in a free state as generated by the nuclear burning stages described in the previous chapter). The gravitational pressure tries to compress the particles in the core. For the electrons in the shells of atoms this would mean the filling of all energy levels, or shells with several electrons. This is only doable to some point since two electrons (as fermions) cannot occupy the quantum state ("Pauli Exclusion Principle", see page 776 in Pauli [1925]). Due to this principle a pressure is build up since the electrons cannot be compressed further than the Pauli Principle allows. It is commonly referred to as degeneracy pressure of electrons and works as counterpart to the gravitational pressure. In other words it can prevent the core of a star from contracting further and eventually collapsing. Depending again on the mass of the star before the start of hydrogen burning, there are possible outcomes when the degeneracy pressure begins to have an effect. If both kinds of pressure provide an equilibrium, the star becomes stable resulting in a white dwarf star. This type of star is very dense due to the described reasons and does not have a thermal source anymore, as nuclear fusion cannot proceed further. As these stars are formed after the fusion of carbon and oxygen, they are comprised of the latter and represent one final end of stellar evolution. White dwarfs can form out of stars with masses ≤ 8 $M_\odot$ (Weigert and Wendker [1996]).

In the case of stars with masses higher than this value the final stages of their evolution proceed differently. As mentioned earlier, their nuclear burning stages prolong till the core consists out

of ^{56}Fe. At this stage the core of the star has become too heavy, so that the electron degeneracy pressure cannot counteract against the gravitational pressure anymore. The mass of the core then exceeds a limit value of about 1.38 $M_\odot$ known as "Chandrasekhar Limit" (Chandrasekhar [1931], Mazzali et al. [2007]). It is the limiting mass up to which a white dwarf star would remain stable. In the case that the core of the star exceeds this value, it collapses eventually under the influence of its gravitational pressure and results either in a neutron star, or a black hole.
During its implosion the density of the core grows which leads to an increase of the temperature and consequently of the kinetic energy of the particles. The electrons previously located in the shells of the atoms, become capable of overcoming the Coloumb forces of the protons and enter the nucleus region of atoms. At this point they react with the protons in the core resulting in further neutrons via the following process:

$$\mathrm{p} + \mathrm{e}^- \longrightarrow \mathrm{n} + \nu \tag{1.32}$$

This way a high concentration of neutrons develops which is a process commonly referred to as neutronization. Due to the increasing number of neutrons, it can happen that atoms collide with single neutrons. Their neutral charge prevents them to be repelled by the electrostatic charges of the atom. Therefore they can enter the core region of the atom much easier than a charged particle would be capable of. At this stage the contraction of the star is still ongoing. Similar as in the case of the electrons, also neutrons can develop a degeneracy pressure. When this limit is reached, the star cannot contract anymore. The contracting atmosphere of the star is then blown away in a process which is known as a core-collapse supernova. A large amount of the energy released during this explosion is carried away by neutrinos. Since the details of this mechanism are still not understood, core-collapse supernovae are a subject of numerous studies in the form of data analysis and simulations (Janka [2012], Wongwathanarat et al. [2015]). The remnant of this explosion is a stellar object known as a neutron star (if the mass of the progenitor star was higher than 8 $M_\odot$, Weigert and Wendker [1996], Woosley and Janka [2005]). During the supernova explosion even heavier elements than ^{56}Fe are produced in the stellar remnant. The corresponding mechanisms will be outlined here briefly.
Since the energy necessary to take a nucleus apart has one of the highest values for ^{56}Fe, the process of nuclear fusion comes to a stop after the silicon burning (Equation 1.21). There are two different processes via which heavier elements are built: The "Rapid Process" (r-process) and the "Slow Process" (s-process) (Burbidge et al. [1957]). Both are known as neutron capture processes. The designations rapid and slow mean in comparison with β-decay processes. The r-process takes place when the number of neutrons is already very high in the star. That is, when a high number of ^{56}Fe, or other atoms with a high number of neutrons in their cores, is already contained in the star. Its time scales are assumed to range from about 0.01 to 10 s (Burbidge et al. [1957]). The s-process on the other hand takes place when the density of the available neutrons is low. The suggested time scales for the s-process range from about 100 to 10^5 years for the capture of a neutron (Burbidge et al. [1957]). Hence the process is rather slow in contrast with the r-process. While the s-process is responsible for the generation of isotopes with mass numbers between 23 and 46 and in addition between 63 and 209, the r-process leads to the generation of isotopes with mass numbers ranging from 70 to 209 (Burbidge et al. [1957]). Both processes were originally suggested by Burbidge et al. [1957] as a way to generate heavier

elements than ^{56}Fe and have been subject of numerous studies since then (see for instance reviews by Mathews and Ward [1985] and Reifarth et al. [2014]).

The Neutron Star

Resulting out of a core-collapse supernova, the neutron star is a very dense, stellar object. Its densities range up to $10^{21}\,\mathrm{g/cm^3}$ (Weigert and Wendker [1996]), while the radius of a neutron star is assumed to be in the range of 10 to 12 km (Lattimer and Prakash [2001], Burke and Graham-Smith [2010]). Since the atmospheres of neutron stars at their surfaces are barely known, it is usually difficult to obtain precise values of their radii. The complexity arises from the unknown modifications of this atmosphere and also the strong magnetic field on the emission of a neutron star (see discussion in Zavlin and Pavlov [2002]). However, a currently used method includes observations of their thermal emission at optical and X-ray wavelengths (Lattimer and Prakash [2001]).

The typical mass of a neutron star is assumed to be around 1.4 $M_\odot$. This value results from measurements of neutron stars in binary systems (see for instance Thorsett and Chakrabarty [1999], Stairs [2004] and Figure 3.2 in Lorimer and Kramer [2012]). The measurement of the mass from solitary neutron stars on the other hand remains a problem.

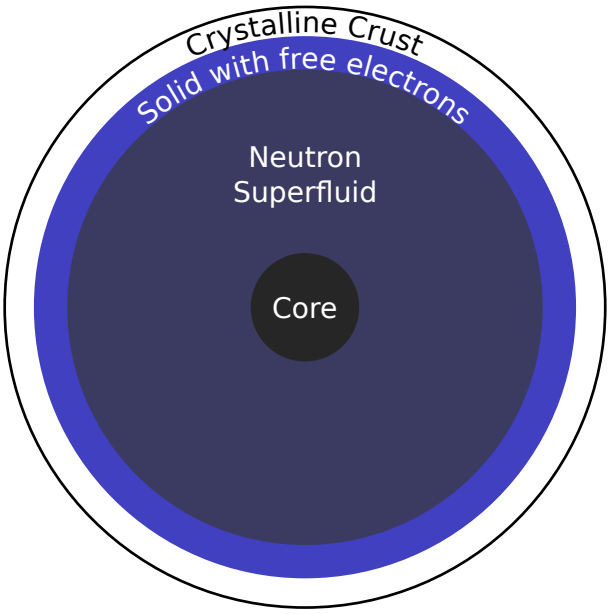

Figure 1.5.: Scheme of the internal structure of a neutron star with a mass of 1.4 $M_\odot$ and a surface radius of 10 km. The scheme was build following Figure 12.1 in Burke and Graham-Smith [2010].

The precise composition of a neutron star is currently not known due to its unknown equation of state. Current theoretical approaches for a neutron star with a mass of 1.4 $M_\odot$ suggest that its interior is composed of several regions (Figure 1.5). The outer part consist of a solid crust which has a density of about $10^6\,\mathrm{g/cm^3}$ (Burke and Graham-Smith [2010]). The outer crust of a neutron star is assumed to be a crystalline lattice consisting of iron nuclei and degenerate electrons (Lorimer and Kramer [2012]). At higher depths of the neutron star interior the density

increases rapidly. At such high densities the electrons overcome the Coloumb forces, enter the core regions of particles where they interact with protons. This leads to the generation of particles with a large number of neutrons in their cores. The process continues till density values of $4 \times 10^{11}\,\mathrm{g/cm^3}$ (Burke and Graham-Smith [2010]) when the most massive generated particles become unstable, leading to the occurrence of free neutrons. The latter form a neutron superfluid (see Migdal [1959] for more details) which is dominant at densities from $2 \times 10^{14}\,\mathrm{g/cm^3}$ to $10^{15}\,\mathrm{g/cm^3}$ (Burke and Graham-Smith [2010]). This density value is assumed to dominate in the core region of the neutron star. According to the current theoretical approaches, the core of a neutron star is a superfluid and superconducting region. However, it needs to be noted that the composition of the core region varies for different theoretical approaches (see for instance Shapiro and Teukolsky [1983]).
The existence of a superfluid region inside of a neutron star has been indicated by observations of anomalies in the rotation of neutron stars known as *Glitches* (Link et al. [1999]). They will be explained further in Chapter 1.4.4.
A detailed overview on current studies of neutron stars can be found in Becker [2009].

1.3. Types of Neutron Stars

Since the discovery of the first neutron star (Chapter 1.1), a large variety of different kinds of neutron stars has been discovered (a general review can be found in Harding [2013]). Figure 1.6 shows a schematic overview of the currently known groups of neutron stars. The two main groups are referred to as radio-loud and radio quiet neutron stars and express the emission characterstics of their members. As the names already indicate, radio-loud objects are the ones from which radio emission can be detected whereas no radio emission can be verified from radio-quiet objects. Pulsars are only one subclass of neutron stars and members of both groups, but also in their case different subgroups have been found. One long-standing example of the latter group was the Geminga pulsar (Blgnami and Caraveo [1992]). Recently, low-frequency observations were made of this object and low frequency radio emission could be verified (Malov et al. [2015]).
Since it is beyond the scope of this thesis to explain all currently known types in detail, only the group of radio-loud neutron stars will be summarised in the following chapter since the Crab pulsar (Chapter 2) also belongs to this group. Furthermore a general and concise overview will be given in this chapter to emphasise the diversity of the currently known neutron stars populations which also indicates why the term "Neutron Star Zoo" is used sometimes in the literature for a description of the different kinds of neutron stars.
More extensive elaborations on the currently known different kinds of neutron stars can be found in Becker [2009]. A review on the currently known types of neutron stars is given by Harding [2013].

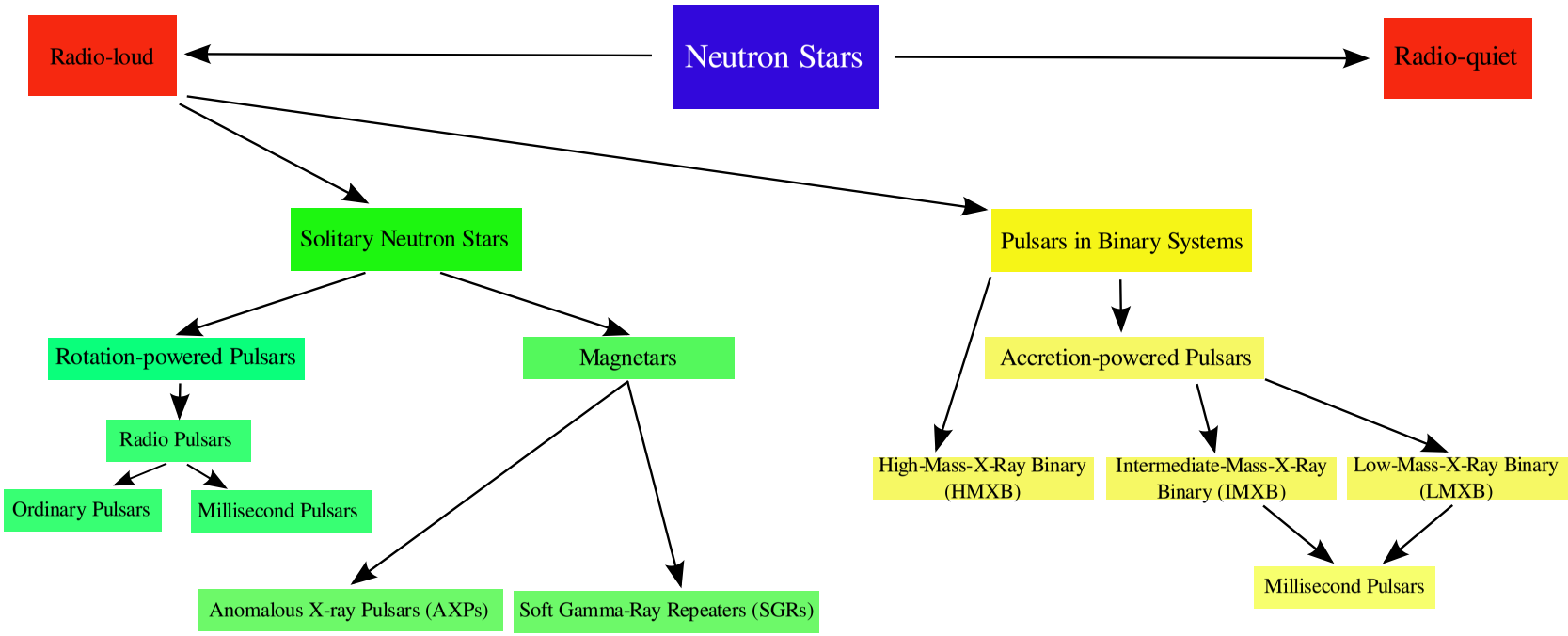

Figure 1.6.: Schematic overview of the currently known kinds of neutron stars.

1.3.1. Radio Loud Neutron Stars

Solitary Neutron Stars

Solitary neutron stars are understood as neutron stars which do not have a companion star. It is assumed that solitary neutron stars are generated in supernova explosions, but only in a few cases corresponding supernova remnants were verified and so far only in one case historical recordings led to a direct identification of a supernova remnant with a supernova explosion (the Crab pulsar, Chapter 2).
To emphasise the currently known diversity of solitary neutron stars, a short summary is given in this chapter.

Rotation-Powered Pulsars
A Rotation-Powered Pulsar (RPP) is a neutron star with a high rotation frequency gained during the core-collapse of the progenitor star (see Chapter 1.2) which is spinning down due to its loss of angular momentum, caused by the emission of magnetic dipole radiation and particle emission (Harding [2013]). Its rotation is the only source of power that such a neutron star has. Its energy is emitted in the form of radiation ranging over (in the cases of some pulsars) all currently accessible wavelength ranges of the electromagnetic spectrum. While the very first pulsar was detected at radio wavelengths (see Chapter 1.1), at present time more than 2000 different kinds of pulsars which are detectable at radio wavelengths are known (Manchester et al. [2005]).
While the spin down process of RPPs takes place in a smooth way, several pulsars have been observed to show deviations from this behaviour in the form of sudden changes in the spin down rate commonly known as "Glitches" (see Chapter 1.4.4).
The group of RPPs consists of ordinary and millisecond pulsars. The difference between both kinds of pulsars is their evolution history and their resulting characteristics. Ordinary pulsars have been proven in the case of the Crab and Vela pulsars to be the remnants of supernova explosions (Chapter 1.1). Their rotation periods are in the range of P$\sim$0.5 s with spin down values of $\dot{\mathrm{P}} \sim 10^{-15}\,\mathrm{ss}^{-1}$ (Lorimer and Kramer [2012]) and their characteristic ages $\tau = P/2\dot{P}$ are less than 100 billion years (Harding [2013]).
Millisecond pulsars on the other hand result from the accretion of matter from a stellar companion in a binary system. It is the common assumption that they originally belonged to RPPs, spun down for several billions of years and when their magnetic fields start to channel the matter from the binary companion, they speed up through this process to very high rotation periods in the range of P$\sim$3 ms with spin down values of $\dot{\mathrm{P}} \sim 10^{-20}\,\mathrm{ss}^{-1}$ (Lorimer and Kramer [2012]) and characteristic ages τ of higher equal 100 billion years (Harding [2013]). Due to this procedure they are often referred to as "recycled pulsars". After their speed up process, they are again RPPs, rotation being their only source of power. Their slowing down takes place more slowly which makes them very stable with regard to their pulsed emission. This is a reason why they are considered in their precision to be even better than atomic clocks (see for instance Rawley et al. [1987]). Millisecond pulsars form about 10 % of the population of RPPs and about 80 % of them are located in binary systems (Harding [2013]). The term millisecond pulsar is a bit misleading since the definition from which rotation period value onwards a pulsar is considered a millisecond pulsar, varies profoundly in the literature[3]. The Crab pulsar for instance has a rotation period of about 33 ms and is not a millisecond pulsar. Therefore in the

[3] http://astro.phys.wvu.edu/GalacticMSPs/GalacticMSPs.txt

latter case the term "Recycled Pulsar" has been introduced since millisecond pulsars are usually the result of a spin up process in a binary system as will be explained further in Chapter 1.3.1. In the case of ordinary pulsars the emitted radiation forms less than 10% of the total spin down power (Harding [2013]). With relation to the different wavelength ranges radio pulsations have been observed to make up about 10^{-4}, or even less of the spin down power. The largest amount of power expressed by pulsed emission is made up by γ-rays around 1 GeV. This has been verified for most (if not all) RPPs (Harding [2013]). In the case of the Crab pulsar for instance the maximum power of its pulsed emission is located in hard X-rays. Due to this property the pulsed γ-ray emission provides the highest amount of information about the particle acceleration processes in the magnetosphere of the pulsar. Originally only seven pulsars were known which emit pulsed emission at γ-rays (commonly known as "The Magnificient Seven", Thompson [2001]). With the advent of the Fermi γ-ray Space Telescope this number was enlarged to more than 100 objects (Abdo et al. [2013]). Due to this extension currently three kinds of γ-ray pulsars are known: Radio-quiet pulsars, radio-loud pulsars and γ-ray millisecond pulsars (Harding [2013]).
An interesting feature of RPPs which have been detected at radio and γ-ray wavelengths is a time delay between their pulsed emission components (Harding [2013]). The pulsed emission of γ-ray pulsars has been observed to arrive at later rotational phase values in comparison with its radio pulses (see Figure 4 in Harding [2013]). This delay is correlated with the separation of the distance of the pulsed emission peaks in γ-rays (Abdo et al. [2010b]). A summary of the emission models for the γ-ray emission of RPPs and which try to explain this time delay at radio and γ-ray wavelengths is given by Harding [2013] and references therein.
RPPs have also been detected to emit pulsed emission at X-ray wavelengths. Currently, there are at least 100 RPPs from which pulsed X-ray emission has been detected (Harding [2013]). This X-ray emission consists of two parts: The non-thermal component and a thermal component ranging from 0.05 to 0.1 keV (a detailed review on this can be found in Kaspi et al. [2006]). An interesting property which has been observed between the thermal and non-thermal pulses is that they are in general not seen at the same rotational phase ranges. On the other hand non-thermal pulsed emission has been observed to be sometimes in phase with γ-ray pulsars. These observed properties imply a variety of different emission mechanisms which are summarised in Harding [2013].
Recently, a new subpopulation of RPPs has been detected. These objects are commonly referred to as Rotating Radio Transient (RRAT)s and were discovered in the course of an examination of single radio pulses (McLaughlin et al. [2006]). Their characteristics have been observed to be more extreme than in the case of other RPPs, but it is currently not known how they fit in the population of RPPs. A full review on these objects can be found in Keane and McLaughlin [2011].
RPPs show a wide range of anomalous properties at radio wavelengths. They range from short time phenomena in the case of for instance single radio pulses, to long time phenomena. A summary of these properties is given in Chapter 1.4.4.

Magnetars

A magnetar is solitary neutron star which has a very high magnetic field on its surface (in the range from 10^{14} to 10^{16} Gauss, Harding [2013]). Currently, magnetars are the objects with the highest magnetic fields known. In contrast with the rotation of rotation-powered pulsars, the magnetic field is assumed to be the source of the free energy of a magnetar. The process in which the magnetic field is decaying, produces the observed electromagnetic radiation.

The first detection of the emission from a magnetar was made on 1979-01-07, when a γ-ray Burst (GRB) with a soft spectrum was detected from the Galactic Center onboard of the Verena spacecraft (Mazets and Golenetskii [1981]). Since its spectrum was softer than from GRBs known at that time, it was first classified as a different type of GRB when another unusual GRB event was detected on 1979-03-05 (Mazets et al. [1979]). In the latter case a hard spectrum, a longer duration and pulsations with a flux which was decaying in an approximately exponential way could be verified (Feroci et al. [2001]). It was localized in a Supernova Remnant (SNR) of the Large Magellanic Cloud (LMC) known as SNR N49 (Cline et al. [1982]). What spoke against the detection of a new class of GRBs was the fact that in the latter case repetitive outbursts of γ-ray emission were detected soon after from the same source (Golenetskii et al. [1984]).
In both cases the source of these outbursts was later identified as a Soft γ-ray Repeater (SGR). Together with Anomalous X-ray Pulsar (AXP)s they belong to the currently known subclasses of magnetars. Both types of neutron stars will be described further in the next chapters.
Currently, a total number of 28 magnetars is known. An up to date list can be found in the magnetar catalog of the Mc Gill pulsar group[4] (Olausen and Kaspi [2014]).

Soft γ-ray Repeater
An SGR is a neutron star which emits non-regular outbursts of γ-rays and X-rays. SGRs have been observed to repeatedly emit bursts of soft γ-ray emission which has become their characteristic (Woods and Thompson [2006]). The durations of these bursts are short, ranging from about 0.1 s (Woods and Thompson [2006]) to several tenths of a second (Harding [2013]). The average energy which has been observed so far ranges from 10^{40} erg to 10^{41} erg (Harding [2013]). The periods during which an SGR is in burst mode can be separated by several years. In the case of some of the currently known SGRs exceptionally bright outbursts of γ-ray emission have been observed (see Figure 1.7). These so-called "Giant Superflares" have been observed to reveal total energies from 10^{45} erg to 10^{47} erg (Harding [2013]). Also the second detected SGR on 1979-03-05 (now known as SGR0526-66) was such a giant superflare (Cline et al. [1980]). With the exception of SGR0526-66, which is located in the LMC, all other SGRs have so far been observed near the Galactic plane.
Further details about the detection and details of giant superflares in the case of other SGRs can be found in Harding [2013]. A general overview of the properties of SGRs is given in Woods and Thompson [2006].

Anomalous X-ray Pulsar
AXPs were detected by Fahlman and Gregory [1981] who discovered pulsations at X-ray wavelengths from a source known as 1E 2259+586 which is located in a SNR known as CTB 109. Being the first X-ray pulsar associated with a SNR, it was first designated as an anomalous X-ray pulsar that was accreting. Interestingly, the existence of an accretion disk, or a companion as a part of a binary system, have not been verified so far. This has also been the case for later discovered AXPs.
The pulsation periods of AXPs have been observed in a range from 5 to 11 s (Harding [2013]). They spin down with large first derivaties of the rotation period, as was shown in the case of the AXP 1E 1841-045 by Vasisht and Gotthelf [1997]. AXPs are bright sources at X-ray

[4] http://www.physics.mcgill.ca/ pulsar/magnetar/main.html

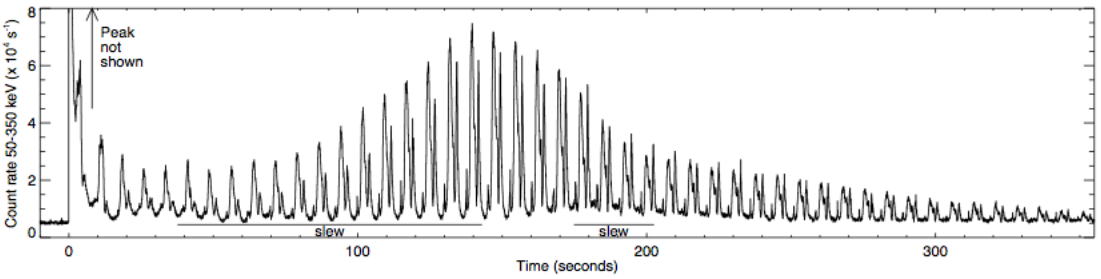

Figure 1.7.: The light curve of SGR 1806-20 (the first observed SGR, Woods and Thompson [2006]) from its outburst in 2005. Pulsations are visible in the tail of the light curve. The figure was adopted from Palmer et al. [2005].

wavelengths (their luminosities reaching up to about 10^{35} erg/s). Similar to SGRs they have high surface magnetic fields in the range from 10^{14} to 10^{15} Gauss. The light curves of both, SGRs and AXPs, look similar which gave rise to the assumption that they are not entirely different types of magnetars. Kaspi et al. [2003] provided evidence of an SGR like outburst from the AXP 1E 2259+586, confirming a resemblance between AXPs and SGRs.

Pulsars in Binary Systems

In contrast with solitary pulsars, pulsars which belong to double star systems are commonly referred to as binary pulsars. Such systems have been detected in a large variety with regard to their components. Some of them consist of one pulsar and one main sequence star for instance, others can have a pulsar and another neutron star, or white dwarf star as companion. The first binary pulsar PSR B1913+16 was discovered in 1974 with the Arecibo radio telescope by Hulse and Taylor [1975]. It was the first object with a indirect verification of the existence of Gravitational Wave (GW)s.

Accretion-Powered Pulsars

Accretion-powered pulsars are neutron stars in a binary system which emit pulses at X-ray wavelengths. Their pulses are generated through the accretion of matter which they channel with their magnetic fields from their companion, or donor star. When the latter exceeds its Roche lobe (the region around the donor star in which the once gravitationally bound matter starts to be transferred on the compact source through an accretion disk, Weigert and Wendker [1996]), an accretion disk forms out. The matter falls on the magnetic poles of the neutron star and creates hot spots on its surface (Figure 1.8). Since the pulsar rotates around its axis, these hot spots occur brighter at X-ray wavelengths than the rest of the star and X-ray pulsations are created.
Reviews on accretion-powered pulsars can be found in for example Kaspi [2008] and Harding [2013]. Based on the composition of the binary system, several different subclasses of binary pulsars have been found, as will be lined out in the next chapters.

[5] http://imagine.gsfc.nasa.gov/science/objects/binary_flash.html

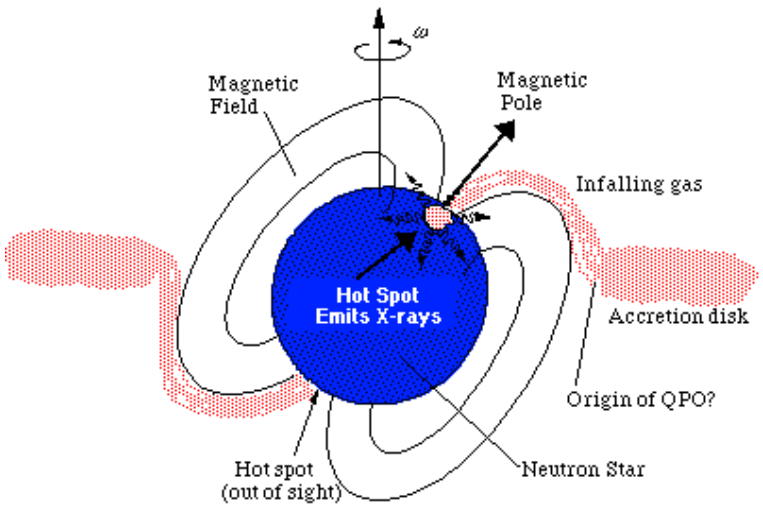

Figure 1.8.: An X-ray pulsar which belongs to a binary system. It channels matter from its companion via an accretion-disk. The matter is falling on the magnetic poles of the neutron star creating hot spots on its surface (Image Credit: H. Brandt, M. Halverson. The picture was adopted from the websites of NASA[5]).

Low-mass X-ray Binaries

A Low-Mass X-Ray Binary (LMXB) is a binary system consisting of a compact source (like a neutron star, or a black hole) and a donor star (which could be a low-mass main sequence star, a white dwarf, or a red giant). Due to the transfer of matter via an accretion disk, LMXBs reveal their highest luminosities at X-ray wavelengths together with a small amount of about 1% of optical emission (Harding [2013]). The neutron star components in a LMXB are assumed to have low magnetic fields in the range of approximately 10^8 Gauss which implies that they are relatively old objects. While accreting matter from the companion star, they are spun up with regard to their angular momentum. Currently, more than 100 LMXBs are known (Harding [2013]). Out of this number more than 24 LMXB systems have been detected to emit X-ray pulsations in a frequency range from 100 to 700 Hz (Chakrabarty [2005]). This discovery strengthened the assumption that LMXBs are progenitors of rotation-powered millisecond pulsars. The final evidence was found with the observed transition from a LMXB to a rotation-powered millisecond pulsar in the case of the source J102347.6+003841 (Archibald et al. [2009]). Radio pulsations in the millisecond range were discovered from this source which about a decade earlier had been observed in the optical range and showed optical emission indicating the existence of an accretion disk. The follow-up observations carried out by Archibald et al. [2009] in the optical range could not verify any optical emission from this system anymore suggesting its transition within a decade. Further radio timing studies of this object have been reported by Archibald et al. [2013].

The X-ray emission from LMXB systems has been observed in a large variety. While some LMXB systems show steady X-ray emission with casual outbursts (which makes them in both states detectable), others are only detectable during their outburst periods. The durations of these outbursts range from 10 to 100 s with total energies ranging from 10^{39} to 10^{40} erg/s (Harding [2013]). Interestingly, some of the LMXBs show pulsations in the millisecond range

during their steady emission state and others during their X-ray outbursts (for more details see Harding [2013]). Furthermore Quasi-Periodic Oscillations (QPO)s in the kHz range have been detected from LMXB (van der Klis [2000]). Some LMXBs show the mentioned millisecond pulsations when they are in the QPO state.
Further details including theoretical approaches for an explanation of the observed emission characteristics of LMXBs can be found in Harding [2013] and references therein.

Intermediate X-ray Binaries
A Intermediate-Mass X-Ray Binary (IMXB) is a system which consists of a compact source like a neutron star, or a black hole and a donor star with a mass ranging from $1.0 M_{\odot}$ to $5.0\ M_{\odot}$ (a systematic study of the evolution of IMXBs as well as LMXBs can be found in Podsiadlowski et al. [2002]). They represent a progenitor state of LMXB systems.

High-mass X-ray Binaries
A High-Mass X-Ray Binary (HMXB) is a system which consists of a compact object (like a neutron star, or a black hole) and a high mass star (that is, with a mass larger than $5 M_{\odot}$) of type O, B, or Be. One crucial difference between HMXBs and the previously mentioned binary systems (LMXBs and IMXBs) is the way the matter from the donor star is transferred to the compact source (definitions are given in Chaty [2011] and later in this chapter).
Also in the case of HMXB pulsations were found, but with durations ranging from 1 to 1000 s (Harding [2013]) they are much longer in contrast with LMXBs. Following the considerations in Harding [2013], the resulting magnetic field of the neutron star should be in the range of 10^{12} Gauss. In the spectra of some HMXBs absorption features have been detected (Heindl et al. [2004]) indicating the occurrence of cyclotron resonant scattering in an energy range from 10 to 50 keV (Harding [2013]). In accordance with the calculations elaborated by Harding [2013] this results in a magnetic field of the neutron star in the range from 10^{12} to 10^{13} Gauss. Due to this stronger magnetic field in contrast with LMXBs, the Alfvén radius (the distance at which the kinetic energy density of the gas equals the magnetic energy density) of the neutron star in a HMXB system is much larger. Consequently, the matter from the companion star is channelled more strongly via the magnetic field lines of the neutron star on its polar cap surface. Depending upon the composition of the donor star, different types of HMXBs have been found (a full review of the different types of HMXB systems is given in Chaty [2011]. The accretion of matter can take place via an accretion disk. When the companion star exceeds its Roche lobe (similar to LMXB systems), a circumstellar disk develops which is crossed by the compact object of the HMXB system when it orbits the companion star on a eccentric orbit, or when the latter ejects a slow stellar wind which is radially emitted from the equator of the companion star (Chaty [2011]).
Prominent HMXBs are for instance Cygnus X-1 (in this case the compact source is assumed to be a black hole, Grinberg et al. [2013]) and Vela X-1 (Kreykenbohm et al. [2008]).
Theoretical approaches providing explanations how HMXB systems might work, are reviewed by Harding [2013] and references therein. Observational characteristics and a classification of HMXBs are reviewed by Chaty [2011].

1.4. Pulsars

As lined out in the last chapter, pulsars constitute only one subgroup of neutron stars. One of their most remarkable characteristic is the regular occurrence of their pulses. The accuracy of the latter is comparable in its precision to atomic clocks (Matsakis and Foster [1996], Lorimer [2008]).
In this chapter a short outline of the basic properties of pulsars is given beginning with a description of the way to categorize them (Chapter 1.4.1), a verification of the canonical pulsar (Chapter 1.4.2), the observational aspects of radio pulsars which make them available as tools for studies of the Interstellar Medium (ISM) (Chapter 1.4.3) and a description of the so far observed anomalous properties of radio pulsars (Chapter 1.4.4).

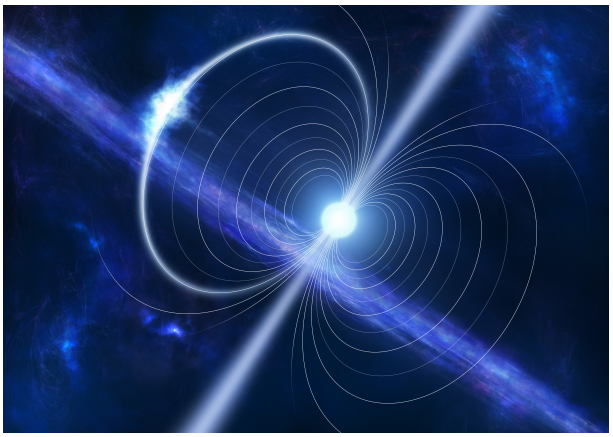

Figure 1.9.: Artist´s impression of a pulsar with closed field lines building up the light cylinder (Image Credit: Inga Nielsen).

1.4.1. The $P - \dot{P}$ Diagram

The two characteristics with which pulsars are nowadays described, are their rotations periods P and the first derivative of the latter, commonly referred to as the spindown $\dot{P}$. Currently, more than 2000 pulsars are known (Manchester et al. [2005]). A simple tool to categorize them is referred to as "P-$\dot{\text{P}}$ Diagram" . In such a diagram the observed rotation periods are arranged on the abscissa and the respective spindown values on the ordinate (Figure 1.10). The common way is to express the values on both axes on logarithmic scale. The largest group of pulsars shown in Figure 1.10 is visible on the upper right side of the diagram in the form of an island. The pulsars belonging to this group are usually referred to as ordinary, or normal pulsars (compare Chapter 1.3.1). As can be easily deduced from Figure 1.10, this group is currently the largest. The second largest group visible in the diagram is located in the lower left corner. This is the group consisting of millisecond, or recycled pulsars (Chapter 1.3.1). Both groups of pulsars differ in their observed rotation periods, spindown values, as well as their evolution histories (see description in Chapter 1.3). A conspicuous property of this diagram is that all pulsars are located apparently along a line which connects both groups. In the lower right corner the diagram is empty. This region is known as the graveyard region and the line along which the known pulsars are located is commonly referred to as death line. According to their

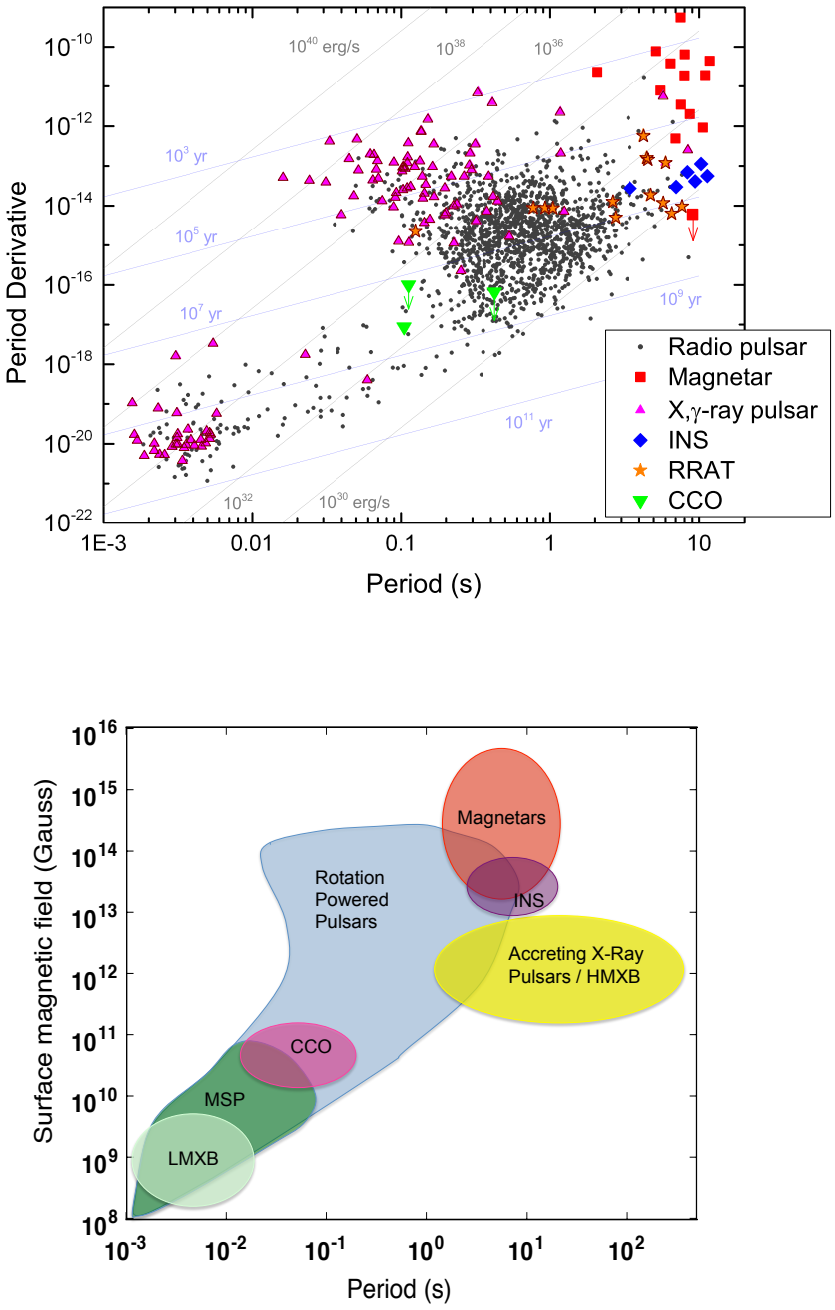

Figure 1.10.: A P-$\dot{\text{P}}$ diagram of all currently known radio pulsars and other neutron stars (upper figure) and a scheme of all currently known populations of neutron stars (lower figure). Both figures were adopted from Harding [2013].

designations they describe the state of RPPs which do not posses enough energy anymore to emit radio waves. The pulsars in this graveyard region are therefore regarded as switched off since they cannot be detected anymore at radio wavelengths.
Another characteristic of pulsars which can be deduced from the P-$\dot{\text{P}}$ diagram, is how pulsars are aging. The rotation periods of pulsars have been observed to increase with time (Burke and Graham-Smith [2010], Lorimer and Kramer [2012]). The quantity describing this process is the already mentioned first derivative of the rotation period, or the spindown. Since the only source of energy of a pulsar lies in its rotation, the emission of the latter leads to a slow down with time. Consequently, the rotation frequency

$$\nu_r = \frac{1}{P} \tag{1.33}$$

decreases with time. The evolution of the rotation frequency with time is usually approximated by a power-law:

$$\dot{\nu_r} = -k \cdot \nu_r^n \tag{1.34}$$

The quantity k in Equation 1.34 is a constant while the exponent n is commonly referred to as the braking index of a pulsar. How this index is determined, depends upon the approximation which is made for the corresponding pulsar. Usually pulsars are approximated as magnetic dipoles. The loss of their energy is expressed in terms of magnetic dipole radiation. In such a case the resulting braking index has been determined as n = 3 (see Chapter 3.2.1 in Lorimer and Kramer [2012]). However, corresponding observations have shown deviations from this value (the braking index is usually calculated with the second derivative of the rotation frequency which is known only for a few pulsars due to timing noise, see Chapter 1.4.4). According to Kaspi and Helfand [2002] the values for the braking index vary from 1.4 to 2.9, implying a different spindown behaviour than is expressed by the approximation of a pulsar by a magnetic dipole. In spite of these problems, the aging process of pulsars can be expressed by the usage of their rotation periods and the derivaties. In the P-$\dot{\text{P}}$ diagram ordinary young pulsars like the Crab pulsar are located in the upper left corner (see also Figure 3.1) and move down and right across the diagram when they lose their rotational energy.
Apart from radio pulsars, other kinds of neutron stars are included in Figure 1.10 as well, in order to emphasise the relation between all of them.

1.4.2. The Canonical Pulsar

A pulsar is nowadays understood as a highly magnetized sphere which is also a superconductor (Lorimer and Kramer [2012]). The observed emission from an isolated RPP such as the Crab pulsar, is assumed to be generated in a region around the star which is referred to as its magnetosphere. An overview of the concept of a pulsar magnetosphere together with a basic theoretical approach for the generation of the observed radio and γ-ray emission, is given in this chapter.

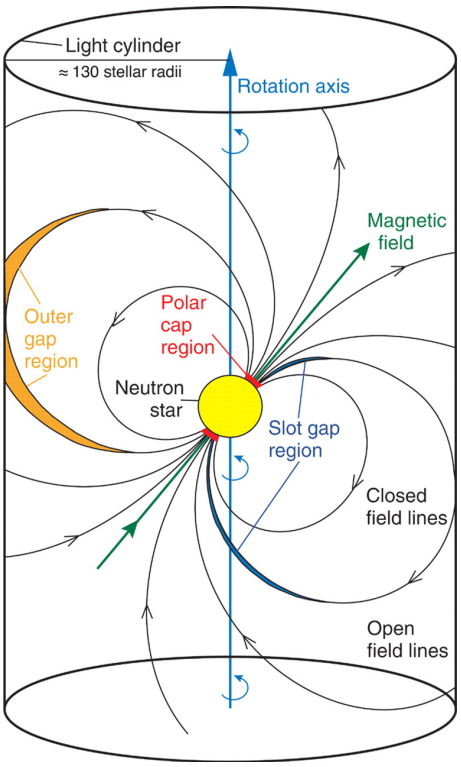

Figure 1.11.: Scheme of a pulsar with its co-rotating magnetosphere indicating the different regions for particle acceleration (see text). The figure was adopted from Aliu et al. [2008].

The Pulsar Magnetosphere (Goldreich-Julian Model)

The magnetosphere of a pulsar is understood as a geometrical region extending from its surface to a certain distance which is commonly referred to as light cylinder radius R_{LC} (Figure 1.11, Equation 1.35). The generation of a pulsar magnetosphere can be explained by the Goldreich-Julian model (Goldreich and Julian [1969]). It needs to be noted that the considerations of this model are only applicable to a pulsar with an aligned rotational and magnetic field axis, commonly referred to as aligned rotator.
After the gravitational collapse of its progenitor star, a pulsar has a very high magnetic field. In addition to this the conservation of angular momentum during the gravitational collapse, results in a high rotation frequency of the pulsar (see Chapter 1.2). The rotation of the pulsar leads to the generation of an additional electric field via the process of electromagnetic induction. Under the assumption that the pulsar is a perfectly conducting sphere, the electric field compensates the magnetic field at any point inside of the sphere, resulting in a force-free state. Assuming the existence of a vacuum around the pulsar (as was common in the early days of pulsar studies), this results in the induction of an electric field outside of the star by its charged surface. The corresponding electric field, or Lorentz force, has an effect on the charges in the surface. According to the calculations of Goldreich and Julian [1969] it is about 10 times higher in value than the corresponding gravitational force, leading to the charged particles being pulled out of the surface of the pulsar. These charged particles are moving along the field

lines of the magnetic field building up a region around the pulsar which is filled with plasma, co-rotating with the star and is commonly referred to as pulsar magnetosphere. The radius of this region is set by the distance at which the co-rotating plasma reaches the speed of light:

$$R_{\mathrm{LC}} = \frac{\mathrm{c}}{\Omega} \tag{1.35}$$

The magnetosphere of a pulsar is illustrated in Figure 1.11. Hence according to the theoretical approach by Goldreich and Julian [1969] the vacuum condition around the pulsar cannot be maintained.
Resulting from the calculations of Goldreich and Julian [1969] (see Equation 2 in Goldreich and Julian [1969]), the distribution of the charged particles depends on the quantity θ which is the polar angle of a coordinate system that is centered on the star (see Figure 1.12). Charged particles located above the magnetic pole (with small values of θ) have an opposite sign than charged particles in the equatorial region (with high values of θ). That means the charged particles are separated in the magnetosphere. The separation takes place for a certain value of θ which is approximated as $\arccos(\sqrt{1/3})$ (Lorimer and Kramer [2012]). This line is commonly referred to as the "Null Line" (Figure 1.12). If the described separation is complete for all charged particles, the electric fields outside of the pulsar are shielded and again a force-free state is reached. Consequently, no acceleration of particles can take place:

$$\vec{E} \cdot \vec{B} = 0 \tag{1.36}$$

The number density at the magnetic pole (for θ=0) after a complete separation of the charged particles, is known as "Goldreich-Julian Density" n_{GJ}:

$$n_{\mathrm{GJ}} = \frac{\Omega B_S}{2\pi \mathrm{ce}} \tag{1.37}$$

In Equation 1.37 the quantity Ω corresponds angular velocity of the pulsar, B_S being the magnetic field strength at the surface of the pulsar, c being the speed of light and e the elementary charge (the equation was adopted from the calculations in Lorimer and Kramer [2012]). The Goldreich-Julian density is a maximum value of the number density and often referred to in scientific literature.
The resulting pulsar magnetosphere is subdivided into different regions (Figure 1.11, Figure 1.12) according to the type of the field lines of the magnetic field: The open field lines along which particles can move out of the magnetosphere, and closed field lines on which they stay within the light cylinder. The location of the open field lines defines a specific area in a pulsar magnetosphere which is referred to as polar cap (Figure 1.11). It is located above the magnetic poles of the pulsar.
In areas of the pulsar magnetosphere in which the magnetic and electric field compensate each other, no acceleration of the charged particles can take place. However, there are several regions in which an acceleration process is possible. They will be explained further in the next chapter.
The idea of a co-rotating magnetosphere was first set up by Deutsch [1955] and later modificated for the aligned rotator by Goldreich and Julian [1969]. Prior to this considerations pulsars were assumed to be rigidly rotating spheres in a vacuum. However, it needs to be noted at this point that the charged particles used by Goldreich and Julian [1969] were electrons and

protons. This was later modified by Ruderman and Sutherland [1975] among others according to their calculations.

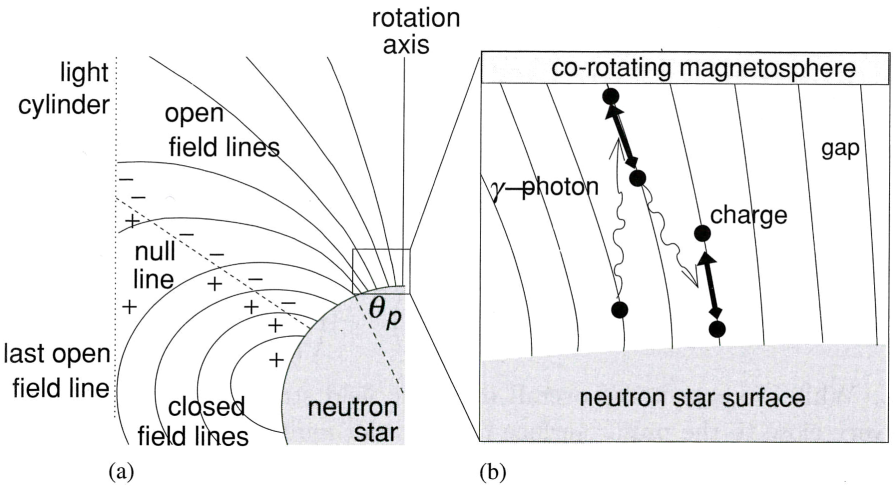

Figure 1.12.: The construction of a pulsar magnetosphere according to the considerations of Goldreich and Julian [1969]. The figure was adopted from Lorimer and Kramer [2012].

Acceleration in a Pulsar Magnetosphere

Several acceleration regions in a pulsar magnetosphere have been assumed to exist in order to explain the observed pulsed emission from pulsars (see overview in for instance Lorimer and Kramer [2012]). It depends which kind of observed emssion is addressed. Here, only the radio and γ-ray emission will be briefly discussed.
A characteristic of the acceleration region is that the compensation of the magnetic and electric field as explained in the last chapter, is not given anymore, which leads to an acceleration process:

$$\vec{E} \cdot \vec{B} \neq 0 \tag{1.38}$$

Consequently, the gap regions are drained of plasma and the corresponding particles are not replaced fast enough from other parts of the magnetsosphere.
The observed pulsar radio emission is assumed to be generated near the polar cap of a pulsar (see last chapter) in an acceleration region which is correspondingly known as polar gap (Figure 1.11). According to the work of for instance Ruderman and Sutherland [1975], the charged particles which are drawn out of the surface of the pulsar, are accelerated by the induced electric field. On their way along the magnetic field lines they emit curvature radiation which leads to the generation of γ-ray photons (Ruderman and Sutherland [1975]). According to the calculations of Erber [1966] a γ-ray photon can be converted due to the existing high magnetic field of the pulsar in electron positron pairs. The generated particles can produce further particles and thus create a secondary pair plasma (see Sturrock [1971] for details). Numerical simulations of the generation of electron positron pairs were carried out by Arendt and Eilek

[2002]. According to these calculations the process of pair cascades can increase the existing plasma density by factors ranging from 10 to 10^4. The common assumption is that the observed radio emission from pulsars is generated by this secondary pair plasma in the polar gap. The corresponding mechanism is currently not understood. In general three different mechanisms for the radio emission are proposed in the literature: Antenna mechanisms, maser mechanisms and relativistic plasma emission mechanisms.
Antenna mechanisms cause emission which is sent out by bunches of particles. This way the emitted power is much higher than in the case of one emitting particle. Such bunched emission in the form of curvature radiation was proposed in the theoretical approaches by Sturrock [1971] and Ruderman and Sutherland [1975].
Maser emission mechanisms have been proposed in a variety of different kinds. An overview of possible maser emission mechanisms is given in Melrose [2004].
The lastly mentioned relativistic plasma emission mechanisms are based on plasma instabilities. Some of the difficulties of the corresponding theoretical approaches are building an instability which grows fast enough. Another aspect of the problem is letting the resulting plasma turbulence escape directly, for which usually an additional conversion is included. Since there are various models addressing this problem, only a few are named here. Different scenarios referring to the growing of the plasma instability and the following plasma turbulence release are discussed in for instance Melrose [1992], Asseo [1993] and Ganse et al. [2012].
So far, only the radio emission from a pulsar has been addressed. Changing now to the probable origin and mechanism behind the observed γ-ray emission, leads to a different region in the pulsar atmosphere than the polar gap. The regions which are nowadays assumed to be responsible for the γ-ray emission are known as outer gaps (see Figure 1.11). An outer gap is located near the earlier described null line which is responsible for the separation of charged particles. The outer gap emission model was originally developed by Cheng et al. [1986a] (as a model specifically built for young pulsars like the Crab and the Vela pulsar as shown in Cheng et al. [1986b]) and modified later by Romani [1996]. According to Cheng et al. [1986a], the outer gap is a region in the form of a slab which is limited on one side by a layer of charged particles resulting from the boundary of the closed field lines area. Its other boundary is formed by a corresponding layer of charged particles, resulting from the region of open field lines. Its limitation towards the star is set by the null line. In other words, it is a gap which is located outside the region of the closed magnetic field lines. It lies in larger distance from the surface of the pulsar in comparison with the polar gap which means that it is not exposed too such a high magnetic field as the polar gap. Therefore the particles which are accelerated in the outer gap cannot be accelerated directly to such high energies as in the polar cap. Hence the particles which are in the end responsible for the generation of the γ-ray emission need to already have high Lorentz factors (relativistic effects need to be included at this point) before the acceleration process. Consequently, the process leading towards γ-ray emission is taking place in several steps.
Without going into detail with the current available models, a brief outline how the γ-ray emission from pulsars is assumed to be generated will be given here. The charged particles which are drawn out of the surface of the pulsar, are accelerated afterwards by the induced electric field. Since they move on bent field lines, they emit curvature radiation up to γ-ray wavelengths. The γ-photons generate electron positron pairs. The location of the outer gap is determined by the efficiency of this process. Since the momentum of these pairs also has a component which is perpendicular to the magnetic field of the pulsar, they emit synchrotron radiation. This process can lead to the creation of further electron positron pairs which results

altogether in a cascade. The described process is also the reason why the outer gap cannot be located further away from the last closed magnetic field line of the pulsar magnetosphere. In the latter case the supply of γ-photons would be missing preventing the development of the cascade. However, in some updated versions of the outer gap model, specified on the Crab pulsar, the generation of the γ-ray emission can also take place due to Inverse Compton (IC) scattering (Hirotani [2006]).
Reviews with corresponding references for the generation of the observed non-radio emission from pulsars can be found in Lorimer and Kramer [2012].

1.4.3. Observational Aspects of Pulsars

Due to the large distances between observers on Earth and pulsars, the latter are seen as point sources. At radio wavelengths pulsars are known as rather weak sources. That is, their mean flux densities (the integrated intensity of a pulsed profile which is averaged over the pulse period) and their peak flux densities (the maximum intensity of a pulsed profile) are no large quantities, making longer observation times necessary. The mean flux density spectra of most pulsars can be approximated by the following power law:

$$\mathrm{S_{mean}(f)} \propto \mathrm{f}^{\alpha} \tag{1.39}$$

In Equation 1.39 the quantity f refers to the observing frequency and α is known as the spectral index. The relation expressed by Equation 1.39 is valid only for pulsars which have flux density spectra following a simple power law model. With the increasing number of pulsar discoveries, deviations from a simple power law model were verified in the form of a broken power law, or a turn over towards lower frequencies (see Figure 1.4 in Lorimer and Kramer [2012]). An extensive analysis of the flux density spectra of 281 pulsars was carried out by Maron et al. [2000]. They verified that at an observing frequency of higher than 100 MHz approximately 5 % from the sample of 281 pulsars showed a more complex course in their flux density spectra than expressed by Equation 1.39. For pulsars with flux density spectra describable by a single power law model, spectral indices in the range from 0 to -4 were found. A mean value established by Maron et al. [2000] was determined as α_{mean}=-1.8 $\pm$0.2.
The negative spectral indices of pulsars are the reason why their strongest signals are observable at low frequencies. This characteristic makes pulsar signals susceptible to the effects caused by the ISM. Depending upon the distance of a pulsar, its age and its geometrical orientation towards the observer's line of sight, emphasise the necessity of observations with radio telescopes with large collection areas. The propagation effects of the ISM on a pulsar signal also make a certain combination of hard- and software equipment necessary for successful pulsar observations.
The effects of these propagation effects can be summarized into three types: Dispersion, scintillation and scattering. These effects will be described in this chapter shortly with references for further reading.

Dispersion
Depending upon the frequency at which the pulsar is observed, dispersion can have the most visible effect on its signal. The plasma in the ISM causes a shift of the pulse arrival times at lower frequencies in comparison with their counterparts at higher frequencies (Figure 1.13, Figure 5.1).

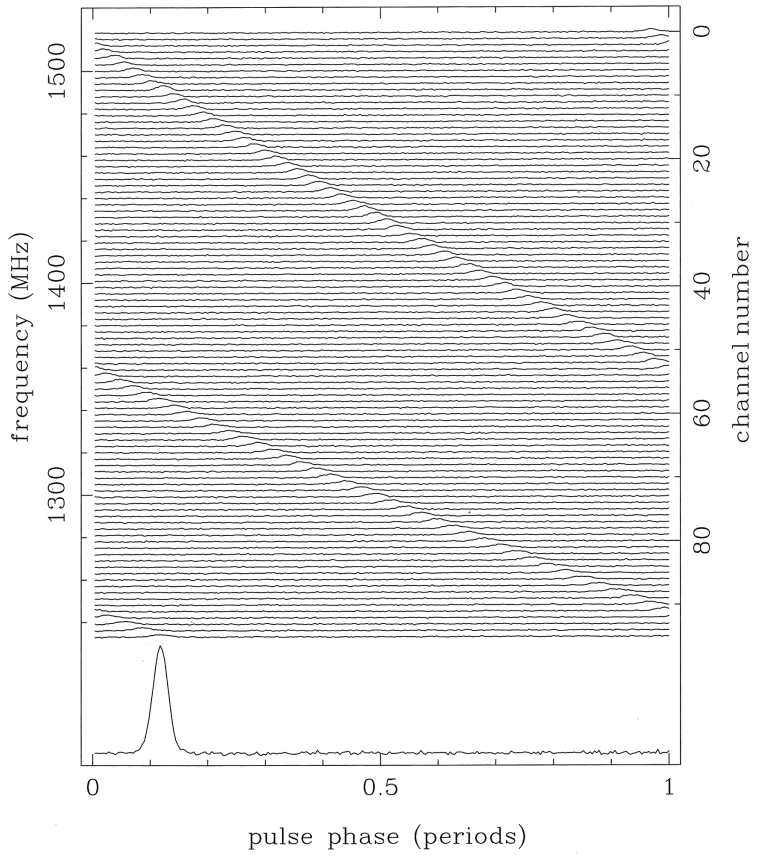

Figure 1.13.: Dispersed parts of the pulsar signal from PSR B1356-60 in a phase-frequency plot to emphasise the effects of dispersion caused by the ISM. The dispersion measure (DM) in this case is 295 $\frac{\mathrm{pc}}{\mathrm{cm}^3}$. The figure was adopted from Lorimer and Kramer [2012].

This kind of distortion is not only inherent to pulsars, but to all kinds of objects whose signals travel through the ISM and most prominent at long wave radio wavelengths.
When radio waves travel through the ISM, they interact with its free electrons. Under the assumption that the ISM is homogeneous, the refractive index for a radio wave amounts to

$$\mu = \sqrt{1 - \frac{\nu_\mathrm{p}^2}{\nu^2}} \tag{1.40}$$

with ν being the frequency at which the observations were carried out and ν_p being the plasma frequency

$$\nu_p = \sqrt{\frac{e^2 n_e}{\pi m_e}} \simeq 8.5\,\mathrm{kHz}\sqrt{\frac{n_e}{\mathrm{cm}^{-3}}} \tag{1.41}$$

with e being the charge of an electron, m_e the mass of an electron and n_e the electron number density. Equation 1.40 indicates that waves with higher frequencies are refracted less than the ones with lower frequencies, implying the reason why radio observations of pulsars are heavily affected by dispersion and γ-ray observations for instance are not.
The different index of refraction for a wave in dependence of its frequency, leads to different arrival times of its parts. Taking the group velocity into account

$$v_g = \mathrm{c}\mu \tag{1.42}$$

results in a time delay between two different frequencies f_1 and f_2 of the propagating radio signal:

$$\Delta t = t_1 - t_2 = d \cdot (f_1^{-2} - f_2^{-2}) \cdot DM \simeq 4.15 \times 10^6 \,\mathrm{ms} \cdot (f_1^{-2} - f_2^{-2}) \cdot DM \tag{1.43}$$

The quantitiy d is known as dispersion constant:

$$d = \frac{\mathrm{e}^2}{2\pi\,\mathrm{m_e\,c}} \tag{1.44}$$

A full derivation of Equation 1.43 is given in Chapter 4.1.1 in Lorimer and Kramer [2012].
The quantity DM is known as *Dispersion Measure* and expresses the integrated electron number density along a distance x between the pulsar and the Earth:

$$DM = \int_0^x n_e \, dl \tag{1.45}$$

Depending upon the location of the pulsar in the Milky Way, its distance and the corresponding amount of electrons between the location of the pulsar and the Earth, the DM values can vary a lot.
So far, a homogeneous ISM has been assumed. In reality, it is rather inhomogeneous, and the electron density varies and is subject to temporal changes which is reflected by changes of the DM values (see Figure 4.1 in Lorimer and Kramer [2012]). The differing electron number density leads to further corruptions of the radio pulsar signal known as scintillation (Figure 1.10 in Lorimer and Kramer [2012]) and scattering (Figure 1.15).

Scattering
Scattering arises (in a simplified form) from distortions as different concentrations of electrons cause differences in the refractive index $\Delta\mu$ which on the other hand result in phase shifts of parts of the radio wave. When the signal arrives on Earth, it has encountered a certain number of these phase shifts $\Delta\Phi$. According to the thin screen model developed by Scheuer [1968], the result of these phase shifts is understood as a bending of the whole wavefront on a thin screen and causes a broadening of the pulsar signal in the form of an exponential tail (Figure 1.15).

The resulting decay time of the exponential function, or scattering time, caused by a distortion of the ISM of length a after traveling the distance x between the pulsar and Earth can be determined as:

$$\tau_s = \frac{\mathrm{e}^4}{4\pi^2 \mathrm{m}_\mathrm{e}^2} \frac{\delta n_e^2}{a} \frac{x^2}{f^4} \propto \frac{x^2}{f^4} \tag{1.46}$$

According to Equation 1.46, the scattering time becomes larger at lower frequencies which is one reason why pulsar radio observations are preferably being carried out at higher frequencies. The negative spectral indices of pulsars (Maron et al. [2000]) are the reason why their mean flux densities become higher towards lower frequencies. The scattering effect smears the pulsar signal away and thus diminishes their mean flux densities momentarily. In other words, their integrated intensities become larger towards lower frequencies, but their instantaneous intensities are diminished by the scattering effect. The latter causes the instantaneous intensity of a pulsar to be drawn nearer to the noise level leading eventually to its disappearance (see Giant Metre-Wave Telescope (GMRT) observations taken at 325 MHz in Figure 1.15).

Scintillation
One further effect evoked by the ISM is known as scintillation. To the human eye scintillation occurs in the form of variations of the brightness of an object (like of the stars at night). Also in the case of radio observations of pulsars, the effect of scintillation is revealed by variations of the intensity of the pulsar signal. Similar to scattering, it is also caused by different electron number density values in the turbulent ISM. After traveling through the ISM, the pulsar signal has different phase values since parts of the signal were disrupted by it. Referring to Equation 1.46 these phase values can be determined via the following estimation:

$$\delta\Phi \sim 2\pi\, f\, \tau_s \tag{1.47}$$

Through the process of constructive and destructive interference, the whole wavefront contains an interference pattern when it arrives at Earth. The resulting signal has consequently parts with higher and with lower intensity as shown in Figure 1.14. The process of interference can only take place under certain conditions. In the case of scintillation the phase patches of the waves should not differ by more than approximately one radian. Since the phase of a signal also depends on the frequency, some frequencies are not included in the process of interference. In other words, the bandwidth of the waves which go through the process of interference is limited. This bandwidth is commonly referred to as scintillation bandwidth Δf. The resulting consequence for the process of interference can be determined via:

$$2\pi\, \Delta f\, \tau_s \sim 1 \tag{1.48}$$

Taking Equation 1.46 and Equation 1.47 into account, the following estimate for the scintillation bandwidth can be made:

$$\Delta f \propto \frac{1}{\tau_s} \propto f^4 \tag{1.49}$$

Consequently, the effect of scintillation is not only visible in the phase and thus the time of the signal, but it can be also scaled in relation to the observing frequency.

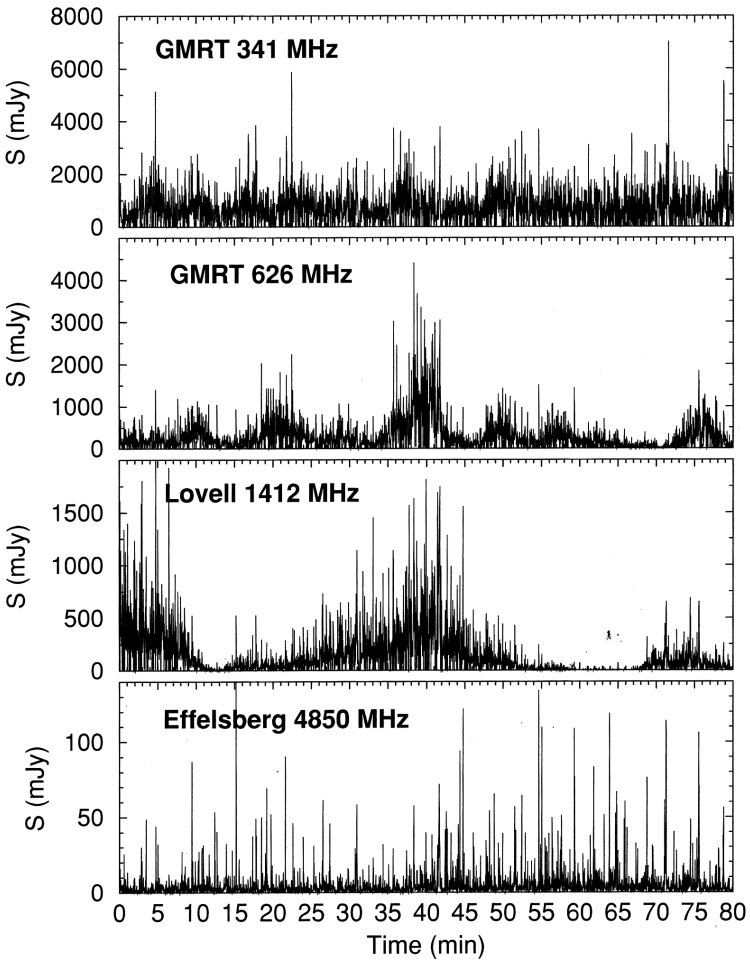

Figure 1.14.: Measurements of the flux denstity of the slow rotating pulsar PSR B1133+16 resulting from observations with the GMRT, the Lovell and the Effelsberg radio telescope. Intensity modulations caused by interstellar scintillation are visible at 626 MHz and 1412 MHz. The figure was adopted from Lorimer and Kramer [2012]).

Some of the described effects affect pulsar observations in most cases (like for example dispersion). Others are more prominent at lower than at higher frequencies (like scattering, or scintillation). In all cases they are taken into consideration before carrying out observations.
In spite of all these distortions, the characteristic signature or finger print of a pulsar is its average pulsed profile. It is determined by averaging several thousand successive single pulses which

differ in intensity, shape and width due to the influence of the ISM. The Average Profile (AP) of a pulsar is subject to these distortions too (Figure 1.15), but contains a much higher S/N and is thus stable at least for a certain time as the pulsar is slowing down due to the loss of rotational energy. Its temporal stability defines the current pulse period of a pulsar (Chapter 1.4.2).
In order to find such a repeating signal, nowadays computational expensive searches are being carried out in the form of scans of DM values and period parameters. In the years following the detection of the first pulsar CP 1919, these techniques were not yet developed and from the

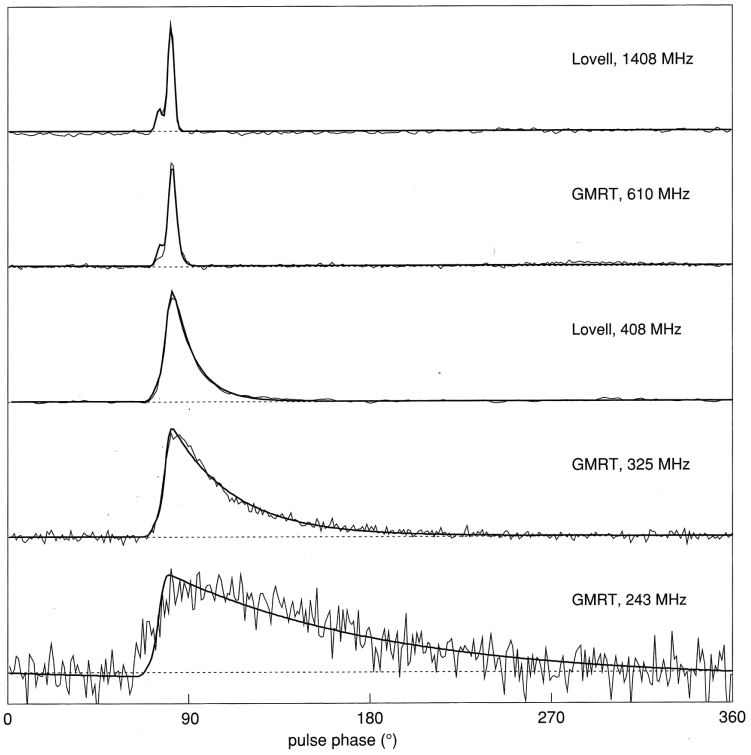

Figure 1.15.: Multifrequency observations of PSR B1831-03. The observations towards lower frequencies show a broadening of the pulse profile caused by scattering effects. The figure was adopted from Lorimer and Kramer [2012]).

computational point of view not executable. Nevertheless new pulsars were found very rapidly also at other wavelengths than at radio (Comella et al. [1969]).
Some of these pulsars were not discovered via searching techniques, but by their single pulses. In spite of all the complications regarding radio observations of pulsars mentioned earlier, these single pulses were bright enough to be detected rather by accident. One of these newly discovered pulsars was the Crab pulsar located in the Crab Nebula SNR (Staelin and Reifenstein [1968]). Later single pulse studies revealed that the Crab pulsar emits these single, bright pulses in addition to its regular pulsed emission. Their much higher flux densities were the reason they were referred to as "Jumbo Pulses" (Sutton et al. [1971]), or as "Giant Pulses" (Argyle and Gower [1972]).
What began with the discovery of the Crab pulsar has nowadays evolved into an independent

research branch.

1.4.4. Anomalous Behaviour of Radio Pulsars

As stated in the previous chapters, one characteristic of pulsars is their stable, pulsed emission. According to the basic theoretical approaches described earlier in this chapter, a pulsar is a spinning body which has a large moment of inertia. It is slowing down due to the loss of rotational energy in the form of electromagnetic emission resulting from a magnetic field of a rotating dipole that is attached to the star. This loss causes a decrease of the rotational frequency and consequently an increase of the rotation period. In order to learn more about the physics of pulsars, this slowing down process is monitored and compared with a model to identify deviations between both. The corresponding technique is known as pulsar timing (see Chapter 5 in Lyne and Graham-Smith [1990], or Chapter 8 in Lorimer and Kramer [2012] for details). However, with the help of this technique radio pulsars were discovered to deviate from their predicted behaviour on time scales from weeks, months to years. To uncover such deviations, usually a large number of single pulses is needed which are added up yielding in an AP of the pulsar. Indicated as long timescales phenomena, they will be described further in the next chapter.
The emission from radio pulsars has been studied on various time scales. As indicated in the case of radio giant pulses, deviations have been observed to also occur on very short time scales in the case of single radio pulses. To emphasise that radio giant pulses are only one form of short timescale deviations, a short overview of anomalous single pulses is also given in this chapter.

Long Timescales Irregularities

Anomalous behaviour (anomalous referring to deviations from the predictions by a respective model) of radio pulsars on long time scales is usually expressed by timing noise, or glitches. Timing noise is associated with a quasi-random walk behaviour of one, or more rotational parameters (like for instance the rotation period, or the rotation frequency) of a pulsar (Lorimer and Kramer [2012]). Originally identified by Boynton et al. [1972] as a random walk process, or noise, nowadays it is known that timing noise is predominantly red noise (Lyne [1999]). It occurs continuously, but in a random way and is assumed to be intrinsic to the pulsar. The random walk process is usually categorized in three different types: Phase noise, slowdown noise and frequency noise (Lyne and Graham-Smith [1990]). A common way to identify timing is noise is via the determination of the second derivative of the pulsar spin frequency (see Chapter 8.4 in Lorimer and Kramer [2012] for details).
A correlation between the strength of timing noise and the period derivative of pulsars has been found (Cordes and Helfand [1980]), implying that young pulsars like the Crab pulsar exhibit a high amount of timing noise (as will be also reflected in Chapter 5.1 of this thesis). Younger pulsars are therefore subject to regular monitoring programs on timescales of years (see for example the results obtained for the Crab pulsar by Lyne et al. [2015]).
Currently, several models for the generation of timing noise exist (an overview can be found in Chapter 4 in Hobbs et al. [2006a]). However, these models cannot explain all observed aspects of pulsar timing noise (Cordes and Helfand [1980]). A further complicating factor is that RPP have been observed to not necessarily reveal only one type of random walk, but to exhibit also discrete jumps in other parameters (Hobbs et al. [2006a]). In order to provide a

thorough understanding of the slowing down process of a pulsar (and also in the context of a GW detection), timing studies are currently one main focus of observational pulsar physics. More abrupt changes in the rotation parameters of a pulsar are known as glitches. A glitch is a sudden jump in the rotation frequency of a pulsar (Lorimer and Kramer [2012]). When a pulsar experiences a glitch, its rotation frequency increases suddenly. Hence the Time of Arrival (TOA)s of the pulsar arrive earlier. After the glitch most pulsars experience an exponential decay towards the rotation state before the glitch (see Figure 1.16). They have been observed to occur mostly in younger pulsars (Shemar and Lyne [1996]). The Crab and Vela pulsar have been observed to show the currently highest number of glitches known.

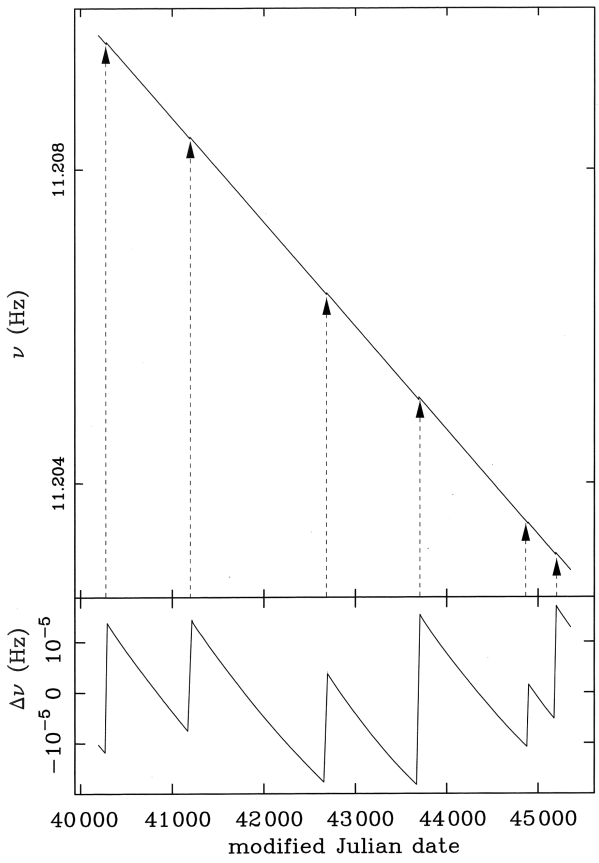

Figure 1.16.: Glitches of the Vela pulsar (figure adopted from Lorimer and Kramer [2012]). The upper plot shows the rotational frequency ν in dependence of time. Jumps in the rotational frequency are indicated with arrows. The lower plot shows the same data subtracted from the general spindown model ($\Delta\nu$).

Regarding their time of occurrence glitches are rare phenomena and are therefore subject to long timescale studies. Recently, a study consisting of 45 years of Crab pulsar data (Lyne et al. [2015]) revealed the occurrence of 24 glitches, 15 ocurring in a time interval of 11 years. Reconstructing the spin down process of the Crab pulsar by isolating the largest glitches, Lyne et al. [2015] found out that on average its glitches increase its spin down rate by about 6 %

thus disturbing its monotonous spin down process.
The reason for the occurrence of glitches is still not understood. One of the first proposed theoretical approaches for glitches tried to explain them as a consequence of star quakes (Baym et al. [1969]). However, this approach is not applicable to all known pulsars with glitches (Lorimer and Kramer [2012]). A summary of theoretical approaches for pulsar glitches can be found in Chapter 4 in Hobbs et al. [2006a].
Glitches have been found and monitored in more than 100 pulsars (Espinoza et al. [2011]). An up to date catalogue of pulsar glitches is mainted by the Jodrell Bank Observatory (JBO)[6].
Another form of anomalous behaviour of radio pulsars is known as mode changing (Lyne [1971]). As will be explained further in the short timescales irregularities section, radio pulsars have been observed to switch themselves off for a certain time. To reach this state, they go through a transition between their bright mode (B-mode) and quiet mode (Q-mode). It should be noted that pulsars which undergo mode changing, do not necessarily have these two modes, but can also have more (see for instance Rankin et al. [1988]). Such processes are transitions of the AP of a pulsar and are therefore detectable on longer time scales. While being in B-mode a pulsar is detectable via its AP. In the Q-mode it is emitting much less radiation and is therefore harder to detect (albeit not completely switched off as in the case of nulling, see next chapter). Recently, a Q-mode of the pulsar PSR B0823+26 has been detected which is about 100 times weaker than its B-mode (Sobey et al. [2015]). Pulsars which undergo mode changing indicate different emission properties as was shown for the pulsar PSR B0943+10 (Bilous et al. [2014]).

Short Timescales Irregularities

While long timescales irregularities are usually examined with data spans which last months or years by the usage of APs, pulsars have also been observed to show irregularities on time scales ranging from microseconds, to nanoseconds. To examine this kind of irregularities, one needs to observe single pulses from radio pulsars (see Figure 1.17 for a comparison between single radio pulses and an AP). They have been studied since the detection of pulsars and in spite of the mentioned disruptions which affect them (see Chapter 1.4.3), revealed various aspects of pulsar physics which will be summarized shortly here. As shown in Figure 1.17 single pulses are anything but stable with regard to their form. However, such single pulses have been also observed to suddenly switch themselves off for a duration of several rotation periods (Figure 1.18). This phenomenon is referred to as nulling (Backer [1970]). The duration of the nulling varies for different pulsars and can range from a few pulses to a few minutes (see Chapter 13.1 in Lyne and Graham-Smith [1990] for more details). Although assumed at first to be a random process, it has been verified that in the case of some pulsars the nulling does not occur at random (Redman and Rankin [2009]). In spite of various studies, it is not yet understood from the theoretical point of view how a pulsar can switch itself off for a certain time. Pulsar nulling studies are therefore an active branch of single pulse research.
Another anomalous single pulse phenomenon is known as drifting subpulses (Drake and Craft [1968]). The individual pulses of a pulsar as shown in Figure 1.17, can consist of several components which are commonly referred to as subpulses. Drifting in their case means moving in pulse longitude (Figure 1.18). For a characterization of drifting subpulses two other quantities apart from the rotation periods (in the case of drifting subpulses referred to as P_1) are defined: A characteristic spacing between subpulses referred to as P_2 and the period P_3 at which a pattern of pulses crosses the pulse window (Lorimer and Kramer [2012]). More details on this

[6] http://www.jb.man.ac.uk/pulsar/glitches.html

can

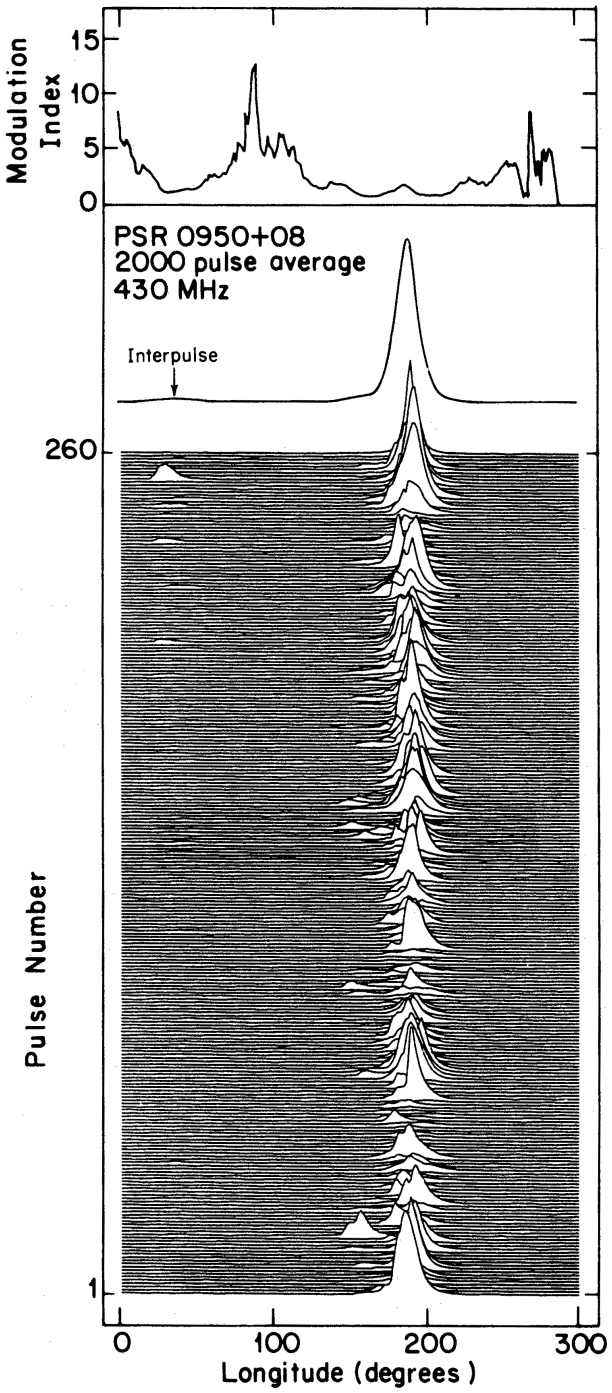

Figure 1.17.: Sequence of single radio pulses from the pulsar PSR B0950+08 which are added up to form the AP. The figure was adopted from Hankins and Cordes [1981].

be found in Backer [1973]. The theoretical approach for drifting subpulses is known as rotating

carousel model of subbeams which are located within a hollow emission cone (see Ruderman and Sutherland [1975], or Chapter 3 in Lorimer and Kramer [2012] for more details).

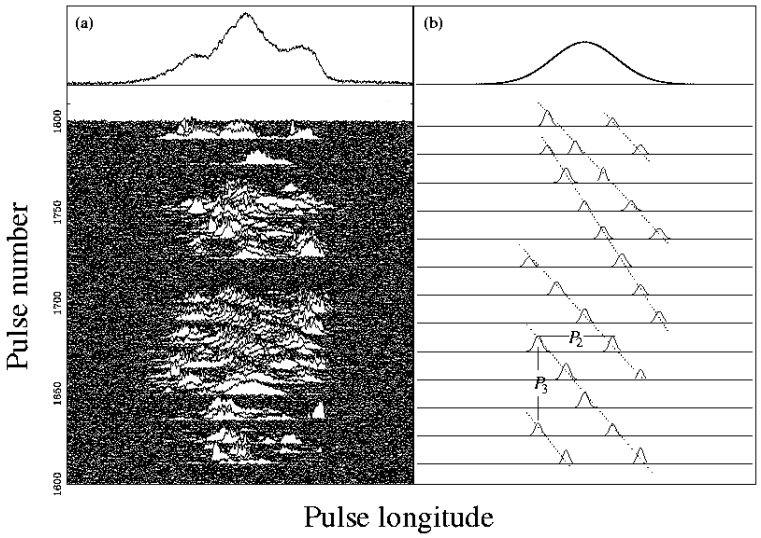

Figure 1.18.: Single pulses from PSR B1944+17 which show both, nulling and drifting subpulses. The observations are shown in the left figure (a)) and a scheme of the drifting subpulses is shown in the right figure (b)). In both cases the respective integrated AP is shown on top. The figure was adopted from Lorimer and Kramer [2012].

Apart from the giant pulse emission which is the central aspect of this thesis and explained in detail in Chapter 3, further anomalous single pulses are known as giant micropulses. Although a micropulse structure was already discovered shortly after the detection of pulsars (Craft et al. [1968]), giant micropulses from the Vela pulsar were discovered much later by Johnston et al. [2001]. They are assumed to be related to giant pulses, but their characteristics differ. Conspicuous differences between giant pulses and giant micropulses are the quasi-periodical occurrence of the latter and pulse widths ranging from 50 to 400 µs (Johnston et al. [2001]). However, similar as in the case of giant pulses, the origin and mechanism of giant micropulses are still not understood and subjects of ongoing single pulse studies of pulsars.

In spite of the differences between the sorts of described anomalous behaviour, a relation is assumed to exist between mode changing, nulling and drifting subpulses (Lorimer and Kramer [2012]) making it an active branch of pulsar physics studies.

1.5. Thesis Outline

The motivation for this thesis is focussed on the long existing question how the Crab pulsar works. As will be illustrated in detail in the next chapter, the nature of the Crab pulsar is rather complex which makes an overall theoretical approach hardly feasable. The Crab pulsar is located at a distance of about 2 kpc and is therefore easier to observe than many other

known pulsars. The latter reason makes it a numerously observed and studied object for a deeper understanding of pulsar physics. In spite of careful studies of the emission characteristics of the Crab pulsar, the understanding of these properties via theoretical approaches seems to be still at its very beginning. The mechanism behind and origin of the observed Crab pulsar emission is of central interest and has been examined for more than 40 years. Single radio pulses provide a rich morphology and therefore an insight into the ongoing processes in a pulsar magentosphere. The detection of Crab pulsar radio giant pulses has provided a powerful tool for the investigation of its radio emission. In the quest to unravel the mechanism behind the radio emission from the Crab pulsar (in the form of its radio giant pulses) and its γ-ray emission, a multiwavelength observational campaign was carried out with the Effelsberg radio telescope, the Westerbork Synthesis Radio Telescope (WSRT) and Major Atmospheric Imaging Cherenkov telescopes (MAGIC). The corresponding results are presented in this thesis.
These observations are necessary to answer the central question if radio giant pulses from the Crab pulsar correlate with its γ-ray emission. A further consequence of this question is if Crab pulsar giant pulses can be regarded as a connection of the Crab pulsar emission throughout the whole electromagnetic spectrum. An answer to the latter question might give a decisive impetus to possible emission mechanism of Crab pulsar radio giant pulses. Besides, the study presented here might provide further information about the mechanism of the coherent radio emission and non-coherent emission at higher wavelengths which is still an open chapter in Astrophysics.

The thesis tries to contribute to these open questions. It starts out with an introduction of neutron stars and pulsars in Chapter 1. After a short description of the detection of the first pulsar (Chapter 1.1), the stellar nucleosynthesis for the formation of a neutron star is explained in Chapter 1.2. A more general overview of currently known kinds of neutron stars (other than from pulsars) is given in Chapter 1.3. A basic description of the observational and theoretical properties of radio pulsars can be found in Chapter 1.4.

Chapter 2 gives an overview of the emission characteristics of the Crab pulsar. Apart from its detection at radio wavelengths (Chapter 2.1), a summary of the multiwavelength emission properties of the Crab pulsar is given in Chapter 2.2. In the latter case an emphasis is given on the radio and γ-ray emission from the Crab pulsar.

The phenomenon of radio giant pulses is introduced in Chapter 3. First, a summary of the observed properties of giant pulses from the Crab pulsar is given (Chapter 3.1), followed by an overview of already carried out correlation studies between the radio giant pulses and multiwavelength emission (Chapter 3.2). Afterwards the giant pulse emission in other pulsars is described (Chapter 3.3). The final part of this chapter is dedicated to a short overview of the existing theoretical approaches for giant pulses (Chapter 3.4).

Chapter 4 introduces the facilities with which the data for this thesis were taken. However, since a multiwavelength study represents the core of this thesis, a short introduction in the way of work is given for radio telescopes (Chapter 4.1) and Imaging Air Cherenkov Telescope (IACT)s (Chapter 4.4). A description of the Effelsberg radio telescope is given in Chapter 4.2, of the WSRT in Chapter 4.3 and of MAGIC in Chapter 4.5. In the latter case only the hardware componets which were used are described.

The analysis of all used data sets is described in Chapter 5. First the reduction and the

analysis of the radio data is given in Chapter 5.1. It is followed by a corresponding description of the reduction and analysis of the γ-ray data in Chapter 5.2. The search for a correlation via the calculation of time differences, the Pearson correlation approach and the determination of flux enhancements, is described in Chapter 5.3.

A summary of the analysis and the resulting conclusions are given in Chapter 6.

2. The Crab Pulsar

The Crab pulsar (PSR B0531+21, PSR J0534+2200) is a neutron star located in the supernova remnant also known as M1, or the Crab Nebula (Figure 2.1). Originally observed by Chinese astronomers during the supernova explosion in 1054 AD (the connection between the supernova explosion in 1054 AD and the Crab Nebula is extensively discussed by Duyvendak [1942] and Mayall and Oort [1942]), the nebula was identified to be connected with the neutron star shortly after its discovery (Lovelace et al. [1968]).

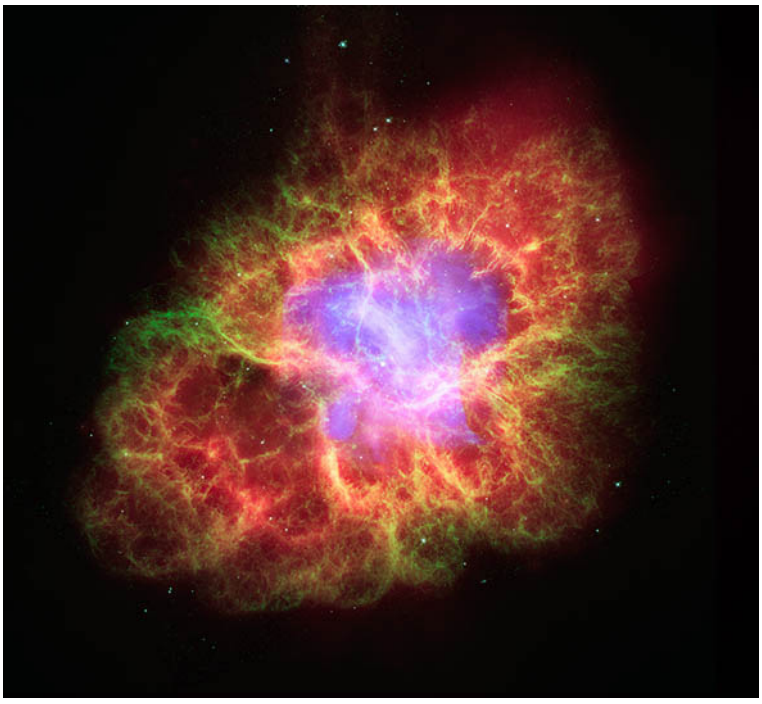

Figure 2.1.: The Crab Nebula in the Taurus constellation. The image is an overlap of four images in total taken at X-rays (1.5 keV, Chandra ACIS, light blue), optical (500 nm and 656 nm, Hubble WFPC2, green and dark blue) and infrared wavelengths (24.0 μm, Spitzer MIPS, red) [Image Credit: X-Ray: NASA/CXC/J.Hester (ASU); Optical: NASA/ESA/J.Hester & A.Loll (ASU); Infrared: NASA/JPL-Caltech/R.Gehrz (Univ. Minn.)]

The Crab pulsar is currently the youngest pulsar known and provided the very first proof of neutron stars being connected with supernova explosions. It is a RPP, belonging to the group of ordinary pulsars (Chapter 1.3).
A summary of basic Crab pulsar parameters is given in Table 2.1. A review on the Crab Nebula can be found in Hester [2008].

Parameter	Value
Designation	PSR B0531+21
Constellation	Taurus
Right Ascension (R.A.) [h m s]	05 34 31.93830
Declination (Dec) [deg ' "]	+22 00 52.1758
Rotational Period [s]	0.033392
Rotation Frequency [Hz]	29.946923
Original Rotation Frequency [Hz]	58
Mean Braking Index	2.342

Table 2.1.: A summary of the parameters of the Crab pulsar. The R.A. and Dec values were adopted from the SIMBAD Astronomical database[1]. The rotation period, rotation frequency (current and original) as well as the braking index were adopted from Lyne et al. [2015].

2.1. Discovery

The Crab pulsar was discovered by its unusually bright single pulses observed at 112 MHz with the 300 foot (91 m) radio telescope at Green Bank (Staelin and Reifenstein [1968]). The respective observations were carried out on 1969-10-17, -19 and -21. Staelin and Reifenstein [1968] denoted at first two pulsating objects and named them NP 0527 and NP 0532. They detected one single bright pulse from NP 0527 and three from NP 0532 (Figure 2.2). An examination of the pulse dispersion values resulted in $(1.58 \pm 0.03) \cdot 10^{20}$ electrons/cm^3 (NP 0527) and $(1.74 \pm 0.02) \cdot 10^{20}$ electrons/cm^3 (NP 0532). The authors reported the latter source to be more active and also more dispersed.

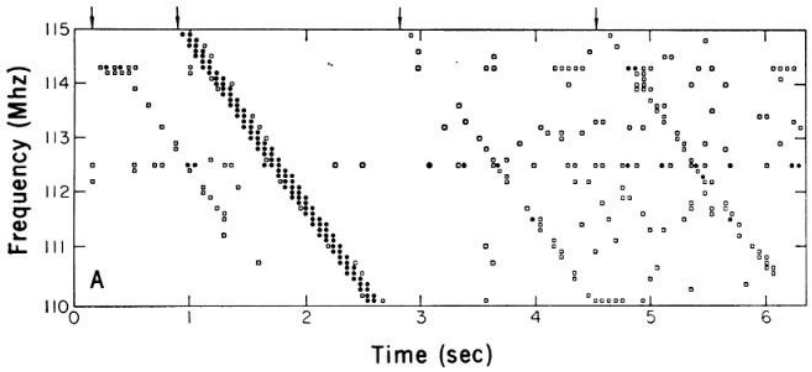

Figure 2.2.: Time-frequency diagram of single, bright pulses from NP 0532 observed on 1968-10-21 (Staelin and Reifenstein [1968]). The diagram consists of four single pulses, one bright one and three weaker ones. The pulses are not straight since they were not dedispersed. The irregular structures in the diagram are a result of RFI.

[1] http://simbad.u-strasbg.fr/simbad/

They determined the position of NP 0527 to R.A.(1950)=5h 27m ±6m, Dec(1950)=22° 30' ±2° and of NP 0532 to R.A.(1950)=5h 32m ±3m, Dec(1950)=22° 30' ±2°. Neither the association with the Crab Nebula was known at that time, nor the fact that the emission came from a rotating, magnetized neutron star. Nevertheless the authors stated that the measured dispersion values matched the estimated distance of the Crab Nebula (Trimble [1968]).
Already then Staelin and Reifenstein [1968] did notice the apparent non-periodicity of these single, bright pulses (more details are given in Chapter 3). They nevertheless determined upper limits of 0.25 s and 0.13 s for the rotation periods of NP 0532 and NP 0527 and emphasised the necessity of observations with higher time resolution for a clear determination of the rotation periods. At this point the authors concluded that the existence of the latter would decide if both discovered objects were the recently discovered radio pulsars (Hewish et al. [1968]), or a new class of radio sources.

2.2. Multiwavelength Characteristics of the Crab Pulsar

One distinctive characteristic of the Crab pulsar is that it emits its pulsed emission over the entire electromagnetic spectrum, ranging from radio to γ-wavelengths (Figure 2.3). Since the properties of the multiwavelength emission from the Crab pulsar are not uniform throughout the electromagnetic spectrum, in the following chapters an overview of its multiwavelength characteristics is given.

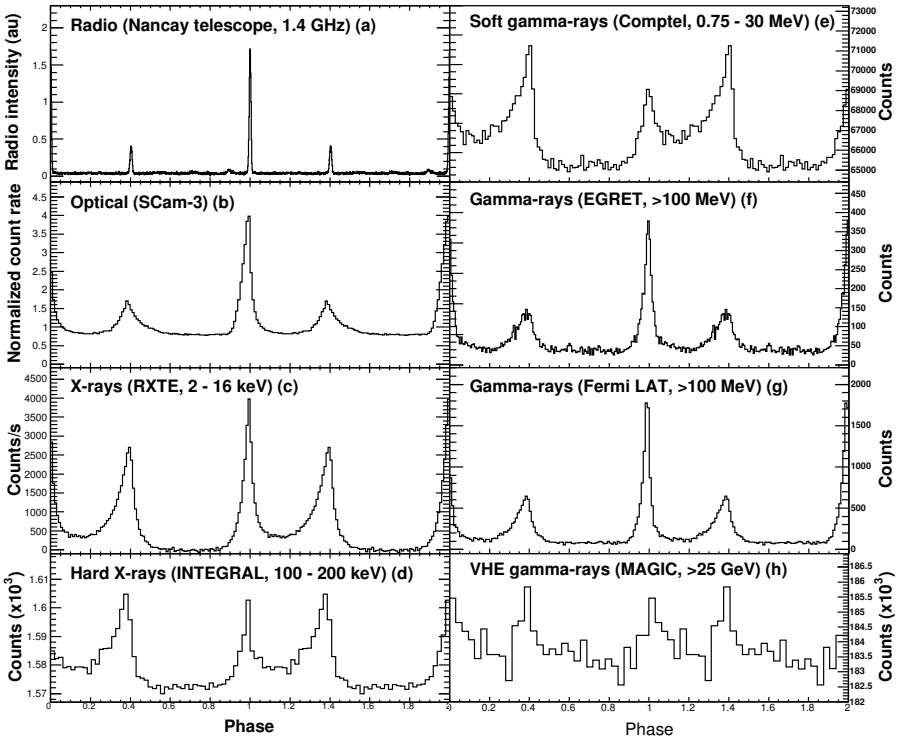

Figure 2.3.: Multiwavelength emission from the Crab pulsar indicating its pulsed emission consisting of the Main and the Interpulse from radio to γ-rays. The figure was adopted from Abdo et al. [2010a].

2.2.1. The Crab Pulsar at Radio Wavelengths

Rotational Period
The pulses found by Staelin and Reifenstein [1968] were sporadic and did not reveal any kind of periodicity. Subsequent studies of this source known as NP 0532 by Lovelace et al. [1968] with the Arecibo radio telescope revealed the heliocentric periodicity of the pulses to be 33.09114 ± 0.00001 ms (dated on 1968-11-15). The authors could verifiy the position of the pulsating source within 10' from the Crab Nebula center and noted at 195 MHz a pulse width of 3 ms (averaged over a total of 25 000 pulse periods) of Main Pulse (P1) at half of its intenstity. Already with these early observations they verified the existence of Interpulse (P2) which trails P1 by 14 ms and has 1/4 of the intensity of P1.
These first measurements were confirmed by Comella et al. [1969] who continued to observe the Crab pulsar with the Arecibo radio telescope at 111.5 MHz and 196.5 MHz. They determined the rotational period of the Crab pulsar to 33.09112±0.000 03 ms (dated on 1968-11-15).
Further periodicity measurements carried out with the Arecibo radio telescope in a frequency range from 318 MHz to 430 MHz were reported by Richards and Comella [1969]. They determined the barycentric period of 33.091121±0.000 007 ms and measured that it changes by 36.48±0.04 ns UTC/day (resulting from a least squares linear fit to the rate in Table 1 in Richards and Comella [1969]).

Radio Timing
The technique of pulsar timing (Chapter 1.4.4) is a method to observe TOAs of a pulsar and compare them with an already existing model. For solitary pulsars like the Crab pulsar timing observations can provide information about the position of a pulsar, its annual parallax and proper motion (see Chapter 8 in Lorimer and Kramer [2012] for details). Regarding the physics of a pulsar, a monitoring of its slow down process can give information about its aging process and possible composition. Due to their unknown equation of state, the composition of pulsars is still a topic of investigation in pulsar science. In this chapter a concise overview will be given which results have been drawn from timing observations of the Crab pulsar.
The slow down rate of the Crab pulsar was determined for the first time by Comella et al. [1969]. In other words, the very first timing observations (Chapter 1.4.4) were reported at optical wavelengths. Since radio observations can be also carried out during the day, they provide the possibility to cover much longer time spans and are therefore more adequate for regular monitoring of a pulsar. The reason for the delayed release of the proper radio TOA values was the (at first) lacking development of a procedure to correct the radio TOAs for the distortions caused by the ISM with sufficient accuracy and the proper conversion of the corresponding radio ephemerides towards infinite frequencies. This technique was developed by Counselman and Rankin [1971] including multipath delay distortions.
A first report about the regular monitoring of the Crab pulsar was given by Roberts and Richards [1971] who observed the Crab pulsar with the Arecibo radio telescope either at one, or simultaneously at two frequencies ranging from 430 MHz, 318 MHz, 196.5 MHz, 111.5 MHz and 73.8 MHz. They found irregularities in the radio TOAs indicating that the slow down process of the Crab pulsar is not linear. These irregularities also included jumps in the rotational phase which are nowadays referred to as glitches (Chapter 1.4.4). However, the main conclusion that can be draw from this work is that the TOA residuals can be fitted with a single cubic phase fit versus time polynomial. This result was applied by Rankin et al. [1971a] and Rankin et al. [1971b] who carried out timing studies of the Crab pulsar with the Arecibo

radio telescope at 430 MHz. The result of this fitting procedure revealed an irregular behaviour of the TOA residuals in comparison with the suggested polynomial fit (see Figure 1 in Rankin et al. [1971a]). Later studies by Groth [1975a], Groth [1975b] and Groth [1975c] established the behaviour of the TOAs from the Crab pulsar to be dominated by a random walk process nowadays known as timing noise (Chapter 1.4.4). Various investigations of this random walk behaviour have been made (see for instance Cordes [1980]).

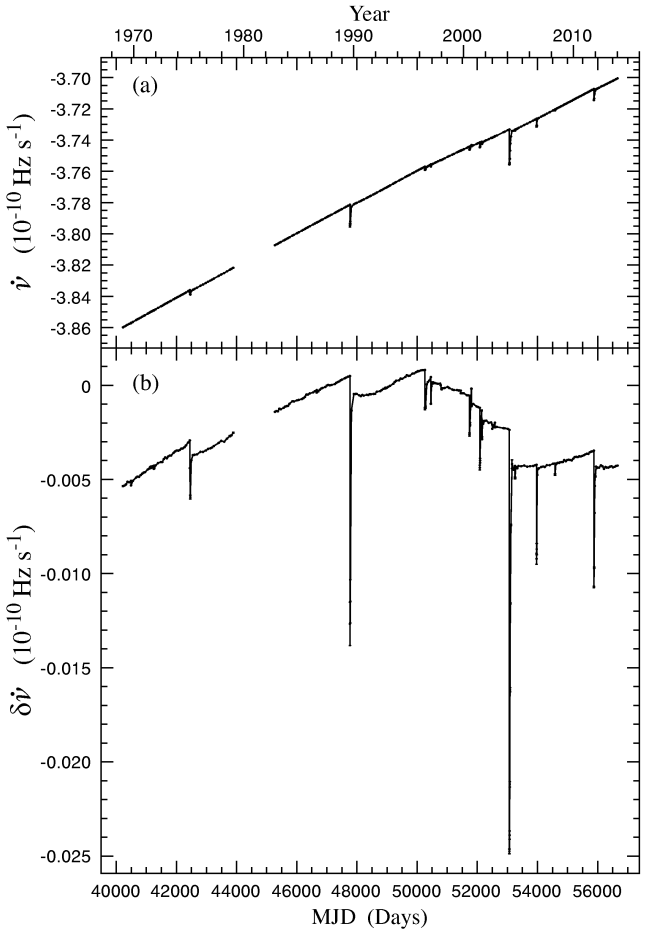

Figure 2.4.: The spin down rate $\dot{\nu}$ of the Crab pulsar resulting from observations monitored over a time span of 45 years. The upper figure (a) shows the spin down. The lower figure (b) shows the same spin down subtracted by a linear model ($\delta\dot{\nu}$). The figure was adopted from Lyne et al. [2015].

The slow down process of the Crab pulsar is overlapped with timing noise and glitches. To comprehend its evolution, regular monitoring programs via timing observations of the Crab pulsar were organized (Demianski and Proszynski [1983], Lyne et al. [1988]). Some of them are still carried out today by for instance the JBO (Lyne et al. [1988]) as well as by the Nancay radio telescope (L. Guillemot, private communication). These observations have revealed several

glitches throughout the years (Lyne et al. [1993]), but also different phenomena as for instance echoes of the regular pulsed emission due to interactions with an ionized cloud from the Crab Nebula (Backer et al. [2000], Graham Smith et al. [2011]). Recently, JBO observations of the Crab pulsar resulting from a time span of 45 years have been published (Lyne et al. [2015]). From this work a decrease of the Crab pulsar rotation rate (currently at about 30 Hz) by 0.5 Hz since 1984 could be verified. This process is interrupted by occurring glitches (Figure 2.4) which have led to an increase of the slow down rate by about 6 % according to Lyne et al. [2015]. The elimination of the glitches out of the respective data sets resulted in the determination of a braking index of 2.519 (and 2.342 for the entire data set, see Lyne et al. [2015] for details) delivering one of the most accurate values currently known.

Average Emission Profile

As already pointed out earlier (Chapter 1.4.4), the AP is constructed from averaging over a large number of detected individual pulses. In other words, it is constructed from data spans which cover (in time) many rotations of a pulsar. The obtained AP can be used to study the effects of the ISM, but also the structure of the magnetic field via the beam geometry (see below for more details). According to the Lighthouse model a pulsar is only seen if the beam, which is emitted along the magnetic poles, sweeps through the observers line of sight. This implies the existence of one or two AP components of a pulsar (depending how the observer is located towards the beams of the pulsar). In reality the AP of pulsars are more complicated with regard to the number and occurrence of their components (see Chapter 3 in Lorimer and Kramer [2012]) as will be described here briefly for the Crab pulsar.

The AP of the Crab pulsar at radio wavelengths is rather complex. As is shown in Figure 2.5 it has seven emission components which apparently never occur altogether at one frequency: A Precursor (Rankin et al. [1970], Boriakoff and Payne [1973]), a P1 and P2 (Lovelace et al. [1968], Comella et al. [1969], Rankin et al. [1970]) the latter occurring in two different forms as the Low Frequency Interpulse (LFIP) and High Frequency Interpulse (HFIP) (Moffett and Hankins [1996]), the High Frequency Component (HFC) 1 and 2 (Figure 3.6, Moffett and Hankins [1996]) and the Low Frequency Component (LFC) (Moffett and Hankins [1996]).

According to Figure 2.5 and the results of previous studies as described by Hankins et al. [2015], the Precursor is visible only at lower frequencies up to about 0.6 GHz. It cannot be found anymore at higher frequencies. The P1 component is visible at frequencies below about 5 GHz and vanishes at higher frequencies. The P2 component on the other hand is visible continuously from 0.43 GHz up to 28 GHz, but undergoes a shift in the rotational phase of about 7° between 3.5 GHz and 4.9 GHz and splits up into two components, the LFIP and the HFIP. Radio giant pulses with emission bands in their dynamic spectra have been observed at the phase ranges of the HFIP (Chapter 3.1). The two HFC components occur in a frequency range from 1.4 GHz to 28 GHz. However, both components drift in rotational phase and occur at higher phase values with increasing frequency. Lastly, the LFC emission component is visible only at lower frequencies, that is from 0.61 GHz to 4.2 GHz. With regard to the occurrence of these emission components, the AP of the Crab pulsar can be subdivided into a low-frequency profile (below 5 GHz) and a high-frequency profile (above 5 GHz).

The detailed study carried out by Hankins et al. [2015] has revealed several characterstics of these emission components. A comparison of their phase ranges shows that apart from both HFC components the drift amount is rather small in the other components of the AP (see Figure 2 in Hankins et al. [2015]). Due to the influence of the ISM (Chapter 1.4.3) the width of an AP component becomes stable at higher frequencies. However, an analysis of the widths

of all AP components at the described frequencies by Hankins et al. [2015], has revealed that the

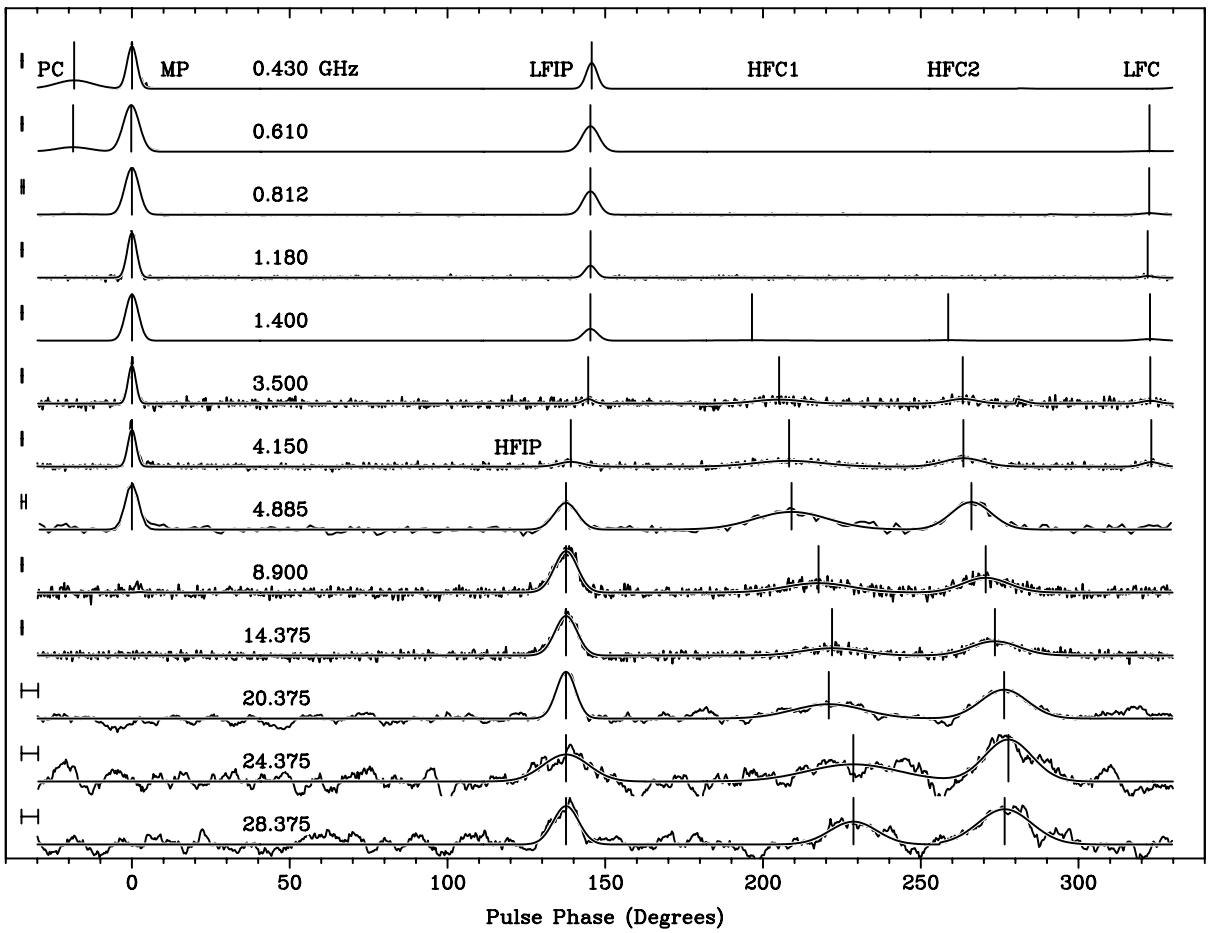

Figure 2.5.: The average emission profile from the Crab pulsar for different frequencies ranging from 0.43 GHz to about 28 GHz. The following emission components are included in this figure: The Precursor (PC), the Main pulse (MP), the LFIP at frequencies below 4 GHz, the HFIP at frequencies higher than 4 GHz, the HFC 1 and 2 and the LFC. The figure was adopted from Hankins et al. [2015].

width of the HFC 2 component is increasing at higher frequencies (see Figure 3 in Hankins et al. [2015]). As stated by Hankins et al. [2015] such an effect has not been observed in another pulsar yet. The described profile evolution with frequency of the Crab pulsar can currently not be explained by a theoretical approach.
A further interesting evolution of the AP of the Crab pulsar was recently reported by Lyne et al. [2013]. According to their observations (carried out at 0.61 GHz and 1.4 GHz, hence in the range of the low-frequency radio profile) resulting in a data set of 22 years length, the distance between the P1 and P2 components is increasing with a rate of $0.62° \pm 0.03°$ per century. Since the origin of the AP emission components lies in the magnetosphere of the pulsar and the radio emission is assumed to be generated near the magnetic poles of the star (Chapter 1.4.2),

this result implies that the magnetic field line axis is moving towards the equator of the pulsar. These findings indicate that the physics of the Crab pulsar are complex which makes it a constant object of research.

2.2.2. A view of the Crab Pulsar at γ-wavelengths

Detection

The detection of the pulsed emission from the Crab pulsar at optical and X-ray wavelengths (Chapter 2.2.3) was the prelude for searches also at γ-wavelengths.

A first approach was carried out by Vasseur et al. [1970] with a balloon experiment using multiplate spark chambers as detector that were sensitive to γ-rays above 50 MeV. Vasseur et al. [1970] observed the Crab pulsar during two flights on 1969-07-11 and on 1969-09-08. An analysis of the direction of the detected events resulted in no direct coincidence with NP 0532 (R.A.=85.75°, Dec=21° resulting from the measurements of Vasseur et al. [1970] in contrast with the previously known coordinates R.A.=83.17°, Dec=22° for NP 0532 at the time when this work was published). The authors noted that systematic errors could be the reason for this. In parallel to the work of Vasseur et al. [1970] the results of other balloon experiments in search for γ-ray emission from the Crab pulsar at energies above 0.6 MeV were reported by Hillier et al. [1970]. The data taking was carried out on 1970-08-02 and resulted in 90 min of observations. Figure 2.6 shows the result of the analysis of these measurements. Due to fluctuations between the time channels, they were summed in groups of two channels (upper plot in Figure 2.6) and four channels. This was done to smooth out the fluctuations. The two peaks shown in Figure 2.6 were interpreted by Hillier et al. [1970] as the Main pulse in the case of peak B and the Interpulse in the case of peak A. Their interpretation was based on the shape of both peaks: Peak B is narrow in comparison with peak A. The shape of peak A is similar to the one which was found with hard X-ray observations carried out by Floyd et al. [1969]. Hillier et al. [1970] determined significance of both peaks as $4.1\,\sigma$ (peak A) and $2.1\,\sigma$ (peak B). Later studies shifted the focus from balloon flights to satellite missions. The Crab pulsar was discovered with the Energetic Gamma-Ray Experiment Telescope (EGRET) in an energy range from 50 MeV to more than 10 GeV by Nolan et al. [1993]. The phase-resolved emission characteristics of the Crab pulsar were examined by Fierro et al. [1998]. Later investigations with the Astro-rivelatore Gamma ad Immagini LEggero (AGILE) (Pellizzoni et al. [2009]) revealed the characteristics of the Crab pulsar in an energy range from 30 MeV to 30 GeV. Apart from AGILE a regular monitoring programme of the Crab pulsar is carried out by the Large Area Telescope (LAT) of the Fermi Gamma-Ray Space Telescope (Abdo et al. [2010a]) covering an energy range from below 20 MeV to higher than 300 GeV.

A search of the Crab pulsar was also carried out with IACTs and culminated in its detection at energies above 25 GeV with MAGIC (Aliu et al. [2008]). After this detection the pulsed emission of the Crab pulsar has also been found at energies above 100 GeV (VERITAS Collaboration et al. [2011]) and in an energy range from 50 to 400 GeV (Aleksić et al. [2012]). Currently, the Crab pulsar is monitored with both, satellites (AGILE, Fermi LAT) and IACTs (MAGIC, Very Energetic Radiation Imaging Telescope Array System (VERITAS)), providing extensive possibilities of a mapping of its properties at γ-ray wavelengths.

γ-Timing

Since some pulsars cannot be detected at radio wavelengths (the common designation is *radio-quiet*), timing studies of them are not possible to be carried out at these wavelengths. It is

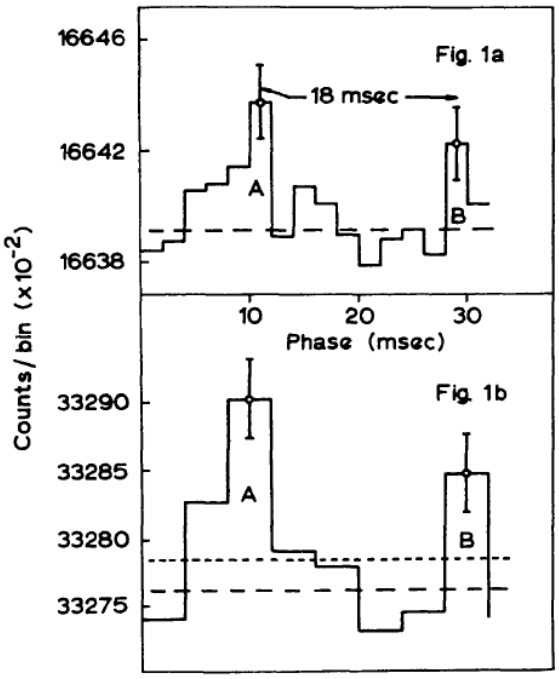

Figure 2.6.: Results from the 90 min of data taken by Hillier et al. [1970]. The upper figure shows counts in 2 ms intervals of the rotational phase while the lower figure shows the analogous result for phase intervals of 4 ms. The dashed lines in both figures are the background levels (see Hillier et al. [1970] for details) and the dotted line in the lower figure corresponds to the average height of the histogram when Peak A is excluded. Both figures were adopted from Hillier et al. [1970].

currently not understood why some pulsars like the Crab pulsar are visible throughout the whole electromagnetic spectrum and others only at some wavelengths. Some pulsars are radio-quiet, but detectable at γ-wavelengths which is the reason why the concept of γ-timing has been introduced. The technique being similar in its aims to the corresponding one at radio wavelengths (an examination of the slow down process with time, the analysis of the possible geometry of the γ-pulses and the precise determination of the position of known and newly discovered γ-ray pulsars, Ray et al. [2011a]), provides nowadays one of the most valuable strategies towards analysing the long-term behaviour of γ-pulsars. A description of the timing procedure in the case of data sets obtained with Fermi LAT can be found in Ray et al. [2011b]. A list of currently known γ-ray pulsars can be found on the webpages of the Fermi LAT mission[2] together with the corresponding timing models[3].
The Crab pulsar has been examined at γ-ray wavelengths with Fermi LAT extensively, albeit with the usage of timing models obtained at radio wavelengths (Abdo et al. [2010a]). The reason for this lies in the large amount of timing noise the Crab pulsar is exhibiting. For such pulsars usually the corresponding radio ephemerides is used since it provides a more accurate

[2] https://confluence.slac.stanford.edu/display/GLAMCOG/Public+List+of+LAT-Detected+Gamma-Ray+Pulsars
[3] https://confluence.slac.stanford.edu/display/GLAMCOG/LAT+Gamma-ray+Pulsar+Timing+Models

timing solution[4].
Interestingly, also pulsars which are radio-quiet, but γ-*loud* have been observed to exhibit rotational instabilities like glitches (as was detected in the case of the radio-quiet Geminga pulsar, Jackson and Halpern [2005]).
The timing of pulsars at γ-ray wavelengths provides a further solution to examine the rotational behaviour of a pulsar in another wavelength range than radio (if it is visible in the latter case). Studying the rotational behaviour of a pulsar at two different wavelength ranges can provide further constraints for corresponding emission models, exceeding the currently existing theoretical approaches which address only one wavelength range.

Average Emission
Analogous to the studies of the radio AP from the Crab pulsar, investigations of its AP at γ wavelengths are primarily used in order to learn more about the beam geometry of the γ-ray emission.

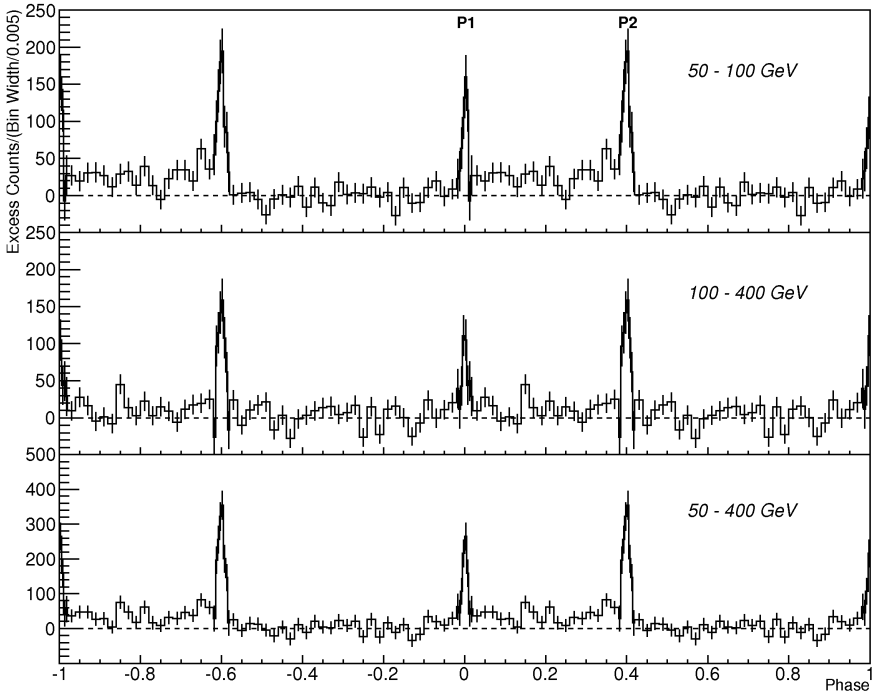

Figure 2.7.: The AP of the Crab pulsar at energies from 50 GeV up to 400 GeV as observed with MAGIC. The bridge emission is most prominent in an energy range from 50 GeV to 100 GeV. The figure was adopted from Aleksić et al. [2014].

The AP of the Crab pulsar at γ-wavelengths looks different than the corresponding one at radio wavelengths. As was mentioned in the last chapter, the radio P1 component disappears at frequencies above 5 GHz (Figure 2.5). Interestingly, it reappears at higher frequencies again (Figure 3.6) and is also visible at γ-wavelengths as is shown by Figure 2.3. However,

[4]http://fermi.gsfc.nasa.gov/ssc/data/access/lat/ephems/

the number of emission components in the γ-AP of the Crab pulsar is smaller than the one previously described at radio wavelengths. It consists predominantly of the P1 and the P2 emission component. These components have been detected at different energies (according to Figure 2.3): 0.75-30 MeV with CGRO COMPTEL (Kuiper et al. [2001]), above 100 MeV with EGRET (Kuiper et al. [2003]), above 100 MeV with Fermi LAT (Abdo et al. [2010a]), above 25 GeV with MAGIC (Aliu et al. [2008]), above 100 GeV with VERITAS (VERITAS Collaboration et al. [2011]) and above 400 GeV with MAGIC (Aleksić et al. [2012]).
These two emission components dominate the AP at γ-wavelengths. However, recently the Bridge emission has been detected at energies above 50 GeV with MAGIC (Aleksić et al. [2014]). It is used to refer to the region between the P1 and P2 ranging from 0.026 to 0.377 values in rotational phase (Aleksić et al. [2014], Figure 2.7). Although various theoretical extensions of the original Outer Gap Model (Chapter 1.4.2) have been constructed to explain the pulsed γ-ray emission from the Crab pulsar (see Abdo et al. [2010a] and Aleksić et al. [2012] for details), currently existing models cannot explain the occurrence of the Bridge emission (see discussion in Aleksić et al. [2014]). However, from the observational point of view the Bridge emission has been noticed at radio wavelengths already by Rankin et al. [1970]. A comparison of the Bridge emission at optical wavelengths indicates it as very weak in terms of intensity (see Figure 2 in Aleksić et al. [2014]).
Another interesting characteristic of the γ-ray emission of the Crab pulsar are the widths of both pulsed emission components P1 and P2. They have been observed to get smaller with increasing energy values (see Figure 3 in Aleksić et al. [2012]). This observed characteristic gives further input in the form of constraints for theoretical emission models.

2.2.3. The Crab Pulsar at other Wavelengths

Since the present thesis focusses on the radio and γ-ray emission of the Crab pulsar, only a short overview is given on its regular pulsed X-ray, optical and infrared emission in this chapter.

Detection
Following its detection at radio wavelengths (Staelin and Reifenstein [1968]), the pulsed emission from the Crab pulsar was also found at X-ray (Fritz et al. [1969]), optical (Cocke et al. [1969], Nather et al. [1969]) and infrared wavelengths (Neugebauer et al. [1969]).
The optical observations revealed the existence of a P1 and P2 emission component, the latter trailing the P1 by 14 ms (Cocke et al. [1969]) and 13.6 ms (Nather et al. [1969]). The rotational period of the Crab pulsar was determined by Nather et al. [1969] to 33.093 464 ms and 33.093 487 ms respectively. Interestingly, Cocke et al. [1969] reported that the optical P2 was usually present and broader than the P1 in their observations. An extensive UBV magnitude analysis showed that the optical pulses were rather blue suggesting the existence of ultraviolet and X-ray pulses.
Pulsations from the Crab pulsar at X-ray wavelengths were detected shortly afterwards (Fritz et al. [1969]). The pulsed components found were P1 and P2, both separated by 12 ms. The pulsed signal was detected with a period of 33.095 ms.
The detection of the pulsed signal from the Crab pulsar at infrared wavelengths was reported by Neugebauer et al. [1969] (see Figure 1 in Neugebauer et al. [1969]). Later studies by Eikenberry et al. [1997] resulted in the determination of a rotation period of 33.4395 ms.

Timing Studies
As mentioned earlier (see Chapter 2.2.1), the very first timing studies were carried out at optical wavelengths. Nather et al. [1969] found out that the Crab pulsar is slowing down by 39.2 ns per day. Contemporaneous timing studies at optical wavelengths are carried out with fast photometers, like for instance Iqueye (Zampieri et al. [2014]), or OPTIMA (Straubmeier et al. [2001]). Currently, in most cases optical timing studies of the Crab pulsar are used for a comparison of the TOAs of the P1 component with the respective one at radio wavelengths (see Chapter 2.2.4 for details).
Since some pulsars only emit their pulsed emission in certain wavelengths, also the concept of X-ray timing studies has been introduced in the past (Jackson and Halpern [2005], Livingstone et al. [2009]). A long-term X-ray timing study of the Crab pulsar has been reported by Rots et al. [2004]. According to their measurements the time difference between the X-ray P1 and P2 is about 13.4 ms (0.400 in rotational phase values) constantly throughout the duration of eight years of their observations.
To understand the emission properties of the Crab pulsar at X-ray wavelengths, the corresponding timing studies (such as reported by Rots et al. [2004]) are currently used for the determination of the time delay between the P1 component at X-ray and radio wavelengths (Chapter 2.2.4).

Average Emission
The AP of the Crab pulsar at X-ray, optical and infrared wavelengths is (as far as it is currently known) not marked by as many different emission components as at radio wavelengths (see Figure 2.3). At optical as well as at X-ray wavelengths a P1 and P2 emission component has been found. Noticeably, the emission at the phase ranges between the pulsed emission components (commonly referred to as "OFF Pulse Emission") is higher especially at X-ray wavelengths in contrast with respective results from radio observations indicating also the existence of the Bridge emission (Chapter 2.2.2).
At infrared wavelengths also the P1 and P2 emission components have been detected (Figure 3.6, Neugebauer et al. [1969], Becklin et al. [1973], Pennypacker [1981], Middleditch et al. [1983], Ransom et al. [1994], Eikenberry et al. [1997]). However, in some cases additional features in the cases of these two pulsed emission components were reported. Pennypacker [1981] noticed a structure in the trailing edge of the P1 emission component which is not visible in the optical AP of the Crab pulsar. This structure looks like an additional, but much weaker emission component which overlaps in rotational phase with P1 and is named "Shoulder" (see Figure 1c in Pennypacker [1981]). Confirming these results, Middleditch et al. [1983] reported an excess after the P2 component, naming it "Postcursor". However, these two features have not been confirmed by later studies (Ransom et al. [1994]) and their existence remains an open question. Another interesting feature of the Crab pulsar AP at infrared wavelengths is an increase of the P1 width, as well as of the distance in rotational phase between P1 and P2 (Ransom et al. [1994], Eikenberry et al. [1997]). The lack of further explanations of the additional features in the infrared AP of the Crab pulsar, emphasises the necessity of further studies in the future.

2.2.4. Time Delays between Emission at different Wavelengths

The pulsed multiwavelength emission from the Crab pulsar has been numerously examined as described in the previous chapters. In spite of these studies which have lead to a new picture

of the Crab pulsar (Figure 2.2), it has been discovered that the pulsed emission components (meaning in this case P1 and P2) are not aligned in time. The corresponding measurements were carried out at optical, X-ray and γ-ray wavelengths and are summarized in Table 2.2.

Wavelength	Time Delay [μs]	Reference
Optical	255 $\pm$ 21	Oosterbroek et al. [2008]
X-rays	344 $\pm$ 40	Rots et al. [2004]
Hard X-rays	280 $\pm$ 40	Kuiper et al. [2003]
γ-rays (EGRET)	241 $\pm$ 29	Kuiper et al. [2003]
γ-rays (Fermi LAT)	281 $\pm$ 23	Abdo et al. [2010a]

Table 2.2.: A summary of the measured time delays between the radio P1 and the corresponding pulsed emission components at other wavelengths. The table was adopted from Abdo et al. [2010a].

With the described time differences the optical P1 is leading the radio P1 (Oosterbroek et al. [2008]), X-ray P1 is leading the radio P1 (Rots et al. [2004] and Kuiper et al. [2003]) and the γ-ray P1 is also leading the radio P1 (Kuiper et al. [2003], Abdo et al. [2010a]).

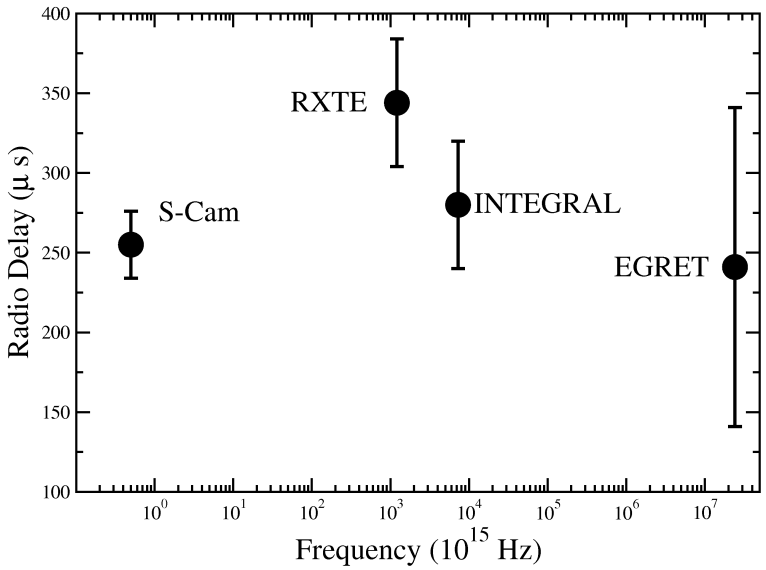

Figure 2.8.: The radio time delay at different wavelengths. The optical observations were carried out with the S-Cam (see Oosterbroek et al. [2008] for details). The larger error bars (the errors in this figure were computed by Oosterbroek et al. [2008] and are therefore not the same ones as shown in Table 2.2) in the case of the other observations result from the comparison with non-simulatenously taken radio observations. The figure was adopted from Oosterbroek et al. [2008].

As pointed out by Oosterbroek et al. [2008], the time delays between the radio P1 and the mul-

tiwavelength emission are approximately constant (Figure 2.8). This result suggests a similar mechanism responsible for the optical to γ-ray emission of the Crab pulsar and consequently also points to similar emission regions in the magnetosphere. A theoretical approach which produces multiwavelength APs similar to the ones resulting from past observations of the Crab pulsar, is proposed by Takata and Chang [2007].
Since it is assumed that the various components of the AP of the Crab pulsar are developing at different heights in the magnetosphere (see Romani and Yadigaroglu [1995] for a discussion of possible emission zones), such multiwavelength timing measurements provide crucial constraints for the construction of corresponding emission models.

3. Radio Giant Pulses

Radio giant pulses are regarded as a different form of pulsar radio emission. They have been only detected in a small number of pulsars so far and their emission mechanism has remained not understood until now. Detected for the first time in the case of the Crab pulsar, has made the latter a subject of numerous single pulse studies.
In this chapter a summary of the characteristics of Crab pulsar giant pulses is given together with an overview of correlation studies already carried out at other wavelengths, a short summary of other giant pulse emitting pulsars, and an overview of their current theoretical understanding.

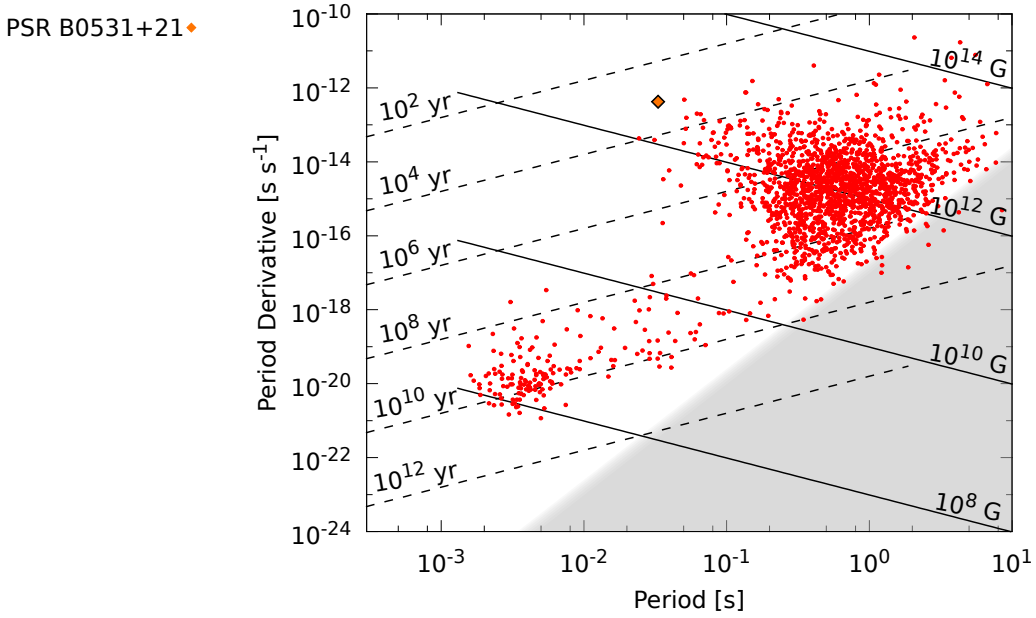

Figure 3.1.: A P-$\dot{\text{P}}$ diagram of all currently known radio pulsars similar to Figure 1.10 indicating the differences between ordinary pulsars (upper right group) and recycled pulsars (lower left group). The Crab pulsar is emphasised in orange color. The dashed lines mark certain characteristic ages while the solid lines stand for surface magnetic field strengths. The grey area to the lower right marks the region in which pulsars cannot be detected at radio wavelengths anymore ("Graveyard" region). Its boundary is blurred since the threshold from which on pulsars belong to the graveyard region depends upon the assumed structure of their magnetic fields (see discussion in Chen and Ruderman [1993]). The data for this plot was taken from the ATNF catalogue (Manchester et al. [2005], http://www.atnf.csiro.au/research/pulsar/psrcat, catalogue version 1.50, software version 1.49).

3.1. Crab Pulsar Giant Pulses

Detection

The Crab pulsar was discovered accidentally by its bright single pulses shortly after the discovery of the first pulsar (Staelin and Reifenstein [1968]). In search for dispersed pulses originally, Staelin and Reifenstein [1968] reported the detection of four single pulses from NP 0532 (the designation used for the Crab pulsar at that time) at a frequency from 110 till 115 MHz observed with the 300 foot Green Bank radio telescope. Already at the time of their observations, they described the observed single pulses as sporadic and isolated with the shortest distance of 0.21 s between each other (corresponding to about 6 pulse periods with the nowadays known rotation period of ∼33 ms of the Crab pulsar) emphasising the later confirmed apparently non-periodical occurrence of radio giant pulses. The association of NP 0532 with the Crab Nebula was not verified at that time putting a neutron star as the source of such sporadic pulses in question.

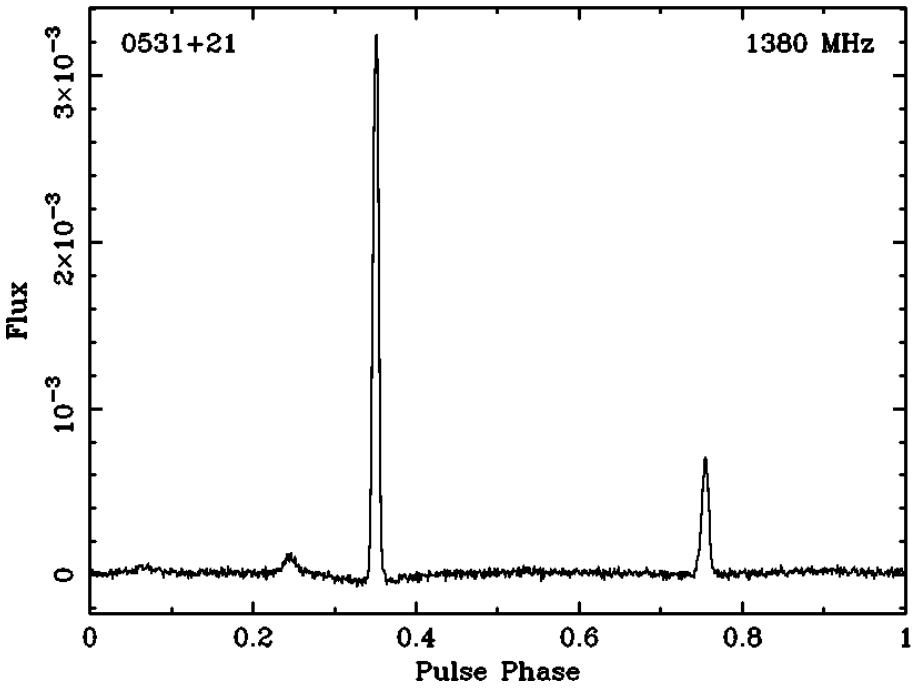

Figure 3.2.: The Crab pulsar observed with the WSRT on 2012-02-20 in the L band (flux is given in arbitrary units). Its AP consists of the bright P1 around the phase of 0.35, the P2 at about 0.75 in phase and the precursor at 0.25 in phase.

The periodicity of the Crab pulsar was discovered with the Arecibo radio telescope (Lovelace et al. [1968], Comella et al. [1969]). The respective source was localized within these measurements to be in the Crab Nebula (see Chapter 2.2.1).
Radio giant pulses reveal certain characteristics which distinguish them from the regular radio pulses from the Crab pulsar. These properties became prominent already during the first studies after the detection of the Crab pulsar.

Flux Densities

The high flux densities of giant pulses are the original reason for their designation to be "giant" and one of their first properties which was discovered apart from their apparently non-periodical occurrence (Staelin and Reifenstein [1968]).

Large flux densities were repeatedly observed to be connected with the width, or duration of radio giant pulses. In the case of the Crab pulsar high time resolution observations with the Arecibo radio telescope at 5.5 and 8.6 GHz (Hankins et al. [2003]) and from 6 to 8.5 GHz and 8 to 10.5 GHz (Hankins and Eilek [2007]) led to the detection of giant pulses with widths in the nanoseconds range. Hankins et al. [2003] reported the detection of giant pulses shorter than 2 ns with intensities higher than 1000 Jy. Giant pulses with a width of less than 0.4 ns and a corresponding flux density of more than 2 MJy were later observed by Hankins and Eilek [2007]. As will be described in more detail in the next chapters, these short pulses were only discovered at the phase ranges of P1.

The observed correlation between the widths of giant pulses and their flux densities was examined in detail by Popov and Stappers [2007]. They carried out Crab pulsar observations with the WSRT at 1.2 GHz and found a correlation between their peak flux densities and their widths. They found no giant pulses with durations longer than 16 µs and peak flux densities larger than 1000 Jy and determined several groups of giant pulses according to their widths (Figure 3.3). One conclusion of their measurements was that Crab pulsar giant pulses can be subdivided into two groups with effective pulse widths of 4.1 µs and 8.2 µs.

As indicated by the mentioned studies high peak flux densities are one specific attribute of giant radio pulses in the case of the Crab pulsar. The typical radio giant pulse can be characterized by its non-periodicity having an energy which is higher than ten times the average pulse energy (Karuppusamy et al. [2011]). Such properties has also been observed in other giant pulse emitting pulsars like for instance in the case of the millisecond pulsar PSR B1937+21 (Soglasnov et al. [2004], see Chapter 3.3).

Phase-bound Occurrence

Radio giant pulses were discovered at the phases of the P1 component, as it was shown by subsequent studies after the detection of the Crab pulsar (Heiles and Campbell [1970]).

P2 giant pulses were detected at 146 MHz some time later (Gower and Argyle [1972]). In this case, a total amount of 402 giant pulses were found of which 30 were verified at the phases of the P2. An analysis of the shapes of P1 and P2 giant pulses resulted in similarities which suggested a similar emission mechanism for both pulse components.

Later searches for giant pulses at the other 5 regular emission components
(Moffett and Hankins [1996]) of the Crab pulsar remained unsuccessful. Jessner et al. [2010] carried out observations of the Crab pulsar with the Effelsberg radio telescope at 8.5 GHzand 15.1 GHz. They found 29 giant pulses ocurring at the phase ranges of the P1 and 85 at the ones of the P2. They could not find any at the phase ranges of both HFC 1 and 2 (Figure 3.6). Similar results were recently reported by Hankins [2012] who carried out high time resolution observations with the GBT, the GAVRT and the Arecibo telescope. Although they detected single pulse at the phase ranges of HFC 1 and 2, they did not identify them as giant pulses due to their intensity distributions in the form of a Gaussian and featureless dynamic spectra (in comparison with the dynamic spectra for P1 and P2 giant pulses as shown in Figure 3.7).

Repeated searches for Crab pulsar giant pulses at the phase ranges of the precursor also remained unsuccessful, suggesting a different emission mechanism for it in contrast with P1 and P2 (Popov et al. [2006]).

According to the results from the mentioned studies radio giant pulses are phase-bound, but only to the phase ranges of P1 and P2.

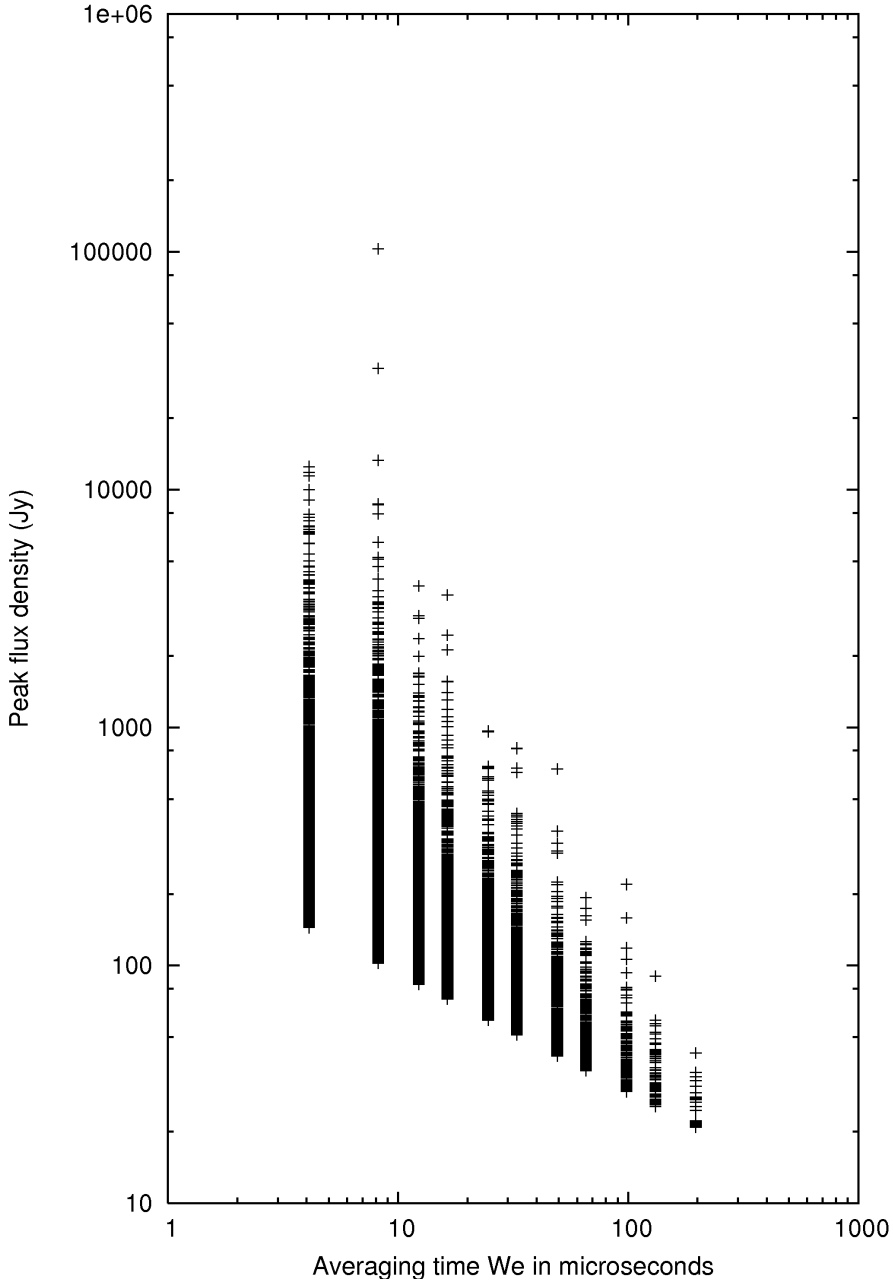

Figure 3.3.: Peak flux densities versus effective pulse widths of Crab pulsar giant pulses (Popov and Stappers [2007]).

Pulse Widths

The widths of giant pulses vary in the range of milliseconds to nanoseconds. Their short widths were already noticed shortly after the detection of the Crab pulsar. Single pulse studies carried out with the 300 foot Green Bank telescope revealed that the bright pulses, with which the Crab pulsar was originally discovered occurred on time scales of milliseconds (Staelin [1970]). Staelin [1970] discovered eight bright single pulses at 115 and 157.5 MHz emphasising that even with a corresponding time resolution of 10 ms and 3.6 ms they could not resolve the rise times of the pulses indicating more complex structures.

Heiles and Campbell [1970] found a narrow structure of the bright single pulses falling below 120 µs which is the time resolution of their instrument indicating brightness temperatures of about 10^{31} K. Such high brightness temperatures cannot be emitted by a thermal source, but are resulting from coherent emission mechanisms (see review in Hankins et al. [2009]).

With progressing time and technological development (including the possibilty to carry out coherent dedispersion procedures via software), deeper investigations of the complex structures of giant pulses could be approached.

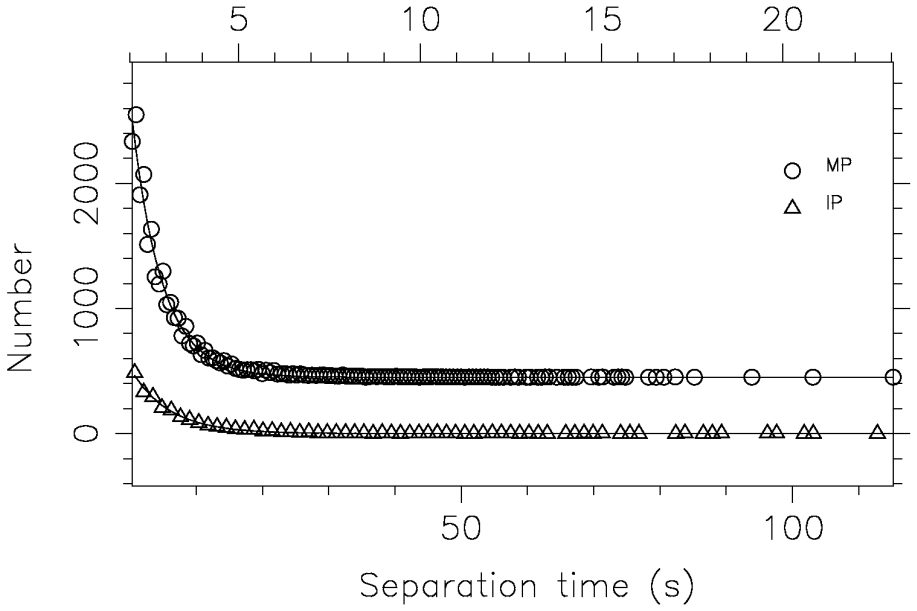

Figure 3.4.: Distribution of separation times of successive giant pulses determined by Karuppusamy et al. [2010]. MP stands for Main pulse, or P1, whereas IP stands for then Interpulse, or P2.

Hankins et al. [2003] carried out high time resolution observations of P1 giant pulses using the Arecibo radio telescope at 5.5 GHz and 8.6 GHz (with 0.5 GHz and 1 GHz bandwidth) and detected subpulses (Chapter 1.4.4) with pulse widths down to 2 ns. They verified that giant pulses with widths in the microseconds range consist of numerous single subpulses , commonly referred to as "Nanoshots" due to their short durations (see Figure 2 in Hankins et al. [2003]). With the assumed distance to the Crab pulsar (2 kpc), they determined a corresponding source diameter of 60 cm and a brightness temperature up to 10^{37} K, making Crab pulsar giant pulses one of the brightest known sources in the Universe.

Later studies by Hankins and Eilek [2007] with the Arecibo radio telescope at higher frequencies (6-8.5 GHz and 8-10.5 GHz) and a bandwidth of 2.2 GHz confirmed the earlier results of P1 giant pulses (Hankins et al. [2003]) and revealed crucial differences between the giant pulses ocurring at the phases of P1 and P2. P1 consists of several short "bursts" of microsecond duration. These burts can be resolved into several overlapping pulses of nanoseconds duration. Hankins and Eilek [2007] noticed that the latter become quite bright occassionaly (for comparison a pulse of less than 0.4 ns duration exceeds an intensity of 2 MJy). The dynamic spectra of such P1 giant pulses reveal these nanoshort giant pulses in the case of P1 (compare Figure 2 with Figure 5 in Hankins and Eilek [2007]).
The Crab pulsar is the only ordinary pulsar for which the pulse width distribution of giant pulses has been studied extensively. Some additional observations have been performed for millisecond pulsars (see page 81).

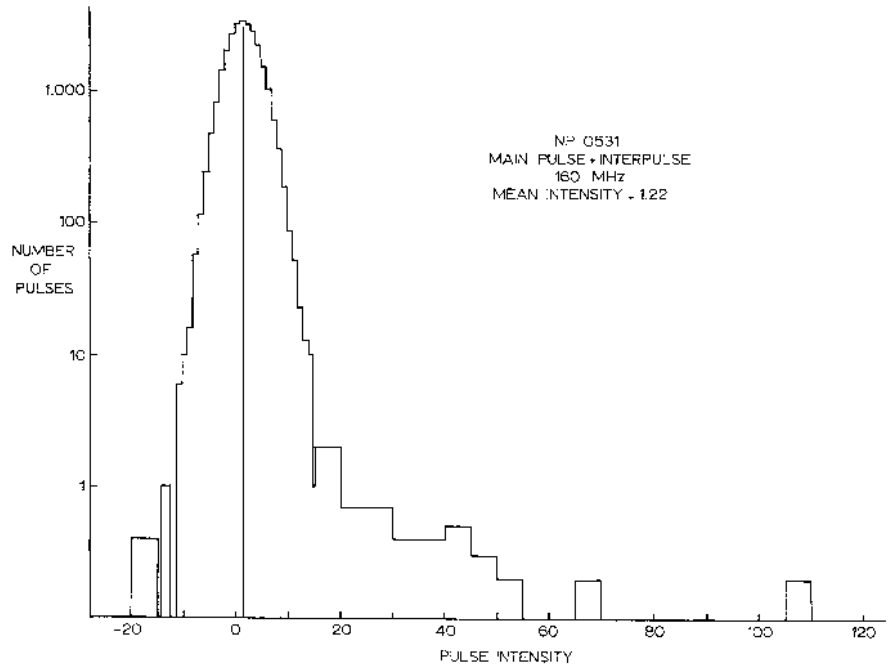

Figure 3.5.: Distribution of pulse intensities from the Crab pulsar as observed at 160 MHz by Sutton et al. [1971].

P2 giant pulses on the other hand were observed to have different time signatures. Each P2 pulse observed by Hankins and Eilek [2007] could be resolved into single pulses of microsecond durations. Their dynamic spectra consist of emission bands (Figure 3.7) which last not more than a few microseconds. They occur in sets of two to three bands which are proportionally spaced and tend to drift upwards in frequency. These emission bands were only observed in the case of the phase shifted P2 at frequencies higher than 4 GHz (HFIP, Figure 3.6). These high time resolution observations revealed via its giant pulse emission that the P1 and the P2 of the Crab pulsar are apparently formed differently in its magnetosphere which contradicts existing magnetospheric models.

Statistical studies of giant pulse widths were reported by Popov and Stappers [2007]. Their results revealed that the peak flux density of a giant pulse correlates with its effective width (see Figure 1 in Popov and Stappers [2007]) confirming also the results of Hankins et al. [2003]. Significant differences between P1 and P2 giant pulses were independently confirmed with high time resolution observations taken with the Effelsberg radio telescope at 8.5 GHz and 15.1 GHz with a bandwidth of 500 MHz (Jessner et al. [2010]). Also in this case, narrowband structures were detected in the case of P1 giant pulses and emission bands with regard to P2 giant pulses (Figure 11 in Jessner et al. [2010]) although no determination of the spacing in the latter case was possible due to the smaller bandwidth. No giant pulses with comparable nanoseconds duration like in the case of P1, or the characteristic emission bands of P2 were found at the HFC 1 and 2 components (Moffett and Hankins [1996]) emphasising different emission regions for these AP components.
Recent high time resolution studies including also the GAVRT, the Arecibo telescope and the Green Bank Telescope (GBT) confirmed the existence of these emission bands only in the case of the P2 at frequencies above 4 GHz (Hankins [2012]; T. Hankins, private communication). Also in this case, no giant pulses at the phases of the HFC 1 and 2 components were found confirming the results of Jessner et al. [2010] and stating the uniqueness of both, P1 and P2.

Poisson Statistics

Each giant pulse is apparently an independent event not connected in any case to another giant pulse. Single pulses studies carried out with the Arecibo radio telescope at 430 MHz indicated no correlation between strong single pulses at the phases of P1 and P2 within one rotation period (Heiles and Campbell [1970]). According to these measurements, strong pulses occurred once per approximately 10^4 pulse periods, that is about 5 min, suggesting that the single bright pulses associated with P1 are emitted independently of the ones being associated with P2.
A detailed study of the distribution of time separation between giant pulses was carried out by Lundgren et al. [1995]. They observed the Crab pulsar with the Green Bank 43 m radio telescope at a center frequency of 800 MHz and 812.5 MHz. Out of a total of 10^7 pulse periods and 3 x 10^4 resulting giant pulses, they determined a rate of one giant pulse every 383 periods exceeding a threshold of 125 Jy. For the determination of this rate an exponential distribution of the time lags between giant pulses resulting from Poisson statistics was assumed. Lundgren et al. [1995] verified no correlation between the flux density of previous, or next coming pulses thus confirming the correctness of their assumption.
An examination of giant pulse rates in the case of P1 and P2 was carried out by Karuppusamy et al. [2010]. In this case the Crab pulsar was observed with the WSRT in a frequency range from 1311 MHz to 1450 MHz. They confirmed the exponential distribution of the separation times of giant pulses in their data for P1 and P2 (Figure 3.4). With a threshold of 3.9 Jy they determined one giant pulse every 0.9 s in the case of the P1 and one every 5.81 s at the phase ranges of the P2 component.
So far no other results have been published which contradict with the assumption that radio giant pulses can be described by a Poisson process. Consequently, each observed giant pulse in the case of the Crab pulsar is apparently an independent event not connected to other giant pulses.

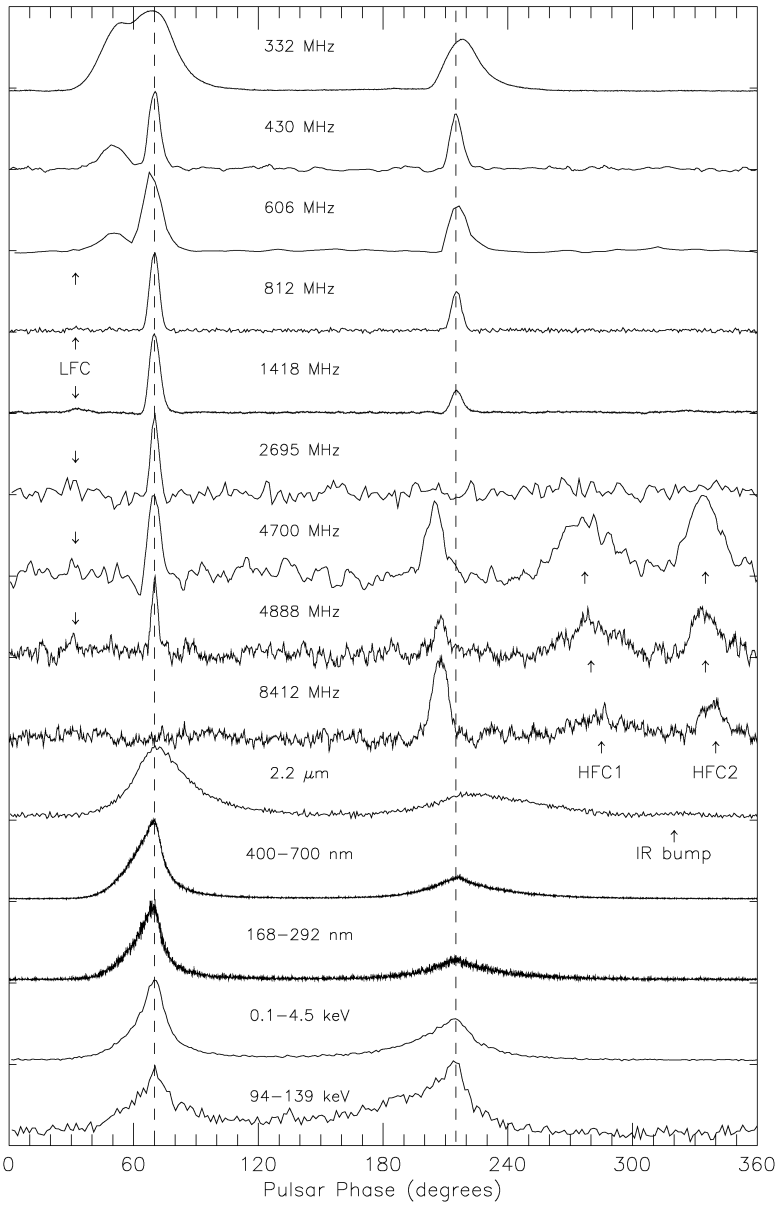

Figure 3.6.: Emission profiles of the Crab pulsar [Moffett and Hankins [1996]].

Power Law Intensity Distributions and Spectral Densities

Radio giant pulses are a different and distinctive form of pulsar emission. Observations of individual pulses by Sutton et al. [1971] carried out with the 300 foot Green Bank radio telescope revealed the existence of two different populations of single pulses visible at 160 MHz at the phase ranges of P1 (Figure 3 in Sutton et al. [1971]). The resulting intensity histograms consist of a low intensity distribution which has the form of a Gaussian (accounting for the regular pulses) and a High Energy (HE) tail which is caused by single bright pulses which were

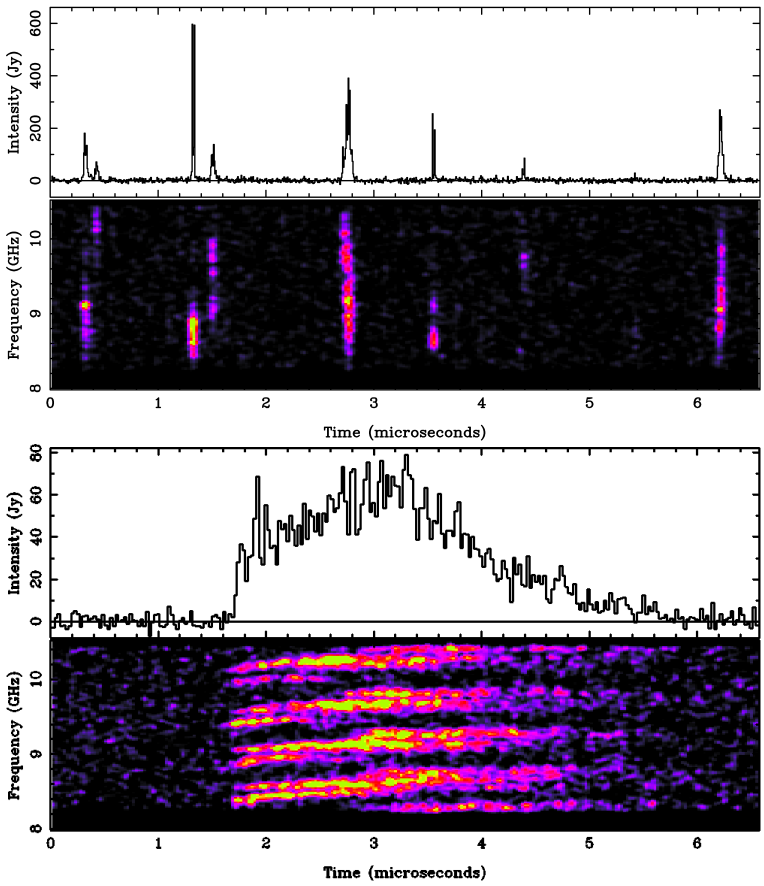

Figure 3.7.: Total intensity and dynamic spectra of P1 pulses (upper plot) revealing giant pulses of nanoseconds duration and P2 giant pulses consisting of emission bands of microseconds duration (lower plot). Both plots were adopted from Eilek and Hankins [2007].

referred to by the authors as "Jumbo Pulses". This discovery was standing in deep contrast with observations of other pulsars which showed only one population of pulses (see for example the study of PSR B1919+21 carried out by Lovelace and Craft [1968] and of PSR B1133+16 by Lang [1969]). An investigation of the arrival times of all single pulses confirmed the existence of two different kinds of pulses in the case of the P1 and the P2, but not the precursor.
Studies of the pulse height distributions of P1 radio giant pulses were carried out by Argyle and Gower [1972] at 146 MHz with the 46 m radio telescope of the Algonquin observatory. They resulted in the determination of a power law distribution of their intensities drawing thus a further difference to the more complex distributions of regular pulses (Hesse and Wielebinski [1974], Burke-Spolaor et al. [2012]). This property inherent to radio giant pulses has been confirmed by numerous further studies (see for example Lundgren et al. [1995]).
The spectral indices of P1 giant pulses were examined initially by Argyle and Gower [1972]. They determined a spectral index of -2.5 in the case of P1 giant pulses at 146 MHz.
A multiwavelength study carried out with the 43 m Green Bank telescope at 800 MHz and 812 MHz by Lundgren et al. [1995] revealed that giant radio pulses have power law intensity

distributions with an exponential index of -3.3 (no distinction between P1 and P2 giant pulses was made within this study).
Multifrequency observations from 0.43 GHz to 8.8 GHz taken with the Arecibo radio telescope revealed parts of power law intensity distributions in the case of both, P1 and P2 giant pulses (Cordes et al. [2004]). A comparison of the intensity distributions of P1 giant pulses observed at 0.43 GHz and 8.8 GHz indicates a steepening from low to high frequencies (compare Figure 2 and 3 in Cordes et al. [2004]). This steepening confirms earlier studies by Argyle and Gower [1972] and Lundgren et al. [1995].
Extensive studies of the cumulative probability distributions of observed giant pulses by Popov and Stappers [2007] revealed differences for P1 and P2 in the form of breaks in the power law indices for P1 giant pulses. Besides, the distributions seem to be different for short and long P1 giant pulses (changing power law indices) emphasising the existence of different giant pulse populations in the case of P1.

Wideband Occurrence
Giant pulses show a wideband occurrence. Not found originally by Sutton et al. [1971], further investigations carried out with the Arecibo radio telescope indicated a wideband behaviour of Crab pulsar single, bright pulses (Heiles and Rankin [1971b]). Simultaneous observations were arranged at 318 MHz, 111 MHz and at 111 MHz, 74 MHz. The authors verified that bright single pulses which occurred at 318 MHz were usually not classified as bright at 111 MHz implying a changing spectral index. They reported that a bright single pulse observed at 318 MHz tends to produce a pulse at 111 MHz which is approximately eight times stronger in intensity than the average pulse at 111 MHz and the other way round (Heiles and Rankin [1971a]). Similar behaviour was observed for pulses at 111 MHz and 74 MHz emphasising a broad band behaviour. The first statistically solid proof of their broad band occurrence was delivered by Sallmen et al. [1999] who carried out dual frequency observations of the Crab pulsar at 1.4 GHz with the Jansky Very Large Array (JVLA) and the 25 m Green Bank telescope at 0.6 GHz. About 70 % of simultaneously observed giant pulses resulted from this work indicating an emission bandwidth of at least 0.8 GHz. Further simultaneous observations of Crab pulsar giant pulses at 23 MHz (UTR-2 radio telescope), 111 MHz (BSA transit radio telescope, Pushchino Radio Astronomy Observatory) and 600 MHz (TNA-1500 Kalyazin radio telescope) marked their first detection in the low frequency range (Popov et al. [2006]). As a result of these observations 12 giant pulses were simultaneously detected at 23 MHz, 600 MHz and 21 at 111 MHz and 600 MHz. The authors nevertheless emphasise that they did not find any giant pulses occurring simultaneously at 23 MHz and 111 MHz which in this case seems somewhat peculiar, but can be attributed to possible influences of the ISM.

Polarization Properties
Crab pulsar radio giant pulses occurring at the phase ranges of P1 and P2 show different polarization characteristics. One of the first studies was carried out by Graham et al. [1970] who used the Mark I Jodrell Bank radio telescope at 408 MHz with a bandwidth of 330 kHz. The authors discovered a total amount of 70 % of linear polarization in the case of single, bright pulses occurring at the phases of P1 and a smaller amount in the case of P2. No circular polarization could be verified from this study.
Further investigations of Crab pulsar single pulses with the Arecibo radio telescope at 430 MHz (8.2 kHz bandwidth) showed different amounts of linear and circular polarization in the case of P1 and P2 (Heiles and Campbell [1970]). High degrees of circular and linear polarization were

observed across the pulse width of single, bright pulses at the phase ranges of P1. One interesting aspect of this study was the detection of a correlation of the circular polarization Stokes parameter V with the arrival time of the pulse. It was observed to be negative for pulses which arrived before the center of the P1 AP emission and positive for later ones, indicating a change of left-hand to right-hand polarization. The authors also reported a higher amount of linear polarization in the case of single, bright P1 pulses, but without a correlation of their TOAs. The detected correlation of circular polarization with pulse TOAs implied that differences in the latter were caused by the pulsar and not by for example propagation effects. Besides at the time of this study, only single bright pulses at the phase of P1 were detected and not in the case of P2, or the Precursor. This was also understood as an exclusion of propagation effects as a possible reason for the detected single bright pulses.
Searching repeatedly for bright, single pulses at the phases of the Interpulse and the precursor to make a comparison with the results of Graham et al. [1970], further polarization studies were carried out at 430 MHz with the Arecibo telescope using a bandwidth of 300 kHz (Rankin [1970]). No correlation between the circular polarization and pulse TOA in the case of P1 could be found. The amount of linear polarization was with an amount of 25 % much smaller than previously reported by Graham et al. [1970]. They verified less than 10 % of circular polarization were contradicting the previous results (Heiles and Campbell [1970]). A deeper investigation of the linear polarization of the Crab pulsar regular pulse components was carried out by Manchester et al. [1972] at 114.1 MHz, 127 MHz, 147 MHz and 158.75 MHz. They verified that in the case of the Precursor its high degree of linear polarization prevailed towards the lower frequency range excluding it as a source of giant pulses.
To verify that giant radio pulses occur at the phase ranges of P1 and not the Precursor for instance, Faraday rotation patterns of the average emission of the Crab pulsar and its radio giant pulses were examined at 146 MHz with the 46 m radio telescope at Algonquin Observatory by Argyle [1973]. Resulting in 3.2 % of linear polarization only, confirmed that giant pulses are weakly polarized in contrast with the strongly linear polarized Precursor confirming earlier results (Graham et al. [1970]).
Extended polarimetric studies of the Crab pulsar at 1.4 GHz, 4.9 and 8.4 GHz were carried out by Moffett and Hankins [1999] with the JVLA. The authors determined at 1.4 GHz the polarization of the Main pulse to be 25 % and the one of P2 to be 15 %. The corresponding polarization angles were reported to be nearly the same (about 120°). The LFC (visible from 812 MHz till 4888 MHz in Figure 3.6) was measured to have a linear polarization of more than 40 % (compare Figure 1 in Moffett and Hankins [1999]). It is interesting that the authors detected already at this frequency low level emission from the HFC 1 and HFC 2 components (visible from 4700 MHz to 8412 MHz in Figure 3.6). They reported both components to have a linear polarization of more than 50 % with a polarization angle of 180°. Comparing the polarization properties of all emission components at 4.9 GHz (Figure 2 in Moffett and Hankins [1999]), the authors confirmed the existence of the HFC 1 and 2 components with a linear polarization between 50 % and 100 % same as for P2 at this frequency (note that the latter is already shifted at this frequency by about 10° in rotational phase as shown in Figure 3.6). The P1 is reported to have the same amount of linear polarization as observed at 1.4 GHz. At 8.4 GHz it is not visible and consequently no respective polarization properties could be verified by the authors (Figure 3 in Moffett and Hankins [1999]). The P2 as well as both HFC components were observed to have a reduced amount of linear polarization at this frequency. A further interesting property found out by Moffett and Hankins [1999] resulted from a comparison of the polarization angle of the P2 at 1.4 and 4.9 GHz (adressing the non-shifted LFIP and the shifted HFIP

as seen in Figure 3.6). According to this the difference between its polarization angle is 90°. Together with its changing polarization at both frequencies, this comparison provides evidence that both P2 components are not the same. With their three frequency measurements Moffett and Hankins [1999] showed the complex polarimetric behaviour of the emission components of the Crab pulsar.

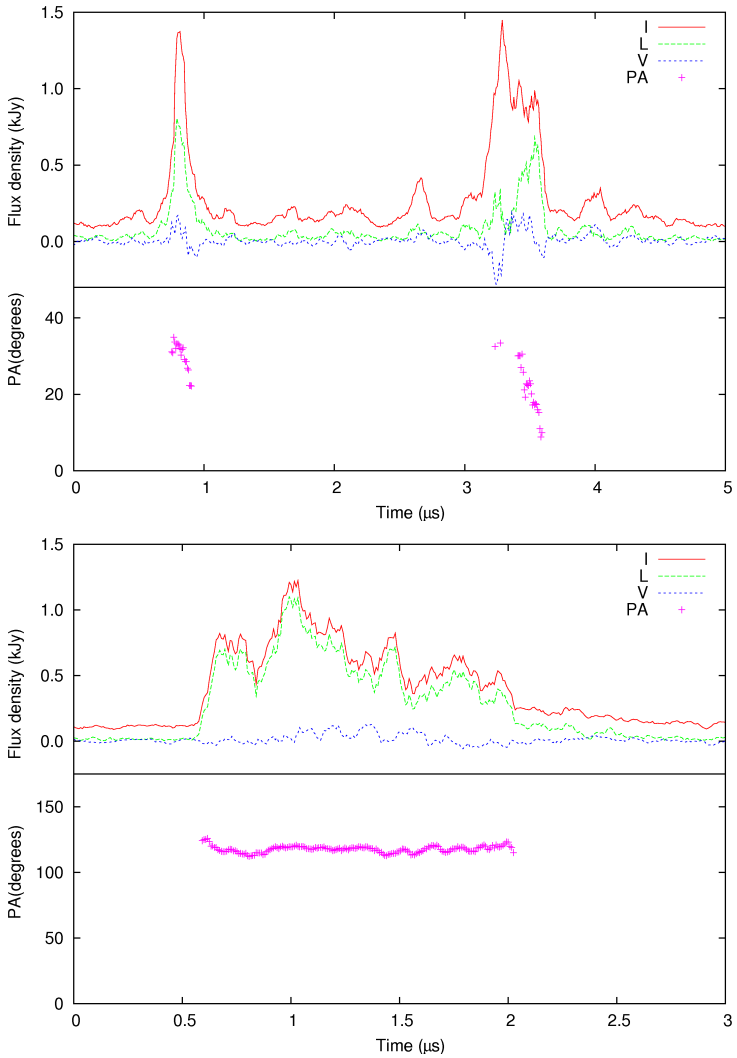

Figure 3.8.: A radio giant pulse observed at 8.5 GHz near the rotational phase of P1 (upper plot) and at 15.1 GHz at the rotational phase of P2 (lower plot). In both plots the red line accounts for the total intensity I, the blue line for the circular polarization V and the green line for the linear polarization L. PA stands for the polarization angle and is indicated by black crosses (Jessner et al. [2010]).

Later polarization studies devoted specifically to Crab pulsar radio giant pulses carried out at 8.5 and 15.1 GHz (Jessner et al. [2010]) revealed that the polarization characteristics of the P1 giant pulses and the P2 giant pulses are different. Having a deeper look at the upper plot in

Figure 3.8 one can recognize P1 giant pulses with nanosecond duration once reported for the first time by Hankins et al. [2003]. An astonishing feature is that the circular polarization in their case changes its sign from pulse to pulse. A similar feature is not seen in the case of P2 giant pulse as shown in the lower plot of Figure 3.8. Besides, changes of the linear polarization seem in some cases to be accompanied by changes of the circular polarization as clearly as shown for P1 giant pulses in Figure 3.8. Such a trend is not visible in the case of the observed P2 giant pulses.
Jessner et al. [2010] observed P1 giant pulses to show an amount of linear polarization between 30 % and 50 % with changes of the position angle between $\pm 20°$ and 40°. P2 giant pulses indicate a high amount of linear polarization up to 100 % and variations of the position angle in the range of $\pm 5°$. According to these observations P1 and P2 giant pulses show different polarization characteristics at high frequencies. The authors emphasise that such differences are not visible at lower frequencies. The reason for this changing behaviour is according to them not understood.
A recent study carried out by Slowikowska et al. [2014] who observed the Crab pulsar at 1.38 GHz with the WSRT, resulted in the determination of the amount of linear polarization of 24 % (P1 component) and of 21 % (P2 component). The authors could not detect significant differences of the polarization position angle between both emission components. Measuring also the polarization of the "Low Frequency Precursor" (LFP, the same as the LFC reported by Moffett and Hankins [1999]) resulted in a linear polarization of about 98 % and a circular polarization of about 20 %. The position angle of the LFP component was measured to +40 with regard to P1, or P2. The authors also detected a high frequency micropulse structure with a width of about 10 µs in the case of P1. They assigned it to radio giant pulses from the Crab pulsar, but made no further inquiries with regard to that.

3.2. Correlation Studies of Crab Pulsar Giant Pulses

In search for an answer about the possible emission mechanism, several correlation studies at different wavelengths were carried out. Since the Crab pulsar is known for its pulsed emission to be detectable over large parts of the electromagnetic spectrum, various studies adressing the emission at different wavelengths were carried out. A summary of past correlation studies is given in Table 3.1.

Optical Correlation Studies
The Crab pulsar belongs to a small group of pulsars, detectable at visible wavelengths (Shearer and Golden [2002], Mignani et al. [2010a], Zharikov and Mignani [2013a]).
A correlation study of its optical photons and radio giant pulses was carried out initially by Shearer et al. [2003] using the WSRT at 1357.5 MHz and the William Herschel Telescope (WHT) at which the TRIFFID optical photometer was mounted (Ryan et al. [2006]). A comparison of the optical P1 coinciding in time with a radio giant pulse and the one without a radio giant pulse, revealed an increase of the optical flux by 3 % in the first case. No changes in the optical Interpulses which coincided with P2 radio giant pulses were detected emphasising thus further differences between the Crab pulsar P1 and P2. Besides, the optical pulse was observed to arrive about 100 µs before the radio pulse.

The optical correlation of radio giant pulses was independently confirmed by Collins et al. [2012] who observed the Crab pulsar simultaneously with the Jodrell Bank radio telescope and the New Technology Telescope (NTT) equipped with the high time resolution photometer IquEYE (Naletto et al. [2009], Barbieri et al. [2012]). Also in this case, a delay of about 178 µs was observed between the average pulse at optical and radio wavelengths.
Extensive studies of the correlation between optical photons and radio giant pulses were carried out by Strader et al. [2013] who observed the Crab pulsar simultaneously with the GBT at 1.5 GHz (800 MHz bandwidth) and the 200 inch (5 m) Hale telescope at which the ARCONS spectrophotometer was mounted (Mazin et al. [2013]). They verified an increased optical peak flux by about 11 % for pulses with a giant radio Main pulse occurring near the optical pulse peak, about 3 % for pulses with giant radio Main pulses which arrive after the optical pulse peak and about 2.8 % for optical Interpulses when a giant Main pulse occured. The latter case was already observed by Shearer et al. [2003]. According to these measurements the increase of the optical flux depends upon certain phase at which a radio giant pulse arrives. A comparison of the spectral characteristics of optical pulses with and without accompanied radio giant pulses showed no differences indicating the same emission mechanism for both kinds of optical pulses. Also in this case, a lag between the arrival times of radio and optical pulses of about 202 µs was observed suggesting similarly as in previous studies that the mechanism which causes a link between the optical (incoherent) emission and the (coherent) radio emission might be not a direct one.
The correlation between radio giant pulses and optical photons from the Crab pulsar is the only detected multiwavelength correlation at the time of writing.

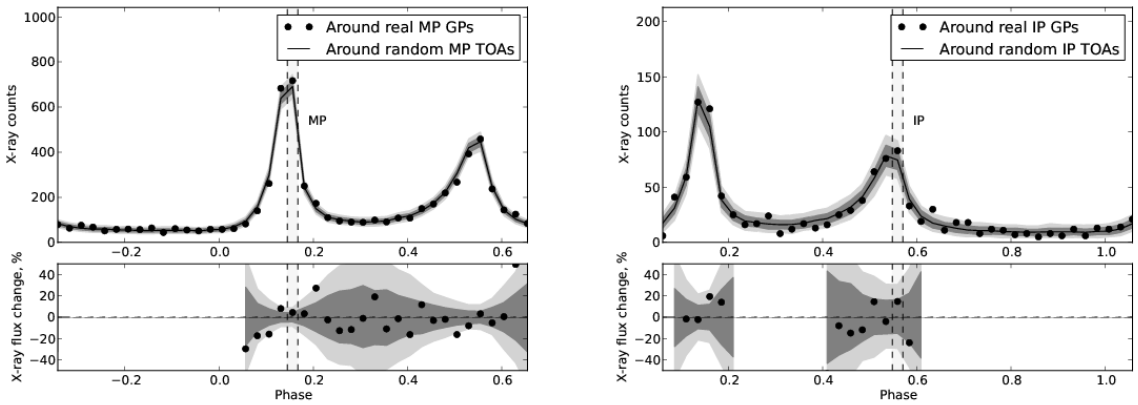

Figure 3.9.: Upper plots: X-ray counts in radio emission region around P1 giant pulses (left plot) and around P2 giant pulses (right plot) expressed in both cases by dashed lines; lower plots: Relative changes of X-ray flux (see Bilous et al. [2012] for details).

X-ray Correlation Studies
The first correlation study at soft X-rays was carried out by Bilous et al. [2012] who carried out simultaneous observations with the GBT at 1.5 GHz and the Chandra X-ray satellite in the energy range from 1.5 to 4.5 keV. A total of 5.4 hours of simultaneous observations resulted from this study. The authors searched for an enhancement of the X-ray flux in various

time windows around radio giant pulses. They compared the X-ray flux in time windows, or rotations in which giant pulses occurred with the one during which no giant pulses appeared. They searched for a correlation in the emission region around the Main pulse and the Interpulse separately (Figure 3.9, Bilous et al. [2012]). The measured change of the X-ray flux was not more than $2\,\sigma$ in this case. In a further approach they also searched for an enhancement of the X-ray flux in a bigger time window, that is of one pulsar period and in one period windows shifted by the size of the window up to 15 pulsar periods. Also in this case the X-ray flux did not change more than $2\,\sigma$ in the same rotation period in which radio giant pulses were detected (Figure 5 in Bilous et al. [2012]). To examine if radio giant pulses and X-ray pulses are emitted simultaneously, they also searched for a correlation between both on timescales of radio giant pulses with 20 phase offsets (Figure 5 in Bilous et al. [2012]). In all three cases no significant increase of the X-ray flux could be verified.
Preliminary results from a correlation study of radio giant pulses and hard X-ray pulses were reported by Mikami et al. [2013]. The authors have observed the Crab pulsar simultaneously at 1.4 GHz with the 34 m Kashima and the 64 m Usuda radio telescope and with the Suzaku X-ray satellite in an energy region from 15 to 75 keV. The total observation time was about 12 hours from which a number of $1.3 \cdot 10^4$ P1 giant pulses resulted. The study focusses on P1 giant pulses which exceed a threshold of $5\,\sigma$. Preliminary results show an enhancement of the hard X-ray flux by $2.7\,\sigma$ during simultaneously occurring P1 radio giant pulses (Figure 3.10). A recent update on this study was reported by Mikami et al. [2014]. Although they searched in broader energy range (from 35 till 315 keV) than previously for enhancements of the X-ray flux during occurring Main pulse giant pulses, the authors could not find an enhancement similar in range to the one observed at optical wavelegths by for instance Strader et al. [2013]. They determined a flux enhancement of $1.0\,\sigma$ and set an upper limit of 70 % during an occurring Main pulse giant pulse. In spite of not finding a statistically solid enhancement of the X-ray flux, the authors emphasise that new satellite missions like ASTRO-H will improve the statistics of photons and thus enable further searches for a correlation of radio giant pulses and X-ray photons from the Crab pulsar.

γ-ray Correlation Studies
The first approach at γ-wavelengths was carried out by Argyle et al. [1974] who observed the Crab pulsar simultaneously for 10 hours with the 25 m radio telescope of the Dominion Radio Astrophysical Observatory at 146 MHz and with the 10 m Whipple Cherenkov telescope at the Mount Hopkins Observatory (nowadays known as the Fred Lawrence Whipple Observatory). In these 10 hours, 300 radio giant pulses were detected of which 183 were identified as P1 giant pulses and 57 with P2 giant pulses. The energy threshold of the Whipple telescope was estimated to about 2×10^{11} eV (with an collection area of $1.4 \times 10^8\,\mathrm{cm}^2$). The time accuracy of 200 µs with which the TOAs of the air showers were detected, allowed for correlation searches at various time scales. In this course, scans for a correlation for one rotation period of the pulsar were carried out for P1, P2 and for both. The same procedure was carried out for five rotation periods. In each case TOA histograms centered around the TOAs of radio giant pulses were constructed and searched for any kind of correlation (see Figure 1 in Argyle et al. [1974]). No statistically significant excess could be determined from this data leaving the question of a correlation open.
As γ-ray studies with earth-bound telescopes belonged to a very young and new branch of observational astronomy, later correlation studies focussed mainly on satellite experiments.
Simultaneous observations of Crab pulsar giant pulses were carried out with the 43 m Green

Bank radio telescope at 0.8 and 1.4 GHz and the Oriented Scintillation Spectrometer Experiment (OSSE) on board of the Compton Gamma-Ray Observatory (CGRO) (Lundgren et al. [1992], Lundgren et al. [1995]). The authors could not verify larger increases of the γ-ray flux in a range from 50 to 220 keV than a factor of 2.5 (during simultaneously occurring giant radio pulses).

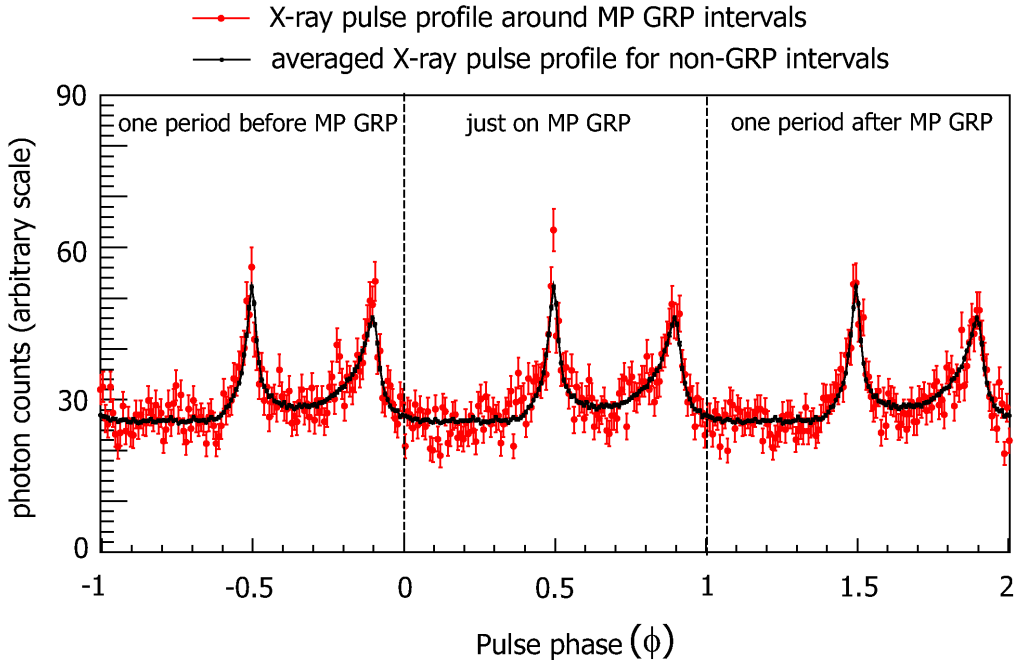

Figure 3.10.: The hard X-ray AP (red curve) around occurring P1 giant pulses in contrast with the X-ray AP with no giant pulses (black curve). The figure was adopted from Mikami et al. [2013].

Extensive searches for correlations between radio giant pulses and γ-rays were carried out with the GBT, the 43 m Green Bank radio telescope and Fermi satellite using Fermi LAT (Bilous et al. [2009], Bilous et al. [2011], Mickaliger et al. [2012]). These searches focussed mainly on a correlation between radio giant pulses occurring at the phases of P2 at frequencies larger than 4 GHz (see Table 3.1 for details) at which the latter is shifted by about 10 degrees in rotational phase (commonly referred to as HFIP. See Figure 2 in Moffett and Hankins [1996]). The scientific motivation for the studies with Fermi LAT were given by a model proposed by Lyutikov [2007]. In spite of repeated attempts (even with a data set of 107 hours of simultaneous observations resulting in 92022 detected radio giant pulses and 393 γ-ray photons in the case of Mickaliger et al. [2012]), no significant correlation was found suggesting that changes in the pair creation rate are unlikely a possible source of radio giant pulses (Bilous et al. [2009]). 38 years after the first correlation study involving IACTs (Argyle et al. [1974]) a further attempt was carried out with the GBT and the VERITAS array as the successor of the Whipple telescope (Aliu et al. [2012]). In a commont attempt, 11.6 hours of simultaneously taken observations were gathered which resulted in the detection of 15366 radio giant pulses (at 8.9 GHz) and 30093 VHE events (> 150 GeV). The search for a correlation was also in this case motivated

by the Lyutikov model (Lyutikov [2007]) and concentrated therefore mainly on P2 giant pulses. The search for increases of the γ-ray flux before, during and after a simultaneously occurring giant pulse, resulted in upper limits declining also in this case changes in pair creation rates being a possible source of radio giant pulses.
The energy ranges examined with IACTs do not cover a large area yet and leave especially the area below 150 GHz unexplored (Table 3.1). In order to determine if the emission mechanism of giant radio pulses is triggered by changes in the coherence of the respective radio beam, changes in the beaming direction, or variations in the pair creation rate (Bilous et al. [2009]), continuous studies are needed which will cover the remaining energy ranges creating the motivation for our study presented here.

Energy Range	Instruments	Flux Enhancements during radio GPs	Reference
Optical (600-750 nm) 1357.5 MHz	William Herschel Telescope & WSRT	7.8σ (3 %) increase	Shearer et al. [2003]
Optical (400-1100 nm) 1.5 GHz	Hale telescope & GBT	11.3 % increase (P1)	Strader et al. [2013]
Soft X-rays (1.5-4.5 keV) 1.5 GHz	Chandra Satellite & GBT	$\leq$2σ (10 %) (P1)	Bilous et al. [2012]
Hard X-rays (15-75 keV) 1.4 GHz	Suzaku Satellite & Kashima, Usuda radio telescope	2.7σ (21.5 %) increase (P1)	Mikami et al. [2013]
Hard X-rays (35-315 keV) 1.4 -1.435 GHz	Suzaku Satellite & Kashima radio telescope	1.0σ (70 %) increase (P1)	Mikami et al. [2014]
Soft γ-rays (50-220 keV) 0.8 GHz	CGRO OSSE & 43 m Green Bank telescope	$<$1σ (250 %)	Lundgren et al. [1995]
γ-rays (0.1-5 GeV) 8.9 GHz	Fermi LAT & GBT	$<$400 % (95% CL) (P2)	Bilous et al. [2011]
γ-rays (0.1-100 GeV) 0.33 & 1.2 GHz 8.9 GHz	Fermi LAT & 43 m Green Bank telescope & GBT	$\leq$3.2% (P1), $\leq$2.3% (P2)	Mickaliger et al. [2012]
VHE γ-rays ($>$200 GeV) 0.146 GHz	Whipple IACT & 25 m Dominion radio telescope	$<$3σ	Argyle et al. [1974]
VHE γ-rays ($>$150 GeV) 8.9 GHz	VERITAS IACT & GBT	$<$500-1000 % (95 % CL) P2	Aliu et al. [2012]

Table 3.1.: Summary of past Crab pulsar giant pulse correlation studies. CL stands for confidence level. Some of the values were adopted from Table 1 in Mikami et al. [2013].

3.3. Radio Giant Pulse Emission in other Pulsars

Radio giant pulses have been found in a number of different pulsars which belong to two different pulsar populations consisting of ordinary pulsars as well as millisecond pulsars (see Figure 3.11).
At the time of writing it is not clear if different sorts of radio giant pulses do exist. Hence apart from commonalities between the radio giant pulses from the later discovered pulsars, also differences to the classical Crab pulsar giant pulses are outlined in this chapter. Details of all currently know giant pulse emitting pulsars can be found in Table 3.2.

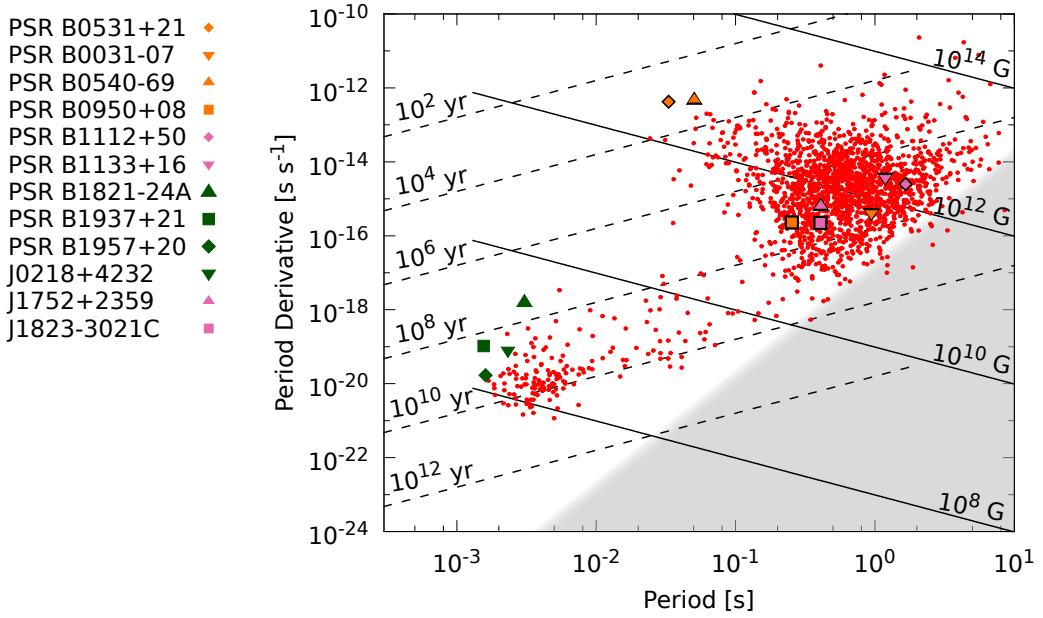

Figure 3.11.: The same image as shown in Figure 3.1 with named giant pulse emitters belonging to the group of ordinary, as well as recycled pulsars. The data for this plot was taken from the ATNF catalogue (Manchester et al. [2005], http://www.atnf.csiro.au/research/pulsar/psrcat, catalogue version 1.50, software version 1.49).

a) Ordinary Pulsars
The group of ordinary pulsars which were found to emit radio giant pulses consists currently of PSR B1112+50 (Ershov and Kuzmin [2003]), PSR B0540-69 (Johnston and Romani [2003]), PSR B1133+16 (Kramer et al. [2003]), PSR B0031-07 (Kuzmin et al. [2004]) and PSR J1752+2359 (Ershov and Kuzmin [2006]). In the following chapters only the details of their radio giant pulse emission will be discussed.

Flux Densities
Very high flux densities are one specific characteristic of radio giant pulses. The detection of single, exceptionally bright pulses led to the discovery of giant pulses also in the case of other

ordinary pulsars than the Crab pulsar. The second ordinary pulsar with this kind of anomalous single pulse emission was PSR B1112+50 in which case single pulses were observed at 111 MHz once per 150 regular pulses with flux densities up to 0.18 kJy (Ershov and Kuzmin [2003]). According to these measurements they contain a peak flux density which is higher by a factor of 80 in contrast with the peak flux densities from regular pulses.
The next pulsar detected to emit radio giant pulses was PSR B0540-69 (Johnston and Romani [2003]), also known as the "Crab Twin" (meaning in other words its close position in Figure 3.11 to the Crab pulsar and similarities of its plerion. Specific information about the latter in contrast with the Crab pulsar is given in Manchester et al. [1993b]). Johnston and Romani [2003] reported the detection of only two giant pulses. The brighter one had a flux density higher by a factor of at least 5000 in comparison with the mean single pulse flux density (Johnston and Romani [2003]). Later studies of this pulsar led to the detection of 141 giant pulses (Johnston et al. [2004]). The mean flux density of the brightest ones was determined to be 10.4 mJy (in contrast with the flux density of 24 µJy of the detected integrated profile).
Single, very bright pulses were also discoverd in the case of PSR B1133+16 by Kramer et al. [2003] who observed the pulsar at four different frequencies (341, 626, 1412, 4850 MHz). The confirmation of them to be giant pulses was later provided by Karuppusamy and Stappers [2008] who examined them in a frequency range from 116 to 173 MHz and identified them to have short widths of about 1 ms and flux densities of about 2000 Jy. Later studies of this pulsar by Karuppusamy et al. [2011] in a frequency range from 110 to 180 MHz confirmed the existence of single, bright pulses, but stated that they were of not giant pulse nature since they did not meet the required minimum energies of 10 times the energy of the AP.
Another pulsar found to emit radio giant pulses was PSR B0031-07 (Kuzmin et al. [2004]). The strongest giant pulses found during the study of Kuzmin et al. [2004] revealed a peak flux density higher by a factor of 120 than the average pulsed emission (that is 530 Jy in the case of the brightest radio giant pulse). In an continuous study Kuzmin and Ershov [2004] detected one strong pulse with a peak flux density of 1100 Jy at a frequency of 40 MHz (in contrast to that they determined the peak flux density of the average emission to 2.7 Jy). Also in the case of this pulsar Karuppusamy et al. [2011] concluded that at a frequency range from 110 to 180 MHz it contains single, bright pulses, but they do not qualify as giant pulses not reaching energies higher than ten times the energy of the average emission. Consequently, this remains a topic of controversy and needs further observations in the future.
A further giant pulse emitter from the group of ordinary pulsars is PSR J1752+2359. It exhibits single pulses with peak flux denstities exceeding the ones from the AP by a factor of 260 (Ershov and Kuzmin [2006]).
Also in the case of other ordinary pulsars than the Crab pulsar high flux densities are an essential characteristic of radio giant pulses independently of the age of the pulsar.

Phase-bound Occurrence

Also in the case of other pulsars than the Crab pulsar, radio giant pulses have been observed to be phase-bound, that is ocurring only at certain rotational phases. Usually these are the phase ranges of the regular pulses. In the case of PSR B1112+50 a clustering of the widths of the single, bright pulses by a factor of 5 around the center of the AP has been observed (Ershov and Kuzmin [2003]). An interesting commonality with the classical Crab pulsar giant pulses (Karuppusamy et al. [2010]) was the observed occurrence of single, bright pulses in the form of groups of pairs and triples according to the observations reported by Ershov and Kuzmin [2003].

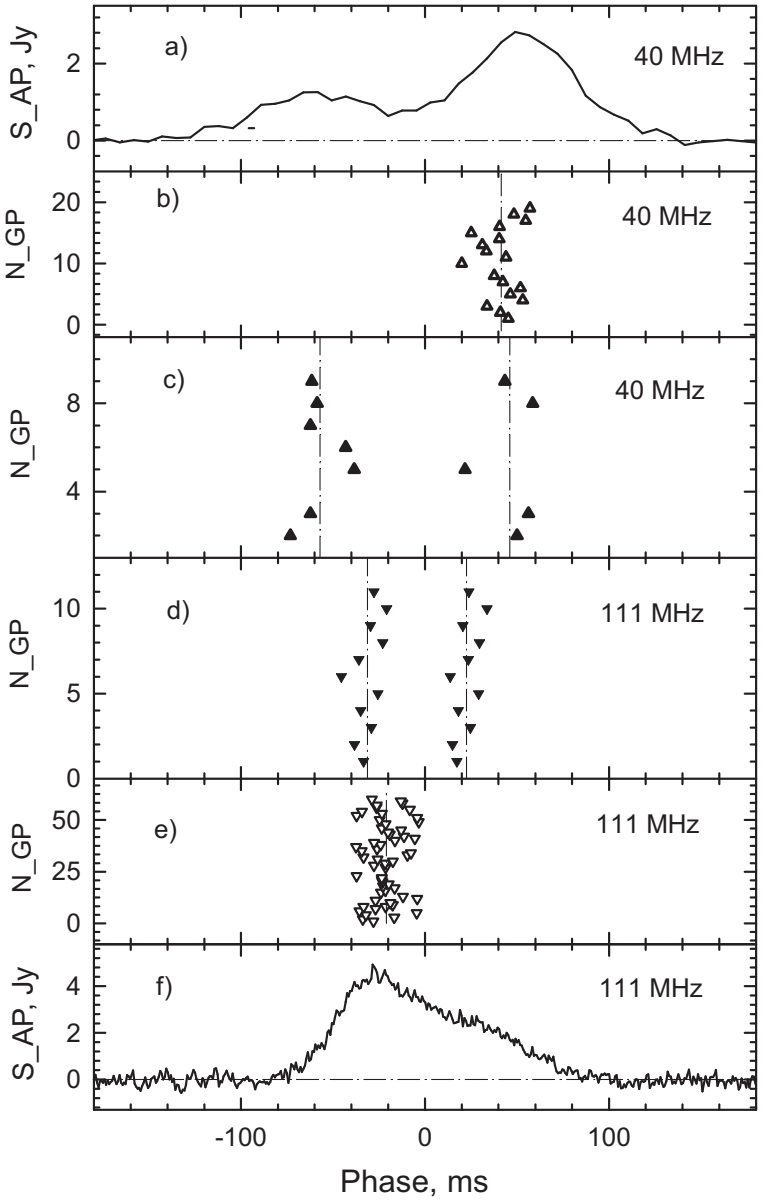

Figure 3.12.: a) Integrated profile of PSR B0031-07 at 40 MHz; b) Phase values of single giant pulses observed at 40 MHz; c) Phase values of double component giant pulses observed at 40 MHz; d) Phase values of double component giant pulses detected at 111 MHz; e) Single pulse phase values of giant pulses detected at 111 MHz; f) Integrated profile of PSR B0031-07 at 111 MHz (Kuzmin and Ershov [2004]).

The occurrence of radio giant pulses only at certain ranges of the rotational phase was also confirmed in the case of PSR B0540-69 (Johnston and Romani [2003], Johnston et al. [2004]). Similar to the giant pulses from the Crab pulsar do the giant pulses from PSR B0540-69 also occur at two specific rotational phase ranges (0.36-0.45 and 0.61-0.66, Johnston and Romani [2003]). It turned out to be problematic to detect the average emission of this pulsar which

is the reason why the X-ray emission profile was used at first to determine the phases of the detected radio giant pulses (see Figure 1 in Johnston and Romani [2003]). The detection of the average emission was later achieved at 1.4 GHz by Johnston et al. [2004] and confirmed also one further specific property of radio giant pulses: Their narrow widths in contrast with the average emission from the pulsar.
In the case of PSR B1133+16 Kramer et al. [2003] discovered that the rotational phase of its single, bright pulses was located at the trailing edge of the leading component of its double pulsed AP (see Figure 17 in Kramer et al. [2003]). High time resolution observations of this pulsar carried out at 4.85 and 8.35 GHz confirmed this result (Figure 3.14, Krzeszowski et al. [2014]). Similar to the Crab pulsar are the brightest pulses located at narrow phase ranges within the average emission profile.
Also in the case of other giant pulse emitting pulsars this kind of radio emission has been observed to be very narrow in contrast with the AP emission. The giant pulses detected from PSR B0031-07 were discoverd to be narrower by a factor of 20 in comparison with the integrated radio emission profile and clustered in its central part (Kuzmin et al. [2004]).
Dual frequency measurements at 40 and 111 MHz carried out by Kuzmin and Ershov [2004] revealed that one part of the detected giant pulses cluster in a window of ± 10 ms in rotational phase near the maximum of the second component of the AP. An interesting feature discovered by Kuzmin and Ershov [2004] was that the phases of its detected giant pulses do not coincide at 40 MHz and at 111 MHz, but are shifted (see Figure 3.12). Giant pulses at 40 MHz do occur at the phase ranges belonging to the second component of the AP (part a) and b) in Figure 3.12) whereas giant pulses detected at 111 MHz occur near the maximum of the first component of the AP (part e) and f) in Figure 3.12). According to the considerations of Kuzmin and Ershov [2004] the reason for this could be either that two emission regions do exist for the giant pulses of this pulsar (similar to the Crab pulsar), or that the giant pulse emission region shifts with frequency. In a search for dual component giant pulses Kuzmin and Ershov [2004] found indeed 12 giant pulses at 111 MHz and five at 40 MHz consisting of two components which are prevalent either at the higher, or at the lower frequency. A comparison of part c) and d) in Figure 3.12 shows that the trailing part of double component giant pulses (part c) coincide with the phases of single giant pulses detected at this frequency (part b)). At 111 MHz the phase values of double component giant pulses of the leading component (part d) coincide with the phase values of single giant pulses detected at this frequency (part e)). According to Kuzmin and Ershov [2004] these observations back up the existence of two emission regions for giant pulses in the case of PSR B0031-07. Double component giant pulses are not uncommon and have been detected also in the case of the Crab pulsar (Karuppusamy et al. [2010]) as well as confirmed in the case of PSR B0031-07 by Karuppusamy et al. [2011] who detected double component pulses in the frequency range from 110 to 180 MHz (see Figure 3 in Karuppusamy et al. [2011]).
One other giant pulse emitter known as PSR J1752+2359, emits giant pulses which cluster at rotational phases near the middle of the AP as was reported by Ershov and Kuzmin [2006].
Deducing from the reported observations the emission phases of radio giant pulses from ordinary pulsars are apparently coinciding with the average emission from the pulsar. The existence of double component giant pulses was verified at the time when this thesis was written for the Crab pulsar and PSR B0031-07.

Power Law Intensity Distributions and Spectral Indices
A distribution of the intensities of radio giant pulses which follows the course of a power-law

has been observed to be a specific characteristic of the latter (see Figure 3.13). This is currently one of the strongest arguments in favour of radio giant pulses (together with high flux densities). The value of the power-law index varies with each pulsar: $\alpha \simeq$-3.6 (PSR B1112+50, Ershov and Kuzmin [2003]), α=-4.8 (PSR B0031-07, Kuzmin and Ershov [2004]), α=-3.0$\pm$0.4 (PSR J1752+2359, Ershov and Kuzmin [2006]).
In the case of PSR B1133+16 it was unclear in the beginning if its single, bright pulses observed by Kramer et al. [2003] were of giant pulse, or giant micropulse nature (details on the latter can be found in Cairns [2004]) since no power-law distribution of their intensities could be verified by Kramer et al. [2003]. This was achieved later with low frequency measurements carried out by Karuppusamy et al. [2011] (see Figure 5 in Karuppusamy et al. [2011]). It was mentioned by Karuppusamy et al. [2011] that higher sensitivity measurements and resulting better statistics in the low frequency range (achieveable for example with LOFAR) could help to improve this result.
Hence also in the case of other ordinary pulsars than the Crab pulsar (as far as was reported by the referenced authors), the intensities of the brightest single pulses follow a power-law distribution independently of the age, rotation period, or first derivative of the latter.

Polarization Properties
Polarization studies of giant pulses are usually carried out for the Crab pulsar (Chapter 3.1) and millisecond pulsars (see page 81). However, some studies of single pulse polarisations exist as is shown for PSR B1133+16 by Karastergiou et al. [2002] and for PSR B0031-07 by Suleimanova and Pugachev [2002].

Wideband Occurrence
Due to poor statistics and maybe also to the complexity of single pulse observations, the wideband occurrence of giant pulses in the case of other pulsars than the Crab pulsar has not been extensively examined yet.
An extensive analysis of giant pulses from PSR B1112+50, PSR B1133+16 and PSR B0031-07 was carried out by Karuppusamy et al. [2011]. All three pulsars were observed in a frequency range from 110 to 180 MHz with the WSRT. The observations of PSR B1112+50 revealed the assignment of the observed pulses to a definite phase range as problematic since the pulsar has double peak structure which is prevalent at higher frequencies (1400 MHz, Wright et al. [1986]) and is blurred towards lower frequencies (328 MHz, Weltevrede et al. [2006]).
In the case of PSR B1133+16 Kramer et al. [2003] could identify 40 bright single pulses at 4850 MHz with a mean flux density higher than ten times the mean (a threshold which was originally set by Karuppusamy et al. [2010] for Crab pulsar giant pulses). The three brightest pulses could be also identified simultaneously at lower frequencies (see Figure 17 in Kramer et al. [2003]). The fact that this pulsar shows also other forms of anomalous single pulse phenomena like pulse nulling (Herfindal and Rankin [2007]), makes the analysis of its single pulses more complex. Bhat et al. [2007] stated that pulse nulling does not occur simultaneously at all frequencies in the case of this pulsar which does not limit the analysis of broadband single pulses. Karuppusamy et al. [2011] could verify the bright, single pulses from both AP components throughout the whole frequency range from 110 to 180 MHz. This kind of behaviour is not seen at higher frequencies as was recently shown by high time resolution observations of this pulsar at 4.85 and 8.35 GHz (Krzeszowski et al. [2014]). Figure 3.14 shows clearly that most of the pulses with higher fluxes do occur prominently at the trailing edge of the first component

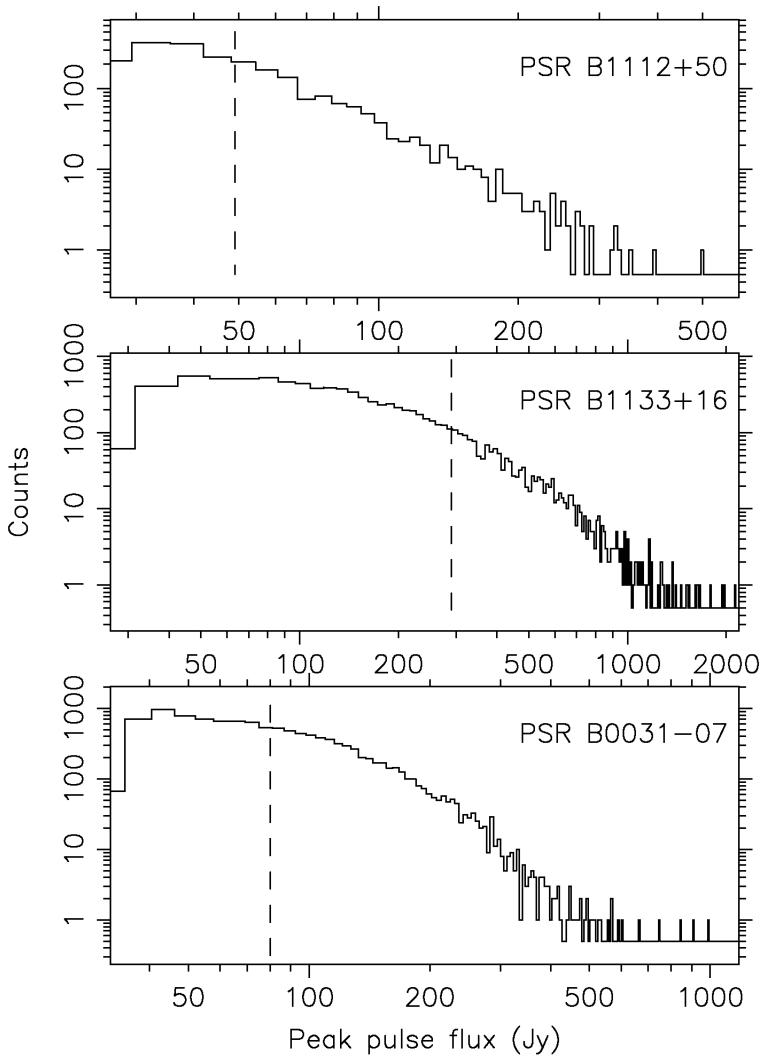

Figure 3.13.: Peak flux distributions (counts of giant pulses observed in a given bin of the peak flux) of single, bright pulses from slow rotating pulsars PSR B1112+50, PSR B1133+16 and PSR B0031-07 (Karuppusamy et al. [2011]).

of the average emission profile. The second component of the latter seems to be the source of pulses with low fluxes (compare the observations made at 4.85 and 8.35 GHz in Figure 3.14). In spite of the vast frequency range at which this pulsar was already examined (from 16.7 MHz to 32 GHz according to Krzeszowski et al. [2014]), the frequency range at which this transition takes place is not known.

Also for the slow rotating pulsar PSR B0031-07 two giant pulses simultaneously observed at 40 and 111 MHz were reported by Kuzmin and Ershov [2004]. The investigations of this pulsar indicated that its giant pulse rate depends upon the observing frequency. Kuzmin and Ershov [2004] observed a giant pulse at 40 MHz to occur approximately once in 85 rotation periods, whereas at 111 MHz the occurrence was once in 11 000 periods. The authors emphasise the necessity of further investigations of this pulsar to examine its wide band behaviour among

others.
The occurrence of the single pulses from PSR B0031-07 was also confirmed in a frequency range from 116 MHz to 173.75 MHz (see Figure 3 in Karuppusamy et al. [2011].

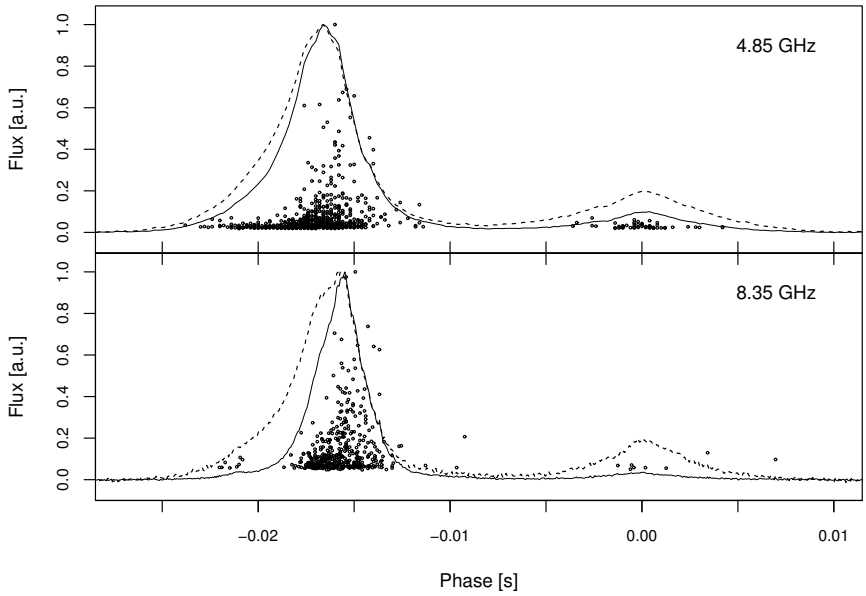

Figure 3.14.: Flux measuerements resulting from high time resolution observations of PSR B1133+16 consisting of the AP (dotted line), the profile resulting from single pulses with a S/N ratio of more than $20\,\sigma$ (solid line) and single pulses with S/N$\geq$ 20 (dots) (Krzeszowski et al. [2014]).

Brightness Temperatures
Radio giant pulses have been observed to have very high brightness temperatures which imply the involvement of coherent emission processes. This was examined extensively in the case of the Crab pulsar (see previous chapter), but also has been determined for other radio giant pulse emitting pulsars. For PSR B1112+50 a value of $T_B \geq 10^{26}$ has been determined (Ershov and Kuzmin [2003]). The authors reported at this point that better statistics were needed for the determination of a more precise value. A value of T_B=3.51·10^{26} K was later published by Karuppusamy et al. [2011].
High brightness temperatures have been also reported in the case of other ordinary pulsars which emit radio giant pulses: T_B=1.32·10^{27} K (PSR B0031-07, Karuppusamy et al. [2011]), $T_B \geq$ 2·10^{28} K (PSR J1752+2359, Ershov and Kuzmin [2006]), T_B=1.93·10^{27} K (PSR B1133+16, Karuppusamy et al. [2011]).
Radio giant pulses emitted by ordinary pulsars are characterized by high brightness temperatures which is a further commonality with the "classical" Crab pulsar giant pulses.

High-energy Emission

In search for a possible explanation why only certain pulsars apparently show radio giant pulses, also the existence of HE emission (meaning in this context at higher frequency ranges than radio) in the case of some of the mentioned pulsars has been discussed as a potential commonality in search for a solution of the emission mechanism behind radio giant pulses.

The pulsed emission from the Crab pulsar was also discovered at X-ray wavelengths and searches for a correlation between radio giant pulses and X-ray photons were carried out, but so far without any success (see Chapter 3.2).

The only extragalactic pulsar so far detected to emit radio giant pulses, PSR B0540-69, was originally discoverd by its X-ray emission (Seward et al. [1984]). Its detection at radio wavelengths was achieved a couple of years later at 640 MHz (Manchester et al. [1993a]). As already mentioned in one of the previous chapters, PSR B0540-69 emits radio giant pulses in two phase regions (0.36-0.45 and 0.61-0.66, Johnston and Romani [2003]). These regions occur 6.7 ms before and 5.0 ms after the midpoint of the X-ray pulse profile (Johnston et al. [2004]). Hence also this pulsar exhibits radio giant pulses which have broader counterparts in phase at X-way wavelengths similar to the Crab pulsar. The reported observations leave several questions open about the possible emission region of radio giant pulses in the outer magnetosphere of PSR B0540-69. Shortly after its discovery PSR B0540-69 was also discovered at optical wavelengths (Middleditch and Pennypacker [1985]). Its optical magnitude was determined to 22.7 making it the second brightest pulsar after the Crab pulsar. The light curve of the pulsar at optical wavelengths was discovered to consist of one broad peak (Middleditch et al. [1987]) similar to the one discovered at X-ray wavelengths (Seward et al. [1984]) suggesting similar emission regions in the magnetosphere of the pulsar. The faintness of PSR B0540-69 at optical wavelengths makes it an object to be adressed with very large optical telescopes. The advent of the E-ELT will possibly enable first correlation studies of its radio giant pulses with optical photons (Mignani et al. [2010b]). PSR B0540-69 has been also detected at infrared wavelengths as was recently reported by Mignani et al. [2012]. Its pulsed emission is similar as in the case of the Crab pulsar, detectable over large ranges of the electromagnetic spectrum making it accessible to various kinds of single pulse studies.

Another giant pulse emitting pulsar which was detected also at X-rays, was PSR B1133+16 (Kargaltsev et al. [2006]). An optical counterpart of this pulsar was detected by Zharikov et al. [2008] and later confirmed by Zharikov and Mignani [2013b]. So far this pulsar has not been detected at γ-ray wavelengths with the Fermi satellite (Krzeszowski et al. [2014]). Due to insufficient statistics no single pulse correlation studies were carried out at the time when this thesis was written.

b) Millisecond Pulsars

The list of millisecond pulsars which are known to emit radio giant pulses, currently contains PSR B1937+21 (Wolszczan et al. [1984]), PSR B1821-24 (Romani and Johnston [2001]), PSR B1957+20 (Joshi et al. [2004], Knight et al. [2006b]) and PSR J1823-3021A (Knight [2007]). To emphasise differences and commonalities with the giant pulse emission from ordinary pulsars (especially with the Crab pulsar), a concise overview of the properties of giant pulses from millisecond pulsars is given in this chapter.

Flux Densities

The flux densities of radio giant pulses in the case of millisecond pulsars are also remarkably higher than the corresponding quantities of their regular pulses.

The original millisecond pulsar PSR B1937+21 discovered by Backer et al. [1982] was examined shortly after its discovery with regard to its single pulses by Wolszczan et al. [1984]. The authors observed the pulsar at 431 MHz and around 1400 MHz with the Arecibo radio telescope and detected single pulses which occurred once about every 400 000 rotation periods. They determined the peak flux densities of these pulses to be two orders of magnitude above the noise level. They did not find any direct indication for radio giant pulses at this time and reported that the intensity histograms of single pulses at the phase of the P1 and the P2 did not show anything unusual, but they verified for the first time the existence of single, bright pulses in the case of this pulsar. Subsequent studies carried out by Sallmen and Backer [1995] gave the first hint that this pulsar might emit giant pulses like the Crab pulsar.

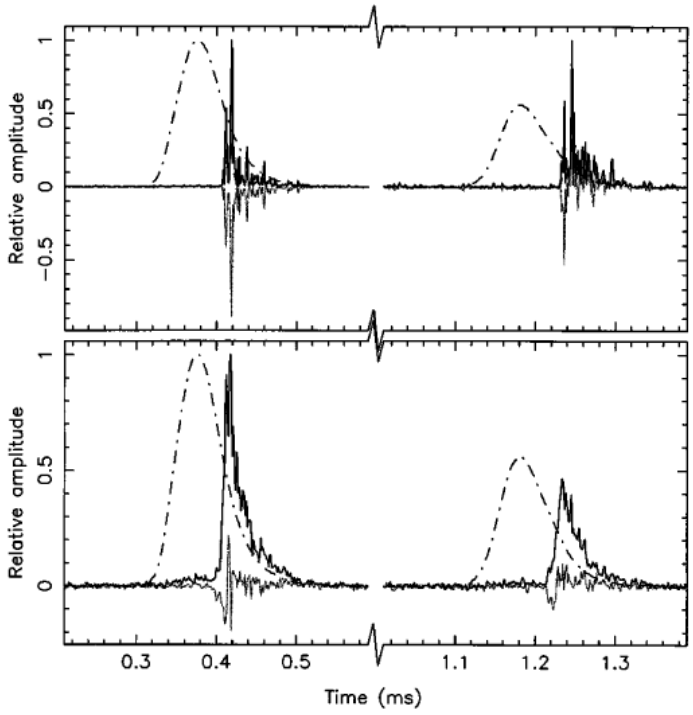

Figure 3.15.: Giant pulses at the phase ranges of P1 and P2 from PSR B1937+21 detected by Cognard et al. [1996]. The top figure shows the brigthest single pulses and the bottom figure presents the average shapes of 60 strongest pulses in the region of its P1 and P2. The solid line corresponds to the total intensity and the dot-dashed line is the AP of all $1.7{\cdot}10^6$ single pulses detected by Cognard et al. [1996] (Figure 2 from Cognard et al. [1996]).

The authors observed the pulsar at 430 MHz with the Arecibo radio telescope. Examining the energy of the recorded pulses they determined the them to extend from the average pulse energy by about six times. Their data provided also one very bright pulse with an energy of about 20 times the average pulse energy confirming earlier observations by Wolszczan et al. [1984]. A re-analysis of this data with full time resolution led to the detection of several strong pulses with pulse energies in the range from 100 to 400 times the average pulse energy (Backer [1995]).

The single pulses were extensively studied by Cognard et al. [1996] who observed the pulsar with the Arecibo radio telescope at 430 MHz. They detected a total of $1.7 \cdot 10^6$ single pulses from PSR B1937+21 and verified that one pulse in about 10 000 pulses had a flux density of more than 20 times the mean flux density in the on pulse phases (that is, the phase ranges of the pulsed emission). With their analysis they gave proof that the single, bright pulses observed in the case of this pulsar were of giant pulse nature identifying the second giant pulse emitter after the Crab pulsar. The first (non-simultaneous) multifrequency studies in the case of this pulsar were reported by Kinkhabwala and Thorsett [2000]. They observed PSR B1937+21 with the Arecibo radio telescope at 430 MHz, 1420 MHz and 2380 MHz. They determined an integrated flux density of the brightest pulses in their sample of at least 80 Jy µs. An extensive study of radio giant pulses from PSR B1937+21 was carried out by Soglasnov et al. [2004] who observed the pulsar at 1650 MHz with the 70 m NASA/JPL radio telescope. They identified about 309 giant pulses in their data set, some of them exceeding the peak flux density of 65 000 Jy (see Figure 1 in Soglasnov et al. [2004]. For comparison: The peak flux density of Crab pulsar giant pulses with nanosecond duration was reported by Hankins and Eilek [2007] to be higher than 2 MJy). Regarding their energies, Soglasnov et al. [2004] found out that the energies of the strongest and the weakest P1 giant pulses amount to 60 and 0.3 times the mean energy of a non-giant, or normal P1. In the case of P2 they observed the strongest and the weakest giant pulses to be 50 and 0.4 times the mean energy of a normal P2. This comparison shows that similar as in the case of the Crab pulsar, also PSR B1937+21 exhibits stronger P1 giant pulses. However, multifrequency observations of the Crab pulsar revealed that its regular emission components change their intensities at lower and higher frequencies (Moffett and Hankins [1996]).
The detection of radio giant pulses in the chronologically second millisecond pulsar PSR B1821-24 was reported by Romani and Johnston [2001]. From their sample of 16 single pulses exceeding the S/N by $4\,\sigma$, they determined the brightest one to have an integrated energy of $\sim$755 Jy µs (in contrast with 9.3 Jy µs being the energy of an average pulse and a $\sim$3 mJy continuum flux). Since this energy amounts to 81 times the average energy, exceeding the set threshold of ten times the average energy (Karuppusamy et al. [2011]), the single, bright pulses qualify in this case as giant pulses according to the calculations of Romani and Johnston [2001].

Phase-bound Occurrence
Also in the case of millisecond pulsars giant pulses were observed to occur only at certain phase ranges. In the case of PSR B1937+21 giant pulses were observed to occur near the phase ranges of its P1 and P2 by Backer [1995]. One specific difference to the giant pulses of the Crab pulsar became obvious from their study: The giant pulses from this pulsar were detected at the trailing edges of the regular pulsed components (at a distance of about 25 µs according to Backer [1995]). This result was later confirmed independently by Cognard et al. [1996] who determined the time delay between the average giant pulse and the integrated profile to be 38±4 µs for the P1 and 52±4 µs for the P2 (Figure 3.15). The authors described the detected radio giant pulses to have short rise times of approximately 5 µs (Figure 3.15). They emphasised therefore the importance of the detected giant pulses with regard to high precision timing measurements. The occurrence of radio giant pulses at the trailing edges of the AP as seen by Cognard et al. [1996] and Backer [1995] at 430 MHz, was also detected at 1420 and 2380 MHz by Kinkhabwala and Thorsett [2000]. The authors determined the time distance between the peak of the P1 and the average giant pulse to be in the range from 57 till 58 µs and between the peak of the P2 and the corresponding giant pulse from 65 to 66 µs for all three frequencies. Kinkhabwala

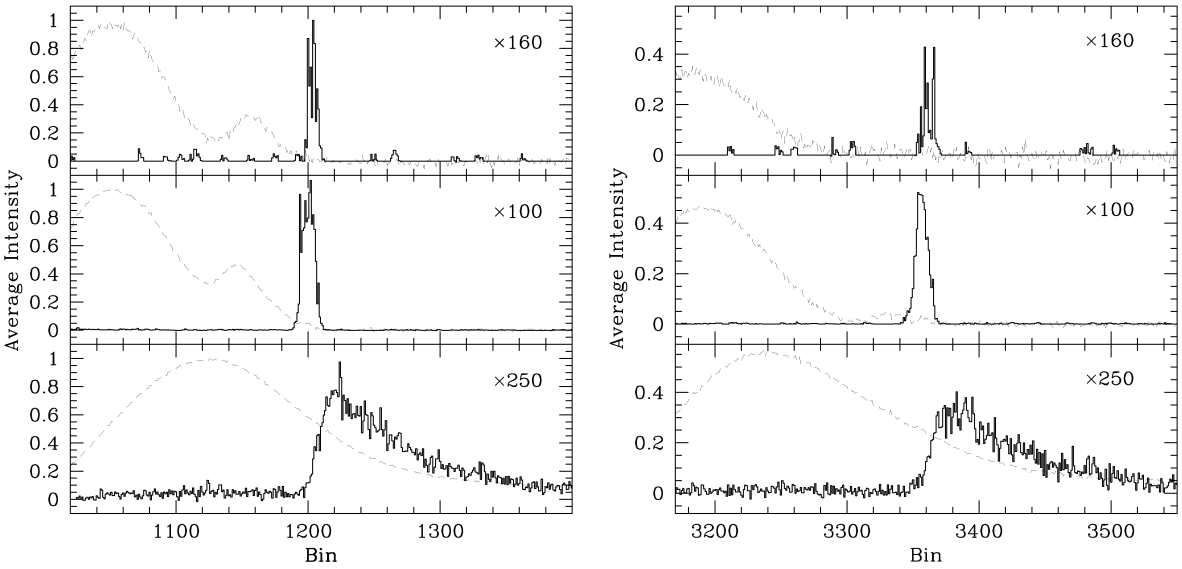

Figure 3.16.: Phase ranges of giant pulses from PSR B1937+21 for the P1 (left plot) and the P2 (right plot) at 2380 MHz (top), 1420 MHz (middle) and 430 MHz (bottom). The solid line stands in both cases for the average giant pulse emission and the dashed line represents the normal emission (Figure 2 and 3 from Kinkhabwala and Thorsett [2000]).

and Thorsett [2000] verified the emission window of the detected radio giant pulses of less than one degree of the rotational phase of this pulsar. The phase ranges of occurrence of giant pulses for P1 and P2 are shown in Figure 3.16. The narrow emission windows of radio giant pulses in the case of PSR B1937+21 (less than 10 µs according to Kinkhabwala and Thorsett [2000]) show a fundamental difference to Crab pulsar giant pulses, which have been observed to occur in the whole range of the pulsed components of the AP like in the case of P1 giant pulses with nanosecond widths (compare Figure 3.7). While most of the first studies of PSR B1937+21 were carried out at 430 MHz, a further investigation of its giant radio pulses was reported by Vivekanand [2002]. They detected seven radio giant pulses at 326.5 MHz with the Ooty Radio Telescope. Six of them were associated with the phase ranges of the P1 and only one with the P2 (see Figure 2 in Vivekanand [2002]). Examining only P1 giant pulses due to these statistics, Vivekanand [2002] determined that the respective giant pulses arrived in a phase window of about 47 µs confirming earlier results by Kinkhabwala and Thorsett [2000]. Furthermore they determined the distance between the mean pulse phase of giant pulses and the peak of the average P1 to be about 8 ns which was not in agreement with the compared observations by Kinkhabwala and Thorsett [2000]. Vivekanand [2002] commented on this as a result of their insufficient observational equipment for observations of this pulsar. An extensive study of the giant pulses from PSR B1937+21 were carried out by Soglasnov et al. [2004]. From their sample of 309 giant pulses they detected 190 at the phase ranges of the P1 and 119 at P2 phase ranges. They confirmed the occurrence of giant pulses at the trailing edges of the AP (see Figure 7 in Soglasnov et al. [2004]). An interesting feature of the giant pulses from PSR B1937+21 noted by Soglasnov et al. [2004] is that while P1 giant pulses are blended with

the end of the trailing edge of the average emission profile, P2 giant pulses occur outside the average emission window (see Figure 13 in Soglasnov et al. [2004]). In other words, P1 giant pulses coincide in phase with the regular emission and Interpulse giant pulses do not. This can be seen as a further difference to Crab pulsar giant pulses. Soglasnov et al. [2004] measured the phase windows where giant pulses did occur in their data set. They determined the center of P1 giant pulses delayed by 58.3±0.3 µs from the peak of the strongest pulsed component of the average P1 emission. In the case of P2 giant pulses they calculated their center of emission as delayed by 65.2±0.5 µs with regard to the average P2 emission. With these values they confirmed the results reported earlier by Kinkhabwala and Thorsett [2000]. The total range where giant pulses occur was determined as 10.7 µs for P1 giant pulses and 8.7 µs in the case of P2 giant pulses. With regard to P1 giant pulses Soglasnov et al. [2004] could even make a more accurate subdivision by determining 97 % of the giant pulses in their data to occur within an emission window of 5.8 µs and the remaining 3 % at ranges with a width of 4.8 µs (see Figure 8 in Soglasnov et al. [2004]). This way they confirmed the characteristic of giant radio pulses to occur only at specific and narrow ranges of the rotational phase.
Although extensively studied, PSR B1937+21 is not the only millisecond pulsar with radio giant pulse emission. In the case of PSR B1821-24 Romani and Johnston [2001] reported the occurrence of the brightest pulses in a narrow region of the first component of its AP (see Figure 3.17). The AP of this pulsar consists of three different components referred to as P1, P2 and P3 (Figure 3.21). Backer and Sallmen [1997] reported about a variable behaviour of the P2 component which is more prominent at higher frequencies whereas the P1 component is dominant at lower frequencies. Radio giant pulses from PSR B1821-24 have been so far detected at the trailing edge of the P1 and P3 emission component (Bilous et al. [2015]). It is still an open question why no giant pulses occur at the phase range of the P2 component.

Power Law Intensity Distributions and Spectral Indices

The first extensive studies in the case of PSR B1937+21 were carried out by Cognard et al. [1996]. They determined the index of the power-law distribution of single, bright pulses to be α=-1.8. Later studies by Kinkhabwala and Thorsett [2000] confirmed this result with approximately the same value of α at 430 MHz, 1420 MHz and 2380 MHz (see Figure 7, 8 and 9 in Kinkhabwala and Thorsett [2000]). At the latter frequency the authors observed that P1 giant pulses are brighter than P2 giant pulses. This had been already found by Cognard et al. [1996] (see Figure 3 in Cognard et al. [1996]).
Examinations of the energy distribution of radio giant pulses from PSR B1937+21 at the P1 and at the P2 carried out by Soglasnov et al. [2004], confirmed the existence of a power law with an index of α=-1.40±0.01 (Figure 3.18). The authors could not identify a difference between the distributions of giant pulses from the P1, or the P2. Extrapolating this power law to lower energies, they argued that if it would continue towards lower energies as well, a peak in the average emission profile of the pulsar should be visible which has not been observed so far indicating the existence of a cutoff. The flattening of the curves in Figure 3.18 at lower energies, is caused by interstellar scintillation. The effect makes it impossible to see a sharp cutoff of the energy distributions of giant pulses towards the detection threshold. Under the assumption that the power law distribution of giant pulses is also valid below their threshold, Soglasnov et al. [2004] corrected the rate of occurrence of giant pulses. The corrected curve is shown in Figure 3.18 by the dashed line which extends the power law fit to the energy corresponding to the detection threshold of this experiment. Estimating the low energy cutoff of giant pulses,

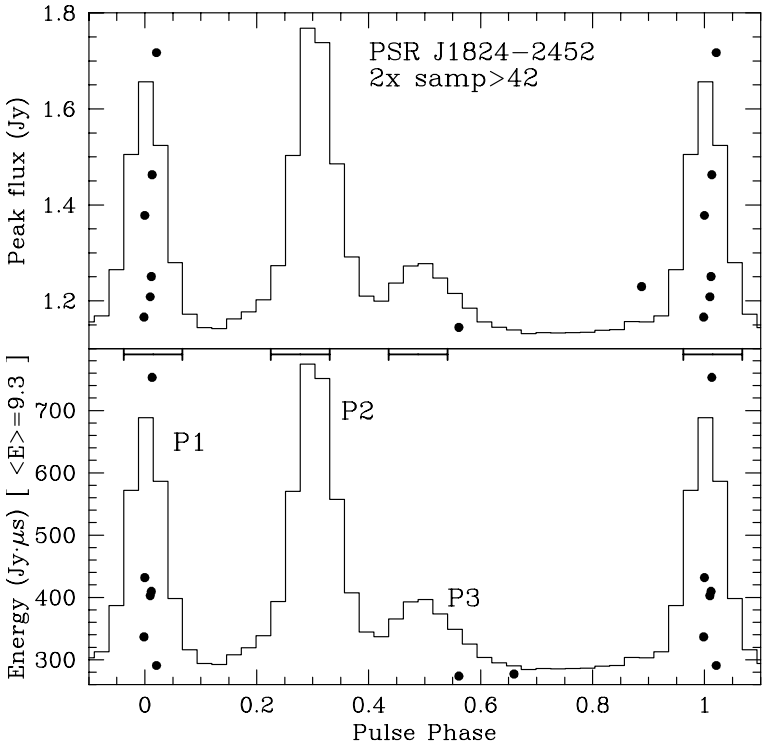

Figure 3.17.: Upper plot: Integrated profile of PSR B1821-24 with peak fluxes of brightest pulses scattering at the phase ranges of the P1 component; lower plot: Integrated energy of brightest single pulses overplotted with the integrated profile (Figure 1 from Romani and Johnston [2001]).

Soglasnov et al. [2004] suggested that P1 giant pulses have a cutoff at a flux density of 16 Jy and P2 giant pulses at 5 Jy. Besides, they verified the occurrence of radio giant pulses in the case of P1 and P2 also below their detection threshold by subtracting the giant pulse profile with the P1 and P2 APs resulting in the necessity to multiply giant pulse profiles by different factors in order to get no pulse component in the difference profiles (see Figure 13 in Soglasnov et al. [2004]).
Wideband observations of the millisecond pulsar PSR B1821-24 carried out by Bilous et al. [2015] indicate a power law energy index of giant pulses occurring at the P1 and P3 component (Figure 3.21) of -1.8±0.3. This value is consistent with previous measurements carried out by Knight et al. [2006a] in which case the power law index is -1.6.

Pulse Widths
Apart from the Crab pulsar, the widths of the giant pulses from PSR B1937+21 and PSR B1821-24 have been examined. Already Cognard et al. [1996] noticed the short rise times of about 5 µs in the case of the giant pulses from PSR B1937+21. A fitting procedure of average giant pulses with Gaussians by Kinkhabwala and Thorsett [2000] revealed that at a frequency of 430 MHz giant pulses at the phase ranges of P1 and P2 have widths of 6.6 µs and 6.4 µs respectively. At 1420 MHz they determined the widths as 4.3 µs for the P1 and 4.1 µs for the P2. At 2380 MHz they calculated the widths as 3 µs for the P1 and 4 µs for the P2.

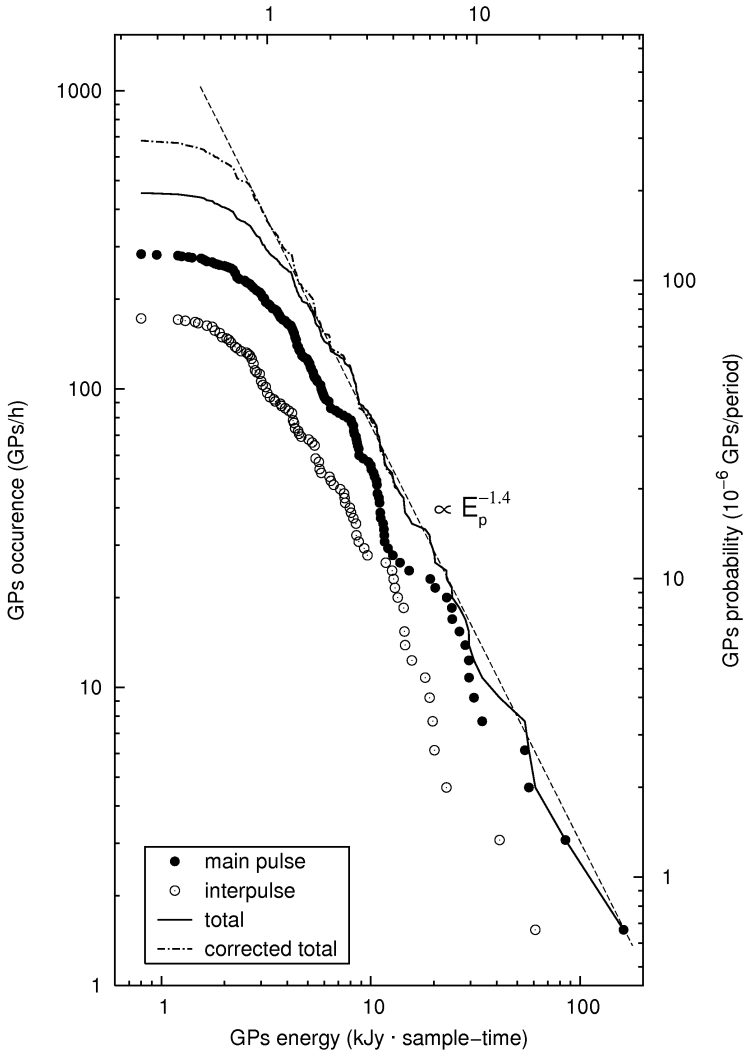

Figure 3.18.: Cumulative distributions of giant pulse energies in the case of PSR B1937+21 at the phase ranges of the P1 (filled circles) and the P2 (open circles). The cumulative distribution of all giant pulses altogether is shown by the solid line. The dashed line is the least square power law fit to the energies of giant pulses as stated in Soglasnov et al. [2004] (Figure 12 from Soglasnov et al. [2004]).

An extended study of the widths of giant pulses from PSR B1937+21 was carried out by Soglasnov et al. [2004]. Aiming for a correction of the effects caused by interstellar scattering in the data, Soglasnov et al. [2004] estimated the intrinsic widths of the giant radio pulses from PSR B1937+21 by determining the response of a scattering medium to a pulse in the form of a δ function (details are given in Chapter 3.1.3 of Soglasnov et al. [2004]). They compared the resulting response minute by minute with the widths of the observed giant pulses in their data (the latter were also averaged minute by minute for this purpose) and found an agreement in shape, separation and number of spikes. Simulating giant pulses with widths of 15, 30 and 45 ns, they found the best match between simulated and real giant pulses with widths of about

15 ns. The authors subdidived between giant pulses consisting of only one sharp peak and with a more complex structure. Their estimation of a width about 15 ns is valid in the first case (see Figure 6 in Soglasnov et al. [2004]). Since a full correction of the interstellar scattering effects are not feasable, Soglasnov et al. [2004] concluded that the true width of giant radio pulses could be also smaller than 15 ns. Similar to the Crab pulsar, also the giant pulses from PSR B1937+21 exhibit pulse widths down into the nanoseconds range albeit they have not been fully resolved in both cases (compare Hankins and Eilek [2007] with regard to the Crab pulsar). Short pulse widths have also been reported by Knight et al. [2006a] with regard to PSR B1821-24. According to their measurements its giant pulses are 100 ns wide at maximum. The shortest detected giant pulse in their data set has a width of 20 ns. Short widths of the giant pulse emission from PSR B1821-24 are also indicated by Bilous et al. [2015] ranging from 10 µs to 20 µs and from 41 µs to 164 µs (see Chapter 4.2 in Bilous et al. [2015] for further details). However, the authors note that in the first case the giant pulses from PSR B1821-24 are unresolved.
Very short widths ranging from microseconds to nanoseconds are apparently also a characteristic millisecond pulsars which emit giant pulses.

Polarization Properties
The polarization properties of radio giant pulses in the case of other giant pulse emitting pulsars than the Crab pulsar, were studied mostly in the case of PSR B1937+21. Cognard et al. [1996] reported that the P1 was linearly polarized to more than 50 % with little circular polarization whereas the P2 had a maximum linear polarization of about 13 % with some percent of circular polarization. A recent polarimetric study of giant pulses from PSR B1937+21 in a frequency range from 2052 till 2116 MHz has been reported by Zhuravlev et al. [2013]. They observed a random behaviour of the polarization of radio giant pulses. While they found clear polarization patterns and evolution of the polarization angle for the AP emission components of this pulsar, some of the observed giant pulses showed a high amount of linear and circular polarization of both signs without any definite evolution their polarization angles (see Figure 3 and 4 in Zhuravlev et al. [2013]). According to Zhuravlev et al. [2013] the Stokes parameters of the giant pulse distributions are random (see Figure 5 in Zhuravlev et al. [2013]).
Knight et al. [2006a] examined the polarimetric behaviour of the first discovered millisecond pulsar in a globular cluster named PSR B1821-24 (Lyne et al. [1987]). They report a circular polarization of about 60 % of its radio giant pulse emission with an apparently random behaviour of the position angles (see Figure 6 in Knight et al. [2006a]).
A similar behaviour as reported by Zhuravlev et al. [2013] for PSR B1937+21, has been reported by Bilous et al. [2015] for PSR B1821-24. According to their broadband polarization studies from 720 till 2400 MHz the spectra of giant pulses from PSR B1821-24 are patchy and the amount of linear and circular polarization changes apparently at random within a single patch and among different patches as well (see Figure 4 and 5 in Bilous et al. [2015]). An interesting result which they draw from their observations is that the P3 component shows a jump in the position angle (by about 15°) of the linear polarization at the trailing edge where the giant pulse emission window is (Figure 3.21). A definite description of the polarimetric behaviour of giant pulses from PSR B1821-24 is still to be gained.

Wideband Occurrence
The wideband occurrence of giant pulses was also examined in the case of millisecond pulsars albeit not that extensively as in the case of the Crab pulsar. Simultaneous dual-frequency observations of giant pulses from PSR B1937+21 were carried out by Popov and Stappers [2003].

They observed the pulsar with the WSRT in a frequency range from 2210 to 2250 MHz and with the 64 m Kalyazin radio telescope from 1414 to 1446 MHz. The authors detected ten giant pulses at frequencies between 2210 and 2250 MHz and 15 giant pulses between 1414 and 1446 MHz. Nevertheless they could not detect simultaneously observed giant pulses in both frequency ranges which represents a clear difference to the broadband giant pulses from the Crab pulsar. Popov and Stappers [2003] argued that the absence of simultaneously giant pulses could be a distinctive characteristic of PSR B1937+21.
A recent wideband study of PSR B1821-24 carried out by Bilous et al. [2015] has led to the detection of 476 giant pulses in a frequency range from 720 till 2400 MHz. However, not all of them were detected simultaneously at different frequencies (see Table 2 in Bilous et al. [2015] for details).

Brightness Temperatures
High brightness temperatures are also a feature of giant pulses in the case of millisecond pulsars. Soglasnov et al. [2004] determined in the case of the brightest giant pulses which they found (65 000 Jy as stated in the previous chapters) and the corresponding widths of smaller than, or equal to 15 ns, brightness temperatures of at least 5×10^{39} K commenting on them as the highest observed values in the Universe at the time of their publication. For the weakest giant pulse in their data set (that is at the low end cutoff of their cumulative energy distribution shown in Figure 3.18), they calculated brightness temperatures of higher than 10^{36} K. Consequently, also in the case of PSR B1937+21 giant pulses exhibit very high brightness temperatures similar as it was observed for the Crab pulsar (see for example Hankins and Eilek [2007]).
However, PSR B1937+21 is not the only giant pulse emitting millisecond pulsar with this characteristic. Knight et al. [2006a] reported th detection of giant radio pulses from PSR B1821-24 at 2700 MHz with brightness temperatures of 5×10^{37} K. Apparently this is a characteristic inherent to both, ordinary and millisecond pulsars, which exhibit radio giant pulse emission.

High-energy Emission
A common property of most of the currently known giant pulse emitting millisecond pulsars is a pulsed X-ray emission profile. The original millisecond pulsar PSR B1937-21 was discovered at X-ray wavelengths above 2 keV by Takahashi et al. [2001]. They reported the existence of a pulse profile consisting of one pulsed component in the case of this pulsar. Later studies by Nicastro et al. [2002] proved the existence of double peak structure also at X-ray wavelengths (see Figure 2 in Nicastro et al. [2002]). An extensive timing analysis was carried out by Cusumano et al. [2003] who verified the existence of the double peak pulsed profile up to about 20 keV. The most interesting result from this work is the detection that the radio and X-ray AP of this pulsar are not exactly aligned in rotational phase (Figure 3.19). Since the giant pulses from this pulsar occur at the trailing edges of its regular AP components as was reported earlier, they are well aligned with the components of the X-ray AP. This suggests a common region of origin in the magnetosphere of PSR B1937-21. However, Cusumano et al. [2003] note that they did not find any enhancement connected to radio giant pulses in the X-ray data they used for the study. The phase alignment of radio giant pulses and X-ray photons has been confirmed independently by Guillemot et al. [2012] who discovered PSR B1937-21 at γ-ray wavelengths with Fermi LAT. However, they note that according to their observations the γ-ray and X-ray AP is slightly misaligned suggesting different emission regions in the magnetosphere of the pulsar. The radio and and γ-ray AP on the other hand is phase aligned according to Guillemot et al. [2012]. This is an interesting feature since it describes an additional difference

to the Crab pulsar and its giant pulses.
The second giant pulse emitting millisecond pulsar PSR B1821-24 was detected at X-ray wavelengths (Rots et al. [1998]). They observed the radio and the X-ray P1 pulse component (Figure 3.17) nearly coinciding in time with a lag of 0.02 rotaton periods, or 60±20 µs and the radio pulse leading (see Figure 2 in Rots et al. [1998]). The P3 component in the radio AP (Figure 3.17) leads the second observed X-ray peak observed by Rots et al. [1998] by 250±60 µs. Romani and Johnston [2001] compared the profile consisting of their 16 radio giant pulses with the average radio and X-ray profile (the latter obtained by Rots et al. [1998]). They verified that the giant pulse P1 component lags the P1 component from the average emission profile of the pulsar by about 80 µs.

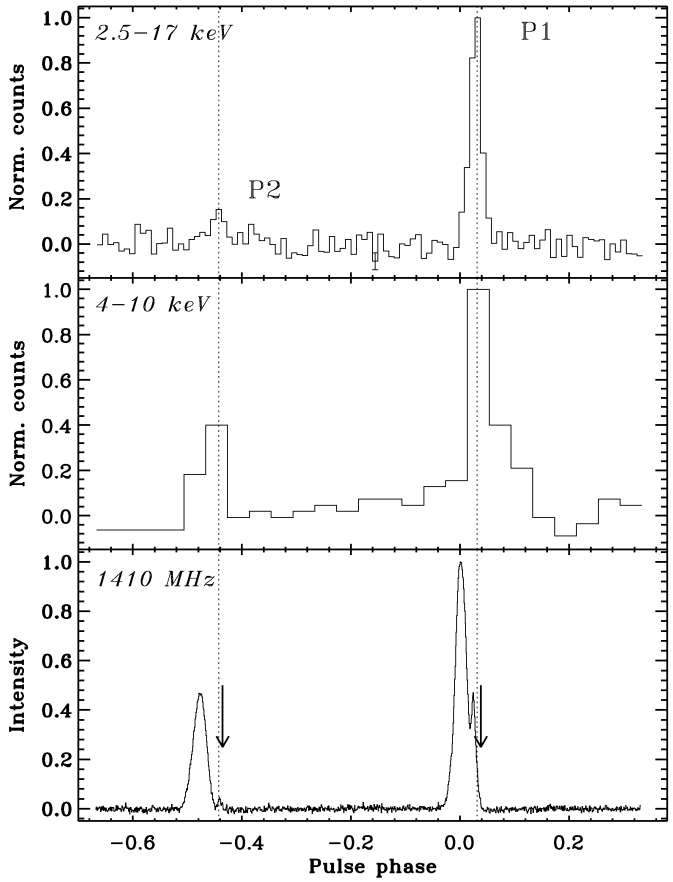

Figure 3.19.: Multiwavelength AP of PSR B1937+21 (Cusumano et al. [2003]). From top to bottom: Pulse profile observed 1) with the RXTE in an energy band from 2 to 17 keV, 2) with BeppoSAX in an energy band from 4 to 10 keV, 3) with Effelsberg radio telescope at 1.4 GHz. The top and middle figure are aligned according to the P1 emission component. The figure was adopted from Cusumano et al. [2003].

A comparison with the X-ray profile determined by Rots et al. [1998] shows that the giant pulse P1 component coincides with the P1 X-ray component (see Figure 3.20). Comparing Figure 3.17 and Figure 3.20 shows that the detected radio giant pulses coincide with the hard X-ray P1 component. Romani and Johnston [2001] suggest this observational characteristic as a criterion for the existence of radio giant pulses in a pulsar.
Recently, the discovery of PSR B1821-24 at γ-ray wavelengths with Fermi LAT has been reported by Johnson et al. [2013]. They detected two peaks in the γ-ray AP of the pulsar (in contrast with the three AP components known from radio observations, see Figure 5 in Johnson et al. [2013]). According to this work the P1 component at X-ray wavelengths, as well as at γ-rays coincides with the phase ranges where radio giant pulses from this pulsar occur, providing extentions to previous studies.

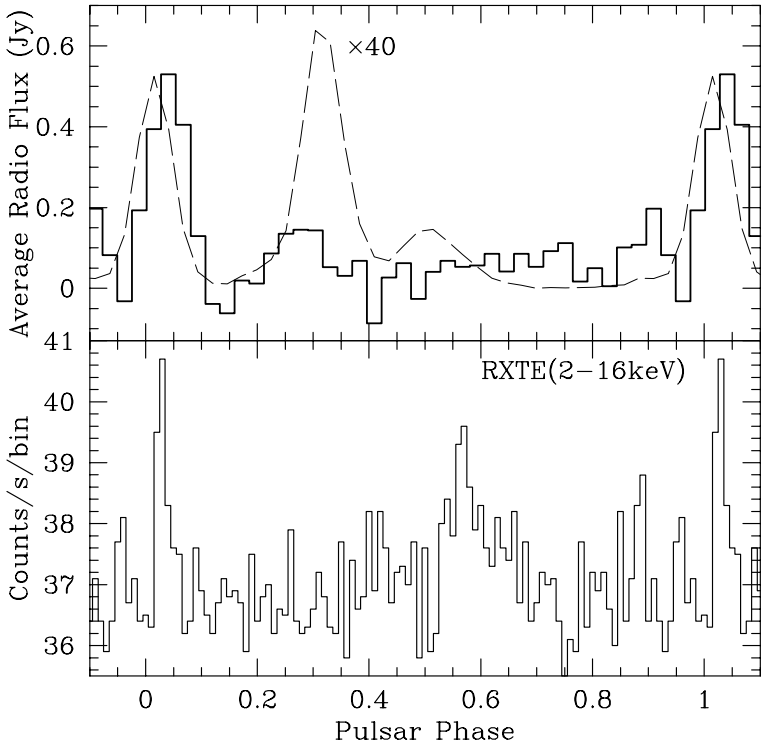

Figure 3.20.: Upper plot: The solid line histogram is the integrated profile of the 16 giant pulses detected from PSR B1821-24 whereas the dotted line is the AP emission from the pulsar; lower plot: X-ray pulse profile as determined by Rots et al. [1998] (Figure 2 from Romani and Johnston [2001]).

An extensive analysis of radio giant pulses from PSR B1821-24 has been reported by Bilous et al. [2015] who carried out a wideband study of this pulsar. A comparison of the radio AP and the radio giant pulses which they detect with the results of Johnson et al. [2013] indicate a similar relationship between radio giant pulses and HE photons as was already indicated for PSR B1937+21: Radio giant pulses from PSR B1821-24 are more closely aligned in phase with the X-ray AP of the pulsar than with its radio AP (compare subfigures a) and c) in Figure 3.21). This relation holds as far as it is currently known for the P1 and P3 emission component. In

other words, the radio giant pulses from PSR B1821-24 occur at the trailing edges of its radio AP. The similarity of the alignment in phase between radio giant pulses HE AP components for PSR B1821-24 and PSR B1937+21 suggests it as a common characteristic of giant pulse emitting millisecond pulsars. More importantly it suggests a common region of origin of both, radio giant pulses and HE photons, also in the case of PSR B1821-24.

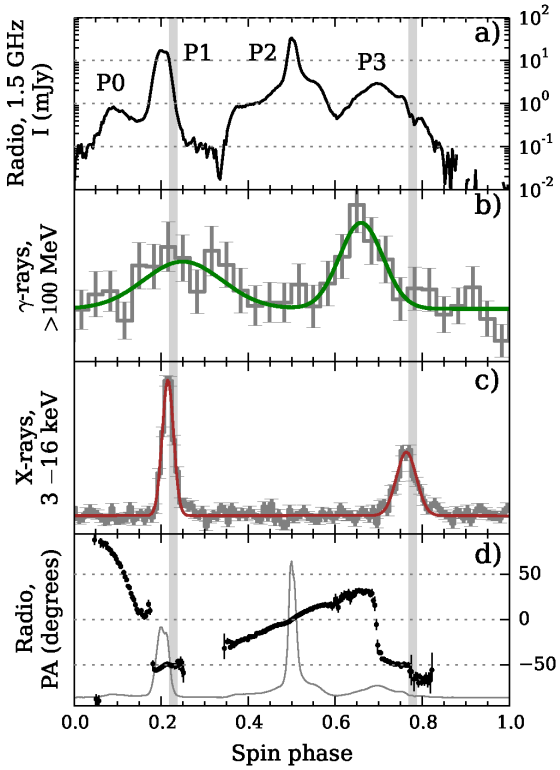

Figure 3.21.: Characteristics of PSR B1824-24A in a frequency range from 1100 to 1900 MHz. The figure was originally adopted from Bilous et al. [2015] and slightly modified for this thesis. According to their conventions the single figures display the following: a) The AP of PSR B1824-24A, b) γ-ray AP adopted from Johnson et al. [2013], c) X-ray AP adopted from Johnson et al. [2013], d) relative position angle of radio emission. The grey areas which are drawn through all figures represent the phase ranges of giant pulse emission.

PSR	P [s][a]	ν [MHz]	Detection*/Reference	S_* [kJy]	S_*/S_{AP}	T_B [K]	α_*
B0531+21	0.33	146	Argyle and Gower [1972]				-2.5
		6-8.5 $\times 10^3$, 8-10.5 $\times 10^3$	Hankins and Eilek [2007]	2×10^6		2×10^{41}	
B1937+21	$1.56 \cdot 10^{-3}$	430	Cognard et al. [1996]		300		
		1650	Soglasnov et al. [2004]	65		$\geq 5 \times 10^{39}$	-1.4
B1821-24	$3.05 \cdot 10^{-3}$	2700	Knight et al. [2006a]	2.3		$\leq 5 \times 10^{37}$	
		720-2400	Bilous et al. [2015]				-1.8
B1112+50	1.66	111	Ershov and Kuzmin [2003]			$\geq 10^{26}$	
		110-180	Karuppusamy et al. [2011]		≥ 10	$3.51 \cdot 10^{26}$	
B0540-69	$50 \cdot 10^{-3}$ [b]	1380	Johnston and Romani [2003]		≥ 5000		
B0031-07	0.94	111.87	Kuzmin et al. [2004]	0.53	120	$\geq 10^{26}$	
		40	Kuzmin and Ershov [2004]	1.1	400	$\geq 10^{28}$	
		110-180	Karuppusamy et al. [2011]		16	$1.32 \cdot 10^{27}$	
B1957+20	$1.6 \cdot 10^{-3}$ [c]	610	Joshi et al. [2004]		129		
		825	Knight et al. [2006b]				-2
J0218+42	$2.32 \cdot 10^{-3}$	793–92, 1341–1469	Knight et al. [2006b]				-1.5
J1823-3021A	$5.44 \cdot 10^{-3}$	685	Knight [2007]		60		-3.1
J1752+2359	0.4	111	Ershov and Kuzmin [2006]		260	$\geq 2 \cdot 10^{28}$	-3.0
B1133+16	1.187	110-180	Karuppusamy et al. [2011]		44	$1.93 \cdot 10^{27}$	

Table 3.2.: Summary of the properties of all currently known giant pulse emitters in chronological order. All quantities labelled with an asterix refer to giant pulses. Note: The rotation period P is not quoted from the same source as the observing frequency ν which refers to the observed radio giant pulses. The flux densities of giant pulses are expressed by S_*, the factor by which the giant pulse emission is higher by S_*/S_{AP}, T_B the brigthness temperature and the power law index (according to the pulse energy distribution) by α_*.

[a] http://www.jb.man.ac.uk/research/pulsar/Resources/epn/browser.html
[b] This value was taken from the ATNF catalogue.
[c] Value adopted from Fruchter et al. [1988].

3.4. Theoretical Approaches

The mechanism behind radio giant pulses has been a topic of debate since their identification as a special form of pulsar radio emission (Chapter 3.1). Currently, no uniform theoretical approach for the generation of radio giant pulses from the Crab pulsar does exist. The developed and published theoretical approaches adress usually only a fraction of their properties. As it has been stated in the last chapters a correlation between radio giant pulses and γ-photons can neither be excluded, nor confirmed (Chapter 3.2). Hence in this chapter theoretical approaches which take only the radio emission into account are introduced as well as approaches which discuss the possible existence of a multiwavelength component of radio giant pulses. Since a discussion of all theoretical approaches is beyond the scope of this thesis, a summary of all currently known (and published) models is given in Table 3.3.

3.4.1. Induced Compton Scattering

This model has been proposed by Petrova [2004], Petrova [2005] and Petrova [2006] and only takes the radio emission with regard to giant pulses into account.
The approach (given in more detail in Petrova [2006]) describes the generation of radio giant pulses due to propagation effects in the plasma of a pulsar magnetosphere. Under the assumption that the magnetosphere of a pulsar contains an electron-positron plasma which is accelerated along the magnetic field lines up to relativistic velocities (the plasma having Lorentz factors of about 100), the process of Compton scattering between these plasma particles and the radio photons which originate inside the pulsar magnetosphere, is induced. Petrova [2006] states that this process is more efficient in the deeper parts of the magnetosphere where the number density of the plasma particles is largest. For this region the approximation of a strong magnetic field is made which basically describes that the radio frequency in the rest frame of an particle is much smaller than the electron gyrofrequency. The process of induced Compton scattering leads to a transfer of radio photons from low to high frequencies. According to the calculations of Petrova [2004], Petrova [2005] and Petrova [2006], this process explains the steep radio spectra of pulsars. Steeper radio spectra of pulsars and the consequently small intensities at high frequencies, imply that this redistribution process leads to a highly efficient amplification of high frequency radiation. According to their numerical calculations, Petrova [2005] state that the optical depth of induced scattering is in general not large which makes the process not efficient. However, since the depth of the scattering process depends upon the number of the scattering particles and the original intensity of the radio radiation (both quantities vary from radio pulse to radio pulse), it can happen that for pulses with high intensities it becomes large, leading to an amplification.
With this approach Petrova [2006] determine the statistics of the amplified intensities which result in an a power law in intensities with an index of -3.26 (see Figure 1 in Petrova [2006]). Besides, within a discussion of the basic characteristics of radio giant pulses, Petrova [2006] determine that for an increase of the intensity of a radio pulse by a few thousand times, the corresponding bandwidth is increased by a factor of a few tenths. They state that the occurrence of radio giant pulses only at certain phase ranges is justified for the Crab pulsar due to frequency dependent refraction of radio waves. Since the scattering region for the described process of intensity amplification is then dependent upon the distribution of the scattering particles within the radio beam, fluctuations of the latter can result in different locations of radio giant pulses at certain phase ranges. According to Petrova [2006], the giant pulses from the

Crab pulsar which have widths in the nanoseconds range result from a focussing effect within the radio beam (more details are given in Chapter 4 in Petrova [2006]).
In summary, this approach tries to explain several properties of radio giant pulses from the Crab pulsar (their power law intensity distributions, bandwidth of occurrence only at radio wavelengths, pulse widths, phase-bound occurrence and their nanoseconds substructure), but no consideration of multiwavelength emission is made by this approach.

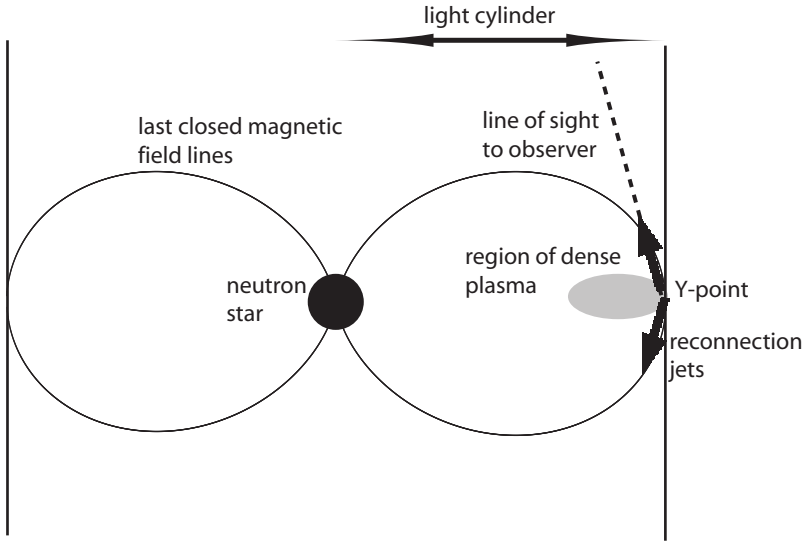

Figure 3.22.: Region around the Crab pulsar in which radio giant pulses are generated according to the theoretical approach proposed by Lyutikov [2007].

3.4.2. Electric Discharge due to Magnetic Reconnection of Field Lines

This approach makes use of actual radio data (Hankins and Eilek [2007]) and was suggested by Lyutikov [2007]. It describes the generation of radio giant pulses on closed magnetic field lines near the light cylinder via the process of anomalous cyclotron resonance (Figure 3.22). The approach tries to explain the occurrence of the emission bands of Crab pulsar giant pulses at the phase ranges of the HFIP at frequencies above 4 GHz (Figure 3.7).
The fitting of the latter results in several requirements which need to be fulfilled by the theoretical approach: The existence of a high density plasma (that is, with densities of about 10^5 times the Goldreich-Julian density, Chapter 1.4.2) which is bound to the closed magnetic field line of the pulsar and the occasional occurrence of a beam of HE particles which move with a γ of approximately 10^7 along the closed field line. In contrast with other models, closed field lines are chosen since this fitting procedure leads to the conclusion that the plasma is not moving relatvistically. To match the observational charactertistics, the magnetic field needs to be at its minimum and the emission region needs to be of small volume. Both properties are associated with the Y-point, where the last closed field line is tangential to the light cylinder (see Figure 3.22). Reconnection at this point which can convert magnetic field energy to kinetic

of fast particles, is the likely source of the relativistic beam.

Mechanism	Plasma Wave Turbulence	Curvature Radiation	Compton Scattering	Magnetic Reconnection
Input	two counter streaming plasma populations	charged particles drifting at relativistic speeds	Electrons / Positrons, low energy radio photons	high density plasma, relativistic particle jets from reconnection
Output	radio pulses with characteristic nanopulses structure	nanosecond radio bursts	higher energy radio photons	banded radio emission via resonance, γ-emission via curvature radiation
Reference	Weatherall [1998]	Gil and Melikidze [2003]	Petrova [2006]	Lyutikov [2007]

Table 3.3.: Summary of currently known theoretical approaches for the generation of radio giant pulses.

4. Instrumentation

4.1. Schematic Overview of a Radio Telescope

The radio signals from celestial sources are usually very weak. A successful detection requires therefore the collection of a sufficient amount of the signal from the source. Consequently, for observations of this kind radio telescopes with large collection areas are needed. Nowadays numerous different types of radio telescopes do exist (constructed according to the types of radio waves they are used to observe). One of the earliest forms of a radio telescope though is a paraboloidal reflector, commonly referred to as a single dish (Figure 4.5). With this kind of reflector the incoming signal is collected and focussed into one point where usually a receiver is located. Paraboloidal reflectors are often used due to their ability to focus incoming radio waves into one point (Figure 4.1).

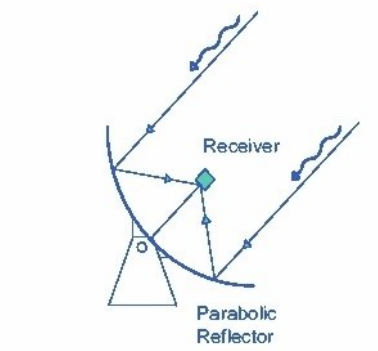

Figure 4.1.: Collection of radio waves with a paraboloidal reflector (Image credit: ASTRON).

The radio waves which move in parallel to the axis of the reflector (that is, on-axis), arrive at the focus in phase. This means that all of them travelled precisely the same distance. Their collection at the focus takes place via a so called feed antenna, or wave guide feed. The latter is an antenna which is used to mediate the signal from the reflector to other parts of the system which result together in a radio telescope. Normally it consists of two receptors which sample orthogonal orientations of polarisation (dual linear, or dual circular). These orientations of polarisation are commonly referred to as polarisation channels (Lorimer and Kramer [2012]). In the next step the resulting signal (with a frequency f_{RF}) is amplified by low-noise amplifier and passed through a bandpass filter. The latter stage is necessary to filter out harmonics caused by other interfering signals which might be overlapping with the original signal from the source. In the next step the frequency of the resulting signal is converted to a lower value with a device called mixer. The reason for this is that signals with lower frequencies

suffer less from cable losses which makes their transmission more efficient. Two input signals are required for the frequency mixer to convert the signal from the source: The signal of the celestial source and the one from a local oscillator (with a frequency f_{LO} that is used as center frequency during conversion, first LO in Figure 4.2) which provides a monochromatic signal. The frequency mixer then produces a new signal which contains several frequency values and not only one, meaning the modulated signal from the source (with an intermediate frequency f_{IF} resulting from the sum f_{RF}+f_{LO} and the difference f_{RF}-f_{LO} of the two input signals) together with other frequencies.

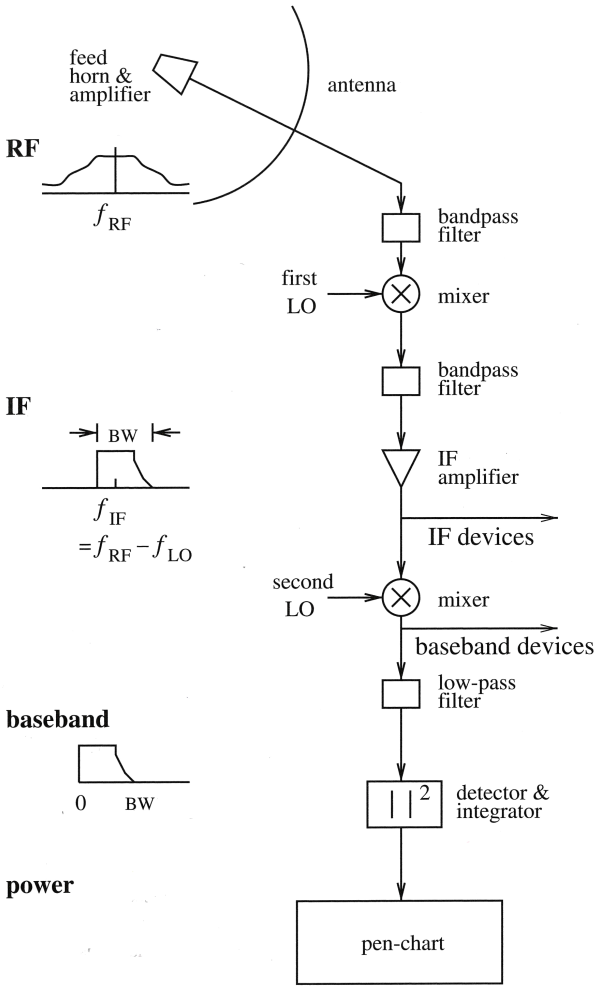

Figure 4.2.: Scheme of the signal path at a radio telescope (figure adopted from Lorimer and Kramer [2012]).

Since the primary aim is to convert the signal of the source down to a lower frequency value (down conversion), only the difference of the frequencies of both input signals is kept. For this purpose the modulated source signal is put through a bandpass after the mixing stage. The resulting signal has then a center frequency f_{IF} in a certain range of frequencies commonly known as bandwidth. It is afterwards amplified (see Figure 4.2). Depending upon the hardware

equipment of the respective radio telescope which is used, this amplified signal can be sent to data acquisition systems after this stage like correlators and filterbanks (see Chapter 5 in Lorimer and Kramer [2012] for details). Another option is to convert it to baseband. This is a signal with a lower cut-off frequency near 0 Hz and an upper one at the maximum bandwidth for which observations with the respective radio telescope are possible. For this another mixing stage with a frequency mixer is required (second LO in Figure 4.2). More information on baseband devices can be found in Chapter 5 in Lorimer and Kramer [2012]. However, if baseband devices are not used, the signal of the source is alternatively put through a low pass filter to filter out frequencies above a specific cut-off frequency. After this stage the actual detection of the signal is carried out by squaring it and plotting its power on a pen-chart (Figure 4.2). Nowadays pen-charts are mostly replaced by technically more sophisticated detection devices (commonly known as pulsar backends) as will be described for the Effelsberg radio telescope in the next chapter.
Coming briefly back to the paraboloidal reflector, it needs to be mentioned that there are different systems of these reflectors used for radio telescopes nowadays (an overview is shown in Figure 4.3).

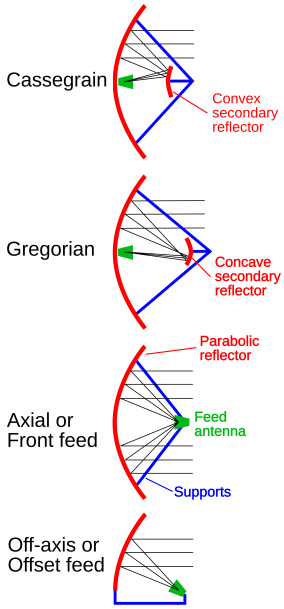

Figure 4.3.: Overview of different types of paraboloidal reflectors (Image Credit: Chris Burks).

The first example in Figure 4.3 is the one, which is discussed in this chapter. Other more complicated constructions are also shown in Figure 4.3 which contain a secondary reflector at the focal point. The Effelsberg radio telescope (Chapter 4.2) for instance contains a secondary reflector which is located shortly before the focal point of the primary reflector (Gregorian system, Figure 4.3). The secondary reflector is of Gregorian style which means that it has a concave shape. In such a system the incoming radio waves are collected by the primary mirror at its focal point (primary focus) and are reflected by the secondary mirror to the focal point of the latter (secondary focus). The Effelsberg radio telescope contains receivers at both foci, thus

enabling a larger range of frequencies at which observations can be carried out (see Figure 4.4).

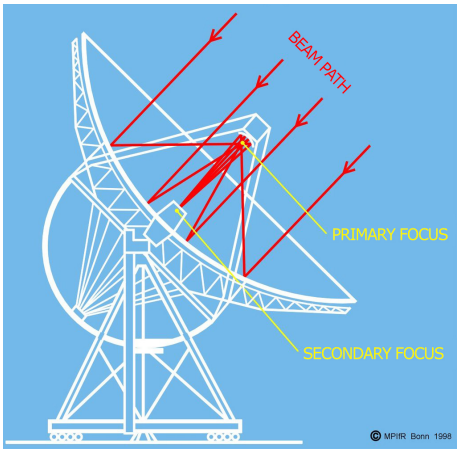

Figure 4.4.: Beam path at the Effelsberg Radio Telescope.

The antennas of the WSRT are paraboloidal reflectors with receivers located at the primary focus (more details are given in Chapter 4.3).
To increase the angular resolution of a single dish, its diameter needs to be enlarged. Since this procedure reaches at some point the limits of the stability of such a construction, the concept of interferometry has been introduced in radio astronomy in the middle of the 20th century. In the radio astronomical context it describes the connection of many single dishes (of smaller diameter). The signals of a celestial source detected with these dishes, are then shifted in phase in such a way by a device known as correlator, so that the signal from all of them is the result of constructive interference. The distance between the single dishes of an interferometer is known as baseline. Usually they can be varied in length. The angular resolution corresponds to the one of a single dish with a primary reflector diameter equal to the total baseline. Interferometers whose single dish outputs can be amplified and combined pairwise in order to provide a large number of different baseline combinations, are referred to as aperture synthesis arrays (Burke and Graham-Smith [2010]). Introduced to increase the resolution of radio telescopes (Ryle and Hewish [1960]), it is nowadays a common technique being applied to a high number of interferometers around the world (like the JVLA in New Mexico/USA for instance). For the study presented here, data from one interferometer, namely the WSRT, is used.

4.2. The Effelsberg Radio Telescope

With a reflector diameter of 100 m the Effelsberg radio telescope is the second largest fully steerable radio telescope worldwide (together with the GBT, in West Virgina/USA) and enables observations in a frequency range from 300 MHz to 90 GHz[1]. Originally constructed from 1968 till 1971, it was officially inaugurated in 1972 and has been in operation since then. A historical overview with regard to the building of the Effelsberg radio telescope can be found in Wielebinski et al. [2011].
Nowadays it is used for a wide variety of scientific observations ranging from compact objects like pulsars to supernovae, HI measurements and Active Galactic Nuclei (AGN) among others. The Effelsberg radio telescope is operated by the Max-Planck Institute for Radioastronomy (MPIfR) in Bonn/Germany.

Figure 4.5.: The Effelsberg 100 m m radio telescope as seen from a valley near the town of Effelsberg in Germany (Image Credit: N. Lewandowska).

4.2.1. Antenna

The Effelsberg telescope has a primary mirror of 100 m in diameter in the form of a paraboloid and a secondary mirror of 6.5 m in diameter in ellipsoid form. The large surface area of the primary mirror amounts to 7850 m^2 and is essential for the detection of weak radio signals like for example from pulsars. Its large diameter also provides a high angular resolution.
The complexity in the construction of an antenna of that size lies in its movements and the

[1] https://eff100mwiki.mpifr-bonn.mpg.de/doku.php?id=information_for_astronomers:user_guide:index

resulting deformation. To keep the form of a parabolic mirror, it was designed with the help of the "Finite Element Method" which describes how a mirror deforms while tilting by numerically solving partial differential equations. Via the homology principle the paraboloidal mirror can keep its shape at different elevations. This principle describes changes of the shape and the position of the reflector which help to keep it in a paraboloidal form (see Chapter 7.5 in Wilson et al. [2009] for more details).
The primary mirror consists of 2352 panels. The high angular resolution is provided by the possibility of a good alignment of all panels. Consequently, the surface accuracy of the primary mirror accounts to 0.55 mm in the best case whereas the secondary mirror reveals a surface error of only 60 µs. The secondary mirror has in addition 96 actuators which compensate for inaccuracies in the homologous structure of the primary mirror.
The system is set up in Gregorian style and mounted on an Alt-Azimuth mount. The limits of the mount are the following:

$$33.5° \leq \text{Azimuth} \leq 503°$$
$$8.2° \leq \text{Elevation} \leq 89°$$

Figure 4.6.: The Seven Beam receiver mounted in the primary focus of the Effelsberg radio telescope (Image Credit: A. Kraus).

4.2.2. Data Flow

As the course of observations with a facility as large as the Effelsberg radio telescope becomes opaque very fast, this chapter shall provide a schematic overview how the signal which is re-

ceived by the radio dish arrives at the computer for further processing.
The word "backend" (Chapter 4.2.4) might not be familiar to everyone. For radio astronomers it is the designation of the detector with which the received data is being processed. On the other hand the receivers are usually referred to as frontends (Chapter 4.2.3).
Referring to Figure 4.7 the signal is being detected by the used frontend. The processing of the signal starts at this point as the polarizations are separated and the signal is amplified. The output signal of this processing stage is further processed by the backend which takes over the computational expensive work consisting of the coherent dedispersion (as in the case of the PSRIX backend). Depending upon the object which was observed, the output data from the backend is put through different pipelines afterwards. In the case of pulsar data like for example from pulsar surveys, it is reduced on a dedicated pulsar cluster machine. The output of this step is stored temporarily on a different machine (PC 207 in Figure 4.7) and fetched either via a fast internet connection, or on tapes by the users at the MPIfR.

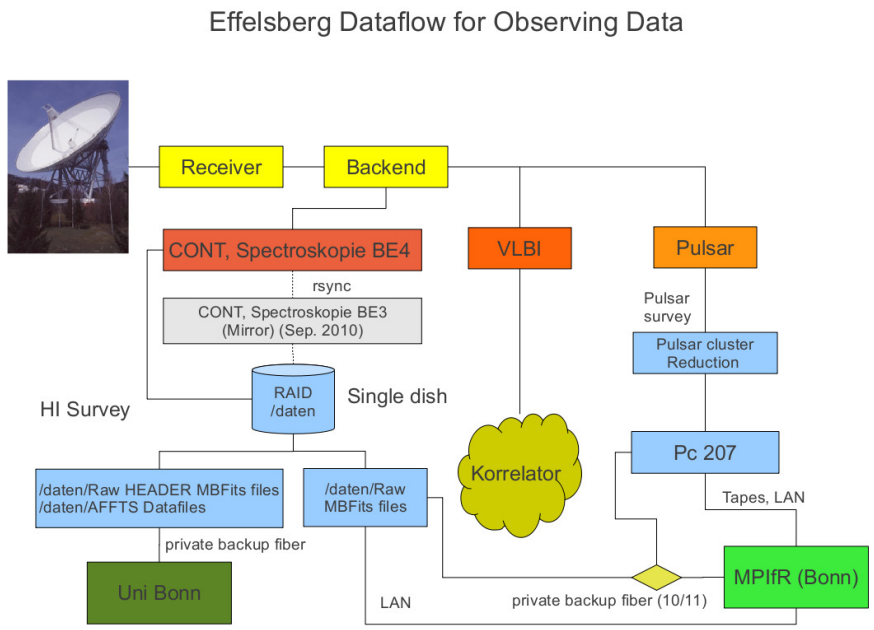

Figure 4.7.: A scheme of the data flow at the Effelsberg radio telescope (Image Credit: Heiko Hafok).

4.2.3. Used Receivers (Frontends)

To accomplish a high variety of radio astrononomical observations, a large number of receivers is mounted at the primary and secondary focus[2]. In the case of the data described in this thesis, two different receivers were used which are described shortly in this chapter.

[2]https://eff100mwiki.mpifr-bonn.mpg.de/doku.php?id=information_for_astronomers:information_of_the_receiver_division:index

P217mm

The 21 cm seven beam receiver belongs to a large group of prime focus receivers available. It covers a frequency range from 1.26 to 1.51 GHz with a center frequency of 1.4 GHz and consists of seven horns arranged in a hexagonal form (Figure 4.6). The seven beam receiver enables the observation of pulsars with a bandwidth of 300 MHz in the protected band from 1.38 to 1.427 GHz in which also the observations used for the study presented here were taken.
Detailed technical information can be found at the websites of the observatory[3][4].

P200mm

Parts of the Crab pulsar observations used for the correlation study were carried out with the P200mm receiver. It contains one horn in contrast with P217mm and covers a frequency range from 1.29 till 1.73 GHz. The receiver is a multi polarimeter box which is usable for several observing modes[5].
For the Crab pulsar observations the pulsar observing mode covering 1.29 till 1.43 GHz with a bandwidth of 100 MHz was used.

4.2.4. Used Detectors (Backends)

For the work presented here one pulsar backend was primarily used which will be shortly explained in the following section.

PSRIX

Currently, there are several backends installed at the Effelsberg telescope for pulsar studies. Due to its high time resolution, the observations obtained for this thesis were carried out with the new PSRIX pulsar backend [6] (Karuppusamy et al. in preparation). It is a baseband recorder based on ROACH boards with HP 5412 switch and 16 high performance nodes. With the PSRIX pulsar backend coherent dedispersion can be carried out. This technique is crucial for the proper reduction of pulsar data without loosing signal due to intra channel smearing during the process of dedispersion. With this capability it makes the detection of narrow and weak pulses possible which would otherwise not be detectable with instruments that were made for incoherent dedispersion.
The PSRIX pulsar backend has a maximum time resolution of 31.25 ns. This together with the coherent dedispersion technique, qualifies it as the proper instrument for the study of radio giant pulses as it makes the detection of a statistically high amount of single pulses possible.

[3] https://eff100mwiki.mpifr-bonn.mpg.de/doku.php?id=information_for_astronomers:rx:p217mm
[4] http://www3.mpifr-bonn.mpg.de/div/electronic/content/receivers/21cm.html
[5] https://eff100mwiki.mpifr-bonn.mpg.de/doku.php?id=information_for_astronomers:rx:p200mm
[6] https://fpra.mpifr-bonn.mpg.de/doku.php?id=pulsarinstruments:psrix

4.3. The Westerbork Synthesis Radio Telescope

The WSRT is a aperture synthesis interferometer currently consisting of 14 single dish radio telescopes located near the small village Westerbork in the Netherlands (Baars and Hooghoudt [1974]).
Originally constructed in 1970 as the SRT (Synthesis Radio Telescope), it was regarded as a low cost telescope constructed via the technique of aperture synthesis pioneered by Ryle and Hewish [1960] and Ryle [1962]. Since its inauguration it has been used for a variety of scientific goals including pulsars, masers, AGN studies among others.
The WSRT is being operated by ASTRON, the Netherlands Institute for Radio Astronomy[7].

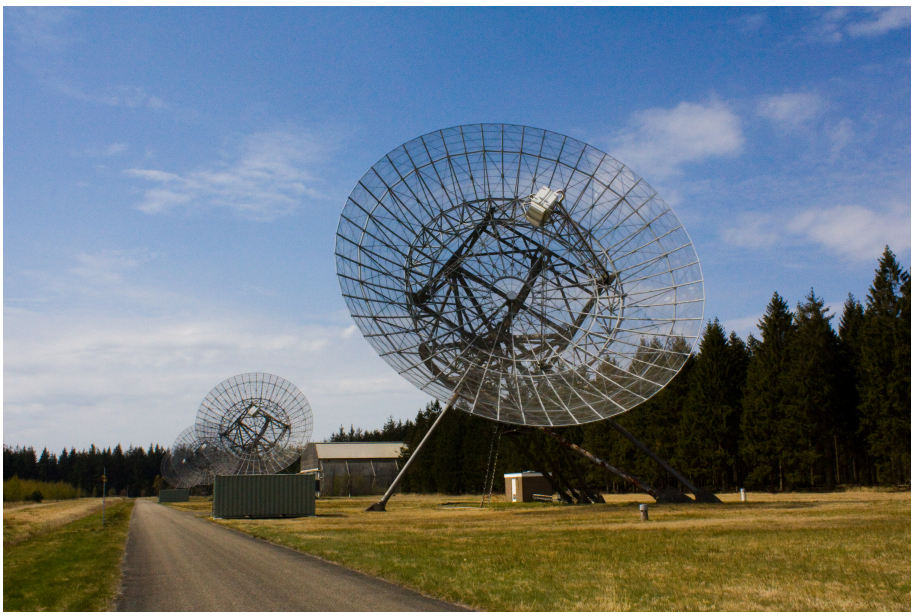

Figure 4.8.: The WSRT near the town of Westerbork in the Netherlands (Image Credit: N. Lewandowska).

4.3.1. The Interferometer

The WSRT is an interferometer which consists of 14 telescopes (from this total number 13 telescopes were used for this study). The whole array is aligned along a 2.7 km long east-west line in order to enable high resolution observations in this direction. When all telescopes are arranged in one line, the resulting radio beam becomes elongated. Consequently, the time resolution in the North-South direction is very poor whereas the one in the East-West direction is high and can be mainted for 12 hours (R. Smits, ASTRON, private communication).
Of the available 14 telescopes 10 are fixed and four are movable on rail tracks labelled A, B, C, D (Figure 4.9). The distance between two telescopes as seen from the respective radio source, also known as baseline, is 144 m between the fixed telescopes. The movable parts of the array enable the changing of the baseline in four different configurations with the minimum distances of 9A = 36 m, AB = 48 m, CD = 48 m. In total the baselines can vary from 36 m to 2.7 km.

[7] http://www.astron.nl/

More information on the used telescope configurations can be found on the website of the observatory[8].

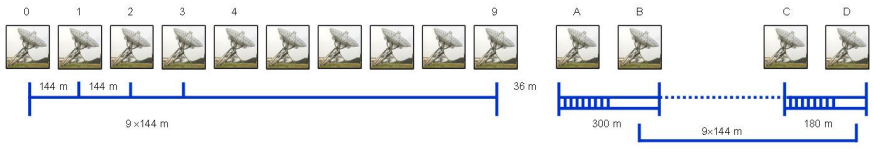

Figure 4.9.: A sketch of the Westerbork array showing 10 fixed antennas and 4 movable ones (Image Credit: ASTRON).

4.3.2. Antennas

The 14 antennas of the WSRT have a diameter of 25 m each and are of parabolic shape consisting of 98 reflector panels (details on the construction of the antennas can be found in Baars and Hooghoudt [1974]). All antennas of the original SRT were build after a template to keep technical differences down to a minimum (see Figure 4 in Baars and Hooghoudt [1974]). Each antenna is mounted on an equatorial mount (instead of Alt-Az as is the case for example for the Effelsberg radio telescope) in order to provide the possibility of tracking a source for a maximum of 12 hours.

4.3.3. Data Flow

In contrast with single dish telescopes the signal is being formed differently in the case of an aperture synthesis interferometer like the WSRT (as explained at the beginning of this chapter). The data flow in the case of the WSRT will be described here shortly on the basis of Figure 4.10. A detailed description is given in Karuppusamy et al. [2008].
The signal from the frontends (Chapter 4.3.4) of all 13 telescopes is transported to the equalizer which compensates for cable losses. Afterwards the signal is transported to the IF to Video Frequency Converter (IVC) where it is split into subbands of 20 MHz width and translated to 20 MHz baseband signals. They are sampled at Nyquist rate in the Analog to Digital Converter (ADC). Passing through the ADC, a geometric delay is added into the baseband signal which is afterwards sent to the correlator and to the adder module (TAAM). In the TAAM the coherent sum of all 13 telescopes in phase is calculated as the equivalent of the signal from a resulting single dish telescope. The resulting signal from all 13 telescopes is afterwards sent to a backend referred to as PuMa II (Chapter 4.3.5) for further processing.

4.3.4. Used Receivers (Frontends)

Currently 13 out of the 14 WSRT antennas are equipped with a Multifrequency Front End receiver (MFFE, Casse et al. [1982], Tan [1991]). These frontends were added to the WSRT in the early 1990s and have been in operation ever since (Tan [1991]). They cover several frequency bands from 110 MHz to 9 GHz, enabling a variety of different kinds of observations

[8] http://astron.nl/radio-observatory/astronomers/wsrt-guide-observations/3-telescope-parameters-and-array-configuration

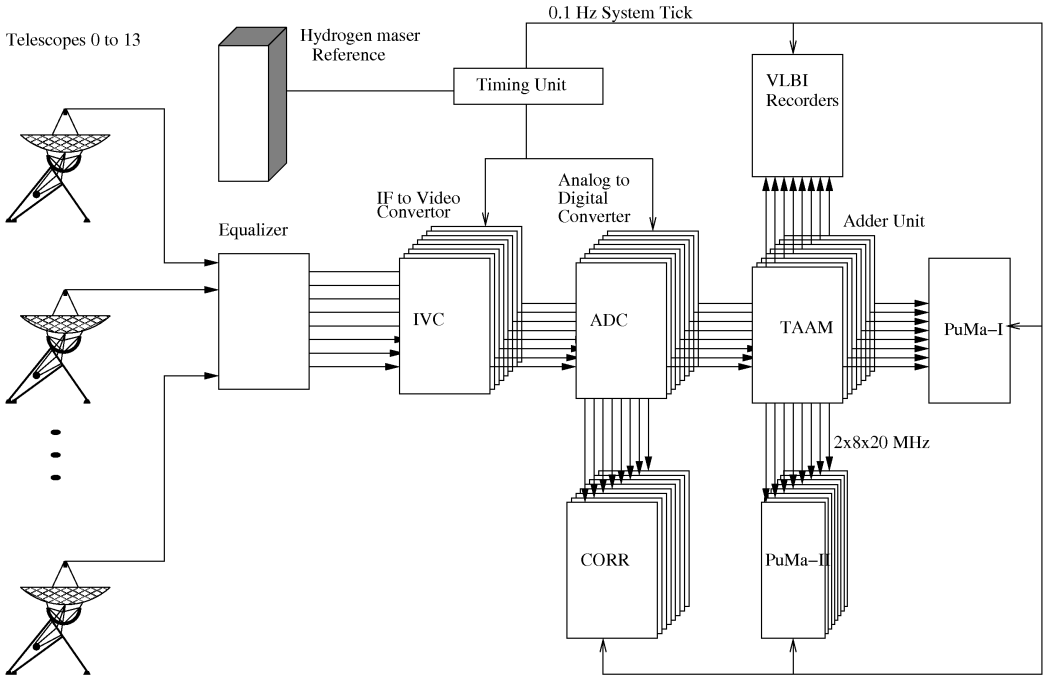

Figure 4.10.: Block diagram of the WSRT (the figure was adopted from Karuppusamy et al. [2008]).

(Karuppusamy et al. [2008]).
Different sensitivities of a MFFE can be achieved by cooling it down via a cryostat (see Table 1 in Tan [1991]). The scheme of a MFFE with the set of available feeds is shown in Figure 1 in Tan [1991]. Their design makes fast switches between different frequency bands in short time possible, emphasising the flexibility of observations with the WSRT.

4.3.5. Used Detector – The PuMa II Pulsar Backend

Due to their weak signals at radio wavelengths, large collection areas and wide bandwidths are crucial for the observations of pulsars. In addition the technique of coherent dedispersion is essential for the reduction of pulsar observations with a minimum amount of information loss due to the smearing of the pulsar signal caused by the ISM. To fulfill these goals a new kind of pulsar backend known as Pulsar Machine II (PuMa II) was built for the WSRT (Karuppusamy et al. [2008]) as the successor of the incoherent dedispersion machine PuMa I (Voûte et al. [2002]). A technical comparison between both backends can be found in Karuppusamy et al. [2008].
PuMa II operates in baseband recording mode and is a coherent dedispersion machine which can process the data taken with a bandwidth of 160 MHz in the form of 8 times 20 MHz subbands. It is therefore capable of dedispersing pulsar data coherently over a bandwidth which is 8 times larger than with the precursor instrument PuMa I, collecting thus a larger amount the signal from a pulsar. It has a best time resolution of 50 ns which is decisive for the observations of

very short pulses like Crab pulsar giant pulses and is also the reason why it was chosen for the study presented here.
All WSRT observations included into this thesis were processed with PuMa II.

4.4. Schematic Overview of an Imaging Air Cherenkov Telescope

An IACT is similar to a optical telescope in what it observes: Optical flashes on timescales of nanoseconds (albeit optical telescopes observe the respective emission usually on much longer time scales). But with this, the similarities already come to an end.
Designed for the observation of very HE γ-ray emission, an IACT consists in general of the following components: An (usually large) optical reflector, an array of Photomultiplier Tube (PMT)s in the focal plane of the reflector which are a significant part of a camera (Figure 4.14), a readout system, a trigger system via which it is decided which observations are recorded, a Data Acquisition System (DAQ) and a calibration system.

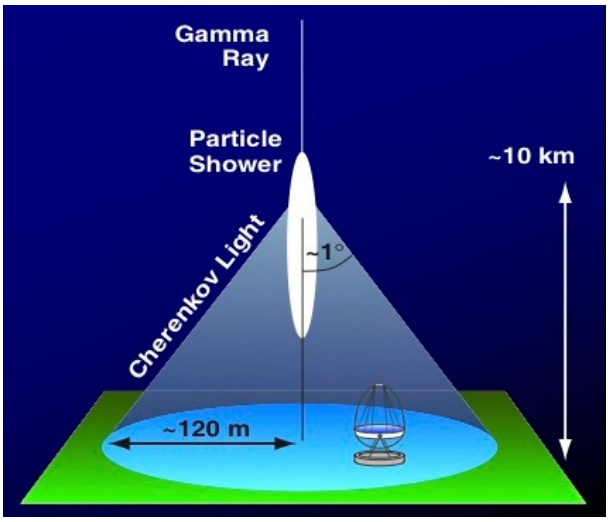

Figure 4.11.: Scheme of the detection of an air shower with a IACT (Image Credit: ISDC[9].

To understand the reason for these components of an IACT, the way how it is operating will be described first and the mentioned components in the next chapter on the basis of the MAGIC telescopes.
Since the atmosphere of the Earth is opaque to γ-ray emission, mostly satellites have been used for the observation of astronomical sources at γ-ray wavelengths. Pioneered in the 1970's with the 10 m Whipple telescope by Trevor Weekes (Weekes et al. [1989]), the approach with which IACTs work is to observe γ-rays indirectly. When a γ-photon (with an energy greater than 10 MeV, Weekes [2003]) enters the atmosphere of the Earth, it collides with one of its molecules and produces consequently a cascade of secondary particles via the process of pair production. Since the original γ-photon traveled with a speed nearly the speed of light, the secondary particles particles also travel with a similar velocity. They even exceed the latter in the medium in which they are moving causing the occurrence of Cherenkov radiation at an height of about 10 to 20 km (see Figure 4.11). These flashes can occur on time scales of 4 ns

to 10 ns and are directly observed by IACTs. Due to the short time scales of these Cherenkov flashes, they are invisible for the naked human eye. In summary, IACTs do not observe the γ-photon directly, but the Cherenkov emission caused by its secondary particles.

The secondary particles interact on their further way with air molecules which results in the emission of secondary γ-rays due to Bremsstrahlung. Both processes, pair production and Bremsstrahlung, continue to take place until the energy threshold for pair production process is reached. This whole process (if caused by a γ-photon) is called an electromagnetic shower, or cascade. Since the direction of the secondary particles does not vary significantly from the direction of the original γ-photon, the whole electromagnetic cascade evolves in the form of a cone around the original trajectory of the γ-photon. Consequently, the Cherenkov radiation is emitted in the form of a cone as well. This way a light pool is created which extends to the ground (Figure 4.11).

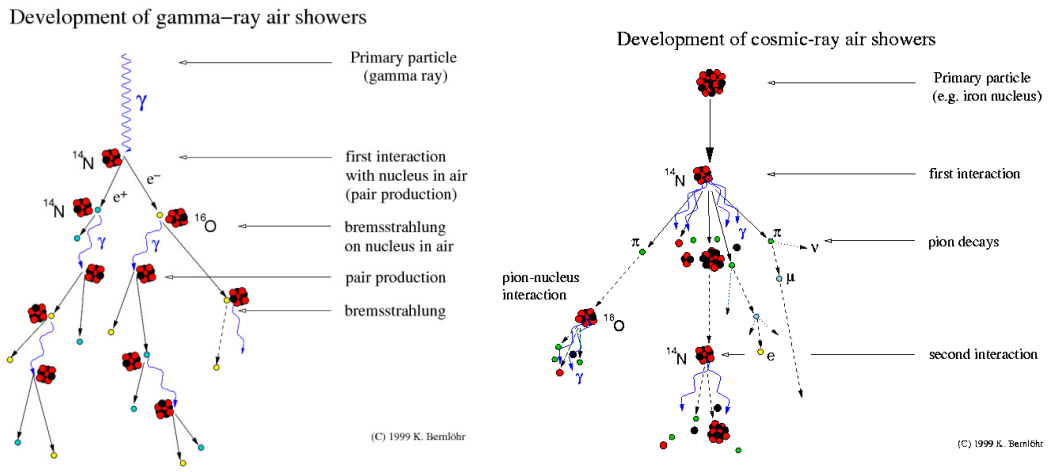

Figure 4.12.: Geometric extension of air showers caused originally by a γ-photon (left picture) and by a hadron (right picture). Image Credit: K. Bernlöhr.

Also belonging to the family of air showers, are hadronic showers (in other words, showers caused by, for instance, protons or iron nucleii). They occur more often than electromagnetic showers (about 1:1000 times) and contribute significantly to the high background emission which is visible with IACTs. In the literature they are referred to as "Cosmic Rays".
While carrying out observations, no subdivision between electromagnetic and hadronic showers is made by an IACT. The subdivision between both kinds of showers is done afterwards during the offline analysis (see Chapter 5.2). One noteworthy difference between both types of showers is their geometric form. While electromagnetic showers were discovered to bunch together and have a rather slim form, hadronic showers have a more extended form (Figure 4.12).
The reason why electromagnetic showers are interpreted as emission from the astronomical source of interest, lies in the nature of photons to have no electric charge. Thus they are unaffected by the magnetic fields of other objects which they pass on their way through the interstellar, or intergalactic medium. This characteristic ensures that the directions of the γ-photons that collide with the atmosphere, correspond with the position of the source which

[9] http://www.isdc.unige.ch/cta/outreach/data

emitted them. The source position is also reconstructed during the offline analysis (Chapter 5.2).
Coming back to the original question of the structure of IACTs (Figure 4.14), it can be deduced that a large reflector is needed to collect as much information of air showers as possible.
The detection of a shower can only take place if the IACT is located within the emission cone of Cherenkov emission. On the ground the latter has a radius of about 120 m, resulting in a shower detection area of about $5 \times 10^4\,\mathrm{m}^2$ (Weekes [2003]). Consequently, the collection area of an IACT needs to be large in order to detect as many air showers as possible. The diameter of the reflector is usually chosen to be large in order to enable also the detection of air showers caused by low energy γ-photons. The reason for this lies in the nature of low-energy γ-ray events to produce cascades which die out fast in the atmosphere. Hence the resulting number of Cherenkov photons which arrive on the ground (and can be thus detected with an IACT) is rather small. To compensate for this effect usually large reflectors are used and more sophisticated trigger systems are developed (like the Sum Trigger in the case of the MAGIC telescopes as will be explained in the next chapter).

4.5. The MAGIC Telescopes

Figure 4.13.: The MAGIC telescopes (M1 located to the left and M2 located to the right) with the Herschel and the NOT optical telescopes in the back at the Roque de los Muchachos observatory on La Palma (Image Credit: N. Lewandowska).

The MAGIC telescopes are a system of two telescopes known as MAGIC 1 and MAGIC 2 (commonly referred to as M1 and M2). Both are located at the Observatorio del Roque de los Muchachos[10] (ORM) on La Palma island, Canary islands (Figure 4.13).
The telescopes are located in a distance of 85 m to each other. MAGIC 1 was inaugurated in

[10] http://www.iac.es/eno.php?op1=2&lang=en

2004 and was operated in single mode till 2009, when the comissioning work on MAGIC 2 was finished. Since then, both telescopes have been in operation as a stereoscopic system.
The MAGIC telescopes are operated by the MAGIC Collaboration which consists of about 150 scientists from 8 different countries[11]. Both telescopes consist of several units which are referred to as subsystems. They are controlled by a central control system for M1 and for M2 (Zanin et al. [2009]). A detailed desciption of all subsystems can be found in (Giavitto [2013]) and (Zanin [2013]). Here only a reference to the significant parts of the hardware is given which are crucial for the basic understanding of pulsar observations with an IACT (Chapter 4.5.1). Detailed performance reports of the MAGIC telescopes can be found in Colin et al. [2009], Cortina et al. [2009], Sitarek et al. [2013]. Reports of the recent upgrade and resulting performance of both MAGIC telescopes are given by Aleksic et al. [2014] and MAGIC Collaboration et al. [2014].
A short overview of the basic subsystens is given below and reflects the signal path. The light from the air shower is reflected by the mirrors on to the camera. The camera pixels are sent to the trigger and the read out. The trigger system then checks for the presence of a signal event, in which case the read out system passes the photon counts to the DAQ for permanent storage.

Telescope Frame
The telescope structure is hold together by a 5.5 tons frame which is made of carbon fiber and aluminium. It was aimed to be of light weight in order to enable fast movements of the telescope in the case of flare alerts, or γ-ray bursts. The carbon tubes of the frame are stiff and prevent this way also deformations of the reflector. The large telescope frame can hold a reflector of respective size and thus guarantees a low energy threshold.
Both telescopes have Alt-Azimuth mounts with which they can be moved in an azimuth range from -90° to +318°. The respective elevation ranges from -70° to +90° (Zanin [2013]). All movements of each of the telescopes are carried out by a drive system which was designed for the purpose of the aimed observations and is explained in detail in Bretz et al. [2009].

Reflector
The reflector has a parabolic form and a diameter of 17 m. Each telescope is built in a tesselated way, that is consisting of individual mirror panels which can be controlled by a mirror alignment system known as Active Mirror Control (AMC). The latter corrects deformations of the mirror tiles via motorized motions (Biland et al. [2008]).
Although the mirror panels of both telescopes cover a surface of about 236 m^2 (Schultz [2013]), there are differences with regard to the structure and number of these mirror panels between M1 and M2. The reflector of the M1 telescope consists of 247 panels which support 964 mirrors that have a surface of about 0.25 m^2 each. Four of such mirrors are located on one support panel (the latter having a surface of about 1 m^2). The reflector of the M2 telescope consists of two different types of mirrors. The inner part is built up out of 143 aluminium mirrors which have a surface of about 1 m^2 each. The outer part consists of 104 mirrors which are made out of glass. Besides, the mirrors are mounted directly on the M2 reflector frame. This is not the case for the M1 mirrors.
More details about the structure and composition of both kinds of mirrors of the M2 telescope together with a detailed comparison between the mirrors from both telescopes are given in Doro

[11] https://magic.mpp.mpg.de

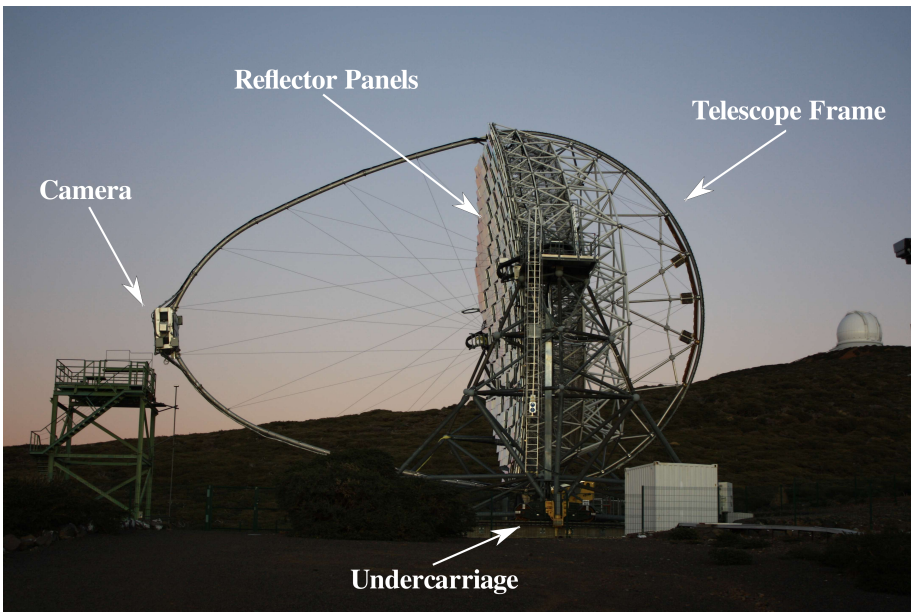

Figure 4.14.: The M1 telescope as seen after sunset with some indicated subsystems (Image Credit: N. Lewandowska).

et al. [2008] and more recently in Schultz [2013].

Cameras
As both MAGIC telescopes are of different age, their cameras were different for some time. The former M1 camera consisted of 576 PMTs of two different sizes which formed the inner and the outer part of the camera. The inner part consisted of 396 PMTs which had a Field of View (FoV) of 0.1°, whereas the outer part was made up of 180 PMTs with an FoV of 0.2°. The M2 on the other hand is uniformly built of 1039 PMTs which have a FoV of 0.1°. The PMTs are often referred to as camera pixels. In the case of M2 the pixels are grouped into seven pieces together. A detailed study of the M2 camera is given in Borla Tridon et al. [2009]. After the construction of both telescopes, the cameras of each were different (a detailed description of both is given in Zanin [2013]). However, after the recent upgrade of both telescopes (Aleksic et al. [2014], MAGIC Collaboration et al. [2014]) the M1 camera is similar in design to the M2 camera. For the study presented here, only post-upgrade MAGIC data have been used.

Readout System
The readout process takes place in several steps. The electrical signals from the PMTs are converted into optical pulses. This is done by the usage of a so called Vertical Cavity Surface Emitting Laser which is connected to optical fibers. These fibers transport the signal to a counting house where they are subdivided into two parts and converted back into electronic signals. One part is then directed to the trigger system and the other one to the DAQ. More details about the readout systems of both telescopes can be found in Jogler [2009] and in Zanin [2013].

Trigger System (Standard Trigger)
The signal coming from all camera pixels cannot be processed continuously. Therefore a trigger system has been included into the hardware of the MAGIC telescopes. A trigger makes a pre-selection of the detected air showers and reduces this way the amount of data. Since most detected air showers are of hadronic origin, this pre-selection is the first part of their exclusion. The standard trigger system of the MAGIC telescopes consists of three levels (Corti et al. [2003]) beginning with the "Level 0 Trigger" (LT0). Depending upon its discriminator threshold (set accordingly with respect to the Night Sky Background (NSB), moon or dark night conditions), it adjusts the signal of individual pixels which are higher than the set threshold.
The "Level 1 Trigger" (LT1) is a topological trigger which is activated as soon as the signal from four next neighbouring (4NN) pixels is higher than the LT0 threshold. Under this condition the recorded air shower (commonly referred to as "Event") is recorded by the DAQ. The reason for the existence of this trigger lies in the compact form of the recorded air showers.
The "Level 2 Trigger" (LT2) was created for the detection of complex patterns of air showers and is not used during standard data taking.
In accordance with the stereo system, another trigger is applied after the LT1 known as "Stereo Coincidence Trigger" (LT3). It is responsible for filtering out events which are only detected by one of the MAGIC telescopes. To determine for which events this is the case, the LT1 signals from both telescopes are delayed in time according to the respective pointing direction of the telescopes. Such a delay is necessary since both telescopes are located in a distance of 85 m (baseline) to each other and the resulting propagation time of the detected emission traveling from one telescope to the other, needs to be taken into account.
The energy threshold resulting out of this kind of trigger system is set to above 60 GeV for the data used in this thesis.
A deeper insight on the trigger system can be found in Paoletti et al. [2008].

Data Acquisition System
The DAQ is used for the recording of the data to disk and storing it so that can be analyzed offline. Consisting of flash ADCs, it is responsible for the digitization of the electronic signals which originally come from the PMTs. The resulting signals are then stored in raw data format (Chapter 5.2).

Calibration System
After the registration of a signal by the PMTs of the camera segments, it needs to be calibrated on the path towards the DAQ. For a proper calibration procedure a calibration box is used which is located in the middle of the reflector of the respective telescope. The box is equipped with light-emitting diodes which are used to illuminate the camera uniformly with light pulses of different frequency and intensity. This way the high voltage of the PMTs is set to form a uniform gain throughout the whole camera. The calibration systems of both MAGIC telescopes have been upgraded recently to newer versions. The data presented in this study has been taken with the upgraded calibration system (Aleksic et al. [2014]).

Clock System
The time setting for the data from the MAGIC telescopes originally consisted of a Rubidium clock and a Global Positioning System (GPS) receiver. Together they provided the time stamp for the DAQ. However, this system has been replaced during the recent upgrade of both tele-

scopes with a single timing unit system[12] (Aleksic et al. [2014]). The time stamp for the data sets presented in this thesis has been set with the new timing system. The timing precision of the new system is 200 ns, same as for the old system. More details are given in Aleksic et al. [2014].

4.5.1. Pulsar Observations with the MAGIC Telescopes

Pulsar observations with the MAGIC telescopes have been very successful in the last years (Aliu et al. [2008], Aleksić et al. [2011], Aleksić et al. [2012], Aleksić et al. [2014]).
The observation of pulsars (mainly of the Crab pulsar at the time of this thesis writing) do not differ significantly from the observations of other sources with the MAGIC telescopes. There are nevertheless two subsystems which are mostly used for pulsar studies. In this chapter these two subsystems are briefly outlined.

Central Pixel (CPIX)
In order to enable a fast detection of a pulsar with an IACT and thus to check the functionality of the telescope and the timing of the system, an optical Central Pixel was installed originally in M1 and later also in M2.
It consists of one PMT which is located at the center of the MAGIC camera. A technical description of the CPIX can be found in (Barrio et al. [2008]). With the help of the CPIX slow variations of different kinds of objects can be examined (emission frequencies ranging from 1 Hz like in the case of blazars till 1 kHz for pulsars and γ-ray bursts).
For pulsar studies a test of the stability of the clock system is crucial for the proper determination of its pulsed emission. Slight changes in the timing of the photons from the pulsar can cause significant changes in its resulting rotational phase and thus corrupt the observations. Therefore frequent tests of the clock systems are essential for successful pulsar γ-ray observations with the MAGIC telescopes.
The analysis of CPIX data in the context of this thesis is given in Chapter 5.2.4.

Sum Trigger
In order to lower the energy threshold even more down to above 25 GeV, another LT1 trigger known as "Sum Trigger" was developed originally for the M1 telescope (Rissi et al. [2009]). At the time when this thesis is written, two Sum Triggers were already developed and mounted at both MAGIC telescopes. Since they were still in commissioning phase at that time, the standard trigger system has been used in the case of the data presented in this study. Due to this fact only the idea and basic functioning of the Sum Trigger is schematically explained. A more detailed description of the former Sum Trigger is given in Rissi et al. [2009]. A status report for the new Sum Trigger system can be found in Haefner [2011], García et al. [2014] and Dazzi et al. [2015].
The idea for the Sum Trigger resulted out of the observations of simulated low energy γ-ray showers (see Chapter 5.2 in Rissi et al. [2009] for details). Based on this, the Sum Trigger is constructed as an analog trigger (while the standard trigger is digital). Its central task is a summation of the analog PMT signals within a set of overlapping patches which consist of N PMTs (for the new Sum Triggers the size of these patches is set to 19 camera pixels, García

[12] http://www.microsemi.com/products/timing-synchronization-systems/timing-synchronization-systems

et al. [2014]). The resulting data is recorded by the DAQ when the sum of the signals of a whole patch exceeds the sum discriminator threshold. The advantage of this technique is that the sum of all signals resulting from a group of camera pixels is used for the trigger decision and not 4NN. That is, small signals from single camera pixels are included in the decision if the observed event will be triggered, or not. Consequently, low-energy events can be observed which otherwise would not have been triggered due to too small signals resulting from the single photons of a PMT. Besides within this patch any charge configuration resulting from the detection of showers is allowed and not only compact ones as in the case of the Standard Trigger. This way a larger diversity of showers can be detected. A visual comparison between both sorts of triggers, the Standard and the Sum Trigger, is shown in Figure 1 of Dazzi et al. [2015].

5. Data Analysis

5.1. Radio Data

5.1.1. Overview of Data Sets

The radio data sets used for this study consist of observations from winter 2012/13 taken non-simultaneously with both the Effelsberg radio telescope and the WSRT. A summary of all radio observations is given in Table 5.1. For the correlation study, all radio observations were taken in the L band, in order to avoid distortions of the signal by RFI (Chapter 5.1.3), as well as to guarantee a high number of single pulses from the Crab pulsar.

Facility	Epoch	ν_{center} [MHz]	BW [MHz]	Δt [min]
Winter 2012/13				
Effelsberg	2012-12-07	1347.5	200	107
WSRT	2012-12-10	1380.0	160	99
Effelsberg	2012-12-17	1347.5	200	120
WSRT	2013-01-08	1380.0	160	21
Effelsberg	2013-01-09	1372.5	-200[1]	104
WSRT	2013-01-10	1380.0	160	119
Effelsberg	2013-01-12	1347.5	200	175
Effelsberg	2013-01-31	1347.5	200	145
WSRT	2013-02-02	1380.0	160	54
WSRT	2013-02-03	1380.0	160	119
Effelsberg	2013-02-06	1347.5	200	244
Effelsberg	2013-02-07	1410.0	75	72
Effelsberg	2013-02-08	1347.5	200	30
Effelsberg	2013-02-09	1347.5	200	118
Effelsberg	2013-02-10	1347.5	200	97
Total Observation Time				**1624**

Table 5.1.: Summary of all Crab pulsar radio observations taken with the Effelsberg telescope and the WSRT indicating the respective observation date (noted as epoch), the center frequency ν_{center}, the bandwidth BW and the observation length Δt.

[1] A negative sign of the bandwidth can result from data taking with an appropriate set of bandpass filters. The corresponding data set in Table 5.1 is not excluded from the sample due to this reason.

5.1.2. Coherent Dedispersion

The recorded radio observations of the Crab pulsar were all reduced offline via an already existing reduction pipeline developed by R. Karuppusamy (MPIfR, Bonn).
The effect most visible when looking at raw pulsar data is known as *Dispersion* (see Chapter 1.4.3). It causes the earlier arrival of pulses observed at higher frequencies than their counterparts at lower frequencies (Figure 5.1). The dispersion effect is caused by the ISM which is a cold plasma located between the pulsar and Earth that causes a frequency dependent refraction of electromagnetic radiation coming from a pulsar. It is therefore crucial to correct the data for this effect in order to make it usable for further analysis. The corresponding procedure is as known as *Dedispersion*.
Since the detection of pulsars, two major reduction methods of this effect were developed. The traditional method has been known as *Incoherent Dedispersion*. In this case the signal from the telescope (the bandpass) is divided into a number of frequency channels by an analog filterbank (see filterbank section in Figure 5.2).
A filterbank is an instrument which can divide the signal from a radio telescope into a specific number of frequency channels. The signal is then detected in each of these channels and shifted by a predicted dispersive delay of the center of each frequency channel using Equation 1.43 in Chapter 1.4.3 (Figure 5.2).
The resulting pulse signals in the single channels are added up afterwards and result in the incoherently dedispersed signal of the whole observing band (see bottom amplitude plot in Figure 5.2). The filterbank technique provides a possibility to reduce huge amounts of radio data and make them accessible to further processing without outages of the respective hardware. Since the dispersive delay is frequency dependend, it takes less computational power to correct each frequency channel (each having a smaller bandwidth than the total observing band) for it individually than without this kind of subdivision. The incoherent dedispersion method is referred to as post-detection technique since the signal is first detected and then reduced. A drawback of this method is that since the pulsar signal from the whole respective frequency channel is shifted to its center frequency by correcting its time of arrival according to Equation 1.43, an amount of dispersion is still enhanced in the resulting signal (that is, in the parts of the signal detected at other frequencies than the center frequency). This effect is known as dispersive smearing and is not reduced by the method of incoherent dedispersion which results in a lower time resolution of the data. The corresponding effect can be seen in the case of millisecond pulsar profiles which do not show their true shape (see the profile of PSR B1937+21 in Figure 1.2 (i) in Lorimer and Kramer [2012]). A deeper overview of analogue filterbanks and the method of incoherent dedispersion can be found in Chapter 5.2. in Lorimer and Kramer [2012].
Consequently, this reduction method was not used for the analysis presented in this thesis.
The second method how the dispersive delay of a pulsar signal can be reduced, is known as "Coherent Dedispersion". It is also known as a pre-detection method since in its case the signal is processed in the form of raw voltages, that is before the detection of the pulsar signal. Usually the signal is recorded on high-speed disks in this case and the forthcoming analysis is made entirely with a corresponding software.
Since pulsars are known as weak objects, the larger the bandwidth which is used for their observations, the more information of the neutron star can be recorded. With the methodof coherent dedispersion the signal with the total bandwidth is processed and not split which prevents the occurrence of dispersion smearing and corrects the signal entirely of its dispersive

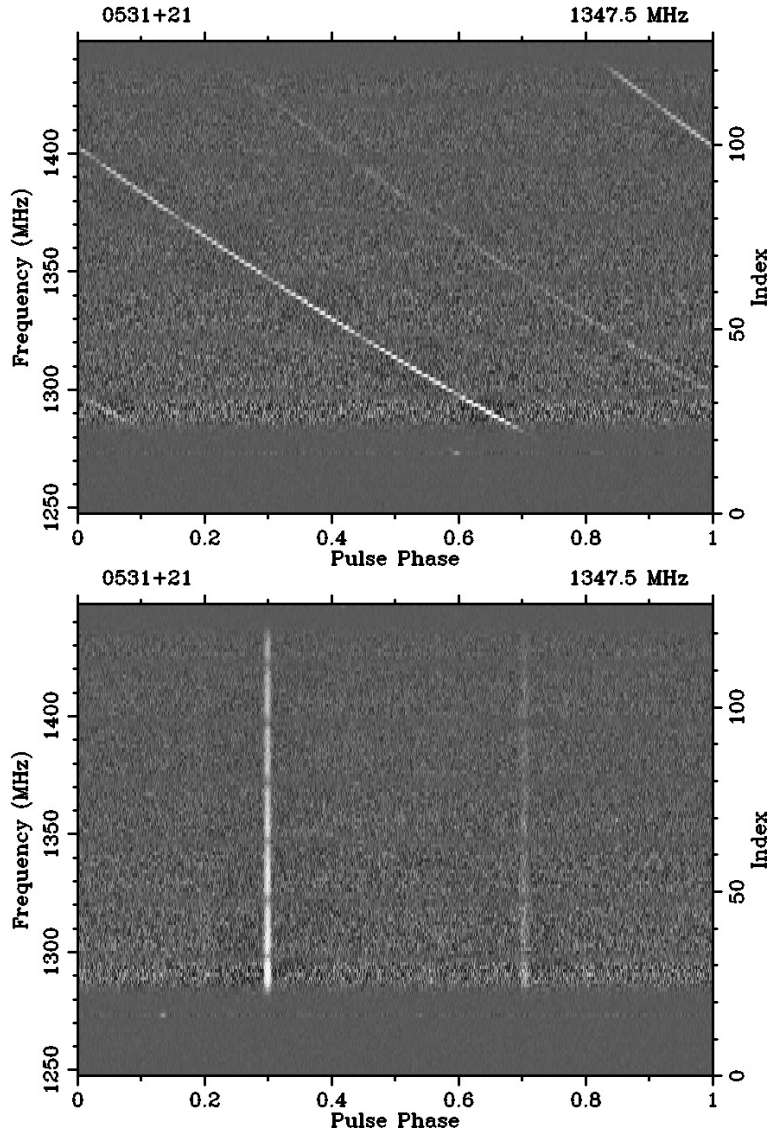

Figure 5.1.: Crab pulsar observations taken with the Effelsberg radio telescope on 09-02-13 before (upper plot) and after dedispersion (lower plot). The lower plot shows two distinct, straight pulses which are known as the Main pulse (P1) and the Interpulse (P2).

delay. During the process of this reduction technique, the pulsar signal is put through a filter known as "Chirp Filter". It causes a delay of the phase by an amount which depends on the frequency of the signal. At first the signal is entirely digitised before the pulsar signal is detected in it, that is with a sampling rate at least twice as high as the highest frequency contained in the signal. Since this is a computationally intensive procedure, the signal (with the total bandwidth) is mixed with a local oscillator down with its frequency to a band going

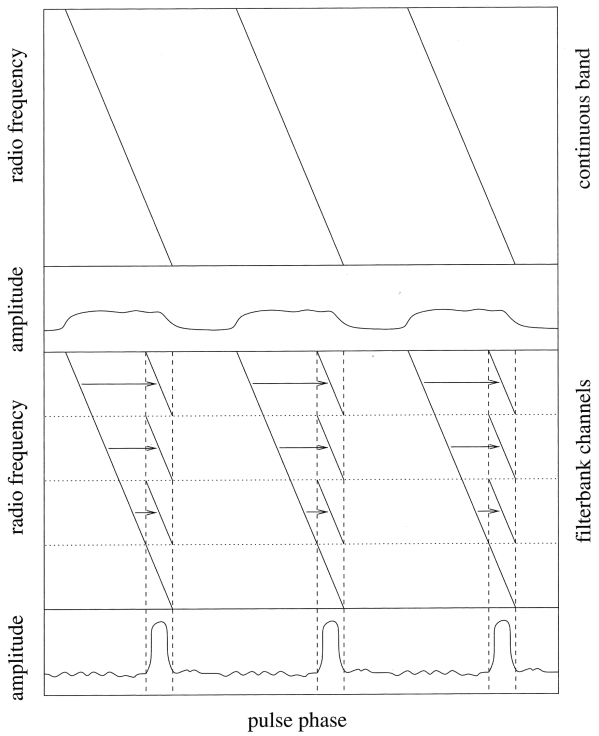

Figure 5.2.: The process of dedispersion as carried out in a filterbank system. The figure was adoptem from Lorimer and Kramer [2012].

from zero to its maximum at the total bandwidth of the signal ("Baseband"). To ease this usually computationally expensive process, the signal is split before the mixing to baseband takes place. The dedispersion procedure is carried out after the data samples were converted into the Fourier domain instead of using the time domain. The phase delay determined by the Chirp function is then applied to the data samples before the signal is recovered afterwards by a inverse Fourier transformation without containing the dispersive delay. Due to the preservation of the entire phase information of the signal, the coherent dedispersion method has been the approved method for high time resolution measurements and is widely used. A detailed explanation of this method is given in Hankins and Rickett [1975].
With regard to the data used for this study, in both cases, the Effelsberg radio telescope and the WSRT, the data was recorded in the form of raw voltages as baseband data and stored in a special file format called "dada"[2]. The reduction of the data was carried out with the open source digital library "Digital Signal Processing for Pulsars" (DSPSR[3], van Straten and Bailes [2011]). With DSPSR a mixed approach was used on the data. That is, single pulse integrations were calculated with a specific number of phase bins (2048 in the case of the WSRT data). A synthetic filterbank with N frequency channels was created (16 channels in the case of the WSRT radio data). These data files were afterwards coherently dedispersed to provide the highest time resolution for the identification of radio giant pulses (16 µs in the case of the Effelsberg data and 4 µs in the case of the WSRT data). For further reference see Chapter 2.4

[2]http://psrchive.sourceforge.net/
[3]http://dspsr.sourceforge.net/index.shtml

in van Straten and Bailes [2011].
Since the dedispersion procedure of all single pulses can lead to an overload of the available space on the corresponding disks, an additional step was included into the pipeline excluding all pulses below a certain threshold. To emphasise the necessity of this step in the data reduction, the following example is given: With a rotation period of 33 ms, the Crab pulsar provides 30 rotations per second which results in 14400 rotations in a 2 hour observation. Since in the case of this study one archive file provides data from one single rotation of the pulsar, a two hour observation can result (in the ideal case) in 14400 archive files (one archive file corresponding to 2.1 MB in the case of the Effelsberg data and to 4.1 MB in the case of the WSRT data) which we also refer to as single pulse files. Depending on the occurrence of the recorded single pulses in these data files, the total amount of data can become very huge. To prevent data loss due to technical problems during recording like breakdowns of the available disks, or simply lack of enough available space, an additional threshold was included into the reduction pipeline by R. Karuppusamy (MPIfR, Bonn) for the data from the Crab pulsar.
For the data from the WSRT, a threshold of $5\,\sigma$ was implemented. In the case of the data from the Effelsberg telescope, a threshold of $7\,\sigma$ was applied to the data. These thresholds were chosen to extract only the bright single pulses from the data and this way also giant radio pulses. The resulting single pulse files containing only bright pulses from the Crab pulsar were used for the forthcoming analysis.

5.1.3. Cleaning of Radio Data

Depending on the frequency at which the observations were carried out, each data set is affected by RFI. For the later correlation analysis all radio data sets were examined and cleaned with two programs from the PSRCHIVE package known as paz and pazi.
To make the search for RFI most effective, all single pulse files from each data set were combined (added up) into one resulting file using the psradd[4] program from the PSRCHIVE package. This way the S/N was increased which made the search for broadband RFI easier. Figure 5.3 shows one example of RFI occuring in one of such combined files from one Effelsberg radio data set. The summed up file was searched afterwards for RFI with the program pazi[5]. It enables the identification and removal of RFI out of frequency channels, subintegrations and phase bins. The latter is carried out manually and thus gives the user the possibility to search for RFI patterns in the data oneself. With pazi affected subintegrations and frequency channels were removed (commonly referred to as "zapped out") from the summed up file which was stored in another format after that.
After this process was completed, the corresponding commands for the automatic RFI excision with the "Pulsar Archive Zapper"[6] (paz) were applied to the single pulse data sets.
The results for all radio data sets are included in the appendix section (Chapter A).

5.1.4. Extraction of Giant Pulses

To identify giant pulses, single pulses need to be extracted from the data. At first, each archive file corresponding to one rotation of the pulsar was integrated ("scrunched") in frequency, time

[4] http://psrchive.sourceforge.net/manuals/psradd/
[5] http://psrchive.sourceforge.net/manuals/pazi/
[6] http://psrchive.sourceforge.net/manuals/paz/

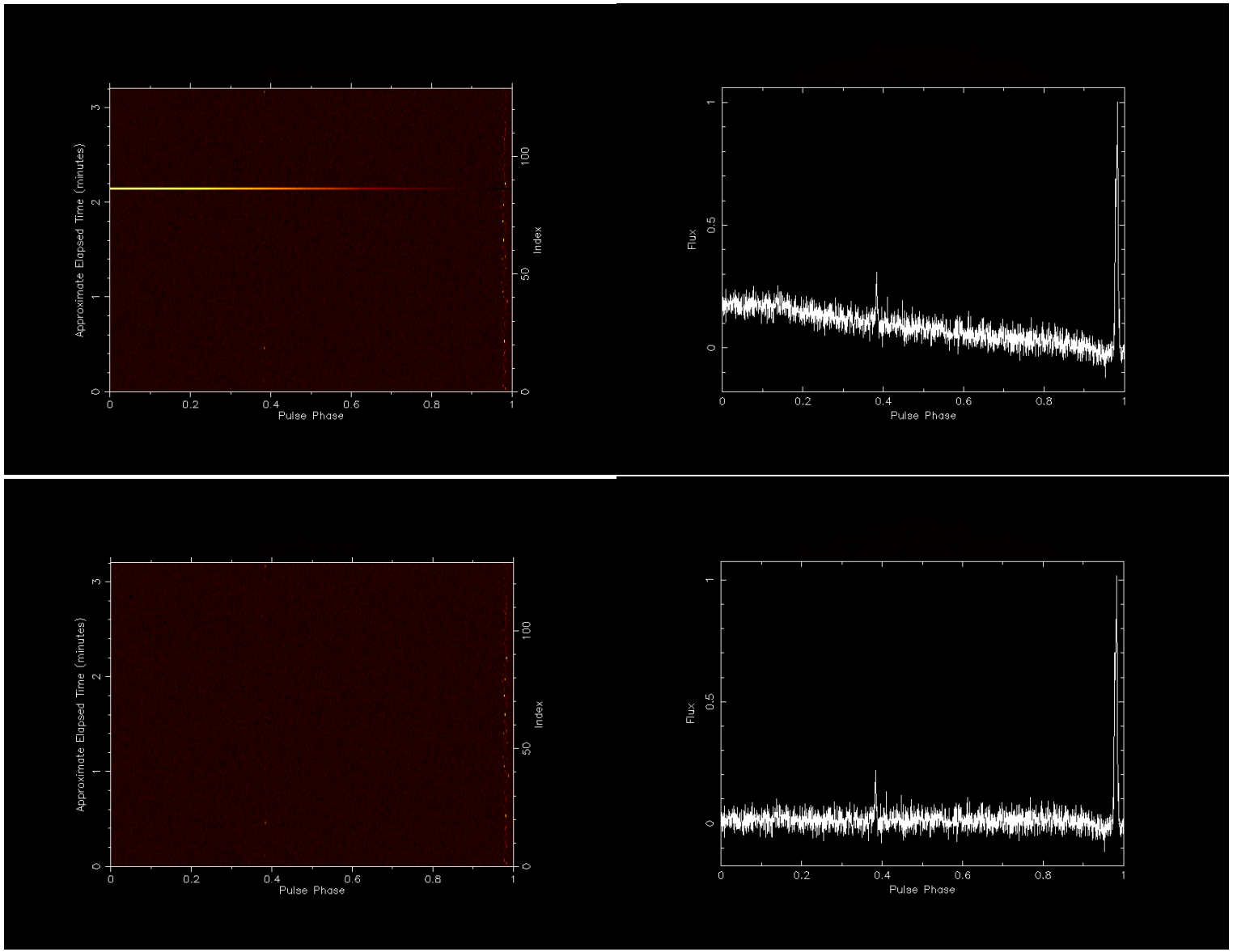

Figure 5.3.: Example of RFI in the Effelsberg data set from 2013-02-06. The figures show the elapsed time of the observations and the respective rotational phase (left panels) and the flux (arbitrary units) in dependence of the rotational phase (right panels). The P1 is located near phase 0.9 whereas the P2 is visible at a phase of about 0.4. The upper (lower) figures show the data before (after) they were were cleaned. The RFI is visible as a bright signal over the whole rotational phase (upper left figure) and causes a higher flux of the non-pulsed emission components as well as the P2 (upper right figure).

and polarization using the "Pulsar Archive Manipulator"[7] (pam) from the PSRCHIVE software package. In the case of the Effelsberg radio data sets this means (2048 phase bins, 128 frequency channels and 4 polarizations per archive file) the conversion in frequency (F), time (T) and polarization (p) to one frequency channel, one phase bin and one polarization of an archive file only. The resulting archive file is commonly referred to as FTp file and represents one data point per file as shown by the scatter plot in for example Figure 5.4, or Figure 5.11. In other words, with this process all phase bins, frequency channels and polarizations of the archive file are integrated away which results in only one of each of these parameters and consequently only one data point. This procedure is carried out for each archive file. In order to extract the strongest pulses from this data, each profile is weighted afterwards with the PSRCHIVE program "Psrwt"[8]. Psrwt provides several ways of weighting of profiles. For each giant pulse in a data set the respective S/N (not their weighted result) was printed into a separate text file. From this text file, parameters like the phase, the topocentric time (SAT) in MJD format, the root mean square (RMS), and a quantity known as Max/RMS (RMS normalized to the global maximum of all data points extracted from FTp files) were extracted and included into a final text file known as rms.txt (see Figure 5.5).
This way the topocentric times of arrival of bright pulses were determined for each data set and used in the further steps of data analysis.
After the extraction of single pulses from all radio data sets, it was noticed that in the case of the WSRT data from 2012-12-10 and 2013-02-02 additional components apart from the pulsed components are clearly visible in their Max/RMS values (see Chapter A.2 and Chapter A.9). Not finding an adequate explanation why additional components (referred to as artefacts from now on) are only visible in the data sets from these two nights, it is assumed they might have their origins in either technical reasons, or improper reduction of the data. Since for the correlation analysis only the barycentered pulsed components are used, both data sets were not excluded from the study, but treated with special care while searching for the existence of a correlation (see Chapter 5.3).

5.1.5. Barycentering of Arrival Times

Introduction
The signal from a pulsar suffers various distortions which cause delays of its TOAs on its way before it is detected with radio facilities on Earth. Travelling through the ISM causes delays in the signal depending upon frequency known as dispersion (Chapter 1.4.3). Apart from dispersion several additional effects occur which affect the TOA of a pulsar signal. They shall be shortly summarized here to explain the necessity of the whole barycentering process.
The total conversion which needs to be carried out for a pulsar signal arriving at a observatory is comprised of several components:

$$t_{BAT} = t_{SAT} + t_{clock} - \frac{\Delta D}{f^2} + \Delta_R + \Delta_E + \Delta_S \tag{5.1}$$

t_{BAT} is the corrected barycentric arrival time (BAT) of the pulsar signal. t_{SAT} is the topocentric site arrival time (SAT) of the pulsar signal at the respective observatory. The term t_{clock} refers to various clock corrections which will be explained in more detail in this chapter. The other

[7] http://psrchive.sourceforge.net/manuals/pam/
[8] http://psrchive.sourceforge.net/manuals/psrwt/

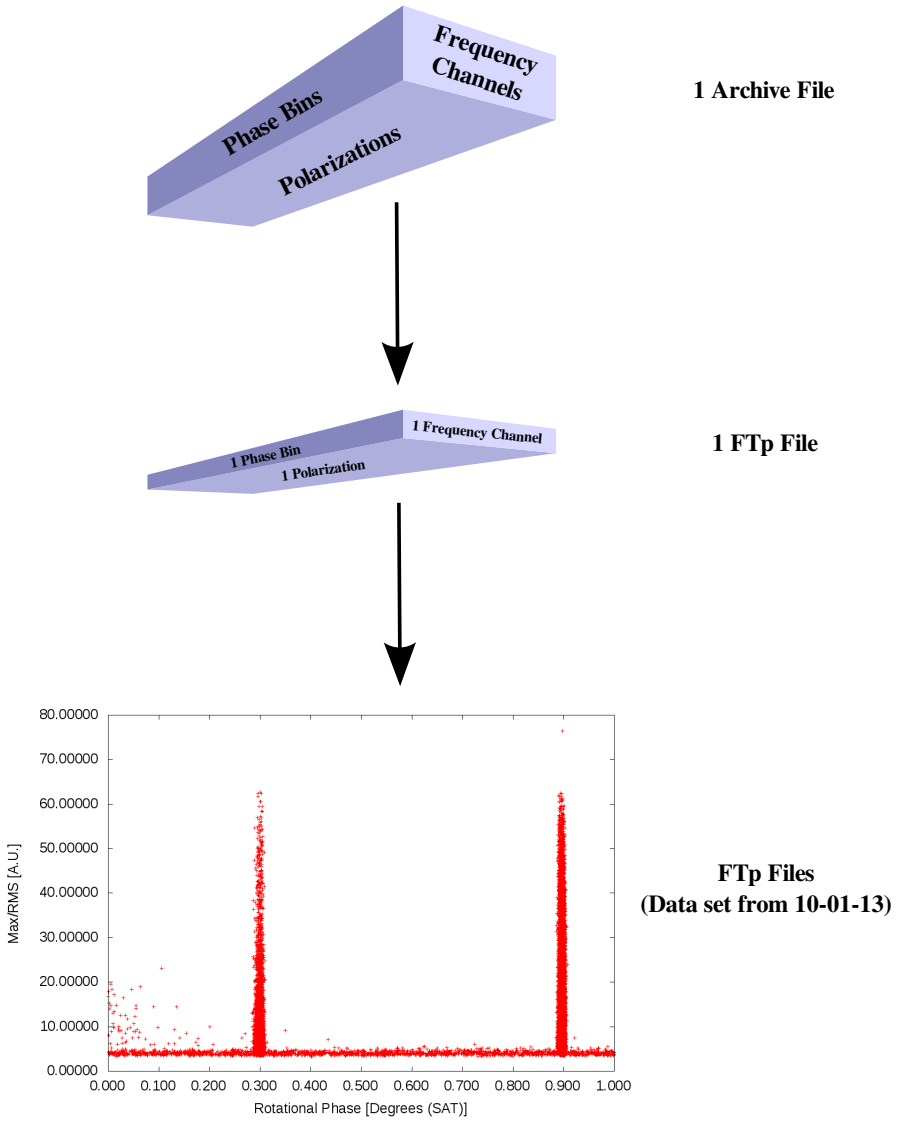

Figure 5.4.: Scheme of the extraction of single pulses from archive files. The archive file is converted into an FTp file via the integration over frequency, time and polarization. The FTp files from one data set are shown by the scatter plot for the data set from 10-01-13.

components in Equation 5.1 are known as the dispersive delay $\frac{\Delta D}{f^2}$ (in dependence of the frequency f at the Solar System Barycenter (SSB), the Roemer delay Δ_R, the Einstein delay Δ_E and the Shapiro delay Δ_S. General information (also with regard to more complex systems

```
phase 0.327026  ./000918/pulse_555430221.FTp epoch 56327.8717032393407664 max/rms 3.64797 rms 0.0116768 sum 0 snr 0
phase 0.53186   ./000918/pulse_555430187.FTp epoch 56327.8716900648654232 max/rms 15.6233 rms 0.0121279 sum 0 snr 0
phase 0.535889  ./000918/pulse_555430257.FTp epoch 56327.8717173547548899 max/rms 3.86137 rms 0.011396 sum 0 snr 0
phase 0.136963  ./000918/pulse_555430258.FTp epoch 56327.8717175890735339 max/rms 16.4352 rms 0.0134537 sum 0 snr 0
phase 0.534668  ./000918/pulse_555430361.FTp epoch 56327.8717578969245405 max/rms 5.44084 rms 0.0115586 sum 0 snr 0
phase 0.131226  ./000918/pulse_555430096.FTp epoch 56327.8716544338699050 max/rms 8.1091 rms 0.0115843 sum 0 snr 0
phase 0.134521  ./000918/pulse_555430349.FTp epoch 56327.8717530629366232 max/rms 7.06264 rms 0.0118491 sum 0 snr 0
phase 0.0101318 ./000918/pulse_555430261.FTp epoch 56327.8717187091299766 max/rms 3.94518 rms 0.011427 sum 0 snr 0
```

Figure 5.5.: Excerpt of the final parameters extracted from all scrunched archive files (FTp files) in the case of the WSRT data set from 04.02.14.

than solitary pulsars) can be found at the Tempo2 webpages[9].
When a pulsar signal is recorded at a observatory, it is tagged with the local site arrival time (usually measured with a OH maser clock). It needs to be converted to a uniform time standard known as Terrestrial Time (TT). This includes several steps. First the local site arrival times are converted to the Coordinated Universal Time (UTC) format. This is done by comparing the site arrival times with the arrival times provided by a Global Positioning System (GPS). The non-uniform rotation of the Earth is the reason for the inclusion of leap seconds. They are included by converting the observed arrival times from UTC format into the International Atomic Time (TAI). The difference between the UTC and TAI format is the sum of leap seconds

$$TAI = UTC + t_{leap} \tag{5.2}$$

In a last step, the arrival times are converted from TAI format into TT(TAI) which means the following conversion:

$$TT(TAI) = TAI + 32.184s \tag{5.3}$$

The reason for the introduction of the 32.184 s offset is of historical origin. The Terrestrial Time (TT) was historically the successor of another time scale known as Ephemeris Time (ET). When TT was introduced, its starting point was set to 01.01.1977, 0 h, 0 m, 32.184 s (p.218 in McCarthy and Seidelmann [2009]) in order to provide a smooth transition from the ET time scale. The time offset of 32.184 s is assumed to be constant and is a necessary factor for a conversion into Terrestrial Time. A deeper overview of the chronologically introduced time scales and conversions is given in McCarthy and Seidelmann [2009].
The physical model of the Earth, known as Geoid, describes the shape of the Earth under the influence of its rotation and gravitation only. In reality, this shape is deformed by tides and winds. TT(TAI) is the time standard of an ideal atomic clock located on the Geoid. Consequently the following clock corrections chains are applied by Tempo2 to the site arrival times in the case of the Effelsberg and WSRT data (all included in t_{clock} in Equation 5.1):

$$\text{eff2gps.clk} \rightarrow \text{gps2utc.clk} \rightarrow \text{utc2tai.clk} \rightarrow \text{tai2tt\_tai.clk}$$

$$\text{wsrt2gps.clk} \rightarrow \text{gps2utc.clk} \rightarrow \text{utc2tai.clk} \rightarrow \text{tai2tt\_tai.clk}$$

[9] http://www.atnf.csiro.au/research/pulsar/tempo2/index.php?n=Main.T2calculator

The quantitative values of these corrections were determined with Tempo2 using its general2 plugin can be found in Table 5.2.

Facility	SAT → GPS [s]	GPS → UTC [s]	UTC → TAI [s]	TAI → TT(TAI)[s]
eff	$1.42 \cdot 10^{-5}$	$6.28 \cdot 10^{-9}$	35	32.1839
wsrt	$-6.81 \cdot 10^{-5}$	$6.28 \cdot 10^{-9}$	35	32.1839

Table 5.2.: Clock corrections applied to the topocentric arrival times (SATs) by the general2 plugin of Tempo2. In the case of the Effelsberg data the data set from 2013-01-12 was used and for the WSRT the data set from 2013-01-10. These corrections have more decimal places than shown here. They are shown here just as an example to give an idea of the orders of magnitude of the clock corrections to emphasise their necessity.

The effects caused by the ISM visible in pulsar radio data, were discussed in Chapter 1.4.3. Taking up on these considerations, it was deduced the radio signal of a pulsar is delayed by the ISM in dependence of its frequency. According to Equation 1.43 the term $\frac{\Delta D}{f^2}$ in Equation 5.1 corrects the arrival times of the pulsar signal for the dispersive delay and converts them into a signal observed at infinitly high frequencies which is not affected by the ISM. The quantity D in Equation 5.1 stands for:

$$\Delta D = DM \cdot d \tag{5.4}$$

(d being the dispersion constant according to Equation 1.44).
The actual barycentering of the signal is carried out by the other terms in Equation 5.1 which will be discussed now in further detail.
The first barycentric correction is carried out by determining the Römer delay Δ_R. The Römer delay represents the time which it takes the light (of the observed pulsar) to travel from the observatory, or the used telescope in this case, to the SSB (see Figure 5.6). It is a geometric effect caused by the nature of the Solar System in which the Earth orbits around the Sun. In other words, when the Earth is closer to the pulsar than the Sun (on its rotation around the latter), then the signal from the pulsar will arrive earlier at the respective observatory on Earth than at the SSB. If the Sun is closer to the pulsar than the Earth, the pulsar signal will arrive earlier at the SSB (Figure 5.6). Consequently, throughout the course of a year the arrival times of the pulsar signal encounter a delay which has a sinusoidal form (see Figure 5.7).
To account for this effect, the Tempo2 software determines the distance from the telescope at the observatory which was used for the observations to the center of the Earth and the distance of the latter to the SSB (marked as vector R in Figure 5.6).

For a determination of the vector R, an ephemeris which reflects the velocities and accelerations of all bodies in the Solar System needs to be used. This ephemeris is released by the Jet Propulsion Laboratory and commonly referred to as "Development Ephemeris" (DE). For the

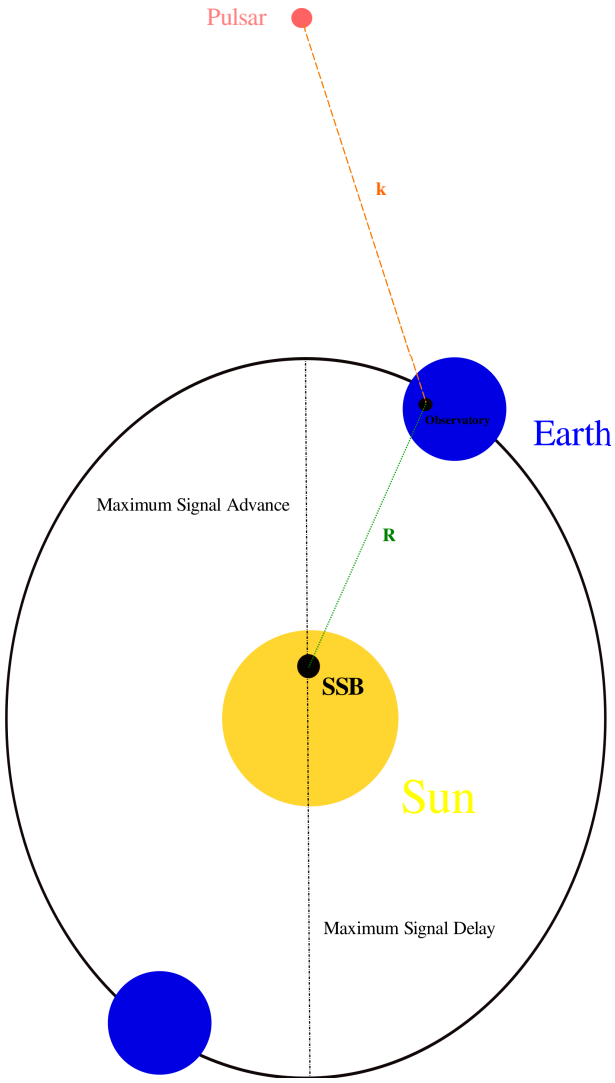

Figure 5.6.: Scheme of the Römer delay caused by the rotation of the Earth around the Sun causing additional time advances, or delays of the signal depending upon the location of the Earth towards the Sun when the distant pulsar is being observed. SSB stands for the Solar System Barycenter, R is the vector from the observatory to the SSB, k is a unit vector pointing from the observatory to the pulsar.

study presented here the DE 200 ephemeris is used whereas for radio pulsar timing procedures a newer version known as DE 405 ephemeris is currently in use. The difference between both is their time of validity. The DE 200 ephemeris is regarded as valid for the time span from 1984 till the end of 2002 whereas the DE 405 ephemeris has been in use for observations from 2003 onwards. The reason why an older ephemeris was used for the study presented here, is shown

by the barycentering procedure in the next chapters.
Referring to Figure 5.6 the Römer delay can be determined via the following equation:

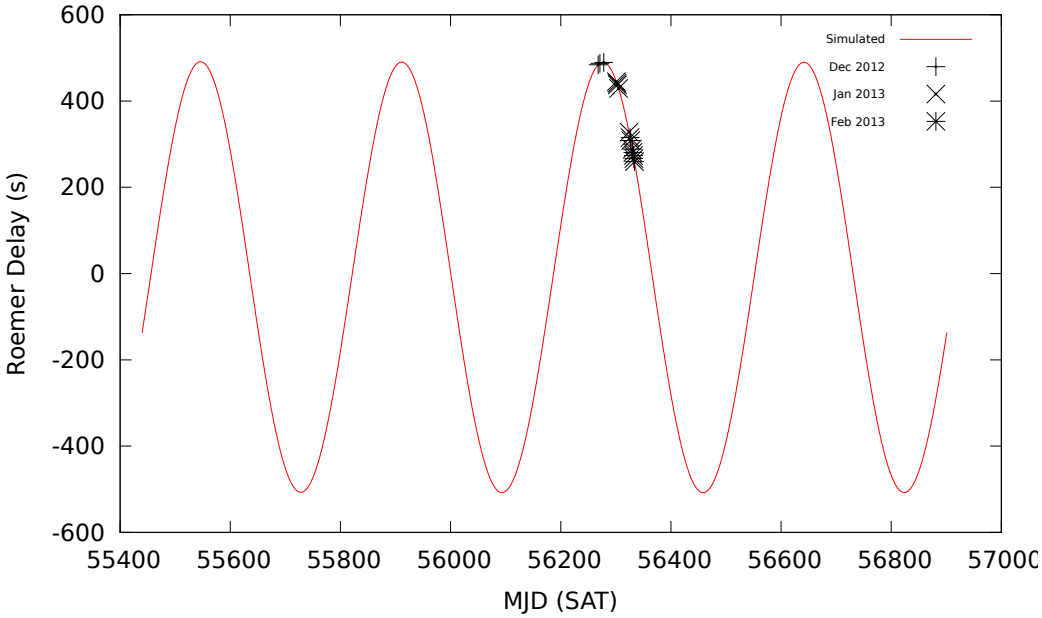

Figure 5.7.: Simulated Römer delay (red sinusoidal curve) in the time span from 01-09-2010 till 01-09-2014. The radio data used for this study are indicated by the black markings.

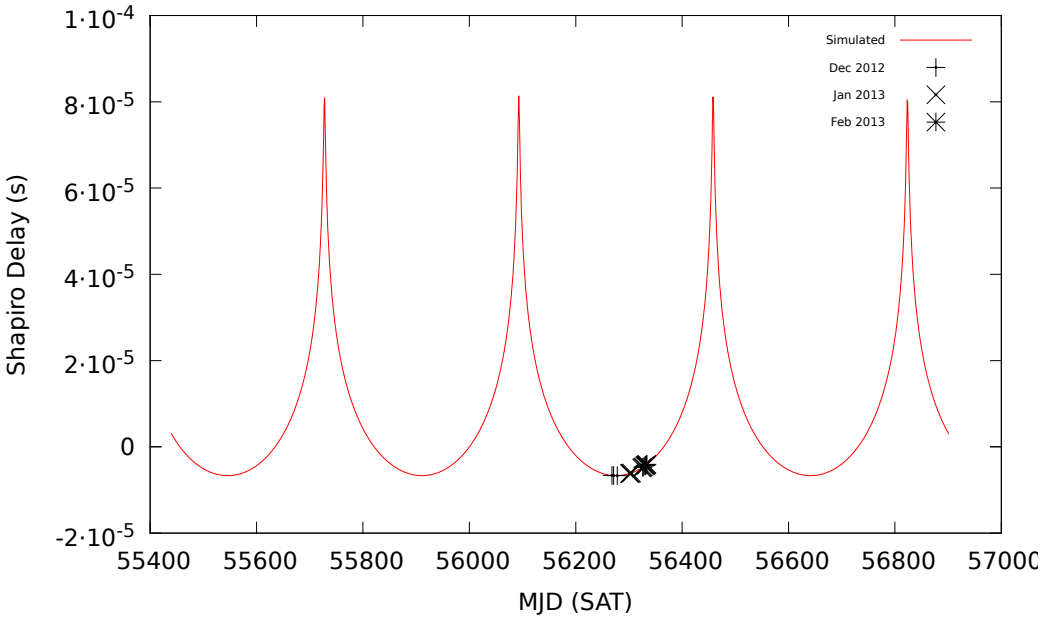

Figure 5.8.: Simulated Shapiro delay (red curve) in the time span from 01-09-2010 till 01-09-2014. The radio data used for this study is indicated by the black markings.

$$\Delta_{\mathrm{R}} = \frac{\mathbf{R} \cdot \mathbf{k}}{\mathrm{c}} \tag{5.5}$$

The quantity c stands for the speed of light and the vectors are marked with bold letters.
The next correction included in Equation 5.1 is commonly referred to as the Einstein delay Δ_E (Figure 5.9). It contains the effects of all redshifts that affect the pulsar signal. The dominant redshift is caused by the gravitational potential of the Sun. Another source is the relative motion of the observatory with respect to the pulsar. The Einstein delay of a signal at the SSB can be computed using the following equation (Edwards et al. [2006]):

$$\Delta_{\mathrm{E}} = \frac{1}{\mathrm{c}^2} \int_{\mathrm{t}_0}^{\mathrm{t}} [\mathrm{U} + \frac{\mathrm{v}^2}{2} + \chi + \phi] \cdot \mathrm{dt} \tag{5.6}$$

The quantity U is the gravitational potential which accounts for the Sun and all planets in the Solar System. The effect of the gravitational potential of the Earth is not included since it is already contained in the calculation of TT(TAI) in Equation 5.3. Since the gravitational potential is larger for objects with higher masses, the pulsar signal is considerably affected by the Sun and by Jupiter. Also smaller celestial bodies can have a measureable influence if the pulsar signal passes close to them. Consequently, in the case of high precision timing, the quantity ϕ in Equation 5.6 needs to be added to account for the influence of asteroids.
The velocity v is the one of the geocentre relative to the SSB. It is important because of the relativistic time dilation on Earth compared to the SSB which is sufficiently close to an inertial frame. Higher order relativistic effects produce a small long term trend that is summarized by χ. All these effects are discussed in more detail by Fukushima [1995] and Irwin and Fukushima [1999].
The mass of an astronomical object causes a curvature of space time which affects both time and space. The effect on time has already been considered in the Einstein delay. The effect on space, the extension of the path relative to the path of the signal if the object would not be there, introduces an additional delay of the pulsar signal which is known as the Shapiro delay Δ_S (Equation 5.1, Figure 5.8). It was originally discussed by (and later named after) Irwin Shapiro who proposed radar experiments with the inner planets of the Solar System in order to test the theory of general relativity originally formulated by Albert Einstein. Naming it the fourth test of general relativity, Shapiro suggested in Shapiro [1964] to send radar signals to Mercury and Venus for a verification of a time delay of their echos. Later observations of the corresponding arrival times (Shapiro et al. [1968]), showed a Shapiro delay of about 160 μs (Figure 3 in Shapiro et al. [1968]) due to the additional path length around the Sun during the superior conjunction of Mercury. The Shapiro delay caused by a number of different objects, can be calculated via the following equation:

$$\Delta_S = -2 \sum \frac{G \cdot m_i}{c^3} \cdot \ln \left[\mathbf{k} \cdot \mathbf{s}_i + |s_i| \right] + \Delta_{S2} \tag{5.7}$$

In this equation m_i is the mass of object i, $\mathbf{k}$ is the unit vector in the direction of the pulsar, $\mathbf{s}_i$ is the vector from object i to the telescope and Δ_{S2} is a correction of second order (see Edwards et al. [2006]). The increases in terms of arrival time which the pulsar signal is going through caused by the Shapiro delay are shown in Figure 5.8.

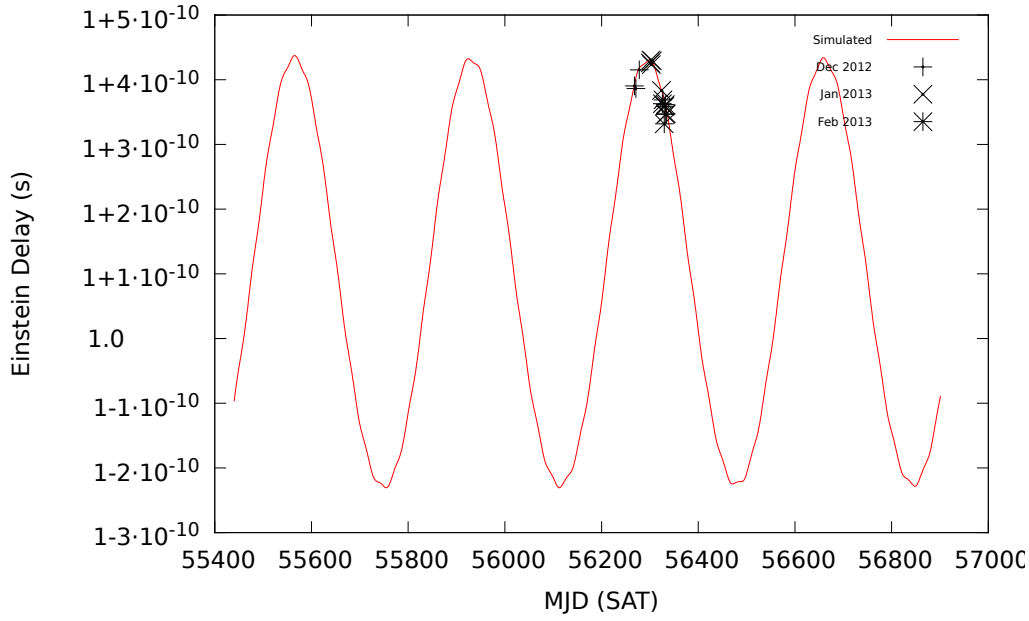

Figure 5.9.: Simulated Einstein delay (red curve) in the time span from 01-09-2010 till 01-09-2014. The radio data used for this study is indicated by the black markings.

To emphasise the magnitudes of the barycentric corrections discussed here, an overview of them is given in Table 5.3 determined from two Crab pulsar radio data sets taken with the Effelsberg radio telescope and the WSRT which were used for this study. As can be deduced from the corrections in this table, the Römer delay has the highest effect on the arrival times of the pulsar signal. Converting the values given in seconds in Table 5.3 into rotations of the Crab pulsar, results in orders of about 13242 (Römer delay), about $1 \cdot 10^{-4}$ (Shapiro delay), 30 (Einstein delay) and about 3 (Dispersive delay). This conversion shall emphasise the necessity of barycentric corrections due to the heavyness of disruptions which the pulsar signal already encountered when it is detected at an observatory on Earth.

Throughout the two hour measurements in the case of these two data sets, the delays changed by the following values (in each case the value from the beginning and the end of the observation was taken):

Facility (Epoch)	Δ_R [s]	Δ_E [s]	Δ_S [s]	Δ_{ISM} [s]
Effelsberg (2013-01-12)	429	1	$-6 \cdot 10^{-6}$	0.13
WSRT (2013-01-10)	437	1	$-6 \cdot 10^{-6}$	0.12

Table 5.3.: Barycentric corrections to the arrival times of the Crab pulsar data sets from 2013-01-12 taken with the Effelsberg radio telescope and from 2013-01-10 taken with the WSRT. The corrections were determined with the general2 plugin from the Tempo2 software package.

Facility (Epoch)	$\delta(\Delta_R)$ [s]	$\delta(\Delta_E)$ [s]	$\delta(\Delta_S)$ [s]	$\delta(\Delta_{ISM})$ [s]
Effelsberg (2013-01-12)	0.51	$3.7 \cdot 10^{-12}$	$5 \cdot 10^{-9}$	$1.6 \cdot 10^{-8}$
WSRT (2013-01-10)	0.31	$4 \cdot 10^{-12}$	$3 \cdot 10^{-9}$	$5 \cdot 10^{-9}$

Table 5.4.: Changes of the barycentric corrections (marked with δ) during an observation time span of two hours in the case of the same data sets as in Table 5.3.

Deducing from Table 5.4, the difference is largest as expected in the case of the Römer delay due to the movement of the Earth around the Sun.
A deeper discussion of the timing model which is used by the Tempo2 software is given in Edwards et al. [2006].
To carry out all of these corrections on the arrival times of the Crab pulsar (and get thus a proper barycentering of the signal), a specific procedure needed to be developed for the barycentering process as will be described in the next chapters.

Preparation for Barycentering – The Observation file
The barycentering of the topocentric radio arrival times is carried out with the pulsar timing software Tempo2. For this step in the analysis, the text files containing the topocentric arrival times (Figure 5.5) need to be converted into arrival time files, also known as observation files, or tim files[10]. Each tim file contains the arrival times of the pulsar signal detected at the respective observatory in the following structure:

```
file   freq   sat   satErr   siteID
```

The file name is in this case the one of the scrunched archive files, or FTp files. Freq is the center frequency of the (taken) observations, sat is the topocentric arrival time and satErr its error. siteID is the code for the site under which Tempo2 recognizes the respective telescope. A list of the available site codes for various radio telescope can be found in the Tempo2 software package as aliases. For this study only the one of the Effelsberg radio telescope and the WSRT were used:

```
eff   g
wsrt  i
```

[10] http://www.atnf.csiro.au/research/pulsar/tempo2/index.php?n=Documentation.ObservationFiles

The first row consists of the abbreviated names for various radio facilities and the second row are the Tempo2 site codes for each observatory. In the case of our Effelsberg and WSRT data sets, the site IDs correspond to g and i. An example of a tim file is shown in Figure 5.10. The tim file is together with the parameter file (next Chapter) the input files for the barycentering process with Tempo2.

```
FORMAT 1
./000386/pulse_169518151.FTp 1380 56271.0657605310230604 0.001 i
./000386/pulse_169518209.FTp 1380 56271.0657831379663231 0.001 i
./000386/pulse_169518322.FTp 1380 56271.0658271295241530 0.001 i
./000386/pulse_169518267.FTp 1380 56271.0658057161713048 0.001 i
./000386/pulse_169518116.FTp 1380 56271.0657471595844172 0.001 i
./000386/pulse_169518140.FTp 1380 56271.0657564188790044 0.001 i
./000386/pulse_169518347.FTp 1380 56271.0658369903243713 0.001 i
./000386/pulse_169518366.FTp 1380 56271.0658443356206420 0.001 i
```

Figure 5.10.: Excerpt of a tim file for the WSRT data set from 2012-12-10.

Preparation for Barycentering – The Ephemeris file
An ephemeris file, mostly called parameter file, is a text file that contains a set of parameters as instructions for the calculations carried out with Tempo2 and a rotation model of the respective pulsar for which the parameter file was originally built. Depending upon the studied pulsar, it can contain a varying number of parameters. For our study here, parameter files for the Crab pulsar, PSR B1133+16 and PSR B1112+50 were used. An example of the used parameter file for the Crab pulsar is given here:

```
PSRJ      J0534+2200              Pulsar Name
RAJ       05:34:31.97232          J2000 Right Ascension
DECJ      +22:00:52.069           J2000 Declination
F0        29.6957720714  2.0      Rotational Frequency
F1        3.7049471e-10  5.2e-16  First Derivative of Rotational Frequency
PEPOCH    56215.00000021756       Epoch of period determination
DM        56.799                  Dispersion Measure
DM1       0.01963                 First derivative of Dispersion Measure
CLK       TT(TAI)                 Definition of used clock correction files
TZRMJD    56215.00000021756       Prediction mode: Time
TZRFRQ    -1                                       Frequency
TZRSITE   @                       Site for which template was built
EPHEM     DE200                   Solar System Ephemeris which needs to be used
UNITS     TDB                     Time format which needs to be used by Tempo2
```

The colors shall only indicate at this point that the parameters included in a parameter file have different tasks. The parameters with the same color belong to the same task. A full description of all parameters which can be included into a parameter file, can be found on the corresponding Tempo2 webpages[11]. Every parameter consists of a label and a value. In some cases like for example the rotational frequency and its derivatives, an uncertainty value

[11] http://www.atnf.csiro.au/research/pulsar/tempo2/index.php?n=Documentation.Parameters

is also given. Not displayed in this example here, but nevertheless common are flags which are located in the line of a parameter and tell Tempo2 this way that it shall fit for it. A flag value of 1 tells Tempo2 to fit this parameter and a value of 0 tells it to hold the respective value fixed.

Barycentering of Radio Data Sets
This part of the analysis turned out to be a bit complicated at first as the Crab pulsar is a young neutron star and exhibits a certain amount of timing noise (Chapter 1.4.4). This results in the fact that for each observation of the Crab pulsar a new ephemeris file needs to be build which is as near in time to the actual observations as possible. What this means in detail will be outlined in the following examples. All data sets were barycenterd using the pulsar timing software Tempo2 (Hobbs et al. [2006b]) in combination with the Barycenter plugin developed by J. Verbiest (MPIfR, Bonn) and V. Kondratiev (ASTRON, Netherlands).
For the barycentering of all radio data sets an ephemeris file was chosen which had been built based on a template for infinite frequencies (TZRFRQ = -1) located at the SSB (TZRSITE = @):

Par File I

```
PSRJ    J0534+2200
RAJ     05:34:31.97232
DECJ    +22:00:52.069
F0      29.6957720714   2.0
F1      -3.7049471e-10  5.2e-16
PEPOCH  56215.00000021756
DM      56.799
DM1     0.01963
CLK     TT(TAI)
TZRMJD  56215.00000021756
TZRFRQ  -1
TZRSITE @
EPHEM   DE200
UNITS   TDB
```

As the first step of the barycentering process, the parameters reflecting the used template, or timing model, were kept fixed (italic letters). Figure 5.11 shows the result of the barycentering process with the "Par File I". The reason for this non-alignment is obvious as the parameter file was built for a different time (MJD=56215) than it was used for (MJD=56268). Since the Crab pulsar prolonged in its rotation, the ephemeris is not valid for the time which our observations adress.
For a data set which spans over three months of time, certain parameters in the parameter file need to be updated. A monthly updated ephemeris model is published by the Jodrell Bank Radio Observatory[12] (Lyne et al. [1993]).

To keep the ephemeris file updated with regard to the observations, the Rotational Frequency

[12] www.jb.man.ac.uk/pulsar/crab/crab2.txt

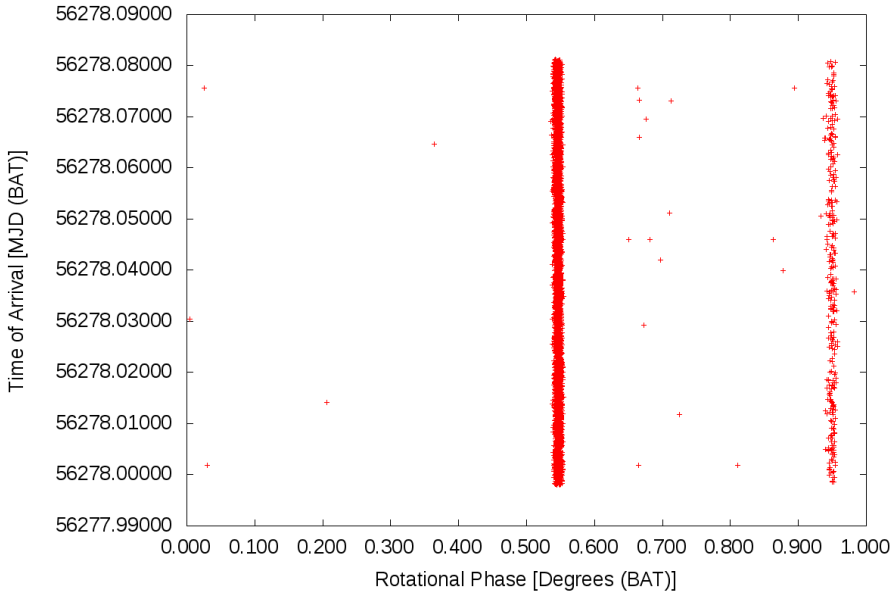

Figure 5.11.: Barycentered (BAT) radio data set from 07-12-12 taken with the Effelsberg radio telescope. The brighter pulse located a phase of 0.5 and 0.6 is P1 while the other one near a phase of 1.0 is P2. The barycentering process was not successful in this case since both peaks are not located at phase 0 and 0.4 as originally expected.

F, PEPOCH, DM and DM1 parameters were updated for each month with the values from the Jodrell Bank Radio Observatory. Here, the parameter file the case for December 2012 is illustrated (italic letters in Par File II):

Par File II

```
PSRJ     J0534+2200
RAJ      05:34:31.97232
DECJ     +22:00:52.069
F0       29.6938196276    3.0
F1       -370430.01E-15   0.73
PEPOCH   56276.000000254050925925 92
DM       56.8554
DM1      -0.27529
CLK      TT(TAI)
TZRMJD   56215.00000021756
TZRFRQ   -1
TZRSITE  @
EPHEM    DE200
UNITS    TDB
```

All TZR parameters were kept fixed during this procedure (italic letters in Par File I). The result of the respective barycentering process is shown in Figure 5.12. Again no alignment is

visible contrary to what was expected since the varying parameter values had been updated:

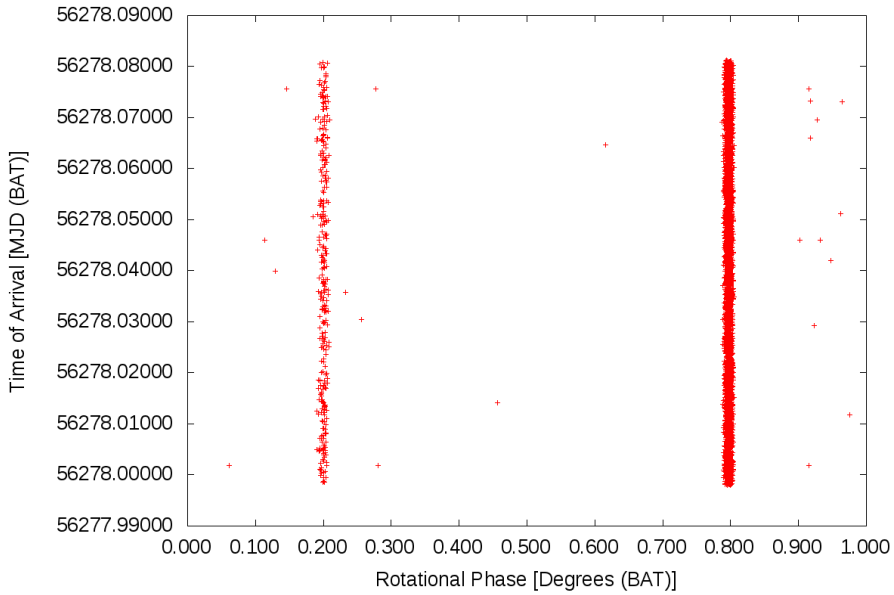

Figure 5.12.: Phase diagram of Crab pulsar observed on 07-12-12 with the Effelsberg radio telescope. This time the barycentering was carried out with the updated Par File II ephemeris. Nevertheless the P1 component is located at phase 0.8 whereas P2 is visible near phase 0.2. Hence even when certain parameters are updated to the respective month in which the observations were taken, the pulse components from the Crab pulsar are not located at the anticipated phase values after barycentering which emphasises that the used ephemeris file in this case is still not the right one.

In the final step of this part of the analysis, another change in the Par File II ephemeris was included as the previous barycentering process was not successful (Figure 5.12). The prediction mode for which the ephemeris file was originally built involves three parameters: TZRMJD, TZRFREQ, TZRSITE. To update the ephemeris file as near as possible in time to the taken observations, in the case of each month, the TZRMJD parameter was substituted by the same value as PEPOCH (Par File III). The result for the data set from 07-12-12 is given in Figure 5.13.

Par File III

```
PSRJ     J0534+2200
RAJ      05:34:31.97232
DECJ     +22:00:52.069
F0       29.6938196276   3.0
F1       -370430.01E-15  0.73
PEPOCH   56276.000000254050925925 92
```

```
DM      56.8554
DM1     -0.27529
CLK     TT(TAI)
TZRMJD  56276.000000254050925925 92
TZRFRQ  -1
TZRSITE @
EPHEM   DE200
UNITS   TDB
```

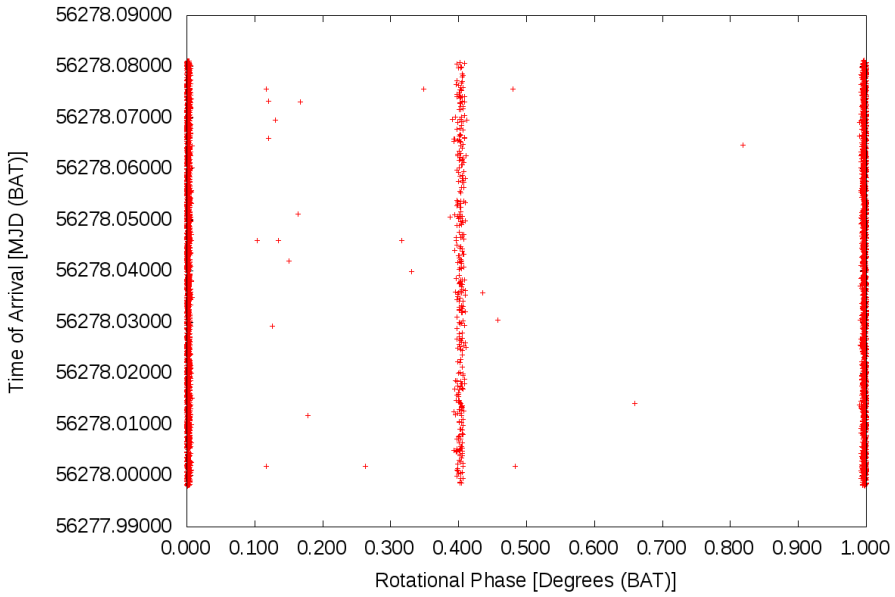

Figure 5.13.: Phase diagram of Crab pulsar observed on 07-12-12 with the Effelsberg radio telescope. This time the barycentering was carried out with the Par File III ephemeris.

This demonstration shows that for the proper barycentering of the Crab pulsar radio data an ephemeris is needed which was built in the same time in which the observations took place. The same procedure was carried out independently for all data sets from all three months. In each case, the F0, F1, DM, DM1 and PEPOCH parameters were updated according to the ephemeris provided by the Jodrell Bank Observatory (JBO) and the TZRMJD value was changed to the one of PEPOCH. In the case of the radio data sets taken with the Effelsberg telescope, a time offset of 97.284 ms needs to be subtracted from the the topocentric TOAs due to a jump between the internal clock of the used pulsar backend and the OH maser clock at the observatory. This procedure was carried out for all data sets taken with the Effelsberg radio telescope.
The results of all barycentered data sets are shown in Figure 5.14 and the resulting ephemeris files for all three months can be found in Chapter A.16.
The resulting radio ephemeris files were used in exactly the same form for the barycentering

of the simultaneously taken γ-ray data sets (Chapter 5.2.4) as an essential step towards a successful correlation study.

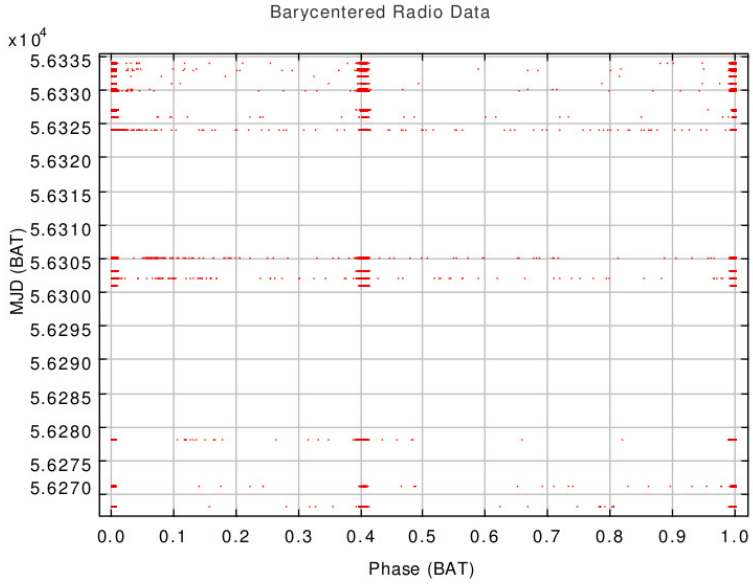

Figure 5.14.: All radio data sets from winter 2012/13 barycentered as described in this chapter. The P1 is located at phase 0.0 and 1.0. The P2 is centered around phase 0.4.

5.2. The MAGIC Pulsar Analysis Chain

5.2.1. Overview of Data Sets

The γ-ray observations presented in this study were carried out with the MAGIC telescopes in stereo mode. All data sets which were used for this study are given in Table 5.5. Since it was not in use when the observations were taken, no data taken with the Sum Trigger was included into this study. All observations were carried out with the standard trigger system providing a threshold of 60 GeV.

Facility	Epoch[13]	Δt [min]	Zd Range [°]	Radio Overlap
Winter 2012/13				
MAGIC	2012-12-07	194	11.8 - 35.0	Eff
MAGIC	2012-12-10	121	14.9 - 15.1	WSRT
MAGIC	2012-12-17	120	15.4 - 14.2	Eff
MAGIC	2013-01-09	177	34.6 - 9.1	WSRT
MAGIC	2013-01-10	112	14.0 - 15.4	Eff
MAGIC	2013-01-11	120	15.5 - 14.1	WSRT
MAGIC	2013-01-13	111	14.9 - 14.1	Eff
MAGIC	2013-02-01	126	15.5 - 15.4	Eff
MAGIC	2013-02-03	123	18.6 - 12.1	WSRT
MAGIC	2013-02-04	119	15.5 - 15.2	WSRT
MAGIC	2013-02-07	135	14.7 - 18.1	Eff
MAGIC	2013-02-08	123	13.8 - 16.6	Eff
MAGIC	2013-02-09	110	13.2 - 14.7	Eff
MAGIC	2013-02-10	118	12.6 - 17.9	Eff
MAGIC	2013-02-11	114	11.1 - 18.7	Eff
Total Observation Time		**1923**		

Table 5.5.: Summary of Crab pulsar observations with the MAGIC telescopes in stereo mode. All listed observations were taken simultaneously with either the Effelsberg radio telescope, or the WSRT as is stated in the last column.

5.2.2. Standard Analysis Chain

The standard analysis chain consists of several steps ranging from the calibration to the background suppression procedure and the determination of a spectrum. All the steps belonging to this part of the analysis have been carried out with the standard software package MARS ("MAGIC Analysis and Reconstruction Software"). It contains a number of C++ programs based on ROOT which have been developed by the MAGIC Collaboration for the analysis of γ-ray data from Imaging Air Cherenkov telescopes (Moralejo et al. [2009]). Each of these programs can be used on a data set of interest by modifying its input card (commonly also referred

[13] Data taken with the MAGIC telescopes are named after the sunrise convention. That is, the date of the observations is set according to the day at which sunrise takes place.

to as rc file). The input card contains all settings for the respective program as well as the path to the input data files and the path where the output should be stored after processing. The order of the analysis steps described here mirrors the order in which the analysis of the MAGIC data was carried out. It needs to be mentioned that the analysis steps in the forthcoming three chapters (processing of raw data, calibration and image cleaning), were done automatically by a pipeline provided by the MAGIC Collaboration. They will nevertheless described here shortly for the completeness of the γ-ray analysis. The manual data analysis carried out by the author of this thesis started with the quality check of the γ-ray data after the image cleaning.
A schematic overview of the analysis chain applied for this thesis is shown in Figure 5.15.

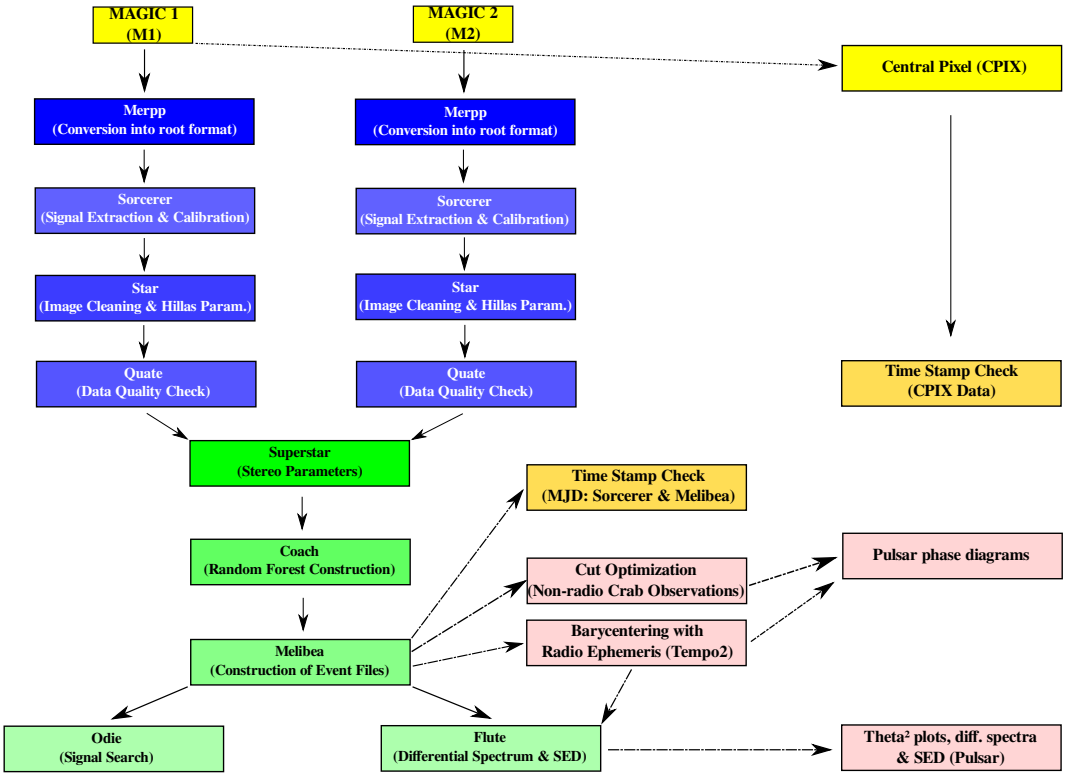

Figure 5.15.: A scheme of the analysis chain applied to the MAGIC data presented in this thesis. The analysis of the data was started by the author of this thesis from Star level onwards.

Processing of raw γ-Ray Data

The very first step of the processing of MAGIC data is the conversion of data files from raw format to root format. This is done by the program "Merpp" from the MARS software package. The raw files do not automatically contain all information about the subsystems of both telescopes. This information needs to be included first which is also done by Merpp. Besides

only data files in root format can be processed further. Consequently, Merpp includes the information about the respective telescope subsystems (starguider, drive system etc.) into the data files and converts them from raw to root format. This procedure is not carried out by the analyzer, but by a automatic reduction pipeline provided and run by the MAGIC Collaboration.

Calibration of γ-Ray Data
After including the information from all subsystems to the raw data with Merpp, the resulting data are ready for calibration. The calibration process is crucial for the further processing of the data as it makes the determination of the charge and the time of arrival of the signal in each camera pixel possible. For an extraction of the pulses which are caused by the signal, it is displayed as a waveform. The corresponding baseline is estimated via pedestal events (events without any pulses caused by a signal, that is a random trigger values. One can understand it as the background noise, or the darkfields as commonly known in the case of optical observations.) in the case of the data presented in this study. The baseline results from a Gaussian fit of the corresponding waveform of a high number of pedestal events. To determine the light pulses caused by the recorded signal, the baseline needs to be subtracted from it so that the integral of the light pulse signal can be calculated. The integral resulting from this subtraction can be extracted via different methods: The spline method, the sliding window method, the digital filter method and the fixed window method. The different methods are discussed in more detail in Albert et al. [2008a]. The extraction of this integral results in the signal in each camera pixel in the units of integrated readout counts. To convert the latter into the unit of photoelectrons, a conversion factor known as F-factor is used. The corresponding conversion is commonly referred to as F-factor method (Mirzoyan et al. [1997]). With the F-factor method the proportionality between the number of photoelectrons and counts is measured under the assumption that fluctuations in the signal are Poisson distributed. According to it a light pulse with a number τ of photelectrons leads to a signal with the following number of readout counts ρ:

$$\rho = \frac{\tau}{\varrho} \tag{5.8}$$

The quantitiy ϱ is a calibration constant. Under the assumption that the fluctuations of the signal are Poisson distributed, their root mean square is calculated via:

$$RMS_{fluctuations} = \frac{\sqrt{\tau}}{\varrho} \tag{5.9}$$

The number of photoelectrons can therefore be determined the following way:

$$\tau = (\frac{RMS_{fluctuations}}{\varrho})^2 \tag{5.10}$$

To approximate this method to reality, an additional non-Poisson component of the photomultipliers of the camera (marked as F^2) needs to be taken into account together with the fluctuations of the pedestal events:

$$\tau = F^2 \frac{\rho^2}{(RMS^2_{signal} - RMS^2_{pedestal})} \tag{5.11}$$

To apply the determination of the calibration constants, calibration pulses are used which are taken after each pedestal run as "Calibration Runs". These runs consist of short light pulses (of about 2 ns duration) emitted from LEDs which are mounted in the mirror dish of the telescope. They have a known intensity comparable to Cherenkov light during air showers and make the calibration procedure thus possible.
The signal extraction and calibration is carried out with the new calibration program "Sorcerer" (developed by J. Sitarek, IFAE) and an automatic pipeline provided by the MAGIC Collaboration.

Image Cleaning and Parametrization of γ-Ray Data
The calibration of the data delivers the number of photoelectrons (the charge) for each camera pixel. This does not mean necessarily that all pixels contain a signal from a shower event. In order to extract the information from the latter, the calibrated data needs to be cleaned in the next anaylsis step. This step is essential as the calibrated data still contain the information from all camera pixels and not only from the ones containing the information from the shower event of interest. Additional signals can be produced by the NSB and can lead to false identifications of a possible shower signal. The process of removing all false signals (that is, which are not caused by the Cherenkov light of a shower) is called the cleaning of a shower image. The image cleaning consists of two different steps. At first a subdivision of all camera pixels is made. There are so far three different procedures available which carry this step out: Absolute Image Cleaning, Time-constrained Absolute Image Cleaning and the Sum Image Cleaning.

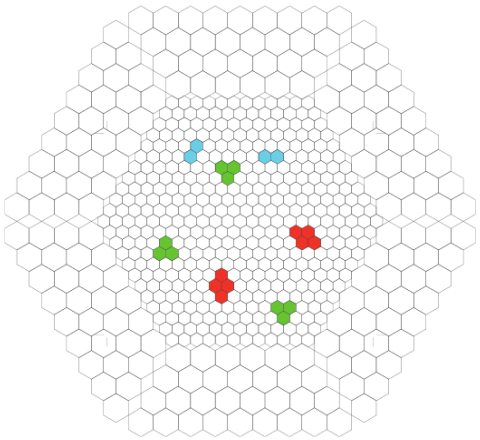

Figure 5.16.: Combinations of next neighbour pixels. The combinations are as follows: 2NN (blue), 3NN (green), 4NN (red). The figure was adopted from Rissi et al. [2009]. It represents a layout of the old M1 camera. For the study presented here, only data with the new M1 camera was used.

The first method makes a comparison between the charge of each camera pixel in two steps. At first the pixels which contain charges with more than 10 photoelectrons are defined as core pixels (Jogler [2009]). It is assumed (not proven yet) to belong to the image of the recorded

shower. Afterwards all camera pixels with at least 5 photoelectrons are selected and defined as boundary pixels if they are adjacent to at least one core pixel. The Absolute Image Cleaning sets the charge from all other camera pixels to zero. The required high photoelectron values for core and boundary pixels make this cleaning procedure not very sensitive to the fluctuations of the NSB. The drawbacks of this method are the non-usage of different noise levels which is crucial if a star is located in the field of view of the MAGIC camera (like it is the case for observations of the Crab Nebula and pulsar with the star ζ Tauri). Consequently, this cleaning method was not used for the data presented in this study.
The Time-constrained Absolute Image Cleaning, or Time Image Cleaning differs from the general Absolut Image Cleaning by using the arrival time of the signals in the selected camera pixels. Apart from selecting the core and boundary pixels the same way as by the Absolut Image Cleaning procedure, a threshold of up to 4.5 ns (core pixels) and 1.5 ns (boundary pixels) is made (both values are set with regard to the mean arrival time of the core camera pixels, boundary camera pixels respectively, Jogler [2009]). This additional constraint in the arrival time of the signal leaves room for a lower threshold of the charge values. Hence in the case of the Time-constrained Absolute Image Cleaning the charge thresholds are set to 6 photoelectrons (core pixels) and 3.5 photoelectrons. With this cleaning method the energy threshold can be lowered which is of crucial importance for the Crab Nebula and pulsar system for instance since the γ-ray emission of the latter is known to be observable with a higher statistical significance towards lower energies (that is, below about 120 GeV, Aleksić et al. [2011]). In spite of the possibility of lowering the energy threshold with this cleaning method, it was not used for the γ-ray data presented in this study either.

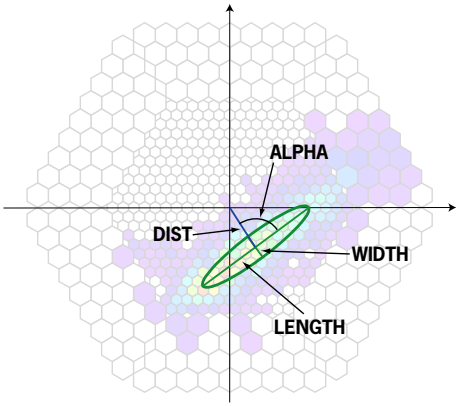

Figure 5.17.: Schematic parametrization of a shower with Hillas parameters (Albert et al. [2008c]).

For the data analysed for the study presented here, the third option known as Sum Image Cleaning was used (Rissi et al. [2009]). The Sum Image Cleaning provides a more elaborated method to clean shower images. In this case not single camera pixels are regarded, but combinations of next neighbour (NN) pixels in several combinations (2, 3, or 4NN, see Figure 5.16). The charges of these pixel combinations are summed up. To prevent unusually large accidental signals of artifical origin in these sums (caused by the NSB, or by afterpulses, Rissi et al. [2009]), the latter are limited to a certain threshold (commonly referred to as "clipped"). In

addition the summed charge needs to lie in small time window of the mean arrival time of the group of camera pixels. If these two conditions are fulfilled, the respective pixels are regarded to belong to the observed shower. With a fixed time threshold of the described kind, the energy threshold can be lowered also in this case and is set to 6 photoelectrons (core pixels) and 3.5 photoelectrons (boundary pixels). The low energy threshold provided by this cleaning method is its advantage for the observation of low energy showers (like in the case of the Crab pulsar). It is the reason why it was used for the cleaning of all γ-ray data sets used in this study. A deeper description of the Sum Image Cleaning is given in Shayduk et al. [2005].
After the image cleaning process, a characterization of each recorded shower image is made. It is done with a set of parameters known as Hillas parameters (Hillas [1985], see schematic shower in the form of an ellipse in Figure 5.17):

SIZE:
: Total amount of light in the shower image (given in photoelectrons). That is, the sum of the signals of the pixels which survived the image cleaning process.

WIDTH:
: Root Mean Square (RMS) of Cherenkov light along minor axis of the ellipse. It describes the transversal development of the shower which is larger in the case of hadronic showers in comparison with γ-ray induced showers. Therefore the width is regarded as a decisive discriminator for the determination of the primary particle.

LENGTH:
: RMS of Cherenkov light along major axis of the ellipse. It describes the longitudinal development of the recorded shower. Also in this case the length is larger for hadronic showers (in contrast with γ-ray induced showers) which makes it a further important discriminator.

ALPHA:
: Angle between the major axis of the shower and connecting line between the Center of Gravity (CoG) of the shower image and the camera center (Figure 5.17).

DIST:
: Angular distance between the Center of Gravity (CoG) of the shower image and the center of the camera (Figure 5.17).

The listed parameters describe characteristics of air shower images and help to distinguish between showers caused by different primary particles. Some other parameters used for the differentiation of air showers (and used for the data quality selection described in the next chapter), are:

Conc -n:
: Fraction of the charge in photoelectrons for the n brightest pixels of the shower. It is used to identifiy the core/compactness of the recorded air shower. Furthermore it is used as a further discriminator for the identification of the primary particle since gamma-ray induced air showers are more compact than hadronic ones.

Number of Islands:

Describes the number of camera pixels arranged in groups ("Islands") which survived the image cleaning process.

Cloudiness:

A parameter that describes the quality of the sky by the following value:

$$\frac{\mathrm{T_m} - \mathrm{T_{low}}}{\mathrm{T_{up}} - \mathrm{T_{low}}} \tag{5.12}$$

The quantity T_m is the temperature measured with the pyrometer mounted on the M1 telescope, T_{low} = 250 K and T_{up} = 200 K representing the worst and best states of weather (for a detailed description of the pyrometer see Chapter 2.2.9 in Zanin [2013]).

A mathematical description of the Hillas parameters can be found in Jogler [2009].
The characterization via the Hillas parameters provides a first subdivision of different air showers. The process consisting of the image cleaning and image paramerization is carried out by the program "Star" which is one further program from the Mars software package and also a part of the automatic data reduction pipeline provided by the MAGIC Collaboration.

Data Quality Check

Since both MAGIC telescopes are standing in the open (that is, without any kind of shelter like a telescope dome), they are subject to (partly rapidly) changing weather conditions. Depending upon the weather conditions when the observations were taken, the quality of the resulting data can decrease if clouds, a high humidity, or Calima (air layer originating from the Sahara desert which is blown over the Canary Islands at certain times of the year reducing the visibility due to the dust which it brings along) were present at the time of the observations. Therefore it is necessary to examine the quality of the data before prolonging with the data analysis. In this context the stability of the Hillas parameters and the additional parameters for the characterization of air showers (see last chapter) are examined and the respective deviations determined. Once available in Star format, the quality of the data was examined by the program quate (developed by M. Gaug, UAB). Quate stands for "Quality Tester". It is used in two steps separately on M1 and M2 data files. During the first run, it determines the mean of the zenith range, the rate above 100, the maximum of the Size, Width, Length, Conc, Number of Islands, Cloudiness and deviations in the azimuth and zenith range. During the second run, cuts are applied on these quantities. These selection cuts can be set manually in the input card (quate.rc, contained in the MARS software package). They are set to $1.5\,\sigma$ from the mean value of the rate distributions by default. For the other parameters, the deviation is set to $2\,\sigma$ from the mean value. Simultaneously with applying cuts, quate extracts all data files according to the deviations of the named parameters and stores them in three different folders named good, bad and out of zenith range. This way a subdivision is automatically created for further analysis. The distributions of the named parameters are shown as an example in Figure 5.18.
To avoid introducing any kind of bias into the γ-ray data sets used for this study, only the zenith range parameter was changed in the input card (to less than 35° since all data sets were taken at low zenith values), in order to select showers with the least amount of contamination caused by the atmosphere. All other parameters were left in the default state.

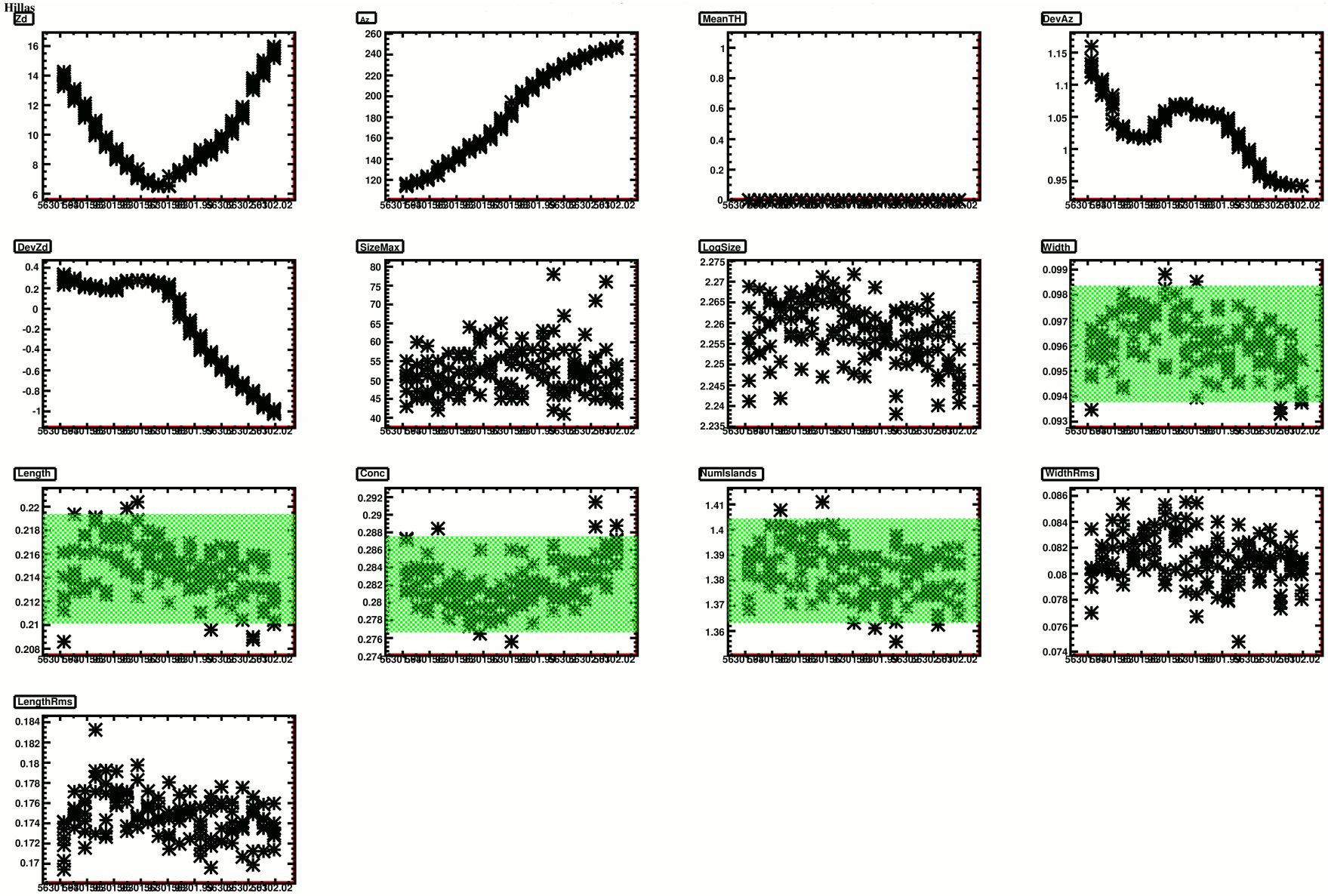

Figure 5.18.: Output of the data quality check of the MAGIC data set from 10-01-2013 taken with M1. The green areas correspond with the values selected for further analysis by Quate.

Construction of Stereoscopic Data

So far, the individual data sets from both telescopes, M1 and M2, were analysed separately. After the data quality selection, the data sets from M1 and M2 which passed the selection cuts ("good" files), are merged together into stereo data files. The result of this merging process is one file per run number which contains the data from both telescopes (and results from the M1 and M2 data files with the same run number). Apart from the merging process, additional parameters are calculated which are commonly referred to as stereo parameters:

Shower Axis Direction:
: The main axis of each recorded air shower is pointing towards the incident direction of the primary particle. Although both telescopes see the projected image of the shower from a different position on the ground, in both cases the main axis is pointing towards the incident direction of the primary particle. The crossing point of both main axes is the shower axis direction of the primary particle. This geometrically reconstructed shower direction technique is working well as long as the angle between both main axes is large enough.

Impact Parameter:
: Is the perpendicular distance between the telescope axis and the shower axis (see part a) in Figure 5.19).

Height of Shower Maximum:
: The reconstructed height of the maximum of the detected air shower above both telescopes. This parameter is used as a further discriminator since the height of the air shower correlates with its energy. Air showers caused by a primary γ-ray particle of higher energy pass through a longer path through the atmosphere before they die out which results in a smaller height value of their maxima. Consequently, low energy air showers have larger height values for their maxima. This way the height of the shower maximum can be used to increase the sensitivity of stereo observations of low energy air showers.

Cherenkov Light Radius:
: The radius of the pool of Cherenkov light on the ground. It is determined under the assumption that it is caused by a single electron with an energy of 86 MeV (critical energy since it equals the energy losses due to excitation or ionization) at the height of shower maximum.

Cherenkov Density:
: The photon intensity on the ground of the Cherenkov light produced by the single electron with an energy of 86 MeV at the height of the shower maximum.

Both parameters, the Cherenkov Light Radius and the Cherenkov Density, are constructed after the reconstruction of the position of the primary particle. They are used to characterize the observed Cherenkov light and calculated under the assumption of an atmospheric model. The shower axis direction and impact parameter are explained schematically in Figure 5.19. The described geometrical reconstruction is referred to as source independent since the position of the respective source was not used. In the case of a source dependent geometrical reconstruction the line from the position of the source to the air shower image is used instead of the main axes (in the case of both telescopes).

The construction of stereo data files means in other words that the direction of the observed shower is reconstructed in the three dimensional space. The corresponding task in software is performed with the program "Superstar" from the MARS software package.

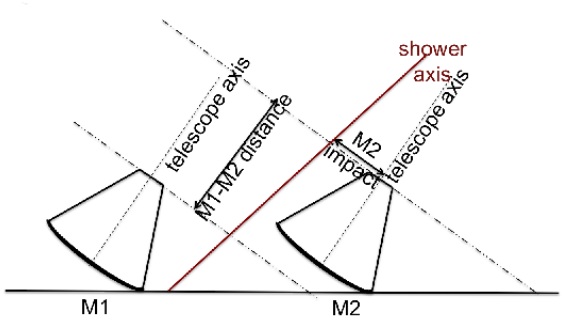

Figure 5.19.: Graphical description of the shower image axis and the impact parameter. The Figure was adopted from Zanin [2013].

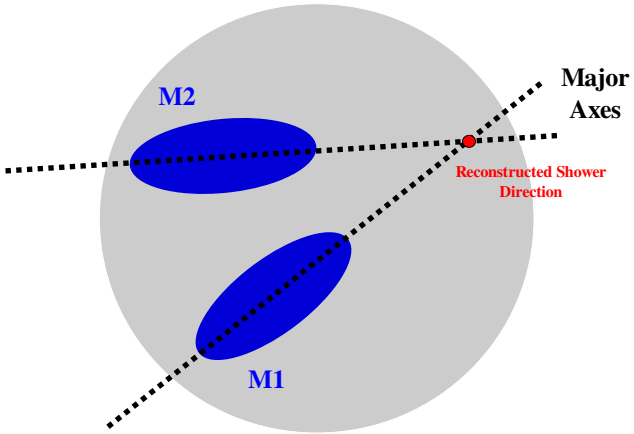

Figure 5.20.: Geometrical Reconstruction of the air shower direction.

Background Discrimination and Energy Reconstruction – Training
The characterization of each shower via the Hillas parameters provides a first estimation which showers were caused originally by a γ-photon, or by other primary particles. IACTs like the MAGIC telescopes can trigger three different kinds of events:

Extensive Air Showers:
Air showers caused by gamma-ray photons, or hadrons.

Muons:

Particles which hit near the telescopes with ultrarelativistic velocities and generate ring structures on the camera.

Accidental Triggers:

Fluctuations of the signal caused by background light from the moon, the NSB, or flashes caused by cars which passed the telescopes on their way up, or down the Roque de los Muchachos vulcano.

For a single telescope the Myon trigger rate is five times smaller than the Hadron rate. The accidental trigger rate is less than 1 Hz. For both telescopes (stereo mode) the latter has a level of a few Hz (Zanin [2013]).
In order to differentiate between the three listed kinds of trigger events, the first filtering process takes already place at hardware level (Coincidence trigger, or L3 trigger, see Zanin [2013] for more details). The L3 trigger rejects all trigger events which were only detected by one telescope. Therefore it is also referred to as stereo trigger. The exclusion of mono events by the L3 trigger results in a much lower trigger threshold of the M1 and M2 telescopes in stereo mode (in contrast with M1 only) since it excludes most of the triggered events. In spite of this exclusion, the background emission cannot be supressed significantly by the L3 trigger. The remaining stereo events have in most cases hadrons as the corresponding primary particles. The next step in the analysis is to select γ-ray induced events only. This is done via the process known as γ/hadron separation.
As mentioned earlier, some of the Hillas parameters of an air shower can be used as discriminators in the idenfitication of γ-ray induced showers. The γ/hadron separation is based on the distributions of image parameters. After the selection of a set of parameters which are adequate for the discrimination between γ and hadron induced air showers, the respective cuts for a differentiation are determined by multidimensional decision trees set up by the "Random Forest" (RF) algorithm (a detailed mathematical explanation is given in Albert et al. [2008b]). The RF algorithm is a statistical learning method which uses a set of image parameters from mono and stereo observations (like SIZE, WIDTH, LENGTH, IMPACT and MaxHeight) and timing information to calculate the probability with which a given shower event was caused originally by a γ-ray photon, or a hadron. This probability is introduced as a new parameter known as "Hadronness". The Hadronness parameter spans from the value 0 till 1 and reflects thus if the considered air shower event was induced by a γ-photon (Hadronness value near 0), or by a hadron (Hadronness value spread from 0 to 1). With a respective cut in the Hadronness parameter (see cut optimization procedure in Chapter 5.2.3), a large fraction of the background emission can be removed from the data.
To guarantee the success of this method of background emission determination, a RF algorithm needs to be trained. For this kind of training Monte Carlo Simulations (MC) simulations of γ-ray induced air showers are used together with data sets commonly referred to as "OFF Data". In the latter case, it is a real data sample which does not contain any signal from a γ-ray source, but only background emission and thus shower events caused by hadrons. A comparison between the Hadronness distributions in dependence of the Size is shown for the simulated γ-ray air showers in the case of MC simulations and for air showers induced by hadrons in the case of the SegueA data in Figure 5.21.
In the case of the study presented here, SegueA data (Table 5.6) was used as OFF data for the RF training and two different sets of MCs (referred to as ST_03_01 and ST_03_02, ST

standing for MAGIC-STereo, 03 for the third hardware change and the last two digits representing analysis periods). SegueA data was chosen for this part of the analysis as it had been repeatedly verified by other analyzers to not contain a γ-ray signal and providing thus a source of background emission. The MC simulations used were specifically built by the MAGIC Collaboration for the epochs covering the time span from December 2012 to February 2013.

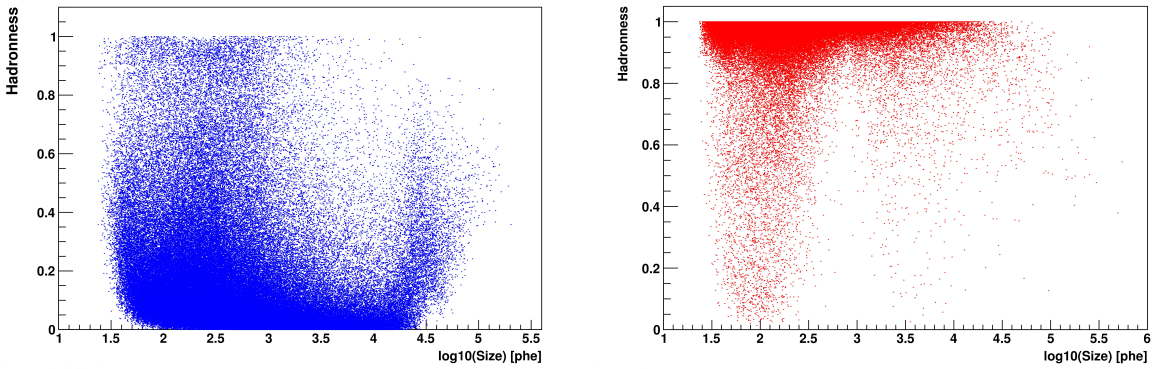

Figure 5.21.: Hadronness distribution as a function of Size for MC simulations for the data set from December 2012 and January 2013 (left plot) and for SegueA data from 18-02-2013 (right plot).

Due to a change of the Point Spread Function (PSF) of the telescopes in the months from December 2012, January 2013 and February 2013 (E. Carmona, private communication), the total Crab Nebula data set was split into two parts: December 2012 and January 2013 (part 1) and February 2013 (part 2). Two different RFs were trained for both parts using only SegueA data from the same month and MC simulations for the respective part (ST_03_01 for part 1 and ST_03_02 for part 2). From this stage of the analysis chain, both data parts were analysed separately.
The RF training is carried out by the program "Coach" for MAGIC stereo data and "Osteria" for MAGIC mono data (in the study presented here only MAGIC stereo data was used). Since the input for Coach needs to be in Superstar format, the SegueA data as well as the used MC simulations were analysed in exactly the same way with the same settings in the respective input cards as the Crab pulsar data until this analysis level.
For the SegueA data the same data quality check was applied with Quate as for the Crab pulsar data (only dark time data was chosen. No moon, or twilight data was included.). The MC simulations were chosen according to the matching PSF and the observing conditions (dark night, or increased NSB due to the Moon for instance). One further discriminating factor was the zenith range for which the MC simulations were built. As all Crab pulsar observations were taken at low zenith ranges (Table 5.5), only MC simulations valid for zenith degrees from 0 till 35 were used for this part of the analysis. This zenith range was set accordingly in the Coach input card.
A further task which can be carried out by RF training, is to determine the direction of the primary particle which induced the air shower. This can be done with Coach by using the following parameter:

`DISP:` `Distance from the center of the shower image to the estimated position of the source`

The method with the DISP parameter was originally proposed by Fomin et al. [1994]. The major axis of the air shower image (under the assumption that it was induced by a γ-ray particle) is a projection of the incoming direction of the shower on the camera plane. Consequently, the position of the source is located on the main axis at a certain difference (from the CoG of the air shower image) which is referred to as DISP (see Figure 5.22). In the case of mono and stereo data the position of the primary particle is reconstructed a bit differently. For mono data one DISP value can be determined with two positions on the main axis on opposite sides of the image centroid which can be taken (positions A and B in Figure 5.22). Which position is more probable to belong to the source of the γ-photon is determined by methods known as Ghost busting. Ghost busting parameters are used to describe the asymmetry of the charge distribution in a shower by comparing the upper part of the air shower (head) and the lower part (tail) (for more details see Zanin [2013]).

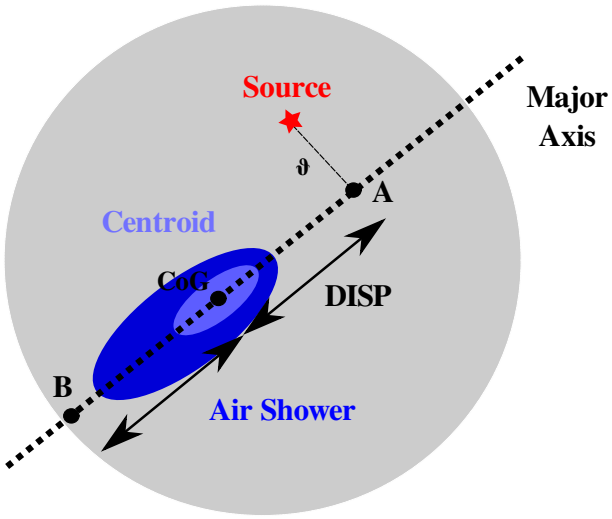

Figure 5.22.: Scheme of the DISP parameter. The grey area represents the camera plane. The true source position is marked in red and the reconstructed source positions are given by A and B. The deep blue shape is a scheme of an air shower induced by a γ-photon and the region in light blue is the centroid of the shower image with the CoG.

With regard to the analysis of stereo data, the determination of the DISP parameter can be improved. For each telescope the DISP parameter is determined individually as described in the case of mono data. Consequently, two possible DISP values result from the paramerization of each air shower image which means four different reconstructed candidate source positions (since a shower is observed by each telescopes individually). Since the ghost busting method is not very successful for low energy events, a different approach is used to determine the appropriate reconstructed position of the source. With it the pair of good reconstructed positions (good means in this case the closer pair to the crossing point of the main axes of both air

shower images) is determined by going through all the possible combinations resulting from the four different reconstructed source positions (see Figure 5.23). The distances (marked with a d in Figure 5.23) between all four combinations are calculated. The pair is eventually chosen whose reconstructed source positions have a smaller distance to each other than a certain value d_{min} (which corresponds to d2 in Figure 5.23). Since this approach works independently of the crossing of the main axes of both shower images, it can be applied to all kinds of air showers (also with parallel main axes) and represents a more efficient strategy of the position reconstruction of the primary particle. It is commonly referred to as stereo DISP method.
The DISP parameter is also trained with MC simulations consisting of γ-ray events (using the DISP-RF method in Coach for stereo data as it was also done for the data presented in this thesis). Further information about the reconstruction of the position of the respective source using the DISP method can be found in Jogler [2009] and Zanin [2013].

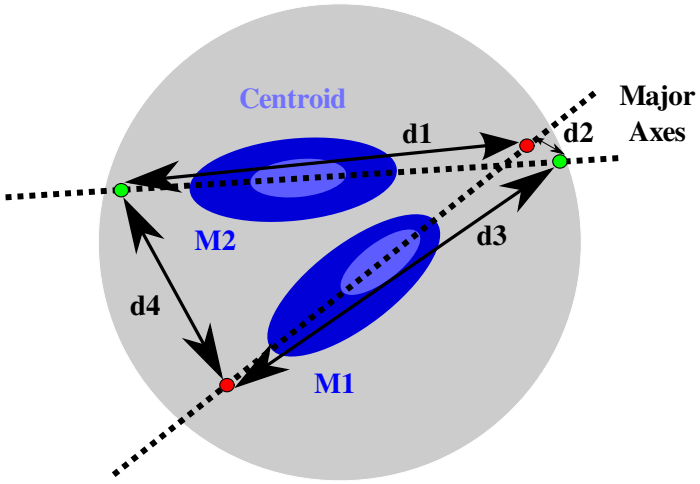

Figure 5.23.: Determination of the DISP parameter for stereo observations. The red points are reconstructed source positions from a γ-ray induced air shower as seen with the M1 telescope. The green points are the reconstructed source positions from the same shower as seen with the M2 telescope.

One further property which can be obtained using Coach is the energy of the primary particle of an air shower. It is estimated using tables which are known as "Look Up Tables" (LUTs). These tables are part of the standard procedure for MAGIC stereo data and they were also calculated for the data used in this study.
An energy LUT is built up by subdividing the used MC simulations of γ-ray induced air showers in bins (with a simulated true energy E_{true}) for every parameter which has an influence on the energy estimation. This results is a multidimensional table in which the mean energy value and its RMS is calculated for each bin. The resulting estimated energy is the value assigned to an event which has parameters that correspond with the ones stored in the respective bin. Since the success of this procedure depends upon the number of available MC simulations and also on the computing power, simplifications are applied which reduce the number of necessary bins. These simplifications run from setting the energy of the primary particle equal to the

the size of the observed shower and fill each bin of the LUT (zeroth order approximation), to corrections between the energy and the size due to their non-linear dependence (first order approximation), to second order approximations which include the zenith range, the leakage parameter and corrections of the geomagnetic field. The resulting estimated energy E_{est} is then determined by the weighted average value (the weight results from uncertainty of each bin) from both telescopes.

Background Discrimination and Energy Reconstruction – Crab Nebula Data
After the optimization of the Hadronness parameter, the DISP parameter and the energy estimation with Coach, the resulting algorithms are applied to the Crab Nebula data which were taken simultaneously with the corresponding radio observations. During this process the same cuts which were applied by Coach on the MC simulations and the SegueA data, are applied on the Crab Nebula data before the calculation of the Hadronness, the DISP parameter and the reconstruction of the energy for each event in this data. This step in the standard analysis (Figure 5.2.2) is carried out by the program Melibea from the MARS software package. After the processing of the Crab Nebula data with Melibea each event has a specific Hadronness and reconstructed energy value together with a reconstructed direction of the shower from the DISP parameter. A first test if a γ-ray signal is available at all in the data, can be already made at this point by checking the Hadronness values (Figure 5.24).

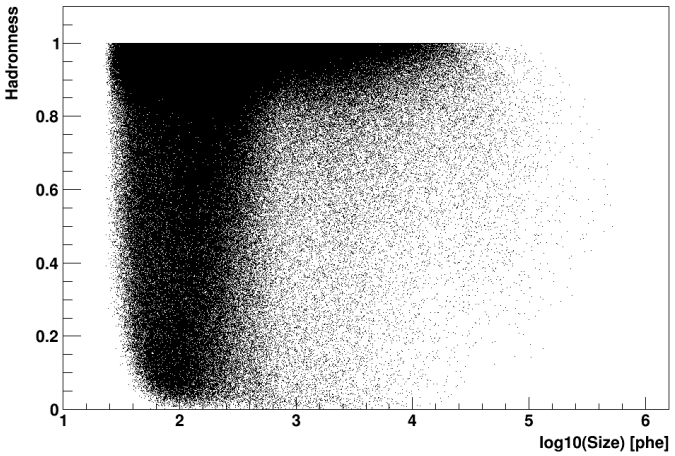

Figure 5.24.: Verification of the γ-ray signal in the total Crab Nebula data set taken simultaneously with radio observations by examining the distribution of Hadronness values in the data resulting from the processing with Melibea.

The fact that the Hadronness values in Figure 5.24 range from the value of 1.0 almost down to 0.0, verify the existence of a γ-ray signal in the Crab Nebula data. The background emission caused by hadronic air showers (indicated by large values of the Hadronness) is nevertheless dominant in the data set and emphasises the reason for a further step in the analysis known as cut optimization (Chapter 5.2.6).
Analogous to the processing with Coach in the last chapter, also Melibea needed to be run

Facility	Epoch	Δt [min]	Zd Range [°]	Usage
Winter 2012/13				
MAGIC	2012-11-18	39	33.4 - 24.8	Coach (part 1)
MAGIC	2012-11-19	62	34.3 - 21.7	Coach (part 1)
MAGIC	2012-11-20	40	31.1 - 22.3	Coach (part 1)
MAGIC	2012-11-21	51	28.0 - 19.0	Coach (part 1)
MAGIC	2012-11-22	77	35.1 - 20.1	Coach (part 1)
MAGIC	2012-11-23	95	34.6 - 16.0	Coach (part 1)
MAGIC	2012-11-24	60	34.5 - 22.2	Coach (part 1)
MAGIC	2012-12-12	68	17.2 - 13.6	Coach (part 1)
MAGIC	2012-12-14	106	19.3 - 16.0	Coach (part 1)
MAGIC	2012-12-15	83	16.3 - 15.7	Coach (part 1)
MAGIC	2012-12-16	114	19.0 - 18.0	Coach (part 1)
MAGIC	2012-12-17	113	18.4 - 17.3	Coach (part 1)
MAGIC	2012-12-19	101	16.3 - 18.1	Coach (part 1)
MAGIC	2012-12-20	133	19.1 - 20.7	Coach (part 1)
MAGIC	2012-12-21	132	18.0 - 21.7	Coach (part 1)
MAGIC	2012-12-22	130	17.0 - 22.3	Coach (part 1)
MAGIC	2012-12-24	24	13.3 - 12.7	Coach (part 1)
MAGIC	2013-01-09	38	16.0 - 23.1	Coach (part 1)
MAGIC	2013-01-10	17	32.0 - 34.9	Coach (part 1)
MAGIC	2013-01-11	71	18.7 - 32.7	Coach (part 1)
MAGIC	2013-01-12	94	16.6 - 34.7	Coach (part 1)
MAGIC	2013-01-13	73	20.3 - 34.2	Coach (part 1)
MAGIC	2013-01-14	95	16.7 - 35.1	Coach (part 1)
MAGIC	2013-01-15	25	29.1 - 35.0	Coach (part 1)
MAGIC	2013-01-16	133	24.1 - 16.0	Coach (part 1)
MAGIC	2013-01-17	93	16.3 - 34.1	Coach (part 1)
MAGIC	2013-01-18	93	17.0 - 35.0	Coach (part 1)
MAGIC	2013-01-19	175	15.4 - 34.0	Coach (part 1)
MAGIC	2013-01-20	30	29.3 - 35.0	Coach (part 1)
MAGIC	2013-01-21	131	12.8 - 35.1	Coach (part 1)
MAGIC	2013-02-07	85	17.9 - 34.6	Coach (part 2)
MAGIC	2013-02-08	97	16.3 - 35.0	Coach (part 2)
MAGIC	2013-02-11	44	22.5 - 30.7	Coach (part 2)
MAGIC	2013-02-15	122	33.5 - 13.1	Coach (part 2)
MAGIC	2013-02-16	49	24.3 - 34.3	Coach (part 2)
MAGIC	2013-02-18	62	16.9 - 34.4	Flute
Total Observation Time		**2955**		

Table 5.6.: All SegueA data sets used for the analysis of the data presented in this study. The last column indicated for which part in the analysis chain the data sets were used. Since the data set was split into two parts (as indicated by the separating double line), part 1 refers to data from December 2012 and January 2013 while part 2 summarizes the data from February 2013.

separately on the December 2012 and January 2013 data (part 1) and on the February 2013 data (part 2). The Melibea outputs of both parts (that is, all three months) are shown in Figure 5.24.
The resulting output files are afterwards barycentered with the same ephemeris files which were determined from the radio data sets (Chapter 5.2.4) as part of the non-standard analysis (Chapter 5.2.3).

Signal Search and Detection
With the DISP method described in the previous chapter, a new parameter known as ϑ was introduced (see Figure 5.22). It is the angular distance between the expected source position on the camera plane and the reconstructed one. Throughout the analysis of γ-ray data from IACTs it has become more common to rather use ϑ^2. Since air showers induced by hadrons have no specific arrival direction due to their charge, their number is proportional to ϑ^2. In contrast with ϑ, the ϑ^2 distribution is flat for showers caused by hadrons and peaks for small values for γ-ray induced showers (see Figure 5.27). The reason for this lies in the isotropic distribution of hadronic showers causing the background emission which is much higher than the γ-ray emission from the respective source of interest. Consequently, a ϑ^2 distribution depicts the hadronic emission in a more extended way than a ϑ distribution would and makes the γ-ray signal from the source easier depictable. The range of the ϑ^2 distribution which is used for the estimation of the background emission and for the subsequent determination of the γ-ray signal from the source is known as signal region.
To understand the signal region in a more thorough way, the observation modes of the MAGIC telescopes need to be explained. Both telescopes, operating in stereo mode, can be either pointed directly on the source (ON observations), or can be moved around it ("wobbled"). In the case of ON observations additional observations OFF the source are needed for a proper background determination. This procedure therefore results in a loss of the observation time on the source and is usually not used. In the case of Woblle observations each telescope is moved between several positions around the source of γ-ray emission. All positions are arranged in two dimensional spherical coordinates consisting of φ (polar angle) and ϑ (azimuth angle). The z axis of the coordinate system is pointed together with the radial distance r towards the source of γ-ray emission. In the case of the Crab Nebula data presented in this study, a azimuth angle of 0.4° is kept with two different polar angles (35° and 215°) following the scheme of the left part of Figure 5.25. The number of hadronic and γ-ray induced air showers is determined from these off source regions (named with a "W" and the corresponding number of the Wobble position). Observations in Wobble mode provide an effective way of observing the γ-ray emission from the source and the background emission simultaneously.
The Crab Nebula in which the Crab pulsar is located, represents a dynamical background and needs to be monitored regularly for a proper background reduction. Apart from two Wobble positions as shown in the left part of Figure 5.25, it has become more common to use four Wobble positions in order to monitor the background emission even more extensively and to reduce the data properly (right part of Figure 5.25). For the Crab Nebula data presented in this study nevertheless the option with two Wobble positions was chosen to avoid the influence of the emission from the star ζ Tauri which in the case of four Wobble positions would occur in the FoV of one of them. The signal of the source is determined by calculating the number of γ-ray events from the source N_{ON} in the signal region. Since it is expected that also air showers induced by hadrons are within this signal region, a cut in the Hadronness parameter is carried out. To estimate the number of hadronic air showers which survived this cut, usually a further

independent data set with no γ-ray signal is used from the which the number of background events N_{OFF} in the signal region is determined.

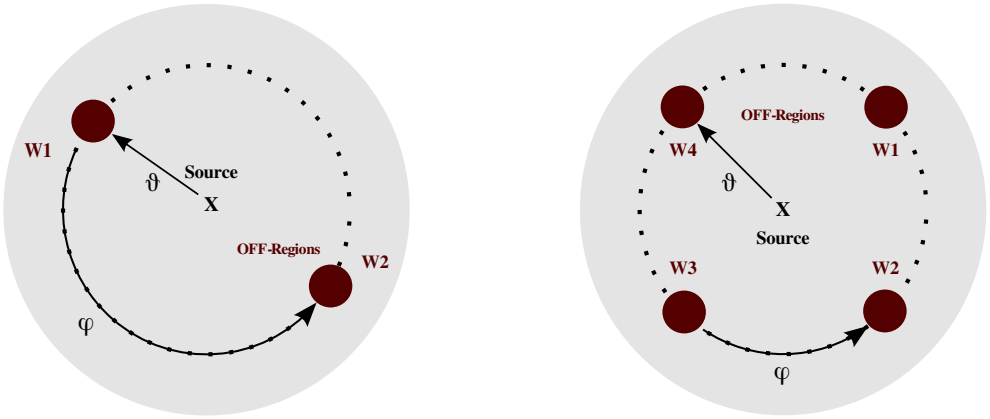

Figure 5.25.: Scheme of Wobble observations carried out with the MAGIC telescopes. The combinations of Wobble positions currently vary between two (left plot) and four (right plot).

The resulting number of air showers caused by γ-photons after the subtraction of background events from the OFF data sample, is known as the number of excess events:

$$N_{ex} = N_{ON} - \xi \cdot N_{OFF} \tag{5.13}$$

The quantity ξ is the fraction between the time which was spent on the source and off the source:

$$\xi = \frac{t_{ON}}{t_{OFF}} \tag{5.14}$$

In this sense it is a normalization factor which makes the counts resulting from observations off the source comparable with the one taken on source (Figure 5.26).

The detection of a signal from a γ-ray source is successful when the number of excess events has a significance of at least $5\,\sigma$. According to the work of Li and Ma [1983] this significance can be determined with the following equation:

$$N_\sigma = \sqrt{2} \cdot (N_{ON} \cdot \ln[(\frac{1+\xi}{\xi}) \cdot (\frac{N_{ON}}{N_{ON} - N_{OFF}})] + N_{OFF} \cdot \ln[(1+\xi) \cdot \frac{N_{OFF}}{N_{ON} - N_{OFF}}])^{\frac{1}{2}} \tag{5.15}$$

Since the γ-ray observations for this study were taken in Wobble mode, the number of ON and OFF events is taken from the same data set.
To approximate the number of background events in the signal region, the ϑ^2 distribution is fitted with a straight line in the region from $(0.1°)^2$ to $(0.4°)^2$. The fit is then extrapolated to

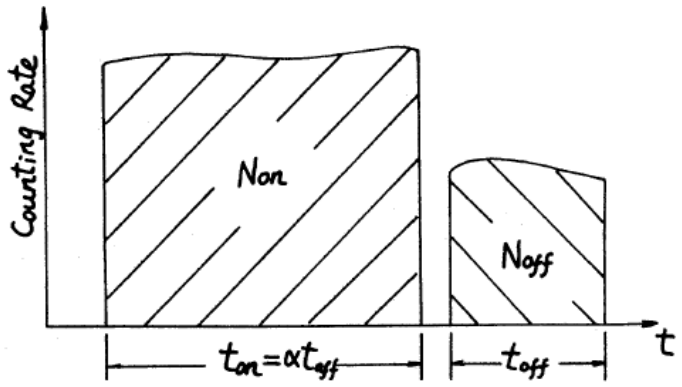

Figure 5.26.: Normalization factor α (in the text explained as ξ in order to avoid confusion with the indices of power law spectra described in Chapter 1.4.3) as explained in Li and Ma [1983]. The figure was adopted from Li and Ma [1983].

the signal region at low ϑ^2 values to properly deduct the number of OFF events from the γ-ray signal from the source. Examples of the ϑ^2 distributions for the Crab Nebula and Crab pulsar signal are shown in Figure 5.27. They were produced with the program Odie from the MARS software package. Although a clear signal is visible in the γ-ray data from all three months, it is nevertheless a signal dominated by the emission from the Crab Nebula and not the pulsar. In order to search for a signal from the Crab pulsar, a more sophisticated approach was applied using the program Flute as will be described in Chapter 5.2.5. With Flute different background reduction methods can be applied also providing the possibility to filter out the γ-ray emission from the Crab pulsar.

5.2.3. Non-Standard Analysis Chain

Since the Crab pulsar is embedded in its plerion, the Crab Nebula, its pulsed emission is outshined by the continuous emission of the latter. This is an instrinsic problem of this system and consequently, the Crab pulsar emission needs to be extracted from the data.
First the γ-ray data needs to be barycentered with the same ephemeris files as used for the barycentering of the radio data sets. This is a crucial step in order to make it comparable with the radio data in the form that the arrival times of the events contained in all data sets are converted to the SSB (see Chapter 5.1.5).
In the second step restrictions (commonly referred to as cuts) of certain parameters need to be performed on the MAGIC data. Although this is a rather common procedure in the case of the data from IACTs, for the Crab Nebula complex it needs to be applied in a specific way which is rather non-standard. Without this cutting procedure, it is not possible to find the γ-ray signal from the Crab pulsar with a significance which is statistically high enough compared to the background emission combined of hadronic and γ-ray air showers also caused by the Crab Nebula. An example of the data sets from December 2012, January 2013 and February 2013 after barycentering, but without any additional cuts is shown in Figure 5.34.

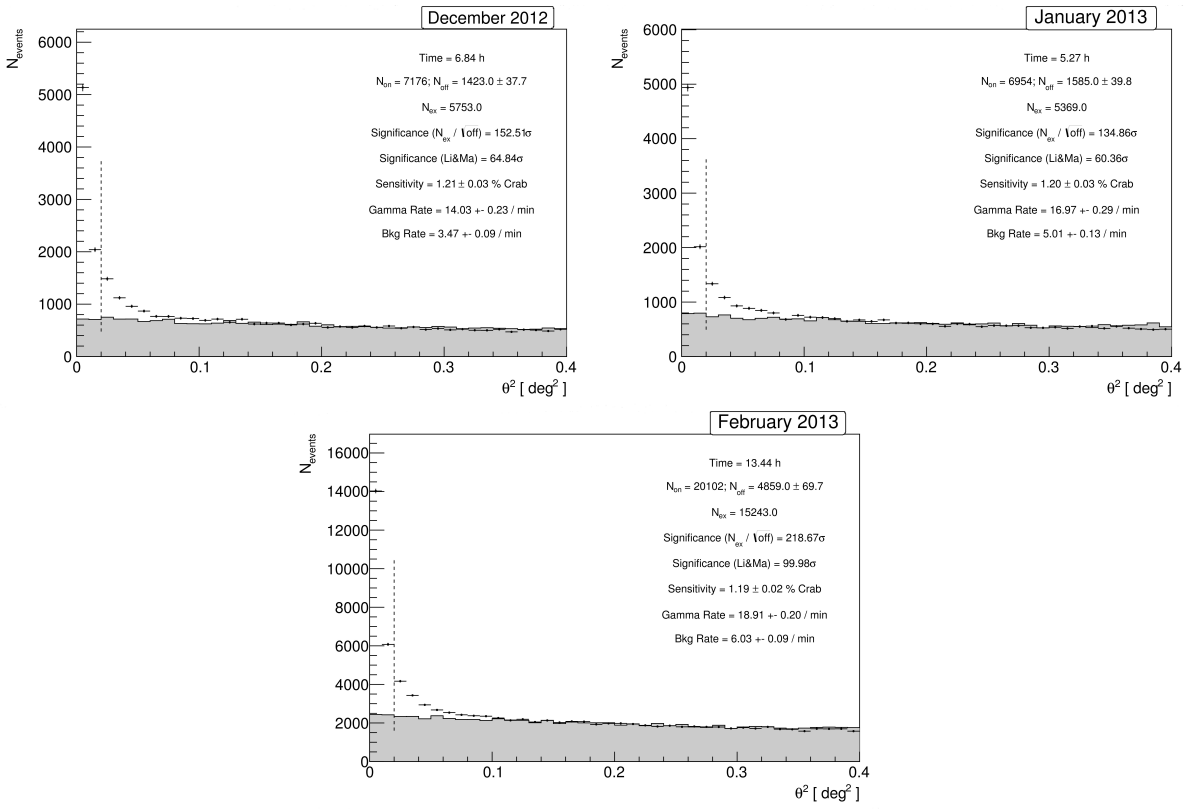

Figure 5.27.: ϑ^2 plots for the Crab Nebula and pulsar data from the three months with radio coverage. The grey areas represent the background emission.

5.2.4. Timing Analysis – γ-ray Data

The proper conversion of the arrival times of all events contained in the MAGIC γ-ray data to the SSB, is a crucial step for a comparison with the arrival times resulting from the radio data. Before the actual barycentering will be carried out, a check if the time stamp in the case of the γ-ray observations was set correctly is made with optical central pixel data, as well as with γ-ray data.

Test of Time Stamp Stability – Central Pixel Data
To test the stability of the time stamp used for the γ-ray observations with MAGIC, optical Central Pixel (Cpix) data was examined. For this part of the analysis, a program called Psearch (developed by M. Lopez, Universidad de Complutense) was used. Figure 5.28 shows the optical pulsar light curve resulting from Cpix observations. During the time span when the data for the correlation study were taken, observations with the cpix were only carried out in December 2012 and January 2013. Consequently, only these data sets were taken into consideration.
As shown in Figure 5.28, in both cases the P1 is visible around phase 0.0 whereas the P2 is present at the phase around 0.4. This speaks for a correct setting of the time stamp by the local GPS and allows for a correlation study between the radio and γ-ray data sets from December 2012 and January 2013. Unfortunately, no cpix data were available for February 2013.

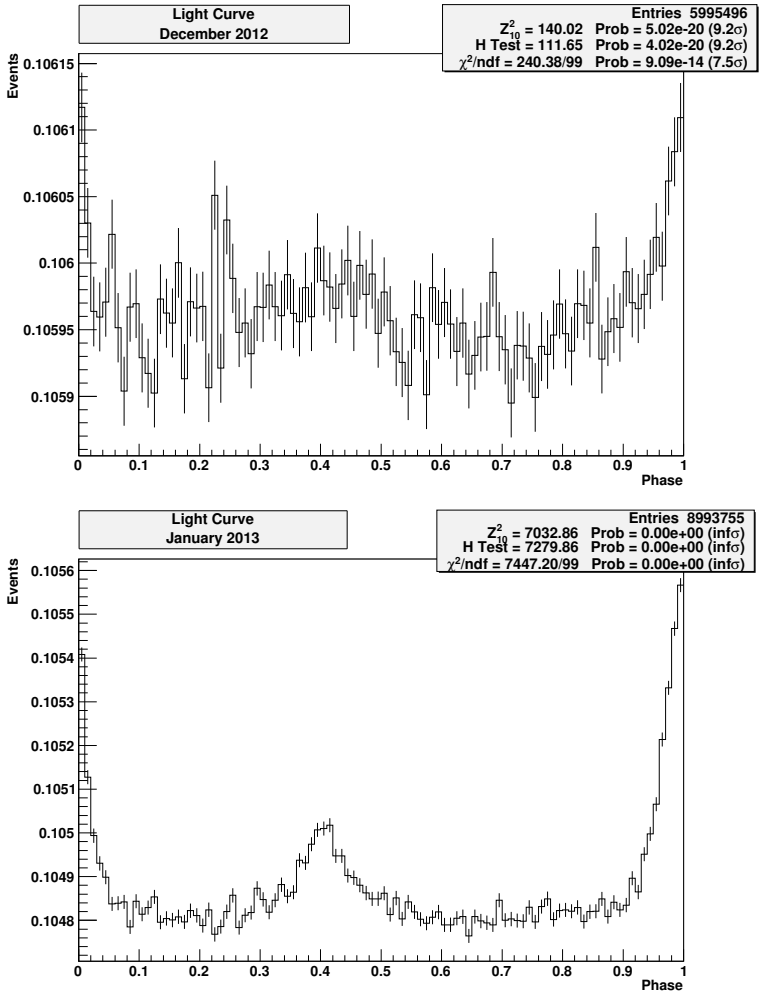

Figure 5.28.: Upper plot: Light curve resulting out of 10 minutes of Crab pulsar observations with the optical cpix on 6.12.12. Lower plot: Light curve as a result of 15 minutes of Crab pulsar cpix data taken on 04.01.13. The probability values are set to zero in the legend since the signal is strong.

Test of Time Stamp Stability – γ-ray Data

To check if the time stamp remained correct throughout the analysis of the MAGIC data, two different steps from the standard analysis chain (Figure 5.15) were compared with each other. The ultimate result of this analysis chain necessary for this study, were the MAGIC data files in Melibea format containing the values of ϑ^2 and Hadronnes with which the showers induced by γ-ray photons can be extracted from the data. For a check of the time stamp the arrival times (marked with the MTime container in the data files) were extracted from each Melibea file. The same was carried out for the calibrated files with the same run numbers in Sorcerer format for each telescope, M1 and M2. The arrival times of these events were extracted and afterwards compared with the ones from the Melibea file with the same runnumber. This way an additional check was included if the times of arrival of the recorded γ-ray events did change

during the process of the standard analysis (Figure 5.15). This procedure was carried out for all data sets from February 2013 as no optical data taken with the cpix was available for this month. The results are shown in Table B.1, Table B.2 and Table B.3. As can be seen in Table B.2 only in the case of two data sets from 04.02.13 a disagreement could be found. Consequently, the files with the two run numbers were excluded from further analysis.

Barycentering of γ-ray Data Sets
The timing analysis of the MAGIC data set was carried out with the Tempo2 plugin (written by G. Giavitto, IFAE) based on the version of the Fermi Tempo2 plugin (written by L. Guillemot, MPIfR) used by the Fermi Collaboration. Both plugins work only with a fully working version of the original Tempo2 timing software for radio data (Hobbs et al. [2006b]). Since all radio data sets used for the correlation study were barycentered with Tempo2 (see Chapter 5.1.5), the corresponding plugin for the simultaneously taken MAGIC data sets was used to keep the amount of systematics as low as possible. An alternative possibility to barycenter MAGIC pulsar data is provided by Psearch. However, due to the described reasons it was not used for this part of the analysis.
To make an alignment of all radio and gamma data sets possible, exactly the same radio ephemeris files were used for the barycentering of the MAGIC data sets. The MAGIC data sets from December 2012, January 2013 and February 2013, were barycentered with the respective radio ephemeris creating thus three differently barycentered data sets. The resulting phase diagrams for each month are shown in Figure 5.35, Figure 5.36 and Figure 5.37, Figure 5.38. They were determined with different cut optimization techniques as will be described in Chapter 5.2.6.

5.2.5. Differential Spectra – Crab Nebula and Crab Pulsar

Although the calculation of differential spectra is carried out as part of the standard analysis (Chapter 5.2.2), their determination in the case of the Crab pulsar can only be carried out after the process of barycentering (since it refers to the pulsed emission phases of the pulsar). Therefore this chapter has been included into the non-standard analysis chain to reflect the order in which the analysis of the γ-ray data was carried out.
For the determination of the differential energy spectra, the program "Flute" is used. Flute is currently the program from the MARS software package with which the differential spectra and spectral energy distributions (SEDs) of an astrononomical source are determined. To explain these quantities in more detail, their mathematical definitions are given below.
The flux of such a source is the number of γ-ray photons N_γ per observation time t and collection area A:

$$\Phi = \frac{d^2 N_\gamma}{dA \cdot dt} \tag{5.16}$$

The differential flux of a source corresponds to the number of γ-rays N_γ per observation time t, collection area A and interval of γ-ray energy E:

$$\frac{d\Phi}{dE} = \frac{d^3 N_\gamma}{dA \cdot dt \cdot dE} \tag{5.17}$$

The total number of γ-rays N_γ per observation time t and collection area A in a specific energy

range (beginning at a specific energy E), also known as the integrated flux, can be determined by:

$$\Phi = \int_{\mathrm{E}}^{\infty} \frac{\mathrm{d}\Phi}{\mathrm{dE}} \cdot \mathrm{dE} \tag{5.18}$$

The spectral energy distribution (SED) is defined as follows:

$$\mathrm{SED} = \frac{\mathrm{d}\Phi}{\mathrm{dE}} \cdot \mathrm{E}^2 \tag{5.19}$$

To determine these quantities, at first the number of γ-rays N_γ needs to be calculated. This number can be determined from the number of excess events, that is from events originating from the astronomical source. Since not all hadronic shower events were eliminated throughout the standard analysis procedure (see background emission in Figure 5.34), the number of such events needs to determined in order to determine the number of excess events. This can be done with Flute which creates ϑ^2 plots (see Figure 5.30) similar as Odie (see Chapter 5.2.2). Since the events from the source and from the background are mixed in the detected signal, the number of background events is estimated by comparing the number of events from the source (ON source distribution shown as black curve in Figure 5.30) with the number of events from the background (OFF source distribution shown as red curve in Figure 5.30). The number of excess events is determined as given by Equation 5.13.
In other words, analogous to Figure 5.27 Figure 5.30 shows the ϑ^2 distributions for two different regions, on the source and off source. Since the observations for this study were carried out in Wobble mode, the telescopes were never directly pointed on the Crab Nebula (see Figure 5.25). The reason for this technique is to gain a better estimation of the background events which is necessary especially for the Crab Nebula being dynamical due to its moving gas and dust structures.
Currently, there are three different modes with which Flute can determine the number of background events: The OFF from Wobble partner mode, the simultaneous background mode and pulsar mode. The OFF from Wobble partner method uses OFF positions from the actual Wobble positions around the source. In the case of two Wobble positions (referred to as W1 and W2) which have the same declination as the observed source, the OFF position from W1 is chosen such that the source would be located in this position when the telescopes would be pointing at the W2 position (corresponding version for four Wobble positions is shown in the left part of Figure 5.29). The simultaneous background method describes the background estimation resulting from a number η of evenly spaced OFF positions from the camera center which result in normalization factor of η^{-1} (right part in Figure 5.29). The pulsar mode is specifically designed for the determination of the background events in the OFF pulse regions in constrast with the number of γ-rays in the ON pulse region of a pulsar. In the case of the Crab pulsar these regions are set from 0.983 till 0.026 (Main pulse), 0.377 till 0.422 (Interpulse) and to 0.52 till 0.87 (OFF pulse emission region) following the conventions in Aleksić et al. [2012].
The normalization factor for the pulsar mode of Flute needs to be determined manually. It can be set in the input card and is (analogous to Equation 5.14) the ratio of the size between the ON (Main pulse and Interpulse) and the OFF pulse regions:

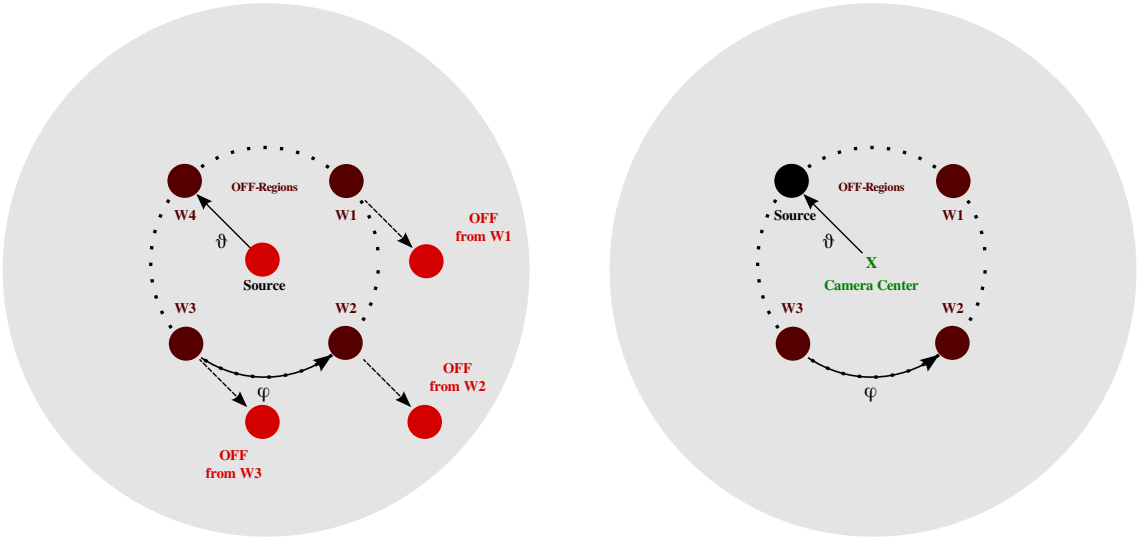

Figure 5.29.: Background determination modes in Flute: OFF from Wobble partner method (left figure) and Simultaneous Background Method (right figure). The brown filled circles are the Wobble positions, the red filled circles the OFF from Wobble partner positions and the black circle in the right figure represents the observed source.

$$\xi = \frac{\Delta_{PhaseON}}{\Delta_{PhaseOFF}} \tag{5.20}$$

It is important to determine this factor in the right way, as otherwise the determination of the background is affected and thus the resulting number of γ-photons from the source. A ϑ^2 plot for the Main and the Interpulse component resulting from the pulsar background mode is shown in Figure 5.30. The resulting differential spectra and SEDs for both pulsed components are shown in Figure 5.31 and Figure 5.32. As already indicated by both Figures, the whole data set was split into two parts consisting of December 2012 & January 2013 data and February 2013 data. This was necessary as new MC simulations were released for the latter data set since the Point Spread Function (PSF) of the telescopes had essentially changed within these three months (E. Carmona, private communication). Consequently, a new RF was determined for the February 2013 data than was used for the processing of the data from December 2012 and January 2013.
To examine if the determination of the differential spectra and SEDs for both pulsed components was carried out in the right way, the whole procedure is carried out for the Crab Nebula as well. For the determination of the background in this case the simultaneous background method in Flute is used. In this case the normalization range is set up in the range from 0.1 to 0.4 degrees (the latter value was used since Wobble observations with exactly this angle were carried out in the case of the MAGIC data which was processed for this project). The resulting differential spectra and SEDs for both divided data samples (December 2012, Janura 2013 and February 2013) are shown in Figure 5.33. The question might arise at this point why

actually the simultaneous background method was used for the Crab Nebula and not the OFF from Wobble partner method. The answer lies in the fact that the Crab Nebula represents an additional background in the case of this system. To get a proper determination of it, a systematic scan of the Crab Nebula is needed which is carried out by the evenly spaced OFF positions mentioned earlier. The OFF from Wobble partner method could also be used in this case, but the simultaneous background method includes a more systematic approach to get a proper determination of the Crab Nebula background.

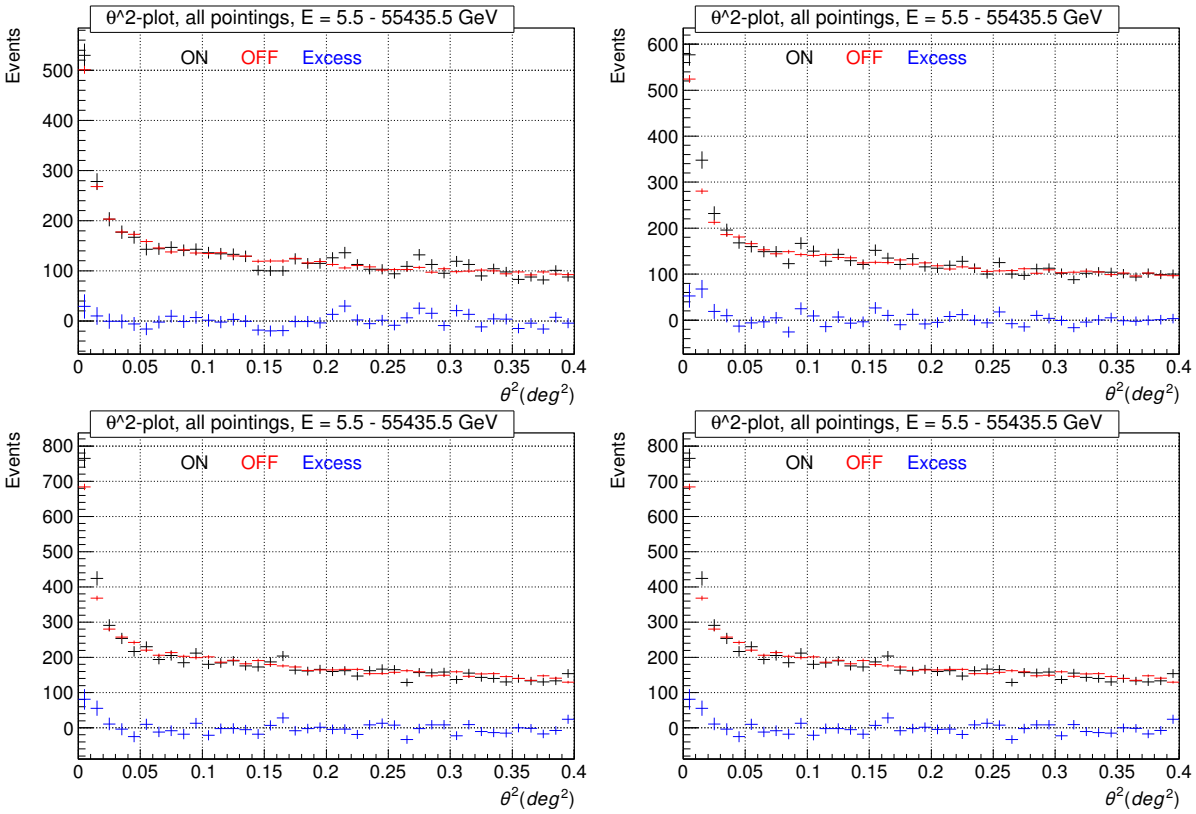

Figure 5.30.: ϑ^2 distributions for the P1 (left row) and P2 component (right row) for December 2012 and January 2013 (top plots) and February 2013 (bottom plots).

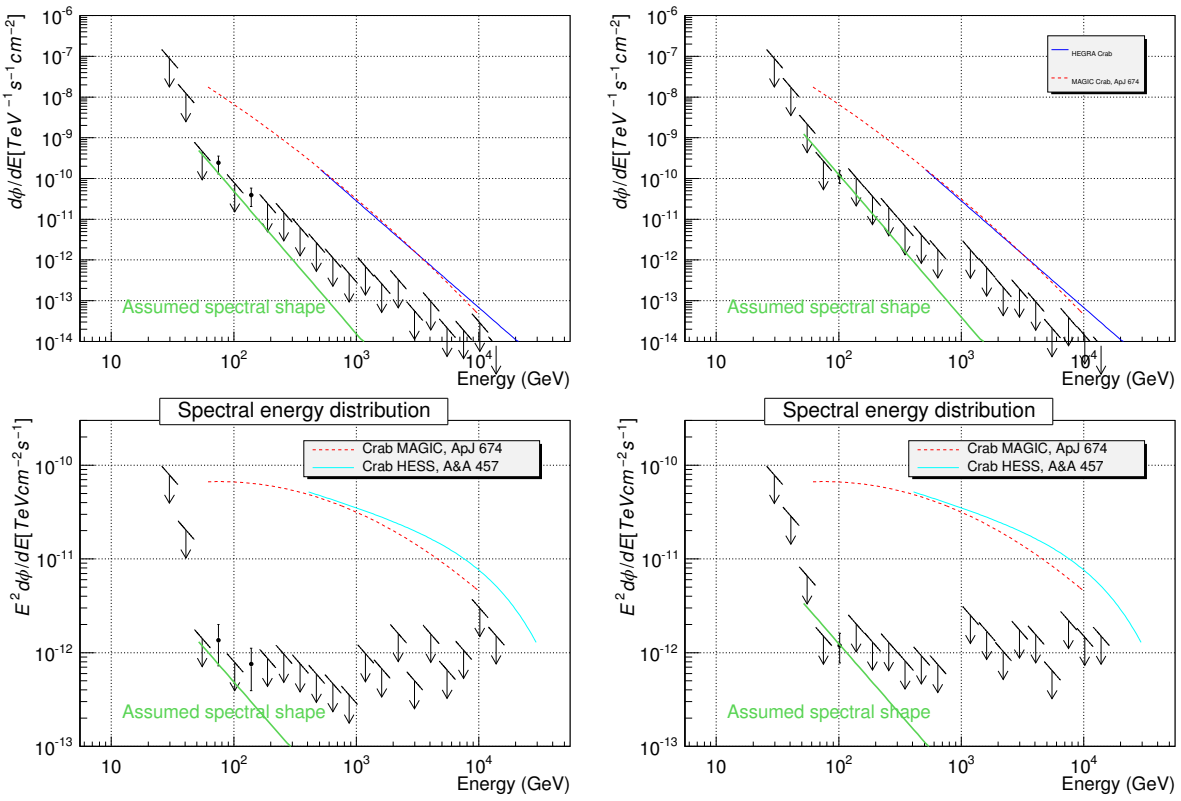

Figure 5.31.: Differential spectrum (top) and spectral energy distribution (bottom) of the Crab Pulsar P1 (left row) and P2 (right row) from December 2012 and January 2013.

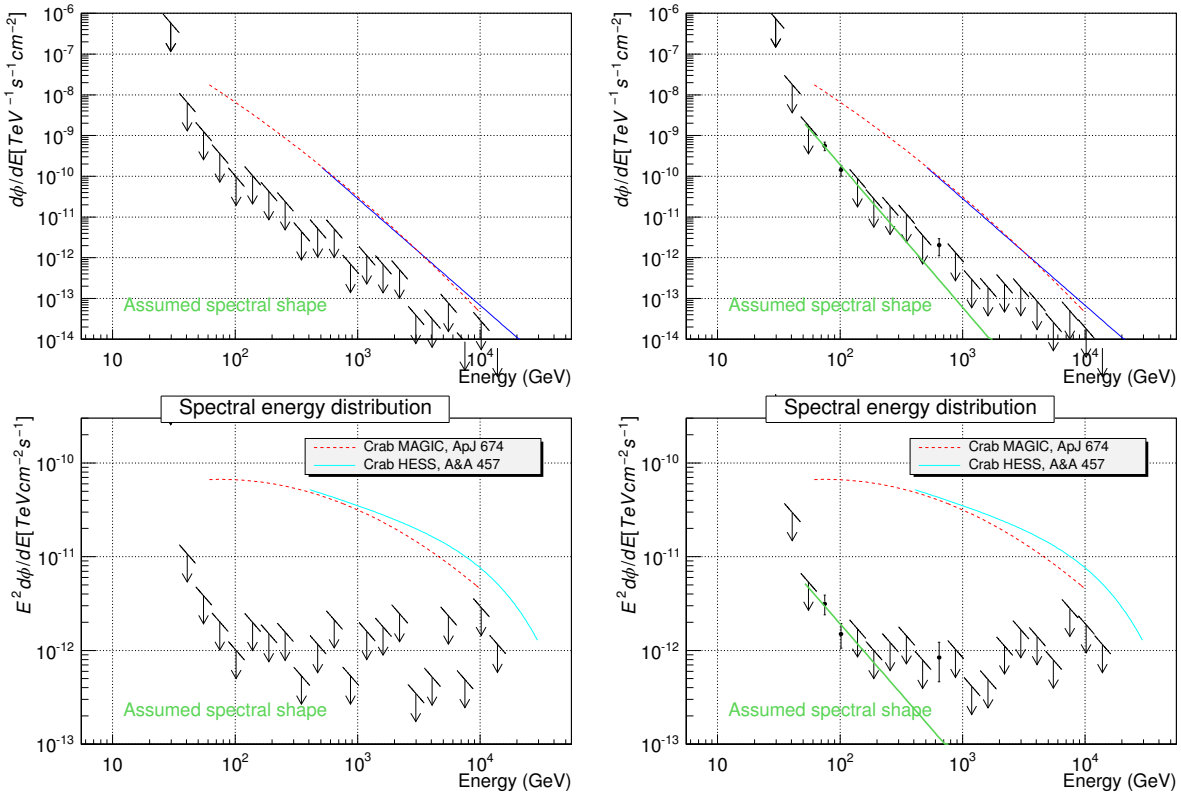

Figure 5.32.: Differential spectrum (top) and spectral energy distribution (bottom) of the Crab pulsar P1 (left row) and P2 (right row) from February 2013. Only upper limits could be determined in this case of the P1 component from the Crab pulsar. One reason for this is the shortness of the data set in contrast with the other two months (Figure 5.31).

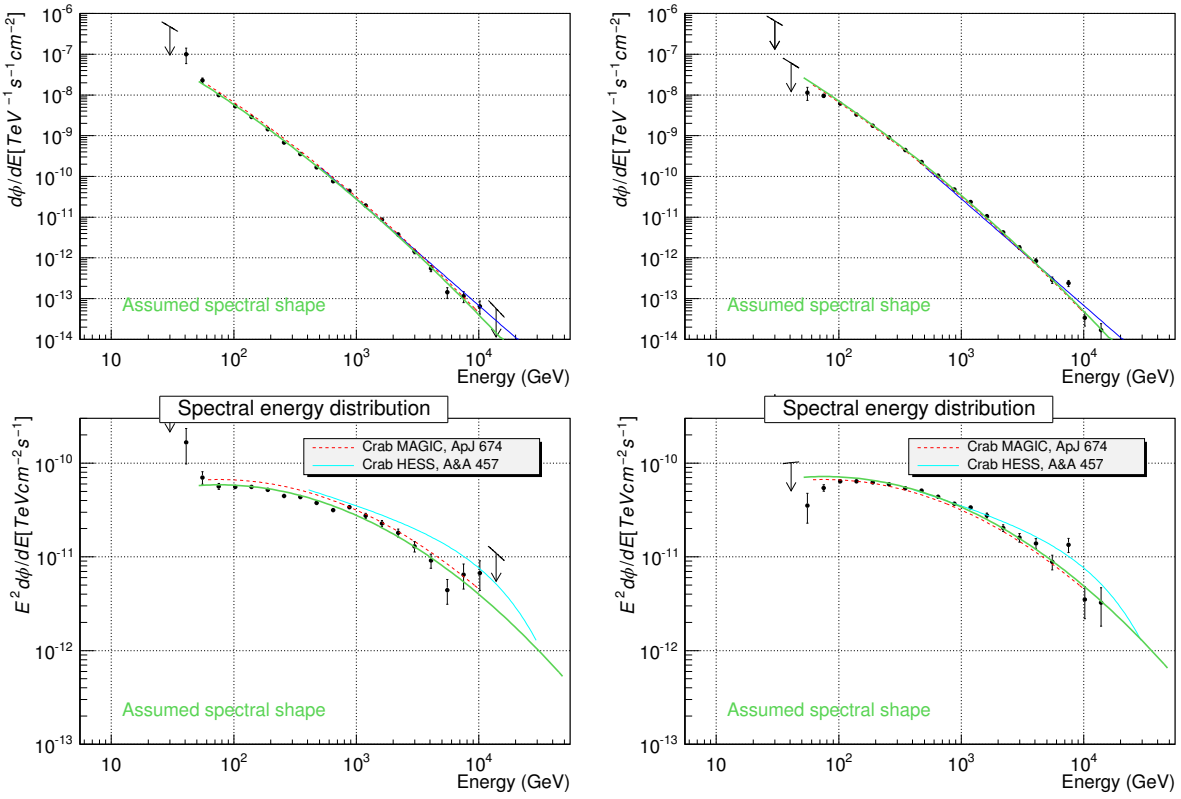

Figure 5.33.: Differential spectrum (top) and spectral energy distribution (bottom) of the Crab Nebula from December 2012 and January 2013 (left row) and from February 2013 (right row).

5.2.6. Cut Optimization – γ-ray Data Sets

For the correlation analysis the highest possible amount of γ-photons from the Crab pulsar needs to be extracted from the data (Table 5.5). In Chapter 5.2.5 the analysis was oriented towards the Crab pulsar and its signal was verified in the corresponding ϑ^2 plots and differential spectra in spite of the high background emission from the Crab Nebula. However, comparing Figure 5.33 with Figure 5.31 and Figure 5.32 nevertheless shows that the Crab Nebula signal is dominant in this data set. The necessity of the cut optimization procedure is emphasised by Figure 5.34 which shows the γ-ray data taken simulatenously with radio data for all three months without additional cuts apart from the ones carried out automatically during the standard analysis. No significantly high pulsed emission from the Crab pulsar is seen in all phase diagrams (although indicated in the data from February 2013 which provides the longest overlap in time with radio observations).
In order to extract the highest amount of γ-ray photons originating from the pulsar and not the nebula, energy dependent cuts in the parameters Hadronness and ϑ^2 are introduced in the further process of the non-standard data analysis into the Crab pulsar data. They need to be energy dependent since the both, the Crab Nebula (CN) and the Crab pulsar (CP), do have different spectra at γ-wavelengths:

$$\frac{dF_{\mathrm{CN}}}{dE} = f_0(\frac{E}{300\mathrm{GeV}})^{-2.31-0.26\cdot\log 10(\frac{E}{300\mathrm{GeV}})} \tag{5.21}$$

$$\tag{5.22}$$

$$\frac{dF_{\mathrm{CP}}}{dE} = (\frac{E}{100\mathrm{GeV}})^{-3.5} \tag{5.23}$$

Equation 5.22 is the result of Crab Nebula observations between 60 GeV and 9 TeV as reported by Albert et al. [2008c] (f_0 being a flux normalisation factor). Equation 5.23 was determined by Aleksić et al. [2012] who observed the Crab pulsar in an energy range from 50 to 400 GeV. To find the appropriate values of the Hadronness, ϑ^2 parameters, data sets from the same source are used which were not taken simulatenously in time with the radio data listed in Table 5.1. To do this all corresponding non-radio Crab Nebula data sets were analysed following the same standard analysis chain as described in Chapter 5.2.2 up to Melibea level (see Table 5.7). After getting all data sets from Table 5.7 into Melibea file format, two different approaches were used in order to find the appropriate energy dependent cuts in the Hadronness and ϑ^2 parameters.

Cut Optimization – Crab Nebula

In the first approach the cuts were optimized on Crab Nebula data. That is, non-barycentered data. For the cut optimization scripts kindly provided by Simon Bonnefoy (Universidad de Complutense) were used. The scripts optimize the cuts on the emission from the Crab Nebula using a quantity known as "Quality Factor" (Q-factor):

$$\mathrm{Q} = \frac{\epsilon_\gamma}{\sqrt{\epsilon_\mathrm{h}}} = \frac{\mathrm{N_{ON}}}{\mathrm{N_{TOTAL}}} \tag{5.24}$$

The quantities ϵ_γ and ϵ_h in Equation 5.24 describe the efficiency of γ-ray induced and hadronic showers. N_{ON} is the number of events resulting from the observations on the source and N_{TOTAL} describes the number of all detected events (γ-ray induced, or hadronic alike) . Consequently,

the Q-factor describes the efficiency of the separation of both kinds of air showers. To extract the highest amount of air showers induced by γ-photons from the source, one usually looks for the highest Q-factor. With the described procedure three OFF regions and one ON region are defined (also in the case of the non-radio Crab Nebula all observations were taken in Wobble mode, see Chapter 5.2.2). Corresponding ϑ^2 distributions for all four positions are determined (Figure B.2). The blue curve in this Figure are the ϑ^2 values from the three OFF source positions and the red curve belongs to the ON source position. The energy range was chosen from 5 GeV (minimum) to 50 TeV (maximum) with 30 energy bins in accordance with previous investigations of the MAGIC Pulsar Working Group (R. Zanin, private communication).
To search for the appropriate Hadronness and ϑ^2 values, the Q-factor is calculated per energy bin resulting from the number of events in the one ON and three OFF positions together for different Hadronness and ϑ^2 values. To extract the highest amount of γ-ray events from the source (and thus to find the optimal cuts in Hadronness and ϑ^2), usually the Hadronness and ϑ^2 values resulting in the highest Q-factor are chosen. The ϑ^2 distributions (Figure B.2) are taken as a sanity check if the separation between ON and OFF positions was sufficient. In coordination with previous examinations of the MAGIC Pulsar Working Group the energy ranges which provide the highest efficiency with regard to the extraction of the Crab pulsar signal, are from 42.9 GeV to 146.4 GeV, 146.4 GeV to 367.8 GeV and from 42.9 GeV to 367.8 GeV. The corresponding cuts in Hadronness and ϑ^2 were applied in these energy bins to the Crab pulsar data taken simultaneously with radio observations (Table 5.5). The described procedure was carried out for each month separately and the resulting phase diagrams were summed up for all three months. The results of this procedure are shown in Figure 5.35 and Figure 5.36 together with one additional phase diagram for the entire energy range from 5 GeV to 50 TeV. The corresponding phase diagram from 42.9 GeV to 367.8 GeV shows a significance of $5.0\,\sigma$ (calculated with Equation 5.15) which in other words means a statistical detection in γ-ray astronomy. An important characteristic of this optimization technique is that the appropriate Q-factor values are chosen basing on the number of events from the Crab Nebula and not from the Crab pulsar. No pulsed γ-ray emission was taken into account by this procedure.

Cut Optimization – Crab Pulsar

Another cut optimization approach which was applied to the non-radio data in Table 5.7 is basing on Crab pulsar data. For this the same data sets as expressed in Table 5.7 were barycentered with the corresponding ephemeris files so that also pulsed emission from the Crab pulsar could be extracted from them. A script kindly provided by Daniel Galindo Fernandez (Universidad de Barcelona) was used to optimize the energy dependent cuts in Hadronness and ϑ^2 parameters on Crab pulsar data. During this procedure combinations of different ϑ^2 and Hadronness values were determined for ranges of the rotational phase of the Crab pulsar covering the Main Pulse (from 0.983 to 0.026), the Interpulse (from 0.377 to 0.422), the OFF pulse region (from 0.52 to 0.87) and the whole rotational phase. Same as in Chapter 5.2.5 the phase ranges were adopted from Aleksić et al. [2012]. This algorithm was carried out for one ON and one OFF position, the latter calculated from the antisource position on the camera plane. For each energy bin the Hadronness and ϑ^2 parameters were optimized to get the maximum significance of the γ-ray signal. To find this maximum, Hadronness values ranging from 0 to 1 and ϑ^2 from 0.002 $(^\circ)^2$ to 0.196 $(^\circ)^2$ were determined throughout the procedure. From a total of 30 energy bins from 5 GeV to 50 TeV the resulting cuts were chosen from 42.9 GeV to 146.4 GeV, 146.4 GeV to 367.8 GeV and 42.9 GeV to 367.8 GeV (in accordance with the settings of the MAGIC Pulsar

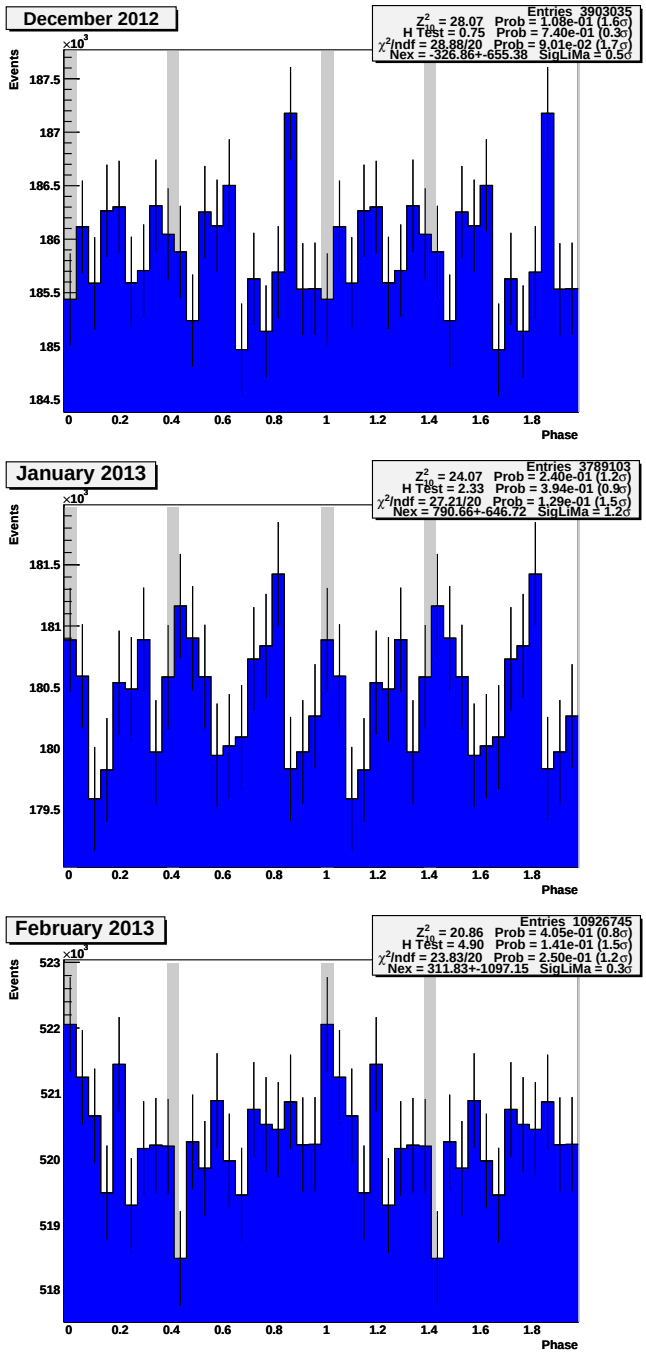

Figure 5.34.: Barycentered MAGIC data from December 2012, January 2013 and February 2013. To emphasise the necessity of cuts, none were included in the Hadronness, or ϑ^2 parameters. The grey fields mark the phase positions of P1 and P2 after barycentering according to the values determined by Aleksić et al. [2012].

Working Group). The optimization procedure was carried out for the non-radio MAGIC data from each of the three months separately. The resulting cuts in Hadronness and ϑ^2 were applied monthwise to the Crab pulsar data which was taken simultaneously with radio observations (Table 5.5) in the same energy ranges. The outcome of all three months was added up and the resulting phase diagrams are shown in Figure 5.37 and Figure 5.38. As is visible in the upper part of Figure 5.38, the significance of pulsed emission is highest with $6\,\sigma$ in the energy range from 42.9 GeV to 367.8 GeV. Comparing this result with the corresponding part of Figure 5.36, verifies that a cut optimization procedure based on Crab pulsar insead of Crab Nebula data, delivers a higher significance of the pulsed emission.
The resulting cuts in Hadronness and ϑ^2 from 42.9 GeV to 367.8 GeV were adopted for the correlation study between radio giant pulses and γ-photons (Chapter 5.3).

Facility	Epoch	Δt [min]	Zd Range [°]
Winter 2012/13			
MAGIC	2012-11-11	216	16.4 - 35.1
MAGIC	2012-11-12	151	17.2 - 20.1
MAGIC	2012-11-13	119	10.8 - 19.1
MAGIC	2012-11-21	38	19.9 - 28.8
MAGIC	2012-11-22	51	19.2 - 9.1
MAGIC	2012-12-05	224	17.5 - 34.9
MAGIC	2012-12-14	207	34.9 - 13.9
MAGIC	2012-12-16	115	16.6 - 12.5
MAGIC	2012-12-20	137	7.0 - 34.5
MAGIC	2013-01-03	93	15.0 - 35.0
MAGIC	2013-01-04	96	15.3 - 35.1
MAGIC	2013-01-05	27	28.1 - 34.9
MAGIC	2013-01-08	199	15.2 - 32.5
MAGIC	2013-01-12	53	34.1 - 22.8
MAGIC	2013-01-14	38	30.1 - 22.5
MAGIC	2013-01-19	53	21.3 - 33.0
MAGIC	2013-01-20	43	25.3 - 34.7
MAGIC	2013-01-31	117	26.1 - 7.0
MAGIC	2013-02-16	150	6.8 - 33.1
MAGIC	2013-02-28	129	6.5 - 29.3
MAGIC	2013-03-01	21	30.0 - 34.8
MAGIC	2013-03-02	144	6.2 - 34.1
MAGIC	2013-03-03	101	6.3 - 25.6
MAGIC	2013-03-09	100	13.0 - 34.7
MAGIC	2013-03-10	105	13.3 - 35.1
MAGIC	2013-03-21	53	23.3 - 35.0
Total Observation Time		**2780**	

Table 5.7.: List of MAGIC data sets which were used for the cut optimization. None of these data sets overlap with radio observations taken for the correlation study. The table is subdivided into three parts to show which data was used for what month (from top to bottom: December 2012, January 2013, February 2013 data).

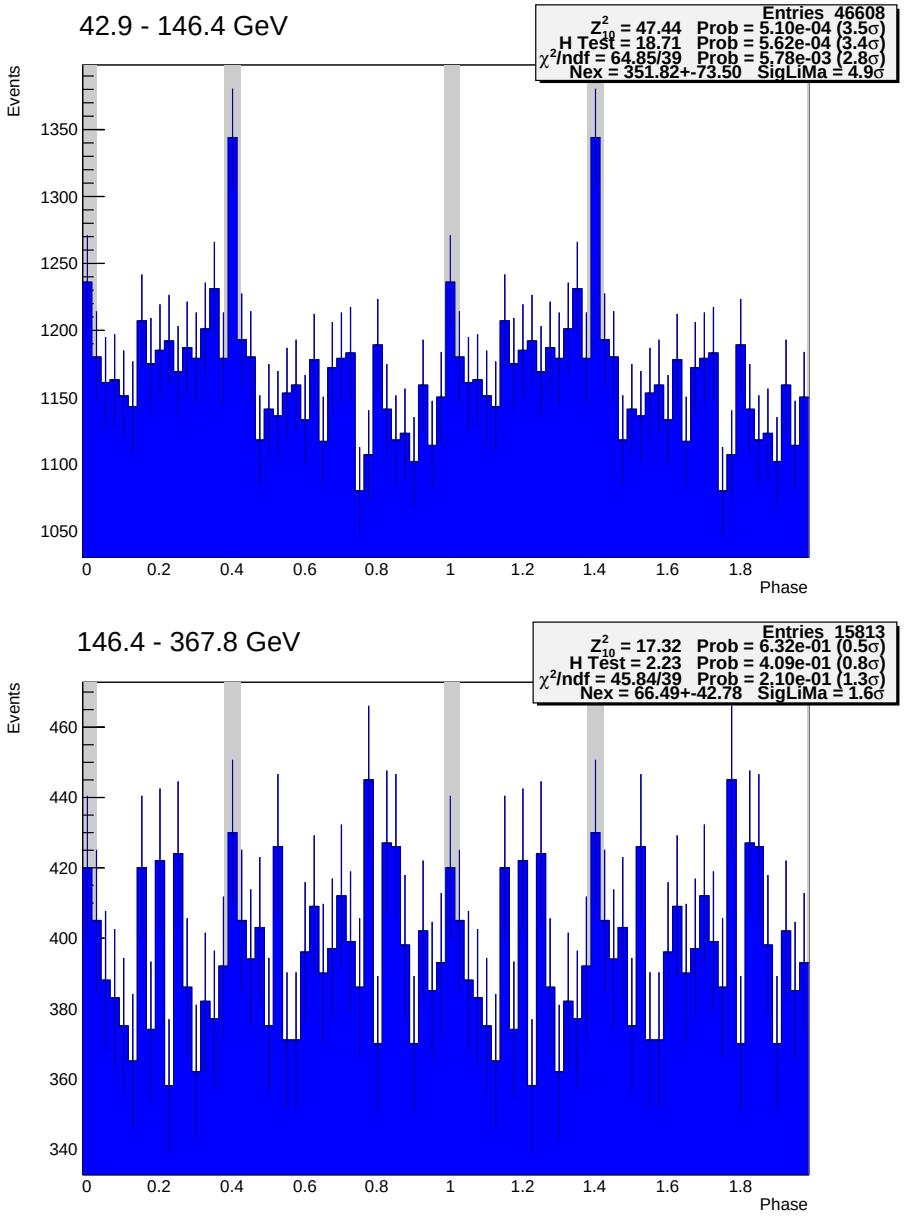

Figure 5.35.: Phase diagrams of MAGIC Crab pulsar data taken simultaneously with radio observations (December 2012, January & February 2013) after including energy dependent cuts in Hadronness and ϑ^2 for an energy range from 42 GeV to 146 GeV (upper figure) and from 146 GeV to 367 GeV (lower figure). The cuts were optimized monthwise on Crab Nebula data (taken non-simultaneously with radio observations). The light curves were determined for each month and added up in this figure, Figure 5.36, Figure 5.37 and Figure 5.38.

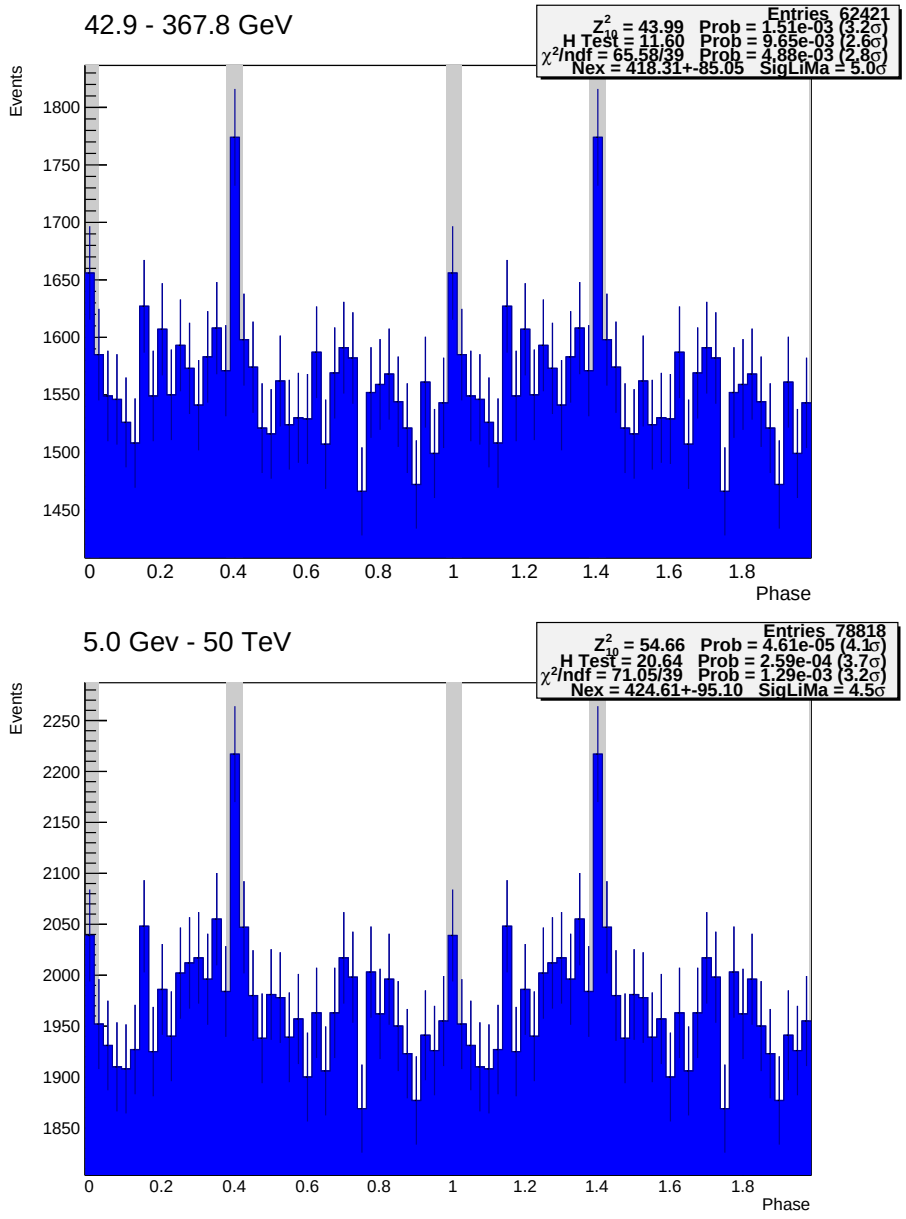

Figure 5.36.: Phase diagrams of MAGIC Crab pulsar data taken simultaneously with radio observations (December 2012, January & February 2013) after including energy dependent cuts in Hadronness and ϑ^2 for an energy range from 42 GeV to 367 GeV (upper figure) and from 5 GeV to 50 TeV (lower figure).

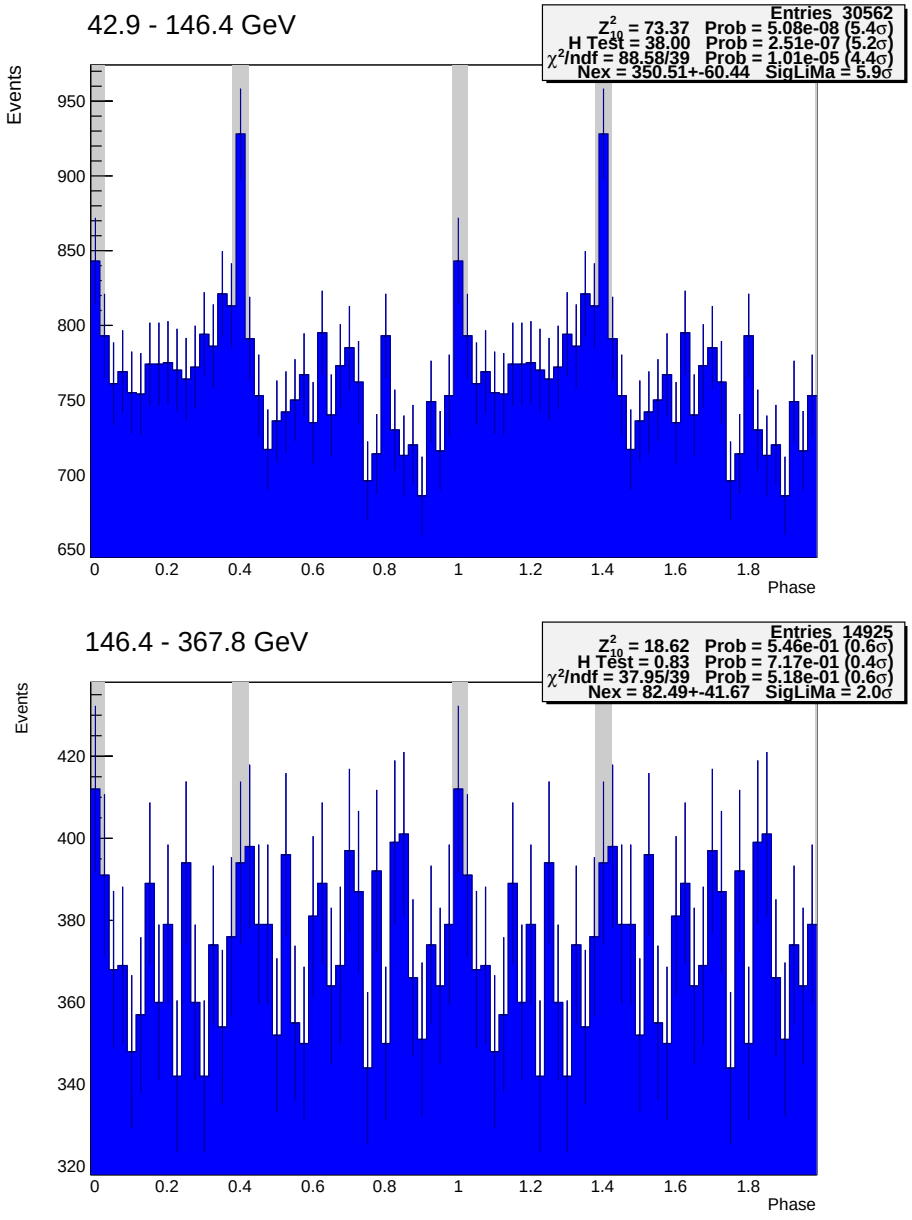

Figure 5.37.: Phase diagrams of MAGIC Crab pulsar data taken simultaneously with radio observations (December 2012, January & February 2013) after including energy dependent cuts in Hadronness and ϑ^2 for an energy range from 42 GeV to 146 GeV (upper figure) and from 146 GeV to 367 GeV (lower figure). The cuts were optimized on Crab pulsar data taken non-simultaneously with radio data and applied monthwise. The resulting phase diagrams were added up in four different energy ranges as in Figure 5.35 and Figure 5.36.

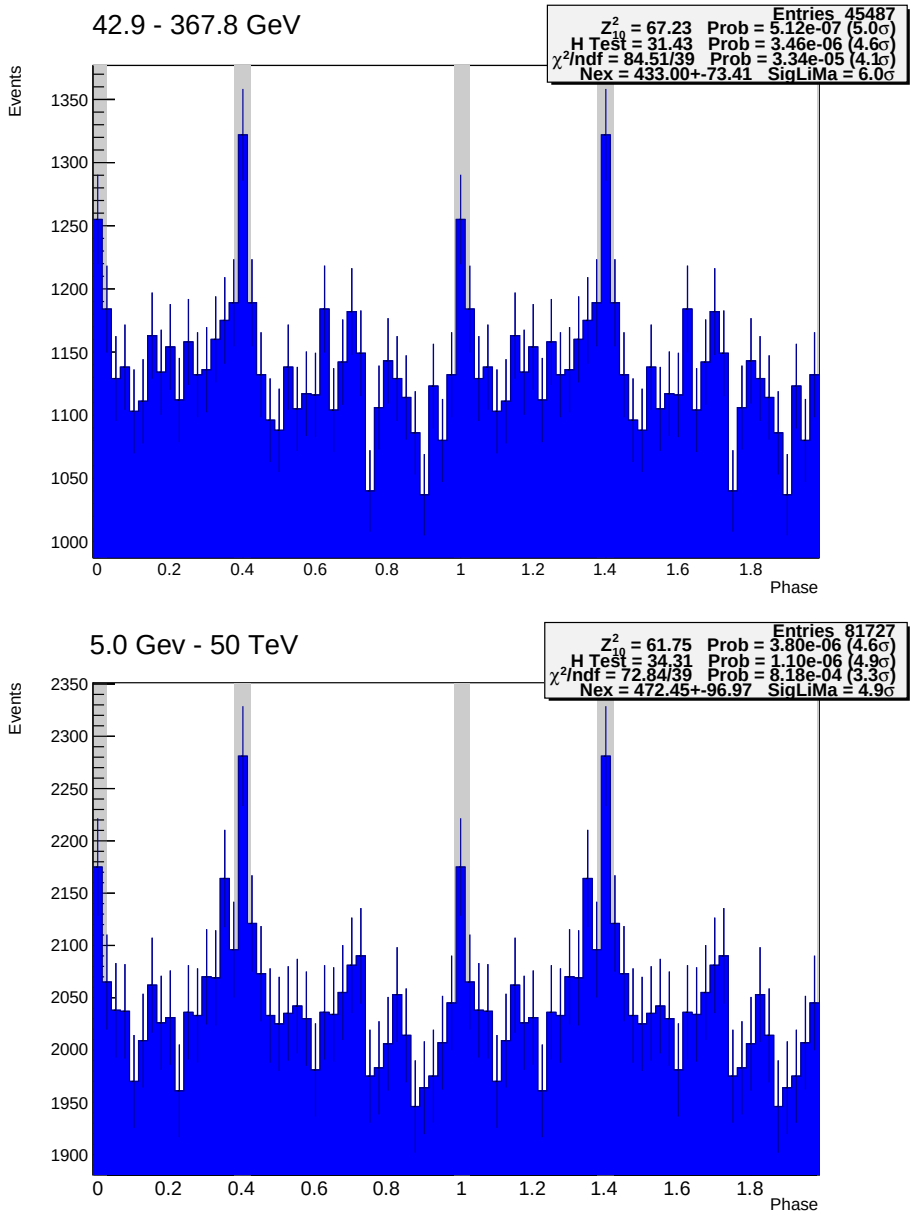

Figure 5.38.: Phase diagrams of MAGIC Crab pulsar data taken simultaneously with radio observations (December 2012, January & February 2013) after including energy dependent cuts in Hadronness and ϑ^2 for an energy range from 42 GeV to 367 GeV (upper figure) and from 5 GeV to 50 TeV (lower figure).

5.3. Correlation Analysis

5.3.1. Approach for Correlation Study

The aim of the study described in this chapter is to find out if a correlation between radio giant pulses and γ-photons from the Crab pulsar does exist. This is an interesting question to ask since currently the radio and γ-ray emission from the Crab pulsar is assumed to originate from different regions in its magnetosphere. Radio giant pulses provide the possibilty to study the Crab pulsar indepedently of its rotation. Due to their short pulse widths ranging from nanoseconds to microseconds, the rotation of the pulsar (ranging in the milliseconds range) can be neglected when a radio giant pulse occurs. Studying radio giant pulses therefore means studying the pulsar in a frozen state. Besides, single pulses provide a direct fingerprint of the state at which the pulsar magnetosphere was when the pulse was emitted. If a correlation between radio giant pulses and γ-photons is found, a common trigger for their emission must have been present. The most likely cause is a localized change somewhere in the magentosphere resulting in the observed multiwavelength properties. If the underlying physical process can be identified, it will lead to a better understanding of the giant pulse emission and possibly give a deeper insight into the emission mechanisms of regular pulses.
Several approaches for the search for a correlation are nowadays known (see for example Chapter 4 in Wall and Jenkins [2012]). Which one is applied in the end, depends on the nature of the data and the correlation one aims to find. Apart from the unknown form of a correlation (if it exists), the nature of the available Crab pulsar data prevents the usage of conventional approaches for correlation searches. Although the data were recorded simultaneously, each event (in the radio and in the γ-ray data) arrives at an individual time at the respective observatory and is marked with a corresponding time stamp. That is, not for each time stamp of a radio event a simultaneous event at γ-rays does exist. Consequently, the events in each data set can be regarded as non-simultaneous values with their TOAs. Since the usual correlation approaches require the existence of concurrent data values (a discussion of this problem in the context of Astrophysics can be found in Edelson and Krolik [1988]), they cannot be applied right away to the data presented in this study.
The search approach for a correlation is subdivided into several sections in this chapter based on the amount of time resolution. That is, with degrading timing information of the recorded events, ranging from the usage of the full timing information in Chapter 5.3.2, to the gradually blurring out of the timing precision due to a binning procedure as described in Chapter 5.3.3 and Chapter 5.3.4.
In Chapter 5.3.2 the differences of the times of arrival ΔTOAs, of radio and γ-ray events are calculated. For this part of the analysis the output of the time stamp check of the γ-ray data together with the corresponding radio data was used (Chapter 5.2.4). This approach is similar to the one presented with Fermi LAT data by Bilous et al. [2011] and aims to search for a correlation of the arrival times of radio and γ-photons in different windows of the rotational phase of the pulsar.
Another approach for a correlation search is described in Chapter 5.3.3. Taking up on the problem with non-concurrent TOAs of radio and γ-ray events, simultaneous values of counts (between the radio and corresponding γ-ray data sets) are constructed by putting the events on the basis of their TOA values in time bins of equal length. A correlation is searched for by examining if both kinds of data sets are linearly correlated via the Pearson correlation coefficient.

A further approach for a correlation search is given in Chapter 5.3.4 and is based on the examination of flux enhancements around occurring radio giant pulses.

5.3.2. Times of Arrival Differences

In this chapter the search for a correlation between radio giant pulses and γ-photons is carried out by using the TOAs of the events from both kind of data sets. The idea behind this approach is to search for pairs of radio and γ-ray events which have small time delays with respect to each other.
This part of the analysis is built up in three steps: The aim is to examine the differences of the arrival times. To deduce if the outcome of these differences shows statistically significant features, a comparison is made with time differences between the events in the γ-ray data and in MC simulations of the radio data sets. These simulations reflect a non-correlated radio pulsar signal. In order to build them, the pulsar signal in the radio data is approximated by Gaussian fits.

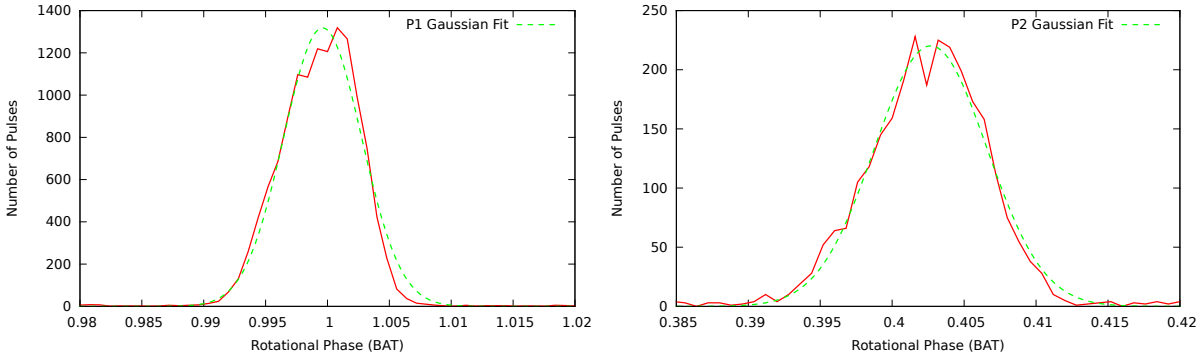

Figure 5.39.: Gaussian fit of P1 (left) and P2 (right) from the barycentered radio data set taken with the WSRT on 2012-12-10 as expressed in Table 5.1.

Extraction of Main and Interpulse – Radio Data

In order to carry out a search for a correlation between γ-photons and radio giant pulses from P1 as well as P2, both regular emission components are fitted with Gaussian fits in the barycentered radio data sets (Table 5.1, Figure 5.39). The fitting procedure is carried out in two steps. To increase the S/N and thus make the fitting procedure with Gaussian curves easier to carry out, all data sets taken with the same telescope at the same center frequency were fitted together in the first step. However, in the case of the Effelsberg data, two data sets were taken at a different center frequency than the others (2013-01-09 and 2013-02-07, compare Table 5.1). Therefore they were fitted separately from the other Effelsberg data sets. Since the radio data sets were in general not taken continuously throughout one month but cover only a small part of each month, the data sets from different months were fitted separately. In the case of each data set the P1 component was fitted with the following Gaussian function:

$$f(t) = a \cdot e^{-\frac{(t-b)^2}{c^2}} \tag{5.25}$$

The coefficients a, b, c stand for the height of the Gaussian, its center and its width. The P2 component was fitted in an analogous way by:

$$g(t) = l \cdot e^{-\frac{(t-m)^2}{n^2}} \tag{5.26}$$

Also in this case the coefficients l, m, n stand for the height of the corresponding Gaussian, its center and its width. In the second step only the height of the respective Gaussian was determined for the single radio data set from each night, the center and width of the Gaussian fit were taken from the corresponding fit of the summarized data set. The two step approach needed to be carried out this way since the available single radio data sets are usually very noisy, which makes the fitting procedure more difficult.
The results of the fitting procedure are summarized in Table 5.8. The bold written entries reflect the Gaussian fit values for the data sets which were aggregated for the fitting procedure. The other entries represent the Gaussian fit values for single radio data sets.

Monte Carlo Simulations – Radio Data

In order to distinguish a correlated signal from a non-correlated one in the further process of the analysis, MC simulations matching the timing information of the radio data sets are constructed. This way, simulated data sets with the same timing information as the real data sets are constructed which contain a purely uncorrelated signal based on independent random numbers. With this procedure it can be excluded that artefacts resulting from the statistical properties of the real data sets, lead to a false interpretation of a correlation between radio and γ-photons.
Before the actual time differences between the arrival times of radio giant pulses and MAGIC photons are determined, the same time differences resulting from non-correlated emission are simulated by constructing MC simulations of the radio data sets and calculating the corresponding time differences with the γ-ray data. The aim behind this procedure is to get an idea how the time differences will look like if no correlation will be found (that is, if they result from non-correlated emission only). The reason why MC simulations were chosen for this procedure is that they provide uncorrelated but otherwise identically distributed arrival times.
The construction of the respective MC simulations is carried out by simulating the available Crab pulsar radio data sets. The reason to choose the radio data and not the γ-ray data lies in the fact that the background emission is much lower in the first case and thus easier ascertainable.
For a proper simulation of the radio data sets, the Gaussian fit parameters obtained in Chapter 5.3.2 and listed in Table 5.8 are used. With these parameters a simulated radio data set is constructed for each night for which radio data are available. The procedure is carried out as follows:
Each MC simulation is built up on the parameters of the Gaussian fit (height, center and width) as determined in the last chapter. The number of pulses is calculated for the range of the corresponding Gaussian fit of P1 (NP1) and P2 (NP2). The total number of pulses (Ntotal) is derived from the number of entries in the corresponding barycentered radio data file (Chapter 5.1). To simulate the pulsed and non-pulsed emission phase regions of the Crab pulsar (Figure 5.40), interarrival times are calculated from the respective radio observations. The differences between consecutive arrival times from the radio data are calculated and converted into seconds. The actual MC simulation is generated with the same start and end time

Facility	Epoch	ν_{center} [MHz]	a	b	c	l	m	n
Winter 2012/13								
Effelsberg	2012-12-07	1347.5	166.9	0.999608	0.00436	8.26	0.40296	0.00498
Effelsberg	2012-12-17	1347.5	333.8	0.999608	0.00436	18.62	0.40296	0.00498
Effelsberg	**2012-12**	1347.5	**510.0**	**0.999608**	**0.00436**	**26.9**	**0.40296**	**0.00498**
WSRT	**2012-12-10**	1380.0	**1318**	**0.99961**	**0.00446**	**220.2**	**0.40268**	**0.00554**
WSRT	2013-01-08	1380.0	378.1	1.00142	0.00445	113.0	0.40459	0.00553
WSRT	2013-01-10	1380.0	1883	1.00142	0.00445	499.0	0.40459	0.00553
WSRT	**2013-01**	1380.0	**2262**	**1.00142**	**0.00445**	**612.0**	**0.40459**	**0.00553**
Effelsberg	**2013-01-09**	1372.5	**336.365**	**1.0012**	**0.00431**	**22.0**	**0.40452**	**0.00556**
Effelsberg	2013-01-12	1347.5	617.0	1.00114	0.00433	40.7	0.4042	0.00539
Effelsberg	2013-01-31	1347.5	160.1	1.00114	0.00433	7.88	0.4042	0.00539
Effelsberg	**2013-01**	1347.5	**777**	**1.00114**	**0.00433**	**48.6**	**0.4042**	**0.00539**
WSRT	2013-02-02	1380.0	598	1.00207	0.00445	103.9	0.40509	0.00548
WSRT	2013-02-03	1380.0	1520	1.00207	0.00445	309.1	0.40509	0.00548
WSRT	**2013-02**	1380.0	**2117**	**1.00207**	**0.00445**	**413.0**	**0.40509**	**0.00548**
Effelsberg	2013-02-06	1347.5	434.0	1.00026	0.00437	21.2	0.40354	0.00608
Effelsberg	2013-02-08	1347.5	99.8	1.00026	0.00437	6.32	0.40354	0.00608
Effelsberg	2013-02-09	1347.5	374.0	1.00026	0.00437	18.79	0.40354	0.00608
Effelsberg	2013-02-10	1347.5	229.7	1.00026	0.00437	10.02	0.40354	0.00608
Effelsberg	**2013-02**	1347.5	**1137**	**1.00026**	**0.00437**	**56.3**	**0.40354**	**0.00608**
Effelsberg	**2013-02-07**	1410.0	**85.0**	**1.00041**	**0.00367**	**3.14**	**0.40365**	**0.00525**

Table 5.8.: Gaussian fit parameters of all radio data sets. The coefficients a,b,c belong to the fit of P1 and l,m,n to the fit of P2.

as the corresponding observation. A random interarrival time is fetched from the differences between the arrival times from the respective radio observations. From this first randomly fetched interarrival time Δt the corresponding phase is calculated using the Taylor expansion formula:

$$\varphi = f_0 \cdot \Delta t + \frac{1}{2} \cdot f_1 (\Delta t)^2 \tag{5.27}$$

The integer part of the phase value is extracted and kept. To determine the fractional part of the rotational phase that results in correctly peaked P1 and P2 pulses, a random value from a uniform distribution of values ranging from zero to one is generated in the next step and it is used to decide if the fractional part is generated by a P1, P2, or OFF pulse event. The decision is made by checking if the value belongs to the fraction of pulses within the P1 Gaussian fit, P2 Gaussian fit, or to the OFF pulse emission regions (Figure 5.40). After this assignment, the phase value of the newly constructed event is calculated by determining its decimal part from the region to which it was assigned and adding the integer part determined earlier via Equation 5.27. The resulting arrival time in MJD format is calculated afterwards in order to make a subtraction with the corresponding γ-ray data sets possible.

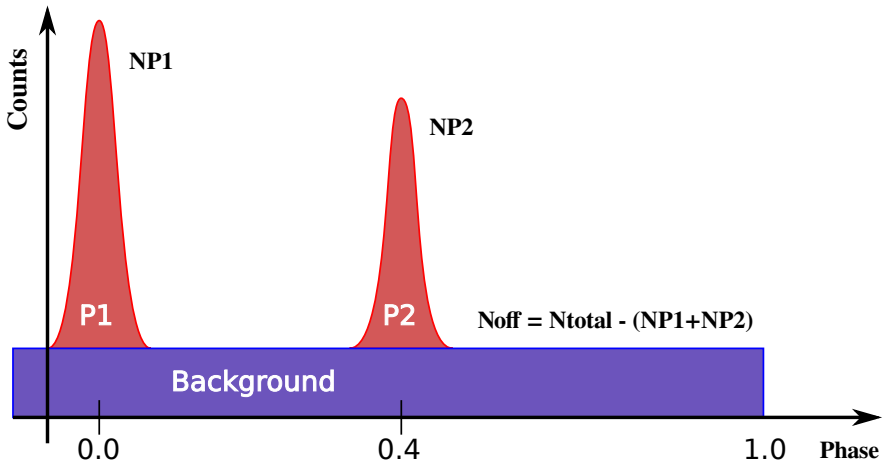

Figure 5.40.: Scheme how MC simulations of the radio data are built. The quantities NP1 and NP2 correspond to the number of pulses within the range of the Gaussian fit of the P1 and the P2 component.

Since the next event is constructed based on the phase position of the previously simulated event, events which are adjacient in phase can be regarded as linked and their construction follows a kind of chain. Nevertheless the simulated events are regarded as random variables in the whole process. The resulting simulations are referred to as Markov Chain Monte Carlo (MCMC) simulations (Brémaud [2013]). They are specified at this point of the thesis to emphasise the difference to the construction of the MC simulations of the γ-ray data sets which will be described in Chapter 5.3.2.
For the first approach towards a search for a correlation, 12 MC simulations are built for each

radio data set. This number of simulations is chosen since it is commonly assumed that the sum of 12 such simulations resembles a normal distribution according to the density of the sum of n uniform random variables (Feller [1957]).
Although the same technique is used to build MC simulations for the Effelsberg and WSRT data sets, the latter are too different to generate a uniform approach for their corresponding simulations. The radio data taken with the Effelsberg radio telescope for instance contains gaps in time throughout a whole observation run. To determine a minimum threshold for these gaps (which will be implemented for the generation of the respective MC simulations), the sizes of all of these gaps are measured in each Effelsberg radio data set. These measurements are done twice, once automatically with a corresponding analysis script and once by eye in order to check the automatic prodecure for errors. Time gaps of different durations are discovered in some of the Effelsberg radio data sets (Table 5.9) albeit not in all. To include all time gaps also in the MC simulations of the affected radio data sets, a threshold of one minute is included into the respective calculations. The idea behind using the same threshold value for all radio data sets which have gaps, is to include also time gaps shorter than those found in the corresponding data set, if some were overlooked. The MC simulations for all radio data sets with gaps are calculated with this threshold. In the case of the Effelsberg radio data sets without gaps, no threshold is included in the calculations of the corresponding MC simulations.
Such a procedure does not need to be carried out for the WSRT radio data sets which are continuous. Nevertheless in this case the data sets are more noisy (see overlap plots in Chapter A.17) in contrast with the Effelsberg data. During the construction of the MC simulations for the WSRT data sets, the noise in the latter has not been included in the calculations (due to re-occuring systematic errors in the further course of the correlation analysis when the noise was included during previous calculations). This is carried out with a cut in the rotational phase values of the corresponding data sets. The cuts are optimized on the radio data sets using the values from the Gaussian fitting process (Table 5.8). An interval of $2\,\sigma$ values around the average is used for the phase cut. The resulting data sets only contain the P1 and the P2 component.
An example of the determined MC simulations together with the corresponding radio data sets from both facilites, is shown in Figure 5.41. The MC simulations for all radio data sets can be found in Chapter A.18.

Epoch	Δt [min] :	1.00	1.58	1.73	1.77	5.83	56.16	104.58
2012-12-17		x	x					
2013-01-09				x	x			
2013-01-31							x	
2013-02-06						x		x

Table 5.9.: Summary of time gaps in the Effelsberg radio data sets.

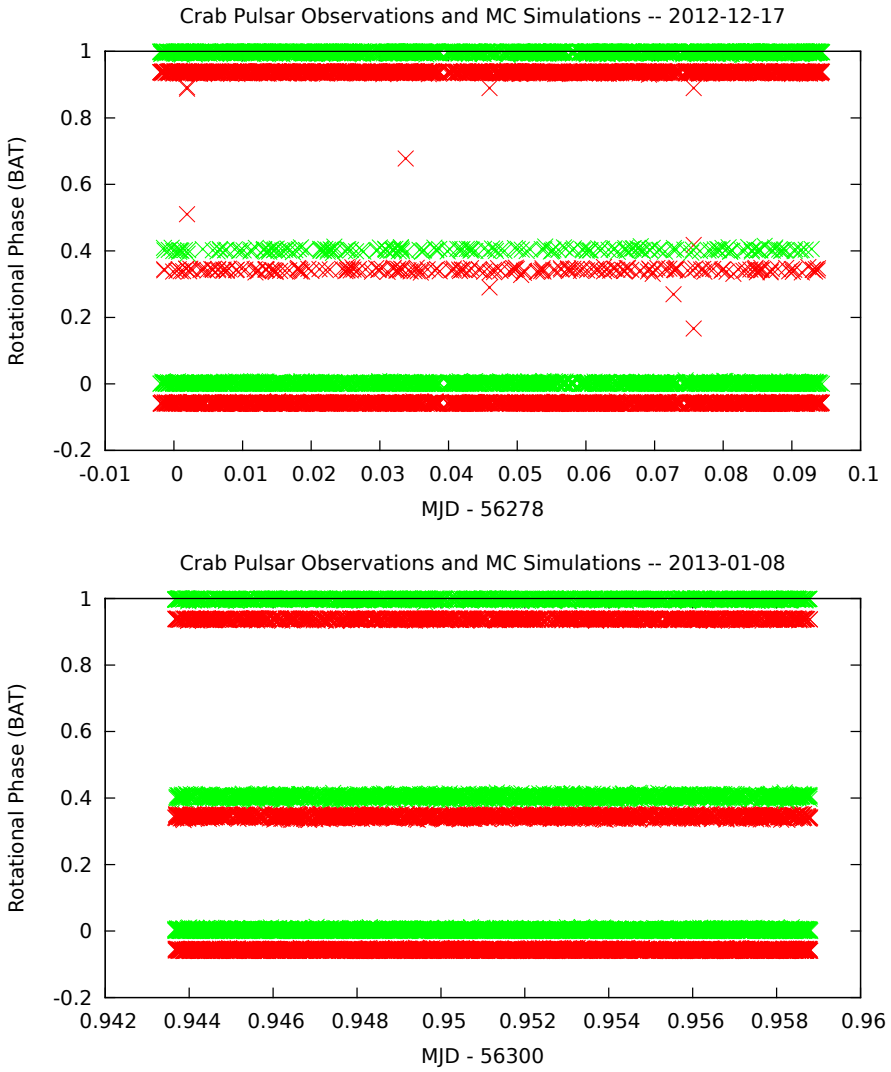

Figure 5.41.: Comparison between radio data sets (red curve) and corresponding MC simulations (green curve). The red curve is shifted by -0.06 on the ordinate to make them easier discernible from the corresponding simulations. Upper figure: Radio observations and MC simulations from 2012-12-17 taken with the Effelsberg radio telescope. Lower figure: WSRT radio observations and MC simulations from 2013-01-08.

Monte Carlo Simulations – γ-ray Data

The construction of MC simulations based on the γ-ray data is necessary for the completion of the search for a correlation as will be shown in Chapter 5.3.4. Analogous to the radio simulations described in the last chapter, also in this case the simulations of the γ-ray data sets are built on the timing properties of the latter and are used to exclude false interpretations of a correlation between radio and γ-photons. However, the procedure for building the appropriate simulations for the available γ-ray data sets, differs due the properties of the latter from the one with which the radio MC simulations were built. They are built in a similar way as described in Aliu et al. [2012], albeit with some modifications.
Analogous to the construction of the radio MC simulations (Chapter 5.3.2), also in this case the statistics of the γ-ray data sets are verified by fitting the pulsed emission components P1 and P2 with Gaussians to determine their number of pulses (NP1, NP2). Unlike in the case of the construction of the radio MC simulations, the total amount of all available γ-ray data sets is used for the Gaussian fitting procedure. That is, the fitting procedure is not carried out for single γ-ray data sets per night due to the much higher background emission in comparison with the radio data. Apart from the pulsed emission components, also the fraction of the number of events contained in the background emission region is determined. The results of this fitting procedure are summarized in Table 5.10.

Components	
a	0.0033
b	1.0003
c	0.0064
l	0.0065
m	0.4050
n	0.0154
BG	0.9902

Table 5.10.: Results of the Gaussian fitting procedure of all γ-ray data sets. Apart from the quantities a and l (refer to text), the notations are analogous to Table 5.8 ("BG" standing for background emission, or OFF pulse emission in this case).

The generation procedure of the γ-ray MC simulations consists of two parts. In the first step of the construction process, barycentered TOAs are extracted from the γ-ray data sets after the final cuts in Hadronness and the ϑ^2 parameters were applied to them (see Chapter 5.2.6). From these data sets the corresponding TOAs of the very first and the very last recorded event are extracted together with the total number of all contained events. To simplify notation, the determined TOAs are referred to as BAT_{min} and BAT_{max}. In the next step the γ-ray data sets without cuts, that is, right after their barycentering (Chapter 5.2.4), are examined (they will be referred to as raw data from now on). Since no cuts have been included in the raw data, the latter contain a much higher number of recorded events. However, also in the case of the raw data sets the barycentered TOAs are extracted for each event and if they are located in time between the values of BAT_{min} and BAT_{max}, they are stored. The resulting barycentered TOAs extracted from the raw data, are afterwards filled (and this way sorted) into time bins.

The bin length is set to one second. This way the trigger rates are estimated from the raw data sets.

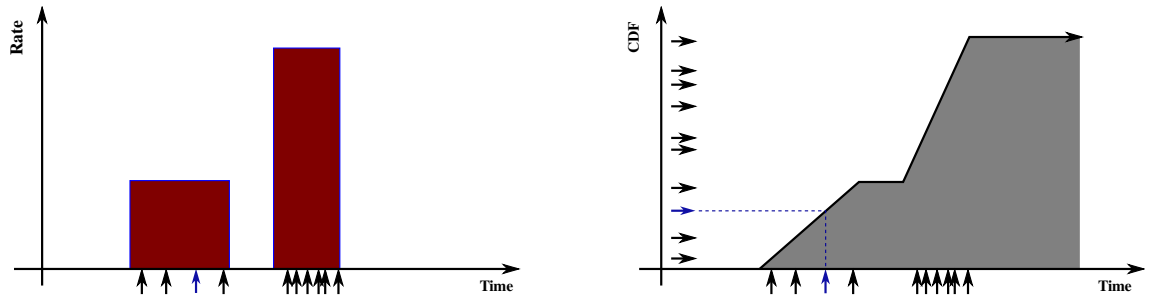

Figure 5.42.: Construction of γ-ray MC Simulations. Left figure: Histogram of raw data events. Right figure: Construction of respective CDF. The arrows in parallel to the abscissa represent event numbers while the ones in parallel to the ordinate stand for the arrival times of the respective events.

In the second part of the construction process the total number of events for the MC simulation is chosen by drawing a Poisson distributed, random number which has a mean value equal to the total number of events in the corresponding γ-ray data file with Hadronness and ϑ^2 cuts. To numerically approximate the TOAs of the recorded raw events, a CDF is calculated out of the histogram of raw events (Figure 5.42). The CDF determines how fast the number of events in the bins of the histogram is growing. Afterwards a random event is picked from the total number of N events between zero and the last element of the CDF. The CDF is an indicator providing information about which bin in the histogram exceeds the randomly picked event for the first time. When this bin in the histogram is found, a uniform, random number u located in it is picked. The respective barycentered TOA is constructed afterwards by calculating the difference between the borders of the bin in which the simulated event has fallen. These borders are ranging from the beginning of the bin to the end of the border multiplied by u. In a consecutive step the rotational phase of the determined barycentered TOA is calculated using the Taylor expansion formula (Chapter 5.3.2). From this calculation only the integer part of the phase is kept.
In the next step it needs to be decided to which emission component the simulated event belongs (that is, P1, P2, or OFF pulse emission). For this purpose a further random number (named r in this context) is chosen. It is checked afterwards on the basis of the integrated areas of the corresponding Gaussian fits (a and l in Table 5.10) if r belongs with its value to P1, P2, or the background emission component. After an assignment to one of the pulsed emission components has been made, a further random number s from the Gaussian distribution of the component to which r was assigned using the position and the width of the respective Gaussian fit (b, c, or m, n in Table 5.10), is drawn. From this number the fractional part of the rotational phase and afterwards the corresponding barycentered TOA is determined. The latter is added to the previously calculated integer part of the barycentered phase value thus constructing the final barycentered phase value of the simulated event. If the random number r is not assigned to one of the pulsed emission components, it is assigned to the background, or OFF pulse emission. With this procedure events of different kind (P1, P2, or BG) are simulated on the

basis of the analysed γ-ray data sets with included cuts in Hadronness and ϑ^2. The resulting MC simulations for all γ-ray data sets are shown in Figure 5.43.

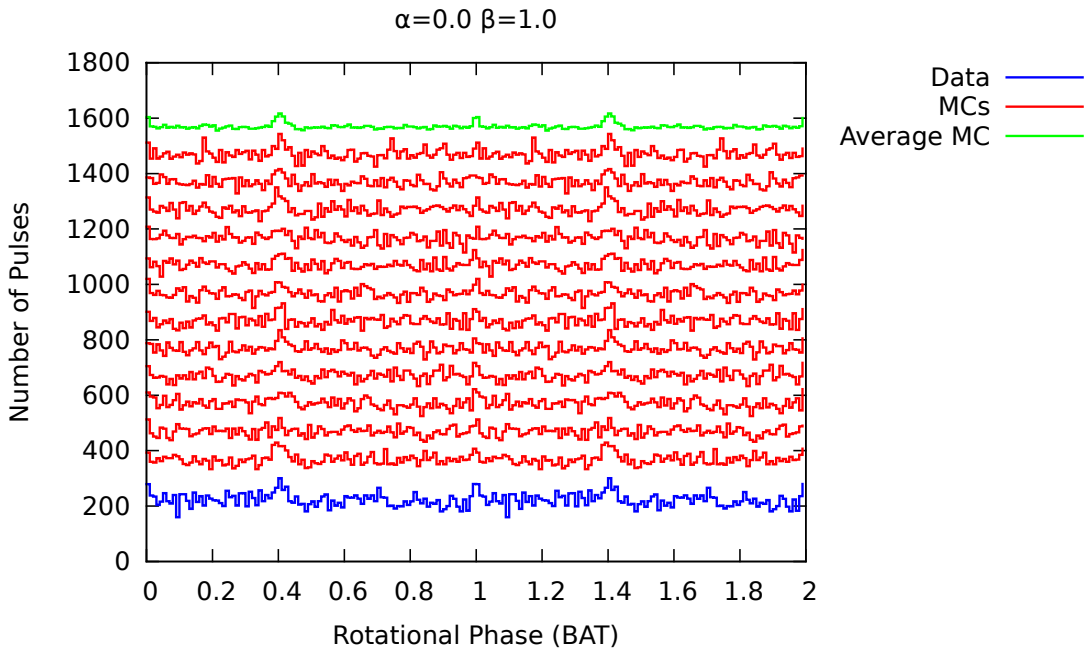

Figure 5.43.: Results of γ-ray MC simulations. The red curves represent the 12 MC simulations, the green curve is the average resulting from them and the blue curve is the sum of the corresponding γ-ray data sets. The P2 component is visible at the phase values around 0.4 and 1.4, while the P1 component is located around 1.0. All curves are shifted on the ordinate to make them easier discernible.

γ-ray Monte Carlo Simulations with injected Pulsar Signal

To examine the outcome of the correlation searches described in Chapter 5.3.4 if a perfect correlation between radio giant pulses and γ-photons would exist (perfect refers to the case when radio giant pulses are directly correlated with γ-photons without any time delay between both), the previously described γ MC simulations are modified. While the basic structure of the simulations stays the same (Chapter 5.3.2), an extension is applied to them in the form of an injection of a perfectly correlated radio signal from the Crab pulsar. To differentiate between different magnitudes of the injection, two new quantities are defined: The parameter α which describes the strength of an injected γ-ray pulsar signal which is perfectly correlated with radio photons and a further parameter named β that describes the strength of an uncorrelated γ-ray pulsar signal. Both parameters are dimensionless, their ratio representing the correlation coefficient.
To ensure a correct injection of simulated γ-photons, the respective MC simulations are only constructed for the time span in which the γ-ray data has an overlap with the radio data. The results shown in Figure 5.43 were constructed for α=0 and β=1, hence representing the case of no correlation between radio giant pulses and γ-photons. The idea behind this approach

is to examine how strong the correlation between radio giant pulses and γ-photons from the Crab pulsar needs to be in order to be detected with the available data sets. The respective correlation search results are shown in Chapter 5.3.4.
Coming back to the modified γ MC simulations, the decision which kind of γ-ray event is simulated, is carried out as described in Chapter 5.3.2, but extended by one further option, namely if the γ-event is correlated with a radio giant pulse, or not. For this purpose the ratio of the integral of the P1 Gaussian fit and the P1+P2 Gaussian fit is calculated. If the afterwards drawn random number is smaller than this ratio, a P1 γ-ray event is simulated. To correlate this event with a radio giant pulse, the latter is drawn out of the radio data and checked if it fits with its phase value to the P1 phase range of the Gaussian fit. In the other case, that is when the random number is larger than the named ratio, a P2 γ-ray event is simulated. Also in this case a radio giant pulse is drawn from the radio data and its phase value is checked if it matches the P2 phase range of the corresponding Gaussian fit. In both cases the drawing of radio giant pulses takes place as long as no a matching candidate is found. If the parameter α is set to zero, no drawing of correlated radio giant pulses takes place.
One result of this injection process is shown in Figure 5.44 for $\alpha = 0.4$ and $\beta = 0.6$, that is for 40 % of injected, perfectly correlated γ-photons and 60 % of uncorrelated γ-photons.

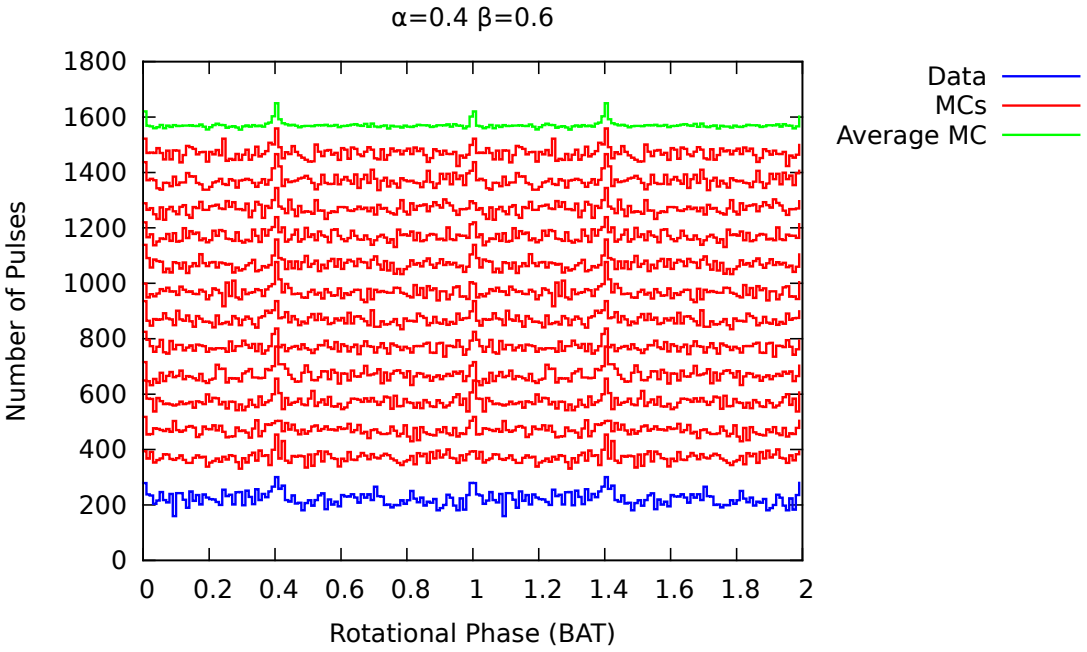

Figure 5.44.: Results of γ-ray MC simulations for. The notations are the same as in Figure 5.43. Analogous to Figure 5.43, all curves are shifted on the ordinate to make them easier discernible.

Comparing Figure 5.43 with Figure 5.44 results in easier discernible P1 and P2 emission components. This is due to the fact that through the injection more correlated γ-photons are located at the narrow radio phase ranges resulting in more prominent emission peaks. In both figures the P2 component is more pronounced than the P1 component. This is in accordance with the

available γ-ray data sets.
All simulations constructed for different values of α and β can be found in Chapter B.3. The reason for the construction of a variety of different γ MC simulations will be explained in detail in Chapter 5.3.4.

Determination of Time Differences – Radio MC vs. γ-ray Data

After the construction of the simulated radio data sets (Chapter 5.3.2), the differences of the arrival times between simulated radio giant pulses and γ-photons are determined. The respective cuts in the Hadronness and ϑ^2 parameters obtained for the Crab pulsar (as described in Chapter 5.2.6) are already included in the MAGIC γ-ray data sets at this point of the analysis. The differences between the 12 radio MC simulations and the γ-ray data from the same night are calculcated afterwards. For this purpose the MC simulations are added up per run for all nights and the statistics of these 12 sums are determined (average, variance and standard deviation). To focus on the search for a correlation, a threshold in the range of $\pm 10\,\mathrm{s}$ is included. It causes the writing out of time differences in time bins ranging from zero to $\pm 10\,\mathrm{s}$.
Several approaches for the search for a correlation were carried out with the time differences between radio and γ-ray photons. For the very first approach no distinction between the pulsed emission components is made in the γ-ray data sets. That is, no cuts in the barycentered rotational phase are included. The result of the corresponding differences is shown in Figure 5.45. It shows the average and the standard deviation of the sums per run of all differences per time bin. The interpretation of the upper figure is the following: The average peaks around a time difference of $0\,\mathrm{s}$ (red curve). To express the regions in which most of the time difference values can be expected, intervals of one standard deviation above and below the average are included into the figure. Based on simulated radio observations, the main point of this figure is to show the time difference values in which a correlation between radio giant pulses and γ-photons does not exist. To show this region in a better way, in the lower plot of Figure 5.45 the average value is set to zero and only the standard deviation is shown. Both plots will be used for comparison with the time differences of radio giant pulses and γ-photons as described in the next chapter.

Determination of Time Differences – Radio Data vs. γ-ray Data

The corresponding time differences between radio data and γ-ray data were calculated with the same procedure as with the radio MC simulations. The only difference in this case is that there is only one radio data set for each night (Table 5.1) and not 12 like in the case of the simulations.
Different sets of time differences are determined from the available data sets. That is, with no cut in the barycentered rotational phase of the γ-ray data, with P1+P2 phase cuts and with single P1 and P2 cuts. Figure 5.46 shows the result for the time differences without a phase cut in the γ-ray data.
The magenta curve in Figure 5.46 reflects the time differences between radio and γ-ray data from which the average of the corresponding time differences resulting from radio MC simulations and γ-ray data were subtracted. The curve shows several deflections towards negative and positive values on the ordinate around the values zero on the abscissa. For their further analysis, the number of time bins is increased. In both, Figure 5.45 and Figure 5.46 it was set to 256 time bins. To examine if the deflections of the magenta curve in Figure 5.46 are an artefact of poor

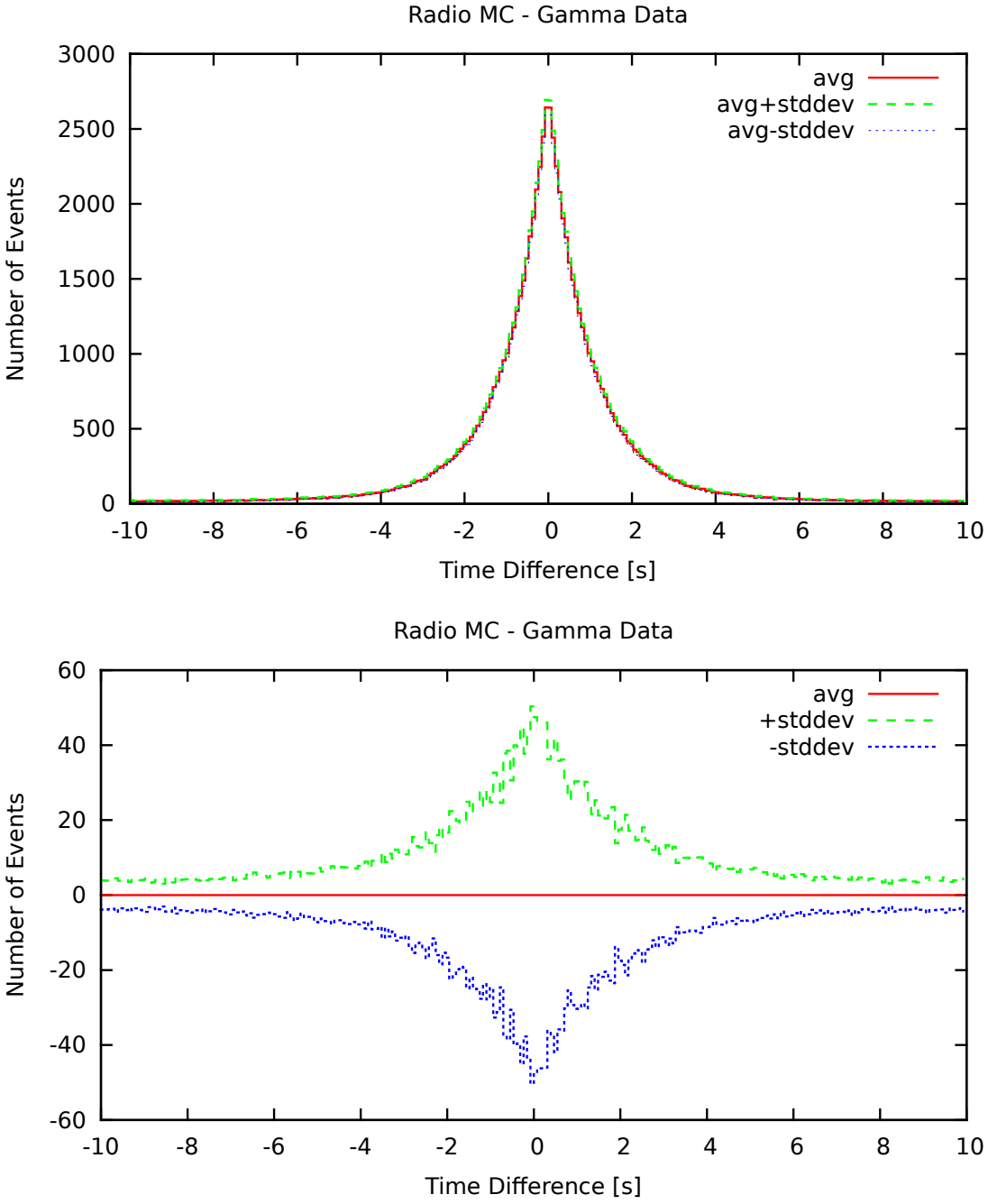

Figure 5.45.: Time differences of radio MC simulations and γ-ray for all nights with overlap in the range of $\pm 10\,\mathrm{s}$. The notations includes the average value (avg) and its standard deviation (stddev). Upper plot: Histogram of all averages per time bin together with standard deviation. Lower plot: The average is subtracted from each bin and the standard deviation is shown with both signs. The time binning is set to 256 bins in both plots.

statistics, or significant, the binning in Figure 5.46 is increased to 1024 time bins and divided in halfs constantly down to 64 time bins. Increasing the number of time bins means in other words to reduce the number of events in each time bin. A consequence of reducing the number of time bins is an increase of the number of events in each time bin. Therefore it provides a way to examine if the deflections of the time differences between the arrival times of radio giant pulses and γ-photons as seen in Figure 5.46, are statistically solid. The corresponding figure for a time binning of 128 and 64 is shown in Figure 5.47. The figures for all constructed time binnings can be found in Chapter C.1.

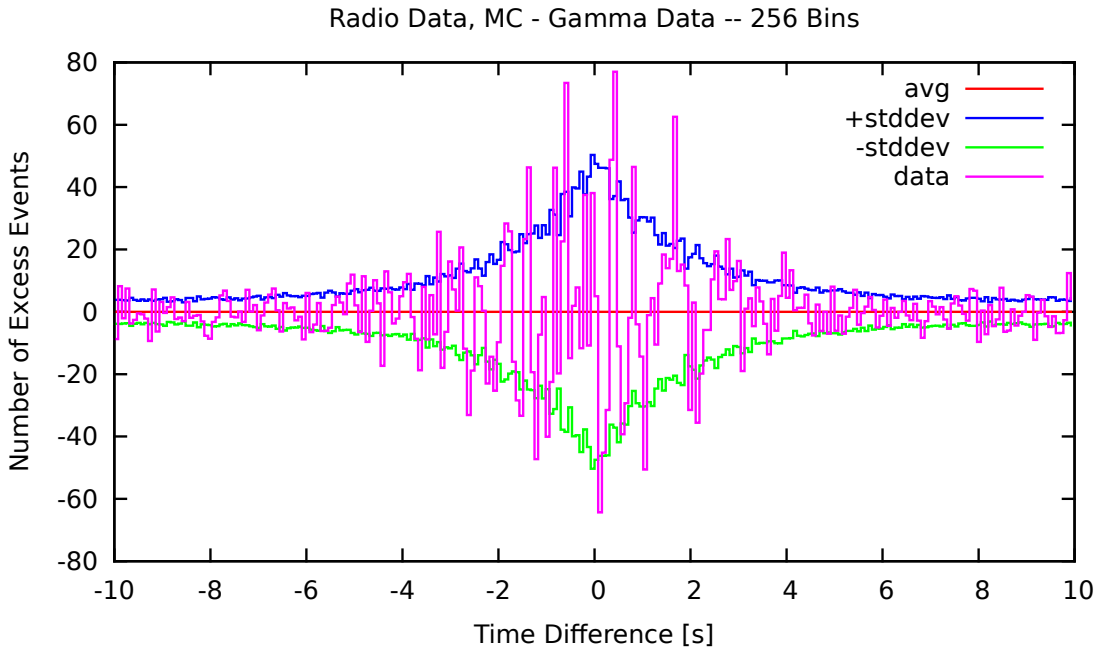

Figure 5.46.: Comparison of time differences: Radio MC simulations and γ-ray data (analogous to lower plot in Figure 5.45) and radio data and γ-ray data (magenta curve labelled "data") for all nights with overlap in the range of 10 s. The other notations are the same as in Figure 5.45. The time binning was set to 256 in this figure.

Comparing Figure 5.46 with Figure 5.47, indicates that the largest deviations towards positive ordinate values seen at about -1.5 s, -0.8 s, 0.2 s and 1.8 s in Figure 5.46 are in all cases apart from the last value rather caused by statistical fluctuations as they are not seen anymore in the lower figure of Figure 5.47, which contains only 64 time bins and provides thus more time differences values per bin. Only the deflection at about 1.8 s remains visible in the last figure, providing an interesting case. The deflections towards negative ordinate values as shown in Figure 5.46 are located at about -2.2 s, -1.5 s, 0.2 s, 1 s and 2.1 s. Apart from the ones located at about -1.5 s and 0.2 s, most of them are not that prominently visible in the corresponding figure with 64 time bins (Figure 5.47), leading to the conclusion of statistical fluctuations as source of their origin. Consequently, only a few of the described deflections are apparently not caused by statistical fluctuations (their significance will be discussed later in the text).

To elaborate if the observed deviations are caused by the Crab Nebula, or the Crab pulsar, the same bin reduction method is carried out for corresponding differences between the arrival times of radio giant pulses and γ-photons, the latter containing only pulsed emission components P1, P2 as well as P1+P2 (Chapter 5.3.2). That is, at this stage of the analysis cuts in the rotational phase are only included in the γ-ray data according to the results obtained by Aleksić et al. [2012]: P1 = [0.983 ; 0.026], P2 = [0.377 ; 0.422].
However, the corresponding time difference results in the case of the P1+P2 phase cut included in the γ-ray data, provide only poor statistics, as is shown in Figure 5.48. Due to this reason it cannot be concluded with the available data sets if the observed deviations as shown in Figure 5.47 are caused by the Crab pulsar. The corresponding time differences for separate P1 and P2 phase cuts in the γ-ray data can be found in Chapter C.1.
Coming back to the deviations seen in the lower part of Figure 5.47, their significance values are determined in the next step. The green curve in this figure represents the negative standard deviation of $1\,\sigma$ whereas the blue curve is the positive standard deviation of the same value (analogous to the upper figure in Figure 5.47 and Figure 5.46). Comparing the deflections towards negative ordinate values at $-1.5\,\mathrm{s}$, $0.2\,\mathrm{s}$ (Figure 5.47) with the green curve, results in an estimated significance of approximately $1.2\,\sigma$ and $1.5\,\sigma$. In the case of the deflection towards positive ordinate values at about $2.1\,\mathrm{s}$, a comparison with the blue curve leads to a estimated significance of about $2\,\sigma$. Consequently, all three deflections are not statistically significant.
The estimated significance values are rather naive significances. In order to determine their correct values, a statistical effect needs to be taken into account which will be explained in the following part of this chapter:
When multiple comparisons are done, like here in the case of a certain number of time bins, the Look-Elsewhere-Effect (LEE) needs to be included in the calculations. It is also known as the effect of multiple comparisons. The LEE is commonly used in particle physics and HE physics (see discussion in Gross and Vitells [2010]) and basically describes (in the context of this thesis) how to determine the probability to find a statistically significant signal if one is looking at many time bins. Here the number of time bins varies between 1024 and 64.
Under the assumption that the observed events follow a normal distribution, one of them (independently if it belongs to radio, or γ-ray observations) has a significance of z times σ. The integration of the normal distribution results in the Error function *Erf* (Abramowitz and Stegun [1965]). Consequently, the fraction of events outside the interval $[-z\sigma; z\sigma]$ has a significance α which can be determined via:

$$\alpha(z) = 1 - \mathrm{Erf}(\frac{z}{\sqrt{2}}) \tag{5.28}$$

Taking into account that the time bins are independent of each other (since one event is only contained in one time bin), the significance of each time bin needs to be determined via the

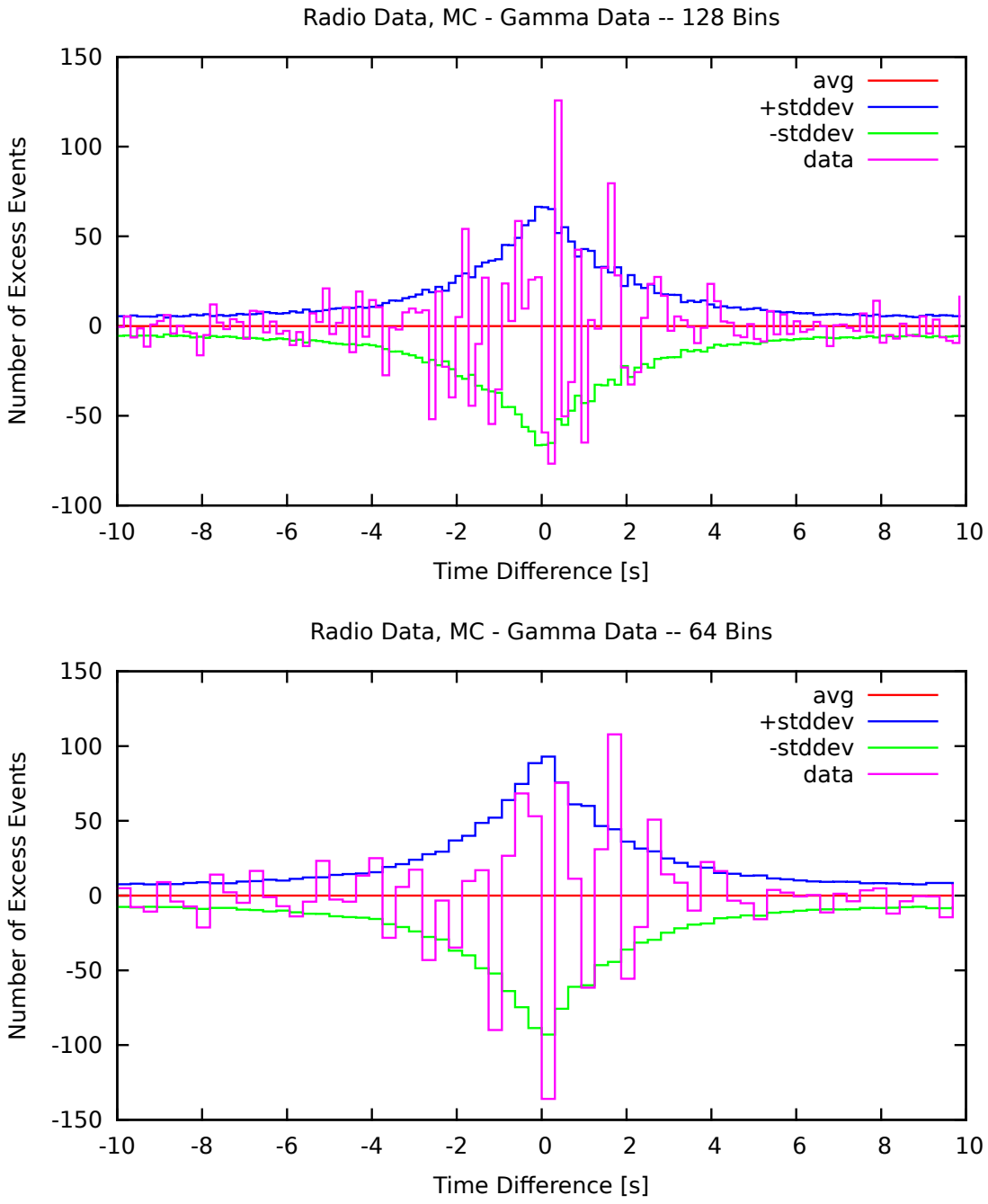

Figure 5.47.: Analogous depiction of the time differences between radio MC simulations + data and γ-ray data for all nights with overlap in the range of $\pm 10\,\mathrm{s}$. The other notations are the same as in Figure 5.45. The time binning was set to 128 in the upper and to 64 in the lower figure.

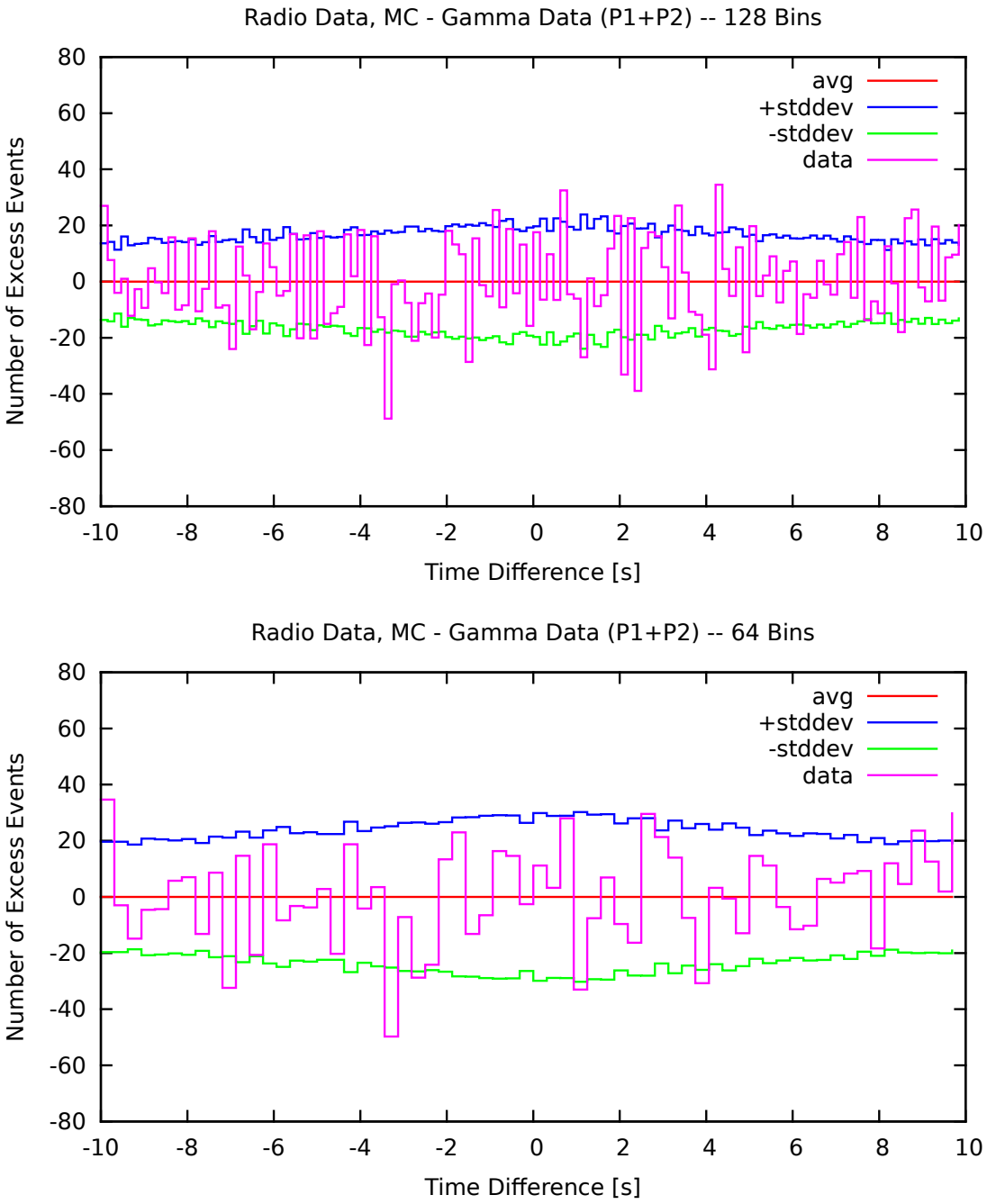

Figure 5.48.: Analogous depiction of the time differences between radio MC simulations + data and γ-ray data for all nights with overlap in the range of $\pm 10\,\mathrm{s}$. The other notations are the same as in Figure 5.45. The time binning was set to 128 in the upper and to 64 in the lower figure.

Dunn-Šidak correction (Šidák [1967]):

$$\alpha_{\mathrm{real}}(\mathrm{z}) = 1 - (1 - \alpha(\mathrm{z}))^{\mathrm{t}} \tag{5.29}$$

The quantitiy t is the number of time bins. Consequently, the real significance of the events inside the normal distribution is not z times σ, but z_{cor} times σ:

$$\mathrm{z}_{\mathrm{cor}}(\mathrm{z}, \mathrm{t}) = \sqrt{2} \cdot \mathrm{InverseErf}(\frac{\mathrm{z}}{\sqrt{2}})^{\mathrm{t}} \tag{5.30}$$

With Equation 5.30 the previously estimated significances for different time bins can be corrected. Figure 5.49 shows the corrected significance values for different time bins ranging from 1024 to 64. An immediate conclusion from this figure is that the corrected significance becomes higher than zero for a naive significance of a bit less than two for a time binning of 64. For higher time binnings the corrected signifance becomes higher than zero for later values of the naive signifance. Consequently, the statistical signifance of the time differences per bin is highest for the lowest number of time bins.

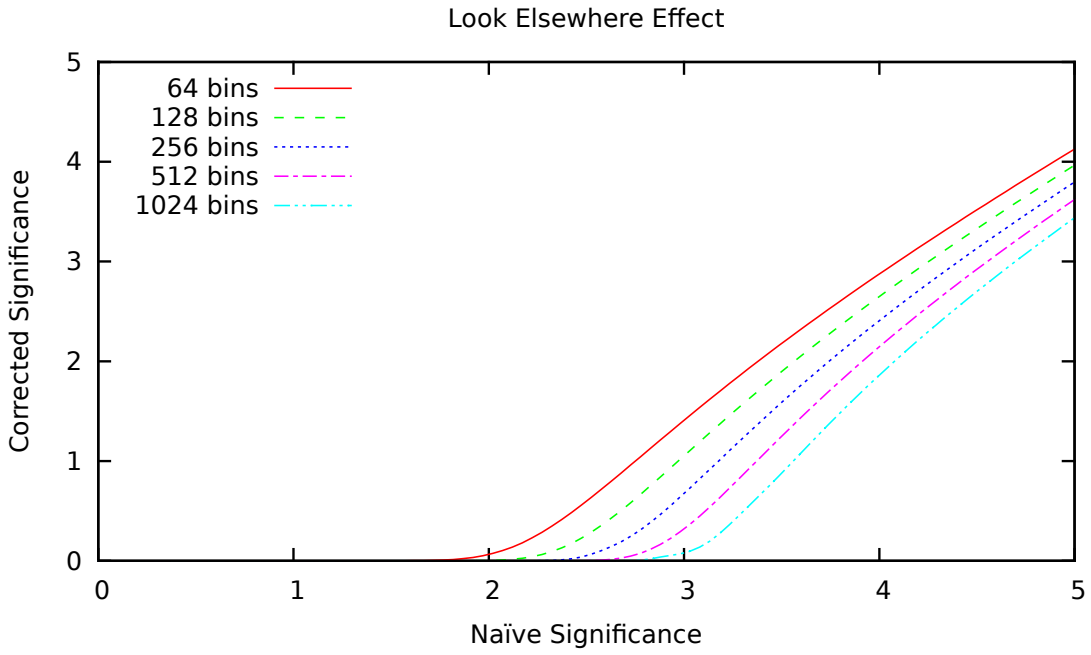

Figure 5.49.: Illustration of the significances corrected with the LEE.

Referring to the observed deflections in Figure 5.46 and Figure 5.47 this means that their estimated, or naive significances, are even lower when corrected for the LEE and therefore even less significant. A naive significance value of two, results in an LEE corrected value of 0.06 when taking the 64 time binning curve in Figure 5.49 into account. Figure 5.50 displays the same time differences as the magenta curve in Figure 5.47 for 64 time bins, but corrected for the LEE. The largest deflections can be seen at approximately $-8\,\mathrm{s}$ and $2\,\mathrm{s}$. The significances

of their excesses are at about $-0.6\,\sigma$ and $0.5\,\sigma$ providing lower values as originally estimated via the naive significance and in accordance with Figure 5.49.
Consequently, with the method described in this chapter and the available radio and γ-ray data sets, no statistically significant correlation between radio giant pulses and γ-photons can be verified.

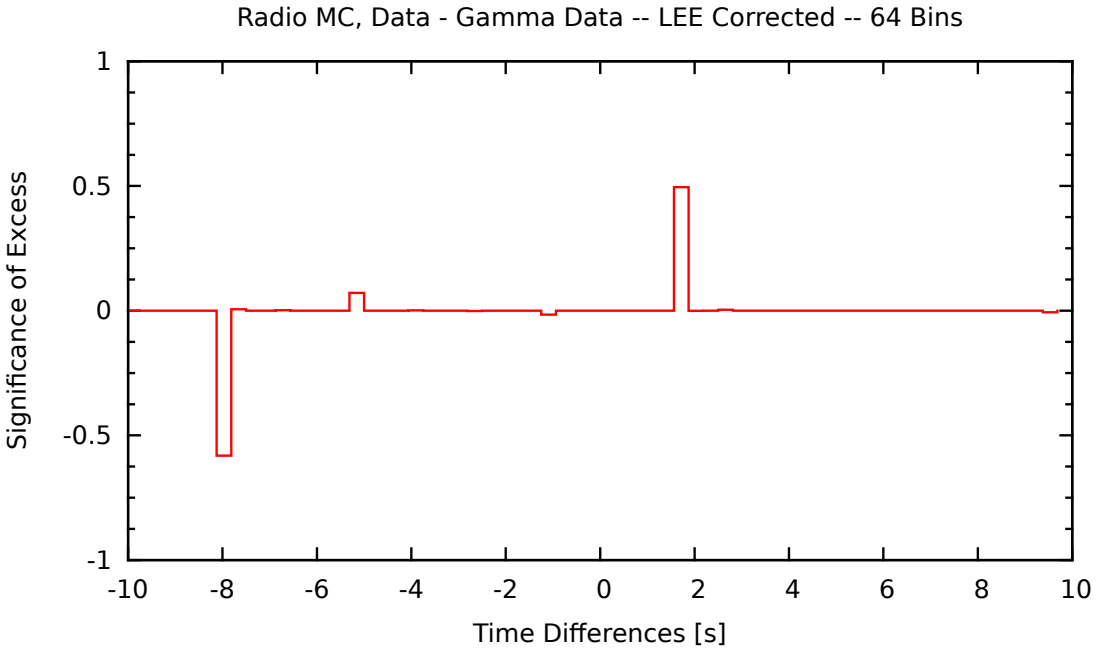

Figure 5.50.: Time differences as expressed in the lower figure of Figure 5.47 corrected for the LEE. As seen in this figure none of the detected deviations displays a statistically significant excess.

5.3.3. Pearson Correlation

In spite of previous obstacles to apply traditional correlation search methods as discussed at the beginning of Chapter 5.3.1, it is also tried to examine the Crab pulsar data used for this study with the Pearson correlation approach (see Chapter 4.2 in Wall and Jenkins [2012]). The goal of this part of the study is to test the following null hypothesis: The radio and γ-ray data sets are uncorrelated.
The Pearson correlation approach is made possible by putting the TOAs from the radio and γ-ray data in concurrent time bins of equal length. It is afterwards tried to determine by means of their TOAs if the number of radio and γ-ray events in these bins are correlated. The length of these bins corresponds to the distances between adjacent TOAs of radio, or γ-photons, that is the inverse rate of radio, or γ-photons. An overview of all average distances Δt determined from each single data set (radio and γ-ray) is shown in Table 5.11. The mean values are given in bold letters. While the average distances resulting from observations taken with the Effelsberg and the MAGIC telescopes are similar, the ones taken with the WSRT are surprisingly different. One reason for this lies in the many OFF pulse events which are prevalent in the WSRT data

even after the barycentering process (see overlap plots in Chapter A.17). This results in a higher count rate as shown by Table 5.11 and consequently, in smaller bin values (the WSRT data sets with the extracted P1 and P2 components are used for this part of the study analogous as for the construction of the corresponding MC simulations). Due to the resemblance of the average distances resulting from the observations taken with the Effelsberg and MAGIC telescopes, the mean value of both (2.34 s, Table 5.12) is used in the forthcoming analysis. Under the assumption that the events located at each of these distances do not depend on each other (which is the basic assumption here since the physics of radio giant pulses are not known), they can be approximated by a Poisson distribution:

$$\mathrm{P(X = k)} = \frac{\mu^{\mathrm{k}}}{\mathrm{k!}} \cdot \mathrm{e}^{-\mu} \tag{5.31}$$

Equation 5.31 describes the probability distribution of a random variable named X with μ being the expected value of X, e being Euler's number and k a number greater equal zero. In the figurative sense X represents the number of events (radio, or γ-ray alike) in an average distance Δt. Consequently, P(X=k) represents the probability to find k events in a time bin. Under this assumption and since it cannot be assumed that the determined average distance of 2.34 s is the ideal one for the correlation search, multiple other values of Δt are also considered, consisting of 4.68 s (Table 5.13), 7.02 s (Table 5.14) and 9.36 s (Table 5.15).
A general drawback of this way of constructing time bins with a specific length, is that some timing information gets lost during the construction of the described bins. Hence the full time resolution becomes unavailable with this approach.
As a first mathematical approach of the search for a correlation, it is investigated if the Crab pulsar radio and γ-ray data used in this thesis are linearly correlated. This is carried out with the Pearson correlation approach (Wall and Jenkins [2012]). If the two kinds of data sets used in this study are labelled as (x_i,y_i), then their Pearson correlation coefficient is determined as:

$$\mathrm{r} = \frac{\sum_{\mathrm{i=1}}^{\mathrm{n}} (\mathrm{x_i} - \bar{\mathrm{x}}) \cdot (\mathrm{y_i} - \bar{\mathrm{y}})}{\sqrt{\sum_{\mathrm{i=1}}^{\mathrm{n}} (\mathrm{x_i} - \bar{\mathrm{x}})^2 \cdot \sum_{\mathrm{i=1}}^{\mathrm{n}} (\mathrm{y_i} - \bar{\mathrm{y}})^2}} \tag{5.32}$$

In Equation 5.32 the quantity n stands for the number of bins from the corresponding data set. The quantities $\bar{x}$ and $\bar{y}$ correspond to the average values of x and y. The latter can be interpreted as counts from the radio data sets (x) and from the γ-ray data sets (y) contained in the constructed bins.
In other words, Equation 5.32 expresses the covariance of two quantities x and y. That is, how much these two quantities change together. A more general expression of the correlation coefficient is given by Equation 5.33:

$$\mathrm{r} = \frac{\mathrm{cov(x, y)}}{\sigma_{\mathrm{x}} \cdot \sigma_{\mathrm{x}}} \tag{5.33}$$

The quantity *cov(x,y)* is the covariance and σ_x as well as σ_x are the standard deviations of the quantities x and y.
The difference between Equation 5.32 and Equation 5.33 lies in the nature of the data they are applied at. While Equation 5.32 is applied on data samples, Equation 5.33 is used for population studies. Consequently, the further approach for the data presented in this study will make use of Equation 5.32.

To search for a linear relationship between the observed radio and γ-photons, the Pearson correlation coefficient (Equation 5.32) is determined for the Effelsberg radio data sets and the simultaneously taken γ-ray data sets, as well as for the WSRT radio data sets and the respective γ-ray data sets. Since both, the corresponding radio and γ-ray data set, contain gaps during the overlap (Chapter A.17), the procedure is carried out after the exclusion of these gaps. The results for several average distances (as discussed earlier in this chapter) are given in Table 5.12, Table 5.13, Table 5.14 and Table 5.15. They contain two quantities, the Pearson correlation coefficient r and a value p. The Pearson correlation coefficient r results in values ranging from -1 to 1. In this context -1 means fully anticorrelated, +1 fully correlated and 0 stands for no correlation. The quantity p is a probability value which ranges from 0 to 1 and describes how likely the apparent correlation is only found due to statistical fluctuations and not because it originates from the Crab pulsar. The smaller the p-value is, the stronger is the evidence for a real correlation, or a non-correlation (depending upon the value of r). To decide if the non-existence of a correlation can be ruled out or not (that is, if a value of r near zero is true), $1\,\sigma$ confidence intervals of the correlation coefficient are included in all corresponding tables. They provide information if the null hypothesis can be excluded, or not in the respective case. An interesting feature expressed in Table 5.12, Table 5.13, Table 5.14 and Table 5.15 is the change of the sign of the Pearson correlation coefficent r from being negative in the case of the correlation of Effelsberg radio data and MAGIC γ-ray data, to being positive in the case of WSRT radio data and MAGIC data (referring only to the total epochs in all named lists at the moment). A feature seen in the latter case comparing the results for all four average distances, is an increase of the Pearson correlation coefficient from 0.0119 to 0.073 with a decreasing probability 0.242 to 0.308 $\cdot 10^{-3}$ (with increasing average distance). Since the determined values of r are near zero (thus suggesting a non-correlation), the corresponding confidence intervals are examined. For all four average distances apart from 2.34 s, a value of zero is not included in the confidence intervals which speaks against the existence of no correlation. The determined correlation coefficient values suggest a statistically weak, or non-significant, correlation for WSRT data taken simultaneously with MAGIC data with increasing average distance. It needs to be noted at this point that although cuts in the rotational phase were introduced into the WSRT data sets in order to reduce the amount of noise (see discussion in Chapter 5.3.2), the resulting pulsed emission components contained in the data sets used for this part of the analysis (P1+P2) are still overlapped with a certain, quantitatively not determinable amount of noise. Therefore it cannot be ruled out that the observed development of the Pearson correlation coefficient might be caused by the leftovers of noise in the data. In the case of the WSRT data sets taken simultaneously with the MAGIC data sets the existence of a correlation cannot be verified with the available amount of data. Hence the null hypothesis cannot be refuted in the case of these data sets.
The corresponding values for the Effelsberg observations which were taken simulatenously with MAGIC, indicate in some sense an opposite behaviour: For all four average distances the Pearson correlation coefficient is negative and goes from -0.0175 to -0.036 (with increasing average distance) with a probability ranging from 0.0318 to 0.0275. In all four cases the value zero is not included in the corresponding confidence intervals objecting the possibility of the null hypothesis. The results rather suggest the existence of an anticorrelation, which becomes statistically more significant with increasing average distance. However, also in the case of these data sets a statistically significant anticorrelation cannot be verified.
The Pearson correlation coefficient for all radio and γ-ray data sets altogether (marked with "Eff/WSRT/MAGIC" in all tables) increases from -0.0029 to 0.0126 with increasing average

distance. Taking the corresponding confidence intervals of r into account, reveals that in all four cases the value zero is contained in them making the exclusion of the null hypothesis not possible. The respective probability values range from 0.649 till 0.321, that is becoming smaller with increasing average distance, but still statistically not significant. In summary no statistically significant correlation, or anticorrelation can be verified when all available data sets (with no limitations like through cuts in the rotational phase) are examined for a linear correlation. The validity of the null hypothesis cannot be excluded.
Apart from the total epochs expressed in Table 5.12, Table 5.13, Table 5.14 and Table 5.15, also the Pearson correlation coefficient and its probability for single night data sets are included (usually with non-bold letters unless the p-value is less than 0.05, indicating a statistically significant probability). One conspicuous property seen in all tables is the change of sign of r with changing average distances. To examine if these changes are correct, the Pearson correlation coefficient is determined for each simultaneously taken radio and γ-ray data set and the corresponding confidence intervals within the ranges of one standard deviation. It is commonly known that from the statistical point of view there are not enough events in the γ-ray data in a time span of two hours at maximum to find a correlation. Hence this method is mainly applied in order to track down the change of sign of r. Interestingly, in the cases of some average distances the correlation coefficients resulting from the data from single nights indicate probability values of less than 0.05. This is the case for the following data sets: 2012-12-07, 2012-12-10 (2.34 s distance), 2012-12-07, 2012-12-17, 2012-12-10 2013-01-10 (4.86 s distance), 2012-12-17, 2013-01-09, 2013-01-10 (7.02 s distance), 2012-12-17, 2013-01-10 (9.36 s distance). One further interesting feature visible in these data sets is that in the case of the Effelsberg data the sign of the corresponding Pearson correlation coefficient is in all named cases opposite to the one resulting from all Effelsberg data sets (marked with "Total" in all tables). This is not shown for WSRT single night data sets. However, the apparently random occurrence of these single nights for different average distances can point to statistical fluctuations as their origin.
The signs of the Pearson correlation coefficient for all single night data sets vary for different average distances seemingly at random. No definite structure behind the sign change can be made out. The corresponding confidence intervals nevertheless indicate the correct sign and value of the respective Pearson correlation coefficent.
To examine the results obtained so far from the Effelsberg and WSRT data further, in the next step cuts in the rotational phase are introduced (at first) in the γ-ray data and the Pearson correlation coefficient is calculated again for all four average distances for the corresponding data files (Table 5.16). For reasons of compactness and since in the previous calculations single nights with statistically significant Pearson correlation coefficients were occurring seemingly at random at different average distances, Table 5.16 summarizes only the results for all nights with an overlap between Effelsberg and MAGIC, WSRT and MAGIC and all radio observations taken simultaneously with MAGIC. An interesting feature expressed by Table 5.16 is that the Pearson correlation coefficient for MAGIC data with a P1 phase cut is negative in the case of the Effelsberg radio data overlapping with MAGIC data and for all available data sets (the latter marked with "Eff/WSRT/MAGIC"). A review of the respective confidence intervals shows that for all average distances apart from 2.34 s and 4.86 s the value of zero is not included, stating that the null hypothesis can only be excluded partly for these data sets (that is, for 7.02 s and 9.36 s). With one exception (a distance of 2.34 s) this is not the case for the WSRT data overlapping with the MAGIC data. In the latter case the results for all average distances rather imply the non-existence of a correlation, albeit the corresponding Pearson correlation

coefficients are statistically not significant. Besides no statistical significance is expressed by the probability values for the Effelsberg data sets overlapping with MAGIC data. Only the Pearson correlation coefficients obtained for all radio and γ-ray data sets with a P1 phase cut have statistically significant probabilities below 0.05. Interestingly, the Pearson coefficient decreases with increasing average distance like the respective probability value (the only exception is shown for a distance of 4.68 s). Examining the corresponding confidence intervals of the correlation coefficient reveal that for all overlapping data sets ("Eff/WSRT/MAGIC") with a P1 phase cut in the MAGIC data, the value of zero is not contained in them emphasising the non-validity of the null hypothesis in their case. In other words, a non-correlation between all three data sets can be refuted. This result suggests the existence of an anticorrelation between radio giant pulses and γ-photons from the Main pulse component P1 from the Crab pulsar. No similar results are expressed in Table 5.16 for the Interpulse component (P2) from the Crab pulsar. To examine further if the results obtained for the P1 component are caused by statistical fluctuations, or if they could be intrinsic, in the next analysis step cuts in the rotational phase in the radio data sets are introduced. At this point the question might arise why cuts in the rotational phase were so far only carried out for the γ-ray data. The reason is the higher background emission in comparison with the radio observations of the Crab pulsar. A limitation of the phase ranges reduces the background emission and if a correlation, or anticorrelation caused by the Crab pulsar can be verified in the present case, the named limitation should reveal it.
The cuts in the barycentered rotational phase applied to the radio data sets result from the Gaussian fitting procedure (Chapter 5.3.2). They are not taken from the work of Aleksić et al. [2012] as it was done for the γ-ray data. It needs to be noted again at this point that cuts in the rotational phase were already included in the WSRT data sets due to the higher level of noise in the data (see Chapter 5.3.2). Hence in the following part of the analysis only the P1 and P2 components from the Effelsberg radio data are extracted. The Pearson correlation coefficient is afterwards calculated again between the radio and γ-ray Crab pulsar data (Table 5.17). The coefficient resulting from radio and γ-ray data containing the P1 component is (similar as in Table 5.16) negative for all Effelsberg radio data sets (marked with "Eff/MAGIC" in Table 5.17), although not significant for all four average time distances. Examining the corresponding confidence intervals reveals that for average distances of 2.34 s and 4.68 s the value of zero is included, but not for the remaining average distances (7.02 s and 9.36 s) which is consistent with the corresponding results from Table 5.16. The correlation coefficent resulting from γ-ray and radio data containing only the P2 component is near zero (suggesting no correlation) with non significant probability values. This is similar with the corresponding result from Table 5.16. The data sets which contain both emission components (P1+P2) display negative correlation coefficients, but also in this case they are statistically not significant. The negative sign of the correlation coefficient is apparently caused by the contained P1 component. In both cases (P2 component only and P1+P2 components) the corresponding confidence intervals contain the value zero which emphasises that the null hypothesis cannot be excluded. Consequently, on the basis of the Effelsberg radio data overlapping with the γ-ray data only, no correlation between both can be verified even with specified rotational phase values from the Crab pulsar.
In the case of WSRT radio data taken simultaneously with MAGIC (marked with "WSRT/MAGIC" in Table 5.17), the Pearson correlation coefficient for the data sets which contain only the P1 emission component is positive except for an average distance of 2.34 s. This is in accordance with the previous results expressed in Table 5.16. The correlation coef-

ficients for all four average distances are near zero, but the respective probability values are statistically not significant, providing effectively no proof, or refutation of a correlation. A similar behaviour is shown for the WSRT and γ-ray which contain the P2 emission component. The corresponding correlation coefficient is near zero with probability values above a value of 0.05. The results for the data sets containing both emission components P1+P2 consist of correlation coefficients which are also near zero, but the respective probabilites are in this case not below 0.05 either. Hence also in the case of the WSRT data sets taken simultaneously with γ-ray data no correlation between both can be verified due to a lack of sufficient statistics.
The corresponding results for the total overlap between all radio and γ-ray data sets (expressed by "Eff/WSRT/MAGIC" in Table 5.17) are more similar to the previous results when phase cuts were only included in the γ-ray data sets (Table 5.16). The correlation coefficients for data sets containing only the P1 emission component are negative for all four different average distances. They become smaller with increasing average distances. The corresponding probability values are below 0.05, but show otherwise no tendency of increase, or decrease. These results are similar to the respective ones shown in Table 5.16. The inclusion of additional phase cuts in the radio data leads to smaller probability values increasing the statistically significance of the determined correlation coefficients. The corresponding confidence intervals of the Pearson correlation coefficient do not contain the value zero, emphasising the non-validity of the null hypothesis in this case. This is consistent with the corresponding results expressed by Table 5.16. In the case of both respective data sets (meaning in Table 5.16 and Table 5.17), a weak anticorrelation between the radio and γ-ray data sets containing only the P1 emission component is suggested.
No similar results have been obtained for the data sets which contain only the P2 emission component, or both. The correlation coefficients are positive in the first case, but statistically not significant. The correlation coefficients resulting from the data sets with P1+P2 phase cuts are negative, but are not statistically significant either. These results suggest that with the present data sets a statistically significant correlation between radio giant pulses and γ-photons cannot be verified, although the null hypothesis can be refuted partly for the P1 data and for all average distances in the case of the P1+P2 data.

Consequently, in most cases no linear correlation can be verified with the available data sets (as discussed the null hypothesis cannot be excluded in their case). Taking a more throrough look at all confidence intervals, results in the observation that the changes of sign of the corresponding Pearson correlation coefficients are not surprising if the value zero is included in the corresponding confidence intervals.
Conspicuous are the results obtained for all data sets containing phase cuts from the P1 emission component in this part of the analysis. Suggested at first by the results obtained for γ-ray data sets with phase cuts (Table 5.16), they have been confirmed by the results received from radio as well as γ-ray data sets with phase cuts (Table 5.17). These results suggest that the observed anticorrelation between radio giant pulses and γ-ray photons from the P1 emission component might be intrinsic. However, as already mentioned the suggested anticorrelation is rather weak. For a solid verification of its veracity more simultaneously taken radio and γ-ray data would be needed.

Epoch	Facility	Average Count Rate [counts/s]	dt [s]
2012-12-07	Eff	0.264	3.78
2012-12-17	Eff	0.420	2.38
2013-01-09	Eff	0.601	1.66
2013-01-12	Eff	0.650	1.54
2013-01-31	Eff	0.320	3.12
2013-02-06	Eff	0.630	1.59
2013-02-07	Eff	0.159	6.28
2013-02-08	Eff	0.624	1.60
2013-02-09	Eff	0.542	1.85
2013-02-10	Eff	0.388	2.58
Average	**Eff**	**0.443**	**2.26**
2012-12-10	WSRT	2.150	0.47
2013-01-08	WSRT	3.858	0.26
2013-01-10	WSRT	3.405	0.29
2013-02-02	WSRT	2.168	0.46
2013-02-03	WSRT	2.564	0.39
Average	**WSRT**	**2.646**	**0.38**
2012-12-07	MAGIC	0.248	4.03
2012-12-10	MAGIC	0.277	3.61
2012-12-17	MAGIC	0.350	2.86
2013-01-08	MAGIC	0.437	2.29
2013-01-09	MAGIC	0.353	2.84
2013-01-10	MAGIC	0.355	2.82
2013-01-12	MAGIC	0.350	2.86
2013-01-31	MAGIC	0.575	1.74
2013-02-02	MAGIC	0.604	1.66
2013-02-03	MAGIC	0.606	1.65
2013-02-06	MAGIC	0.309	3.23
2013-02-07	MAGIC	0.493	2.03
2013-02-08	MAGIC	0.458	2.19
2013-02-09	MAGIC	0.398	2.52
2013-02-10	MAGIC	0.455	2.20
Average	**MAGIC**	**0.414**	**2.42**

Table 5.11.: Counting rates and their reciprocal values for each observation used in this study. The time gaps in the single data sets were not taken into consideration during the calculation of the counting rate.

Epoch	Facility	r	p	[r - 1σ ; r + 1σ]
2012-12-07	**Eff/MAGIC**	**0.082**	**0.00315**	**[0.043; 0.121]**
2012-12-17	Eff/MAGIC	0.0222	0.274	[-0.0065; 0.0508]
2013-01-09	Eff/MAGIC	0.012	0.592	[-0.020; 0.045]
2013-01-12	Eff/MAGIC	-0.014	0.515	[-0.045; 0.016]
2013-01-31	Eff/MAGIC	-0.017	0.572	[-0.061; 0.026]
2013-02-06	Eff/MAGIC	-0.056	0.552	[-0.189; 0.078]
2013-02-07	Eff/MAGIC	-0.0276	0.258	[-0.0620; 0.0069]
2013-02-08	Eff/MAGIC	0.072	0.395	[-0.047; 0.189]
2013-02-09	Eff/MAGIC	-0.011	0.612	[-0.041; 0.019]
2013-02-10	Eff/MAGIC	0.001	0.979	[-0.031; 0.032]
Total	**Eff/MAGIC**	**-0.0175**	**0.0318**	**[-0.0291; -0.0060]**
2012-12-10	**WSRT/MAGIC**	**-0.046**	**0.0114**	**[-0.072; -0.020]**
2013-01-08	WSRT/MAGIC	0.041	0.365	[-0.023; 0.104]
2013-01-10	WSRT/MAGIC	0.0283	0.176	[-0.0013; 0.0578]
2013-02-02	WSRT/MAGIC	-0.002	0.929	[-0.041; 0.036]
2013-02-03	WSRT/MAGIC	0.001	0.98	[-0.027; 0.028]
Total	**WSRT/MAGIC**	**0.0119**	**0.242**	**[-0.0025; 0.0263]**
Total	**Eff/WSRT/MAGIC**	**-0.0029**	**0.649**	**[-0.0119; 0.0061]**

Table 5.12.: Pearson Correlation Coefficient determined for all overlapping radio and γ-ray data sets. The values expressed with bold letters refer to all simulatenously taken Effelsberg and MAGIC observations, WSRT and MAGIC observations and all radio observations (Effelsberg and WSRT) taken simulatenously with MAGIC. No cuts in the rotational phase have been applied on the data sets. The average distance was set to 2.34 s.

Epoch	Facility	r	p	[r - 1σ ; r + 1σ]
2012-12-07	**Eff/MAGIC**	**0.095**	**0.0148**	**[0.040; 0.150]**
2012-12-17	**Eff/MAGIC**	**0.058**	**0.0422**	**[0.018; 0.098]**
2013-01-09	Eff/MAGIC	0.023	0.487	[-0.023; 0.069]
2013-01-12	Eff/MAGIC	0.018	0.554	[-0.025; 0.061]
2013-01-31	Eff/MAGIC	-0.024	0.59	[-0.085; 0.038]
2013-02-06	Eff/MAGIC	-0.113	0.402	[-0.296; 0.078]
2013-02-07	Eff/MAGIC	-0.0458	0.184	[-0.0943; 0.0030]
2013-02-08	Eff/MAGIC	0.079	0.51	[-0.090; 0.244]
2013-02-09	Eff/MAGIC	0.023	0.441	[-0.019; 0.065]
2013-02-10	Eff/MAGIC	-0.018	0.56	[-0.063; 0.026]
Total	**Eff/MAGIC**	**-0.0224**	**0.0524**	**[-0.0387; -0.0061]**
2012-12-10	**WSRT/MAGIC**	**-0.053**	**0.04**	**[-0.090; -0.017]**
2013-01-08	WSRT/MAGIC	0.065	0.303	[-0.025; 0.154]
2013-01-10	**WSRT/MAGIC**	**0.079**	**0.00754**	**[0.037; 0.120]**
2013-02-02	WSRT/MAGIC	0.0496	0.198	[-0.0049; 0.1038]
2013-02-03	WSRT/MAGIC	0.010	0.708	[-0.029; 0.050]
Total	**WSRT/MAGIC**	**0.038**	**0.00833**	**[0.018; 0.058]**
Total	**Eff/WSRT/MAGIC**	**0.0039**	**0.661**	**[-0.0088; 0.0167]**

Table 5.13.: Pearson Correlation Coefficient determined for all overlapping radio and γ-ray data sets. The values expressed with bold letters refer to all simulatenously taken Effelsberg and MAGIC observations, WSRT and MAGIC observations and all radio observations (Effelsberg and WSRT) taken simulatenously with MAGIC. No cuts in the rotational phase have been applied on the data sets. The average distance was set to 4.86 s.

Epoch	Facility	r	p	[r - 1σ ; r + 1σ]
2012-12-07	Eff/MAGIC	0.041	0.387	[-0.026; 0.109]
2012-12-17	**Eff/MAGIC**	**0.069**	**0.0482**	**[0.020; 0.118]**
2013-01-09	**Eff/MAGIC**	**0.093**	**0.0194**	**[0.037; 0.148]**
2013-01-12	Eff/MAGIC	0.030	0.425	[-0.023; 0.082]
2013-01-31	Eff/MAGIC	-0.002	0.968	[-0.078; 0.073]
2013-02-06	Eff/MAGIC	-0.07	0.672	[-0.30; 0.16]
2013-02-07	Eff/MAGIC	-0.032	0.453	[-0.091; 0.028]
2013-02-08	Eff/MAGIC	-0.04	0.792	[-0.24; 0.17]
2013-02-09	Eff/MAGIC	0.0486	0.184	[-0.0031; 0.0999]
2013-02-10	Eff/MAGIC	-0.012	0.765	[-0.066; 0.043]
Total	**Eff/MAGIC**	**-0.0228**	**0.105**	**[-0.0427; -0.0029]**
2012-12-10	WSRT/MAGIC	-0.0541	0.088	[-0.0987; -0.0093]
2013-01-08	WSRT/MAGIC	0.135	0.084	[0.025; 0.241]
2013-01-10	**WSRT/MAGIC**	**0.104**	**0.00381**	**[0.053; 0.154]**
2013-02-02	WSRT/MAGIC	-0.033	0.483	[-0.100; 0.034]
2013-02-03	WSRT/MAGIC	0.0506	0.139	[0.0022; 0.0987]
Total	**WSRT/MAGIC**	**0.047**	**0.00734**	**[0.022; 0.072]**
Total	**Eff/WSRT/MAGIC**	**0.0073**	**0.504**	**[-0.0082; 0.0229]**

Table 5.14.: Pearson Correlation Coefficient determined for all overlapping radio and γ-ray data sets. The values expressed with bold letters refer to all simulatenously taken Effelsberg and MAGIC observations, WSRT and MAGIC observations and all radio observations (Effelsberg and WSRT) taken simulatenously with MAGIC. No cuts in the rotational phase have been applied on the data sets. The average distance was set to 7.02 s.

Epoch	Facility	r	p	[r - 1σ ; r + 1σ]
2012-12-07	Eff/MAGIC	0.095	0.0852	[0.017; 0.172]
2012-12-17	**Eff/MAGIC**	**0.100**	**0.0131**	**[0.043; 0.156]**
2013-01-09	Eff/MAGIC	0.0682	0.136	[0.0035; 0.1323]
2013-01-12	Eff/MAGIC	0.025	0.557	[-0.035; 0.086]
2013-01-31	Eff/MAGIC	-0.025	0.683	[-0.112; 0.062]
2013-02-06	Eff/MAGIC	-0.16	0.394	[-0.41; 0.11]
2013-02-07	Eff/MAGIC	-0.041	0.398	[-0.110; 0.028]
2013-02-08	Eff/MAGIC	0.08	0.651	[-0.16; 0.31]
2013-02-09	Eff/MAGIC	0.035	0.411	[-0.025; 0.094]
2013-02-10	Eff/MAGIC	-0.013	0.769	[-0.076; 0.050]
Total	**Eff/MAGIC**	**-0.036**	**0.0275**	**[-0.059; -0.013]**
2012-12-10	WSRT/MAGIC	-0.020	0.577	[-0.072; 0.031]
2013-01-08	WSRT/MAGIC	0.1211	0.179	[-0.0063; 0.2446]
2013-01-10	**WSRT/MAGIC**	**0.17**	$\mathbf{0.249 \cdot 10^{-4}}$	**[0.12; 0.23]**
2013-02-02	WSRT/MAGIC	0.0746	0.171	[-0.0024; 0.1507]
2013-02-03	WSRT/MAGIC	0.013	0.751	[-0.043; 0.068]
Total	**WSRT/MAGIC**	**0.073**	$\mathbf{0.308 \cdot 10^{-3}}$	**[0.044; 0.102]**
Total	**Eff/WSRT/MAGIC**	**0.0126**	**0.321**	**[-0.0053; 0.0305]**

Table 5.15.: Pearson Correlation Coefficient determined for all overlapping radio and γ-ray data sets. The values expressed with bold letters refer to all simulatenously taken Effelsberg and MAGIC observations, WSRT and MAGIC observations and all radio observations (Effelsberg and WSRT) taken simulatenously with MAGIC. No cuts in the rotational phase have been applied on the data sets. The average time distance was set to 9.36 s.

Epoch	Facility	dt [s]	Phase Cut$_\gamma$	r	p	[r - 1σ ; r + 1σ]
Total	Eff/MAGIC	2.34	P1	-0.0066	0.422	[-0.0181; 0.0050]
Total	Eff/MAGIC	2.34	P2	0.000	0.98	[-0.012; 0.011]
Total	Eff/MAGIC	2.34	P1+P2	-0.0047	0.565	[-0.0163; 0.0069]
Total	Eff/MAGIC	4.68	P1	-0.0116	0.315	[-0.0279; 0.0047]
Total	Eff/MAGIC	4.68	P2	0.0075	0.514	[-0.0088; 0.0238]
Total	Eff/MAGIC	4.68	P1+P2	-0.003	0.809	[-0.019; 0.014]
Total	Eff/MAGIC	7.02	P1	-0.0216	0.125	[-0.0415; -0.0017]
Total	Eff/MAGIC	7.02	P2	0.0139	0.325	[-0.0060; 0.0338]
Total	Eff/MAGIC	7.02	P1+P2	-0.005	0.713	[-0.025; 0.015]
Total	Eff/MAGIC	9.36	P1	-0.0283	0.0815	[-0.0513; -0.0053]
Total	Eff/MAGIC	9.36	P2	0.012	0.459	[-0.011; 0.035]
Total	Eff/MAGIC	9.36	P1+P2	-0.011	0.499	[-0.034; 0.012]
Total	WSRT/MAGIC	2.34	P1	-0.001	0.926	[-0.015; 0.013]
Total	WSRT/MAGIC	2.34	P2	0.0129	0.204	[-0.0015; 0.0273]
Total	WSRT/MAGIC	2.34	P1+P2	0.0088	0.385	[-0.0055; 0.0232]
Total	WSRT/MAGIC	4.68	P1	0.008	0.599	[-0.013; 0.028]
Total	WSRT/MAGIC	4.68	P2	0.0232	0.106	[0.0029; 0.0435]
Total	WSRT/MAGIC	4.68	P1+P2	0.0222	0.123	[0.0018; 0.0425]
Total	WSRT/MAGIC	7.02	P1	0.006	0.721	[-0.019; 0.031]
Total	WSRT/MAGIC	7.02	P2	0.0204	0.245	[-0.0044; 0.0453]
Total	WSRT/MAGIC	7.02	P1+P2	0.0193	0.272	[-0.0056; 0.0441]
Total	WSRT/MAGIC	9.36	P1	0.005	0.822	[-0.024; 0.033]
Total	WSRT/MAGIC	9.36	P2	0.0273	0.178	[-0.0014; 0.0559]
Total	WSRT/MAGIC	9.36	P1+P2	0.0228	0.26	[-0.0058; 0.0515]
Total	Eff/WSRT/MAGIC	2.34	P1	-0.0142	0.026	[-0.0232; -0.0052]
Total	Eff/WSRT/MAGIC	2.34	P2	0.0040	0.535	[-0.0051; 0.0130]
Total	Eff/WSRT/MAGIC	2.34	P1+P2	-0.0070	0.271	[-0.0160; 0.0020]
Total	Eff/WSRT/MAGIC	4.68	P1	-0.0185	0.0394	[-0.0312; -0.0058]
Total	Eff/WSRT/MAGIC	4.68	P2	0.0077	0.39	[-0.0050; 0.0205]
Total	Eff/WSRT/MAGIC	4.68	P1+P2	-0.0072	0.421	[-0.0200; 0.0055]
Total	Eff/WSRT/MAGIC	7.02	P1	-0.0244	0.0262	[-0.0400; -0.0089]
Total	Eff/WSRT/MAGIC	7.02	P2	0.0075	0.497	[-0.0081; 0.0230]
Total	Eff/WSRT/MAGIC	7.02	P1+P2	-0.0115	0.296	[-0.0270; 0.0041]
Total	Eff/WSRT/MAGIC	9.36	P1	-0.029	0.0204	[-0.047; -0.011]
Total	Eff/WSRT/MAGIC	9.36	P2	0.0087	0.494	[-0.0093; 0.0266]
Total	Eff/WSRT/MAGIC	9.36	P1+P2	-0.0140	0.271	[-0.0319; 0.0040]

Table 5.16.: Pearson Correlation Coefficient - Phase cuts only included in γ-ray data (taken from Aleksić et al. [2012]).

Epoch	Facility	dt [s]	Phase Cut$_{\gamma,r}$	r	p	[r - 1σ ; r + 1σ]
Total	Eff/MAGIC	2.34	P1	-0.0074	0.368	[-0.0189; 0.0042]
Total	Eff/MAGIC	2.34	P2	0.0028	0.736	[-0.0088; 0.0143]
Total	Eff/MAGIC	2.34	P1+P2	-0.0038	0.644	[-0.0153; 0.0078]
Total	Eff/MAGIC	4.68	P1	-0.0112	0.333	[-0.0275; 0.0052]
Total	Eff/MAGIC	4.68	P2	0.0068	0.559	[-0.0096; 0.0231]
Total	Eff/MAGIC	4.68	P1+P2	0.001	0.937	[-0.015; 0.017]
Total	Eff/MAGIC	7.02	P1	-0.02053	0.145	[-0.04045; -0.00059]
Total	Eff/MAGIC	7.02	P2	0.000	0.999	[-0.020; 0.020]
Total	Eff/MAGIC	7.02	P1+P2	-0.003	0.818	[-0.023; 0.017]
Total	Eff/MAGIC	9.36	P1	-0.0253	0.119	[-0.0483; -0.0023]
Total	Eff/MAGIC	9.36	P2	0.006	0.694	[-0.017; 0.030]
Total	Eff/MAGIC	9.36	P1+P2	-0.007	0.649	[-0.030; 0.016]
Total	WSRT/MAGIC	2.34	P1	-0.004	0.68	[-0.019; 0.010]
Total	WSRT/MAGIC	2.34	P2	0.003	0.785	[-0.012; 0.017]
Total	WSRT/MAGIC	2.34	P1+P2	0.0088	0.385	[-0.0055; 0.0232]
Total	WSRT/MAGIC	4.68	P1	0.005	0.733	[-0.015; 0.025]
Total	WSRT/MAGIC	4.68	P2	0.005	0.709	[-0.015; 0.026]
Total	WSRT/MAGIC	4.68	P1+P2	0.0222	0.123	[0.0018; 0.0425]
Total	WSRT/MAGIC	7.02	P1	0.001	0.948	[-0.024; 0.026]
Total	WSRT/MAGIC	7.02	P2	0.006	0.725	[-0.019; 0.031]
Total	WSRT/MAGIC	7.02	P1+P2	0.0193	0.272	[-0.0056; 0.0441]
Total	WSRT/MAGIC	9.36	P1	0.002	0.933	[-0.027; 0.030]
Total	WSRT/MAGIC	9.36	P2	0.012	0.546	[-0.016; 0.041]
Total	WSRT/MAGIC	9.36	P1+P2	0.0228	0.26	[-0.0058; 0.0515]
Total	Eff/WSRT/MAGIC	2.34	P1	-0.0152	0.0167	[-0.0243; -0.0062]
Total	Eff/WSRT/MAGIC	2.34	P2	0.0014	0.832	[-0.0077; 0.0104]
Total	Eff/WSRT/MAGIC	2.34	P1+P2	-0.0068	0.284	[-0.0158; 0.0022]
Total	Eff/WSRT/MAGIC	4.68	P1	-0.0192	0.0325	[-0.0320; -0.0065]
Total	Eff/WSRT/MAGIC	4.68	P2	0.003	0.779	[-0.010; 0.015]
Total	Eff/WSRT/MAGIC	4.68	P1+P2	-0.0066	0.46	[-0.0194; 0.0061]
Total	Eff/WSRT/MAGIC	7.02	P1	-0.026	0.0176	[-0.042; -0.011]
Total	Eff/WSRT/MAGIC	7.02	P2	0.001	0.895	[-0.014; 0.017]
Total	Eff/WSRT/MAGIC	7.02	P1+P2	-0.0112	0.308	[-0.0268; 0.0043]
Total	Eff/WSRT/MAGIC	9.36	P1	-0.030	0.0163	[-0.048; -0.013]
Total	Eff/WSRT/MAGIC	9.36	P2	0.004	0.739	[-0.014; 0.022]
Total	Eff/WSRT/MAGIC	9.36	P1+P2	-0.0135	0.288	[-0.0314; 0.0045]

Table 5.17.: Pearson Correlation Coefficient - Phase cuts are included in the γ-ray data (taken from Aleksić et al. [2012]) and radio data (taken from the corresponding Gaussian fits, see Chapter 5.3.2).

5.3.4. Flux Enhancements

The predominant problem with the search for a correlation lies in the unknown physics of the radio giant pulse phenomenon and the resulting unknown existence of a correlation between radio giant pulses and γ-photons. To include a variety of different approaches for the search for a correlation, in this part of the analysis the flux of the γ-ray data is examined around occurring radio giant pulses. This approach is similar to the one presented in Aliu et al. [2012] and is applied with some modifications to the Crab pulsar data used for this study.
In the first part only simulations of all used radio data sets are included to search for a correlation whereas in the second part simulations of the γ-ray data sets are used to determine the correlation level. This technique is an attempt to include possible variations of the non-pulsed emission which could obliterate a correlation.
During the first part of this study the arrival times of the radio and γ-ray events were converted to the SSB (Chapter 5.1, Chapter 5.2). In the case of an existing correlation, they should be arranged within a specific time window around each other. Therefore in both cases (for radio and γ MC simulations) search windows are defined. A search window is an area in time around a radio giant pulse (Figure 5.51) given in units of the rotation period of the Crab pulsar. To make this search comparable, the same search windows as by Aliu et al. [2012] are applied in this study: 1, 3, 9, 27, 81, 243, 729, 2187 Crab pulsar rotation periods. These values are converted into fractional parts of a day and the number of γ-ray events is calculated in each search window around a radio giant pulse. Since a delay between the radio and γ-ray emission of the Crab pulsar cannot be excluded, three different time ranges are defined in which the number of γ-ray events around a radio giant pulse is examined: Before, centered on and after a radio giant pulse (Figure 5.51). These three ranges are examined for each search window resulting in a total of 30 searches for the Effelsberg radio data and MAGIC γ-ray without rotational phase cuts and WSRT radio data with P1 and P2 phase cut.

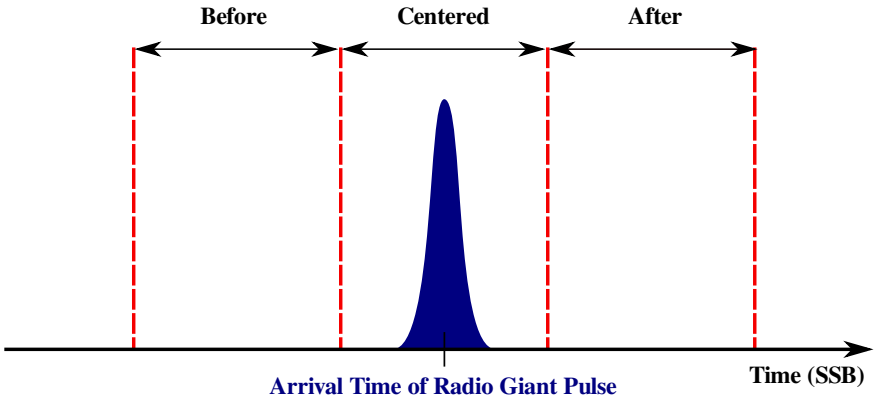

Figure 5.51.: Schematic view of how search windows are located with reference to a radio giant pulse.

Flux Enhancements - Simulated Radio Data

To examine the influence of the non-pulsed emission resulting from the radio data sets on a possible correlation, all radio data sets from the Crab pulsar involved in this study were simulated as described in Chapter 5.3.2. Due to the much lower background emission in the case of the radio data (see Chapter 5.1), it is easier to capture and model it with a MC simulation than in the case of the γ-ray data. However, as described in Chapter 5.3.2 the simulations for the Effelsberg and WSRT data were built up with different techniques.
In the first part of the search for flux enhancements of the γ-ray data the search windows are, as described earlier in this chapter, located on each giant pulse in the radio data (centered). In addition to this they are also located before and after the radio giant pulse (Figure 5.51). The resulting numbers of γ-ray events in dependence of a radio giant pulse are determined for the actual data sets as well as for the corresponding MC simulations. The comparison between the data sets and the MC simulations is shown in Figure 5.52 and Figure 5.53. In the case of Figure 5.52 no cuts in the rotational phase are included in the data. This is done in Figure 5.53. In both figures the results for the search windows of the MC simulations are indicated with error bars. The ones from the data sets are included with crosses. Taking at first only the blue crosses and error bars from Figure 5.52 into account ("MC after", "data after"), it is noticed instantly that for all multiple values of the rotation period they lie within the range of the error bars of the MC simulations.

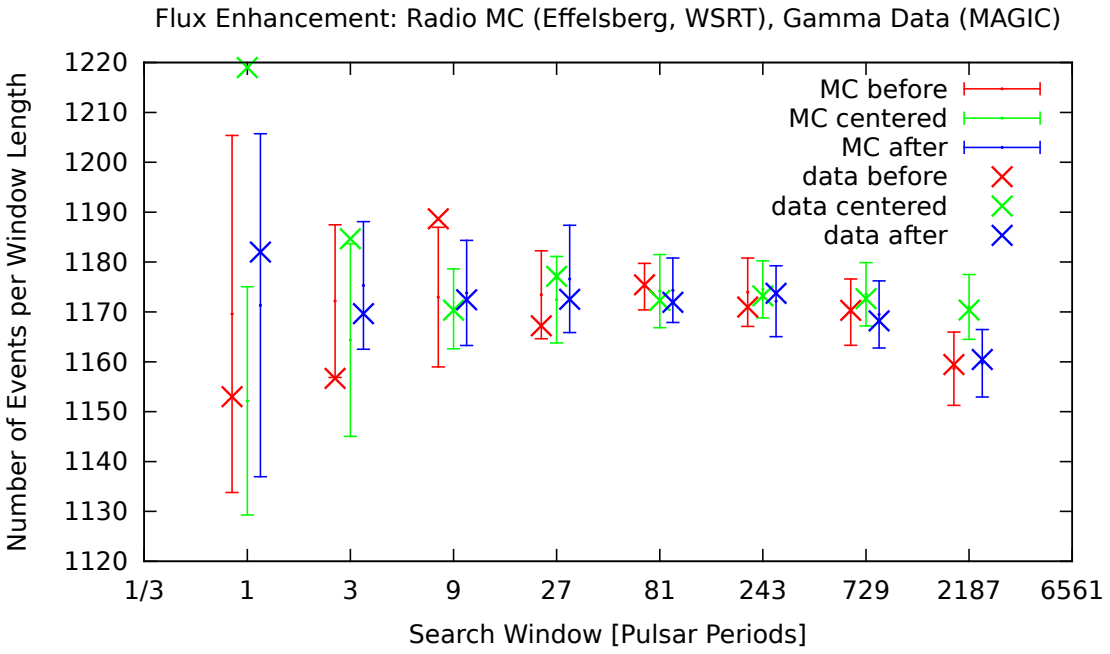

Figure 5.52.: Enhancements of γ-ray flux around occurring radio giant pulses for the total amount of simultaneously taken radio and γ-ray data. The crosses and error bars are shifted to make them easier discernible.

This result implies that the numbers of γ-ray events around a radio giant pulse resulting from the data sets are in the range of the corresponding numbers resulting from the MC simulations indicating no existence of a correlation between radio giant pulses and γ-photons. Taking a look at the corresponding search window in Figure 5.53 changes the result of Figure 5.52 with regard to the number of crosses outside of the error bars range of the corresponding MC simulations (81 and 243 pulsar periods in Figure 5.53). Since no indication of such a development is visible from the other multiple rotation periods in Figure 5.53, in these two cases statistical fluctuations are likely the cause of the deviation.
Referring with the same considerations to the red crosses and error bars in Figure 5.52 ("MC before", "data before"), it is noticed that for two multiple values of the rotation period (three and nine) the results for the data sets are not in the range of the error bars of the corresponding MC simulations. However, since this development does not continue for the other multiple rotation period values, it might be rather caused by statistical fluctuations than something intrinsic from the Crab Nebula + pulsar system. The fact that nothing of this development is seen anymore in Figure 5.53 seems to confirm this indepedently. Since the latter can be also the reason of poor statistics, no definite proof is given that the deviations seen at three and nine pulsar periods are really caused by statistical fluctuations. This still needs to be verified, as will be described later in the text.

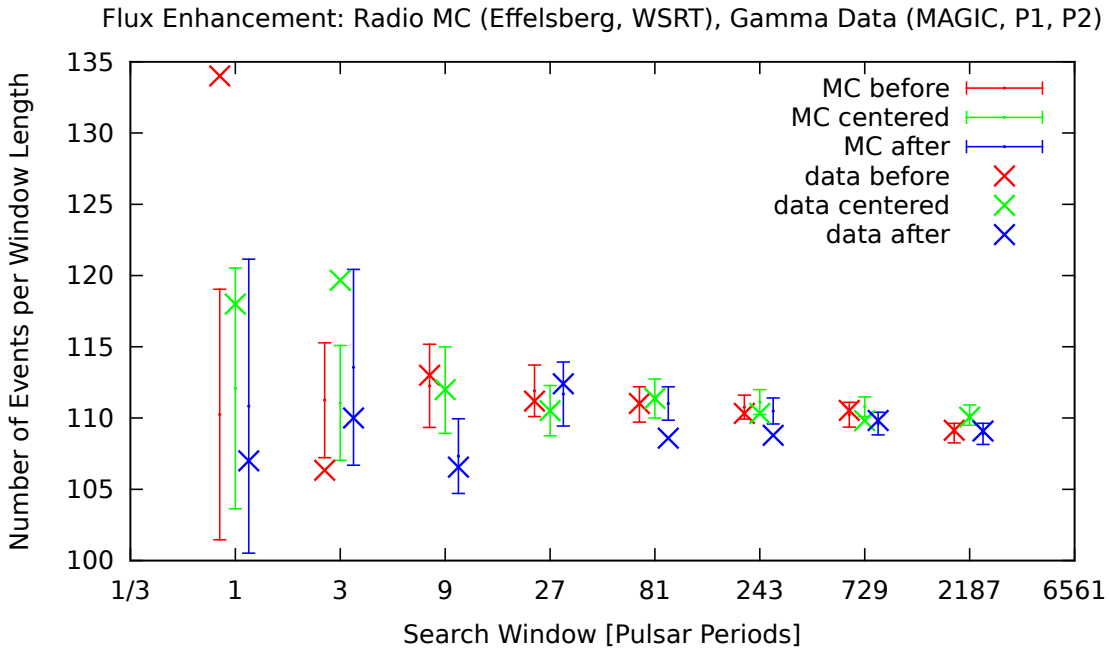

Figure 5.53.: Enhancements of γ-ray flux around occurring radio giant pulses for the total amount of simultaneously taken radio and γ-ray data. In contrast with Figure 5.52 phase cuts were included in this case into the γ-ray data (taken from Aleksić et al. [2012]).

Lastly, the green crosses and error bars in Figure 5.52 ("MC centered", "data centered") are lying in the error bars range of the MC simulations expect for a search window of one and

three pulsar periods (Figure 5.52). This is an interesting result since for a search window of three pulsar periods also a deviation is seen in Figure 5.53 (and the data point for one pulsar period is in the upper region of the error bar of the respective MC simulations). The observed deviations for these search windows will be examined further in the next chapter.
Apart from the carried out comparisons, the veracity of the described deviations can be tested also in a different way. Since so far only one part of all data sets, the radio data, was simulated with the MC approach, in the next chapter the same search for flux enhancements is carried out once more, but with MC simulations based on γ-ray data (Chapter 5.3.2).

Flux Enhancements - Simulated γ-Ray Data

To examine the results from the last chapter, the corresponding analysis is carried out once more, but with γ MC simulations. A description of the algorithm with which the latter were built, is given in Chapter 5.3.2.
The corresponding results are shown in Figure 5.54. The upper figure shows the case for not correlated MC simulations ($\alpha = 0.0$, $\beta = 1.0$, refer to Chapter 5.3.2 for details) and the lower figure for fully correlated MC simulations ($\alpha = 1.0$, $\beta = 0.0$). Interestingly, in the upper figure the deviation of the data in the centered window (green cross in Figure 5.54) is still outside of the range of the corresponding MC simulations for one rotation period as was first noticed in Figure 5.52. This is not seen anymore in the lower figure of Figure 5.54. Hence it can be deduced already at this point that the observed deviation for the centered window at one rotation period, is statistically not very high. Besides another deviation between the flux enhancements for the data and the MC simulations shown in Figure 5.54 belongs to the window located before the radio giant pulse for nine pulsar periods (red cross and respective MC simulation in Figure 5.54). A slight deviation of this kind is already seen also in a window of nine pulsar periods in Figure 5.52.
To quantify the magnitude of the observed deviations, analogous flux enhancement calculations are carried out for the same data, but with modified MC simulations. The corresponding modification lies in the inclusion of various amounts of a correlated and uncorrelated signal from the Crab pulsar (expressed by different values for the parameters α and β). This modification only refers to the centered search window at the moment. The corresponding results (apart from Figure 5.54) can be found in Chapter C.4. A comparison between the results for α values ranging from 0.0 to 0.2, leads to a estimated, necessary amount of correlated γ-photons amount between 0% and 10% in order to get matching results between the data and the MC simulations. To capture this value with high precision, the amount of MC simulations for each value of the quantity α is increased from 12 to 200 in order to improve the statistics of the simulations. Afterwards the flux enhancement calculations are carried out again in exactly the same way as before. The results of these calculations are shown in Figure 5.55. For the purpose of the quantitization of the repeatedly mentioned deviation in the centered window at one rotation period, only the number of events per window length of this one point is included in Figure 5.55 (marked by a horizontal cyan colored line). The red curves in this figure stand for the MC simulations (their average values and standard errors) which have various amounts of injected, correlated γ-photons. The green lines are the $1\,\sigma$ standard deviations of these averages and the blue lines reflect the corresponding $1.96\,\sigma$ standard deviation. The interesting area of this figure is located where the cyan line comes nearest to the average value of the MC simulations. To determine the α value where both, the data and the MC simulations cross, a linear fit is constructed through the average values of the simulations (red dashed line in Figure 5.55).

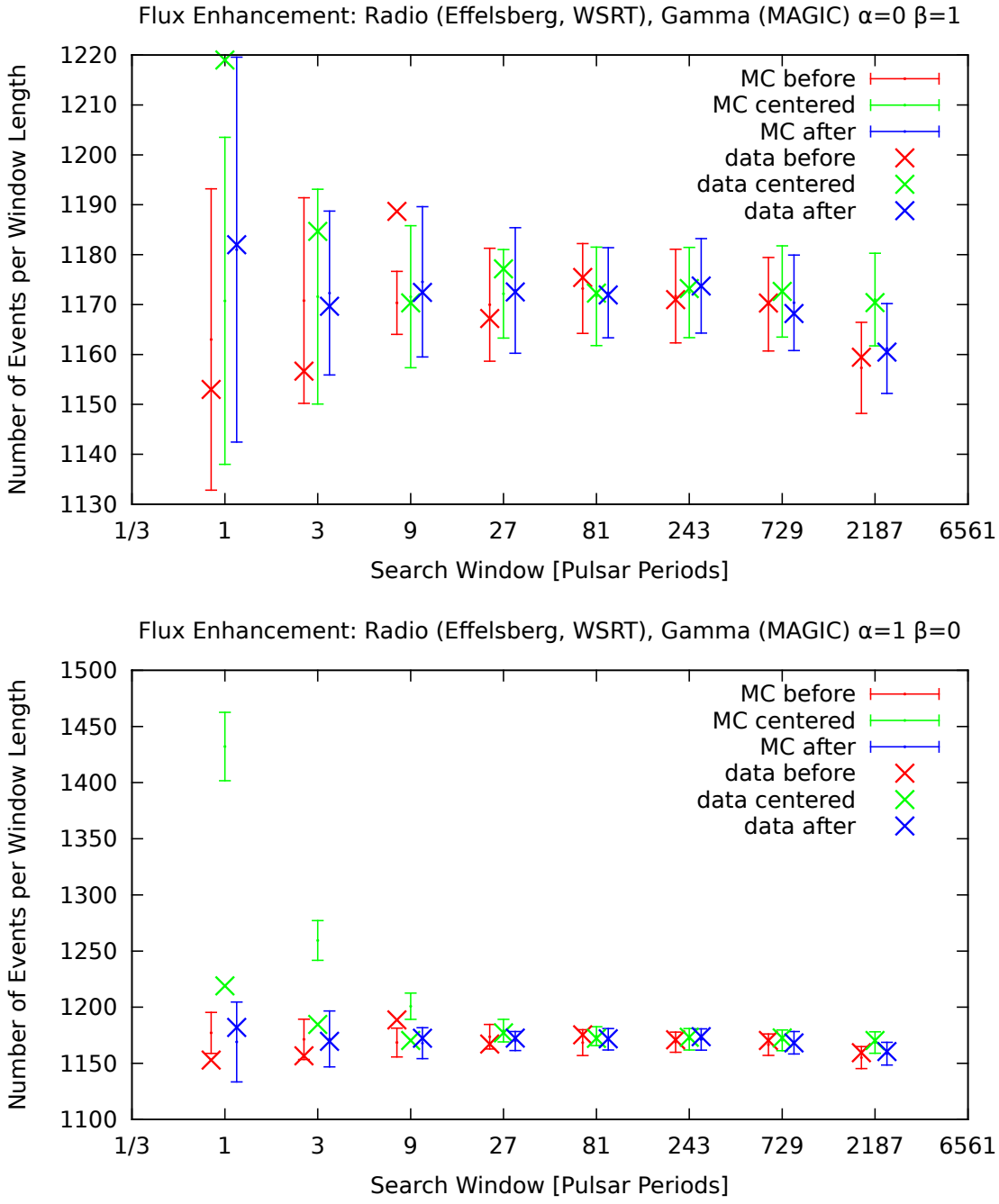

Figure 5.54.: Enhancements of γ-ray flux around occurring radio giant pulses for the total amount of simultaneously taken radio and γ-ray data. In contrast with Figure 5.52 MC simulations based on γ-ray are used for the calculation of these results. No phase cuts are included. These calculations were still carried out with 12 MC simulations. Upper figure: Flux enhancements for 100% uncorrelated MC simulations. Lower figure: Flux enhancements for 100% correlated MC simulations.

Corresponding fits are also build for the $1\,\sigma$ and $1.96\,\sigma$ standard deviation values (green and blue dashed lines in Figure 5.55). The results of the fitting procedure are shown in Table 5.18 for one rotation period of the centered rotation window (P = 1) and for three rotation periods (P = 3). The corresponding calculations have also been carried out for three rotation periods since this data point is still outside the error bars range of the flux enhancement calculations shown in Figure 5.52. Although it is not that prominent anymore in the upper part of Figure 5.54, it is still further away from the average value of the respective MC simulations. To verify the validity of the results for the flux enhancement calculations at one rotation period, the same calculations are carried out for the flux enhancement at three rotation periods.

P = 1			P = 3	
m1	257.4		m1	261.8
t1	1174.72		t1	3522.6
m2	265.4		m2	261.8
t2	1242.2		t2	3649.0
m3	249.4		m3	261.9
t3	1107.3		t3	3396.2

Table 5.18.: The coefficients of linear fits for different α values (for the case of one rotation period and three rotation periods). The values noted with m stand for the slope of the linear fit (given in units of counts in search window per percent of a correlation) and the values marked with a t are intersections with the ordinate (given in counts in search window). The coefficients m1, t1 belong to the linear fit through the average values of the MC simulations, whereas the coefficents m2, t2 and m3, t3 belong to the linear fits through the $1.96\,\sigma$ standard deviation values (see Figure 5.55 and Figure 5.56).

Estimating from the lower figure of Figure 5.55 the α value which reflects the smallest distance between the data point and the average values of the MC simulations, is at about 0.17. For a more precise value the intersection between both corresponding linear curves is calculated. With this procedure an α value of 0.17 ± 0.14 is calculated confirming the earlier estimated results. Hence according to these calculations, an amount of 17 % of γ-photons which are directly correlated with radio giant pulses, is needed to reproduce the deviation of the data point for a search window of one rotation period as expressed in Figure 5.52 and in Figure 5.54. The respective 95 % confidence interval extends to an upper value of 0.45 (the intersection between the cyan and the lower blue line in Figure 5.55). The lower boundary of this confidence interval is located at α values smaller than zero and cannot be determined with the available amount of data sets.
The same calculations are carried out for a search window of three rotation periods (Figure 5.56). With the same values for P = 3 from Table 5.18, the corresponding α value for this search window is determined as 0.12 ± 0.23. This confirms that the results for a search window of one rotation are not caused by statistical fluctuations (albeit the respective error is higher than the actual value of α in this case confirming the lack of sufficient statistics). The upper value of the corresponding 95% confidence interval is determined as 0.60. Since also in the case of three rotation periods the lower border of this confidence interval is located at α values

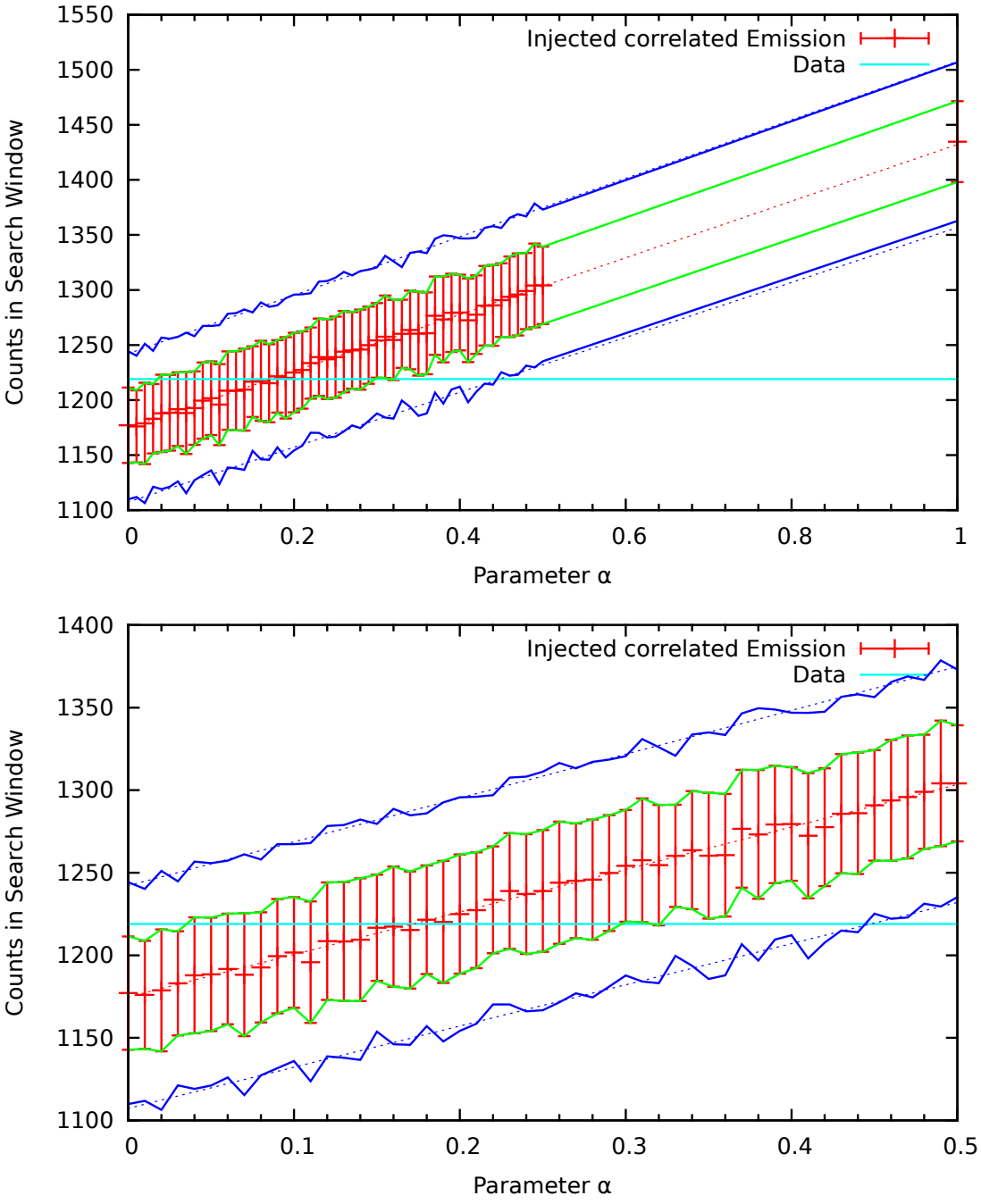

Figure 5.55.: Counts in the centered search window for one rotation period from Figure 5.54 for various values of the parameter α. The cyan line represents the corresponding data point at 1219 counts in the centered window as shown in Figure 5.54. Upper figure: All values for α from 0 to 1. Lower figure: Values for α from 0 to 0.5.

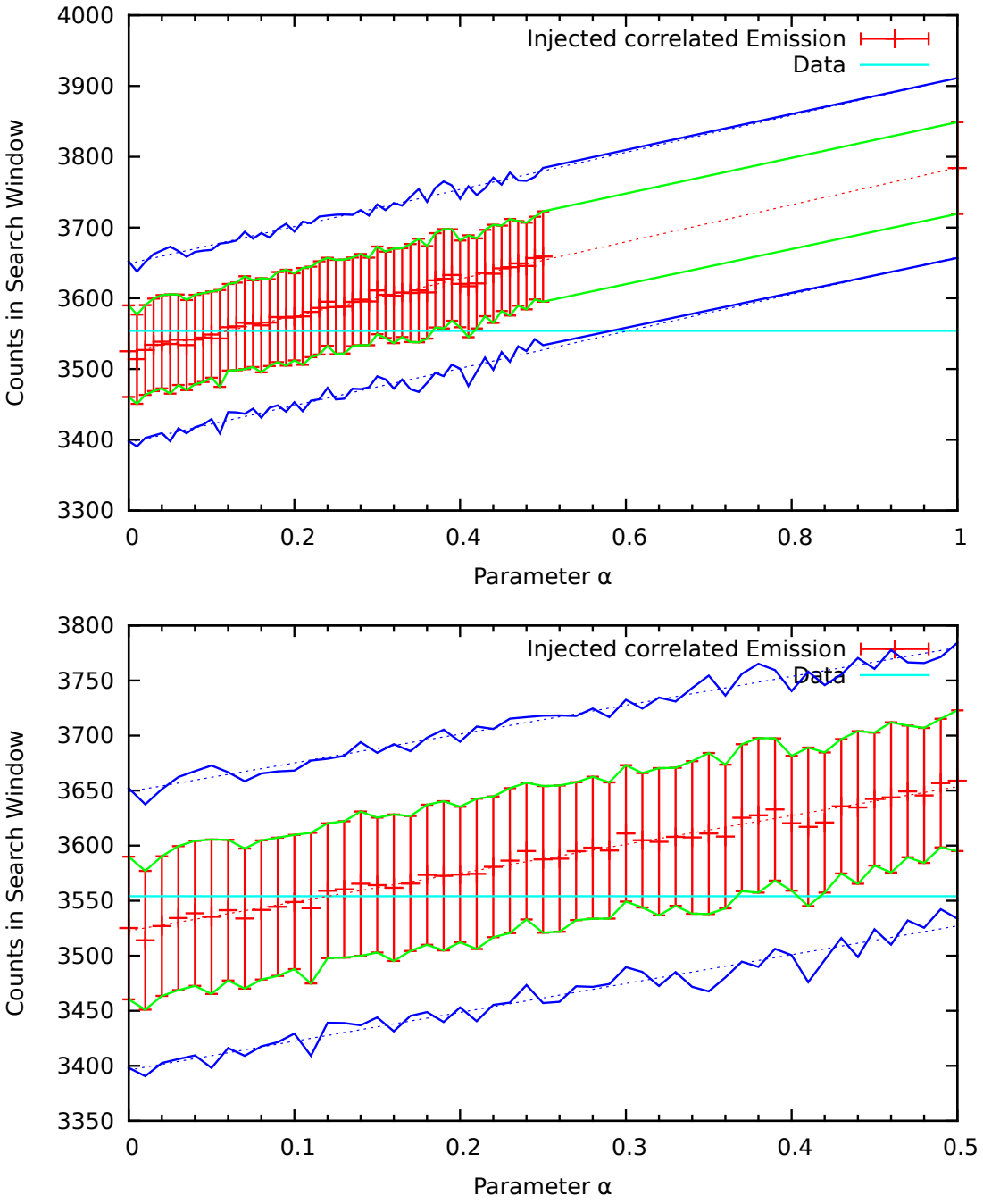

Figure 5.56.: Counts in the centered search window for three rotation periods from Figure 5.54 for various values of the parameter α. The cyan line represents the corresponding data point at 3554 counts in the centered window as shown in Figure 5.54. Upper figure: All values for α from 0 to 1. Lower figure: Values for α from 0 to 0.5.

below zero, an α value equal zero (describing the case of no correlation) cannot be excluded with 95 % confidence.
As can be deduced from the results obtained from the search windows of one and three rotation periods, the excess number of γ-photons on a radio giant pulse becomes higher with shorter search windows. To study this behaviour in more detail, corresponding results for search windows of 1/3 and 1/9 rotation period length are determined (Figure 5.57). This approach goes beyond the procedure described in Aliu et al. [2012]. On the contrary to the previously made assumptions, the α values are not higher, but lower in contrast with the ones resulting from search windows of one and three rotation periods length. This is indeed the case because in search windows which are shorter than one rotation period only one component, either P1 or P2, is included. Which of these components is chosen depends where the radio giant pulse occurs. Consequently, the corresponding α values for shorter time windows than one rotation period, are expected to be approximately half of the original value. In the case of a search window of 1/3 and 1/9 rotation periods length an α value of 0.087 ± 0.079 and 0.090 ± 0.048 is determined. Hence in both cases an increase of the number of γ-photons around a radio giant pulse of about 9 % is seen. The respective errors are high due to the increasing influence of Poisson noise. However, the existence of an enhancement of γ-photons around radio giant pulses of approximately equal value, indicates that it is not caused by statistics, but is indeed intrinsic. The corresponding 95 % confidence intervals extend to an upper value of 0.25 (search window of 1/3 rotation periods) and 0.193 (search window of 1/9 rotation periods). As is also shown in Figure 5.57, the lower borders of the confidence intervals are located below zero. Consequently, an α value equal zero cannot be excluded in this case either.
During the analysis of the data presented in this thesis, not understood features have been identified in some WSRT data sets (Chapter 5.1). Although, these features have been eliminated out of the affected data sets by introducing a cut in the rotational phase (see Chapter 5.3.2), it cannot be guaranteed that these features are not overlapping with the pulsed radio emission in the WSRT data. Therefore a further test is made if the detected enhancement can be regarded as of intrinsic origin. For this purpose the corresponding α values for search windows of one and three rotation periods length are determined for the Effelsberg radio sets only (Figure C.4.3). The corresponding α values are 0.137 ± 0.100 (search window of 1 rotation period) and 0.14 ± 0.17 (search window of 3 rotation periods). The upper borders of the respective confidence intervals are 0.344 and 0.484. This result does not differ much from the calculations based on all radio data sets (Figure 5.55, Figure 5.56) and is compatible within the respective error bars. In other words, there is no indication that the observed enhancement is caused by the additional features detected in the WSRT radio data.
In the next step it is tried to optimize the search for flux enhancements more on the Crab pulsar by including phase cuts (adopted from Aleksić et al. [2012]) in the γ-ray data and in the γ MC simulations. The idea behind this is the following: The previous attempt in examining the flux enhancements in search windows with a length of 1/3 and 1/9 rotation periods (Figure 5.57) has been successful. The phase ranges for the P1 and P2 emission determined by Aleksić et al. [2012] correspond to 1/11 of the rotation period of the Crab pulsar. Therefore it becomes interesting to search for flux enhancements in data sets as well as MC simulations with cuts in the rotational phase. The results of these calculations are shown in Figure 5.58. As can be seen in both figures, the intersection between the linear fit through the average of the MC simulations and the included data point has shifted to smaller α values due to the inclusion of phase cuts. The calculation of the intersection between both linear curves results in the following α: 0.055 ± 0.032 for a search window of 1/3 and 1/9 rotation periods. That means in

both cases an increase of γ-photons resulting from either P1, or P2 centered on a radio giant

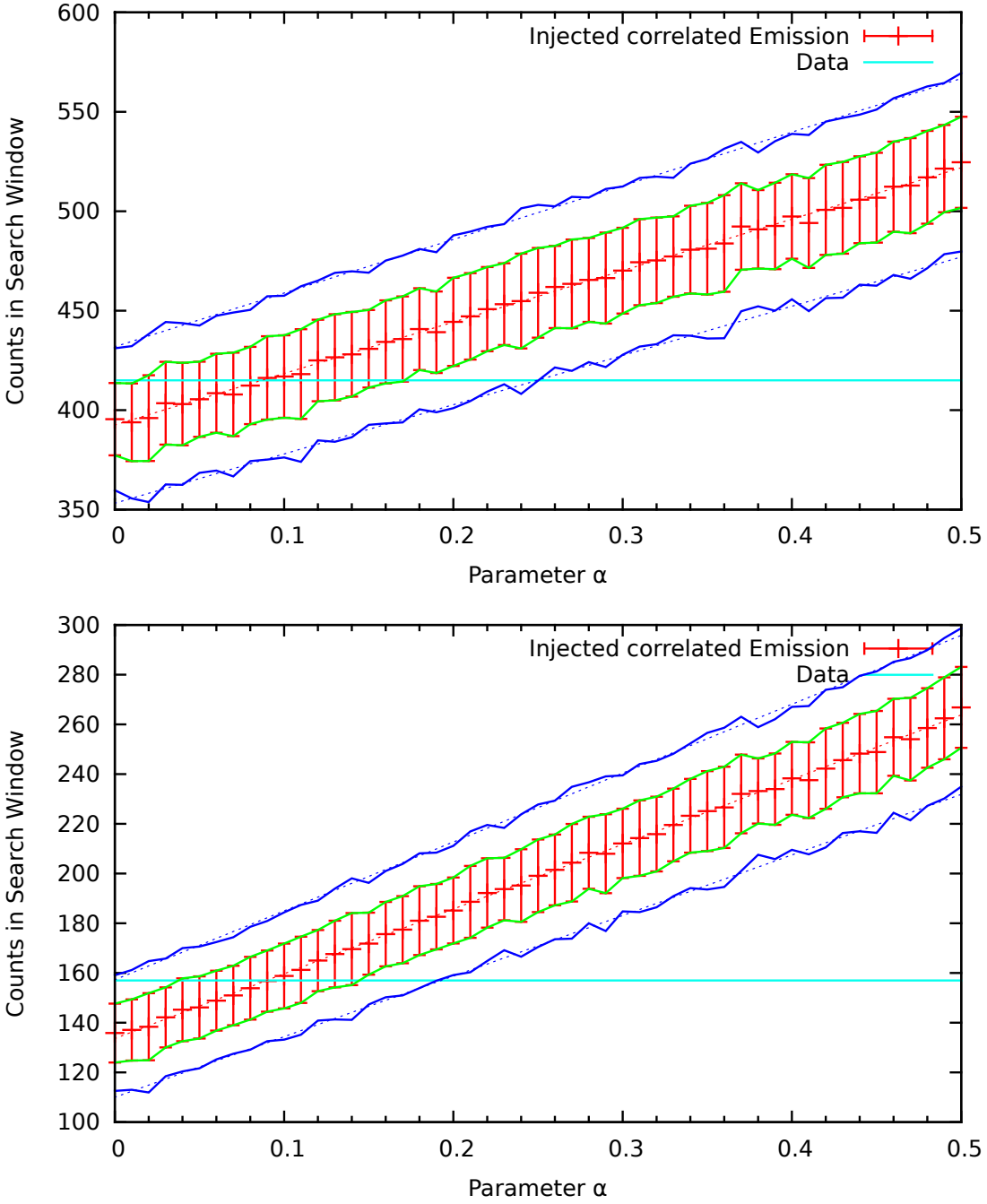

Figure 5.57.: Counts in the centered search window for 1/3 (upper figure) and 1/9 (lower figure) rotation periods from Figure 5.54 for various values of the parameter α. The cyan line represents the corresponding data point at 415 (upper figure) and 157 (lower figure) counts in the centered window.

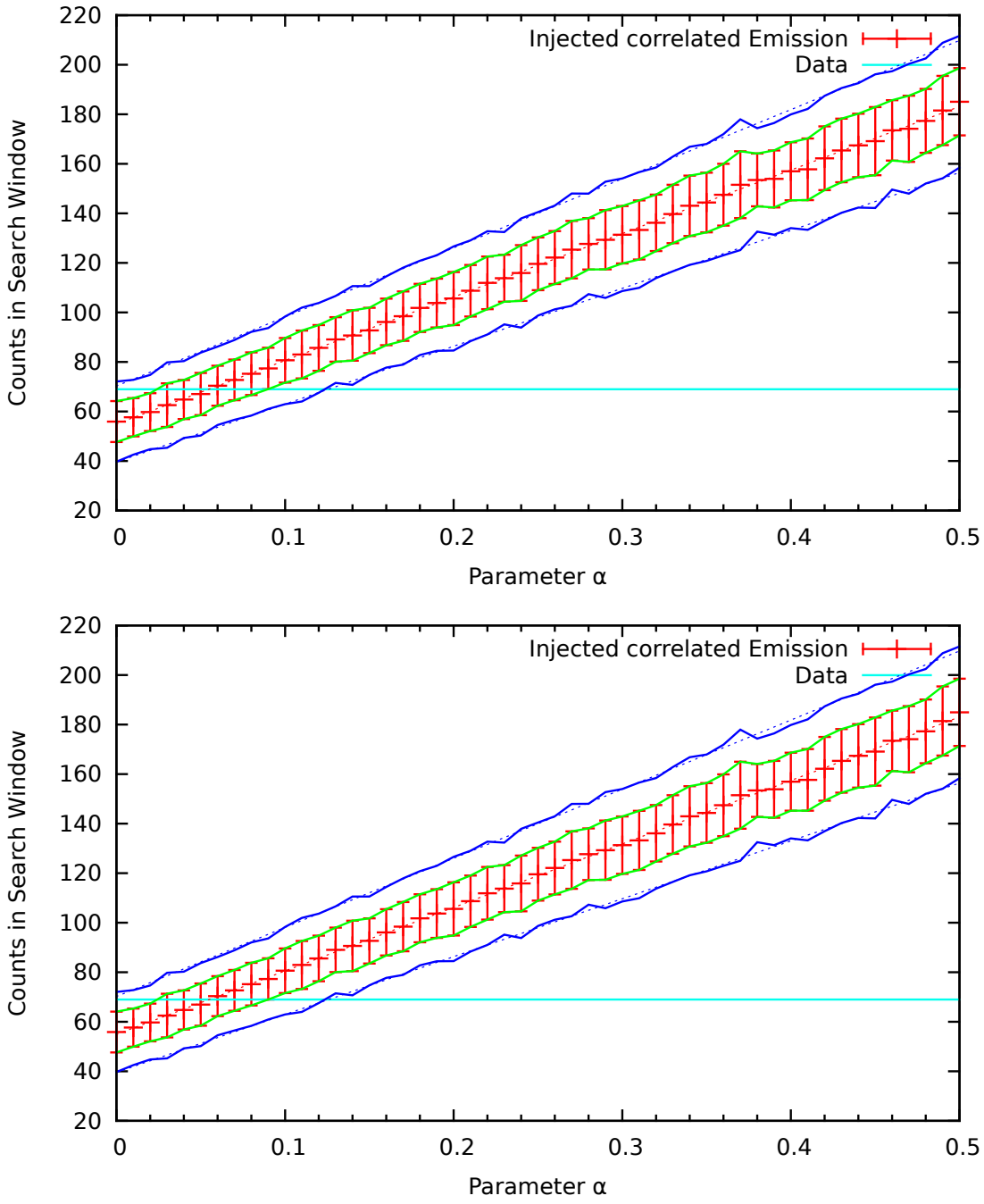

Figure 5.58.: Counts in the centered search window for 1/3 (upper figure) and 1/9 (lower figure) rotation periods from Figure 5.54 for various values of the parameter α. The cyan line represents the corresponding data point at 69 (upper and lower figure) counts in the centered window. Cuts in the rotational phase (adopted from Aleksić et al. [2012]) are included in the γ-ray data and in the γ MC simulations.

pulse (which can also result only one of the two emission componets) of about 6 % has been discovered. The respective upper border of the 95 % confidence interval is in both cases 0.126. However, similar as in the previously discussed cases, the lower border is again located at α values below zero which emphasises that an α value equal zero cannot be excluded.

In summary, the observed deviation between the flux enhancements resulting from the radio and γ-ray data sets and the corresponding radio MC simulations (Figure 5.52) and γ MC simulations (Figure 5.54) for a search window of one rotation period of the Crab pulsar centered on a radio giant pulse, has been quantified as 0.17±0.14. The upper value of the corresponding 95 % confidence interval has been determined as 0.45. The lower value of this interval cannot be determined with the available amount of data.
Since a similar deviation is also seen in Figure 5.52 and Figure 5.54 for search window of three rotation periods, the same calculations are carried out also in this case. The resulting magnitude of the corresponding deviation has been determined as 0.12±0.23 with an upper value of the confidence interval of 0.60. Since the search window of one rotation period is included in the one for three rotation periods, this is an additional test if the 17% increase of the γ-ray flux centered on a radio giant pulses for a one rotation period search window is caused by statistical fluctuations, or if it might be intrinsic. The 12 % increase of the γ-ray flux in this search window suggests that this development might be indeed intrinsic.
To examine the increase of the number of γ-photons centered on radio giant pulses further, the same calculations are made for search windows of 1/3 and 1/9 rotation periods. The magnitudes of the respective calculated deviations are 0.087±0.079 and 0.090±0.048. The determined decrease can be explained by taking into account that such short search windows can only contain one of the emission components P1, or P2. Hence the number of γ-photons centered on a radio giant pulses which occurs at the phase ranges of either P1, or P2 is higher by about 9 %. The corresponding upper value of the confidence interval is in both cases 0.25.
Since the increase of the γ-ray flux can be also found in short search windows of 1/3 and 1/9 rotation periods length, rotational phase cuts are included in the γ-ray data as well as the γ MC simulations. The respective flux enhancement calculations for the same search windows reveal an increase of γ-photons centered on a radio giant pulse of 0.055±0.032, or about 6 % in both cases. The upper border of the confidence interval is for both search windows 0.126.
Consequently, with the third correlation search approach, the examination of flux enhancements between radio and γ-photons, the following relations have been found:
A correlation of 17 % between radio giant pulses and γ-photons if P1 and P2 are included.
A correlation of 9 % if either P1, or P2 are taken into account and a correlation of 6 % when phase cuts are included.
The latter value emphasises that the observed correlation originates from the Crab pulsar. However, due to the fact that the lower border of the corresponding confidence interval cannot be determined, a value for α equal zero (that is, suggesting the existence of no correlation) cannot be excluded entirely from these considerations.

6. Summary and Outlook

Present pulsar emission theories place the origin of radio emission in a region near the magnetic poles of the neutron star known as polar gap and of γ-ray emission in a region near the light cylinder in a region known as outer gap. Charged particles which are accelerated in these regions, are subject to different magnetic field strengths which result in different acceleration mechanisms (Chapter 1.4.2). However, the alignment in rotational phase of the observed multiwavelength emission from the Crab pulsar (Figure 2.3) opposes this assumption and rather suggests a common emission mechanism.
Detailed studies of the emission properties of the Crab pulsar have revealed additional kinds of radio emission beyond the regular pulsed emission (Chapter 3). Among these anomalous radio pulses are giant pulses, which are studied in the present thesis. Their different emission properties suggest a discrete emission mechanism which could be related to the emission at other wavelengths. Besides, investigations of different giant pulse emitting pulsars than the Crab pulsar revealed that although their giant pulse emission is misplaced in the rotational phase with regard to its normal radio emission, it is nevertheless aligned with multiwavelength emission (Figure 3.19). These observations suggest that radio giant pulses might be the still missing link between the pulsed emission at different wavelengths.
In the present work the question of a correlation between radio giant pulses and γ-photons from the Crab pulsar is investigated. For this purpose data taken simultaneously with the Effelsberg radio telescope, the WSRT and the MAGIC telescopes are used. After the analysis of all radio and γ-ray data sets (Chapter 5.1, Chapter 5.2), the search for a correlation between radio giant pulses and γ-photons is addressed from various sides (Chapter 5.3).
First, a subtraction of corresponding TOAs is carried out to check for a clustering at different wavelengths. These differences are put into various time bins in the range of $\pm 10\,\mathrm{s}$ and are searched for statistically significant deviations (Chapter 5.3.2). To differentiate between a real and an artificial correlation signal, MC simulations are constructed, based on the timing properties of the radio data sets. After that, the time differences resulting from the radio and γ-ray data as well as the radio simulations and γ-ray data are compared. These comparisons are carried out for γ-ray data sets with and without cuts in the rotational phase of the Crab pulsar (adopted from Aleksić et al. [2012]). However, in both cases no statistically significant deviation could be determined out of the TOAs. This can be due to insufficient amounts of data, or a lack of sensitivity of this approach, or simply because this method is not the appropriate one to search for this kind of correlation.
In a second correlation search approach both kinds of data sets are examined with the Pearson correlation coefficient (Chapter 5.3.3). With this approach a search for a linear correlation between the radio and γ-ray data sets is carried out by checking the null hypothesis which states that the data sets are not linearly correlated. To search for this kind of correlation, the TOAs of radio giant pulses are placed in time bins. The size of these bins is set according to the inverse count rate resulting from the data sets. The Pearson correlation coefficient is afterwards determined for all data sets nightwise and monthwise. These calculations are carried out for data sets with and without cuts in the rotational phase. Interestingly, the Pearson correlation

coefficient for data sets with a P1 phase cut is negative and has statistically significant probability values. This result suggests the existence of a linear anticorrelation between radio giant pulses and γ-ray photons, resulting from the P1 emission component. However, since the values of the Pearson correlation coefficient are located near zero, the observed linear relationship is apparently very weak (as far as can be deduced from the available data sets). A deeper investigation of the effectiveness of this method involves higher amounts of simultaneously taken radio and γ-ray data.
The third correlation search approach consists of a comparison of the number of γ-photons around occurring radio giant pulses (Chapter 5.3.4). Since the nature and mechanism of a correlation between both is not known, the possibility cannot be excluded that for instance correlated γ-photons are emitted in a certain time distance after, or before the corresponding radio giant pulses. To determine the amount of γ-photons around a radio giant pulse, time windows around the latter (commonly referred to as search windows) in units of the rotation period of the Crab pulsar are defined. To incorporate possible delays between radio giant pulses and γ-photons, each search window is located at three different positions with regard to a radio giant pulse (Figure 5.51). With this setup the number of γ-photons in each search window around a radio giant pulse is calculated. To minimize the possibility of a false detection, the same calculations are carried out for 1) radio MC simulations and γ-ray data and for 2) radio data and γ-MC simulations. Already in the first case a deviation between the results of simulations and actual data sets is noticed for a search window of one and three rotation periods of the Crab pulsar centered on a radio giant pulse (Figure 5.52). Contemplating if the deviations result from the Crab pulsar, cuts in the rotational phase of the γ-ray data are introduced. The corresponding results are shown in Figure 5.53. Interestingly, the number of γ-photons around a radio giant pulse is still higher for a centered search window of three rotation periods, after the introduction of phase cuts. Besides, the respective number for a search window of one rotation period is still in the range of the corresponding simulations, but rather in the upper range of the error bar of the latter.
To examine this increased number of γ-photons around a radio giant pulse further, additional MC simulations of the γ-ray data sets are constructed (Chapter 5.3.2). That means, they are modified with an injected signal from the Crab pulsar. The strength of the injected pulsar signal is included by two different parameters: The parameter α which describes the strength of a perfectly correlated γ-ray pulsar signal and the parameter β which stands for the strength of an uncorrelated γ-ray pulsar signal. The aim of this method is a quantitization of the strength of the noticed deviation.With this procedure an α value of 0.17 ± 0.14 is determined for a centered search window of one rotation period and of 0.12 ± 0.23 for a corresponding search window of three rotation periods length. In other words, the observed number γ-photons is higher by about 17 % in a centered search window of the length of one rotation period when a radio giant pulse occurs. In a centered search window of three rotation periods length, the number γ-photons is higher by about 12 % when a radio giant pulses is observed.
To make sure that the observed enhancements are not caused by the artificial features seen in some of the WSRT data sets, the corresponding calculations are also carried out for Effelsberg radio data only. The resulting α values are 0.137 ± 0.100 (for a search window of one rotation period) and 0.14 ± 0.17 (for a search window of three rotation periods). They do not differ much from the α values calculated for the whole radio data set. Therefore there is no indication that the observed enhancement is caused by artificial features seen in some of the WSRT data sets.
The results obtained so far imply that the number of correlated γ-photons is increasing for shorter centered search windows. To examine this increase further, shorter search windows of

1/3 and 1/9 Crab pulsar rotation period are defined next. Analogous flux enhancement calculations result in an α value of 0.087 ± 0.079 (for a search window of 1/3 rotation periods) and 0.090 ± 0.048 (for a search window of 1/9 rotation periods). Hence the increase in number of γ-photons centered on a radio giant pulse is with about 9 %, smaller than at first anticipated. This results from the fact that only one of the regular emission components of the Crab pulsar (P1, or P2) is included in a search window which is shorter than one rotation period. Consequently, the number of γ-photons centered on a radio giant pulse which occurs at the phase ranges of either P1, or P2 is higher by about 9 %.
Since the length of the regular emission components P1 and P2 is approximately 1/11 of the whole rotation period of the Crab pulsar, according to the results obtained by Aleksić et al. [2012] (and thus only a little shorter than the so far examined search windows), flux enhancement calculations are also carried out for search windows of 1/3 and 1/9 rotation periods but for γ-ray data sets and γ MC simulations with phase cuts adopted from Aleksić et al. [2012]. The resulting α values are 0.055 ± 0.032 in both cases. Hence the number of γ-photons centered on a radio giant pulse which occurs either at the phase range of P1, or P2 is higher by about 6 %. All data selection criteria at this point (folding with rotation period, selection of phase ranges, optimization of cut parameters in the analysis of γ-ray data) are optimized for the emission from the Crab pulsar, suppressing the contribution from the Crab Nebula. Due to the described restriction in rotational phase, these results can be regarded as a correlation between radio giant pulses and gamma photons from the Crab pulsar itself.

The γ-ray flux that occurs in correlation with radio giant pulses, is too weak to explain the total emission from a pulsar. Nevertheless it offers an important glimpse into the processes in a pulsar magnetosphere. To enable a deeper investigation of the discovered enhancement, currently ongoing and also future long-term monitoring programs of the Crab pulsar at different wavelengths need to be coordinated in order to enable the collection of larger amounts of simulatenously taken data.
As explained in Chapter 3.2, previously a 3 % increase of optical photons associated with radio giant pulses at the phase ranges of the P1 emission component was found (Shearer et al. [2003]). Interestingly, correlation studies carried out at hard X-rays by Mikami et al. [2013] led to the identification of a higher number of X-ray photons in a search window centered on P1 radio giant pulse by 21.5 % (see middle panel in Figure 1 in Mikami et al. [2013]). The analysis described by Mikami et al. [2013] indicates similar properties as were encountered during the flux enhancement calculations in this work: A smearing out of the discovered enhancement when the search window is widened and a decrease of the number of X-ray photons together with an increase of their fluctuations when the search window is narrowed. In other words, a dilution of the enhancement for longer time windows and a visible lack of statistics for shorter time windows.
Apart from this result at hard X-rays, no further indication of an enhancement has been found in earlier studies at X-rays or γ-rays while the optical correlation has been confirmed independently (compare Table 3.1). The open question is why this might be the case. As is indicated by Table 3.1, the corresponding results from past studies consist of rather high upper limit values. Taking the results of the work of for instance Bilous et al. [2011] and Aliu et al. [2012] into account, results in upper limits in the range of 400 % to 1000 %. These values reflect a lack of sensitivity necessary to detect a correlation which is of the order of a few percent. Consequently, the existence of a correlation cannot be ruled out in their cases. Continuous and more sensitive future missions are therefore crucial to close the currently existing gap of verified flux

enhancements between optical and γ-ray wavelengths. If this gap can be closed, a first order approximation of the spectral shape of the flux increase during occurring radio giant pulses can be constructed, giving constraints on the responsible physical processes and the respective theoretical approaches.

The theoretical approaches describing the emission from pulsars from the last decade are increasingly of numerical nature instead of providing analytical solutions. However, realistic parameters are outside the reach of fully resolved models due to currently existing constraints in computing time (see for instance Philippov and Spitkovsky [2014] where the ratio of neutron star radius to light cylinder radius is modified due to computational costs). The present theoretical approaches consist of simplified solutions, or approaches with parameters which are optimized to more favourable values. Alternatively, limited regions of interest can be studied, but this approach requires prior knowledge of suitable boundary conditions (see for example Umizaki and Shibata [2010] for simulations of the Y-point). If any such simplifications are made due to for instance limitations in the computing time, they need to be examined carefully for physical correctness.

As has been shown in the present work and numerous other publications, the Crab pulsar is a complex system which has abundant facets within one wavelength range as well as at different wavelength ranges. Its giant pulse emission represents only one type of its anomalous behaviour. The results from the present work do not confirm that the giant pulse emission from the Crab pulsar is the one and only missing link to understand the generation of its regular multiwavelength emission. They show that the mechanism behind the giant pulse emission is of multiwavelength nature and emphasise the necessity of future continuous multiwavelength monitoring programs.

Appendices

A. Radio Data Sets

In this section a summarizing data sheet for every radio data set is included to give an overview over the characteristics of the respective data set.

A.1. 2012-12-07

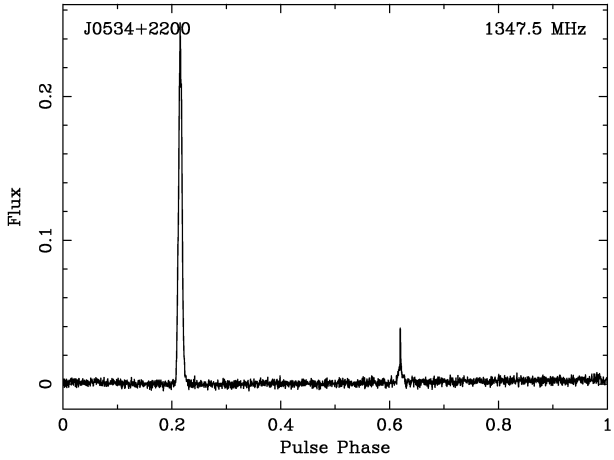

Telescope	Effelsberg
Backend	PSRIX
BW [MHz]	200
ν [MHz]	1347.5
Length [min]	107

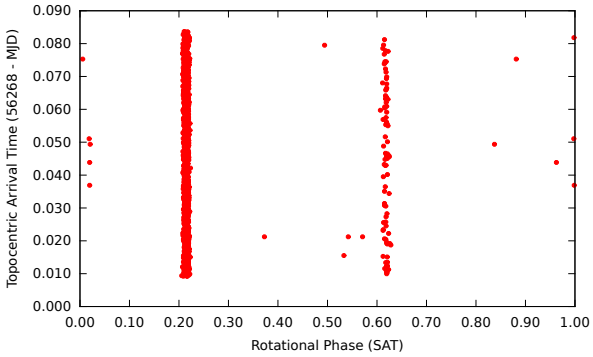

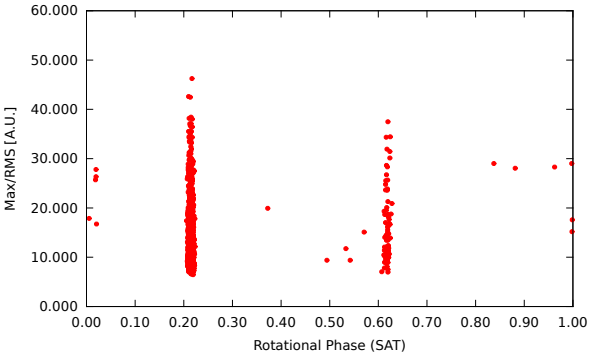

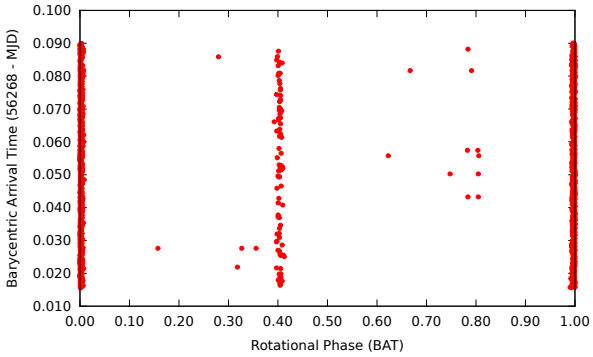

A.2. 2012-12-10

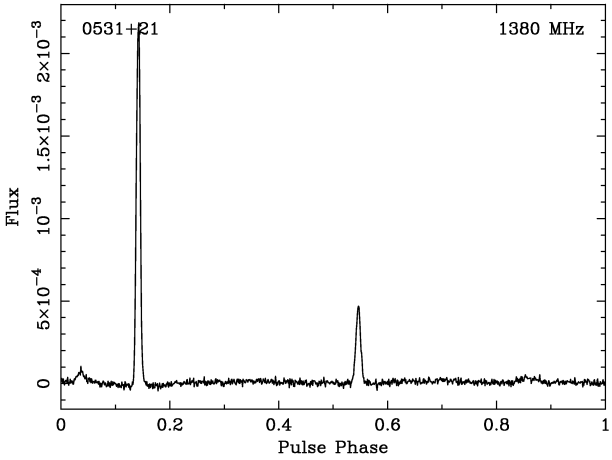

Telescope	WSRT
Backend	PuMaII
BW [MHz]	160
ν [MHz]	1380
Length [min]	120

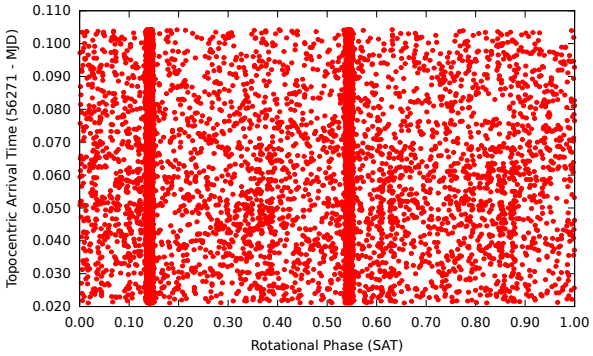

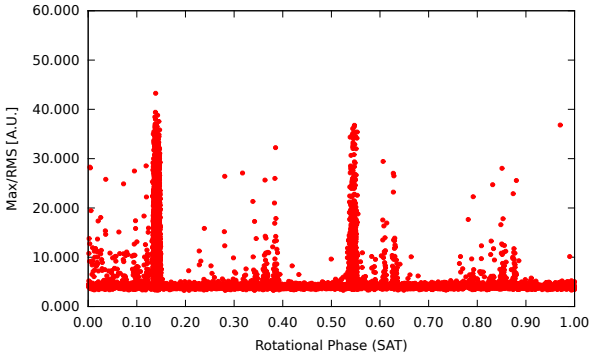

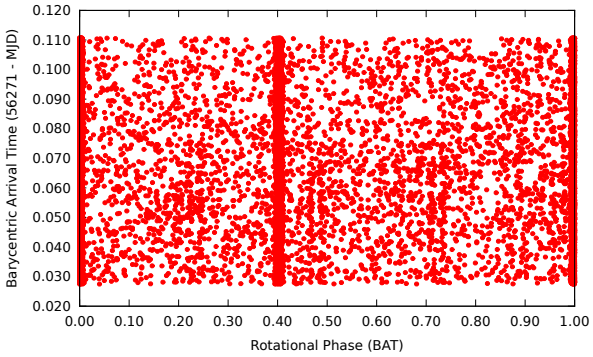

A.3. 2012-12-17

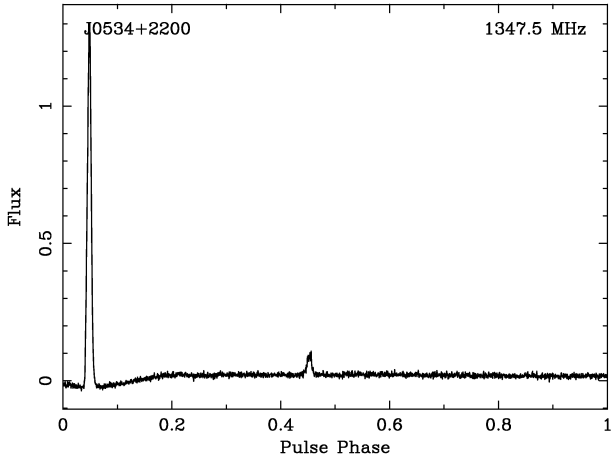

Telescope	Effelsberg
Backend	PSRIX
BW [MHz]	200
ν [MHz]	1347.5
Length [min]	138

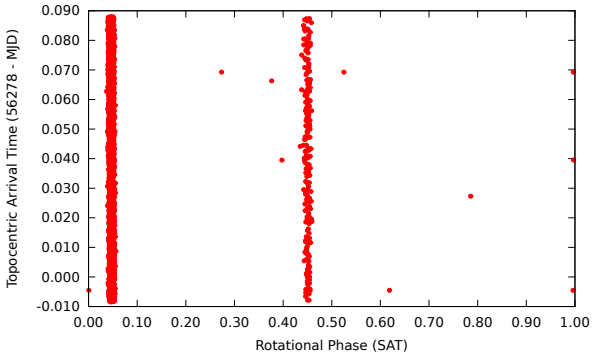

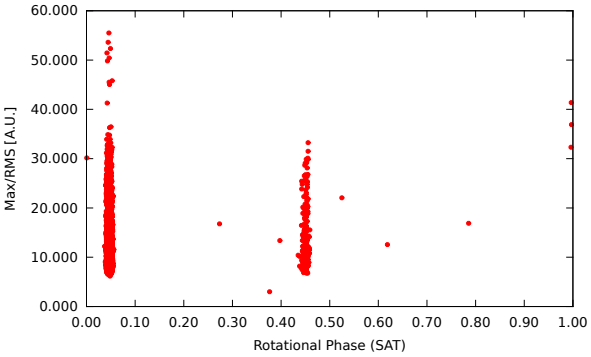

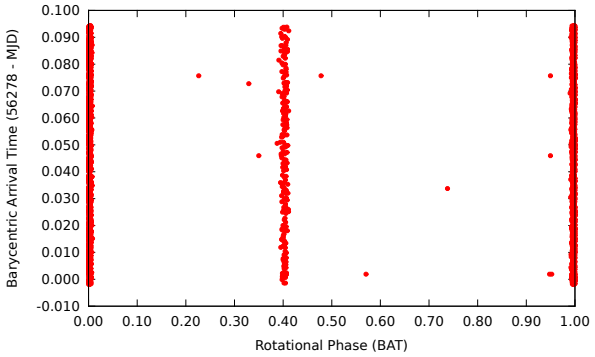

A.4. 2013-01-08

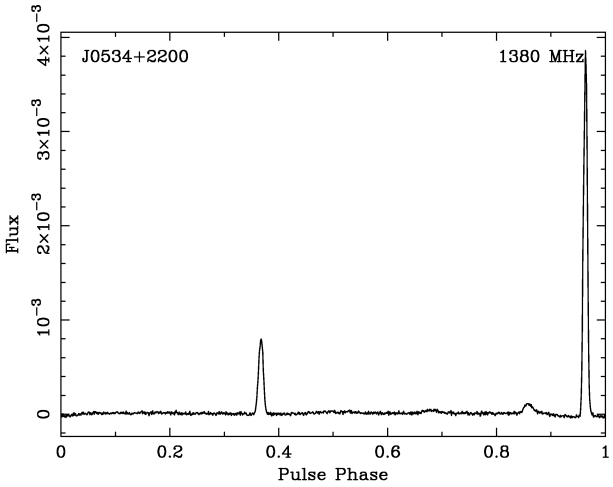

Telescope	WSRT
Backend	PuMaII
BW [MHz]	160
ν [MHz]	1380
Length [min]	120

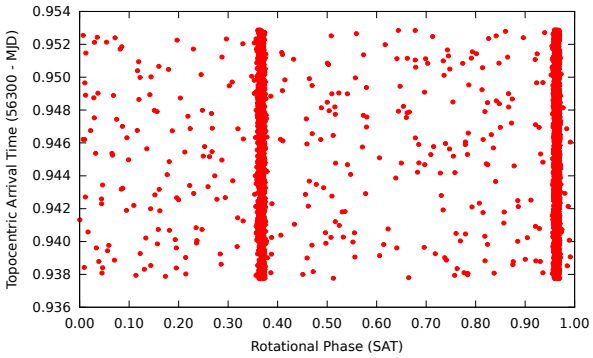

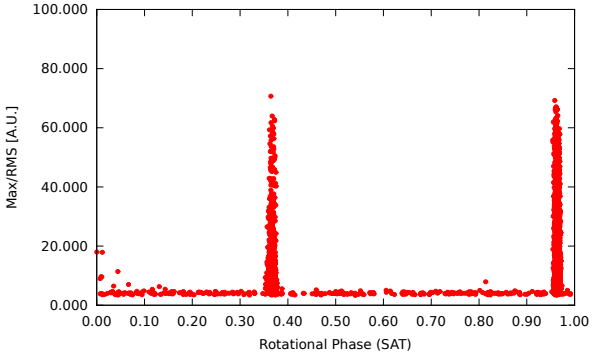

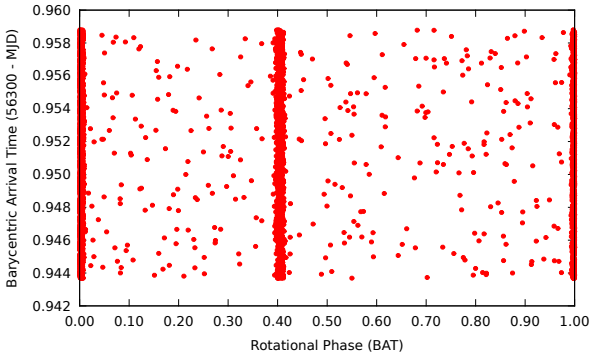

A.5. 2013-01-09

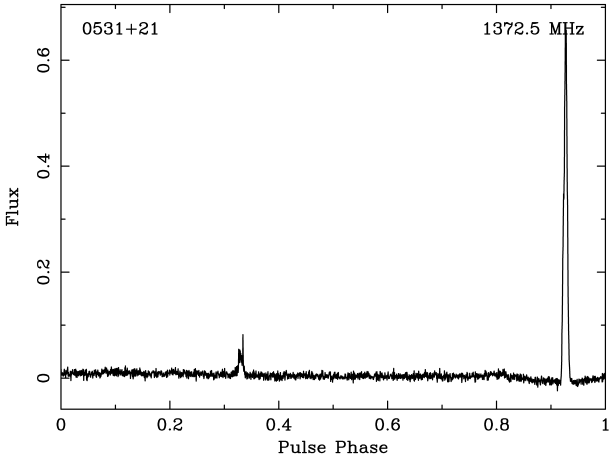

Telescope	Effelsberg
Backend	PSRIX
BW [MHz]	-200
ν [MHz]	1372.5
Length [min]	104

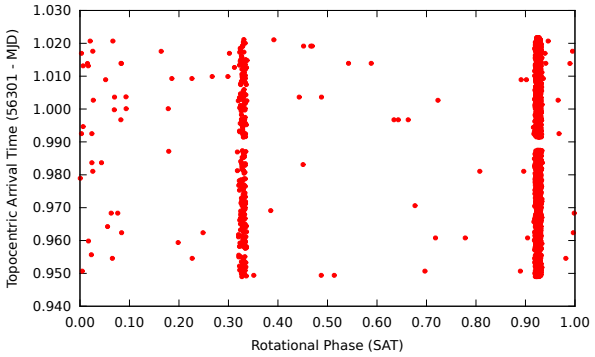

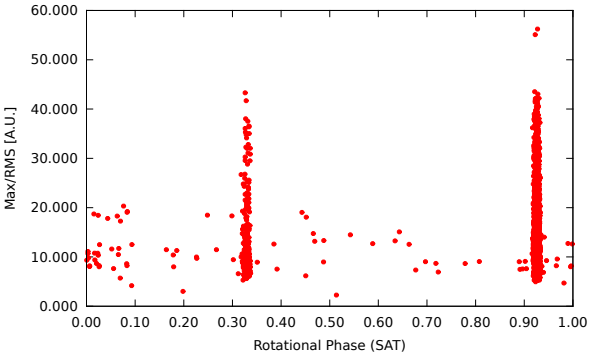

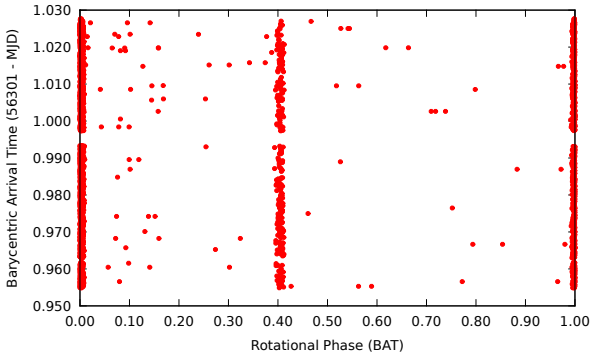

A.6. 2013-01-10

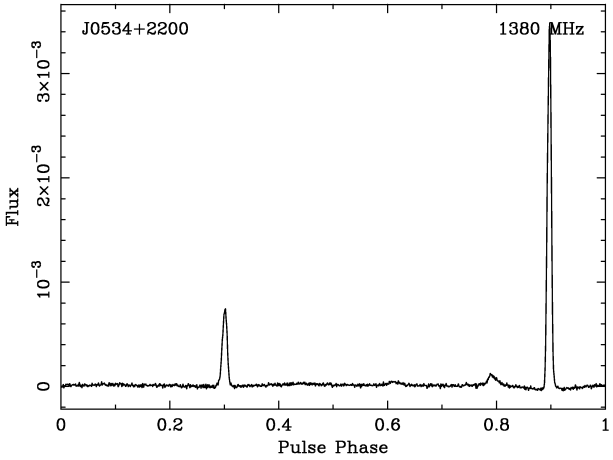

Telescope	WSRT
Backend	PuMaII
BW [MHz]	160
ν [MHz]	1380
Length [min]	120

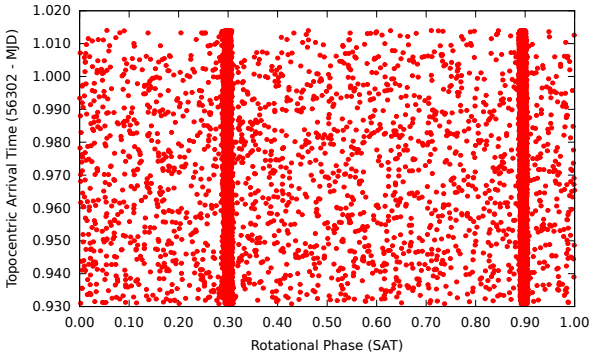

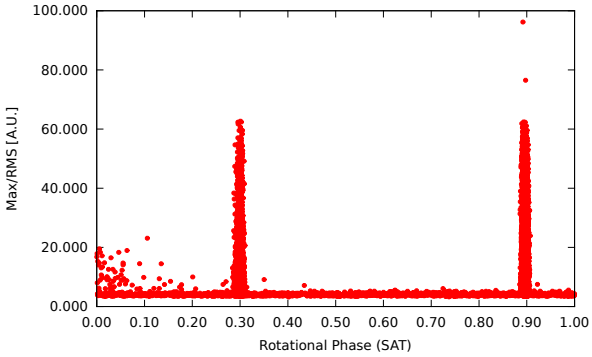

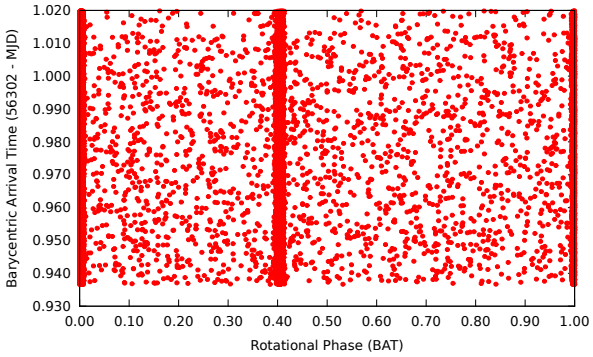

A.7. 2013-01-12

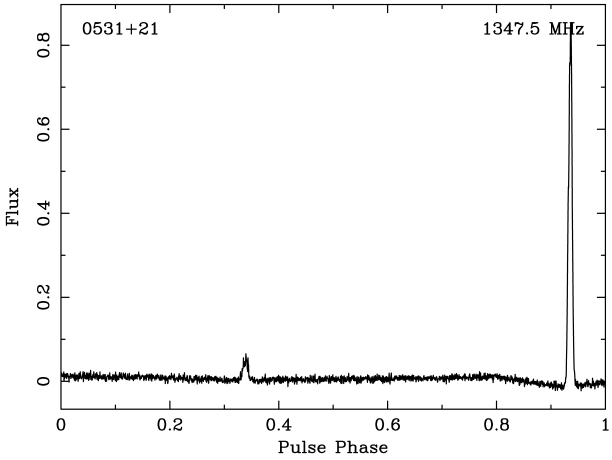

Telescope	Effelsberg
Backend	PSRIX
BW [MHz]	200
ν [MHz]	1347.5
Length [min]	176

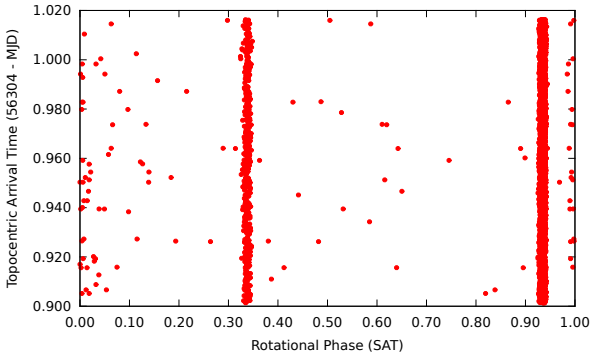

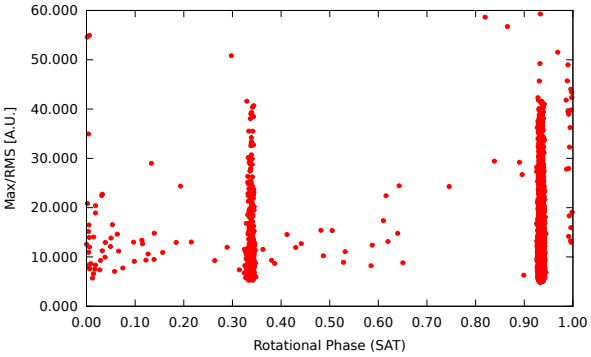

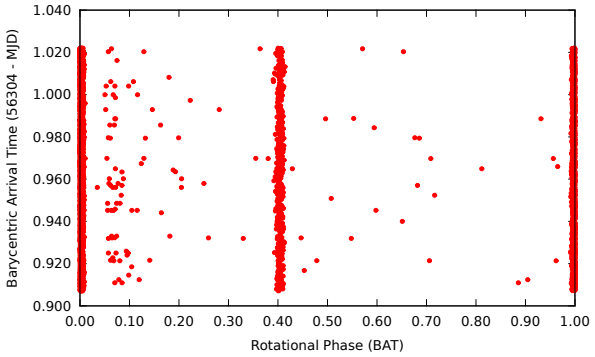

A.8. 2013-01-31

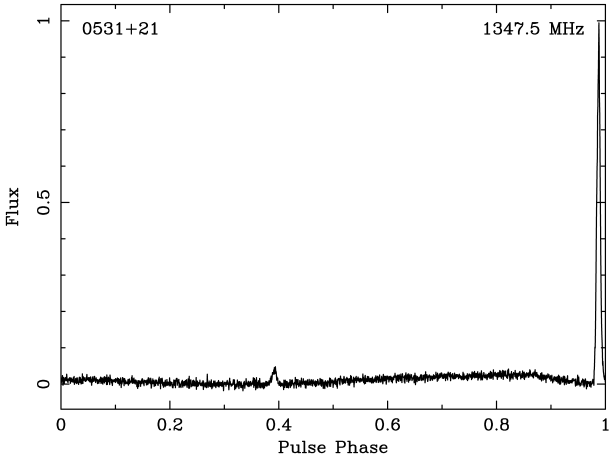

Telescope	Effelsberg
Backend	PSRIX
BW [MHz]	200
ν [MHz]	1347.5
Length [min]	145

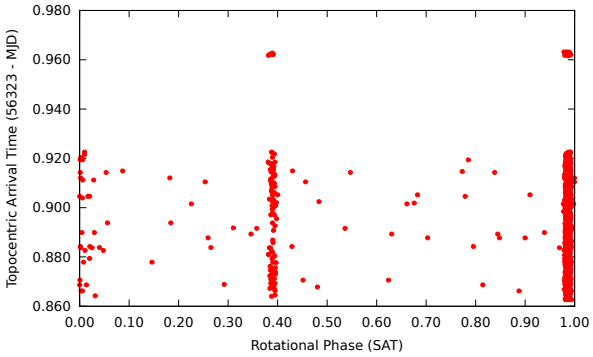

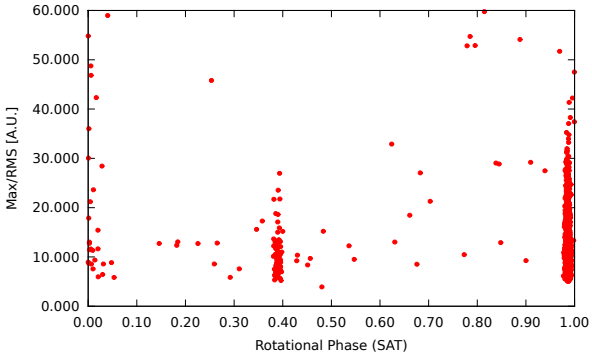

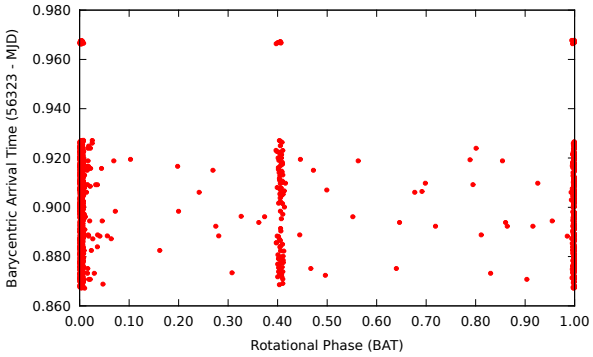

A.9. 2013-02-02

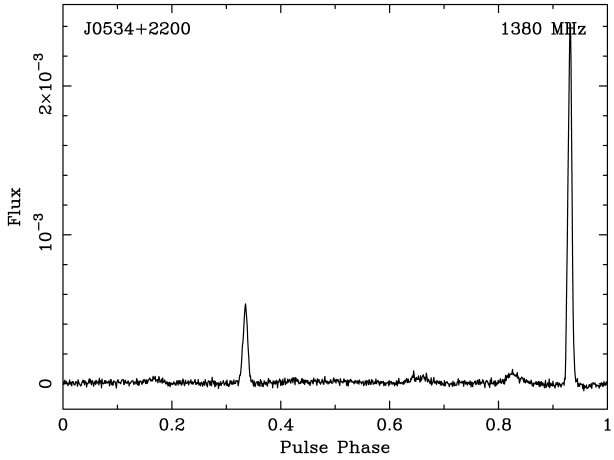

Telescope	WSRT
Backend	PuMaII
BW [MHz]	160
ν [MHz]	1380
Length [min]	54

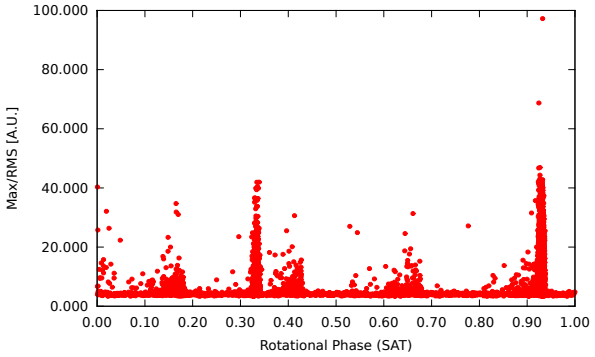

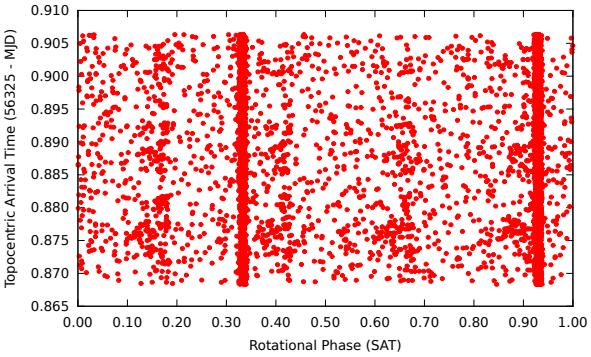

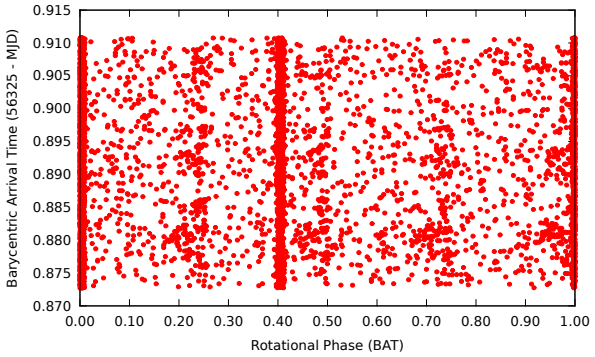

A.10. 2013-02-03

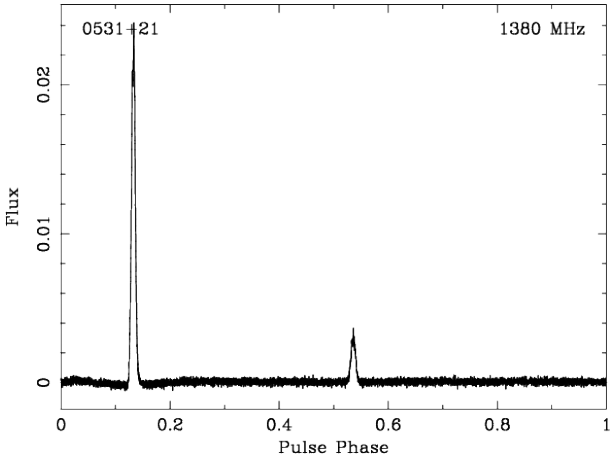

Telescope	WSRT
Backend	PuMaII
BW [MHz]	160
ν [MHz]	1380
Length [min]	120

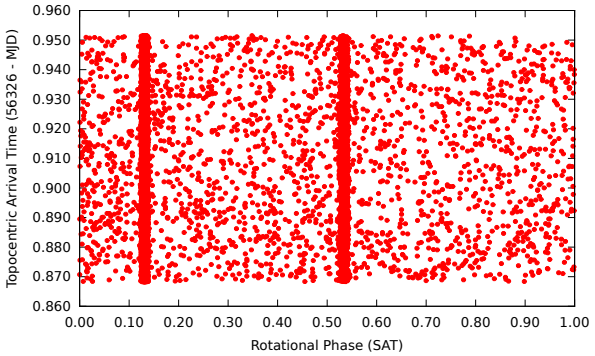

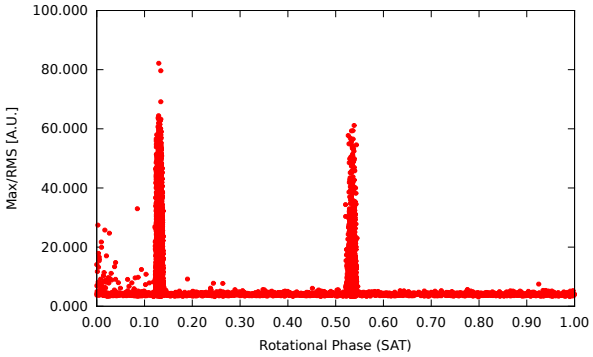

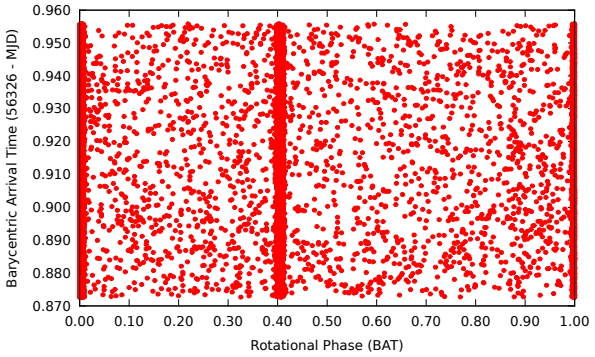

A.11. 2013-02-06

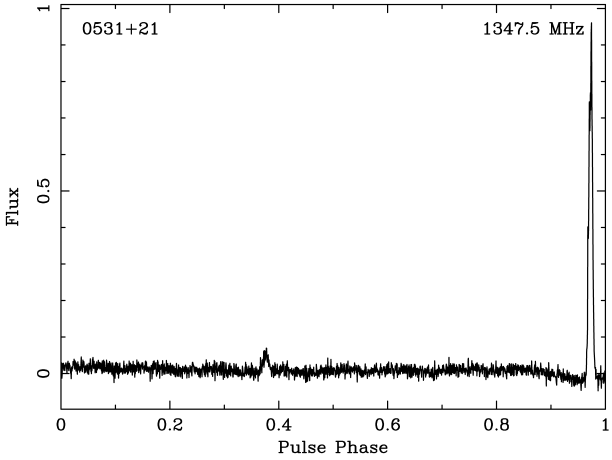

Telescope	Effelsberg
Backend	PSRIX
BW [MHz]	200
ν [MHz]	1347.5
Length [min]	245

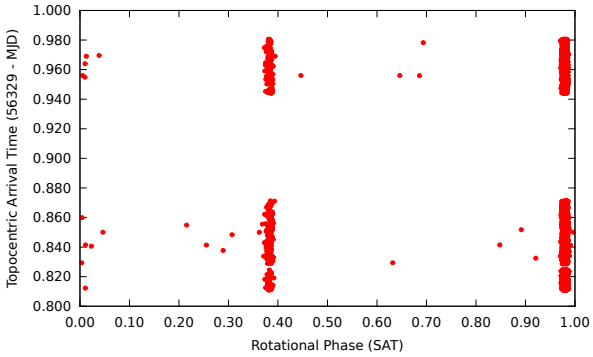

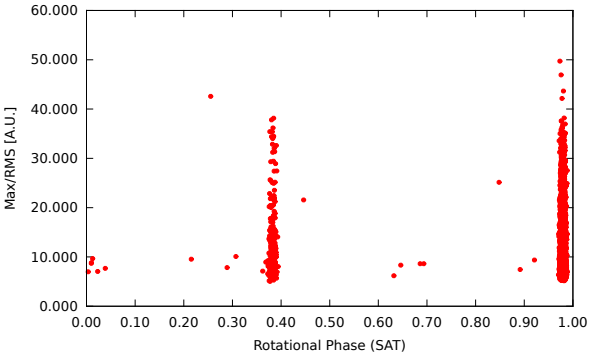

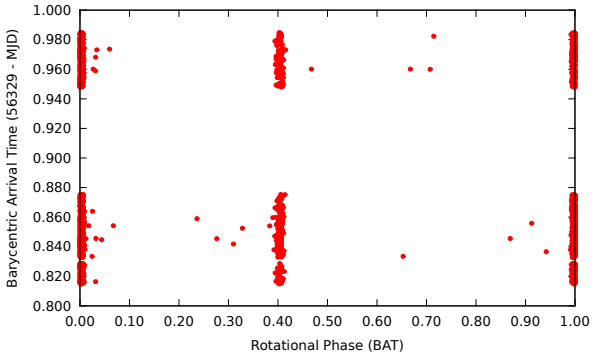

A.12. 2013-02-07

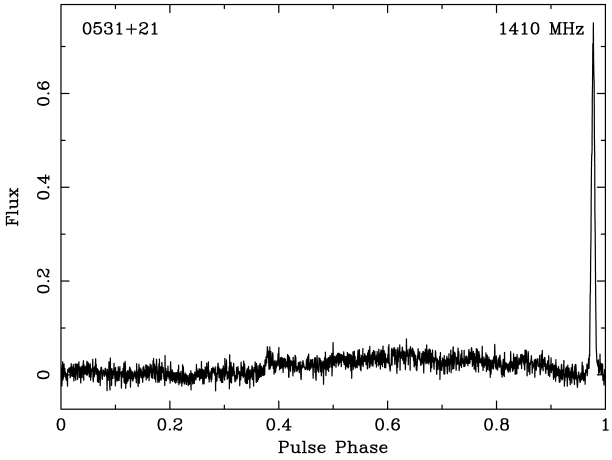

Telescope	Effelsberg
Backend	PSRIX
BW [MHz]	75
ν [MHz]	1410
Length [min]	72

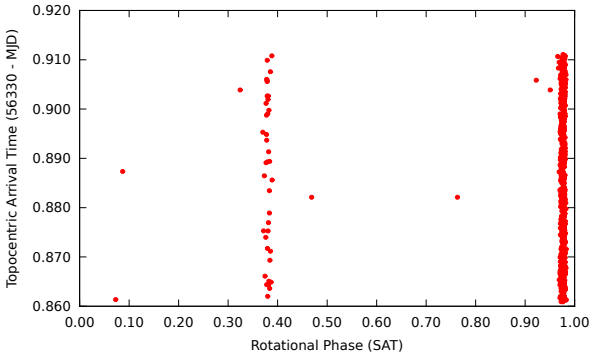

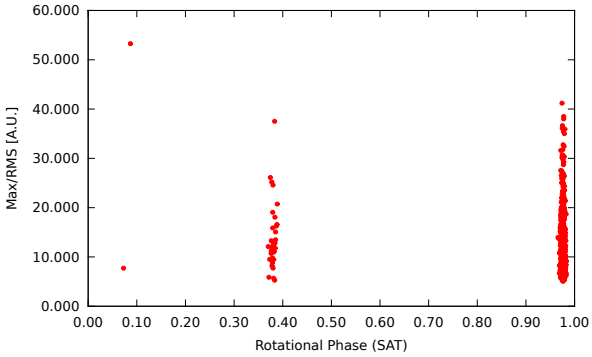

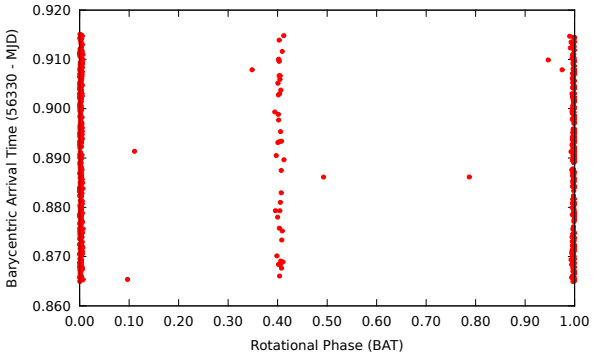

A.13. 2013-02-08

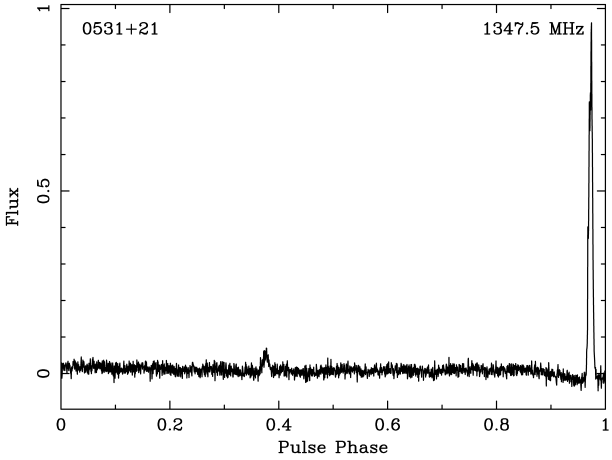

Telescope	Effelsberg
Backend	PSRIX
BW [MHz]	200
ν [MHz]	1347.5
Length [min]	30

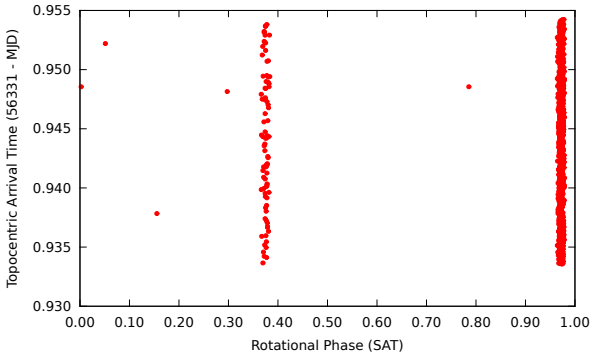

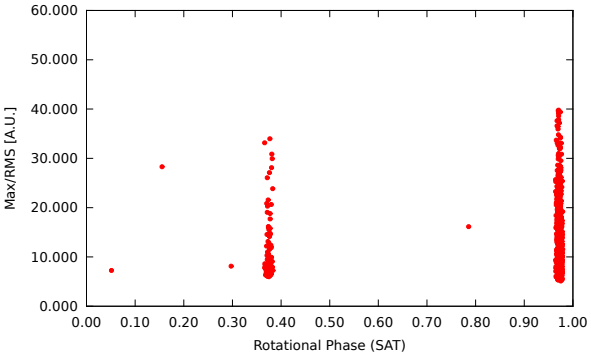

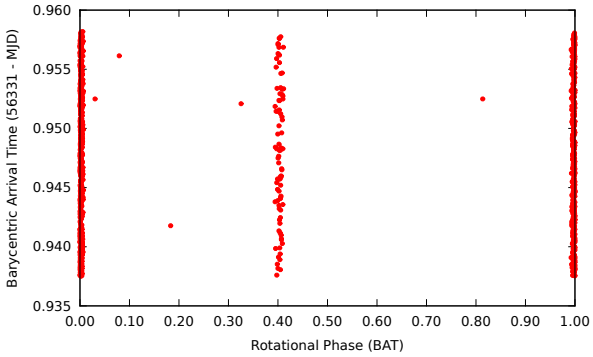

A.14. 2013-02-09

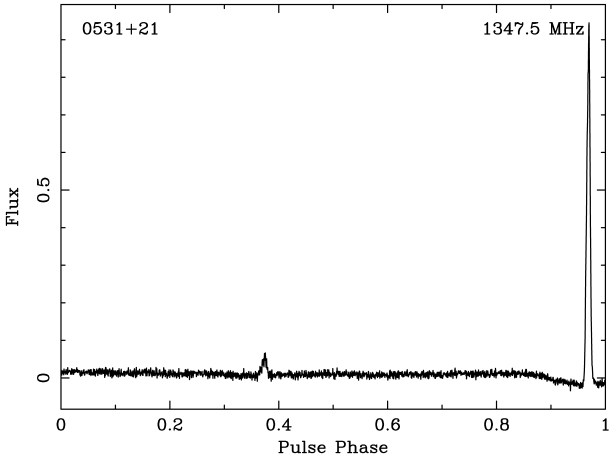

Telescope	Effelsberg
Backend	PSRIX
BW [MHz]	200
ν [MHz]	1347.5
Length [min]	118

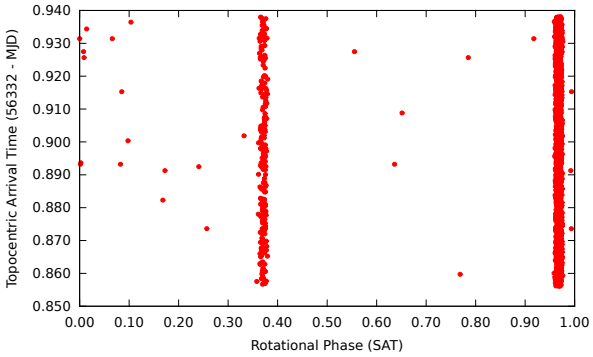

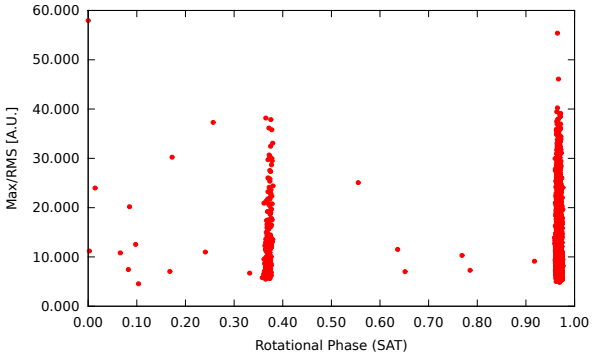

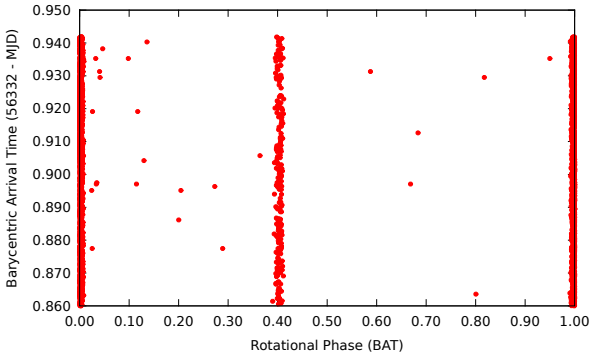

A.15. 2013-02-10

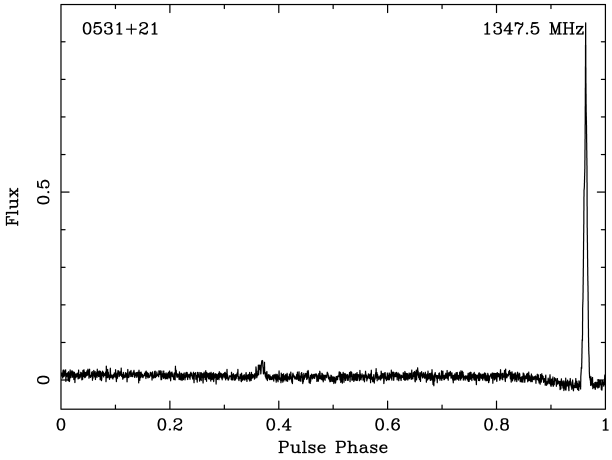

Telescope	Effelsberg
Backend	PSRIX
BW [MHz]	200
ν [MHz]	1347.5
Length [min]	100

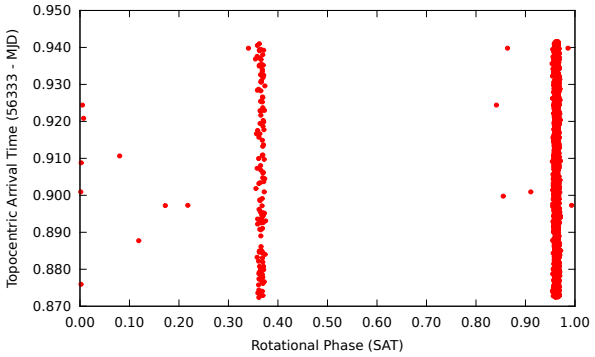

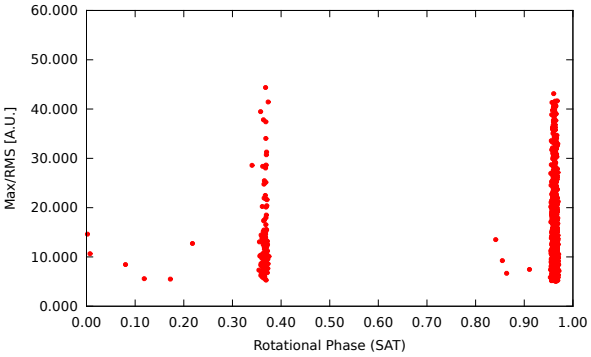

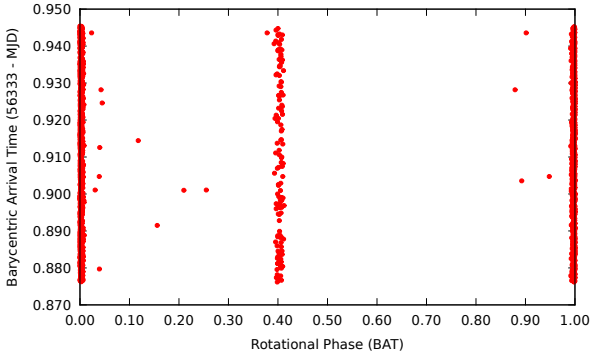

A.16. Radio Ephemeris Files

A.16.1. December 2012

```
PSRJ    J0534+2200
RAJ     05:34:31.97232
DECJ    +22:00:52.069
F0      29.6938196276   3.0
F1      -370430.01E-15  0.73
PEPOCH  56276.00000025405092592592
DM      56.8554
DM1     -0.27529
CLK     TT(TAI)
TZRMJD  56276.00000025405092592592
TZRFRQ  -1
TZRSITE @
EPHEM   DE200
UNITS   TDB
```

A.16.2. January 2013

```
PSRJ    J0534+2200
RAJ     05:34:31.97232
DECJ    +22:00:52.069
F0      29.6928275084   2.0
F1      -370403.39E-15  0.35
PEPOCH  56307.00000032239583330000
DM      56.8396
DM1     0.26402
CLK     TT(TAI)
TZRMJD  56307.00000032239583330000
TZRFRQ  -1
TZRSITE @
EPHEM   DE200
UNITS   TDB
```

A.16.3. February 2013

```
PSRJ    J0534+2200
RAJ     05:34:31.97232
DECJ    +22:00:52.069
F0      29.6918354749   3.0
F1      -370369.40E-15  0.49
PEPOCH  56338.00000007214120370000
DM      56.8238
DM1     -0.64139
CLK     TT(TAI)
TZRMJD  56338.00000007214120370000
```

```
TZRFRQ  -1
TZRSITE @
EPHEM   DE200
UNITS   TDB
```

A.17. Radio & γ-Observations Overlap

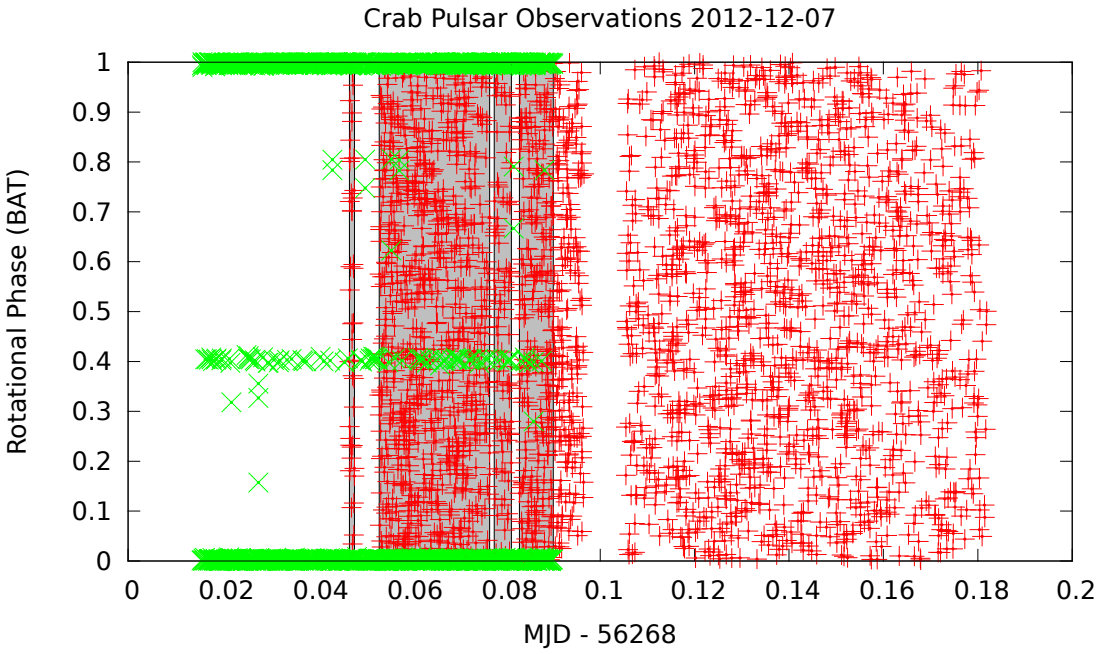

Figure A.1.: Overlap: Radio Observations from 2012-12-07 and γ-Observations from 2012-12-07. The red data points represent the respective γ-ray data set, the green ones the radio data set and the grey areas reflect the time spans of simultaneous observations. The same notations are used for all other figures in this section.

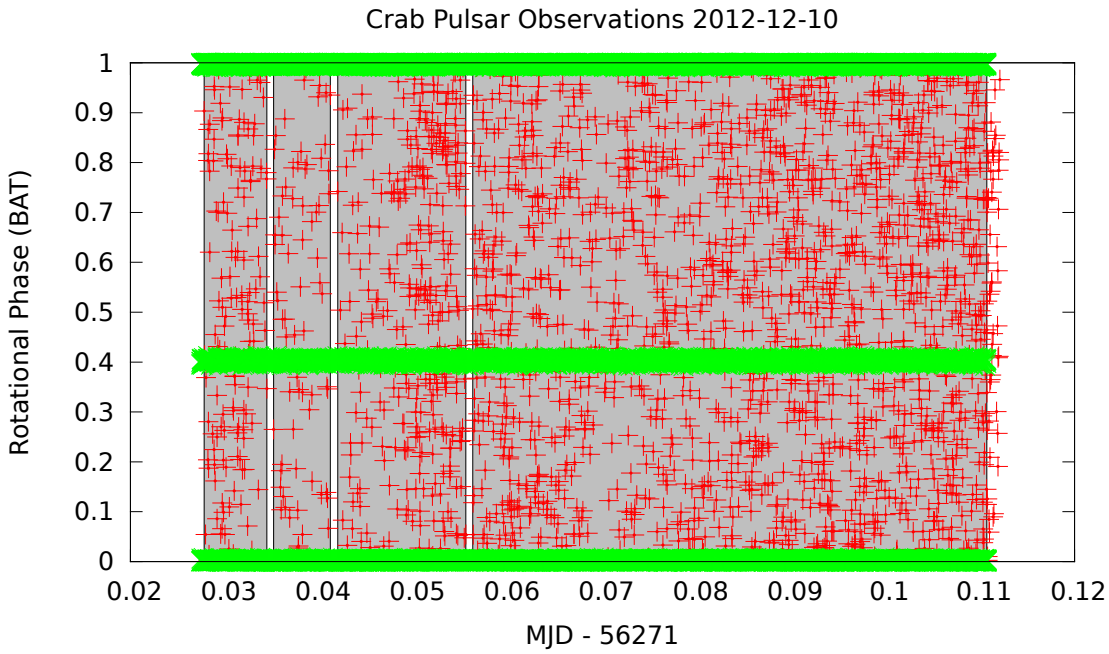

Figure A.2.: Overlap: Radio Observations from 2012-12-10 and γ-Observations from 2012-12-10. The radio observations were carried out with the WSRT.

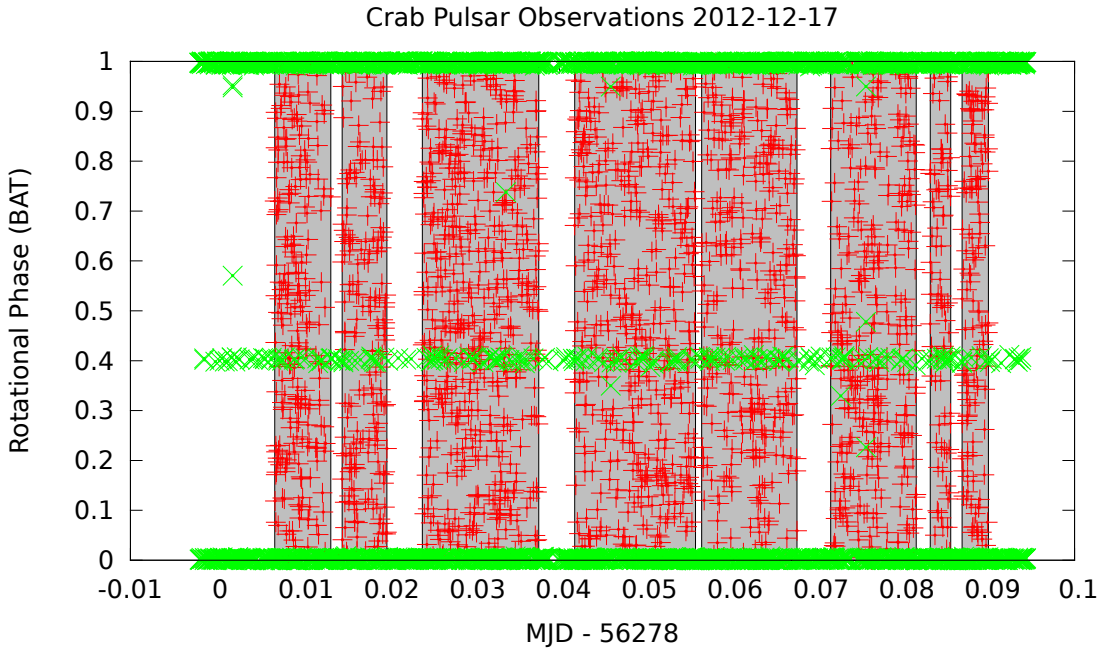

Figure A.3.: Overlap: Radio Observations from 2012-12-17 and γ-Observations from 2012-12-17.

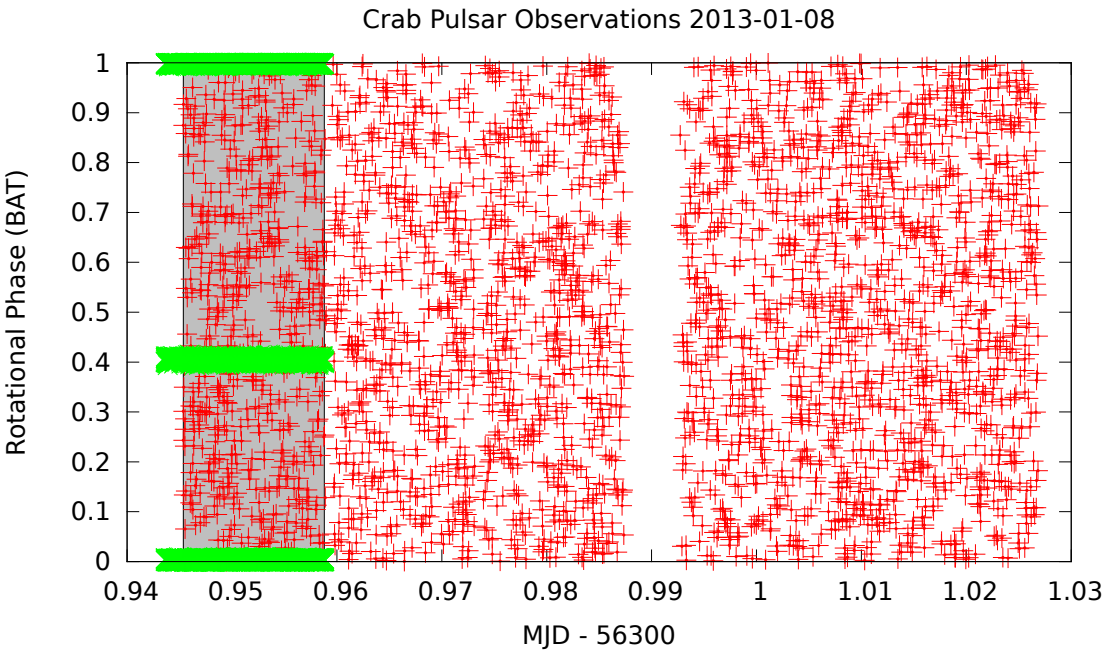

Figure A.4.: Overlap: Radio Observations from 2013-01-08 and γ-Observations from 2013-01-09. The radio observations were carried out with the WSRT.

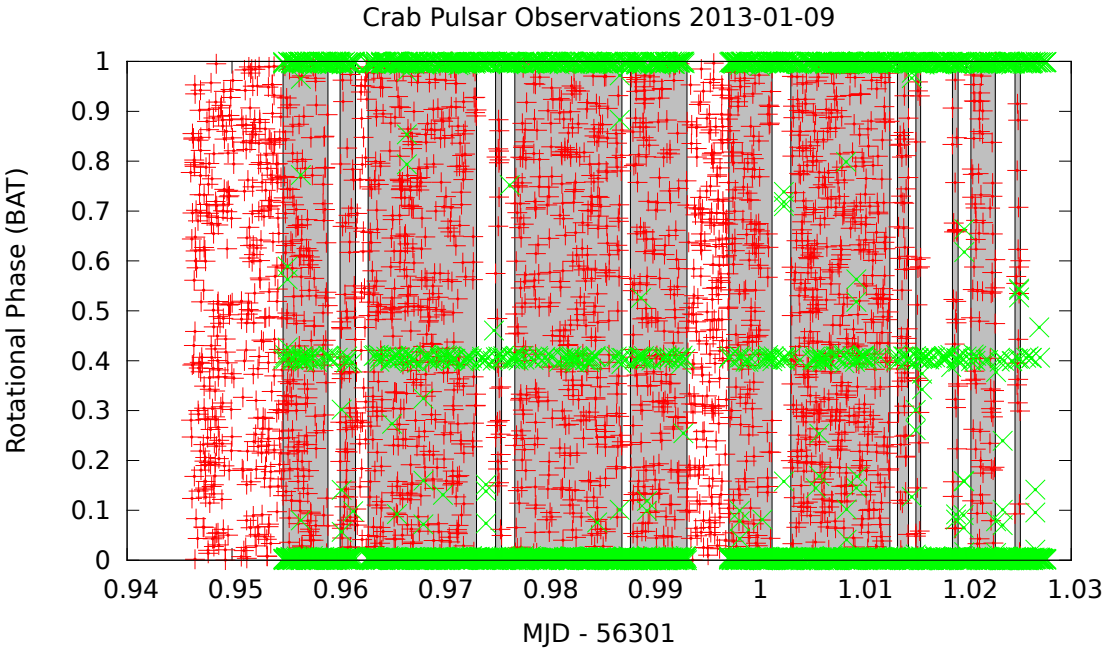

Figure A.5.: Overlap: Radio Observations from 2013-01-09 and γ-Observations from 2013-01-10.

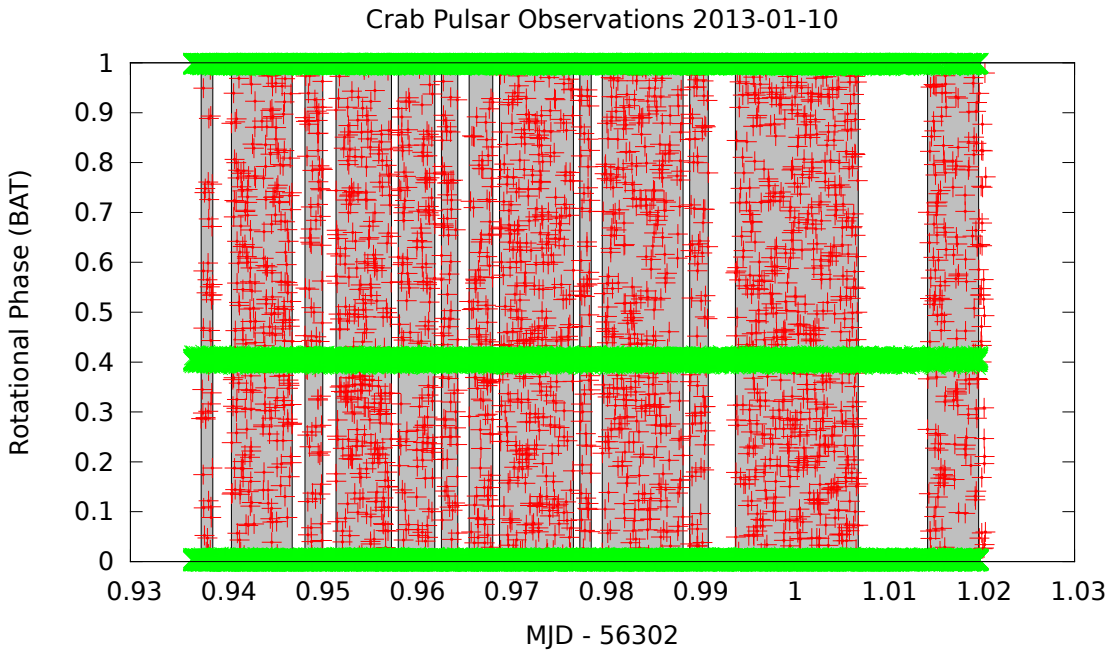

Figure A.6.: Overlap: Radio Observations from 2013-01-10 and γ-Observations from 2013-01-11. The radio observations were carried out with the WSRT.

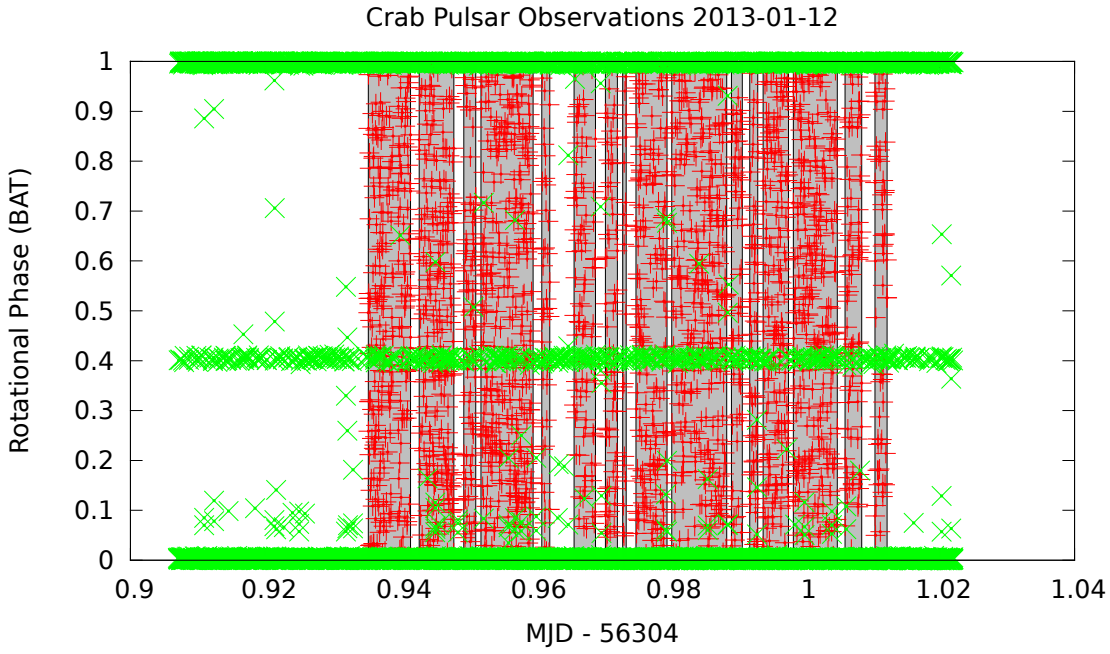

Figure A.7.: Overlap: Radio Observations from 2013-01-12 and γ-Observations from 2013-01-13.

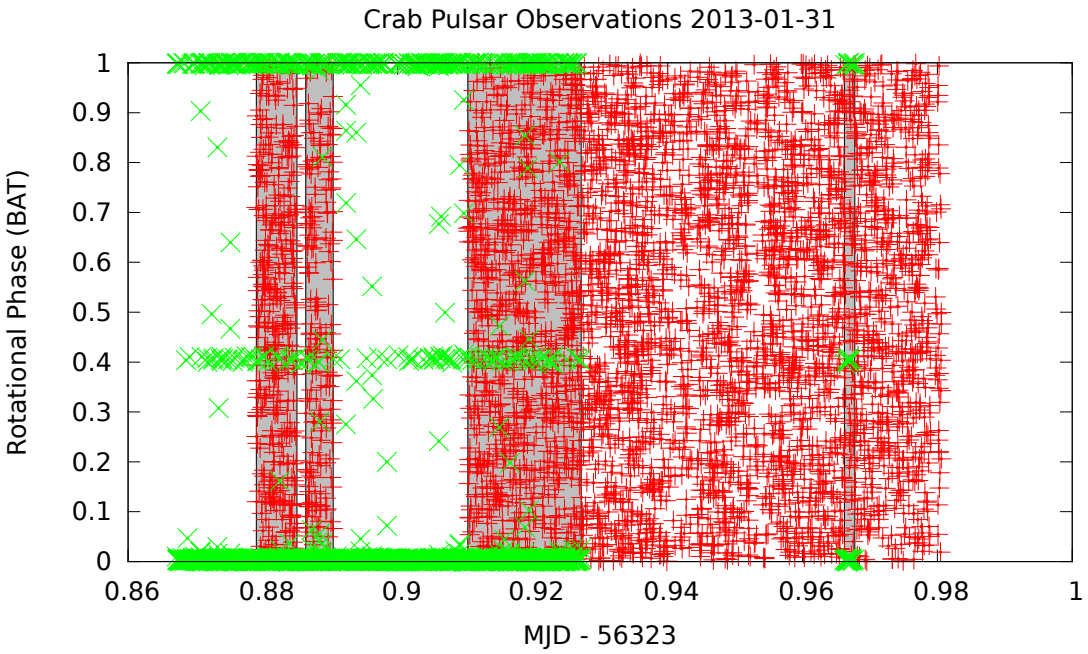

Figure A.8.: Overlap: Radio Observations from 2013-01-31 and γ-Observations from 2013-02-01.

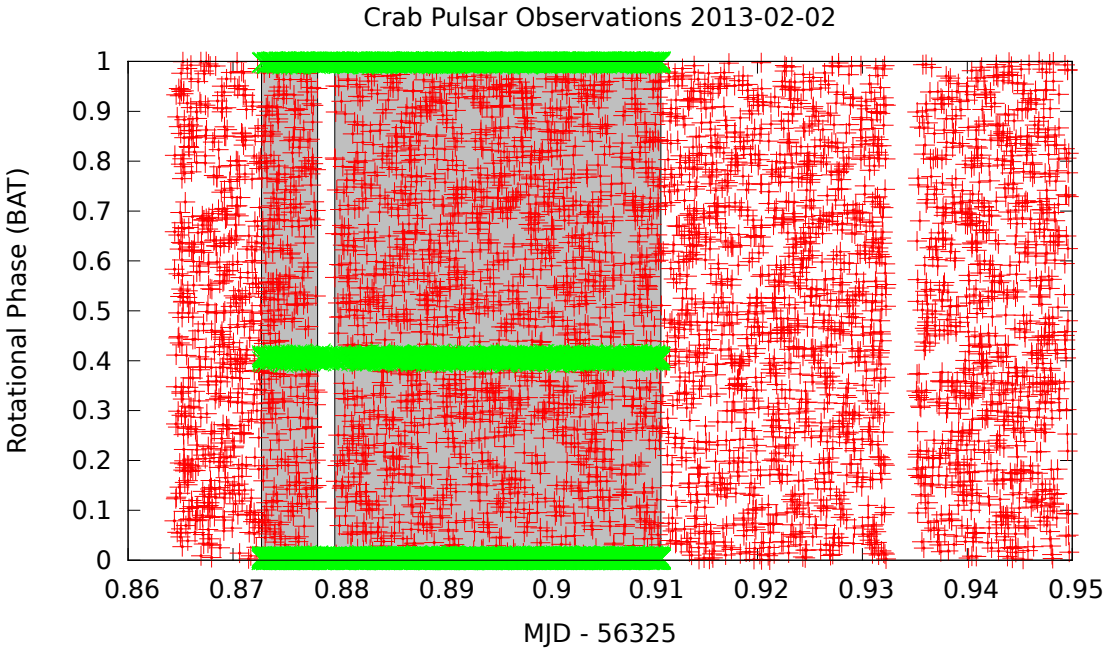

Figure A.9.: Overlap: Radio Observations from 2013-02-02 and γ-Observations from 2013-02-03.

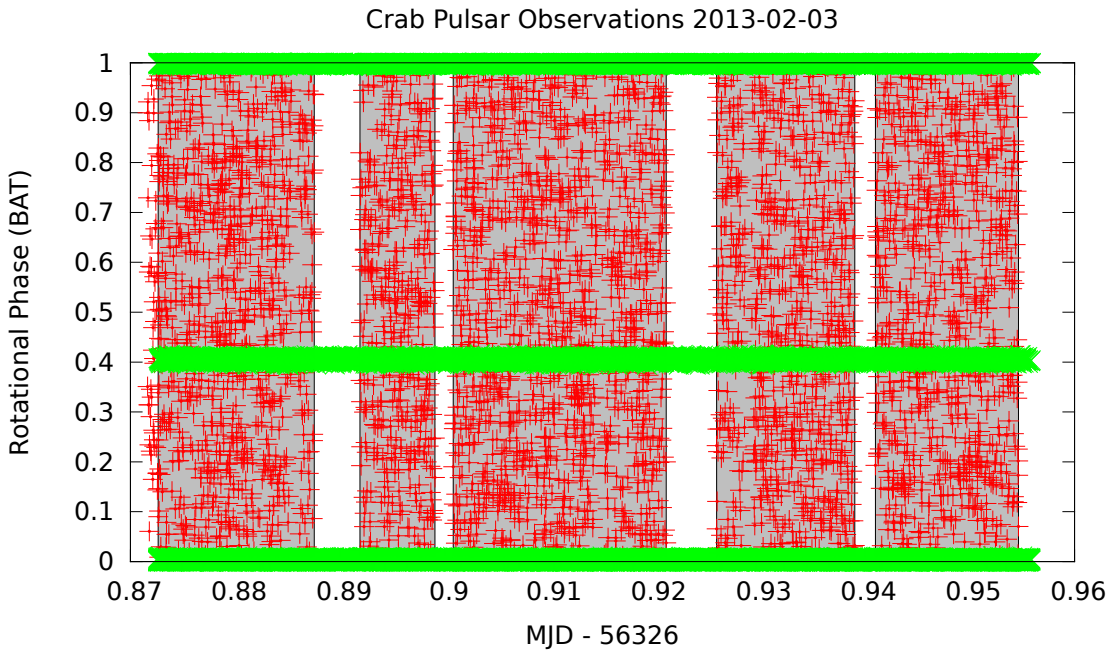

Figure A.10.: Overlap: Radio Observations from 2013-02-03 and γ-Observations from 2013-02-04.

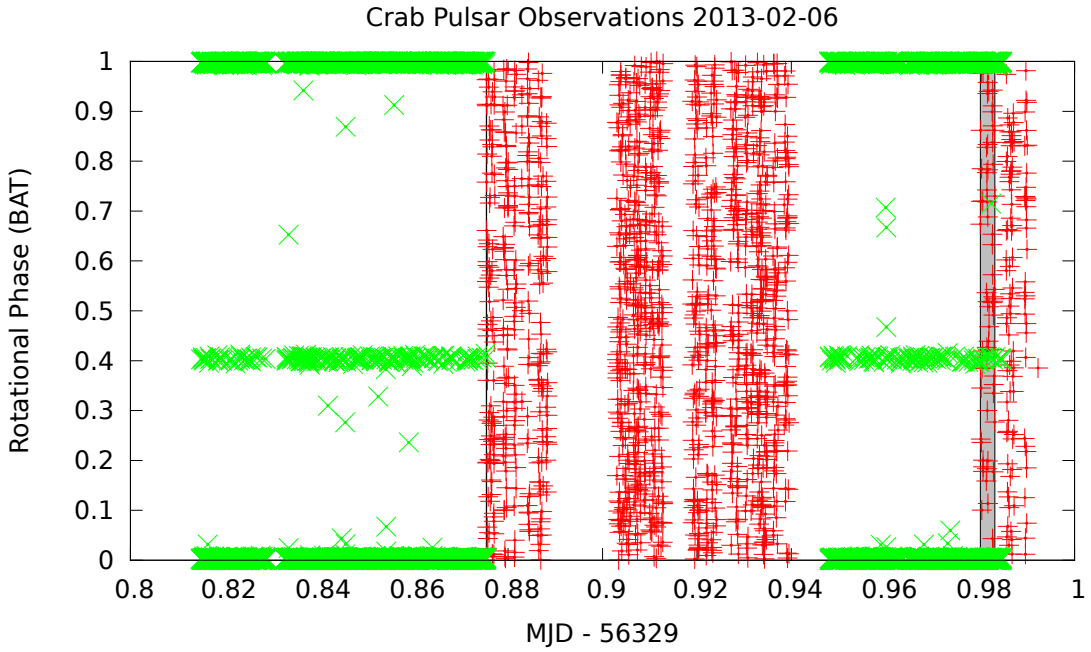

Figure A.11.: Overlap: Radio Observations from 2013-02-06 and γ-Observations from 2013-02-07.

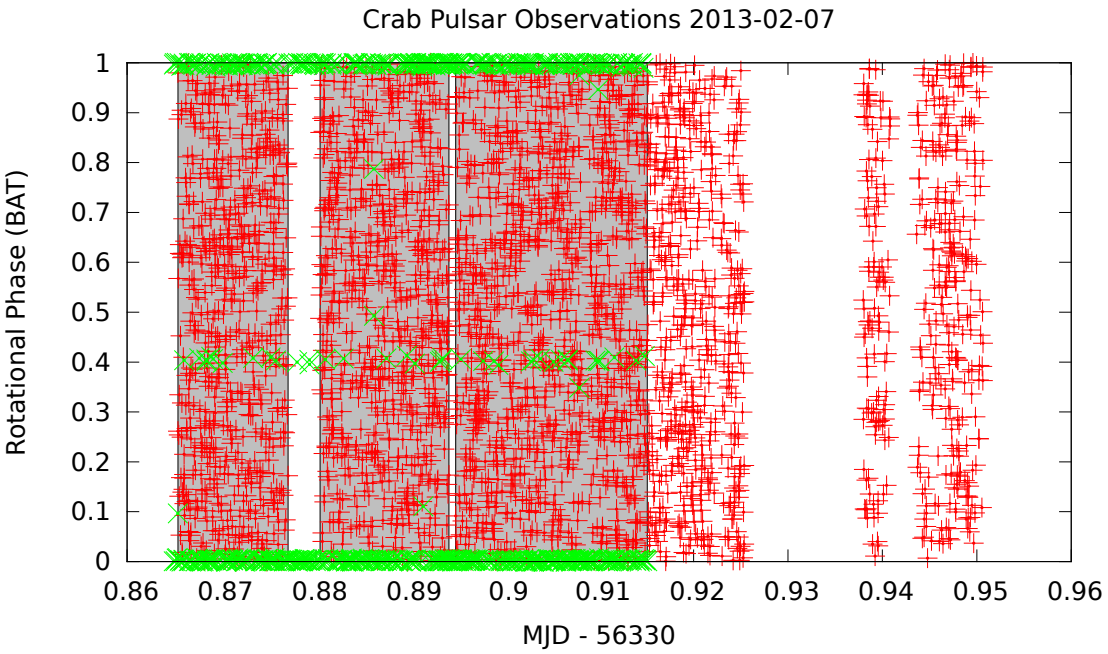

Figure A.12.: Overlap: Radio Observations from 2013-02-07 and γ-Observations from 2013-02-08.

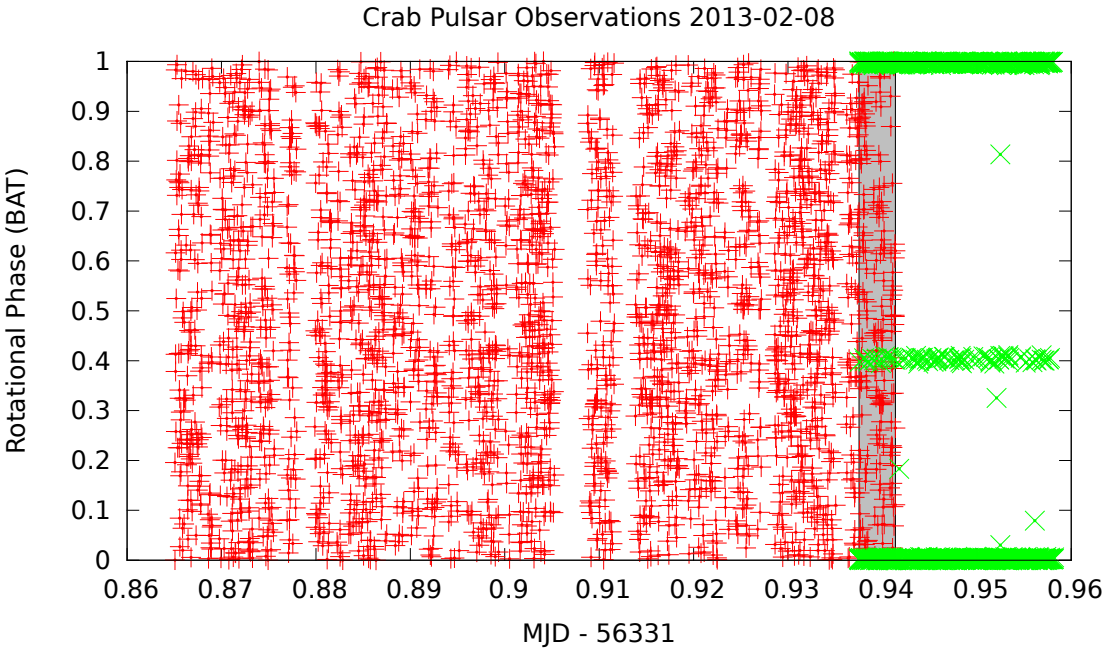

Figure A.13.: Overlap: Radio Observations from 2013-02-08 and γ-Observations from 2013-02-09.

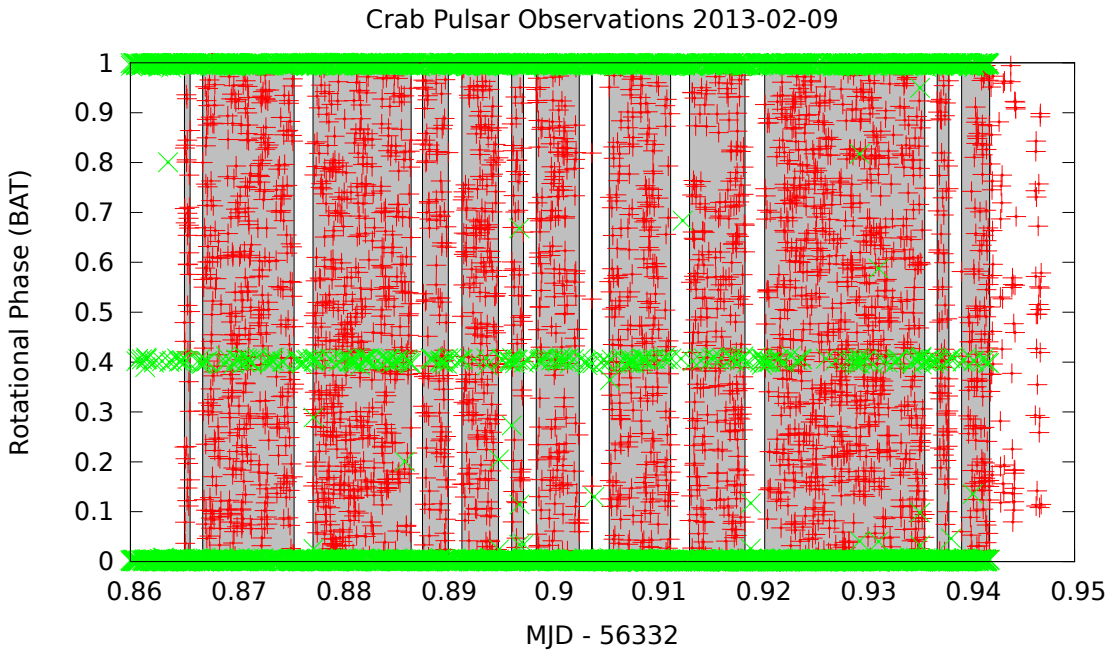

Figure A.14.: Overlap: Radio Observations from 2013-02-09 and γ-Observations from 2013-02-10.

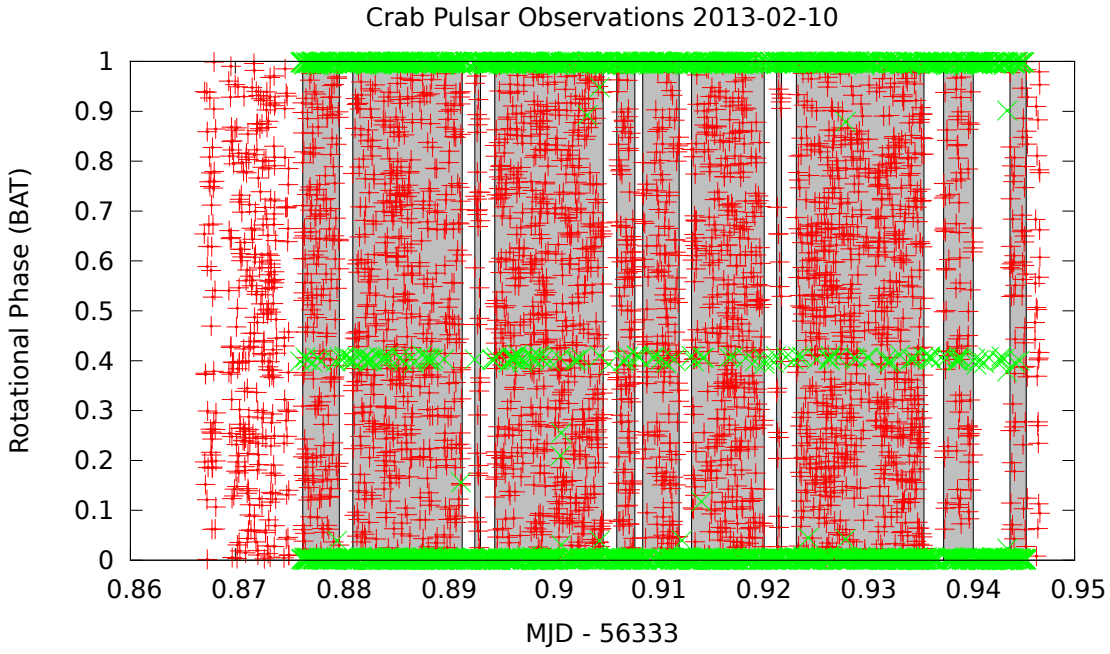

Figure A.15.: Overlap: Radio Observations from 2013-02-10 and γ-Observations from 2013-02-11.

A.18. Radio MC Simulations

A.18.1. 2012-12-07

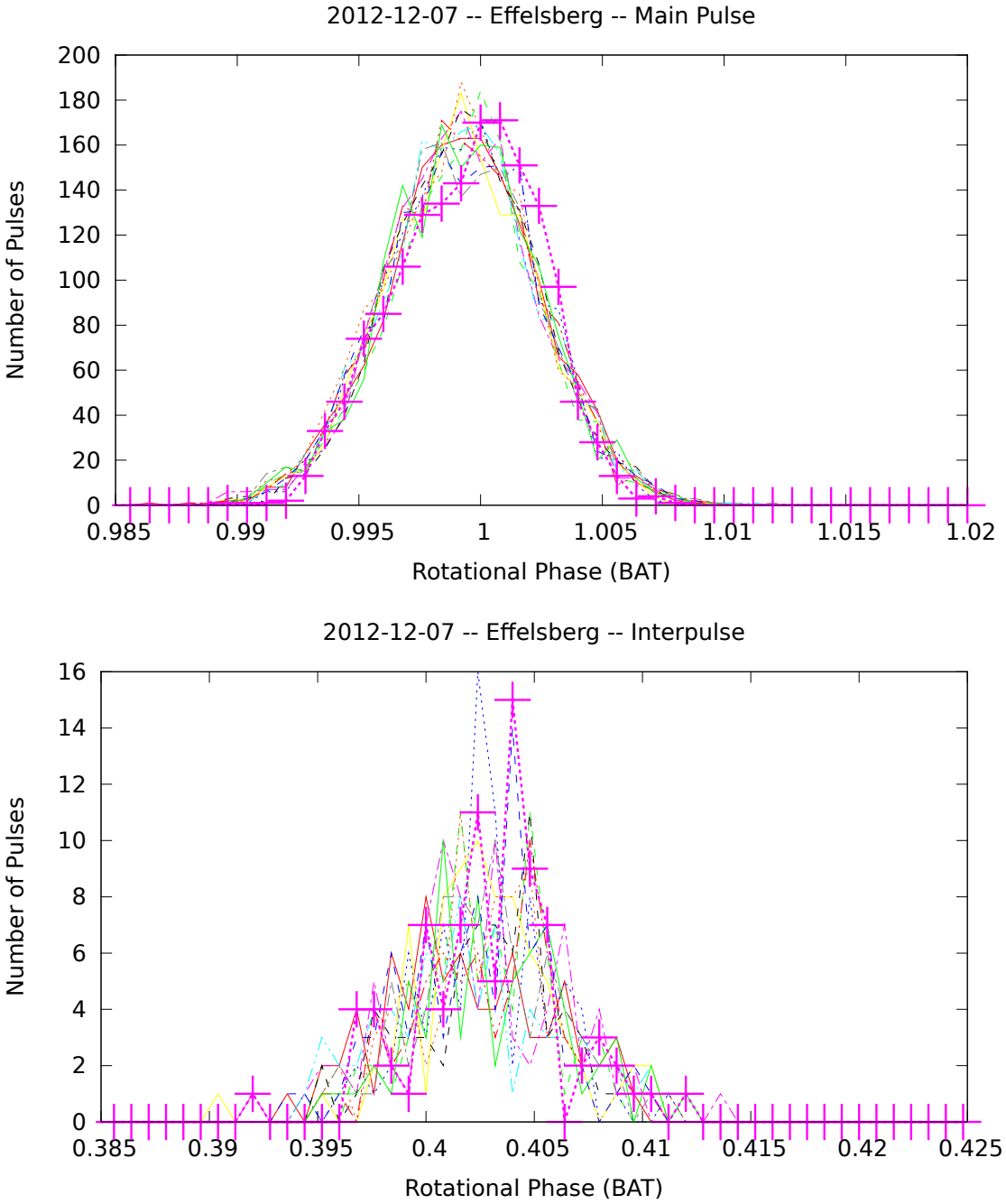

Figure A.16.: MC Simulations of Effelsberg data from 2012-12-07. 12 MC simulations were built for this data set. The magenta crosses represent the Effelsberg data from 2012-12-07.

A.18.2. 2012-12-10

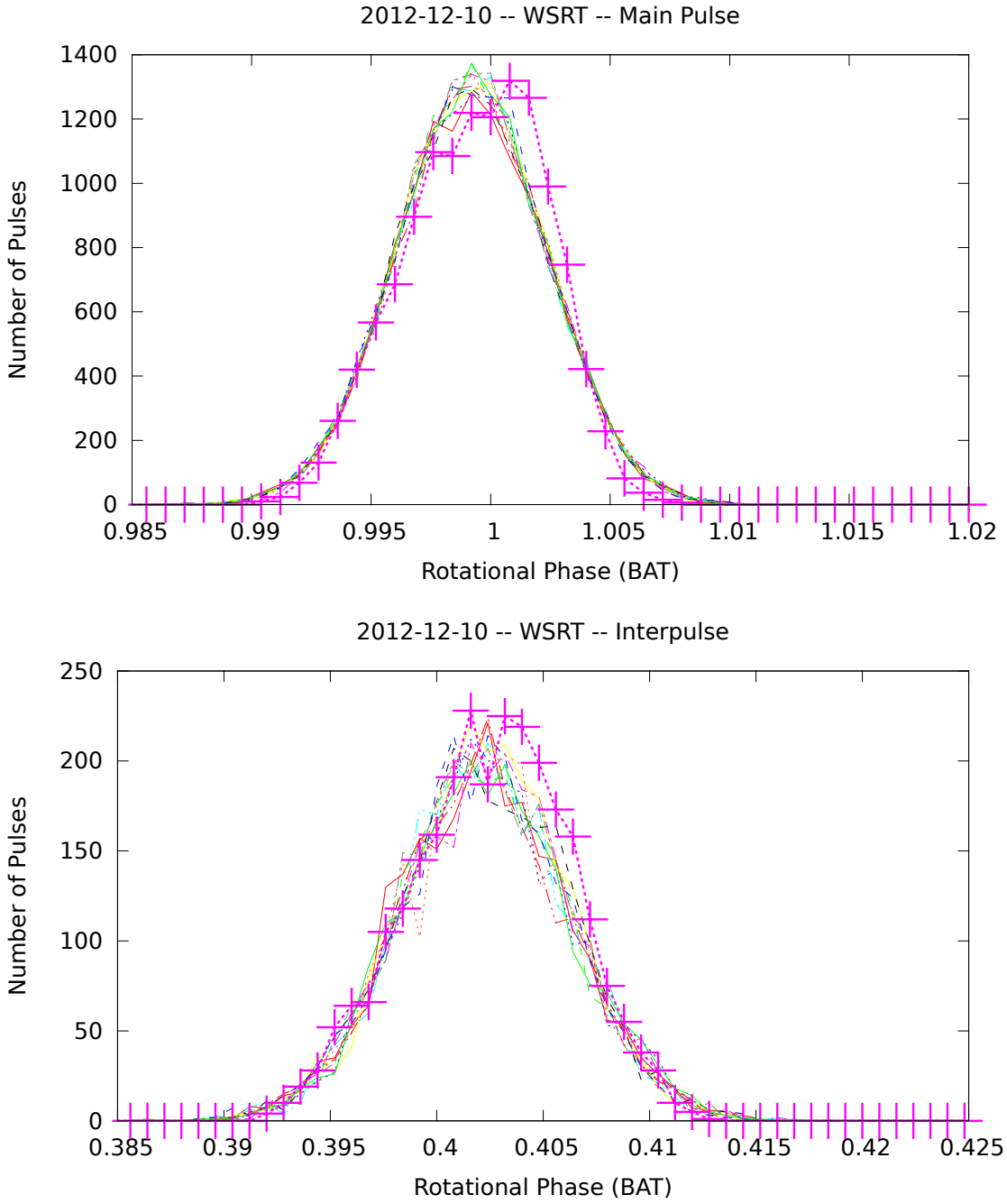

Figure A.17.: MC Simulations of WSRT Data from 2012-12-10. 12 MC simulations were built for this data set. The magenta crosses represent the WSRT data from 2012-12-10.

A.18.3. 2012-12-17

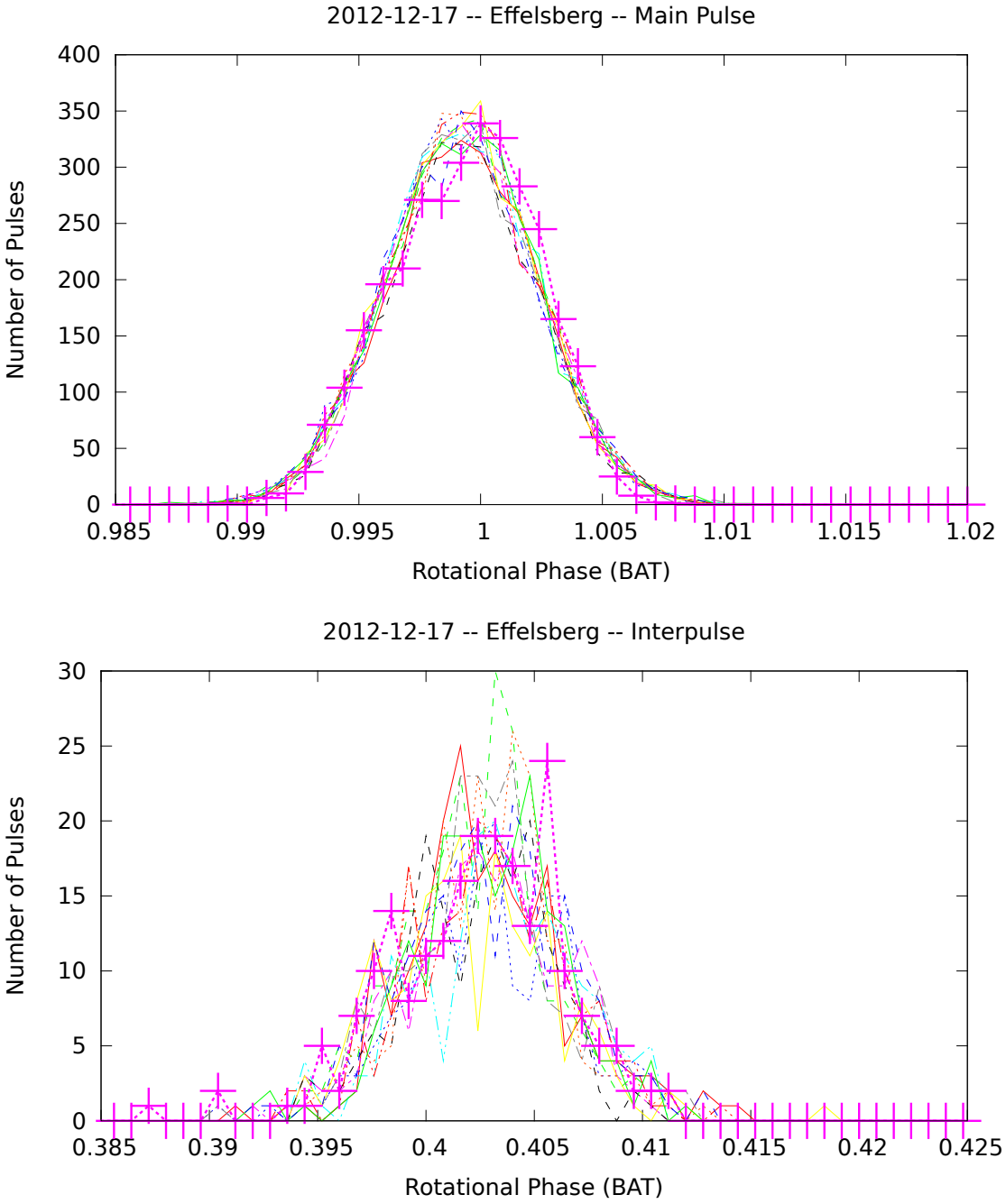

Figure A.18.: MC Simulations of Effelsberg data from 2012-12-17. 12 MC simulations were built for this data set. The magenta crosses represent the Effelsberg data from 2012-12-17.

A.18.4. 2013-01-08

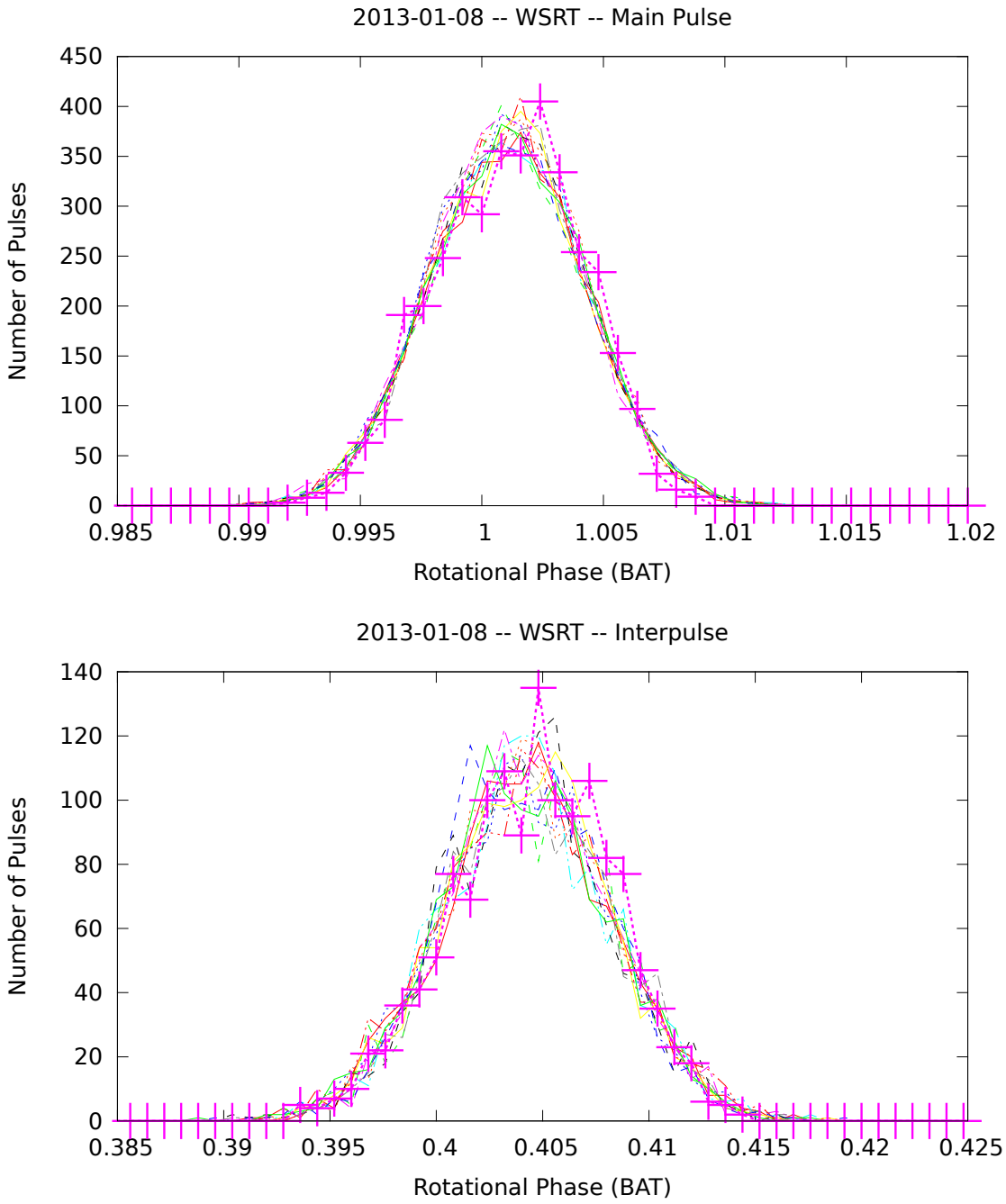

Figure A.19.: MC Simulations of WSRT Data from 2013-01-08. 12 MC simulations were built for this data set. The magenta crosses represent the WSRT data from 2013-01-08.

A.18.5. 2013-01-09

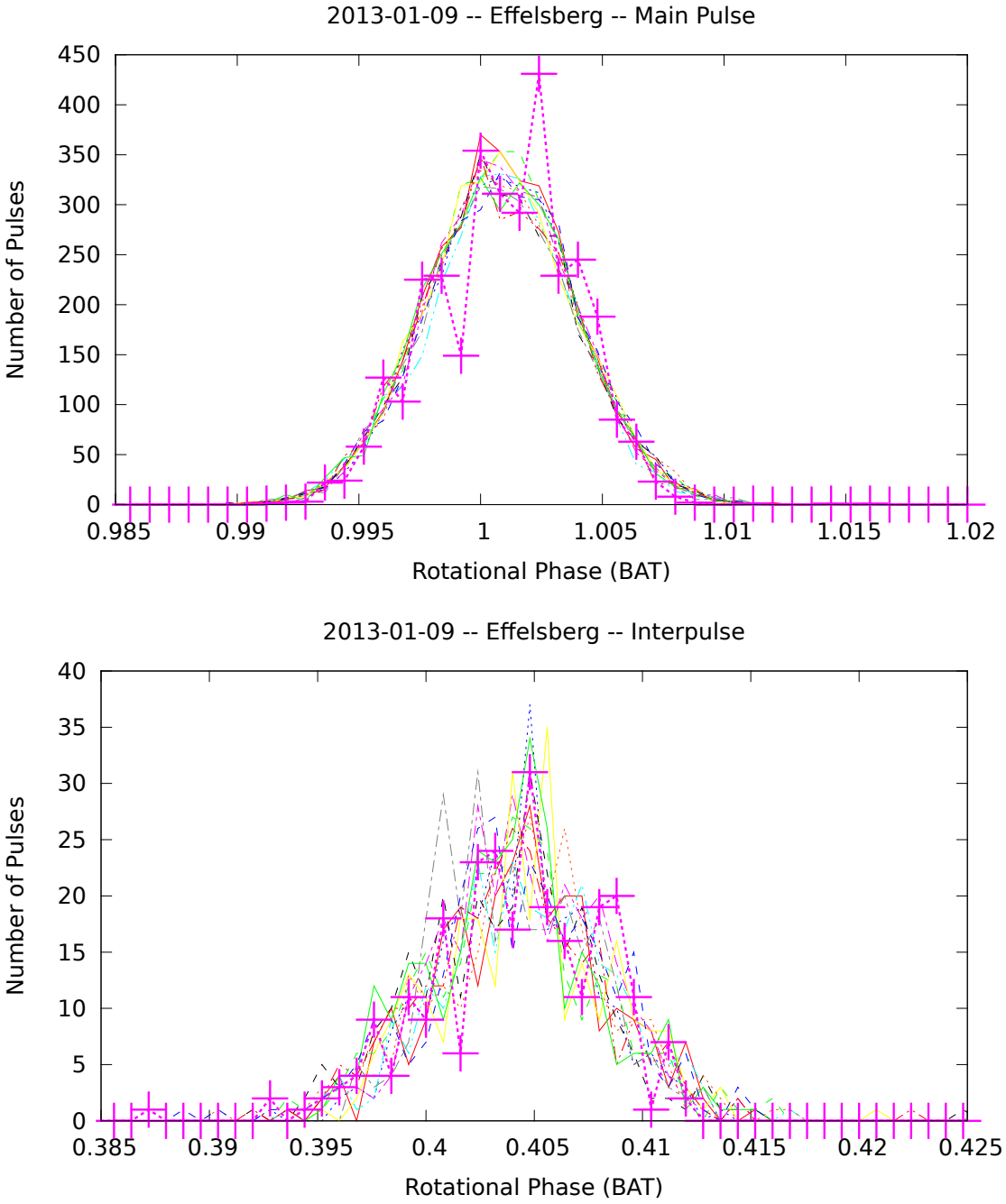

Figure A.20.: MC Simulations of Effelsberg data from 2013-01-09. 12 MC simulations were built for this data set. The magenta crosses represent the Effelsberg data from 2013-01-09.

A.18.6. 2013-01-10

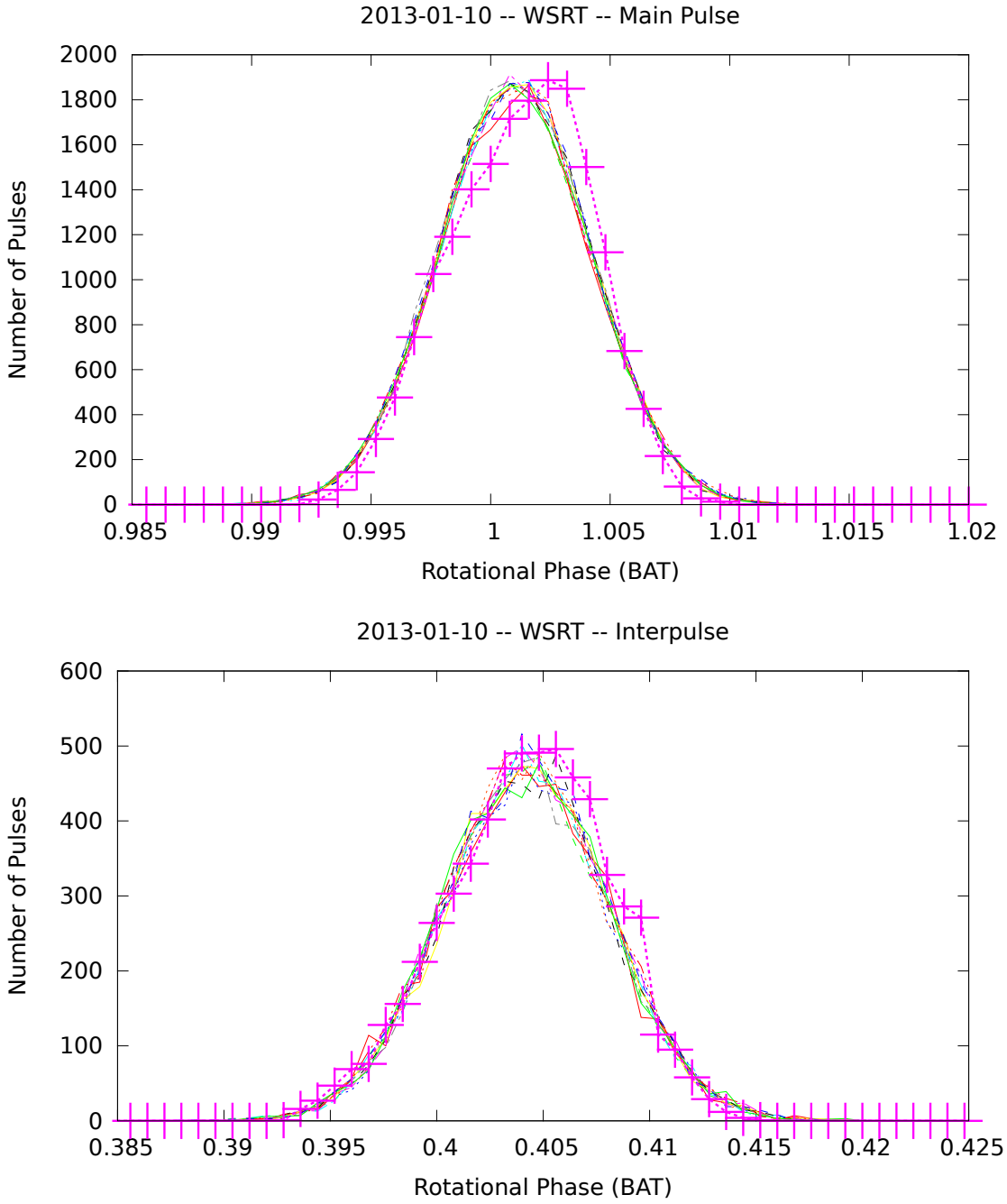

Figure A.21.: MC Simulations of WSRT Data from 2013-01-10. 12 MC simulations were built for this data set. The magenta crosses represent the WSRT data from 2013-01-10.

A.18.7. 2013-01-12

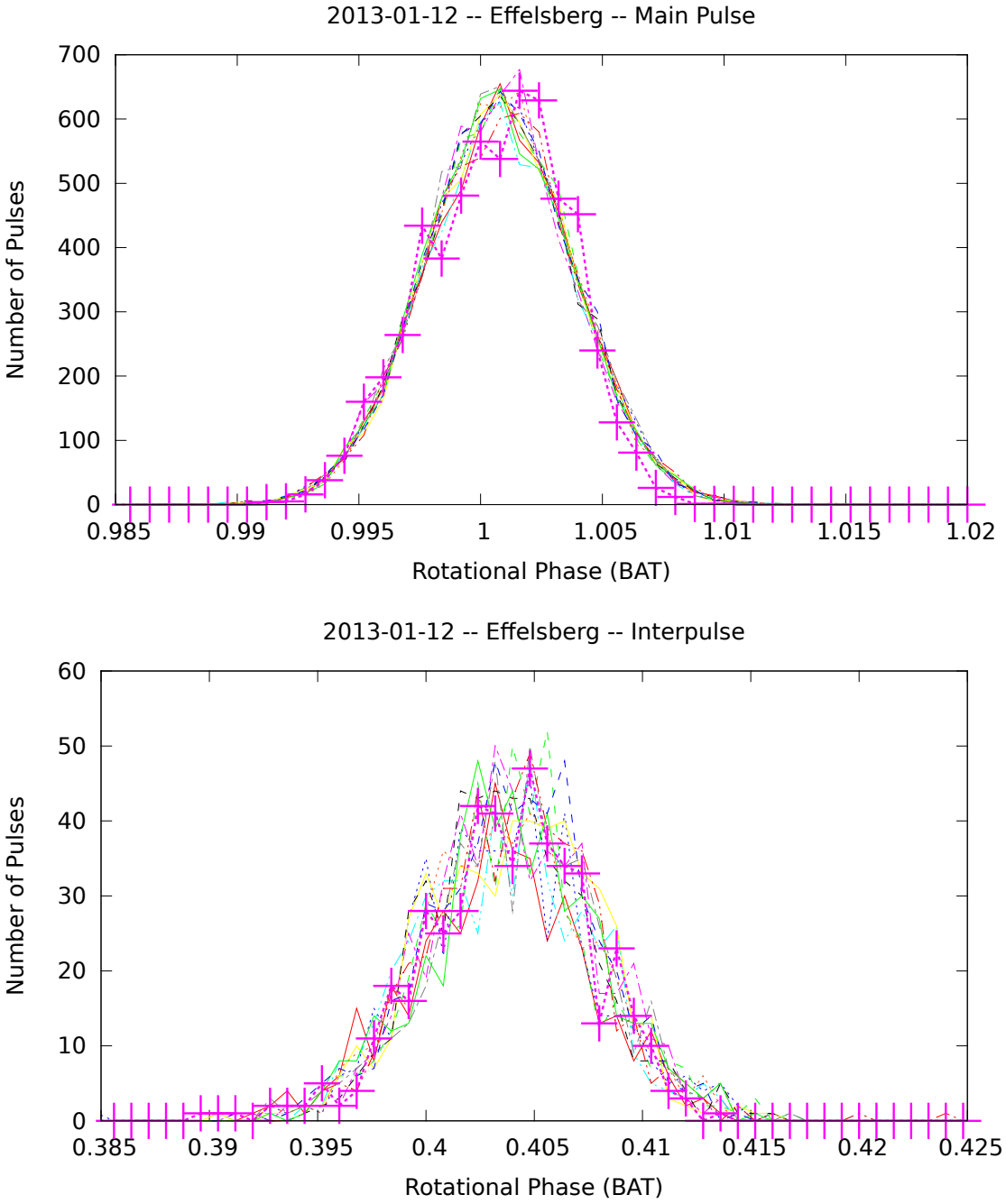

Figure A.22.: MC Simulations of Effelsberg data from 2013-01-12. 12 MC simulations were built for this data set. The magenta crosses represent the Effelsberg data from 2013-01-12.

A.18.8. 2013-01-31

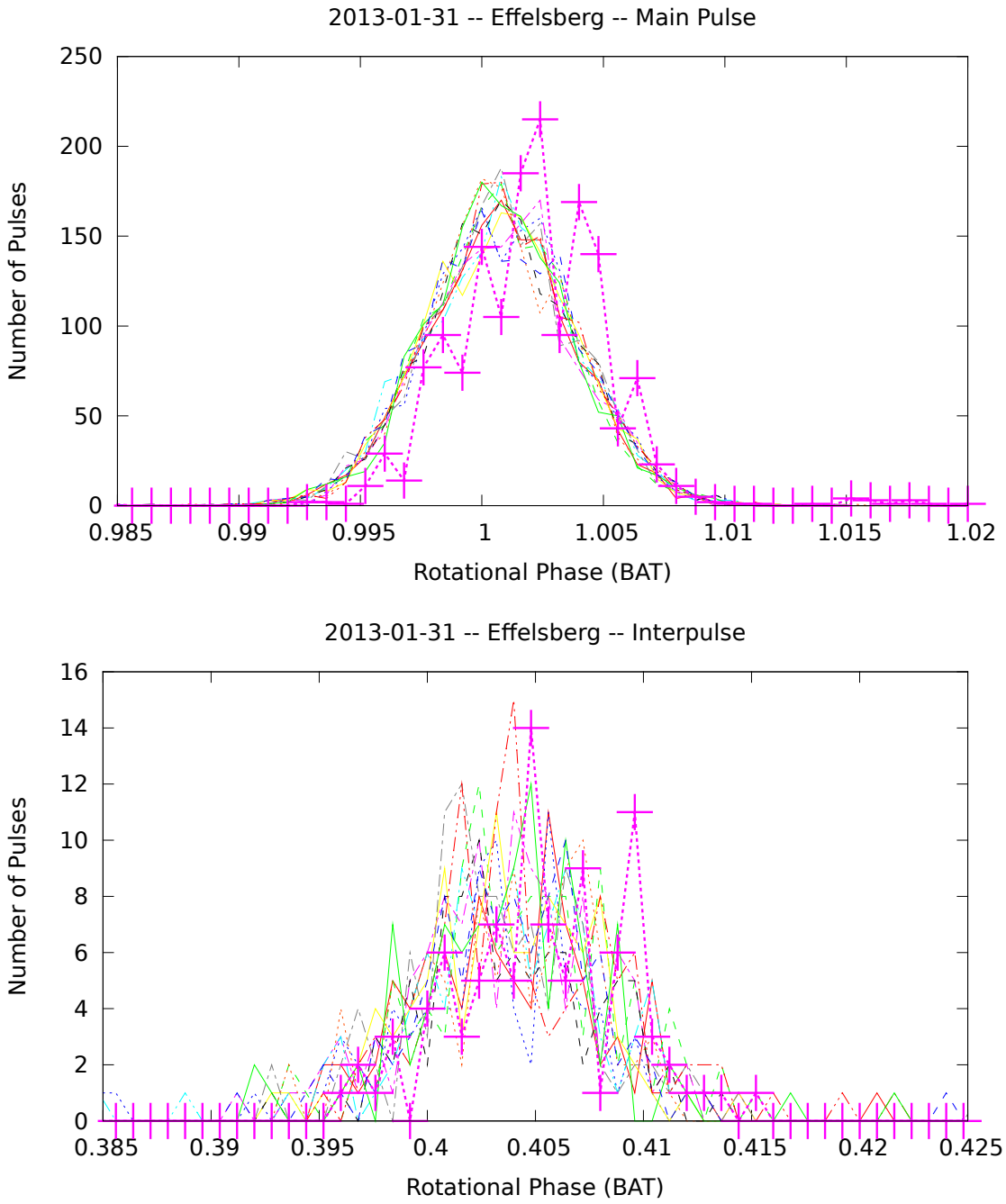

Figure A.23.: MC Simulations of Effelsberg data from 2013-01-31. 12 MC simulations were built for this data set. The magenta crosses represent the Effelsberg data from 2013-01-31.

A.18.9. 2013-02-02

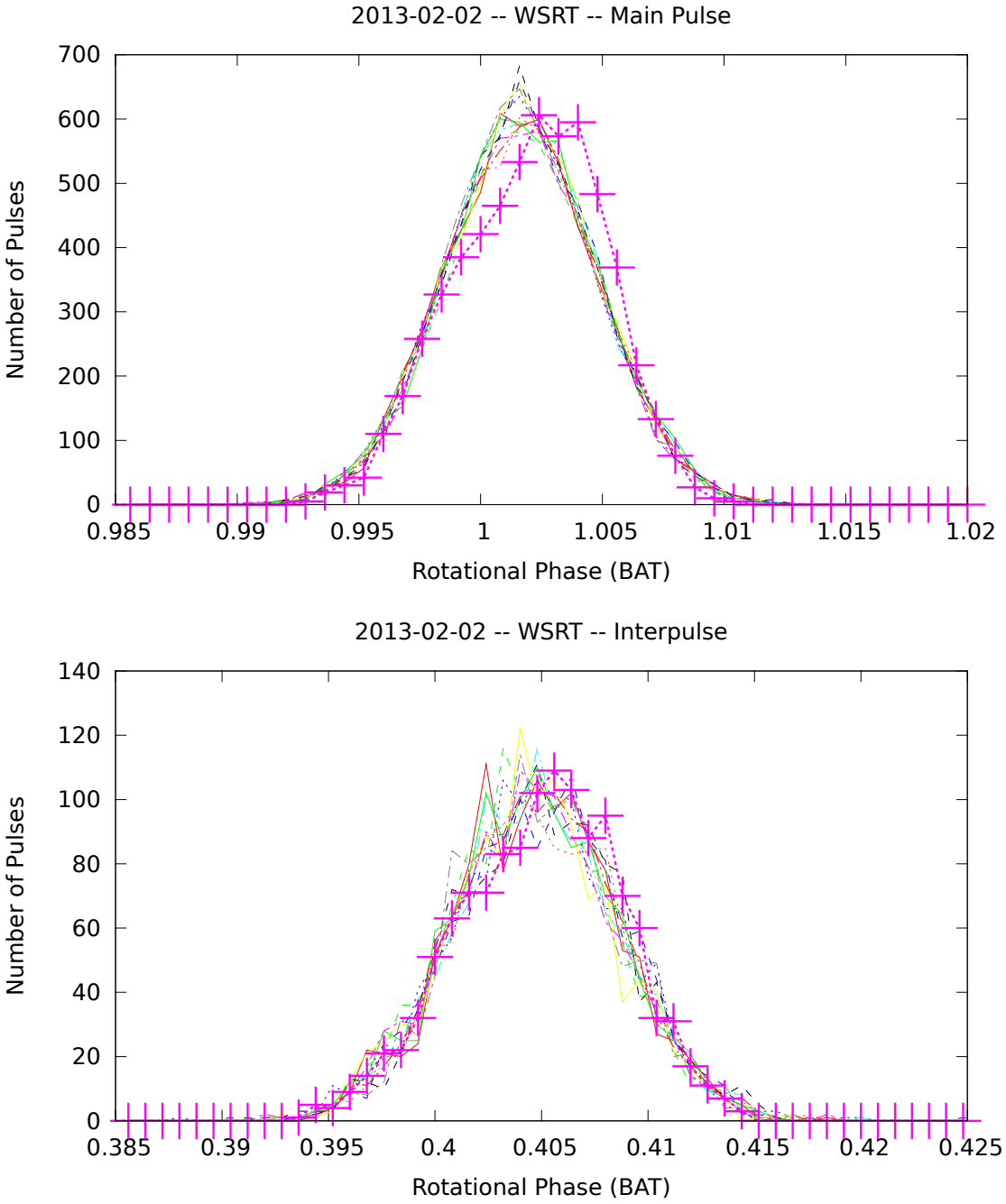

Figure A.24.: MC Simulations of WSRT Data from 2013-02-02. 12 MC simulations were built for this data set. The magenta crosses represent the WSRT data from 2013-02-02.

A.18.10. 2013-02-03

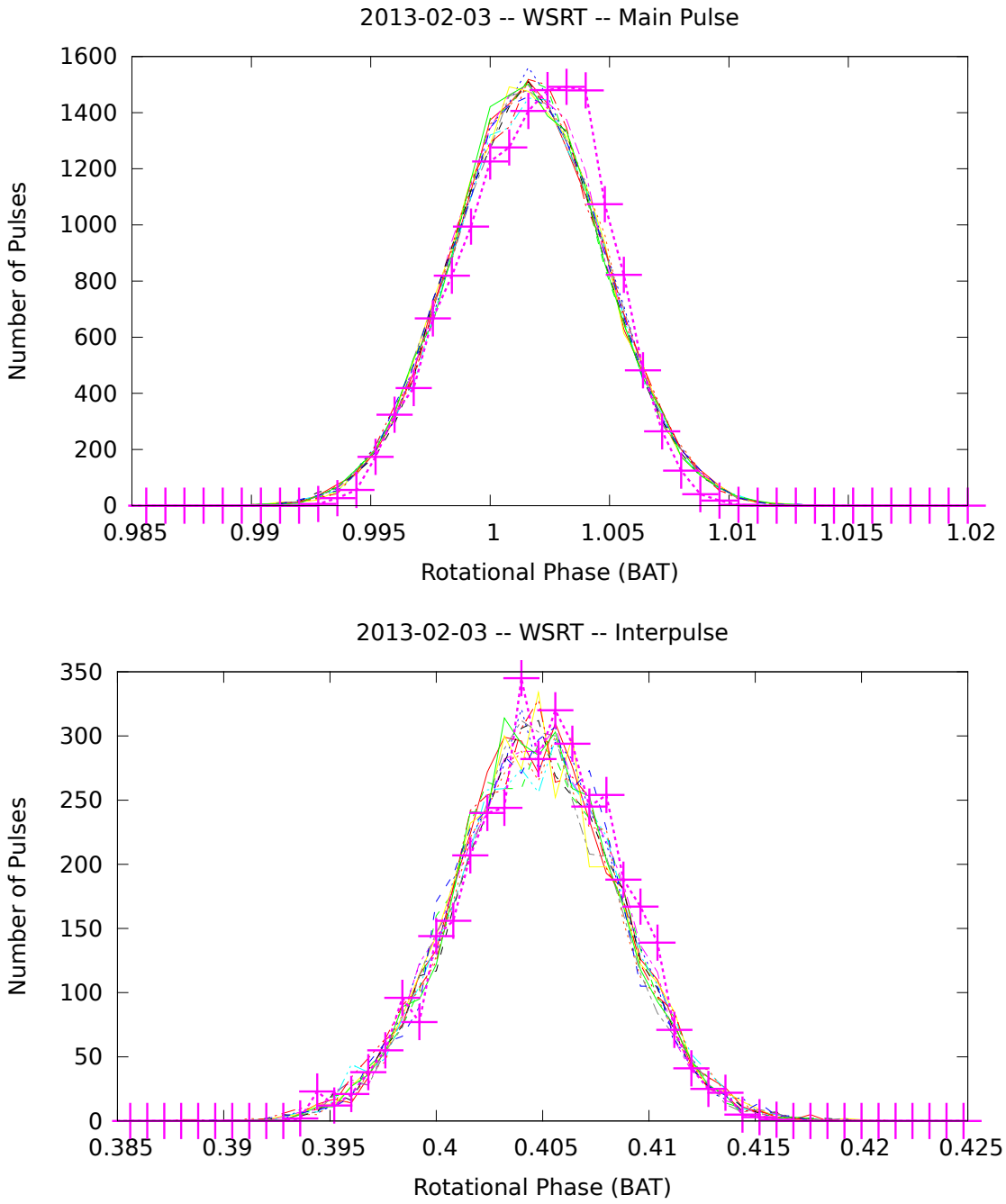

Figure A.25.: MC Simulations of WSRT Data from 2013-02-03. 12 MC simulations were built for this data set. The magenta crosses represent the WSRT data from 2013-02-03.

A.18.11. 2013-02-06

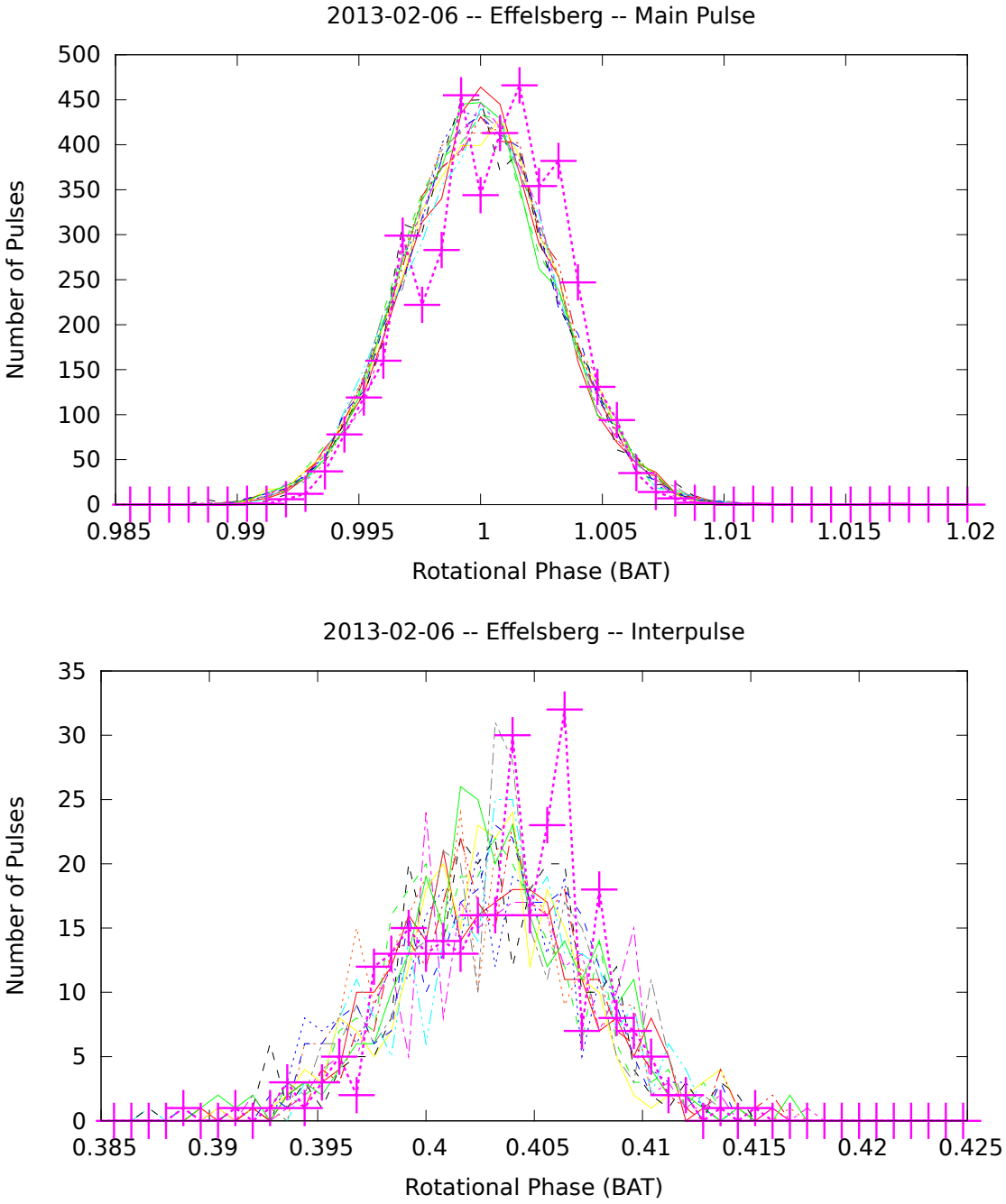

Figure A.26.: MC Simulations of Effelsberg data from 2013-02-06. 12 MC simulations were built for this data set. The magenta crosses represent the Effelsberg data from 2013-02-06.

A.18.12. 2013-02-07

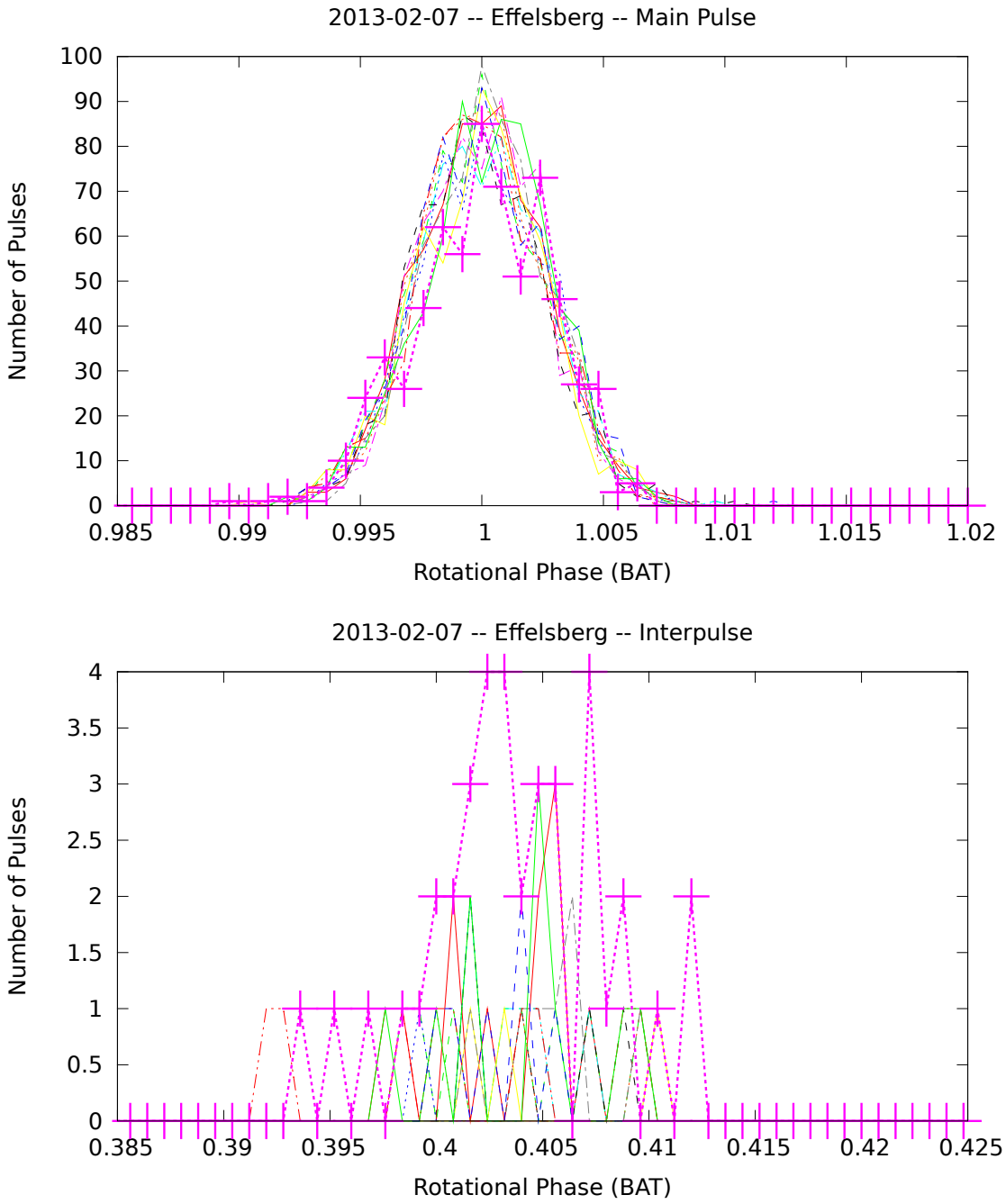

Figure A.27.: MC Simulations of Effelsberg data from 2013-02-07. 12 MC simulations were built for this data set. The magenta crosses represent the Effelsberg data from 2013-02-07.

A.18.13. 2013-02-08

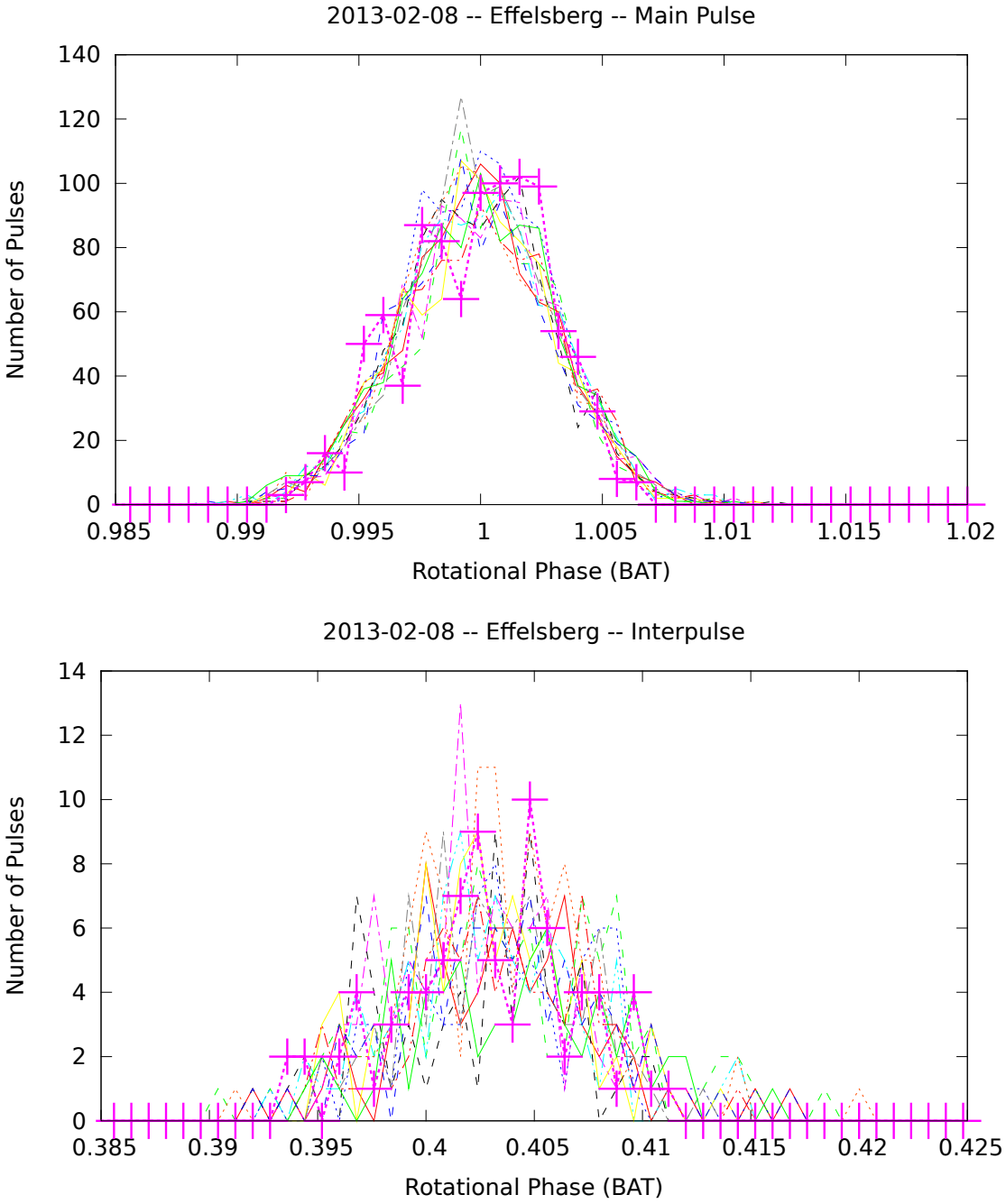

Figure A.28.: MC Simulations of Effelsberg data from 2013-02-08. 12 MC simulations were built for this data set. The magenta crosses represent the Effelsberg data from 2013-02-08.

A.18.14. 2013-02-09

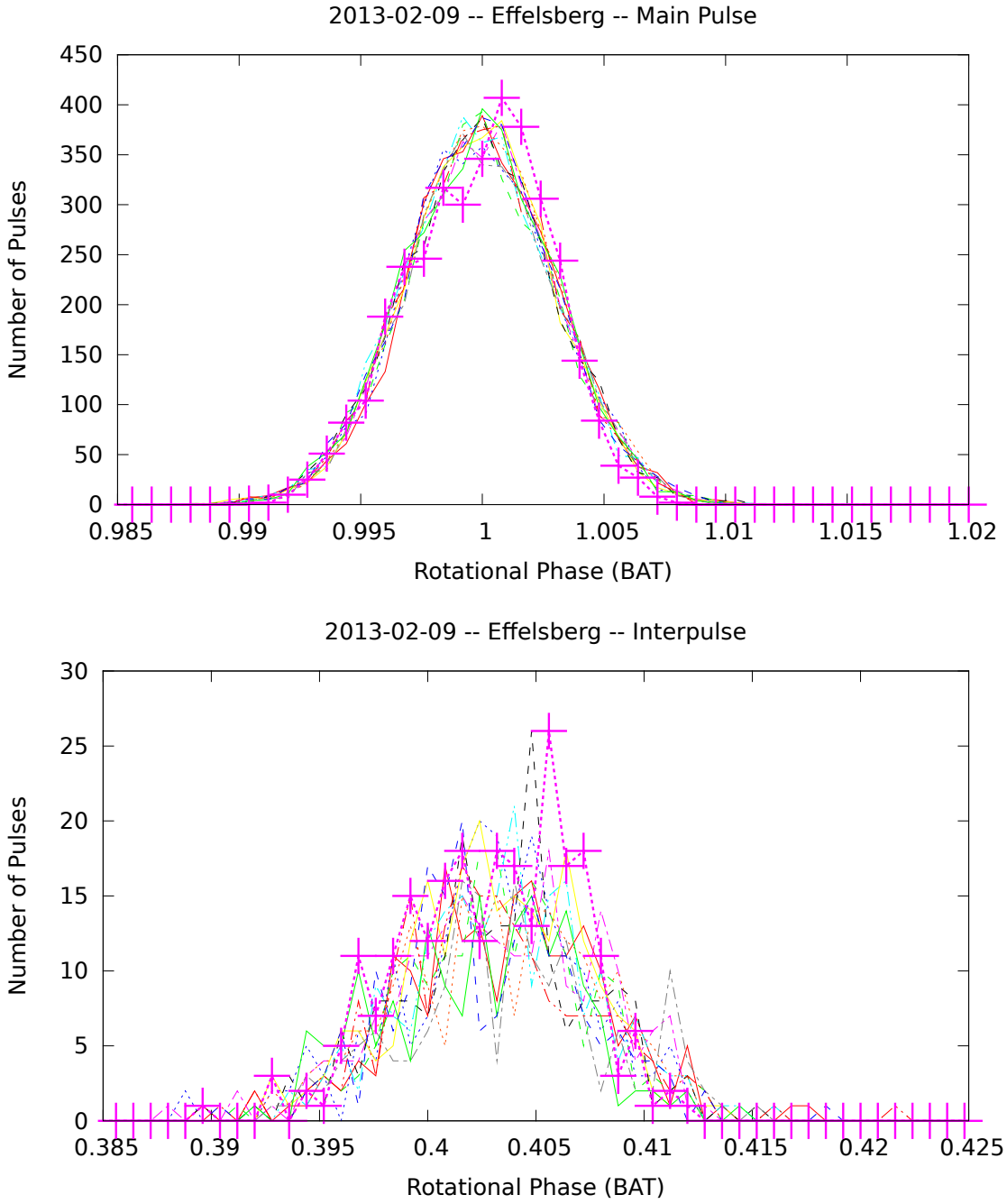

Figure A.29.: MC Simulations of Effelsberg data from 2013-02-09. 12 MC simulations were built for this data set. The magenta crosses represent the Effelsberg data from 2013-02-09.

A.18.15. 2013-02-10

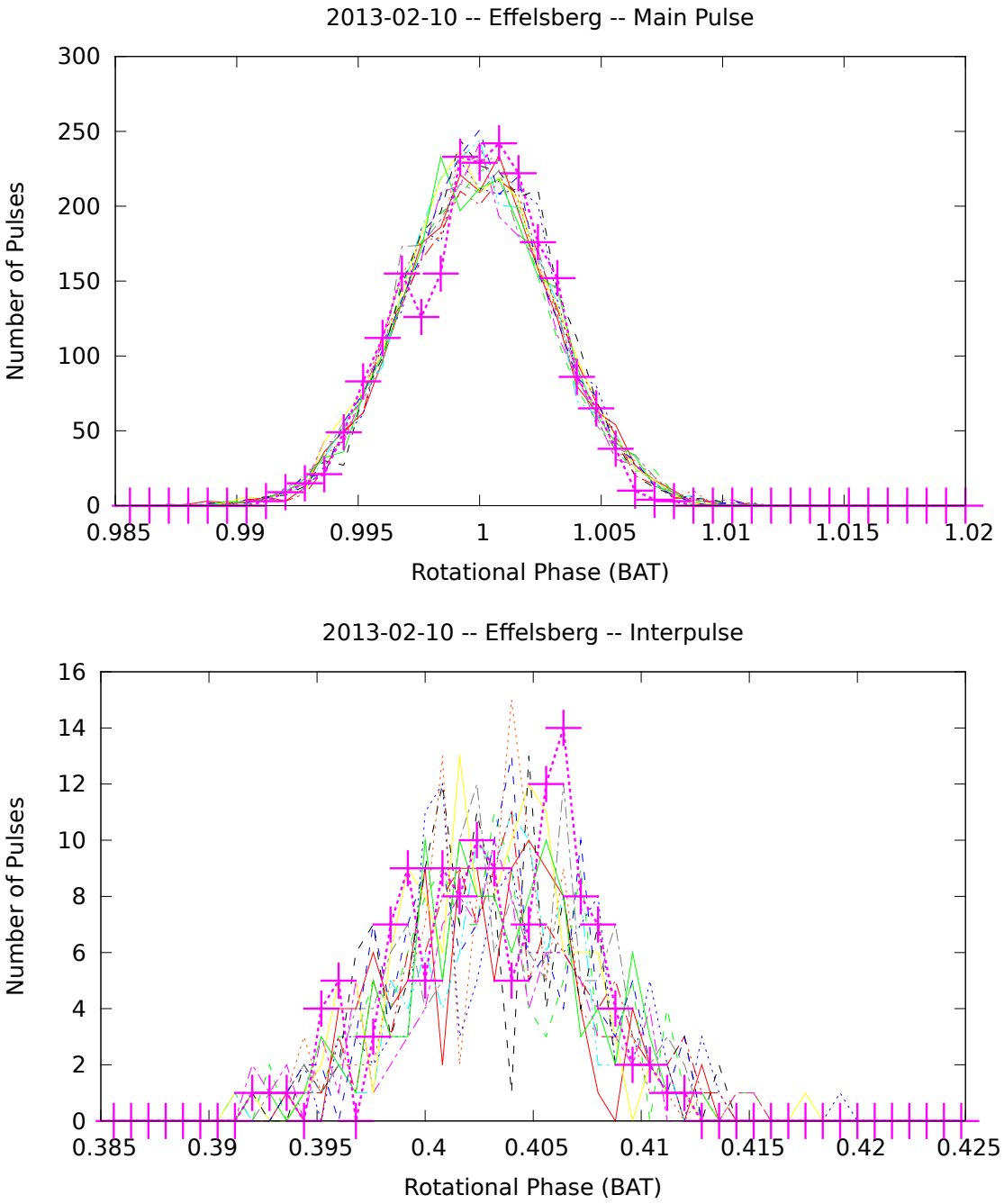

Figure A.30.: MC Simulations of Effelsberg data from 2013-02-10. 12 MC simulations were built for this data set. The magenta crosses represent the Effelsberg data from 2013-02-10.

B. MAGIC Data Sets

B.1. Time Stamp Check – γ-ray Data

Epoch	Runnumber	Y	Q	Y-Q	M1	M2
20130201	05022951	319770	220319	0	x	
		319965	220319	0		x
	05022952	29965	13361	0	x	
		30019	13361	0		x
	05022955	236549	154750	0	x	
		236593	154750	0		x
	05022960	308004	223338	0	x	
		308337	223338	0		x
	05022961	287808	223517	0	x	
		287871	223517	0		x
	05022962	278024	198732	0	x	
		277924	198732	0		x
	05022963	274315	208071	0	x	
		274344	208071	0		x
	05022964	265443	202826	0	x	
		266206	202826	0		x
	05022965	228149	183717	0	x	
		230257	183717	0		x
	05022966	189130	67382	0	x	
		191024	67382	0		x
20130202	05022972	245803	122297	0	x	
		246196	122297	0		x
20130203	05022991	683098	246783	0	x	
		342480	246783	0		x
	05022992	656128	223715	0	x	
		328668	223715	0		x
	05022993	668468	239847	0	x	
		336044	239847	0		x
	05022994	674758	236208	0	x	
		338131	236208	0		x
	05022995	680744	202750	0	x	
		340778	202750	0		x
	05022996	709182	253426	0	x	
		357991	253426	0		x
	05022997	25672	9139	0	x	
		38213	9139	0		x
	05023000	694998	255378	0	x	
		348999	255378	0		x
	05023001	710084	18093	0	x	
		356584	18093	0		x
	05023002	709684	260908	0	x	
		357394	260908	0		x
	05023003	720092	257346	0	x	
		361399	257346	0		x

Table B.1.: A comparison of the number of MJD entries in calibrated files (Sorcerer files, designated with "Y") with merged data (Melibea files, noted by a "Q" in the list).

Epoch	Runnumber	Y	Q	Y-Q	M1	M2
	05023004	707564	28005	0	x	
		358825	28005	0		x
20130204	05023036	289603	137876	9194	x	
		303218	137876	0		x
	05023037	352130	247677	0	x	
		354018	247677	0		x
	05023038	339434	242359	0	x	
		340808	242359	0		x
	05023039	38444	27508	0	x	
		63625	27508	0		x
	05023042	175720	126470	0	x	
		176524	126470	0		x
	05023045	330620	239367	0	x	
		331727	239367	0		x
	05023046	334680	160981	0	x	
		335404	160981	0		x
	05023047	237336	175591	0	x	
		212120	175591	18765		x
	05023050	331161	246322	0	x	
		331723	246322	0		x
	05023053	330127	227367	0	x	
		331257	227367	0		x
	05023054	334427	230375	0	x	
		335315	230375	0		x
	05023055	333394	229803	0	x	
		334607	229803	0		x
	05023056	338136	253698	0	x	
		338962	253698	0		x
	05023057	333898	113883	0	x	
		334707	113883	0		x
20130207	05023209	297221	93655	0		x
	05023211	301257	136478	0	x	
		301441	136478	0		x
	05023212	295406	100856	0	x	
		295279	100856	0		x
	05023213	294947	87406	0	x	
		295247	87406	0		x
	05023216	276754	57058	0	x	
		277192	57058	0		x
	05023217	307281	10468	0	x	
		307564	10468	0		x
20130208	05023261	251316	187575	0	x	
		290738	187575	0		x
	05023264	275241	214956	0	x	
		275473	214956	0		x

Table B.2.: A comparison of the number of MJD entries in calibrated files (Sorcerer files, designated with "Y") with merged data (Melibea files, noted by a "Q" in the list).

Epoch	Runnumber	Y	Q	Y-Q	M1	M2
	05023265	277248	216107	0	x	
		277344	216107	0		x
	05023266	279267	216865	0	x	
		279386	216865	0		x
	05023267	121597	39135	0	x	
		121859	39135	0		x
	05023268	218282	130373	0	x	
		218452	130373	0		x
20130209	05023320	294307	162410	0	x	
		294677	162410	0		x
	05023321	291850	166424	0	x	
		292017	166424	0		x
	05023322	289215	154136	0	x	
		289378	154136	0		x
	05023323	92825	49012	0	x	
		92857	49012	0		x
	05023326	295660	184317	0	x	
		295618	184317	0		x
	05023327	294972	177820	0	x	
		295098	177820	0		x
20130210	05023368	308424	126021	0	x	
		307148	126021	0		x
	05023369	295812	176426	0	x	
		296350	176425	0		x
	05023370	291251	126129	0	x	
		291390	126129	0		x
	05023371	292951	146229	0	x	
		292846	146229	0		x
	05023372	290587	196672	0	x	
		290779	196672	0		x
	05023373	291912	128597	0	x	
		292188	128597	0		x
20130211	05023418	293758	163589	0	x	
		294156	163589	0		x
	05023419	295152	157078	0	x	
		295333	157078	0		x
	05023420	295838	185704	0	x	
		296088	185704	0		x
	05023421	297222	166277	0	x	
		297481	166277	0		x
	05023422	298559	199666	0	x	
		298746	199666	0		x
	05023423	259520	60122	0	x	
		259671	60122	0		x

Table B.3.: A comparison of the number of MJD entries in calibrated files (Sorcerer files, designated with "Y") with merged data (Melibea files, noted by a "Q" in the list).

B.2. Cut Optimization – Crab Nebula

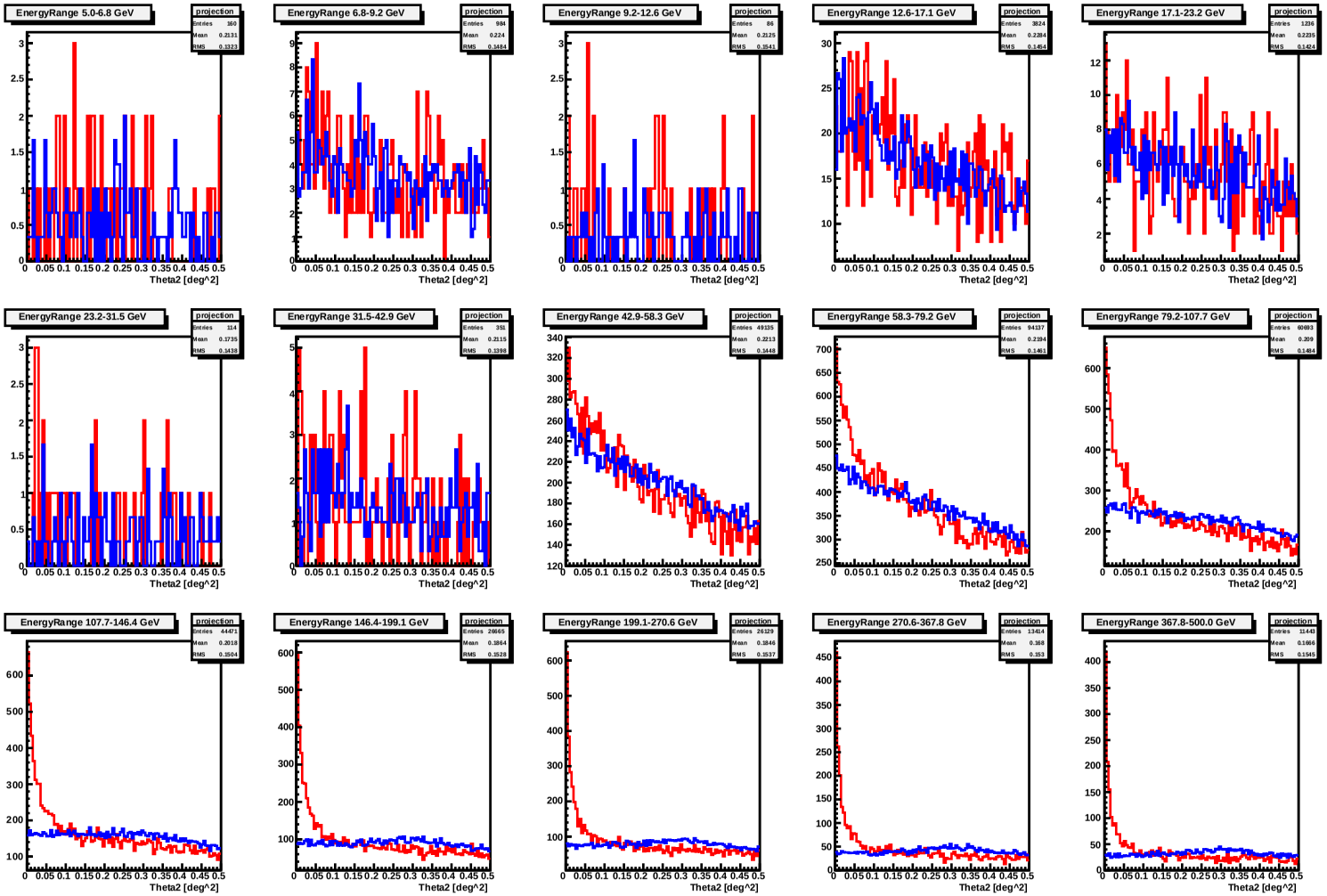

Figure B.1.: ϑ^2 distributions resulting from the non-radio Crab Nebula observations taken in December 2012.

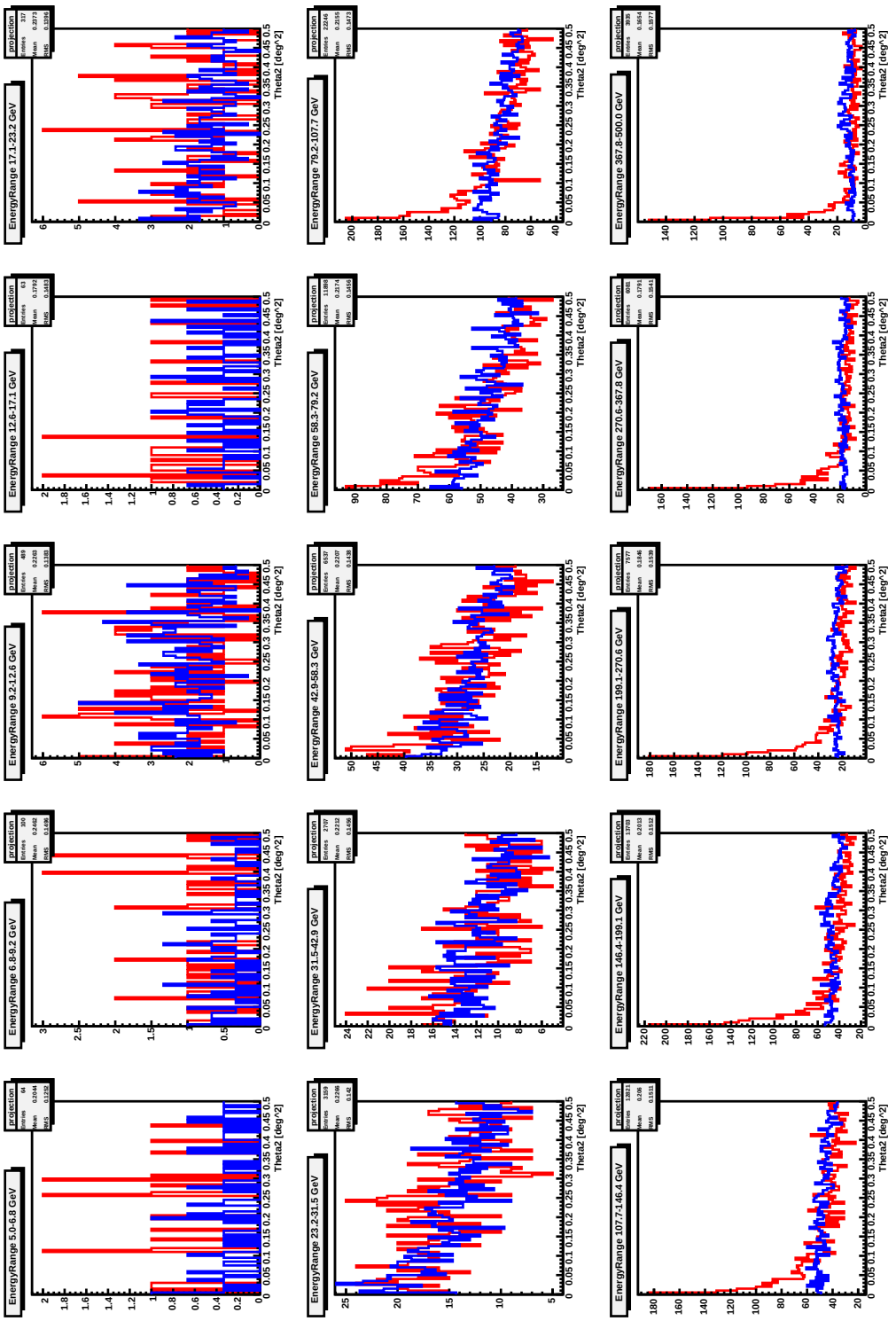

Figure B.2.: ϑ^2 distributions resulting from the non-radio Crab Nebula observations taken in January 2013.

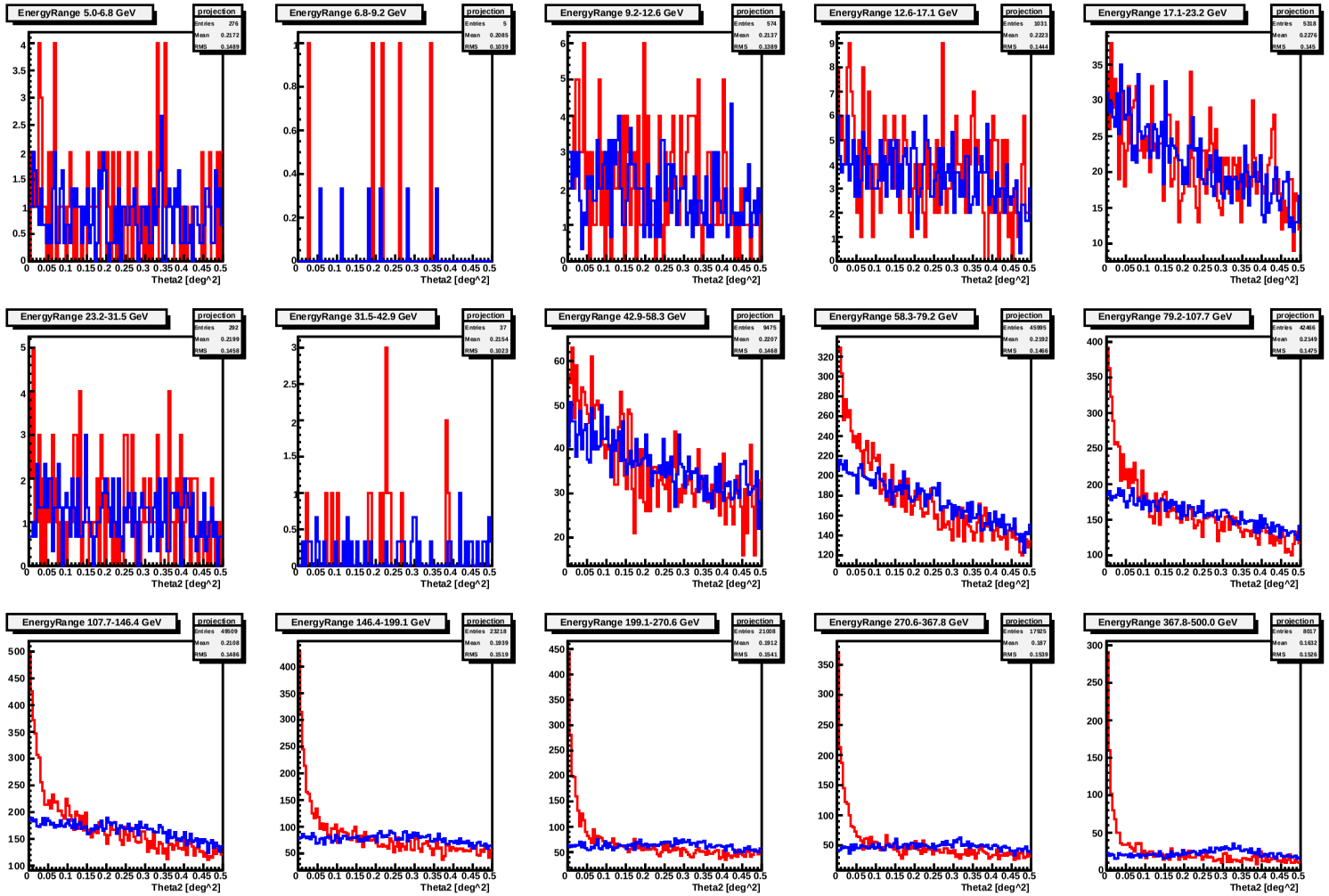

Figure B.3.: ϑ^2 distributions resulting from the non-radio Crab Nebula observations taken in February 2013.

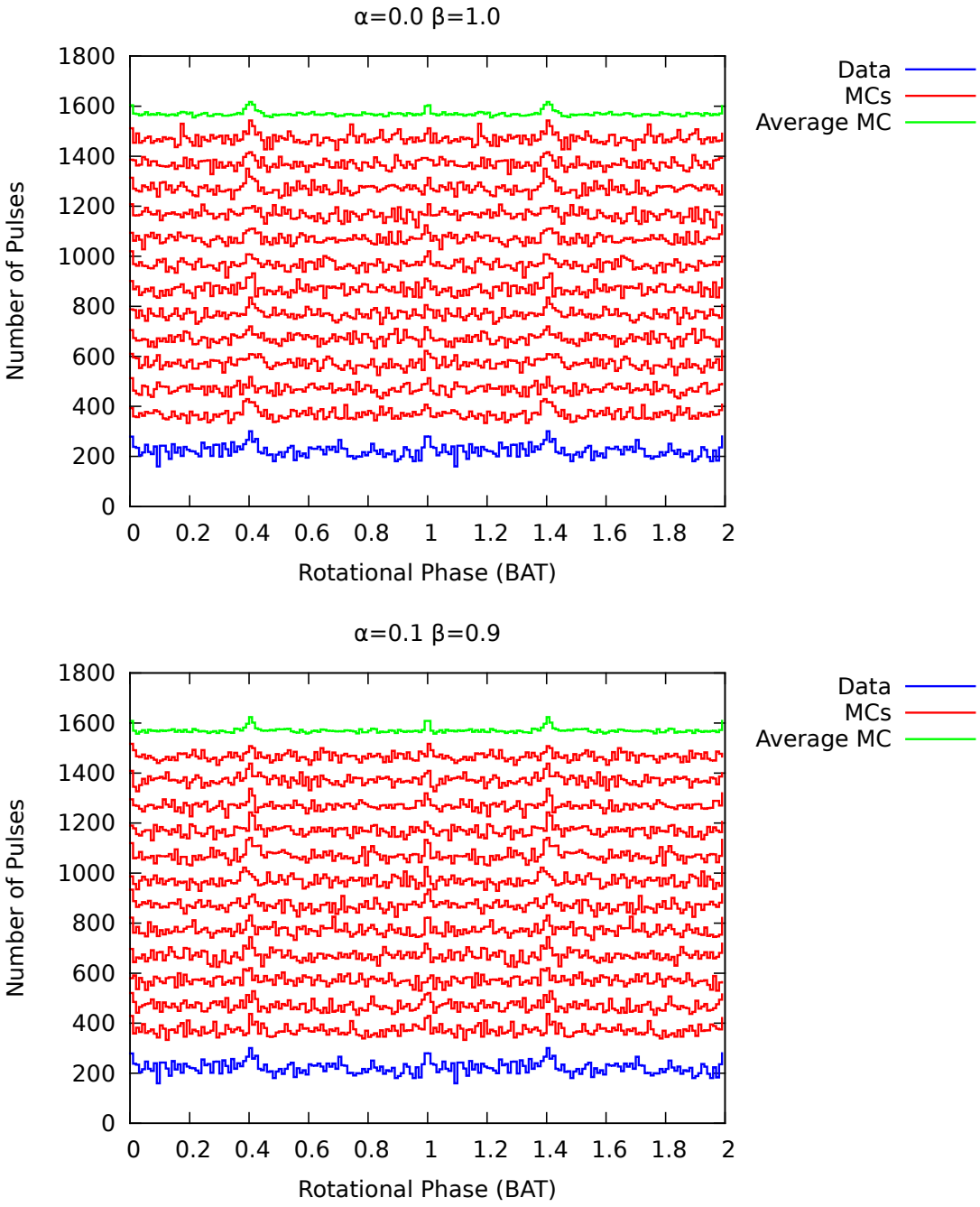
α=0.0 β=1.0
Number of Pulses
Rotational Phase (BAT)
Data
MCs
Average MC
α=0.1 β=0.9
Number of Pulses
Rotational Phase (BAT)
Data
MCs
Average MC

Figure B.4.

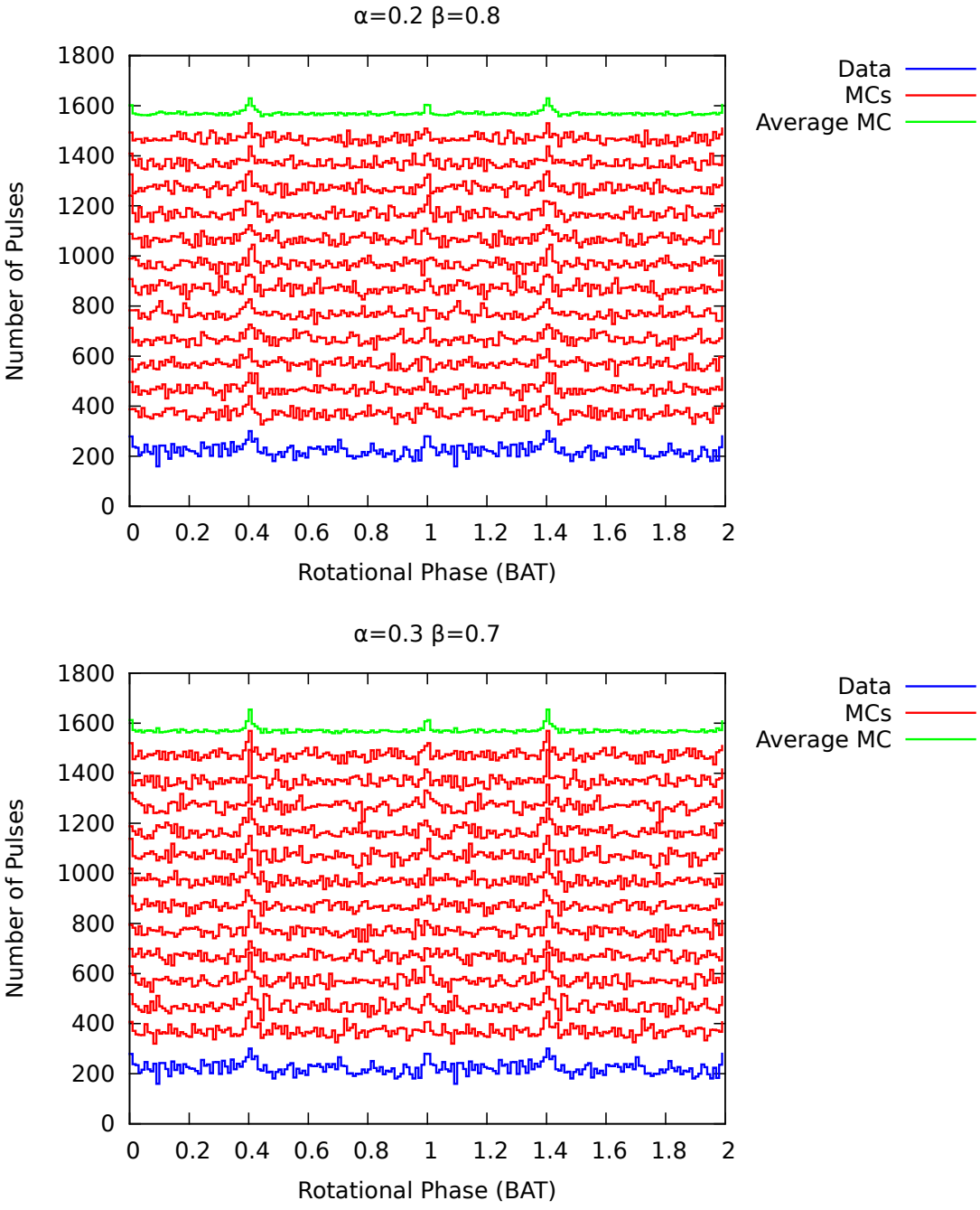
α=0.2 β=0.8
Number of Pulses
Rotational Phase (BAT)
Data
MCs
Average MC
α=0.3 β=0.7
Number of Pulses
Rotational Phase (BAT)
Data
MCs
Average MC

Figure B.5.

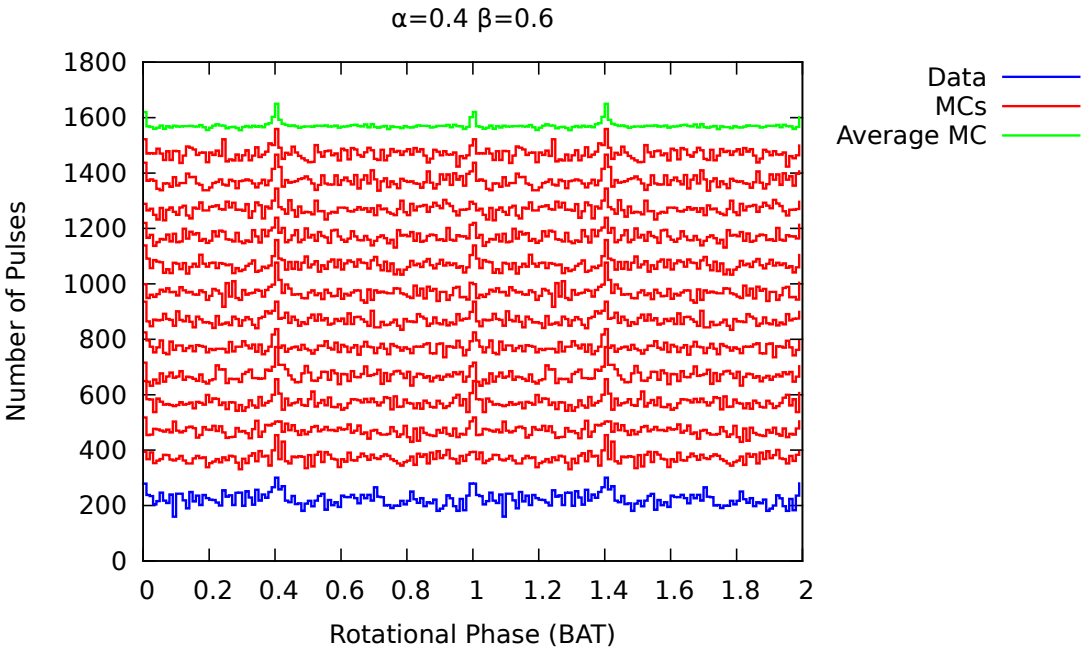
α=0.4 β=0.6
Number of Pulses
Rotational Phase (BAT)
Data
MCs
Average MC
0
200
400
600
800
1000
1200
1400
1600
1800
0
0.2
0.4
0.6
0.8
1
1.2
1.4
1.6
1.8
2

Figure B.6.

C. Correlation Study

C.1. Time Differences: Radio Data – γ-ray Data

C.1.1. No Phase Cuts in γ-ray Data

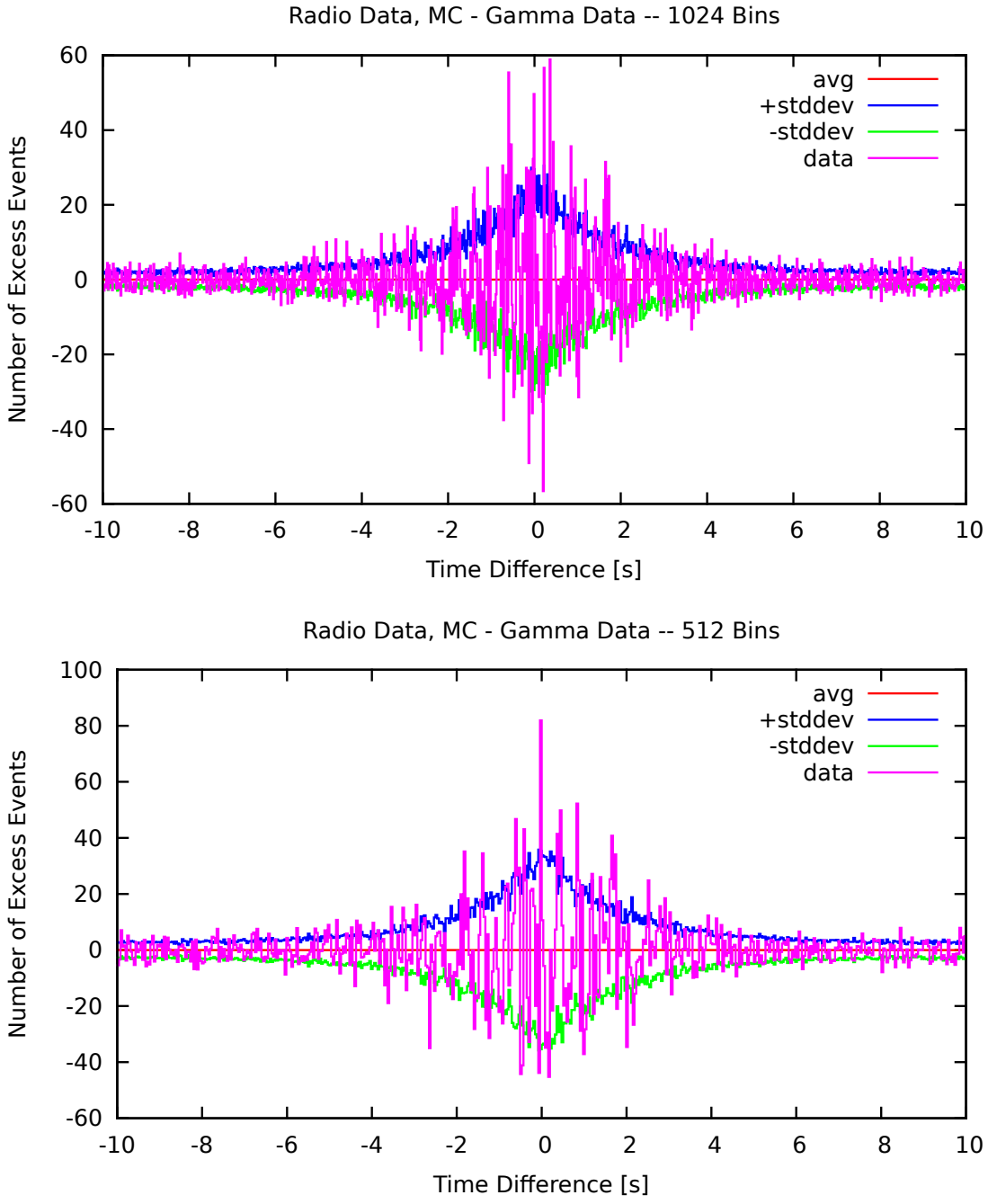
Radio Data, MC - Gamma Data -- 1024 Bins
Number of Excess Events
Time Difference [s]
avg
+stddev
-stddev
data
60
40
20
0
-20
-40
-60
-10
-8
-6
-4
-2
0
2
4
6
8
10
Radio Data, MC - Gamma Data -- 512 Bins
Number of Excess Events
Time Difference [s]
avg
+stddev
-stddev
data
100
80
60
40
20
0
-20
-40
-60
-10
-8
-6
-4
-2
0
2
4
6
8
10

Figure C.1.

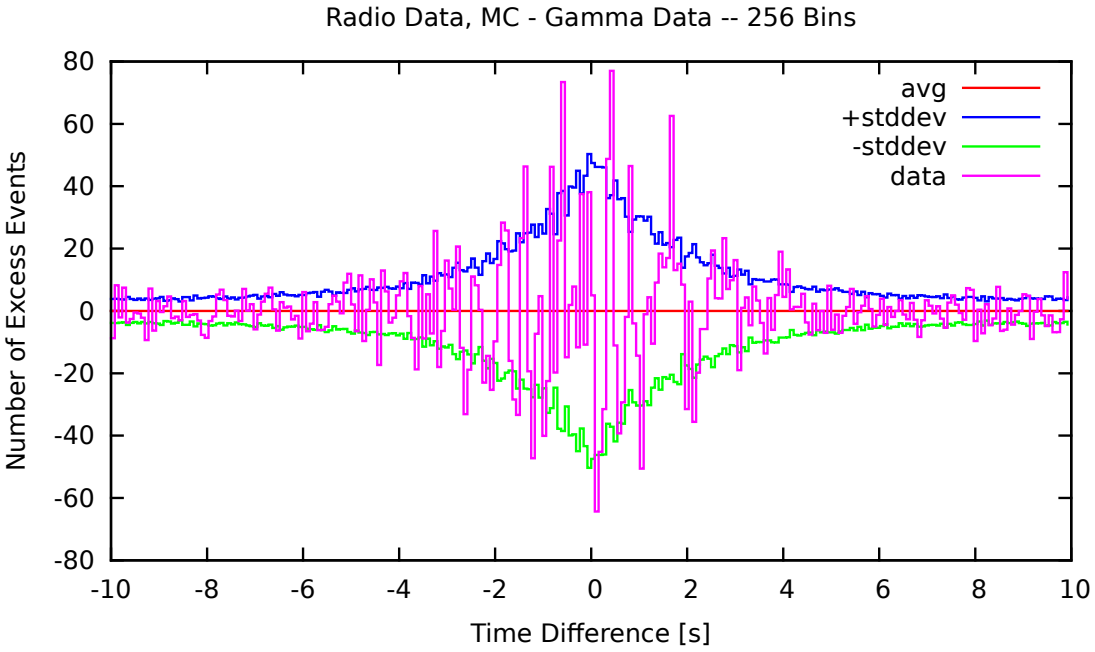
Radio Data, MC - Gamma Data -- 256 Bins
Number of Excess Events
Time Difference [s]
avg
+stddev
-stddev
data
80
60
40
20
0
-20
-40
-60
-80
-10
-8
-6
-4
-2
0
2
4
6
8
10

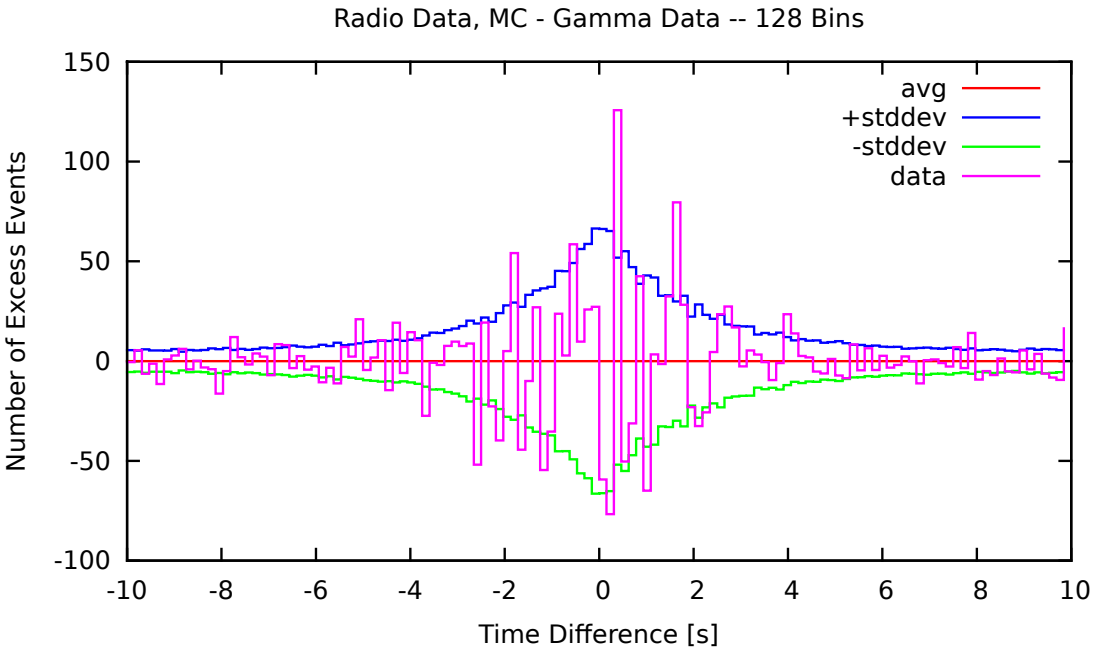
Radio Data, MC - Gamma Data -- 128 Bins
Number of Excess Events
Time Difference [s]
avg
+stddev
-stddev
data
150
100
50
0
-50
-100
-10
-8
-6
-4
-2
0
2
4
6
8
10

Figure C.2.

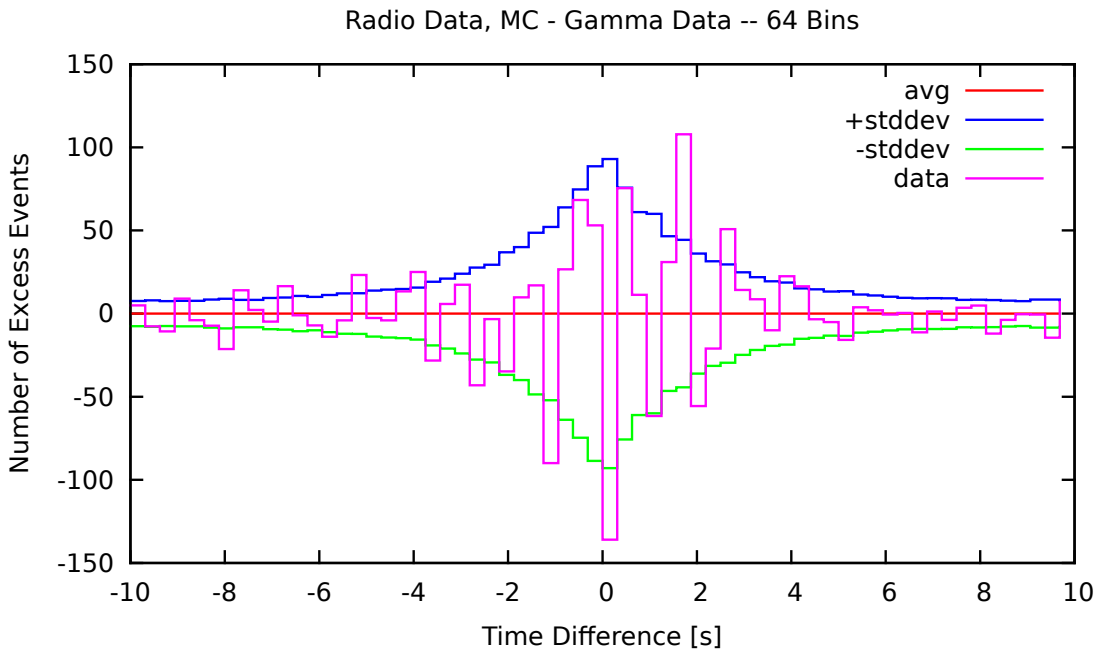
Radio Data, MC - Gamma Data -- 64 Bins
Number of Excess Events
Time Difference [s]
avg
+stddev
-stddev
data
150
100
50
0
-50
-100
-150
-10
-8
-6
-4
-2
0
2
4
6
8
10

Figure C.3.

C.1.2. P1 Phase Cut in γ-ray Data

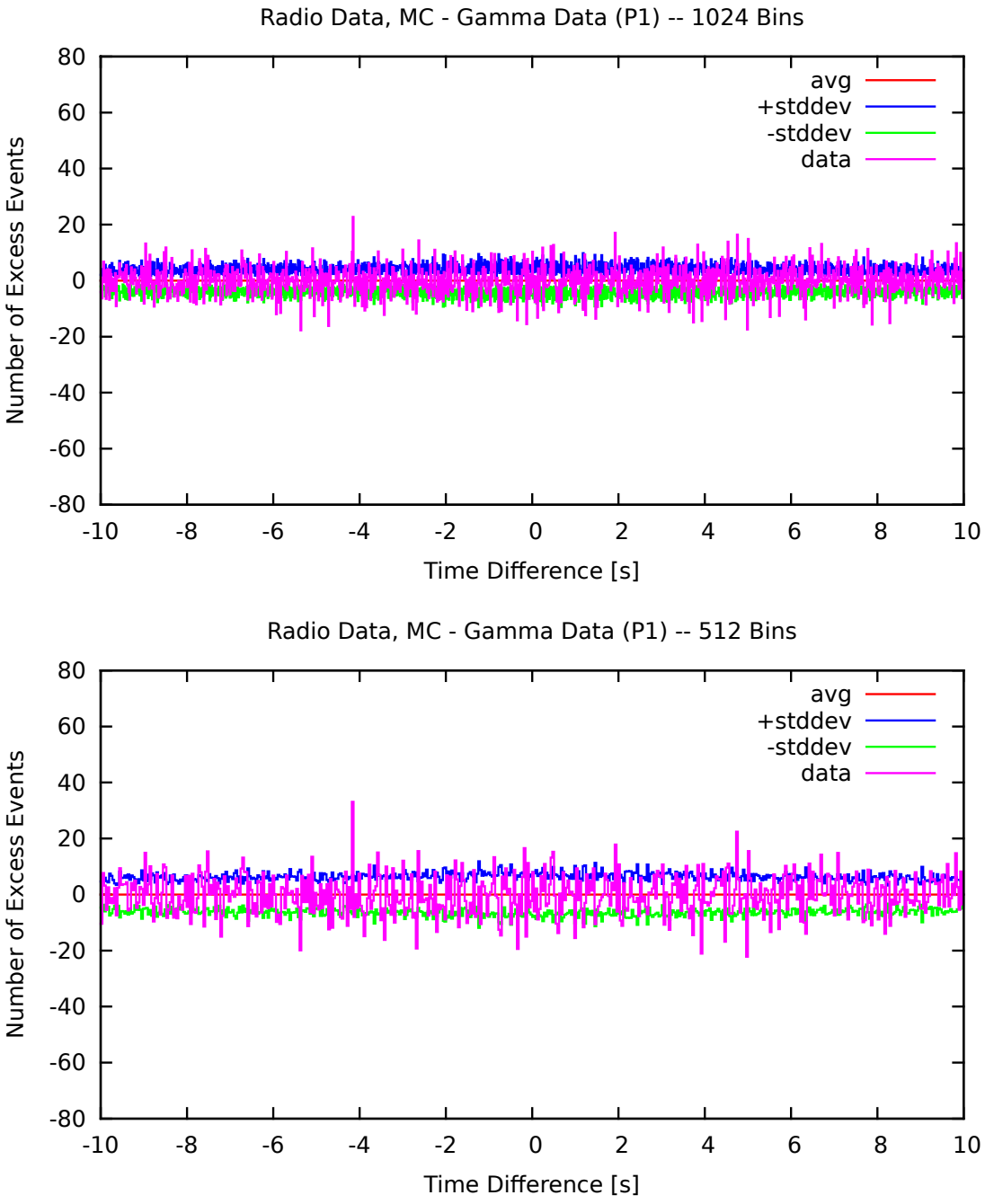

Figure C.4.

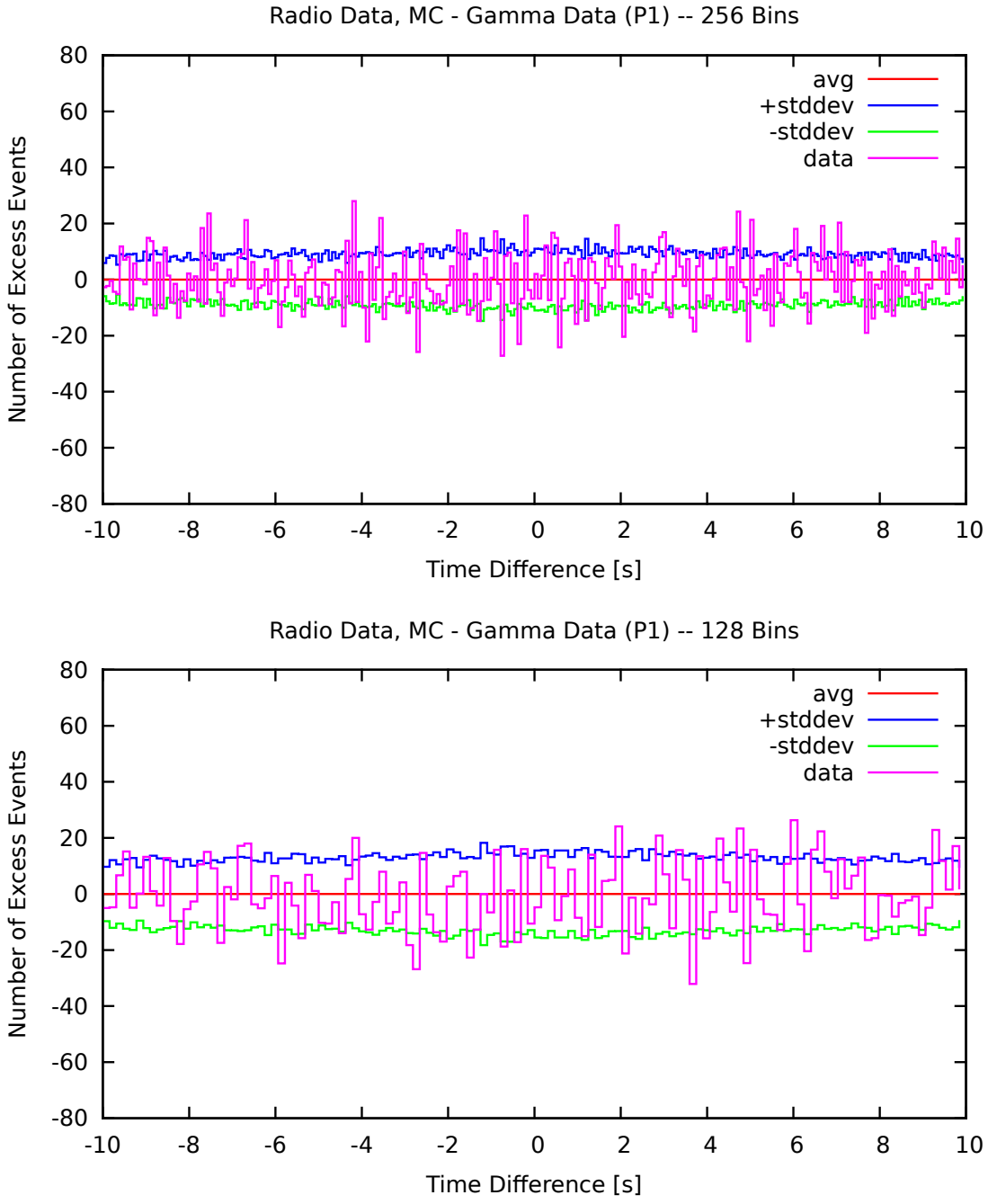
Radio Data, MC - Gamma Data (P1) -- 256 Bins
Number of Excess Events
Time Difference [s]
avg
+stddev
-stddev
data
80
60
40
20
0
-20
-40
-60
-80
-10
-8
-6
-4
-2
0
2
4
6
8
10

Radio Data, MC - Gamma Data (P1) -- 128 Bins
Number of Excess Events
Time Difference [s]
avg
+stddev
-stddev
data
80
60
40
20
0
-20
-40
-60
-80
-10
-8
-6
-4
-2
0
2
4
6
8
10

Figure C.5.

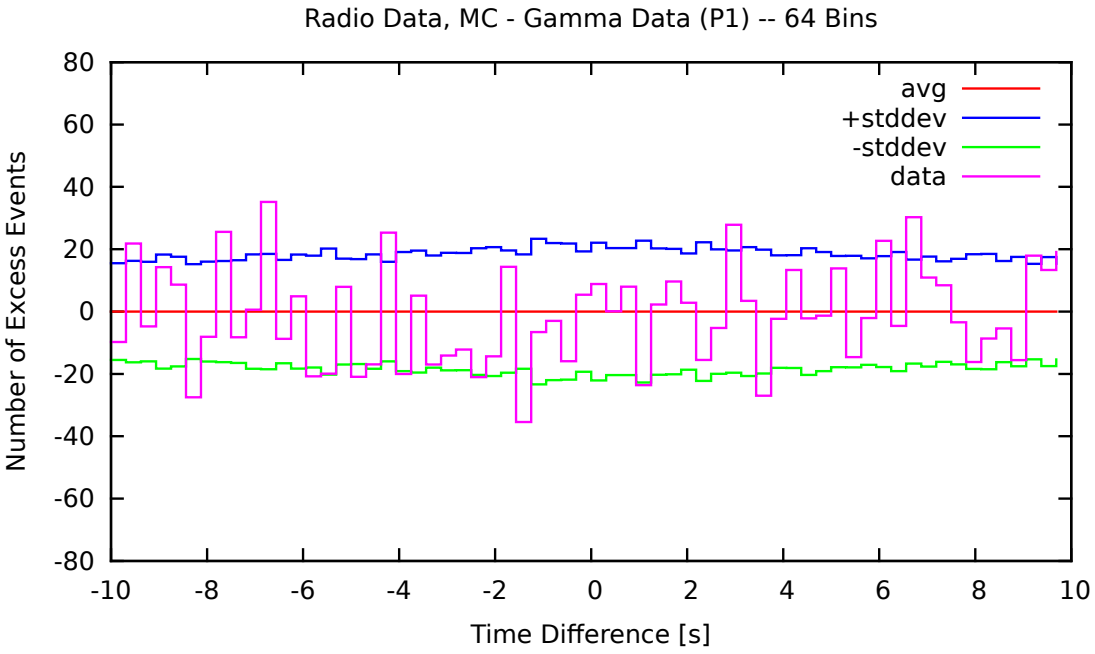
Radio Data, MC - Gamma Data (P1) -- 64 Bins
Number of Excess Events
Time Difference [s]
avg
+stddev
-stddev
data
80
60
40
20
0
-20
-40
-60
-80
-10
-8
-6
-4
-2
0
2
4
6
8
10

Figure C.6.

C.1.3. P2 Phase Cut in γ-ray Data

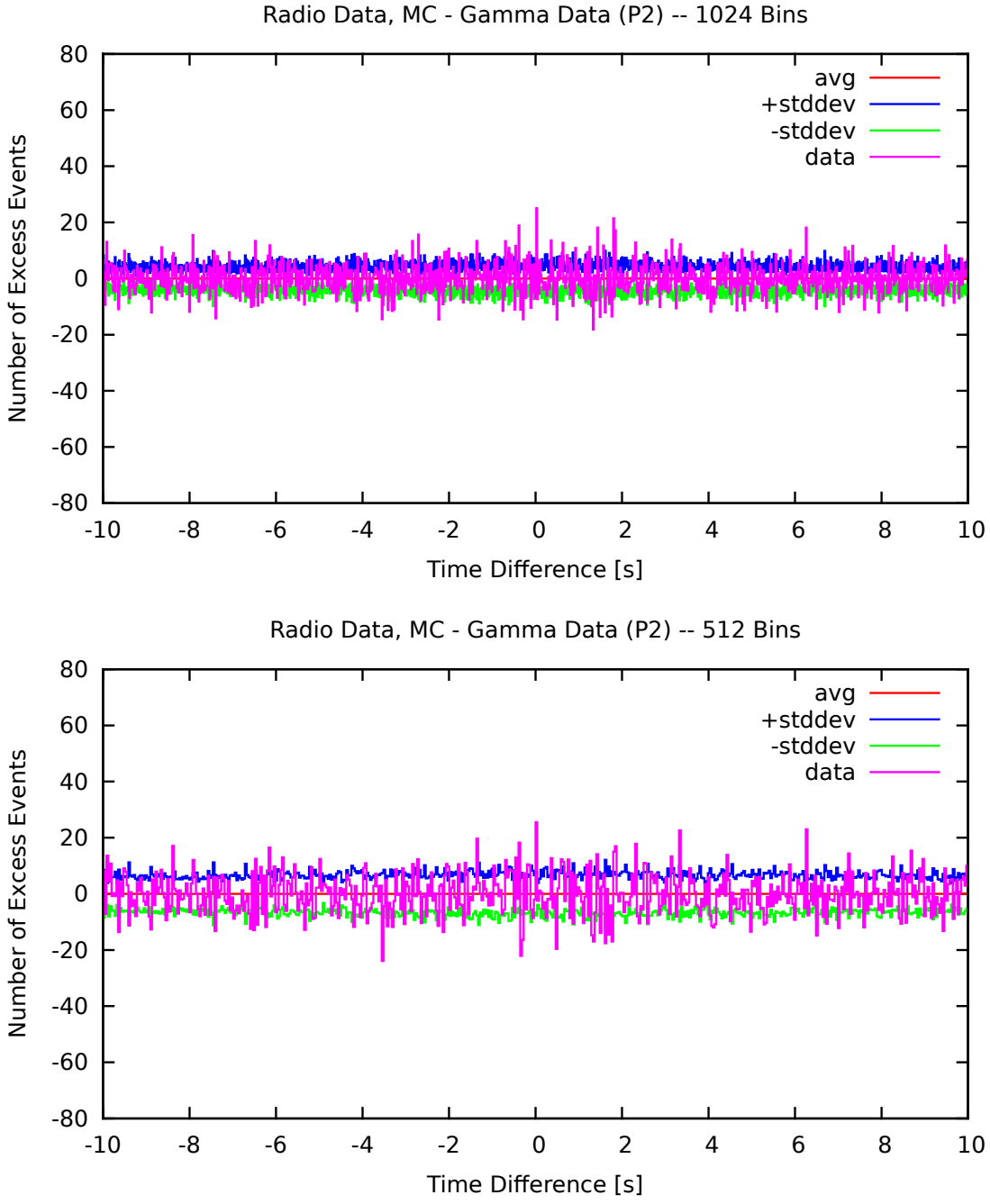

Figure C.7.

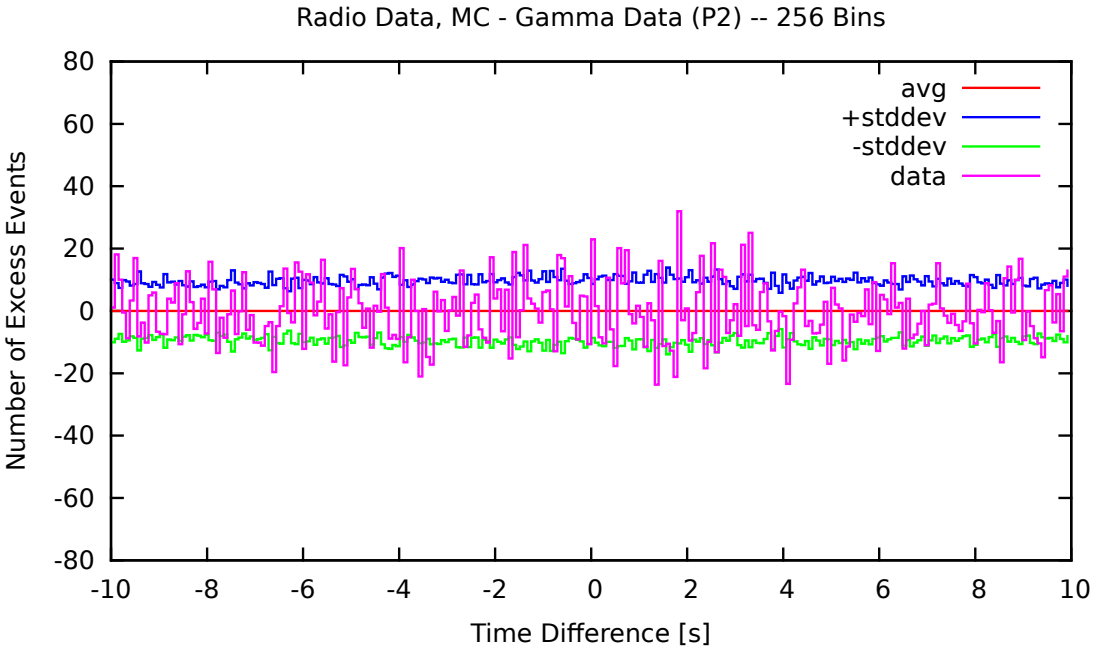
Radio Data, MC - Gamma Data (P2) -- 256 Bins
Number of Excess Events
Time Difference [s]
avg
+stddev
-stddev
data
80
60
40
20
0
-20
-40
-60
-80
-10
-8
-6
-4
-2
0
2
4
6
8
10

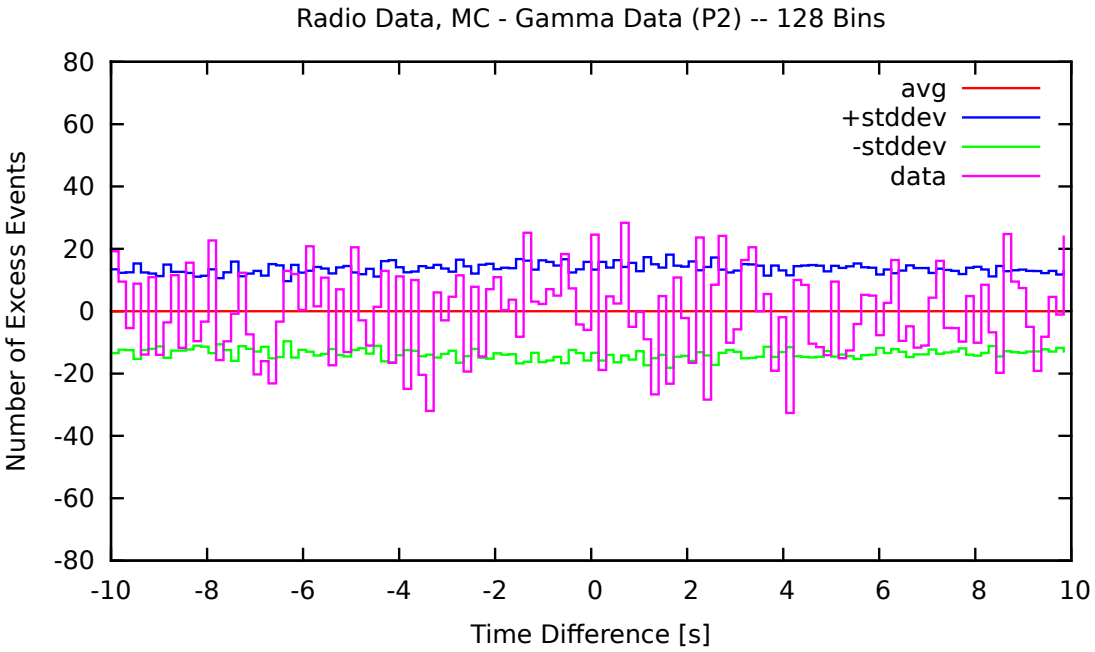
Radio Data, MC - Gamma Data (P2) -- 128 Bins
Number of Excess Events
Time Difference [s]
avg
+stddev
-stddev
data
80
60
40
20
0
-20
-40
-60
-80
-10
-8
-6
-4
-2
0
2
4
6
8
10

Figure C.8.

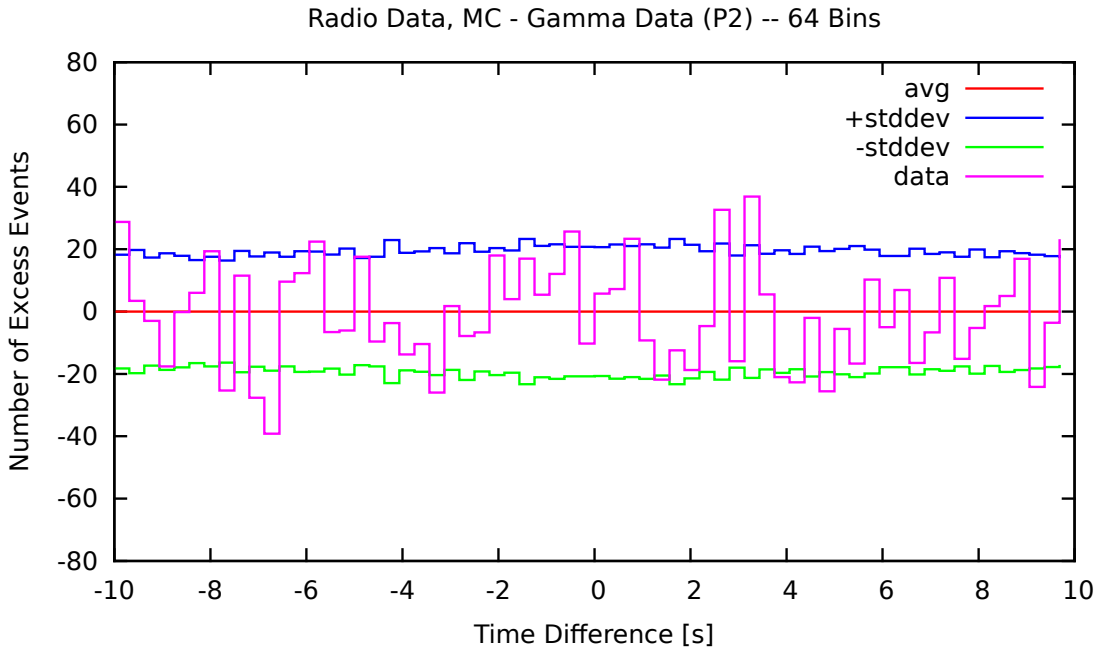
Radio Data, MC - Gamma Data (P2) -- 64 Bins
Number of Excess Events
Time Difference [s]
avg
+stddev
-stddev
data
80
60
40
20
0
-20
-40
-60
-80
-10
-8
-6
-4
-2
0
2
4
6
8
10

Figure C.9.

C.1.4. P1+P2 Phase Cut in γ-ray Data

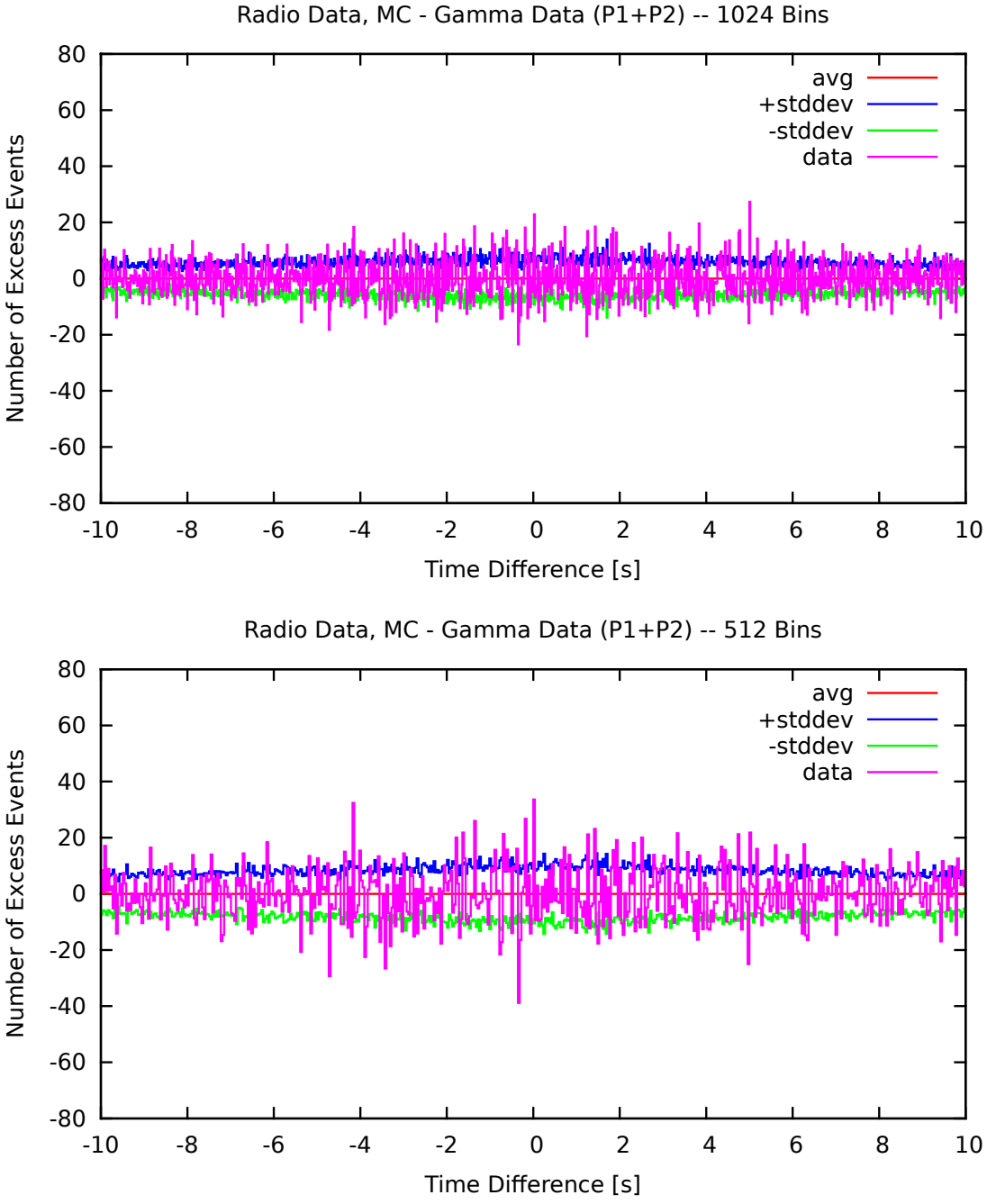

Figure C.10.

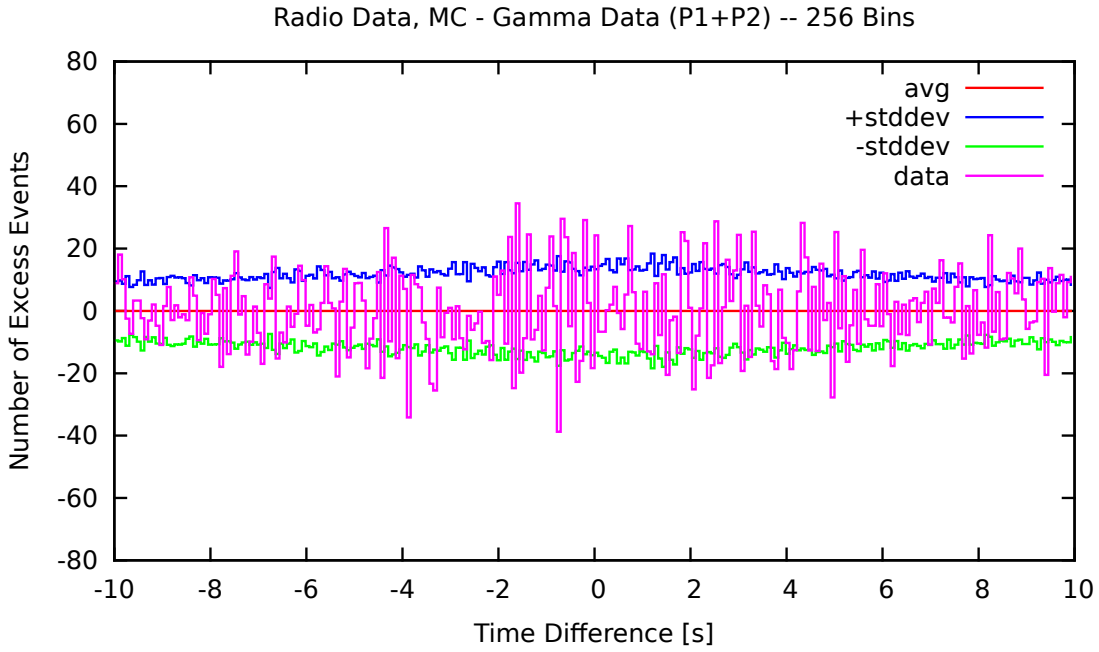
Radio Data, MC - Gamma Data (P1+P2) -- 256 Bins
Number of Excess Events
Time Difference [s]
avg
+stddev
-stddev
data
80
60
40
20
0
-20
-40
-60
-80
-10
-8
-6
-4
-2
0
2
4
6
8
10

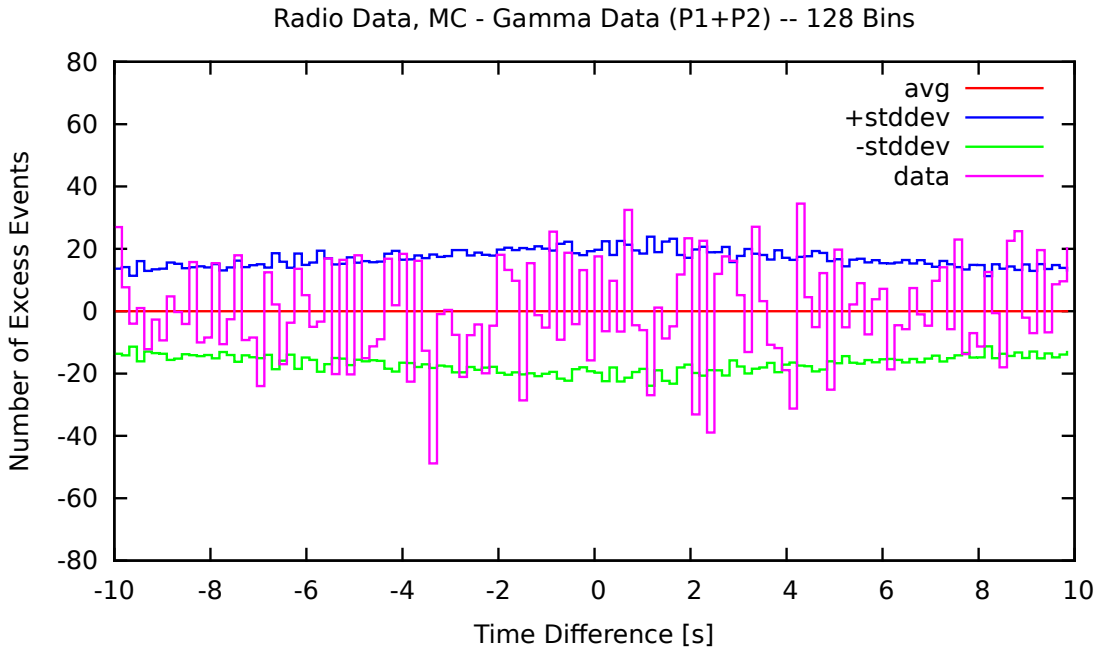
Radio Data, MC - Gamma Data (P1+P2) -- 128 Bins
Number of Excess Events
Time Difference [s]
avg
+stddev
-stddev
data
80
60
40
20
0
-20
-40
-60
-80
-10
-8
-6
-4
-2
0
2
4
6
8
10

Figure C.11.

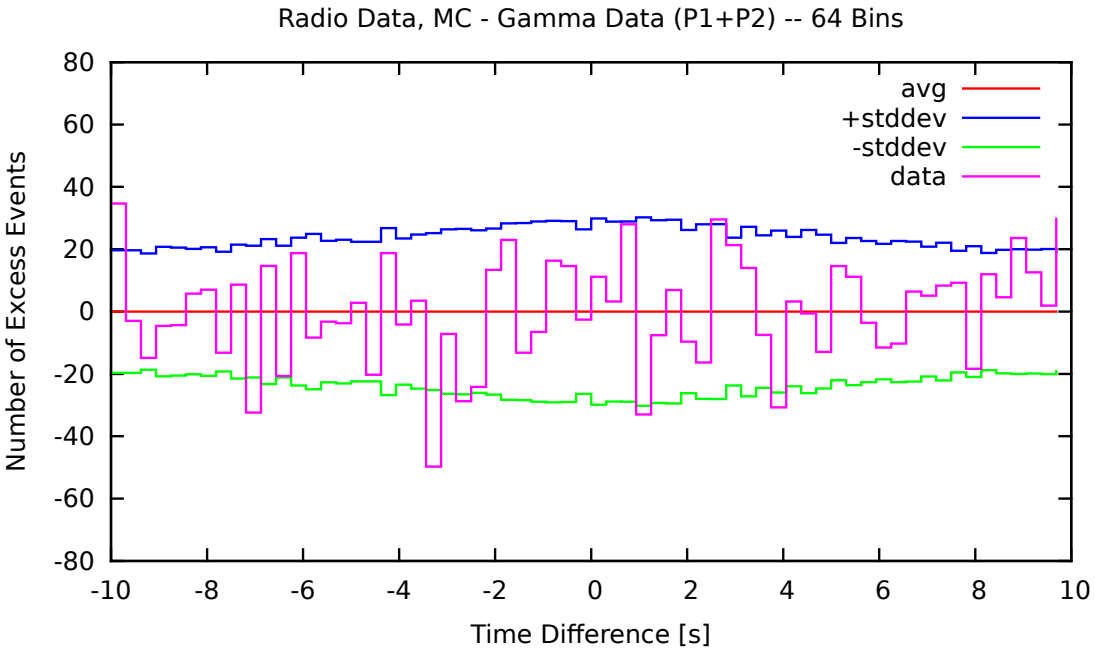
Radio Data, MC - Gamma Data (P1+P2) -- 64 Bins
Number of Excess Events
Time Difference [s]
avg
+stddev
-stddev
data
80
60
40
20
0
-20
-40
-60
-80
-10
-8
-6
-4
-2
0
2
4
6
8
10

Figure C.12.

C.2. Time Differences: Radio Data (Effelsberg) – γ-ray Data

C.2.1. No Phase Cuts in γ-ray Data

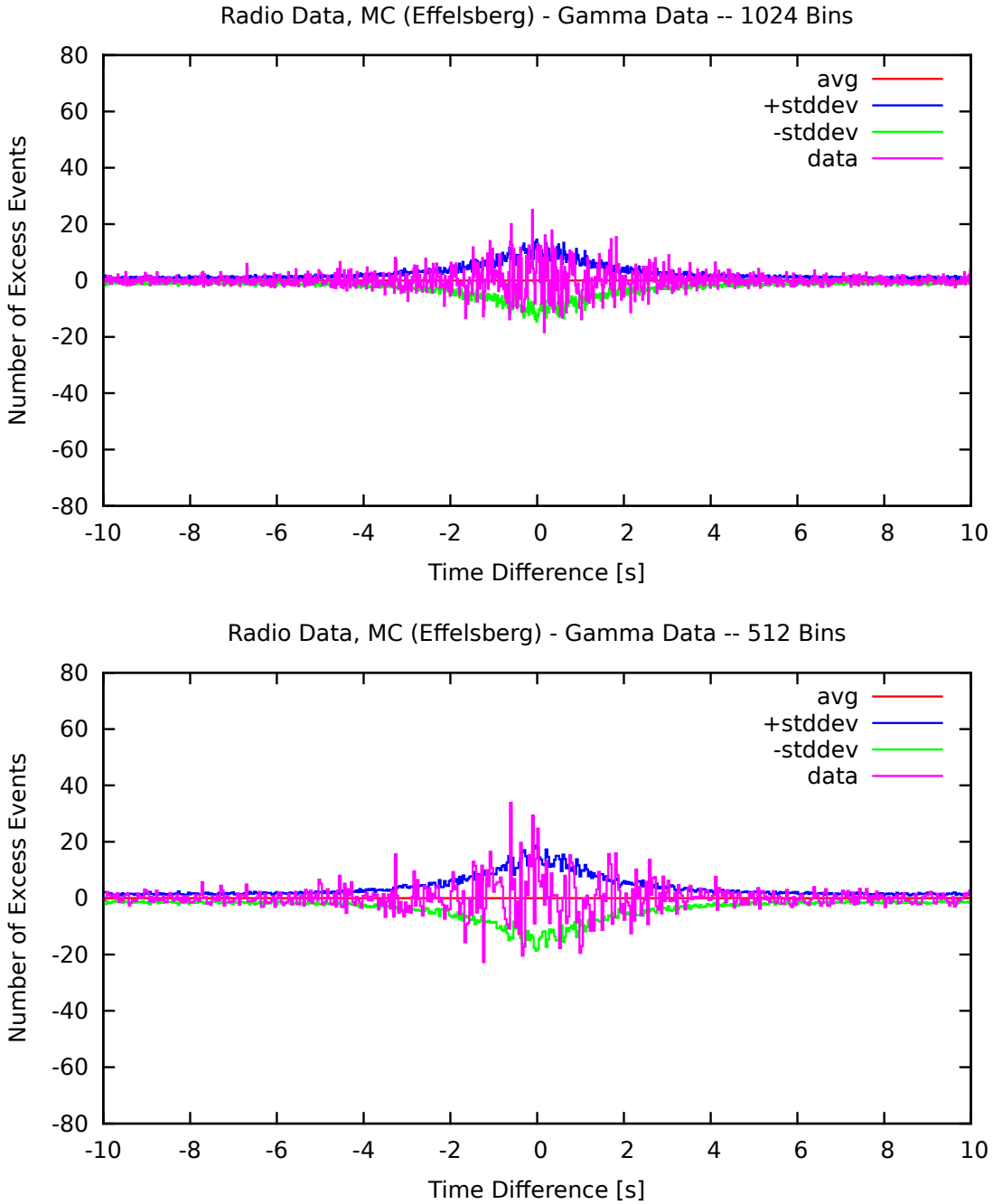

Figure C.13.

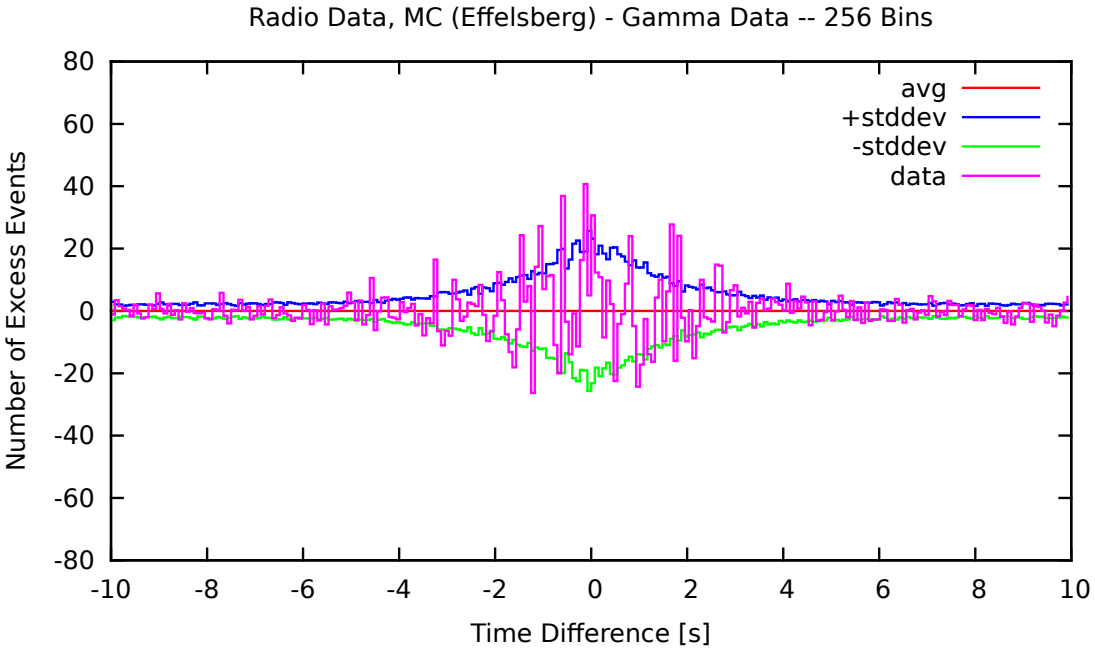
Radio Data, MC (Effelsberg) - Gamma Data -- 256 Bins
Number of Excess Events
Time Difference [s]
avg
+stddev
-stddev
data
80
60
40
20
0
-20
-40
-60
-80
-10
-8
-6
-4
-2
0
2
4
6
8
10

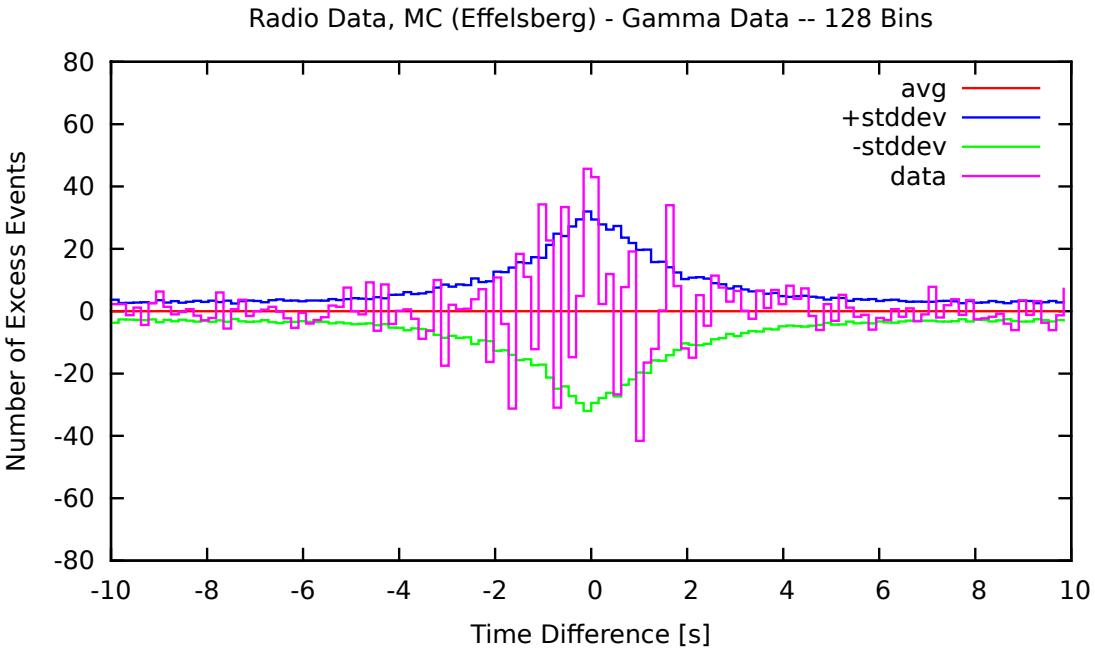
Radio Data, MC (Effelsberg) - Gamma Data -- 128 Bins
Number of Excess Events
Time Difference [s]
avg
+stddev
-stddev
data
80
60
40
20
0
-20
-40
-60
-80
-10
-8
-6
-4
-2
0
2
4
6
8
10

Figure C.14.

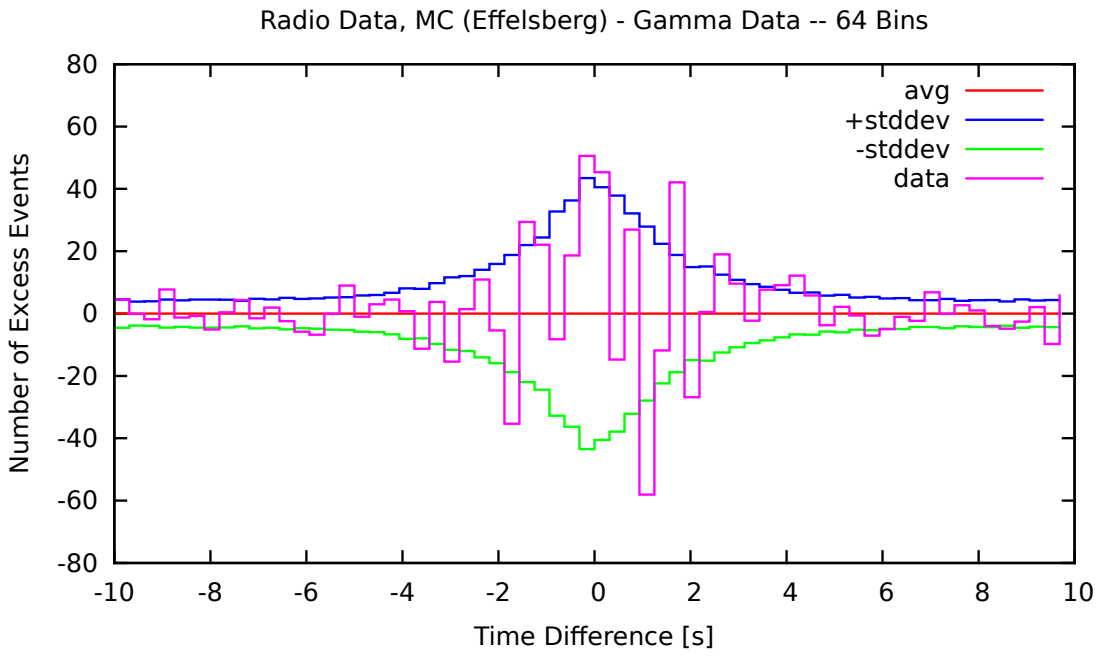
Radio Data, MC (Effelsberg) - Gamma Data -- 64 Bins
Number of Excess Events
Time Difference [s]
avg
+stddev
-stddev
data
80
60
40
20
0
-20
-40
-60
-80
-10
-8
-6
-4
-2
0
2
4
6
8
10

Figure C.15.

C.2.2. P1 Phase Cut in γ-ray Data

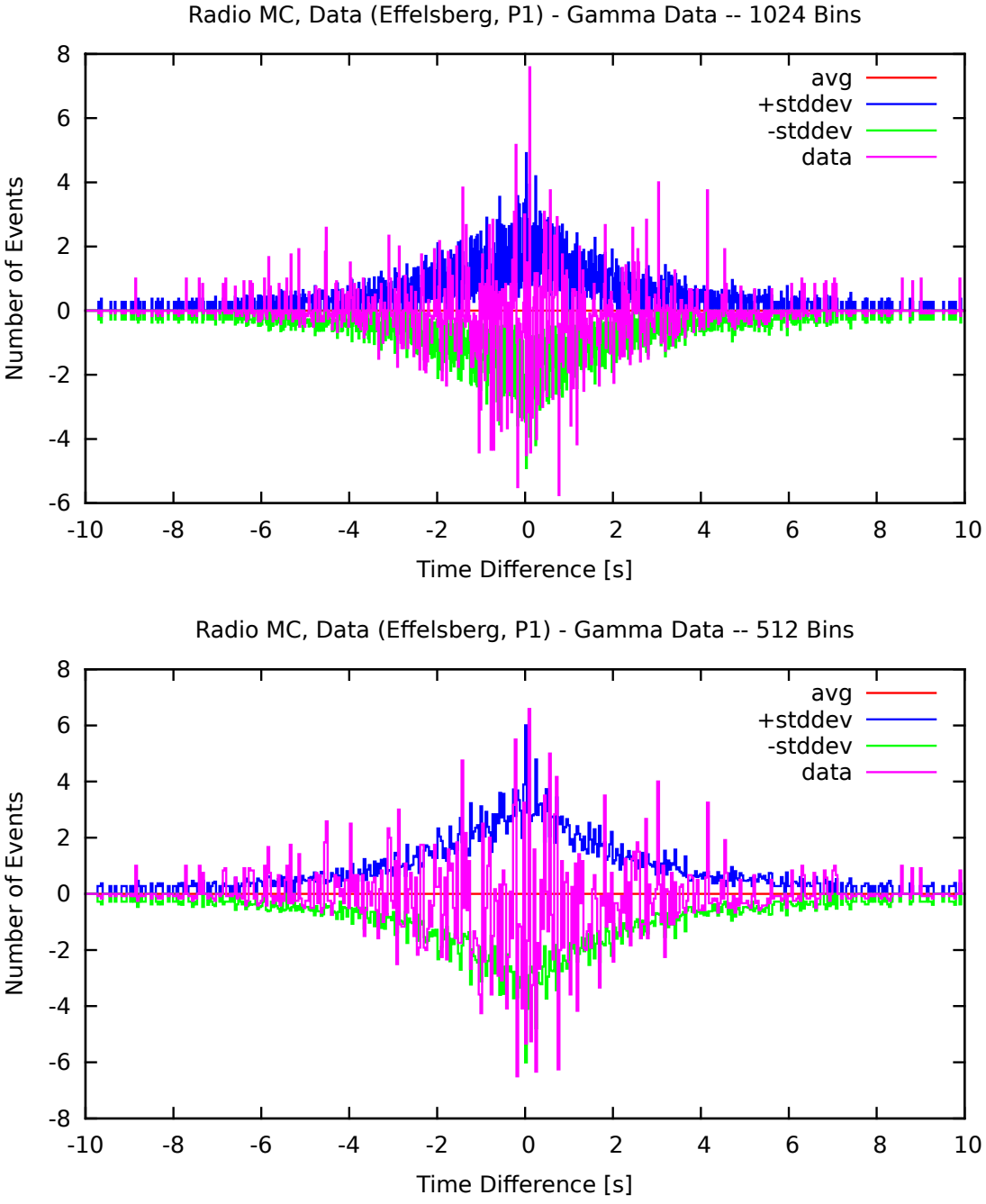

Figure C.16.

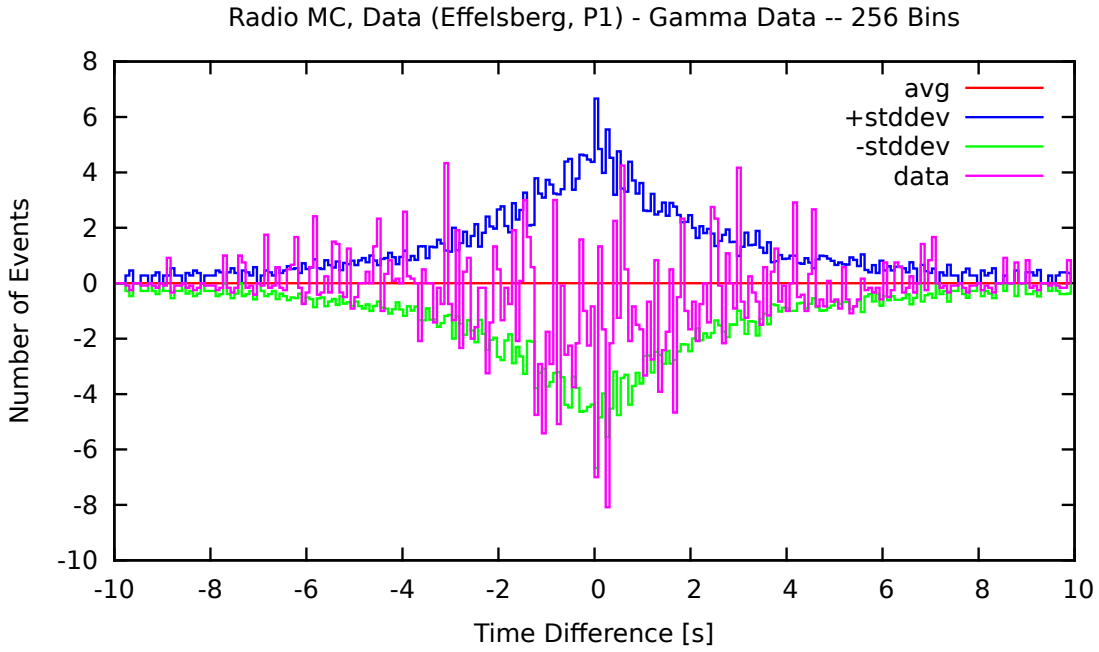
Radio MC, Data (Effelsberg, P1) - Gamma Data -- 256 Bins
Number of Events
Time Difference [s]
avg
+stddev
-stddev
data
8
6
4
2
0
-2
-4
-6
-8
-10
-10
-8
-6
-4
-2
0
2
4
6
8
10

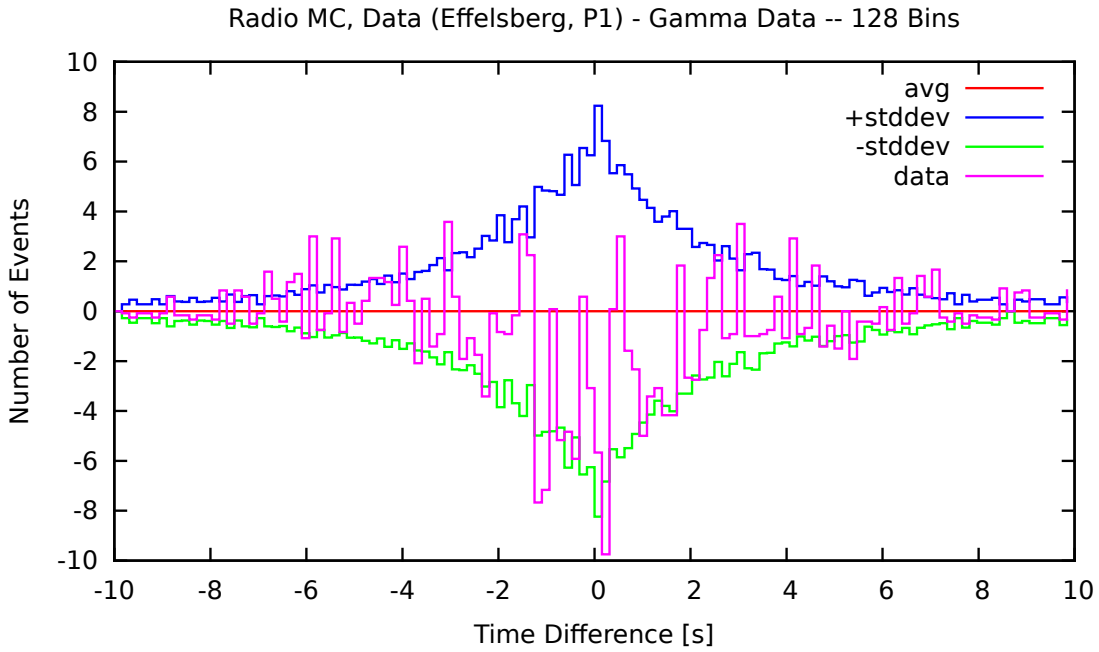
Radio MC, Data (Effelsberg, P1) - Gamma Data -- 128 Bins
Number of Events
Time Difference [s]
avg
+stddev
-stddev
data
10
8
6
4
2
0
-2
-4
-6
-8
-10
-10
-8
-6
-4
-2
0
2
4
6
8
10

Figure C.17.

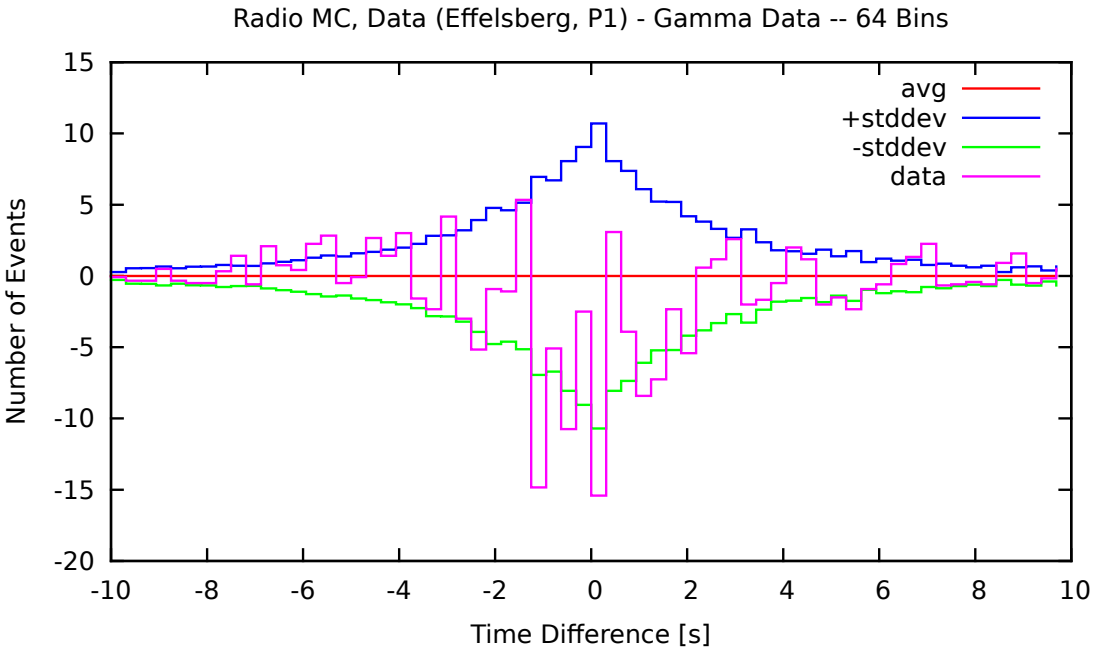
Radio MC, Data (Effelsberg, P1) - Gamma Data -- 64 Bins
Number of Events
Time Difference [s]
avg
+stddev
-stddev
data
15
10
5
0
-5
-10
-15
-20
-10
-8
-6
-4
-2
0
2
4
6
8
10

Figure C.18.

C.2.3. P2 Phase Cut in γ-ray Data

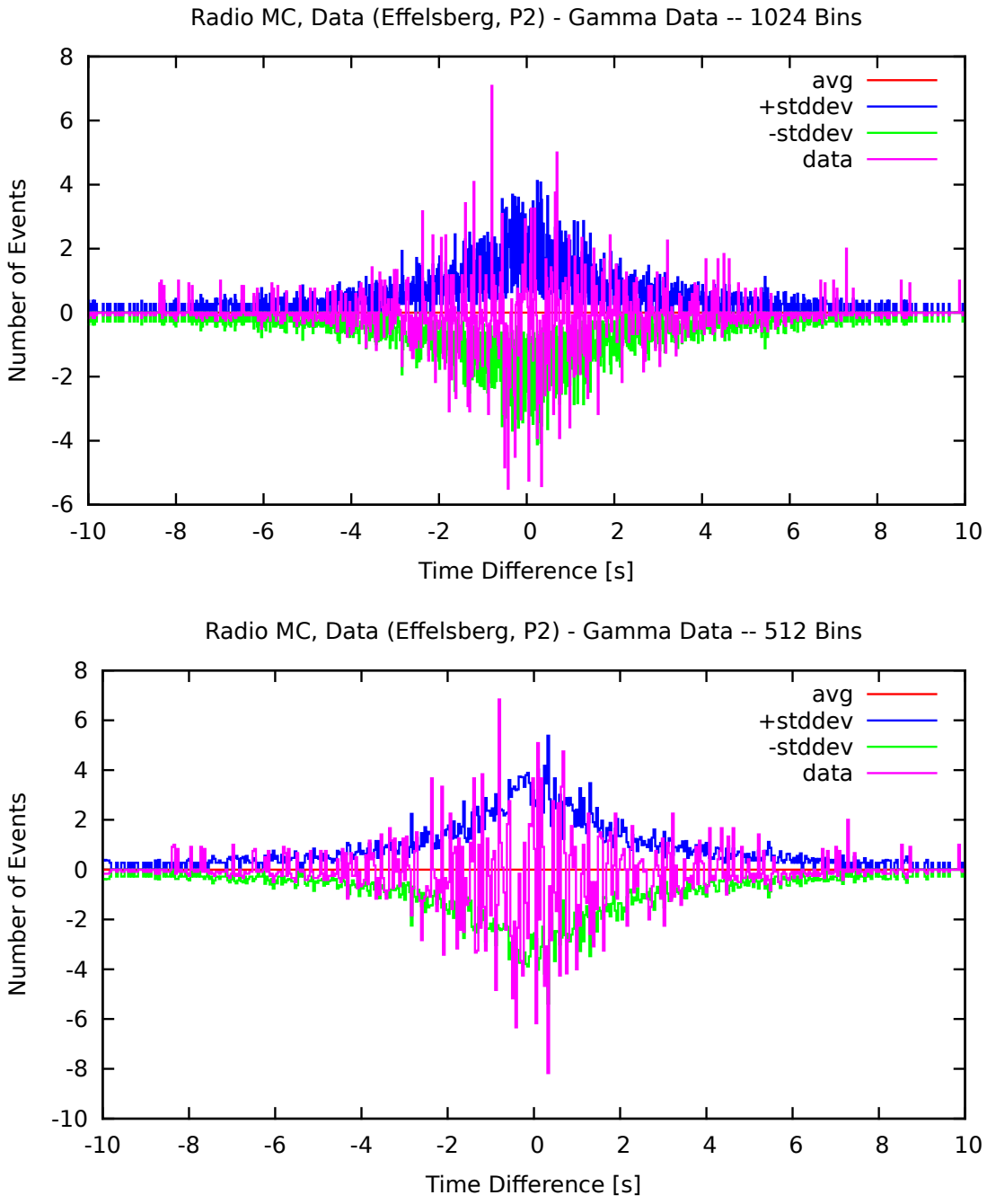

Figure C.19.

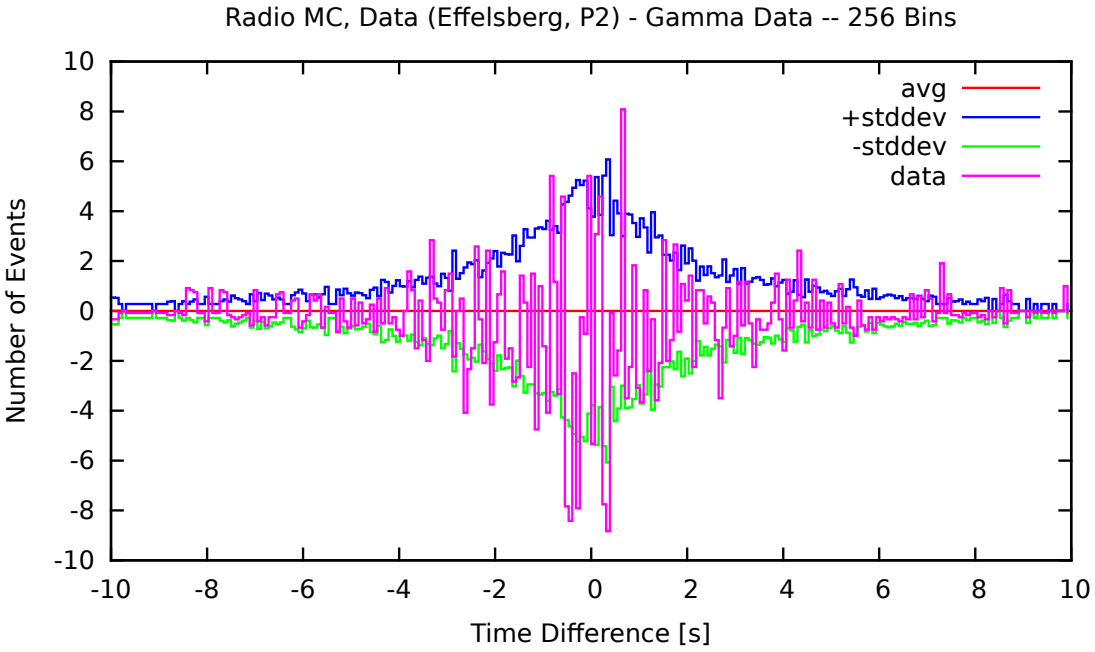
Radio MC, Data (Effelsberg, P2) - Gamma Data -- 256 Bins
Number of Events
Time Difference [s]
avg
+stddev
-stddev
data
10
8
6
4
2
0
-2
-4
-6
-8
-10
-10
-8
-6
-4
-2
0
2
4
6
8
10

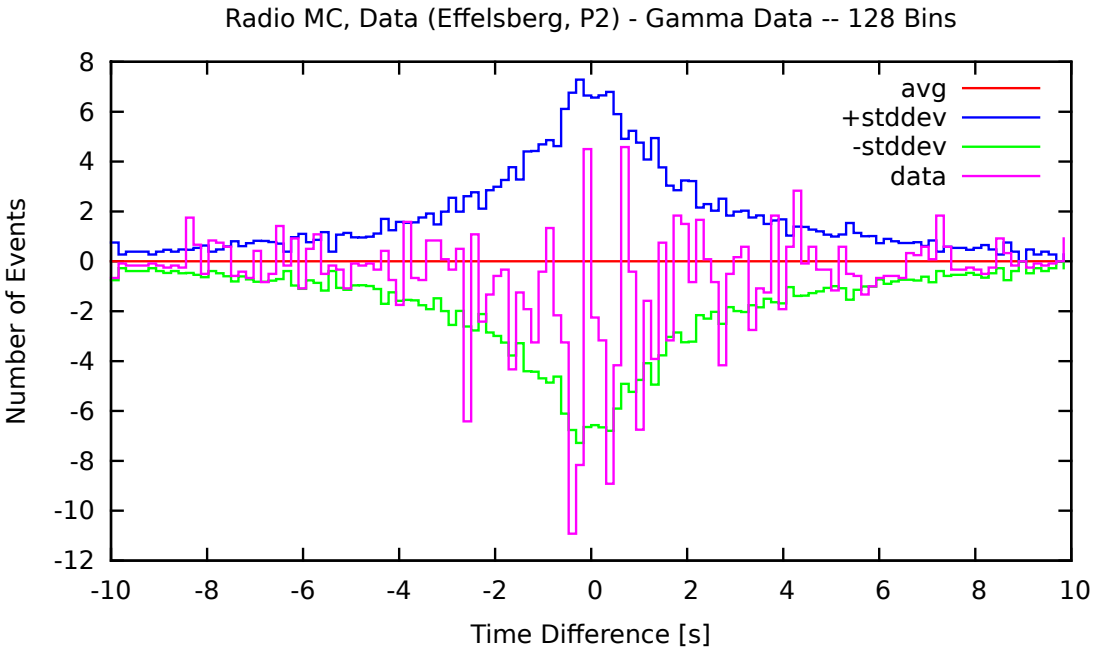
Radio MC, Data (Effelsberg, P2) - Gamma Data -- 128 Bins
Number of Events
Time Difference [s]
avg
+stddev
-stddev
data
8
6
4
2
0
-2
-4
-6
-8
-10
-12
-10
-8
-6
-4
-2
0
2
4
6
8
10

Figure C.20.

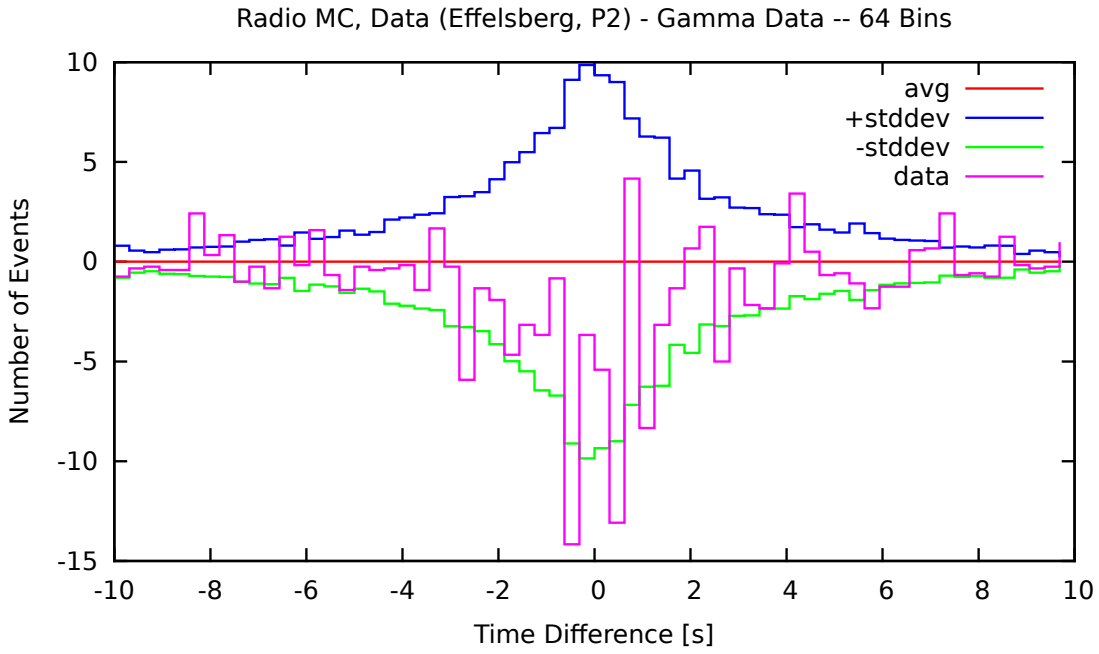
Radio MC, Data (Effelsberg, P2) - Gamma Data -- 64 Bins
Number of Events
Time Difference [s]
avg
+stddev
-stddev
data
10
5
0
-5
-10
-15
-10
-8
-6
-4
-2
0
2
4
6
8
10

Figure C.21.

C.2.4. P1+P2 Phase Cut in γ-ray Data

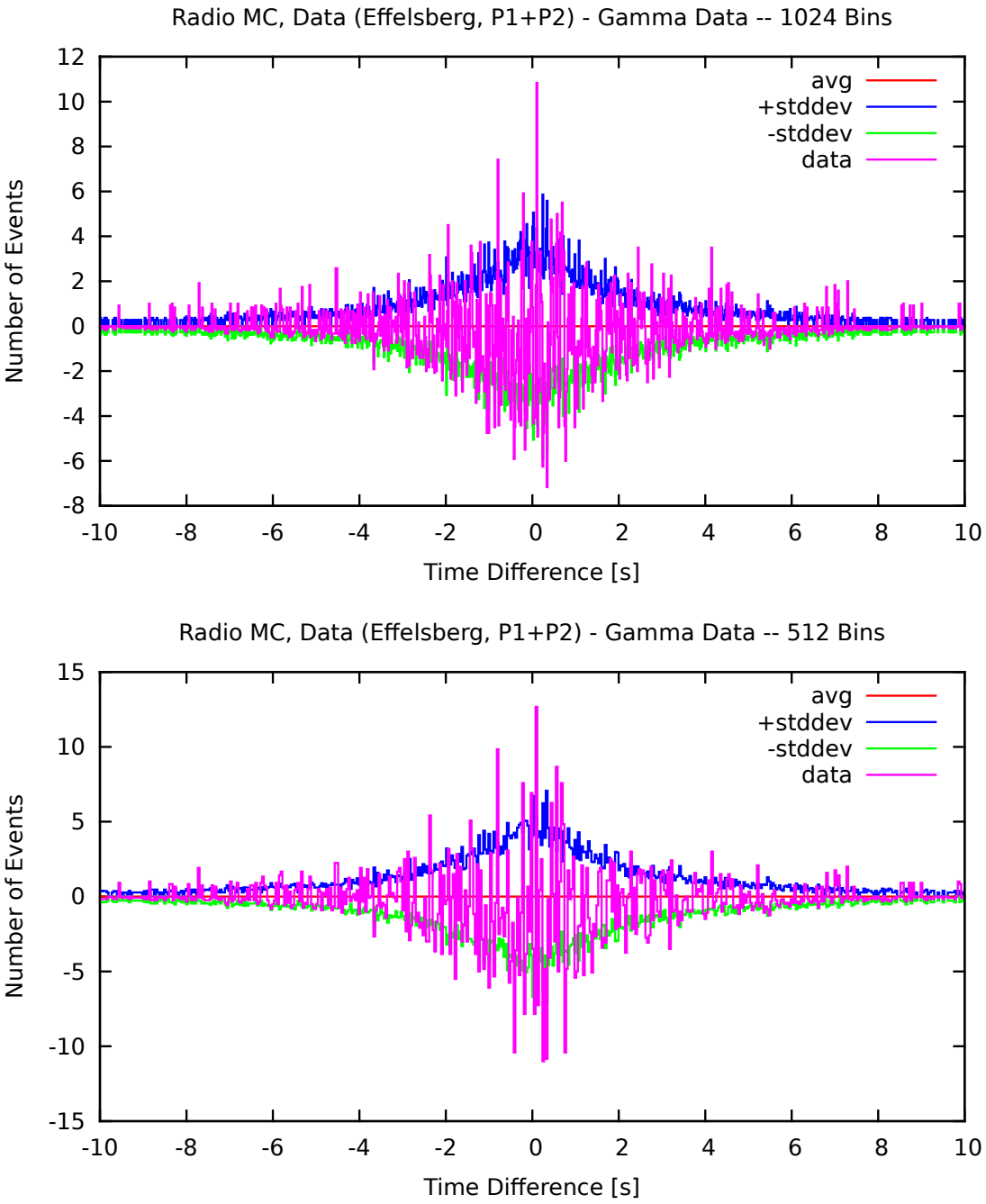

Figure C.22.

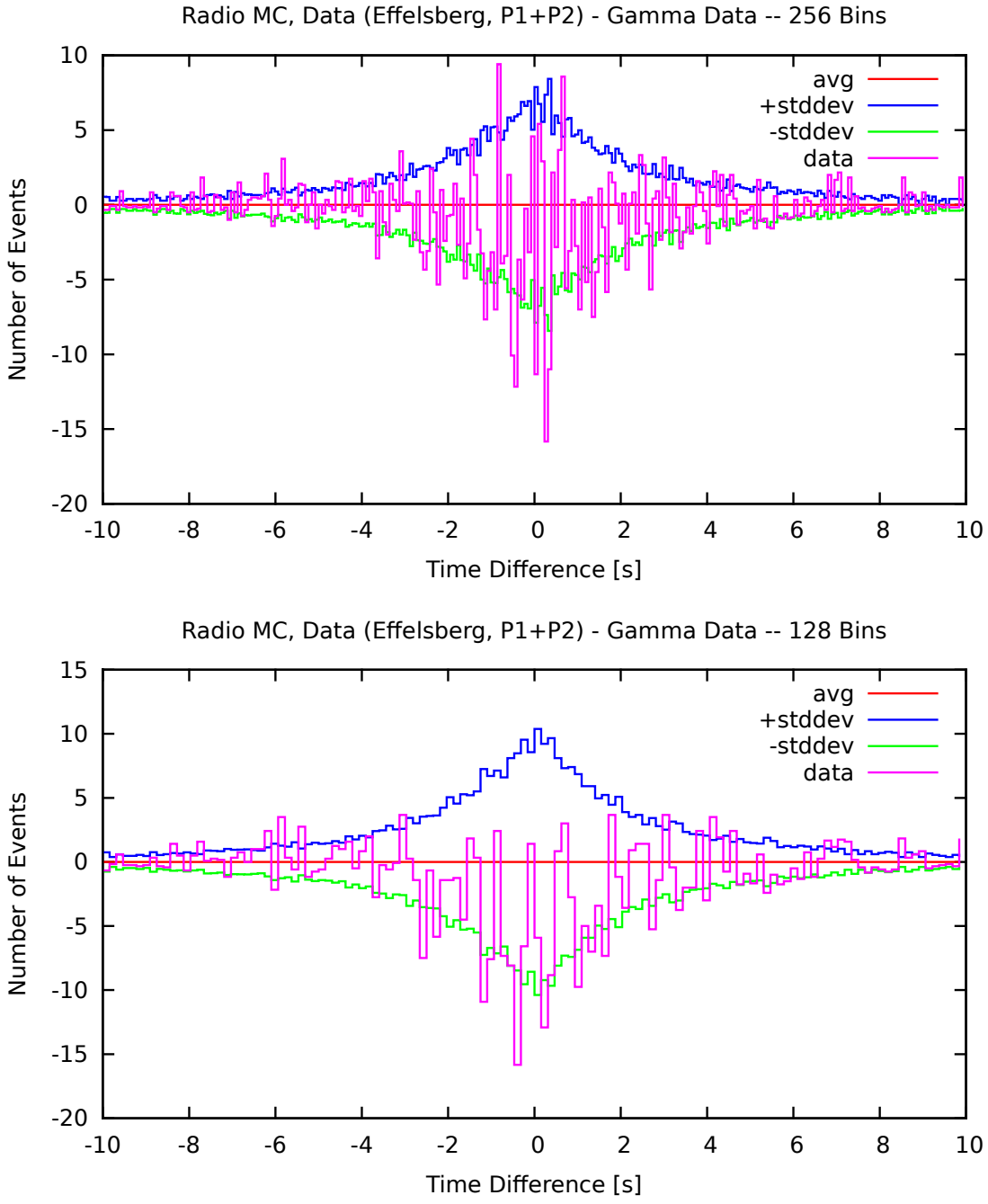
Radio MC, Data (Effelsberg, P1+P2) - Gamma Data -- 256 Bins
Number of Events
Time Difference [s]
avg
+stddev
-stddev
data
10
5
0
-5
-10
-15
-20
-10
-8
-6
-4
-2
0
2
4
6
8
10
Radio MC, Data (Effelsberg, P1+P2) - Gamma Data -- 128 Bins
Number of Events
Time Difference [s]
avg
+stddev
-stddev
data
15
10
5
0
-5
-10
-15
-20
-10
-8
-6
-4
-2
0
2
4
6
8
10

Figure C.23.

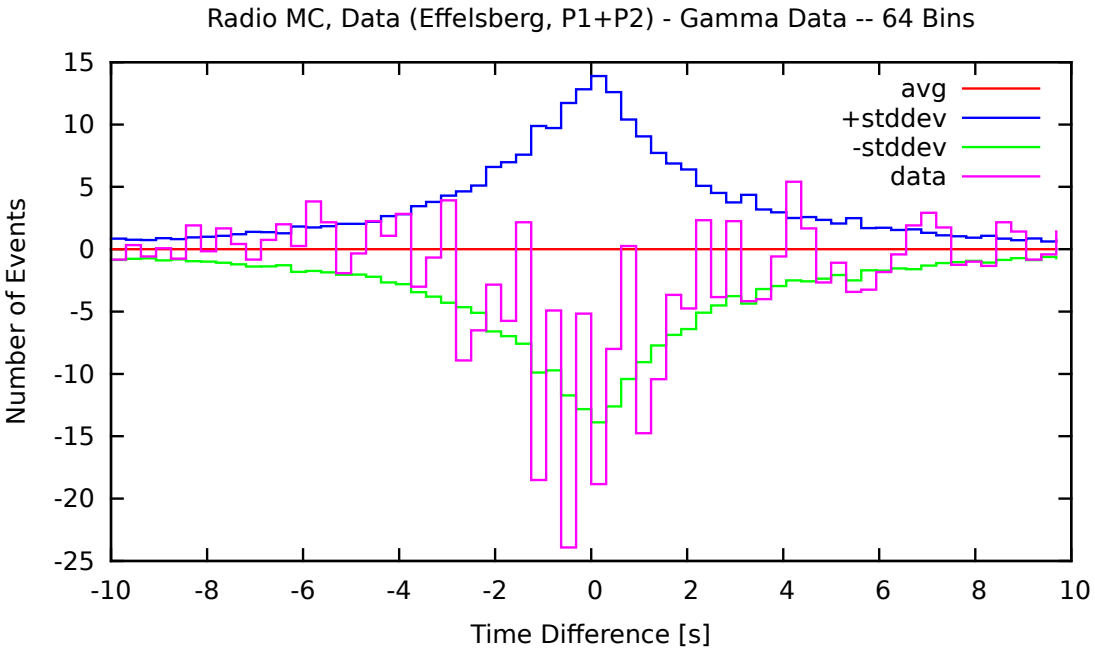
Radio MC, Data (Effelsberg, P1+P2) - Gamma Data -- 64 Bins
Number of Events
Time Difference [s]
avg
+stddev
-stddev
data
15
10
5
0
-5
-10
-15
-20
-25
-10
-8
-6
-4
-2
0
2
4
6
8
10

Figure C.24.

C.3. Time Differences: Radio Data (WSRT) – γ-ray Data

C.3.1. No Phase Cuts in γ-ray Data

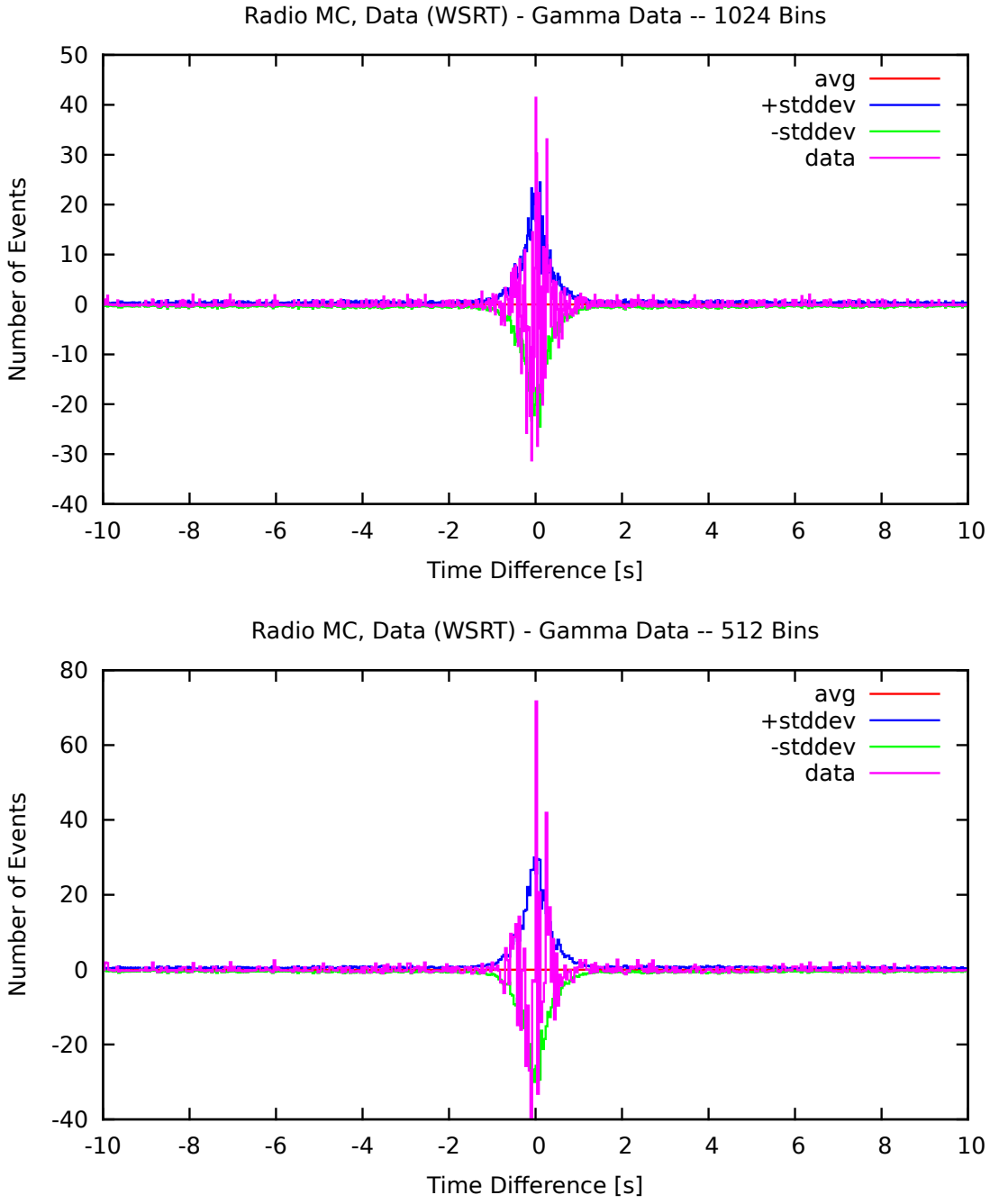

Figure C.25.

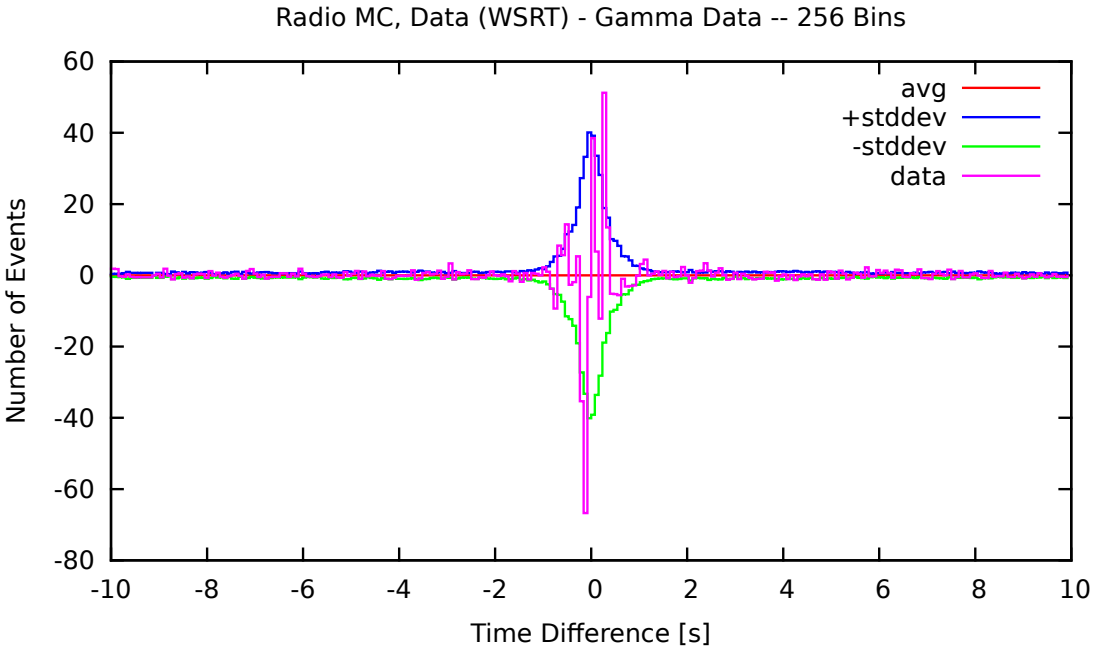
Radio MC, Data (WSRT) - Gamma Data -- 256 Bins
Number of Events
Time Difference [s]
avg
+stddev
-stddev
data
60
40
20
0
-20
-40
-60
-80
-10
-8
-6
-4
-2
0
2
4
6
8
10

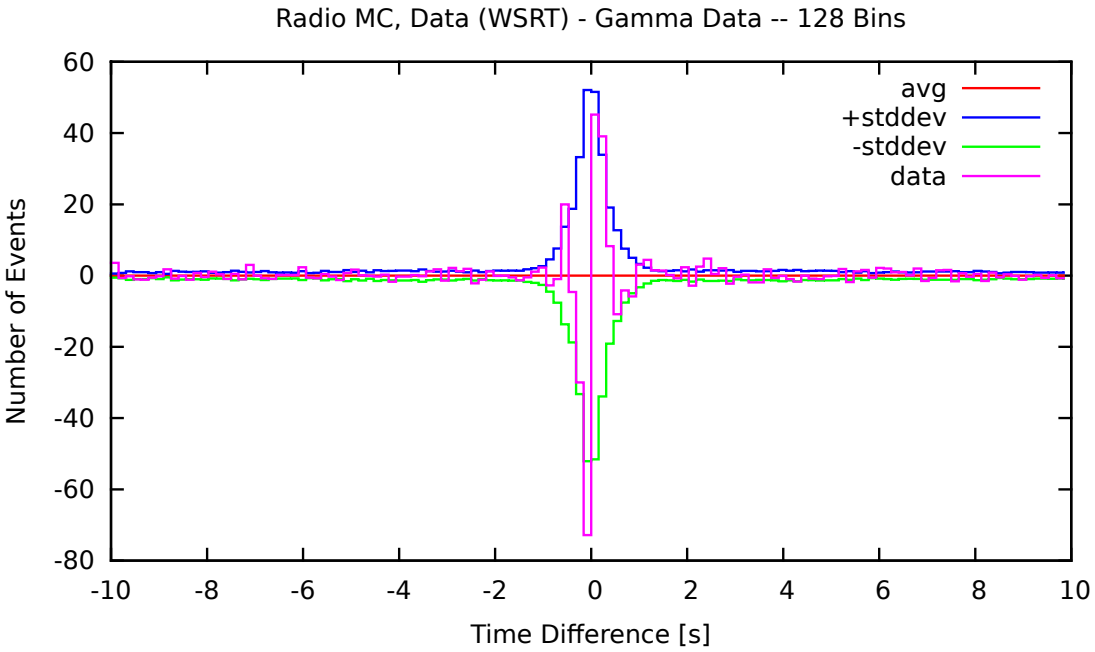
Radio MC, Data (WSRT) - Gamma Data -- 128 Bins
Number of Events
Time Difference [s]
avg
+stddev
-stddev
data
60
40
20
0
-20
-40
-60
-80
-10
-8
-6
-4
-2
0
2
4
6
8
10

Figure C.26.

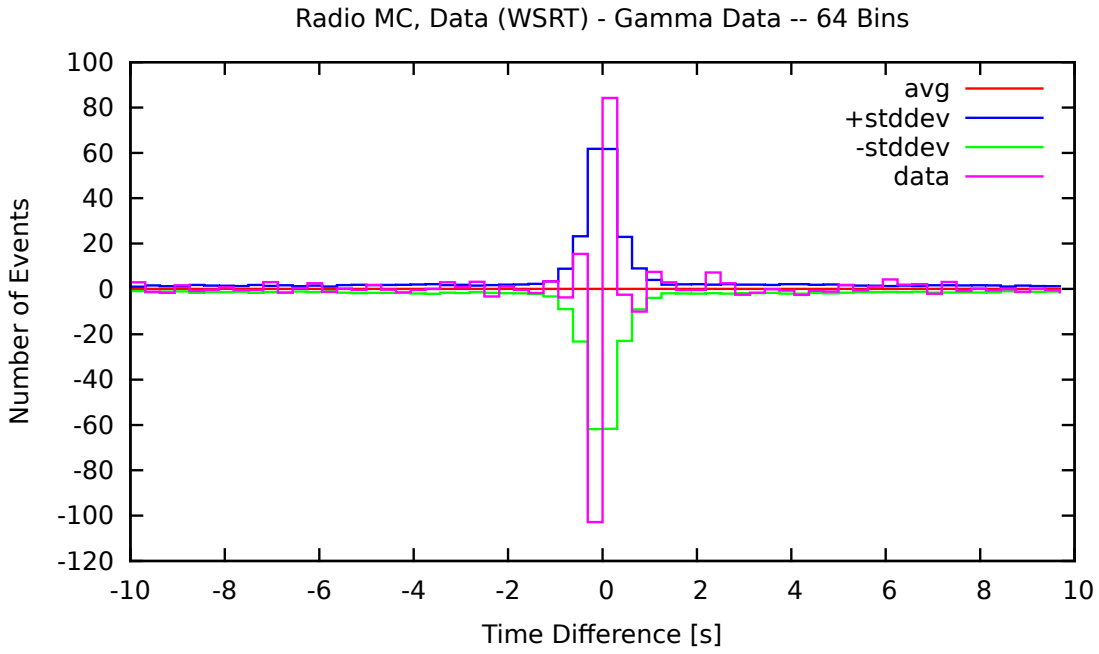
Radio MC, Data (WSRT) - Gamma Data -- 64 Bins
Number of Events
Time Difference [s]
avg
+stddev
-stddev
data
100
80
60
40
20
0
-20
-40
-60
-80
-100
-120
-10
-8
-6
-4
-2
0
2
4
6
8
10

Figure C.27.

C.3.2. P1 Phase Cut in γ-ray Data

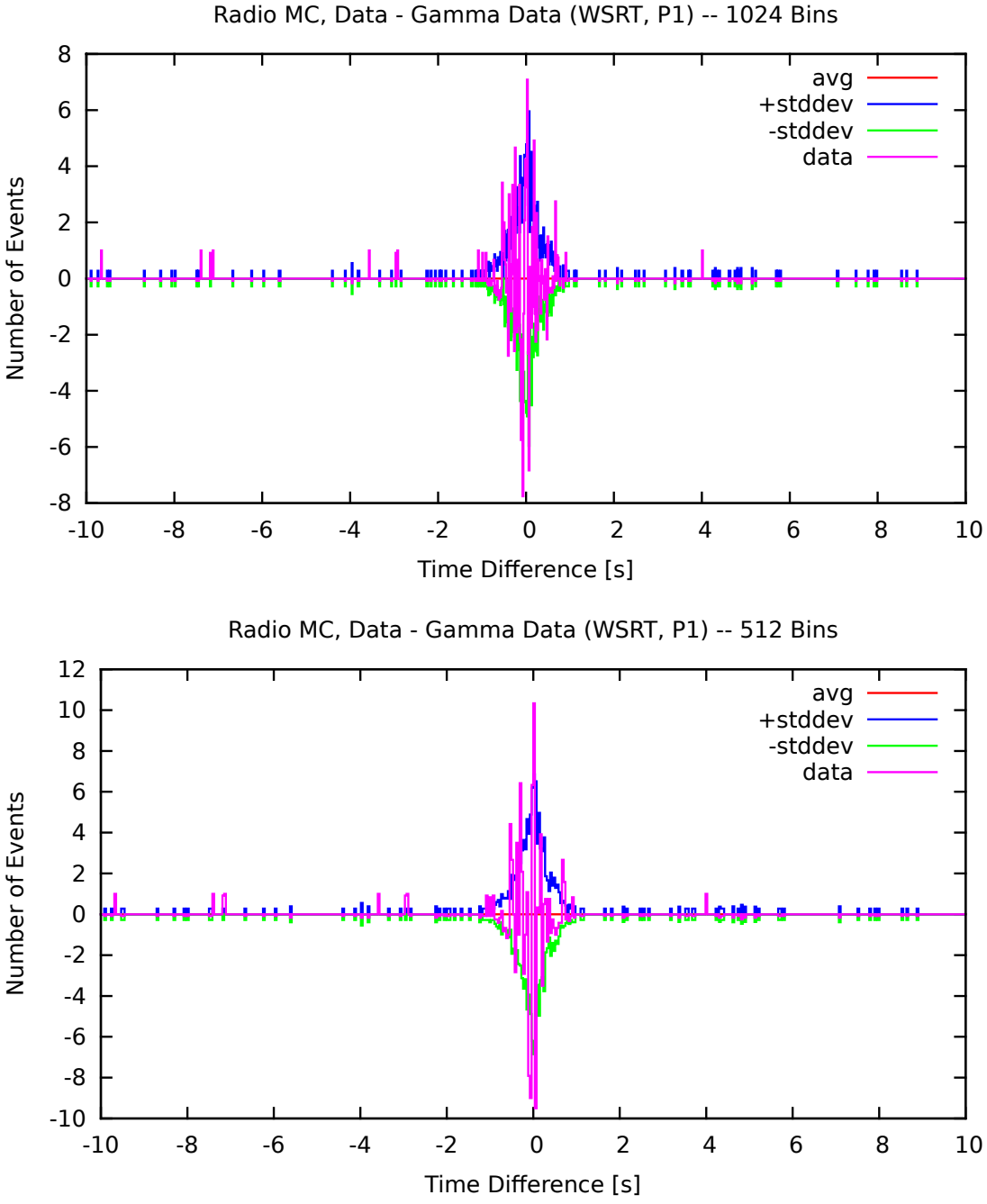

Figure C.28.

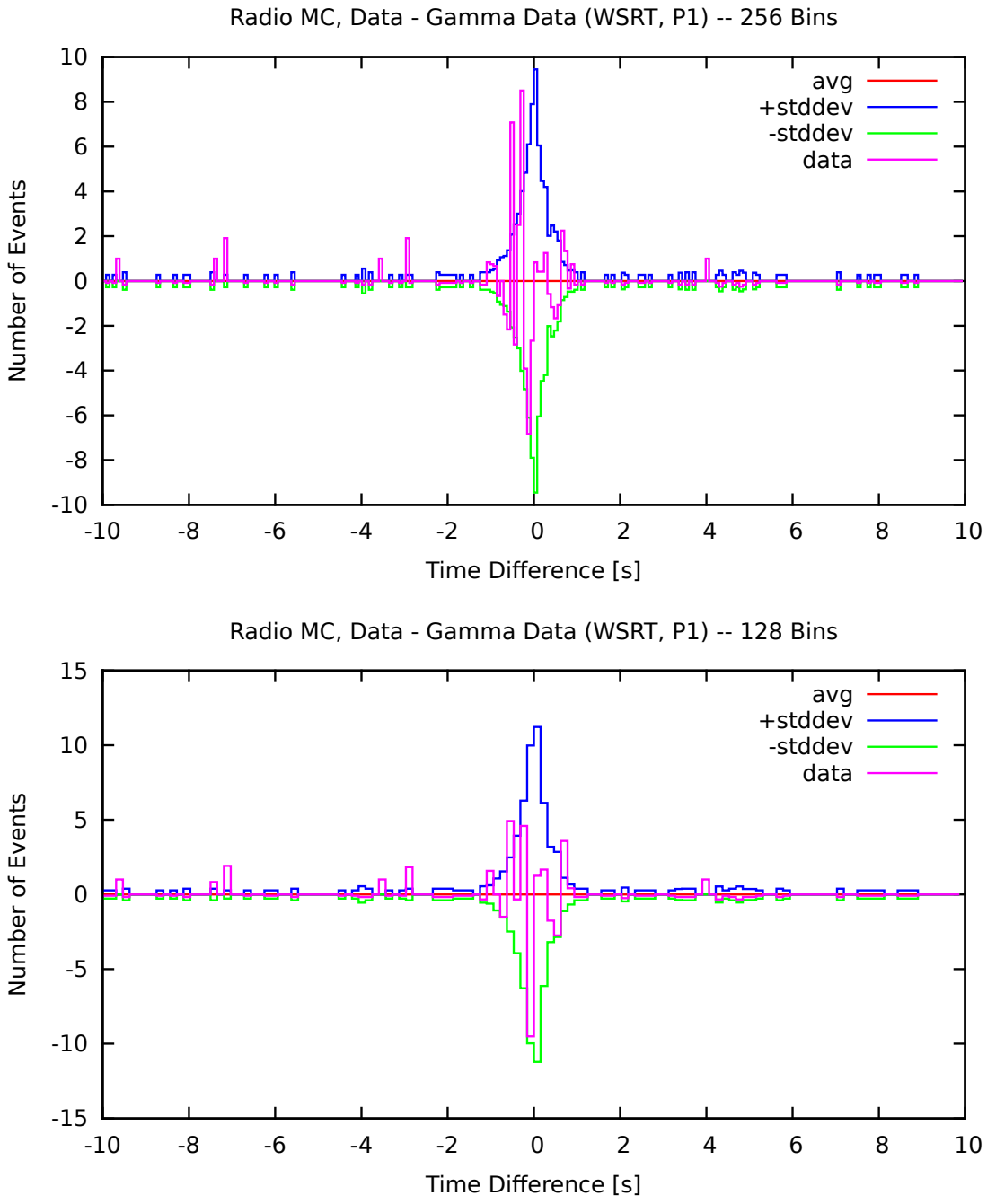
Radio MC, Data - Gamma Data (WSRT, P1) -- 256 Bins
Number of Events
Time Difference [s]
avg
+stddev
-stddev
data
Radio MC, Data - Gamma Data (WSRT, P1) -- 128 Bins
Number of Events
Time Difference [s]
avg
+stddev
-stddev
data

Figure C.29.

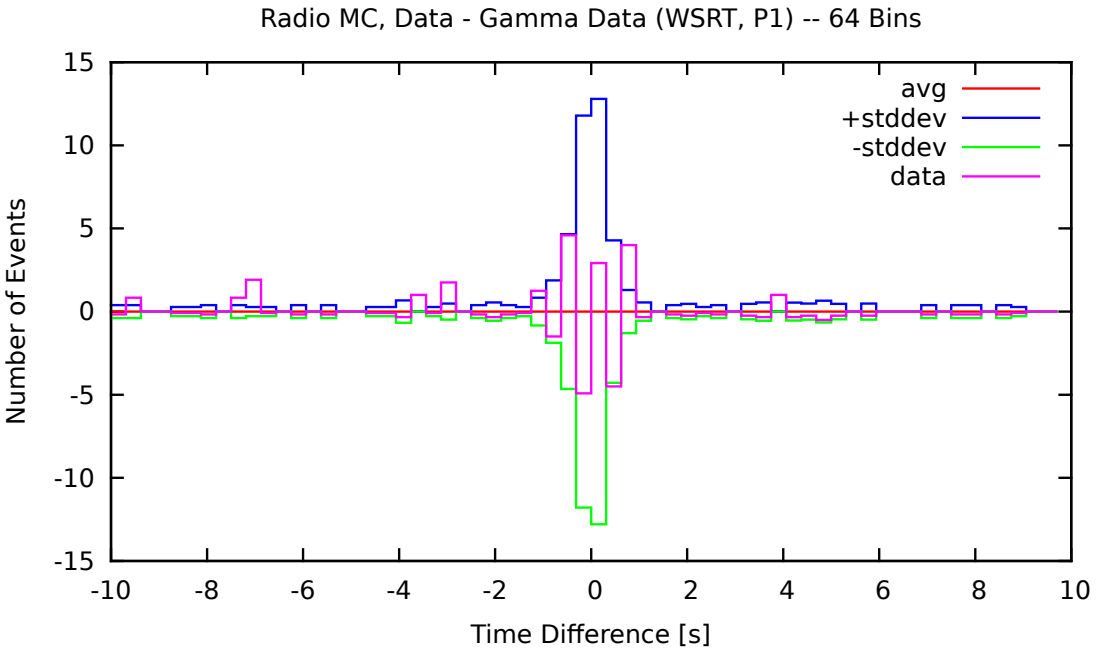
Radio MC, Data - Gamma Data (WSRT, P1) -- 64 Bins
Number of Events
Time Difference [s]
avg
+stddev
-stddev
data
15
10
5
0
-5
-10
-15
-10
-8
-6
-4
-2
0
2
4
6
8
10

Figure C.30.

C.3.3. P2 Phase Cut in γ-ray Data

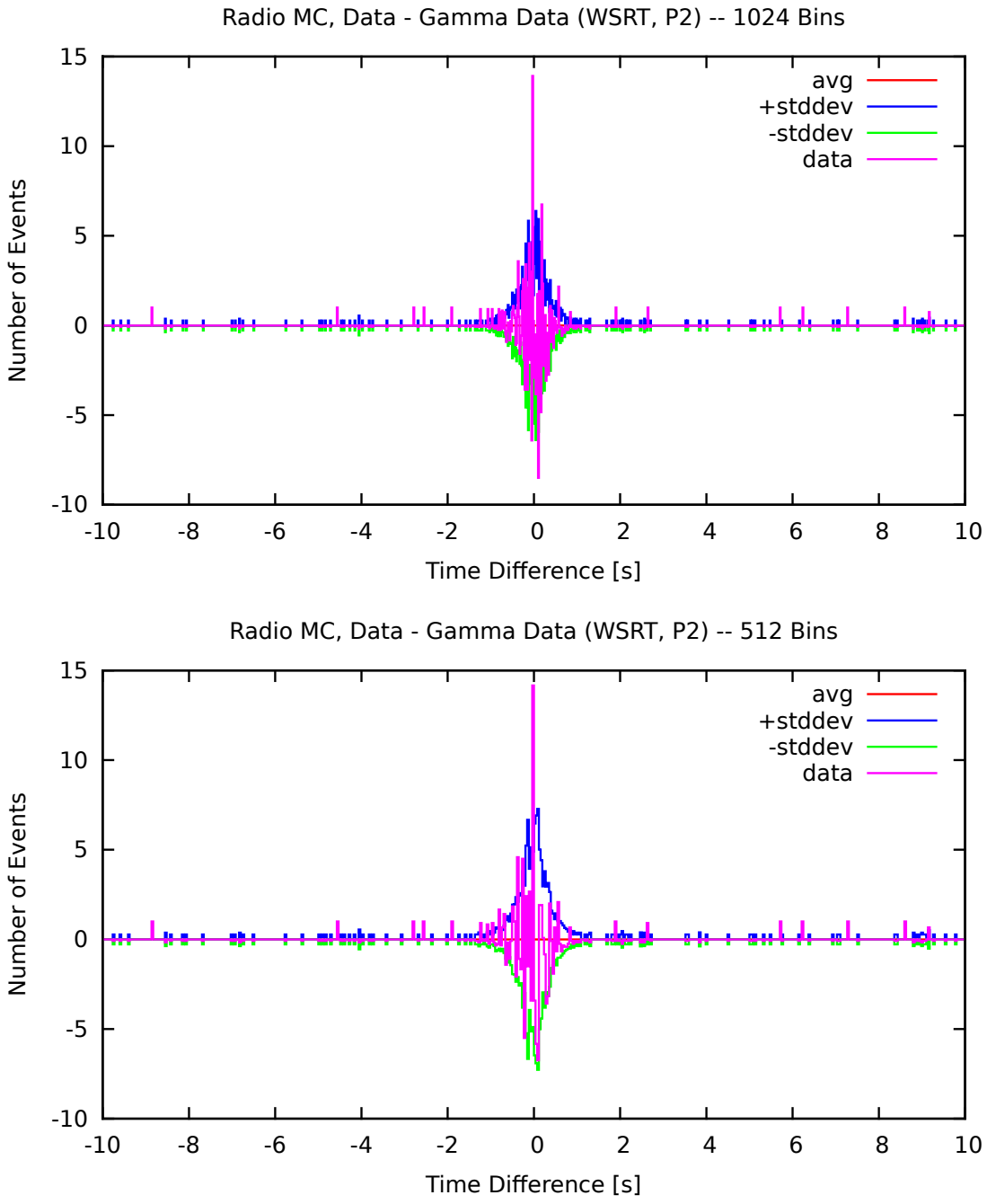

Figure C.31.

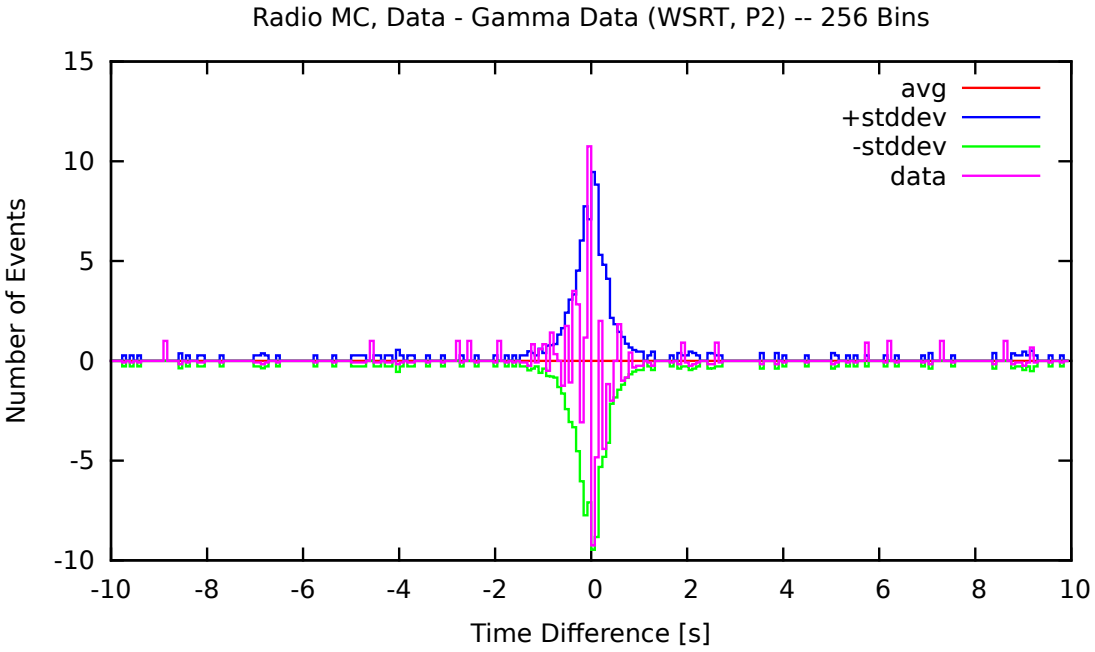
Radio MC, Data - Gamma Data (WSRT, P2) -- 256 Bins
avg
+stddev
-stddev
data
Number of Events
Time Difference [s]
15
10
5
0
-5
-10
-10
-8
-6
-4
-2
0
2
4
6
8
10

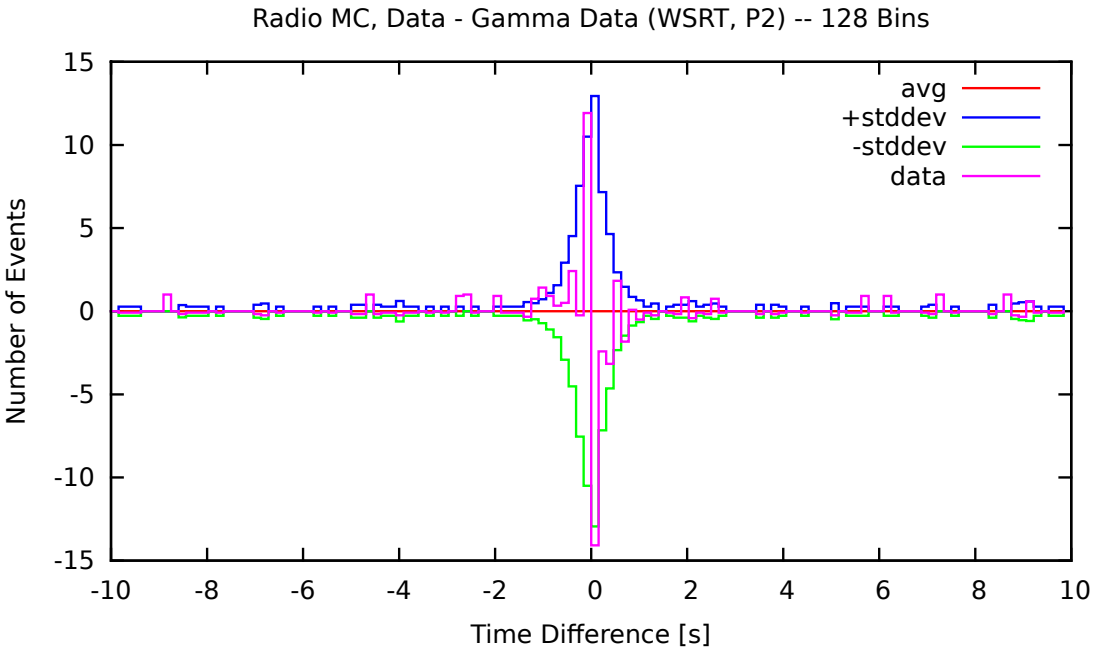
Radio MC, Data - Gamma Data (WSRT, P2) -- 128 Bins
avg
+stddev
-stddev
data
Number of Events
Time Difference [s]
15
10
5
0
-5
-10
-15
-10
-8
-6
-4
-2
0
2
4
6
8
10

Figure C.32.

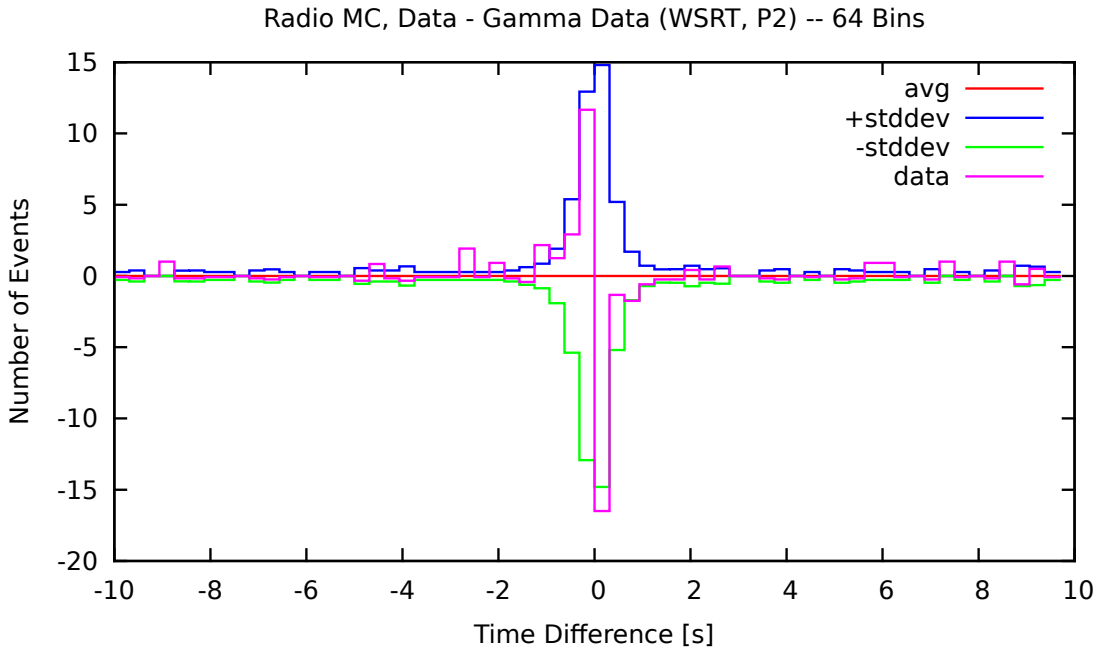
Radio MC, Data - Gamma Data (WSRT, P2) -- 64 Bins
Number of Events
Time Difference [s]
avg
+stddev
-stddev
data
15
10
5
0
-5
-10
-15
-20
-10
-8
-6
-4
-2
0
2
4
6
8
10

Figure C.33.

C.3.4. P1+P2 Phase Cut in γ-ray Data

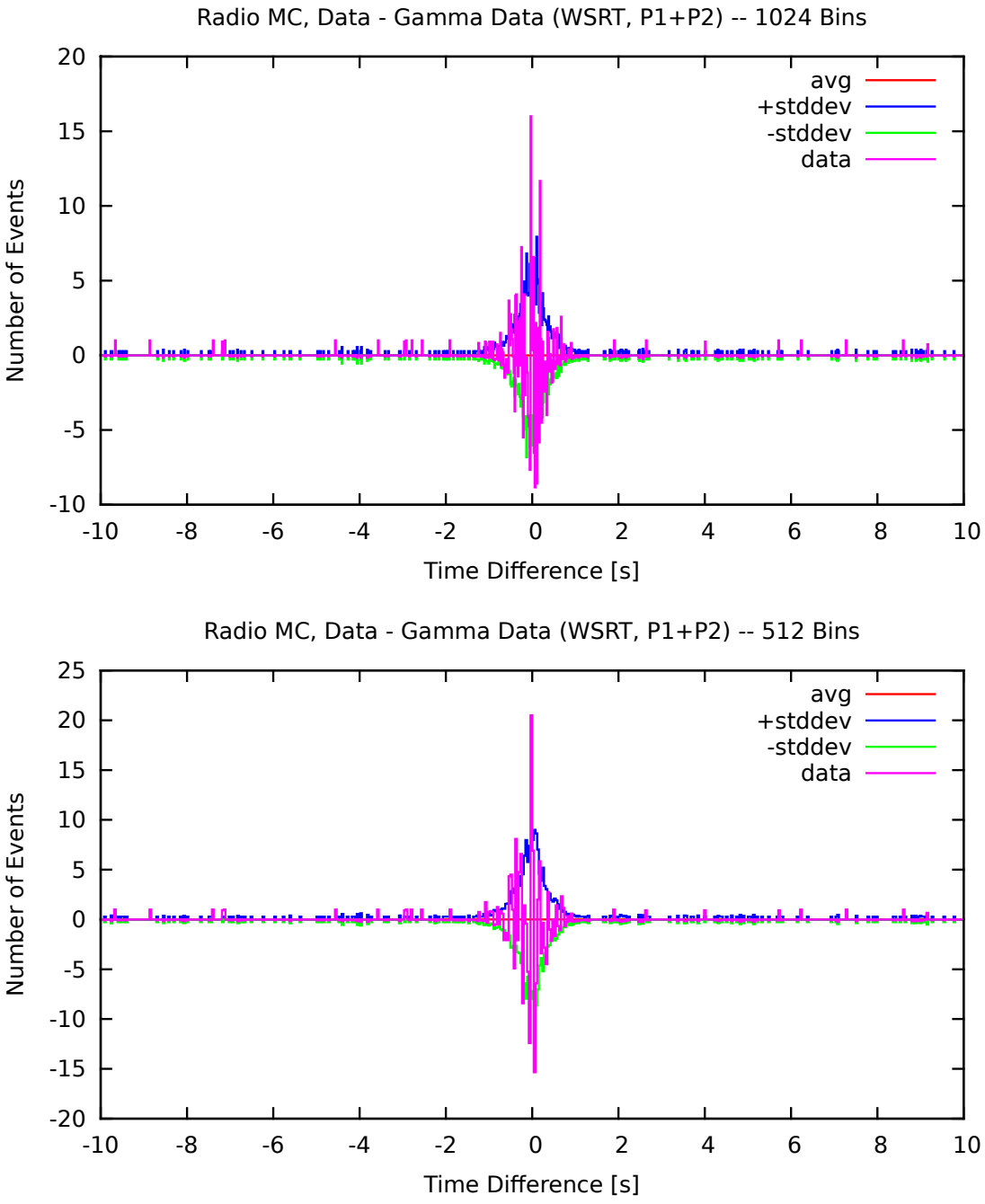

Figure C.34.

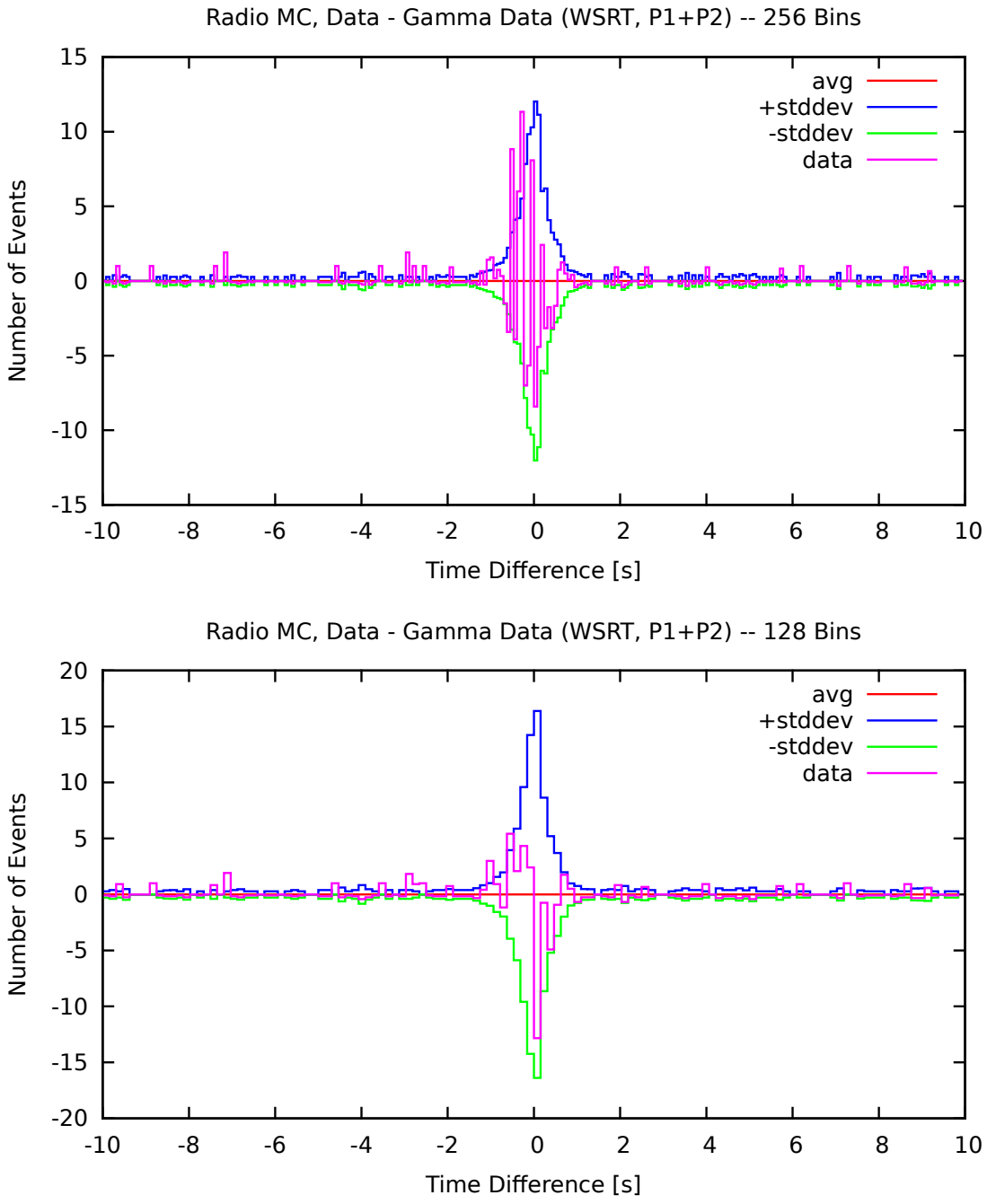
Radio MC, Data - Gamma Data (WSRT, P1+P2) -- 256 Bins
Number of Events
Time Difference [s]
avg
+stddev
-stddev
data
15
10
5
0
-5
-10
-15
-10
-8
-6
-4
-2
0
2
4
6
8
10
Radio MC, Data - Gamma Data (WSRT, P1+P2) -- 128 Bins
Number of Events
Time Difference [s]
avg
+stddev
-stddev
data
20
15
10
5
0
-5
-10
-15
-20
-10
-8
-6
-4
-2
0
2
4
6
8
10

Figure C.35.

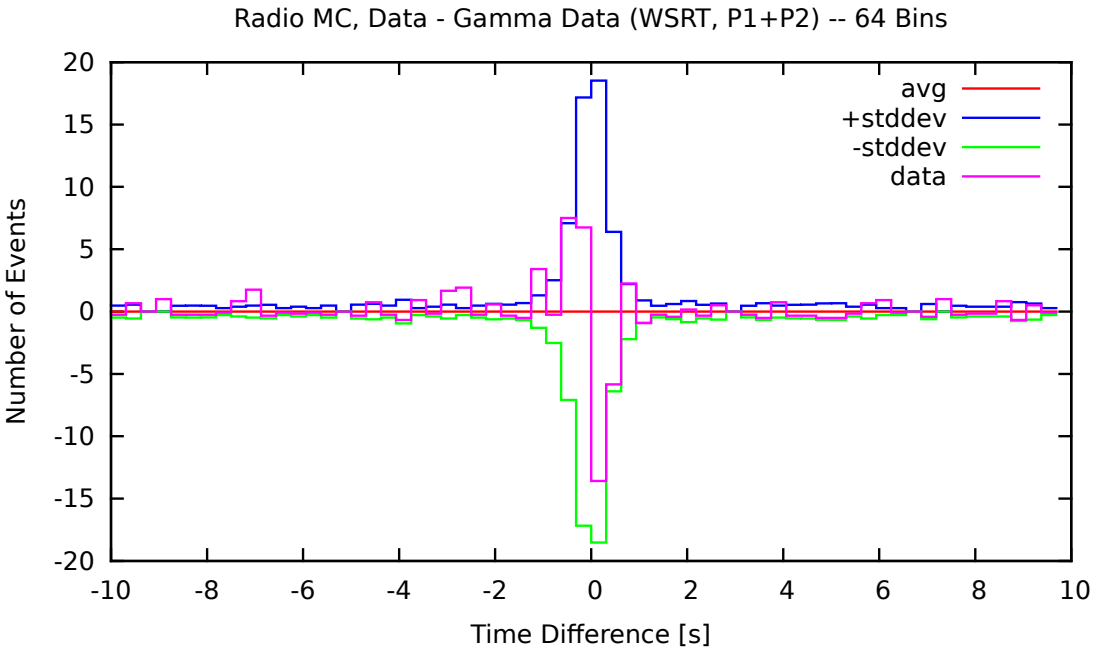
Radio MC, Data - Gamma Data (WSRT, P1+P2) -- 64 Bins
Number of Events
Time Difference [s]
avg
+stddev
-stddev
data
20
15
10
5
0
-5
-10
-15
-20
-10
-8
-6
-4
-2
0
2
4
6
8
10

Figure C.36.

C.3.5. Time Differences – LEE Corrected

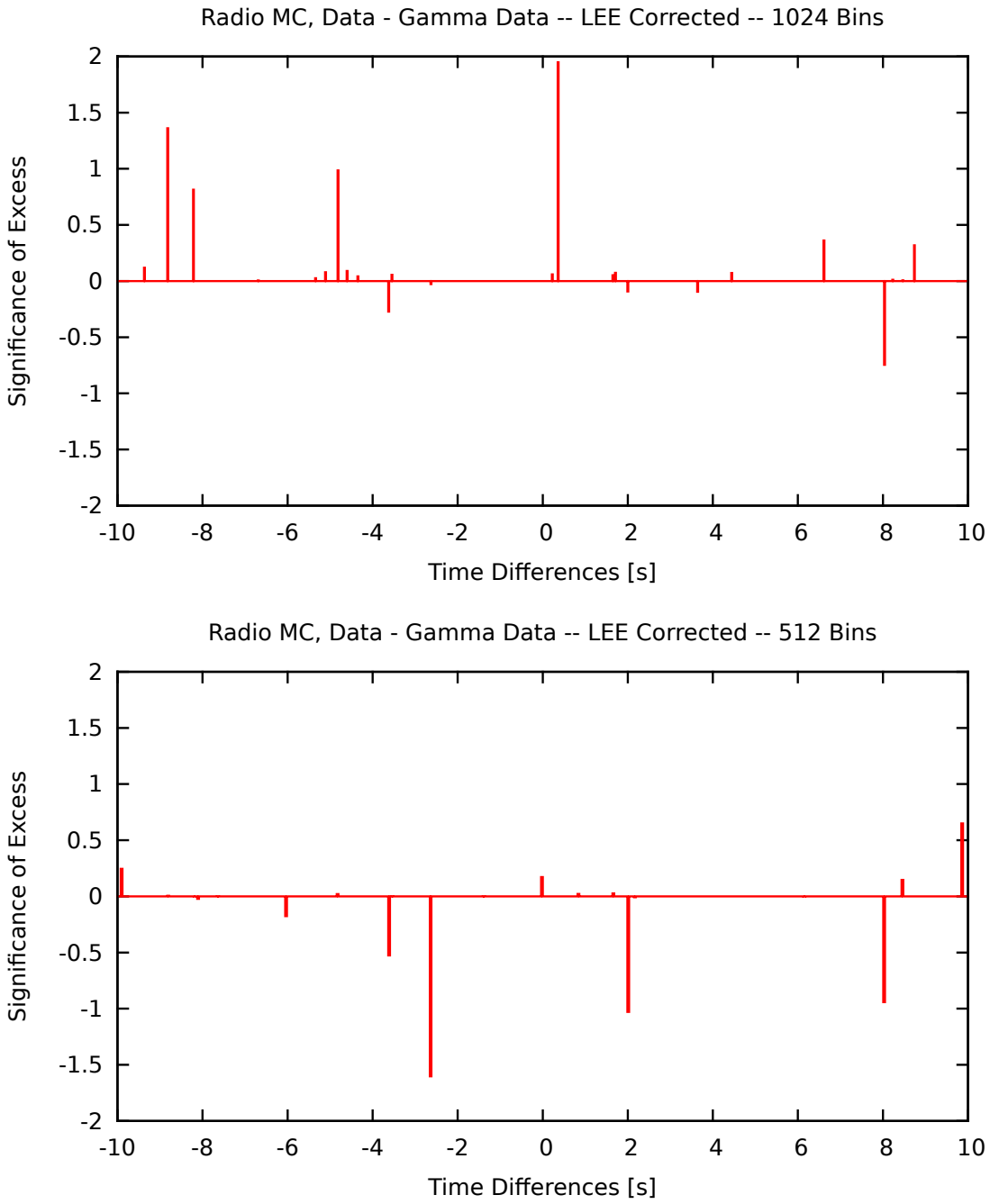

Figure C.37.

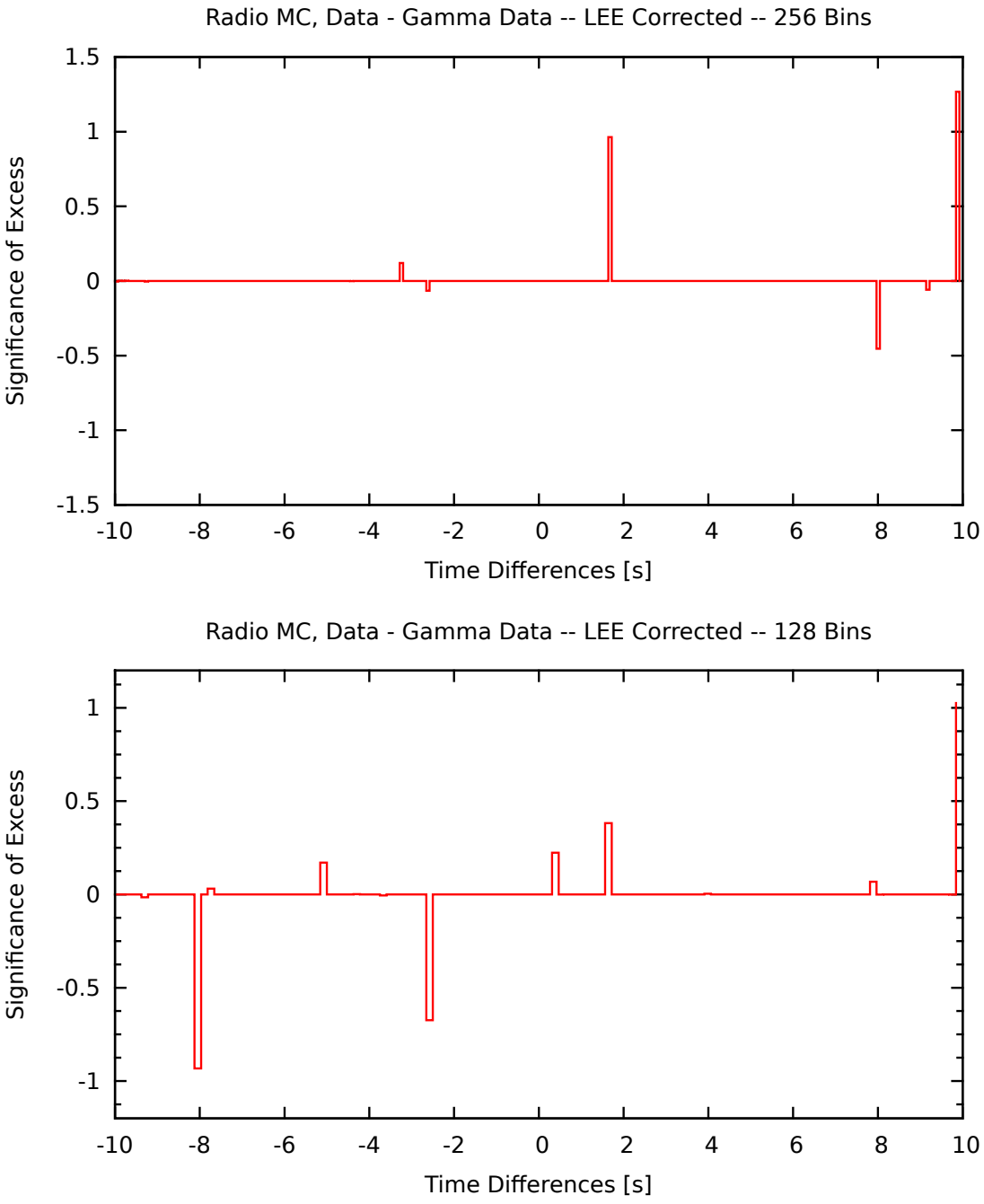
Radio MC, Data - Gamma Data -- LEE Corrected -- 256 Bins
Significance of Excess
Time Differences [s]
1.5
1
0.5
0
-0.5
-1
-1.5
-10
-8
-6
-4
-2
0
2
4
6
8
10
Radio MC, Data - Gamma Data -- LEE Corrected -- 128 Bins
Significance of Excess
Time Differences [s]
1
0.5
0
-0.5
-1
-10
-8
-6
-4
-2
0
2
4
6
8
10

Figure C.38.

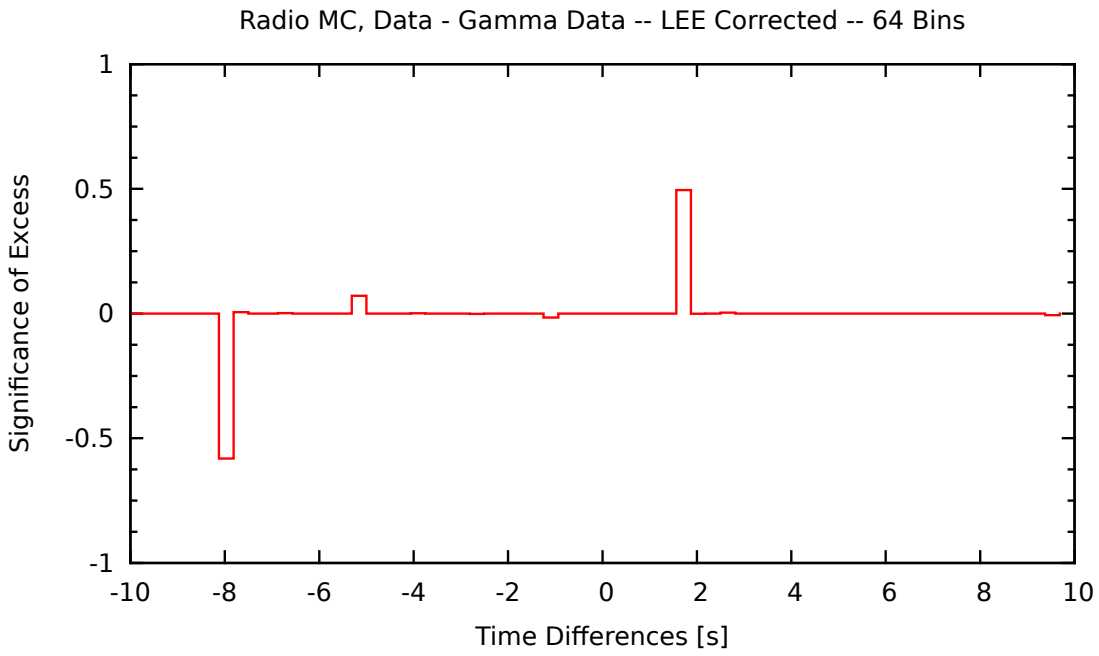
Radio MC, Data - Gamma Data -- LEE Corrected -- 64 Bins
Significance of Excess
Time Differences [s]
1
0.5
0
-0.5
-1
-10
-8
-6
-4
-2
0
2
4
6
8
10

Figure C.39.

C.4. Flux Enhancement – γ-ray MC Simulations

C.4.1. 12 γ-ray MC Simulations

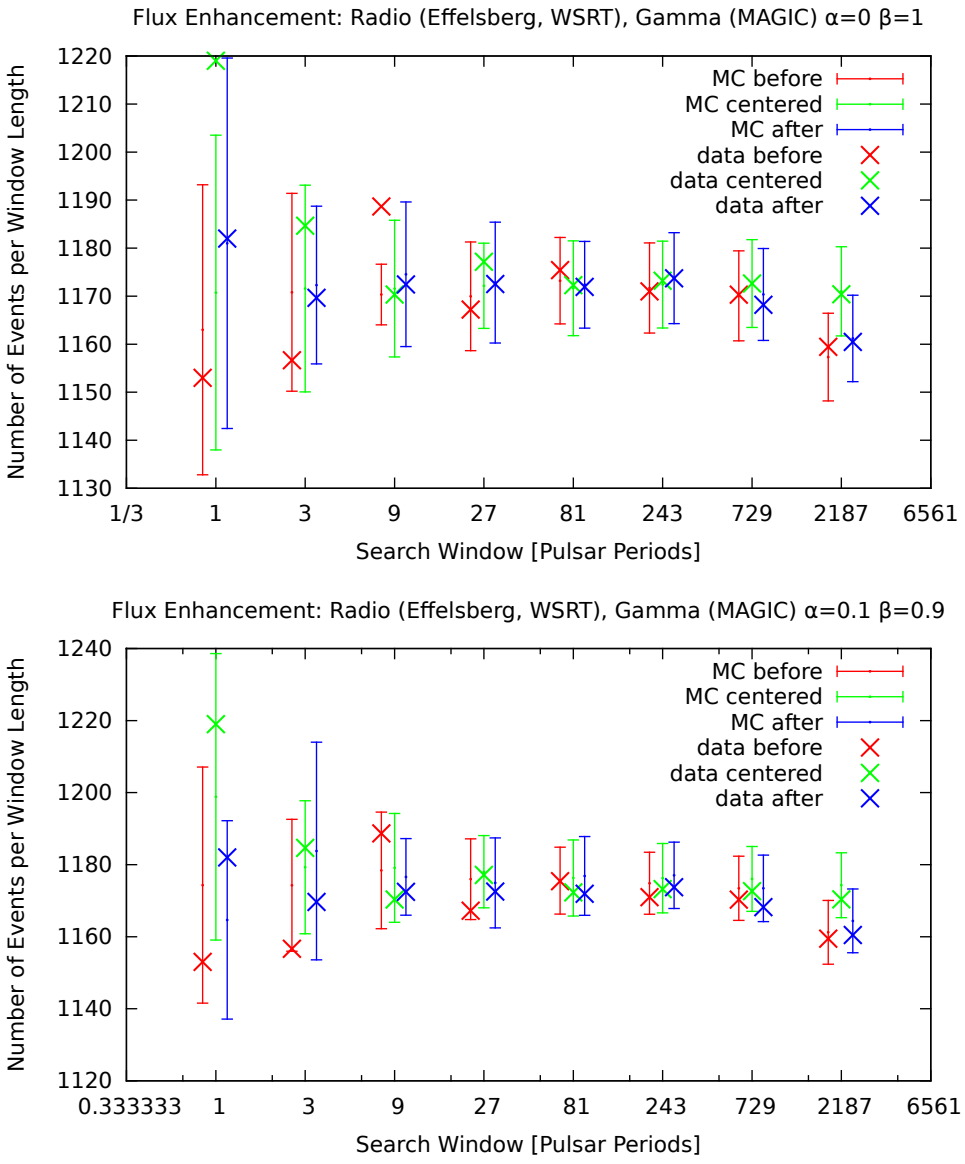

Figure C.40.

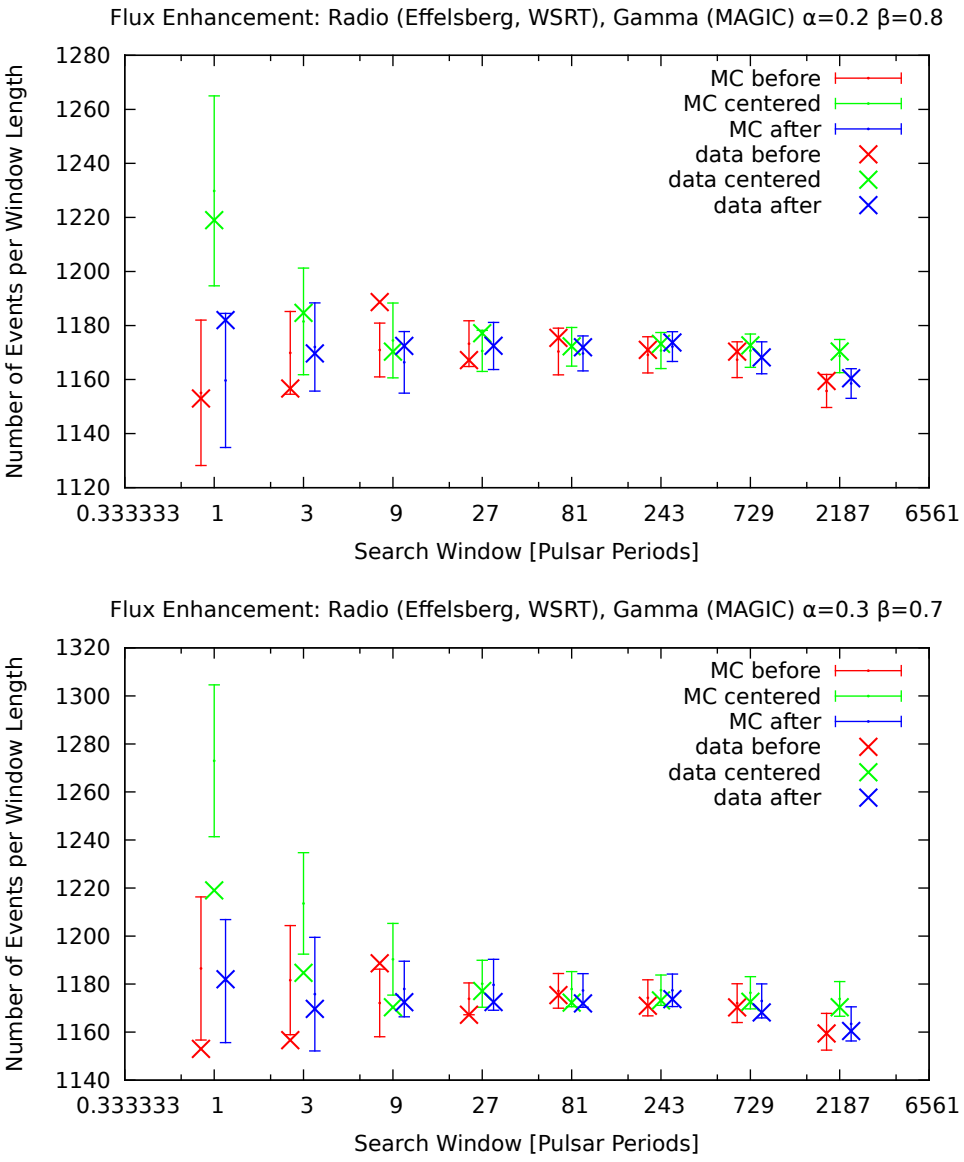
Flux Enhancement: Radio (Effelsberg, WSRT), Gamma (MAGIC) α=0.2 β=0.8
Number of Events per Window Length
Search Window [Pulsar Periods]
MC before
MC centered
MC after
data before
data centered
data after
1280
1260
1240
1220
1200
1180
1160
1140
1120
0.333333
1
3
9
27
81
243
729
2187
6561
Flux Enhancement: Radio (Effelsberg, WSRT), Gamma (MAGIC) α=0.3 β=0.7
Number of Events per Window Length
Search Window [Pulsar Periods]
MC before
MC centered
MC after
data before
data centered
data after
1320
1300
1280
1260
1240
1220
1200
1180
1160
1140
0.333333
1
3
9
27
81
243
729
2187
6561

Figure C.41.

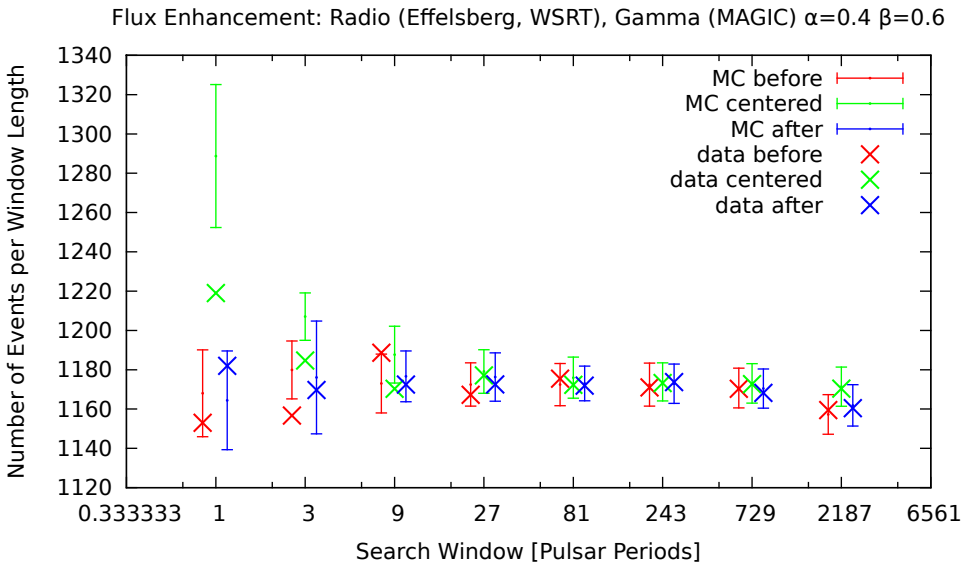
Flux Enhancement: Radio (Effelsberg, WSRT), Gamma (MAGIC) α=0.4 β=0.6
Number of Events per Window Length
Search Window [Pulsar Periods]
MC before
MC centered
MC after
data before
data centered
data after
1340
1320
1300
1280
1260
1240
1220
1200
1180
1160
1140
1120
0.333333
1
3
9
27
81
243
729
2187
6561

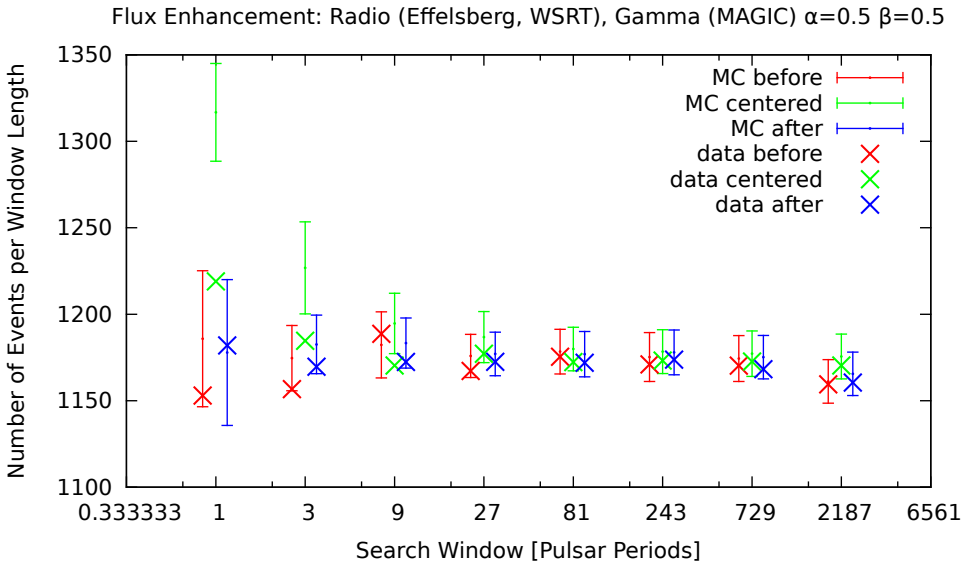
Flux Enhancement: Radio (Effelsberg, WSRT), Gamma (MAGIC) α=0.5 β=0.5
Number of Events per Window Length
Search Window [Pulsar Periods]
MC before
MC centered
MC after
data before
data centered
data after
1350
1300
1250
1200
1150
1100
0.333333
1
3
9
27
81
243
729
2187
6561

Figure C.42.

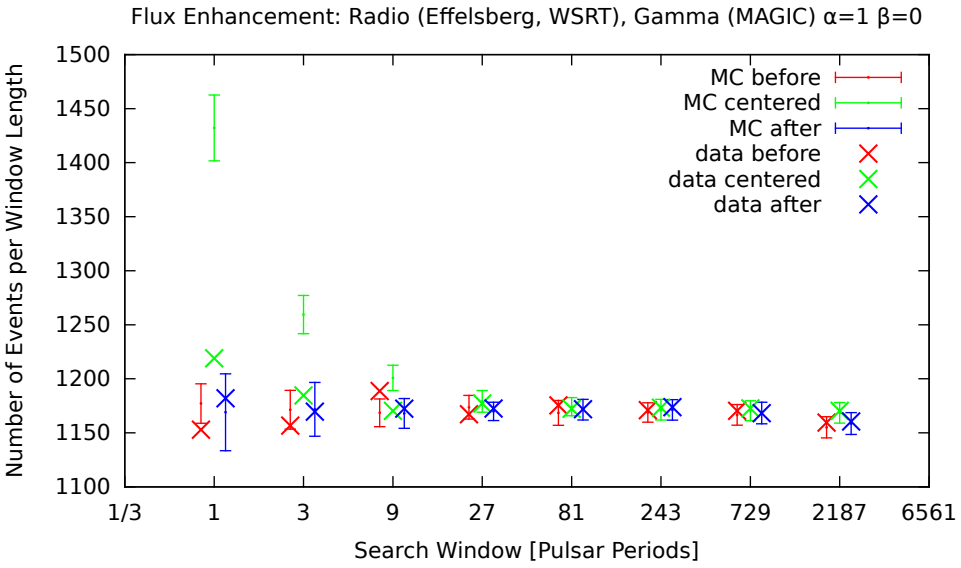
Flux Enhancement: Radio (Effelsberg, WSRT), Gamma (MAGIC) α=1 β=0
Number of Events per Window Length
Search Window [Pulsar Periods]
1500
1450
1400
1350
1300
1250
1200
1150
1100
1/3
1
3
9
27
81
243
729
2187
6561
MC before
MC centered
MC after
data before
data centered
data after

Figure C.43.

C.4.2. 200 γ-ray MC Simulations

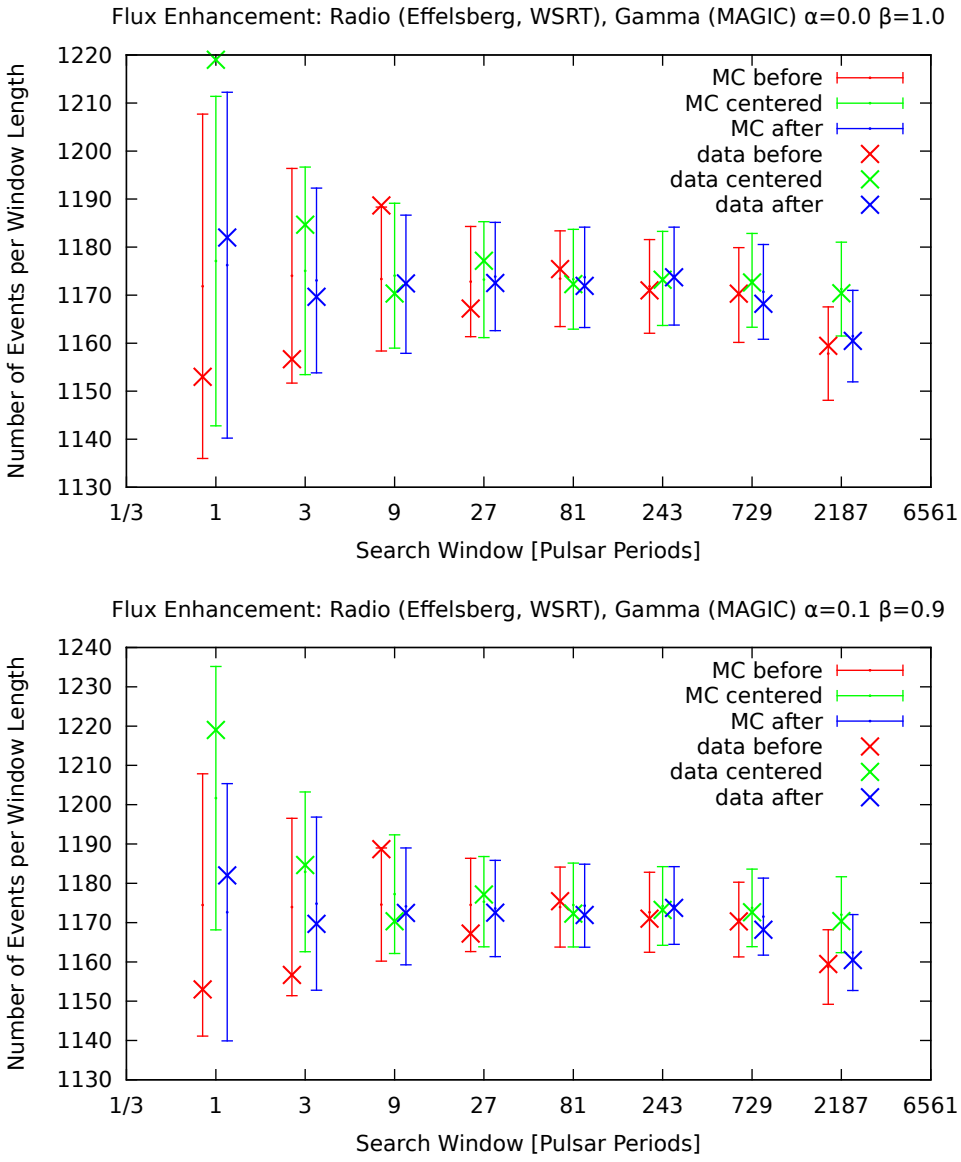

Figure C.44.

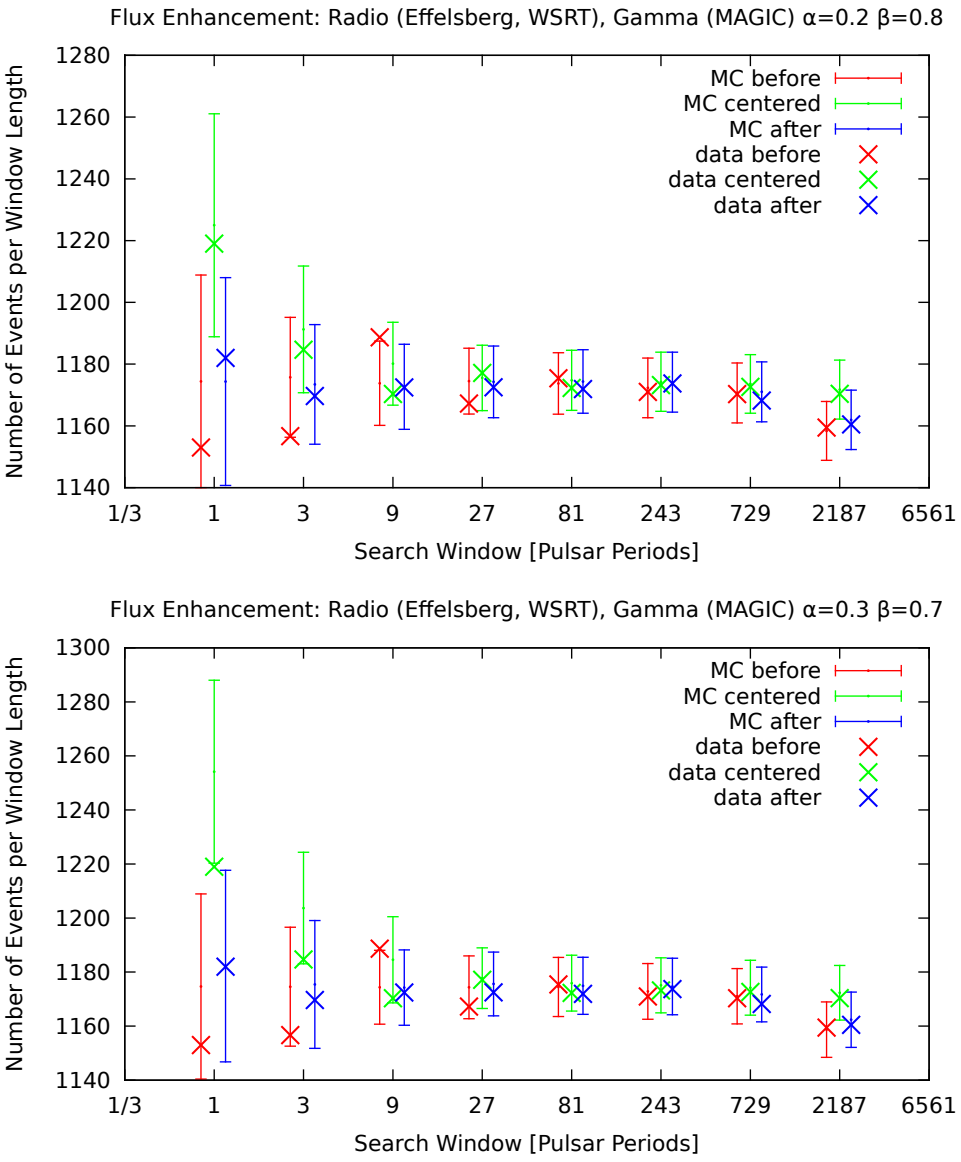
Flux Enhancement: Radio (Effelsberg, WSRT), Gamma (MAGIC) α=0.2 β=0.8
Number of Events per Window Length
Search Window [Pulsar Periods]
MC before
MC centered
MC after
data before
data centered
data after
1280
1260
1240
1220
1200
1180
1160
1140
1/3
1
3
9
27
81
243
729
2187
6561
Flux Enhancement: Radio (Effelsberg, WSRT), Gamma (MAGIC) α=0.3 β=0.7
Number of Events per Window Length
Search Window [Pulsar Periods]
MC before
MC centered
MC after
data before
data centered
data after
1300
1280
1260
1240
1220
1200
1180
1160
1140
1/3
1
3
9
27
81
243
729
2187
6561

Figure C.45.

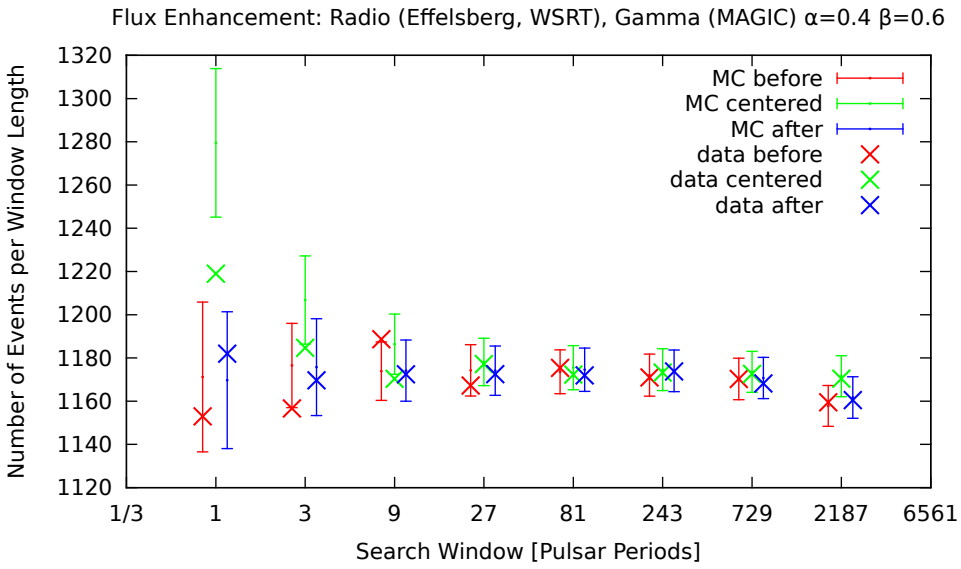
Flux Enhancement: Radio (Effelsberg, WSRT), Gamma (MAGIC) α=0.4 β=0.6
Number of Events per Window Length
Search Window [Pulsar Periods]
MC before
MC centered
MC after
data before
data centered
data after
1320
1300
1280
1260
1240
1220
1200
1180
1160
1140
1120
1/3
1
3
9
27
81
243
729
2187
6561

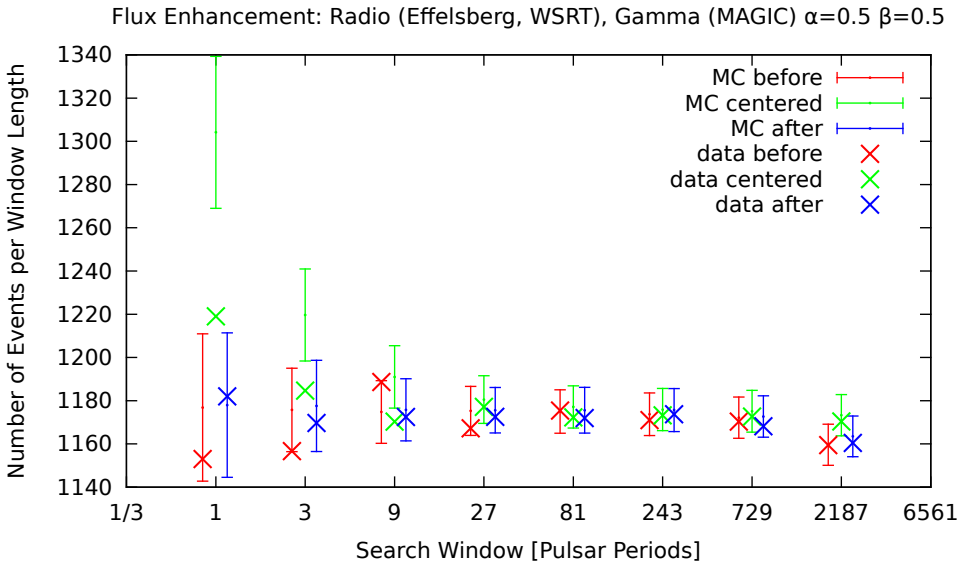
Flux Enhancement: Radio (Effelsberg, WSRT), Gamma (MAGIC) α=0.5 β=0.5
Number of Events per Window Length
Search Window [Pulsar Periods]
MC before
MC centered
MC after
data before
data centered
data after
1340
1320
1300
1280
1260
1240
1220
1200
1180
1160
1140
1/3
1
3
9
27
81
243
729
2187
6561

Figure C.46.

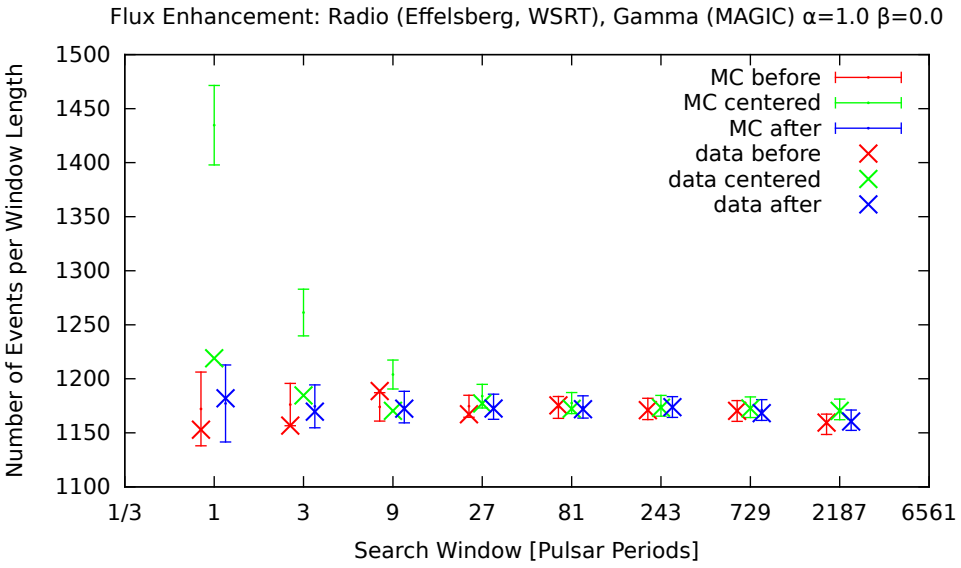
Flux Enhancement: Radio (Effelsberg, WSRT), Gamma (MAGIC) α=1.0 β=0.0
Number of Events per Window Length
Search Window [Pulsar Periods]
1500
1450
1400
1350
1300
1250
1200
1150
1100
1/3
1
3
9
27
81
243
729
2187
6561
MC before
MC centered
MC after
data before
data centered
data after

Figure C.47.

C.4.3. Flux Enhancement: γ-ray MC Simulations and Effelsberg Data

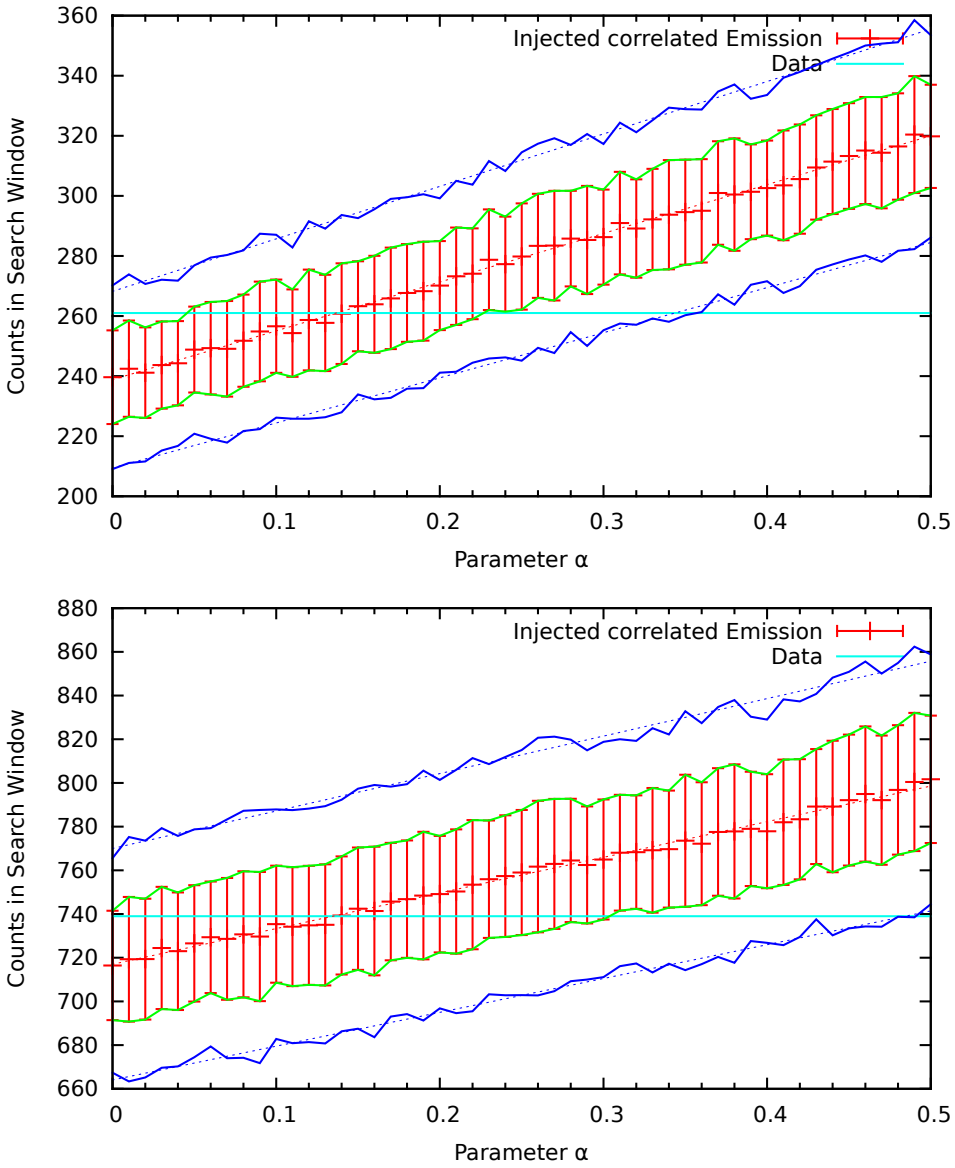

Figure C.48.: Counts in the centered search window for one (upper figure) and three (lower figure) Crab pulsar rotation periods and different values of α. The cyan line is the corresponding data value at 261 (upper figure) and 739 (lower figure) counts.

Bibliography

A. A. Abdo, M. Ackermann, M. Ajello, W. B. Atwood, M. Axelsson, L. Baldini, J. Ballet, G. Barbiellini, M. G. Baring, D. Bastieri, K. Bechtol, R. Bellazzini, B. Berenji, R. D. Blandford, E. D. Bloom, E. Bonamente, A. W. Borgland, J. Bregeon, A. Brez, M. Brigida, P. Bruel, T. H. Burnett, G. A. Caliandro, R. A. Cameron, F. Camilo, P. A. Caraveo, J. M. Casandjian, C. Cecchi, Ö. Çelik, A. Chekhtman, C. C. Cheung, J. Chiang, S. Ciprini, R. Claus, I. Cognard, J. Cohen-Tanugi, L. R. Cominsky, J. Conrad, C. D. Dermer, A. de Angelis, A. de Luca, F. de Palma, S. W. Digel, E. d. C. e. Silva, P. S. Drell, R. Dubois, D. Dumora, C. Espinoza, C. Farnier, C. Favuzzi, S. J. Fegan, E. C. Ferrara, W. B. Focke, M. Frailis, P. C. C. Freire, Y. Fukazawa, S. Funk, P. Fusco, F. Gargano, D. Gasparrini, N. Gehrels, S. Germani, G. Giavitto, B. Giebels, N. Giglietto, F. Giordano, T. Glanzman, G. Godfrey, I. A. Grenier, M.-H. Grondin, J. E. Grove, L. Guillemot, S. Guiriec, Y. Hanabata, A. K. Harding, M. Hayashida, E. Hays, R. E. Hughes, G. Jóhannesson, A. S. Johnson, R. P. Johnson, T. J. Johnson, W. N. Johnson, S. Johnston, T. Kamae, H. Katagiri, J. Kataoka, N. Kawai, M. Kerr, J. Knödlseder, M. L. Kocian, M. Kramer, F. Kuehn, M. Kuss, J. Lande, L. Latronico, S.-H. Lee, M. Lemoine-Goumard, F. Longo, F. Loparco, B. Lott, M. N. Lovellette, P. Lubrano, A. G. Lyne, A. Makeev, M. Marelli, M. N. Mazziotta, J. E. McEnery, C. Meurer, P. F. Michelson, W. Mitthumsiri, T. Mizuno, A. A. Moiseev, C. Monte, M. E. Monzani, E. Moretti, A. Morselli, I. V. Moskalenko, S. Murgia, T. Nakamori, P. L. Nolan, J. P. Norris, A. Noutsos, E. Nuss, T. Ohsugi, N. Omodei, E. Orlando, J. F. Ormes, M. Ozaki, D. Paneque, J. H. Panetta, D. Parent, V. Pelassa, M. Pepe, M. Pesce-Rollins, M. Pierbattista, F. Piron, T. A. Porter, S. Rainò, R. Rando, P. S. Ray, M. Razzano, A. Reimer, O. Reimer, T. Reposeur, S. Ritz, L. S. Rochester, A. Y. Rodriguez, R. W. Romani, M. Roth, F. Ryde, H. F.-W. Sadrozinski, D. Sanchez, A. Sander, P. M. Saz Parkinson, J. D. Scargle, C. Sgrò, E. J. Siskind, D. A. Smith, P. D. Smith, G. Spandre, P. Spinelli, B. W. Stappers, M. S. Strickman, D. J. Suson, H. Tajima, H. Takahashi, T. Tanaka, J. B. Thayer, J. G. Thayer, G. Theureau, D. J. Thompson, S. E. Thorsett, L. Tibaldo, D. F. Torres, G. Tosti, A. Tramacere, Y. Uchiyama, T. L. Usher, A. Van Etten, V. Vasileiou, N. Vilchez, V. Vitale, A. P. Waite, E. Wallace, P. Wang, K. Watters, P. Weltevrede, B. L. Winer, K. S. Wood, T. Ylinen, and M. Ziegler. Fermi Large Area Telescope Observations of the Crab Pulsar And Nebula. *ApJ*, 708:1254–1267, January 2010a. doi: 10.1088/0004-637X/708/2/1254.

A. A. Abdo, M. Ackermann, M. Ajello, W. B. Atwood, M. Axelsson, L. Baldini, J. Ballet, G. Barbiellini, M. G. Baring, D. Bastieri, and et al. The First Fermi Large Area Telescope Catalog of Gamma-ray Pulsars. *ApJS*, 187:460–494, April 2010b. doi: 10.1088/0067-0049/187/2/460.

A. A. Abdo, M. Ajello, A. Allafort, L. Baldini, J. Ballet, G. Barbiellini, M. G. Baring, D. Bastieri, A. Belfiore, R. Bellazzini, and et al. The Second Fermi Large Area Telescope Catalog of Gamma-Ray Pulsars. *ApJS*, 208:17, October 2013. doi: 10.1088/0067-0049/208/2/17.

M. Abramowitz and I. A. Stegun. *Handbook of mathematical functions with formulas, graphs, and mathematical tables*. 1965.

J. Albert, E. Aliu, H. Anderhub, P. Antoranz, A. Armada, M. Asensio, C. Baixeras, J. A. Barrio, H. Bartko, D. Bastieri, J. Becker, W. Bednarek, K. Berger, C. Bigongiari, A. Biland, R. K. Bock, P. Bordas, V. Bosch-Ramon, T. Bretz, I. Britvitch, M. Camara, E. Carmona, A. Chilingarian, S. Ciprini, J. A. Coarasa, S. Commichau, J. L. Contreras, J. Cortina, M. T. Costado, V. Curtef, V. Danielyan, F. Dazzi, A. de Angelis, C. Delgado, R. de Los Reyes, B. de Lotto, E. Domingo-Santamaría, D. Dorner, M. Doro, M. Errando, M. Fagiolini, D. Ferenc, E. Fernández, R. Firpo, J. Flix, M. V. Fonseca, L. Font, M. Fuchs, N. Galante, R. J. García-López, M. Garczarczyk, M. Gaug, M. Giller, F. Goebel, D. Hakobyan, M. Hayashida, T. Hengstebeck, A. Herrero, D. Höhne, J. Hose, C. C. Hsu, P. Jacon, T. Jogler, R. Kosyra, D. Kranich, R. Kritzer, A. Laille, E. Lindfors, S. Lombardi, F. Longo, J. López, M. López, E. Lorenz, P. Majumdar, G. Maneva, K. Mannheim, O. Mansutti, M. Mariotti, M. Martínez, D. Mazin, C. Merck, M. Meucci, M. Meyer, J. M. Miranda, R. Mirzoyan, S. Mizobuchi, A. Moralejo, D. Nieto, K. Nilsson, J. Ninkovic, E. Oña-Wilhelmi, N. Otte, I. Oya, M. Panniello, R. Paoletti, J. M. Paredes, M. Pasanen, D. Pascoli, F. Pauss, R. Pegna, M. Persic, L. Peruzzo, A. Piccioli, N. Puchades, E. Prandini, A. Raymers, W. Rhode, M. Ribó, J. Rico, M. Rissi, A. Robert, S. Rügamer, A. Saggion, T. Saito, A. Sánchez, P. Sartori, V. Scalzotto, V. Scapin, R. Schmitt, T. Schweizer, M. Shayduk, K. Shinozaki, S. N. Shore, N. Sidro, A. Sillanpää, D. Sobczynska, A. Stamerra, L. S. Stark, L. Takalo, P. Temnikov, D. Tescaro, M. Teshima, D. F. Torres, N. Turini, H. Vankov, V. Vitale, R. M. Wagner, T. Wibig, W. Wittek, F. Zandanel, R. Zanin, and J. Zapatero. FADC signal reconstruction for the MAGIC telescope. *Nuclear Instruments and Methods in Physics Research A*, 594:407–419, September 2008a. doi: 10.1016/j.nima.2008.06.043.

J. Albert, E. Aliu, H. Anderhub, P. Antoranz, A. Armada, M. Asensio, C. Baixeras, J. A. Barrio, H. Bartko, D. Bastieri, J. Becker, W. Bednarek, K. Berger, C. Bigongiari, A. Biland, R. K. Bock, P. Bordas, V. Bosch-Ramon, T. Bretz, I. Britvitch, M. Camara, E. Carmona, A. Chilingarian, S. Ciprini, J. A. Coarasa, S. Commichau, J. L. Contreras, J. Cortina, M. T. Costado, V. Curtef, V. Danielyan, F. Dazzi, A. de Angelis, C. Delgado, R. de Los Reyes, B. de Lotto, E. Domingo-Santamaría, D. Dorner, M. Doro, M. Errando, M. Fagiolini, D. Ferenc, E. Fernández, R. Firpo, J. Flix, M. V. Fonseca, L. Font, M. Fuchs, N. Galante, R. J. García-López, M. Garczarczyk, M. Gaug, M. Giller, F. Goebel, D. Hakobyan, M. Hayashida, T. Hengstebeck, A. Herrero, D. Höhne, J. Hose, S. Huber, C. C. Hsu, P. Jacon, T. Jogler, R. Kosyra, D. Kranich, R. Kritzer, A. Laille, E. Lindfors, S. Lombardi, F. Longo, J. López, M. López, E. Lorenz, P. Majumdar, G. Maneva, K. Mannheim, M. Mariotti, M. Martínez, D. Mazin, C. Merck, M. Meucci, M. Meyer, J. M. Miranda, R. Mirzoyan, S. Mizobuchi, A. Moralejo, D. Nieto, K. Nilsson, J. Ninkovic, E. Oña-Wilhelmi, N. Otte, I. Oya, M. Panniello, R. Paoletti, J. M. Paredes, M. Pasanen, D. Pascoli, F. Pauss, R. Pegna, M. Persic, L. Peruzzo, A. Piccioli, N. Puchades, E. Prandini, A. Raymers, W. Rhode, M. Ribó, J. Rico, M. Rissi, A. Robert, S. Rügamer, A. Saggion, T. Y. Saito, A. Sánchez, P. Sartori, V. Scalzotto, V. Scapin, R. Schmitt, T. Schweizer, M. Shayduk, K. Shinozaki, S. N. Shore, N. Sidro, A. Sillanpää, D. Sobczynska, F. Spanier, A. Stamerra, L. S. Stark, L. Takalo, P. Temnikov, D. Tescaro, M. Teshima, D. F. Torres, N. Turini, H. Vankov, A. Venturini, V. Vitale, R. M. Wagner, T. Wibig, W. Wittek, F. Zandanel, R. Zanin, and J. Zapatero. Implementation of the Random Forest method for the Imaging Atmospheric Cherenkov Telescope MAGIC.

Nuclear Instruments and Methods in Physics Research A, 588:424–432, April 2008b. doi: 10.1016/j.nima.2007.11.068.

J. Albert, E. Aliu, H. Anderhub, P. Antoranz, A. Armada, C. Baixeras, J. A. Barrio, H. Bartko, D. Bastieri, J. K. Becker, W. Bednarek, K. Berger, C. Bigongiari, A. Biland, R. K. Bock, P. Bordas, V. Bosch-Ramon, T. Bretz, I. Britvitch, M. Camara, E. Carmona, A. Chilingarian, J. A. Coarasa, S. Commichau, J. L. Contreras, J. Cortina, M. T. Costado, V. Curtef, V. Danielyan, F. Dazzi, A. De Angelis, C. Delgado, R. de los Reyes, B. De Lotto, E. Domingo-Santamaría, D. Dorner, M. Doro, M. Errando, M. Fagiolini, D. Ferenc, E. Fernández, R. Firpo, J. Flix, M. V. Fonseca, L. Font, M. Fuchs, N. Galante, R. García-López, M. Garczarczyk, M. Gaug, M. Giller, F. Goebel, D. Hakobyan, M. Hayashida, T. Hengstebeck, A. Herrero, D. Höhne, J. Hose, C. C. Hsu, P. Jacon, T. Jogler, R. Kosyra, D. Kranich, R. Kritzer, A. Laille, E. Lindfors, S. Lombardi, F. Longo, J. López, M. López, E. Lorenz, P. Majumdar, G. Maneva, K. Mannheim, O. Mansutti, M. Mariotti, M. Martínez, D. Mazin, C. Merck, M. Meucci, M. Meyer, J. M. Miranda, R. Mirzoyan, S. Mizobuchi, A. Moralejo, D. Nieto, K. Nilsson, J. Ninkovic, E. Oña-Wilhelmi, N. Otte, I. Oya, D. Paneque, M. Panniello, R. Paoletti, J. M. Paredes, M. Pasanen, D. Pascoli, F. Pauss, R. Pegna, M. Persic, L. Peruzzo, A. Piccioli, M. Poller, E. Prandini, N. Puchades, A. Raymers, W. Rhode, M. Ribó, J. Rico, M. Rissi, A. Robert, S. Rügamer, A. Saggion, A. Sánchez, P. Sartori, V. Scalzotto, V. Scapin, R. Schmitt, T. Schweizer, M. Shayduk, K. Shinozaki, S. N. Shore, N. Sidro, A. Sillanpää, D. Sobczynska, A. Stamerra, L. S. Stark, L. Takalo, P. Temnikov, D. Tescaro, M. Teshima, N. Tonello, D. F. Torres, N. Turini, H. Vankov, V. Vitale, R. M. Wagner, T. Wibig, W. Wittek, F. Zandanel, R. Zanin, and J. Zapatero. VHE γ-Ray Observation of the Crab Nebula and its Pulsar with the MAGIC Telescope. *ApJ*, 674:1037–1055, February 2008c. doi: 10.1086/525270.

J. Aleksić, E. A. Alvarez, L. A. Antonelli, P. Antoranz, M. Asensio, M. Backes, J. A. Barrio, D. Bastieri, J. Becerra González, W. Bednarek, A. Berdyugin, K. Berger, E. Bernardini, A. Biland, O. Blanch, R. K. Bock, A. Boller, G. Bonnoli, D. Borla Tridon, I. Braun, T. Bretz, A. Cañellas, E. Carmona, A. Carosi, P. Colin, E. Colombo, J. L. Contreras, J. Cortina, L. Cossio, S. Covino, F. Dazzi, A. De Angelis, G. De Caneva, E. De Cea del Pozo, B. De Lotto, C. Delgado Mendez, A. Diago Ortega, M. Doert, A. Domínguez, D. Dominis Prester, D. Dorner, M. Doro, D. Eisenacher, D. Elsaesser, D. Ferenc, M. V. Fonseca, L. Font, C. Fruck, R. J. García López, M. Garczarczyk, D. Garrido, G. Giavitto, N. Godinović, D. Hadasch, D. Häfner, A. Herrero, D. Hildebrand, D. Höhne-Mönch, J. Hose, D. Hrupec, T. Jogler, H. Kellermann, S. Klepser, T. Krähenbühl, J. Krause, J. Kushida, A. La Barbera, D. Lelas, E. Leonardo, E. Lindfors, S. Lombardi, M. López, A. López-Oramas, E. Lorenz, M. Makariev, G. Maneva, N. Mankuzhiyil, K. Mannheim, L. Maraschi, B. Marcote, M. Mariotti, M. Martínez, D. Mazin, M. Meucci, J. M. Miranda, R. Mirzoyan, J. Moldón, A. Moralejo, P. Munar-Adrover, D. Nieto, K. Nilsson, R. Orito, N. Otte, I. Oya, D. Paneque, R. Paoletti, S. Pardo, J. M. Paredes, S. Partini, M. A. Perez-Torres, M. Persic, L. Peruzzo, M. Pilia, J. Pochon, F. Prada, P. G. Prada Moroni, E. Prandini, I. Puerto Gimenez, I. Puljak, I. Reichardt, R. Reinthal, W. Rhode, M. Ribó, J. Rico, M. Rissi, S. Rügamer, A. Saggion, K. Saito, T. Y. Saito, M. Salvati, K. Satalecka, V. Scalzotto, V. Scapin, C. Schultz, T. Schweizer, M. Shayduk, S. N. Shore, A. Sillanpää, J. Sitarek, I. Snidaric, D. Sobczynska, F. Spanier, S. Spiro, V. Stamatescu, A. Stamerra, B. Steinke, J. Storz, N. Strah, T. Surić, L. Takalo, H. Takami, F. Tavecchio, P. Temnikov, T. Terzić, D. Tescaro, M. Teshima, O. Tibolla,

D. F. Torres, A. Treves, M. Uellenbeck, H. Vankov, P. Vogler, R. M. Wagner, Q. Weitzel, V. Zabalza, F. Zandanel, R. Zanin, and K. Hirotani. Observations of the Crab Pulsar between 25 and 100 GeV with the MAGIC I Telescope. *ApJ*, 742:43, November 2011. doi: 10.1088/0004-637X/742/1/43.

J. Aleksić, E. A. Alvarez, L. A. Antonelli, P. Antoranz, M. Asensio, M. Backes, J. A. Barrio, D. Bastieri, J. Becerra González, W. Bednarek, A. Berdyugin, K. Berger, E. Bernardini, A. Biland, O. Blanch, R. K. Bock, A. Boller, G. Bonnoli, D. Borla Tridon, I. Braun, T. Bretz, A. Cañellas, E. Carmona, A. Carosi, P. Colin, E. Colombo, J. L. Contreras, J. Cortina, L. Cossio, S. Covino, F. Dazzi, A. de Angelis, G. de Caneva, E. de Cea Del Pozo, B. de Lotto, C. Delgado Mendez, A. Diago Ortega, M. Doert, A. Domínguez, D. Dominis Prester, D. Dorner, M. Doro, D. Eisenacher, D. Elsaesser, D. Ferenc, M. V. Fonseca, L. Font, C. Fruck, R. J. García López, M. Garczarczyk, D. Garrido, G. Giavitto, N. Godinović, D. Hadasch, D. Häfner, A. Herrero, D. Hildebrand, D. Höhne-Mönch, J. Hose, D. Hrupec, T. Jogler, H. Kellermann, S. Klepser, T. Krähenbühl, J. Krause, J. Kushida, A. La Barbera, D. Lelas, E. Leonardo, N. Lewandowska, E. Lindfors, S. Lombardi, M. López, A. López-Oramas, E. Lorenz, M. Makariev, G. Maneva, N. Mankuzhiyil, K. Mannheim, L. Maraschi, M. Mariotti, M. Martínez, D. Mazin, M. Meucci, J. M. Miranda, R. Mirzoyan, J. Moldón, A. Moralejo, P. Munar-Adrover, A. Niedzwiecki, D. Nieto, K. Nilsson, N. Nowak, R. Orito, D. Paneque, R. Paoletti, S. Pardo, J. M. Paredes, S. Partini, M. A. Perez-Torres, M. Persic, L. Peruzzo, M. Pilia, J. Pochon, F. Prada, P. G. Prada Moroni, E. Prandini, I. Puerto Gimenez, I. Puljak, I. Reichardt, R. Reinthal, W. Rhode, M. Ribó, J. Rico, S. Rügamer, A. Saggion, K. Saito, T. Y. Saito, M. Salvati, K. Satalecka, V. Scalzotto, V. Scapin, C. Schultz, T. Schweizer, M. Shayduk, S. N. Shore, A. Sillanpää, J. Sitarek, I. Šnidarić, D. Sobczynska, F. Spanier, S. Spiro, V. Stamatescu, A. Stamerra, B. Steinke, J. Storz, N. Strah, T. Surić, L. Takalo, H. Takami, F. Tavecchio, P. Temnikov, T. Terzić, D. Tescaro, M. Teshima, O. Tibolla, D. F. Torres, A. Treves, M. Uellenbeck, H. Vankov, P. Vogler, R. M. Wagner, Q. Weitzel, V. Zabalza, F. Zandanel, R. Zanin, and K. Hirotani. Phase-resolved energy spectra of the Crab pulsar in the range of 50-400 GeV measured with the MAGIC telescopes. *A&A*, 540:A69, April 2012. doi: 10.1051/0004-6361/201118166.

J. Aleksic, S. Ansoldi, L. A. Antonelli, P. Antoranz, A. Babic, P. Bangale, M. Barcelo, J. A. Barrio, J. Becerra Gonzalez, W. Bednarek, E. Bernardini, B. Biasuzzi, A. Biland, M. Bitossi, O. Blanch, S. Bonnefoy, G. Bonnoli, F. Borracci, T. Bretz, E. Carmona, A. Carosi, R. Cecchi, P. Colin, E. Colombo, J. L. Contreras, D. Corti, J. Cortina, S. Covino, P. Da Vela, F. Dazzi, A. De Angelis, G. De Caneva, B. De Lotto, E. de Ona Wilhelmi, C. Delgado Mendez, A. Dettlaff, D. Dominis Prester, D. Dorner, M. Doro, S. Einecke, D. Eisenacher, D. Elsaesser, D. Fidalgo, D. Fink, M. V. Fonseca, L. Font, K. Frantzen, C. Fruck, D. Galindo, R. J. Garcia Lopez, M. Garczarczyk, D. Garrido Terrats, M. Gaug, G. Giavitto, N. Godinovic, A. Gonzalez Munoz, S. R. Gozzini, W. Haberer, D. Hadasch, Y. Hanabata, M. Hayashida, J. Herrera, D. Hildebrand, J. Hose, D. Hrupec, W. Idec, J. M. Illa, V. Kadenius, H. Kellermann, M. L. Knoetig, K. Kodani, Y. Konno, J. Krause, H. Kubo, J. Kushida, A. La Barbera, D. Lelas, J. L. Lemus, N. Lewandowska, E. Lindfors, S. Lombardi, F. Longo, M. Lopez, R. Lopez-Coto, A. Lopez-Oramas, A. Lorca, E. Lorenz, I. Lozano, M. Makariev, K. Mallot, G. Maneva, N. Mankuzhiyil, K. Mannheim, L. Maraschi, B. Marcote, M. Mariotti, M. Martinez, D. Mazin, U. Menzel, J. M. Miranda, R. Mirzoyan, A. Moralejo, P. Munar-Adrover, D. Nakajima, M. Negrello, V. Neustroev, A. Niedzwiecki, K. Nilsson, K. Nishijima, K. Noda,

R. Orito, A. Overkemping, S. Paiano, M. Palatiello, D. Paneque, R. Paoletti, J. M. Paredes, X. Paredes-Fortuny, M. Persic, J. Poutanen, P. G. Prada Moroni, E. Prandini, I. Puljak, R. Reinthal, W. Rhode, M. Ribo, J. Rico, J. Rodriguez Garcia, S. Rugamer, T. Saito, K. Saito, K. Satalecka, V. Scalzotto, V. Scapin, C. Schultz, J. Schlammer, S. Schmidl, T. Schweizer, A. Sillanpaa, J. Sitarek, I. Snidaric, D. Sobczynska, F. Spanier, A. Stamerra, T. Steinbring, J. Storz, M. Strzys, L. Takalo, H. Takami, F. Tavecchio, L. A. Tejedor, P. Temnikov, T. Terzic, D. Tescaro, M. Teshima, J. Thaele, O. Tibolla, D. F. Torres, T. Toyama, A. Treves, P. Vogler, H. Wetteskind, M. Will, and R. Zanin. The major upgrade of the MAGIC telescopes, Part I: The hardware improvements and the commissioning of the system. *ArXiv e-prints*, September 2014.

J. Aleksić, S. Ansoldi, L. A. Antonelli, P. Antoranz, A. Babic, P. Bangale, U. Barres de Almeida, J. A. Barrio, J. Becerra González, W. Bednarek, E. Bernardini, B. Biasuzzi, A. Biland, O. Blanch, S. Bonnefoy, G. Bonnoli, F. Borracci, T. Bretz, E. Carmona, A. Carosi, P. Colin, E. Colombo, J. L. Contreras, J. Cortina, S. Covino, P. Da Vela, F. Dazzi, A. De Angelis, G. De Caneva, B. De Lotto, C. Delgado Mendez, M. Doert, D. Dominis Prester, D. Dorner, M. Doro, S. Einecke, D. Eisenacher, D. Elsaesser, E. Farina, D. Ferenc, D. Fidalgo, M. V. Fonseca, L. Font, K. Frantzen, C. Fruck, R. J. García López, M. Garczarczyk, D. Garrido Terrats, M. Gaug, N. Godinović, A. González Muñoz, S. R. Gozzini, D. Hadasch, M. Hayashida, J. Herrera, A. Herrero, D. Hildebrand, K. Hirotani, J. Hose, D. Hrupec, W. Idec, V. Kadenius, H. Kellermann, K. Kodani, Y. Konno, J. Krause, H. Kubo, J. Kushida, A. La Barbera, D. Lelas, N. Lewandowska, E. Lindfors, S. Lombardi, M. López, R. López-Coto, A. López-Oramas, E. Lorenz, I. Lozano, M. Makariev, K. Mallot, G. Maneva, N. Mankuzhiyil, K. Mannheim, L. Maraschi, B. Marcote, M. Mariotti, M. Martínez, D. Mazin, U. Menzel, J. M. Miranda, R. Mirzoyan, A. Moralejo, P. Munar-Adrover, D. Nakajima, A. Niedzwiecki, K. Nilsson, K. Nishijima, K. Noda, N. Nowak, R. Orito, A. Overkemping, S. Paiano, M. Palatiello, D. Paneque, R. Paoletti, J. M. Paredes, X. Paredes-Fortuny, S. Partini, M. Persic, P. G. Prada Moroni, E. Prandini, S. Preziuso, I. Puljak, R. Reinthal, W. Rhode, M. Ribó, J. Rico, J. Rodriguez Garcia, S. Rügamer, A. Saggion, T. Y. Saito, K. Saito, K. Satalecka, V. Scalzotto, V. Scapin, C. Schultz, T. Schweizer, S. N. Shore, A. Sillanpää, J. Sitarek, I. Snidaric, D. Sobczynska, F. Spanier, V. Stamatescu, A. Stamerra, T. Steinbring, J. Storz, M. Strzys, S. Sun, T. Surić, L. Takalo, H. Takami, F. Tavecchio, P. Temnikov, T. Terzić, D. Tescaro, M. Teshima, J. Thaele, O. Tibolla, D. F. Torres, T. Toyama, A. Treves, M. Uellenbeck, P. Vogler, R. M. Wagner, and R. Zanin. Detection of bridge emission above 50 GeV from the Crab pulsar with the MAGIC telescopes. *A&A*, 565:L12, May 2014. doi: 10.1051/0004-6361/201423664.

E. Aliu, H. Anderhub, L. A. Antonelli, P. Antoranz, M. Backes, C. Baixeras, J. A. Barrio, H. Bartko, D. Bastieri, J. K. Becker, W. Bednarek, K. Berger, E. Bernardini, C. Bigongiari, A. Biland, R. K. Bock, G. Bonnoli, P. Bordas, V. Bosch-Ramon, T. Bretz, I. Britvitch, M. Camara, E. Carmona, A. Chilingarian, S. Commichau, J. L. Contreras, J. Cortina, M. T. Costado, S. Covino, V. Curtef, F. Dazzi, A. De Angelis, E. De Cea del Pozo, R. de los Reyes, B. De Lotto, M. De Maria, F. De Sabata, C. Delgado Mendez, A. Dominguez, D. Dorner, M. Doro, D. Elsässer, M. Errando, M. Fagiolini, D. Ferenc, E. Fernandez, R. Firpo, M. V. Fonseca, L. Font, N. Galante, R. J. Garcia Lopez, M. Garczarczyk, M. Gaug, F. Goebel, D. Hadasch, M. Hayashida, A. Herrero, D. Höhne, J. Hose, C. C. Hsu, S. Huber, T. Jogler, D. Kranich, A. La Barbera, A. Laille, E. Leonardo, E. Lindfors, S. Lombardi, F. Longo,

M. Lopez, E. Lorenz, P. Majumdar, G. Maneva, N. Mankuzhiyil, K. Mannheim, L. Maraschi, M. Mariotti, M. Martinez, D. Mazin, M. Meucci, M. Meyer, J. M. Miranda, R. Mirzoyan, M. Moles, A. Moralejo, D. Nieto, K. Nilsson, J. Ninkovic, N. Otte, I. Oya, R. Paoletti, J. M. Paredes, M. Pasanen, D. Pascoli, F. Pauss, R. G. Pegna, M. A. Perez-Torres, M. Persic, L. Peruzzo, A. Piccioli, F. Prada, E. Prandini, N. Puchades, A. Raymers, W. Rhode, M. Ribó, J. Rico, M. Rissi, A. Robert, S. Rügamer, A. Saggion, T. Y. Saito, M. Salvati, M. Sanchez-Conde, P. Sartori, K. Satalecka, V. Scalzotto, V. Scapin, T. Schweizer, M. Shayduk, K. Shinozaki, S. N. Shore, N. Sidro, A. Sierpowska-Bartosik, A. Sillanpää, D. Sobczynska, F. Spanier, A. Stamerra, L. S. Stark, L. Takalo, F. Tavecchio, P. Temnikov, D. Tescaro, M. Teshima, M. Tluczykont, D. F. Torres, N. Turini, H. Vankov, A. Venturini, V. Vitale, R. M. Wagner, W. Wittek, V. Zabalza, F. Zandanel, R. Zanin, J. Zapatero, O. C. de Jager, E. de Ona Wilhelmi, and MAGIC Collaboration. Observation of Pulsed γ-Rays Above 25 GeV from the Crab Pulsar with MAGIC. *Science*, 322:1221–, November 2008. doi: 10.1126/science.1164718.

E. Aliu, S. Archambault, T. Arlen, T. Aune, M. Beilicke, W. Benbow, A. Bouvier, J. H. Buckley, V. Bugaev, K. Byrum, A. Cesarini, L. Ciupik, E. Collins-Hughes, M. P. Connolly, W. Cui, R. Dickherber, C. Duke, J. Dumm, A. Falcone, S. Federici, Q. Feng, J. P. Finley, G. Finnegan, L. Fortson, A. Furniss, N. Galante, D. Gall, G. H. Gillanders, S. Godambe, S. Griffin, J. Grube, G. Gyuk, D. Hanna, J. Holder, H. Huan, G. Hughes, T. B. Humensky, P. Kaaret, N. Karlsson, Y. Khassen, D. Kieda, H. Krawczynski, F. Krennrich, M. J. Lang, S. LeBohec, K. Lee, M. Lyutikov, A. S. Madhavan, G. Maier, P. Majumdar, S. McArthur, A. McCann, P. Moriarty, R. Mukherjee, T. Nelson, A. O'Faoláin de Bhróithe, R. A. Ong, M. Orr, A. N. Otte, N. Park, J. S. Perkins, M. Pohl, H. Prokoph, J. Quinn, K. Ragan, L. C. Reyes, P. T. Reynolds, E. Roache, D. B. Saxon, M. Schroedter, G. H. Sembroski, G. D. Şentürk, A. W. Smith, D. Staszak, I. Telezhinsky, G. Tešić, M. Theiling, S. Thibadeau, K. Tsurusaki, A. Varlotta, S. Vincent, M. Vivier, R. G. Wagner, S. P. Wakely, T. C. Weekes, A. Weinstein, R. Welsing, D. A. Williams, B. Zitzer, and V. Kondratiev. Search for a Correlation between Very-high-energy Gamma Rays and Giant Radio Pulses in the Crab Pulsar. *ApJ*, 760:136, December 2012. doi: 10.1088/0004-637X/760/2/136.

A. M. Archibald, I. H. Stairs, S. M. Ransom, V. M. Kaspi, V. I. Kondratiev, D. R. Lorimer, M. A. McLaughlin, J. Boyles, J. W. T. Hessels, R. Lynch, J. van Leeuwen, M. S. E. Roberts, F. Jenet, D. J. Champion, R. Rosen, B. N. Barlow, B. H. Dunlap, and R. A. Remillard. A Radio Pulsar/X-ray Binary Link. *Science*, 324:1411–, June 2009. doi: 10.1126/science.1172740.

A. M. Archibald, V. M. Kaspi, J. W. T. Hessels, B. Stappers, G. Janssen, and A. Lyne. Long-Term Radio Timing Observations of the Transition Millisecond Pulsar PSR˜J1023+0038. *ArXiv e-prints*, November 2013.

P. N. Arendt, Jr. and J. A. Eilek. Pair Creation in the Pulsar Magnetosphere. *ApJ*, 581: 451–469, December 2002. doi: 10.1086/344133.

E. Argyle. Polarization of Giant Pulses from PSR 0531+21. *ApJ*, 183:973–976, August 1973. doi: 10.1086/152283.

E. Argyle and J. F. R. Gower. The Pulse-Height Distribution for NP 0532. *ApJ*, 175:L89, July 1972. doi: 10.1086/180991.

E. Argyle, G. Baird, J. Grindlay, H. Helmken, and E. Omongain. Search for correlations between giant radio-pulses and 100-GeV gamma-rays from NP 0532. *Nuovo Cimento B Serie*, 24:153–156, December 1974. doi: 10.1007/BF02725954.

E. Asseo. Microtexture in the Pulsar Radio Emission Zone. *MNRAS*, 264:940, October 1993.

W. Baade and F. Zwicky. Remarks on Super-Novae and Cosmic Rays. *Physical Review*, 46: 76–77, July 1934. doi: 10.1103/PhysRev.46.76.2.

J. W. M. Baars and B. G. Hooghoudt. The Synthesis Radio Telescope at Westerbork. General Lay-out and Mechanical Aspects. *A&A*, 31:323, March 1974.

D. C. Backer. Pulsar Nulling Phenomena. *Nature*, 228:42–43, October 1970. doi: 10.1038/228042a0.

D. C. Backer. Pulsar Fluctuation Spectra and the Generalized Drifting-Subpulse Phenomenon. *ApJ*, 182:245–276, May 1973. doi: 10.1086/152134.

D. C. Backer. Millisecond Pulsar Radiation Properties. *Journal of Astrophysics and Astronomy*, 16:165, June 1995. doi: 10.1007/BF02714831.

D. C. Backer and S. T. Sallmen. Polarimetry, Peculiar Mode and X-Ray Alignment of PSR B1821-24. *AJ*, 114:1539, October 1997. doi: 10.1086/118583.

D. C. Backer, S. R. Kulkarni, C. Heiles, M. M. Davis, and W. M. Goss. A millisecond pulsar. *Nature*, 300:615–618, December 1982. doi: 10.1038/300615a0.

D. C. Backer, T. Wong, and J. Valanju. A Plasma Prism Model for an Anomalous Dispersion Event in the Crab Pulsar. *ApJ*, 543:740–753, November 2000. doi: 10.1086/317150.

C. Barbieri, G. Naletto, L. Zampieri, E. Verroi, S. Gradari, S. Collins, and A. Shearer. Aqueye and Iqueye, Very-High-Time-Resolution Photon-Counting Photometers. In E. Griffin, R. Hanisch, and R. Seaman, editors, *IAU Symposium*, volume 285 of *IAU Symposium*, pages 280–282, April 2012. doi: 10.1017/S1743921312000786.

J. A. Barrio, F. Lucarelli, P. Antoranz, and et al. The Central Pixel of the MAGIC Telescope for Optical Observations. *International Cosmic Ray Conference*, 3:1477–1480, 2008.

G. Baym, C. Pethick, D. Pines, and M. Ruderman. Spin Up in Neutron Stars : The Future of the Vela Pulsar. *Nature*, 224:872–874, November 1969. doi: 10.1038/224872a0.

W. Becker, editor. *Neutron Stars and Pulsars*, volume 357 of *Astrophysics and Space Science Library*, 2009. doi: 10.1007/978-3-540-76965-1.

E. E. Becklin, J. Kristian, K. Matthews, and G. Neugebauer. Measurements of the Crab Pulsar at 2.2 and 3.5 Microns. *ApJ*, 186:L137, December 1973. doi: 10.1086/181375.

N. D. R. Bhat, Y. Gupta, M. Kramer, A. Karastergiou, A. G. Lyne, and S. Johnston. Simultaneous single-pulse observations of radio pulsars. V. On the broadband nature of the pulse nulling phenomenon in PSR B1133+16. *A&A*, 462:257–268, January 2007. doi: 10.1051/0004-6361:20053157.

A. Biland, M. Garczarczyk, H. Anderhub, and et al. The Active Mirror Control of the MAGIC Telescopes. *International Cosmic Ray Conference*, 3:1353–1356, 2008.

A. V. Bilous, V. I. Kondratiev, M. A. McLaughlin, M. Mickaliger, D. R. Lorimer, S. M. Ransom, M. Lyutikov, B. Stappers, and G. I. Langston. Constraining Pulsar Emission Physics through Radio/Gamma-Ray Correlation of Crab Giant Pulses. *ArXiv e-prints*, December 2009.

A. V. Bilous, V. I. Kondratiev, M. A. McLaughlin, S. M. Ransom, M. Lyutikov, M. Mickaliger, and G. I. Langston. Correlation of Fermi Photons with High-frequency Radio Giant Pulses from the Crab Pulsar. *ApJ*, 728:110, February 2011. doi: 10.1088/0004-637X/728/2/110.

A. V. Bilous, M. A. McLaughlin, V. I. Kondratiev, and S. M. Ransom. Correlation of Chandra Photons with the Radio Giant Pulses from the Crab Pulsar. *ApJ*, 749:24, April 2012. doi: 10.1088/0004-637X/749/1/24.

A. V. Bilous, J. W. T. Hessels, V. I. Kondratiev, J. van Leeuwen, B. W. Stappers, P. Weltevrede, H. Falcke, T. E. Hassall, M. Pilia, E. Keane, M. Kramer, J.-M. Grießmeier, and M. Serylak. LOFAR observations of PSR B0943+10: profile evolution and discovery of a systematically changing profile delay in bright mode. *A&A*, 572:A52, December 2014. doi: 10.1051/0004-6361/201424425.

A. V. Bilous, T. T. Pennucci, P. Demorest, and S. M. Ransom. A Broadband Radio Study of the Average Profile and Giant Pulses from PSR B1821-24A. *ApJ*, 803:83, April 2015. doi: 10.1088/0004-637X/803/2/83.

G. F. Blgnami and P. A. Caraveo. Geminga: new period, old γ-rays. *Nature*, 357:287, May 1992. doi: 10.1038/357287a0.

V. Boriakoff and R. R. Payne. Crab Pulsar: Precursor Pulse Detection at 606 MHz. *Astrophys. Lett.*, 15:175, December 1973.

D. Borla Tridon, F. Goebel, D. Fink, W. Haberer, J. Hose, C. C. Hsu, T. Jogler, R. Mirzoyan, R. Orito, O. Reimann, P. Sawallisch, J. Schlammer, T. Schweizer, B. Steinke, M. Teshima, and for the MAGIC Collaboration. Performance of the Camera of the MAGIC II Telescope. *ArXiv e-prints*, June 2009.

P. E. Boynton, E. J. Groth, D. P. Hutchinson, G. P. Nanos, Jr., R. B. Partridge, and D. T. Wilkinson. Optical Timing of the Crab Pulsar, NP 0532. *ApJ*, 175:217, July 1972. doi: 10.1086/151550.

Pierre Brémaud. *Markov chains: Gibbs fields, Monte Carlo simulation, and queues*, volume 31. Springer Science & Business Media, 2013.

T. Bretz, D. Dorner, R. M. Wagner, and P. Sawallisch. The drive system of the major atmospheric gamma-ray imaging Cherenkov telescope. *Astroparticle Physics*, 31:92–101, March 2009. doi: 10.1016/j.astropartphys.2008.12.001.

E. M. Burbidge, G. R. Burbidge, W. A. Fowler, and F. Hoyle. Synthesis of the Elements in Stars. *Reviews of Modern Physics*, 29:547–650, 1957. doi: 10.1103/RevModPhys.29.547.

Bernard F Burke and Francis Graham-Smith. *An introduction to radio astronomy*. Cambridge University Press, 2010.

S. Burke-Spolaor, S. Johnston, M. Bailes, S. D. Bates, N. D. R. Bhat, M. Burgay, D. J. Champion, N. D'Amico, M. J. Keith, M. Kramer, L. Levin, S. Milia, A. Possenti, B. Stappers, and W. van Straten. The High Time Resolution Universe Pulsar Survey - V. Single-pulse energetics and modulation properties of 315 pulsars. *MNRAS*, 423:1351–1367, June 2012. doi: 10.1111/j.1365-2966.2012.20998.x.

I. H. Cairns. Properties and Interpretations of Giant Micropulses and Giant Pulses from Pulsars. *ApJ*, 610:948–955, August 2004. doi: 10.1086/421756.

J. L. Casse, E. E. M. Woestenburg, and J. J. Visser. Multifrequency cryogenically cooled front-end receivers for the Westerbork Synthesis Radio Telescope. *IEEE Transactions on Microwave Theory Techniques*, 30:201–209, 1982. doi: 10.1109/TMTT.1982.1131049.

D. Chakrabarty. Millisecond Pulsars in X-Ray Binaries. In F. A. Rasio and I. H. Stairs, editors, *Binary Radio Pulsars*, volume 328 of *Astronomical Society of the Pacific Conference Series*, page 279, July 2005.

S. Chandrasekhar. The Maximum Mass of Ideal White Dwarfs. *ApJ*, 74:81, July 1931. doi: 10.1086/143324.

S. Chaty. Nature, Formation, and Evolution of High Mass X-Ray Binaries. In L. Schmidtobreick, M. R. Schreiber, and C. Tappert, editors, *Evolution of Compact Binaries*, volume 447 of *Astronomical Society of the Pacific Conference Series*, page 29, September 2011.

K. Chen and M. Ruderman. Pulsar death lines and death valley. *ApJ*, 402:264–270, January 1993. doi: 10.1086/172129.

K. S. Cheng, C. Ho, and M. Ruderman. Energetic radiation from rapidly spinning pulsars. I - Outer magnetosphere gaps. II - VELA and Crab. *ApJ*, 300:500–539, January 1986a. doi: 10.1086/163829.

K. S. Cheng, C. Ho, and M. Ruderman. Energetic Radiation from Rapidly Spinning Pulsars. II. VELA and Crab. *ApJ*, 300:522, January 1986b. doi: 10.1086/163830.

T. L. Cline, U. D. Desai, G. Pizzichini, B. J. Teegarden, W. D. Evans, R. W. Klebesadel, J. G. Laros, K. Hurley, M. Niel, and G. Vedrenne. Detection of a fast, intense and unusual gamma-ray transient. *ApJ*, 237:L1–L5, April 1980. doi: 10.1086/183221.

T. L. Cline, U. D. Desai, B. J. Teegarden, W. D. Evans, R. W. Klebesadel, J. G. Laros, C. Barat, K. Hurley, M. Niel, and M. C. Weisskopf. Precise source location of the anomalous 1979 March 5 gamma-ray transient. *ApJ*, 255:L45–L48, April 1982. doi: 10.1086/183766.

W. J. Cocke, M. J. Disney, and D. J. Taylor. Discovery of Optical Signals from Pulsar NP 0532. *Nature*, 221:525–527, February 1969. doi: 10.1038/221525a0.

I. Cognard, J. A. Shrauner, J. H. Taylor, and S. E. Thorsett. Giant Radio Pulses from a Millisecond Pulsar. *ApJ*, 457:L81, February 1996. doi: 10.1086/309894.

P. Colin, D. Borla Tridon, E. Carmona, F. De Sabata, M. Gaug, S. Lombardi, P. Majumdar, A. Moralejo, V. Scalzotto, and J. Sitarek. Performance of the MAGIC telescopes in stereoscopic mode. *ArXiv e-prints*, July 2009.

S. Collins, A. Shearer, B. Stappers, C. Barbieri, G. Naletto, L. Zampieri, E. Verroi, and S. Gradari. Crab Pulsar: Enhanced Optical Emission During Giant Radio Pulses. In E. Griffin, R. Hanisch, and R. Seaman, editors, *IAU Symposium*, volume 285 of *IAU Symposium*, pages 296–298, April 2012. doi: 10.1017/S1743921312000841.

J. M. Comella, H. D. Craft, R. V. E. Lovelace, and J. M. Sutton. Crab Nebula Pulsar NP 0532. *Nature*, 221:453–454, February 1969. doi: 10.1038/221453a0.

J. M. Cordes. Pulsar timing. II - Analysis of random walk timing noise - Application to the Crab pulsar. *ApJ*, 237:216–226, April 1980. doi: 10.1086/157861.

J. M. Cordes and D. J. Helfand. Pulsar timing. III - Timing noise of 50 pulsars. *ApJ*, 239: 640–650, July 1980. doi: 10.1086/158150.

J. M. Cordes, N. D. R. Bhat, T. H. Hankins, M. A. McLaughlin, and J. Kern. The Brightest Pulses in the Universe: Multifrequency Observations of the Crab Pulsar's Giant Pulses. *ApJ*, 612:375–388, September 2004. doi: 10.1086/422495.

D. Corti, M. Mariotti, R. Paoletti, R. Pegna, A. Stammera, and N. Turini. The Trigger System of the MAGIC Telescope: On-Line Selection Strategies for Cherenkov Telescopes. *International Cosmic Ray Conference*, 5:2959, July 2003.

J. Cortina, F. Goebel, T. Schweizer, and for the MAGIC Collaboration. Technical Performance of the MAGIC Telescopes. *ArXiv e-prints*, July 2009.

C. C. Counselman, III and J. M. Rankin. Multipath Delay Distortion of Radio Pulses from NP 0532. *ApJ*, 166:513, June 1971. doi: 10.1086/150978.

C. L. Cowan, Jr., F. Reines, F. B. Harrison, H. W. Kruse, and A. D. McGuire. Detection of the Free Neutrino: A Confirmation. *Science*, 124:103–104, July 1956. doi: 10.1126/science.124.3212.103.

H. D. Craft, J. M. Comella, and F. D. Drake. Submillisecond Radio Intensity Variations in Pulsars. *Nature*, 218:1122–1124, June 1968. doi: 10.1038/2181122a0.

G. Cusumano, W. Hermsen, M. Kramer, L. Kuiper, O. Löhmer, E. Massaro, T. Mineo, L. Nicastro, and B. W. Stappers. The phase of the radio and X-ray pulses of PSR B1937+21. *A&A*, 410:L9–L12, October 2003. doi: 10.1051/0004-6361:20031368.

F. Dazzi, D. Herranz Lazaro, M. Lopez, D. Nakajima, J. Rodriguez Garcia, and T. Schweizer. Performance studies of the new stereoscopic Sum-Trigger-II of MAGIC after one year of operation. *ArXiv e-prints*, August 2015.

M. Demianski and M. Proszynski. Timing of the Crab pulsar - Consequences of the large glitch of 1975. *MNRAS*, 202:437–451, February 1983.

A. J. Deutsch. The electromagnetic field of an idealized star in rigid rotation in vacuo. *Annales d'Astrophysique*, 18:1, January 1955.

M. Doro, D. Bastieri, A. Biland, F. Dazzi, L. Font, M. Garczarczyk, M. Ghigo, E. Giro, F. Goebel, R. Kosyra, E. Lorenz, M. Mariotti, R. Mirzoyan, L. Peruzzo, G. Pareschi, and J. Zapatero. The reflective surface of the MAGIC telescope. *Nuclear Instruments and Methods in Physics Research A*, 595:200–203, September 2008. doi: 10.1016/j.nima.2008.07.073.

F. D. Drake. Pulse Structure of the Pulsating Radio Source in Vulpecula. *Science*, 160:416–419, April 1968. doi: 10.1126/science.160.3826.416.

F. D. Drake and H. D. Craft. Second Periodic Pulsation in Pulsars. *Nature*, 220:231–235, October 1968. doi: 10.1038/220231a0.

J. J. L. Duyvendak. Further Data Bearing on the Identification of the Crab Nebula with the Supernova of 1054 A.D. Part I. The Ancient Oriental Chronicles. *PASP*, 54:91–94, April 1942. doi: 10.1086/125409.

R. A. Edelson and J. H. Krolik. The discrete correlation function - A new method for analyzing unevenly sampled variability data. *ApJ*, 333:646–659, October 1988. doi: 10.1086/166773.

R. T. Edwards, G. B. Hobbs, and R. N. Manchester. TEMPO2, a new pulsar timing package - II. The timing model and precision estimates. *MNRAS*, 372:1549–1574, November 2006. doi: 10.1111/j.1365-2966.2006.10870.x.

S. S. Eikenberry, G. G. Fazio, S. M. Ransom, J. Middleditch, J. Kristian, and C. R. Pennypacker. High Time Resolution Infrared Observations of the Crab Nebula Pulsar and the Pulsar Emission Mechanism. *ApJ*, 477:465–474, March 1997.

J. A. Eilek and T. H. Hankins. Radio emission physics in the Crab pulsar. In W. Becker and H. H. Huang, editors, *WE-Heraeus Seminar on Neutron Stars and Pulsars 40 years after the Discovery*, page 112, January 2007.

T. Erber. High-Energy Electromagnetic Conversion Processes in Intense Magnetic Fields. *Reviews of Modern Physics*, 38:626–659, October 1966. doi: 10.1103/RevModPhys.38.626.

A. A. Ershov and A. D. Kuzmin. Detection of Giant Pulses from the Pulsar PSR B1112+50. *Astronomy Letters*, 29:91–95, February 2003. doi: 10.1134/1.1544530.

A. A. Ershov and A. D. Kuzmin. Detection of Giant Pulses in Pulsar PSR J1752+2359. *Chinese Journal of Astronomy and Astrophysics Supplement*, 6(2):30–33, December 2006.

C. M. Espinoza, A. G. Lyne, B. W. Stappers, and M. Kramer. A study of 315 glitches in the rotation of 102 pulsars. *MNRAS*, 414:1679–1704, June 2011. doi: 10.1111/j.1365-2966.2011.18503.x.

G. G. Fahlman and P. C. Gregory. An X-ray pulsar in SNR G109.1-1.0. *Nature*, 293:202–204, September 1981. doi: 10.1038/293202a0.

J. Faulkner and J. R. Gribbin. Stability and Radial Vibration Periods of the Hamada-Salpeter White Dwarf Models. *Nature*, 218:734–736, May 1968. doi: 10.1038/218734a0.

W. Feller. *An introduction to probability theory and its applications.* 1957.

M. Feroci, K. Hurley, R. C. Duncan, and C. Thompson. The Giant Flare of 1998 August 27 from SGR 1900+14. I. An Interpretive Study of BeppoSAX and Ulysses Observations. *ApJ*, 549:1021–1038, March 2001. doi: 10.1086/319441.

J. M. Fierro, P. F. Michelson, P. L. Nolan, and D. J. Thompson. Phase-resolved Studies of the High-Energy Gamma-Ray Emission from the Crab, Geminga, and VELA Pulsars. *ApJ*, 494: 734–746, February 1998. doi: 10.1086/305219.

F. W. Floyd, I. S. Glass, and H. W. Schnopper. Hard X-Rays from the Crab Pulsar. *Nature*, 224:50–51, October 1969. doi: 10.1038/224050a0.

V. P. Fomin, A. A. Stepanian, R. C. Lamb, D. A. Lewis, M. Punch, and T. C. Weekes. New methods of atmospheric Cherenkov imaging for gamma-ray astronomy. I. The false source method. *Astroparticle Physics*, 2:137–150, May 1994. doi: 10.1016/0927-6505(94)90036-1.

G. Fritz, R. C. Henry, J. F. Meekins, T. A. Chubb, and H. Friedman. X-ray Pulsar in the Crab Nebula. *Science*, 164:709–712, May 1969. doi: 10.1126/science.164.3880.709.

A. S. Fruchter, D. R. Stinebring, and J. H. Taylor. A millisecond pulsar in an eclipsing binary. *Nature*, 333:237–239, May 1988. doi: 10.1038/333237a0.

T. Fukushima. Time ephemeris. *A&A*, 294:895–906, February 1995.

G. Gamow. Zur Quantentheorie des Atomkernes. *Zeitschrift fur Physik*, 51:204–212, March 1928. doi: 10.1007/BF01343196.

U. Ganse, P. Kilian, F. Spanier, and R. Vainio. Nonlinear Wave Interactions as Emission Process of Type II Radio Bursts. *ApJ*, 751:145, June 2012. doi: 10.1088/0004-637X/751/2/145.

J. R. García, F. Dazzi, D. Häfner, D. Herranz, M. López, M. Mariotti, R. Mirzoyan, D. Nakajima, T. Schweizer, and M. Teshima. Status of the new Sum-Trigger system for the MAGIC telescopes. *ArXiv e-prints*, April 2014.

G. Giavitto. *Observing the VHE Gamma-Ray Sky with the MAGIC Telescopes: the Blazar B3 2247+381 and the Crab Pulsar*. PhD thesis, Universitat Autonoma de Barcelona, 2013.

J. Gil and G. I. Melikidze. Curvature radiation and giant subpulses in the Crab pulsar. *ArXiv Astrophysics e-prints*, November 2003.

T. Gold. Rotating Neutron Stars as the Origin of the Pulsating Radio Sources. *Nature*, 218: 731–732, May 1968. doi: 10.1038/218731a0.

P. Goldreich and W. H. Julian. Pulsar Electrodynamics. *ApJ*, 157:869, August 1969. doi: 10.1086/150119.

S. V. Golenetskii, V. N. Ilinskii, and E. P. Mazets. Recurrent bursts in GBS0526 - 66, the source of the 5 March 1979 gamma-ray burst. *Nature*, 307:41–43, January 1984. doi: 10.1038/307041a0.

J. F. R. Gower and E. Argyle. Detection of Strong Interpulses from NP 0532. *ApJ*, 171:L23, January 1972. doi: 10.1086/180859.

D. A. Graham, A. G. Lyne, and F. G. Smith. Physical Sciences: Polarization of the Radio Pulses from the Crab Nebula Pulsar. *Nature*, 225:526, February 1970. doi: 10.1038/225526a0.

F. Graham Smith, A. G. Lyne, and C. Jordan. The 1997 event in the Crab pulsar revisited. *MNRAS*, 410:499–503, January 2011. doi: 10.1111/j.1365-2966.2010.17459.x.

V. Grinberg, N. Hell, J. Wilms, J. Rodriguez, K. Pottschmidt, M. A. Nowak, M. Böck, A. Bodaghee, M. Cadolle Bel, F. Fürst, M. Hanke, M. Kühnel, P. Laurent, S. B. Markoff, A. Markowitz, D. M. Marcu, G. G. Pooley, A. Popp, R. E. Rothschild, and J. A. Tomsick. Cygnus X-1: shedding light on the spectral variability of a black hole. *ArXiv e-prints*, March 2013.

E. Gross and O. Vitells. Trial factors for the look elsewhere effect in high energy physics. *European Physical Journal C*, 70:525–530, November 2010. doi: 10.1140/epjc/s10052-010-1470-8.

E. J. Groth. Timing of the Crab pulsar. I - Arrival times. *ApJS*, 29:431–442, November 1975a. doi: 10.1086/190352.

E. J. Groth. Timing of the Crab Pular II. Method of Analysis. *ApJS*, 29:443–451, November 1975b. doi: 10.1086/190353.

E. J. Groth. Timing of the Crab Pulsar III. The Slowing Down and the Nature of the Random Process. *ApJS*, 29:453–465, November 1975c. doi: 10.1086/190354.

L. Guillemot, T. J. Johnson, C. Venter, M. Kerr, B. Pancrazi, M. Livingstone, G. H. Janssen, P. Jaroenjittichai, M. Kramer, I. Cognard, B. W. Stappers, A. K. Harding, F. Camilo, C. M. Espinoza, P. C. C. Freire, F. Gargano, J. E. Grove, S. Johnston, P. F. Michelson, A. Noutsos, D. Parent, S. M. Ransom, P. S. Ray, R. Shannon, D. A. Smith, G. Theureau, S. E. Thorsett, and N. Webb. Pulsed Gamma Rays from the Original Millisecond and Black Widow Pulsars: A Case for Caustic Radio Emission? *ApJ*, 744:33, January 2012. doi: 10.1088/0004-637X/744/1/33.

D. Haefner. New improved Sum-Trigger system for the MAGIC telescopes. *International Cosmic Ray Conference*, 9:251, 2011. doi: 10.7529/ICRC2011/V09/1326.

T. Hamada and E. E. Salpeter. Models for Zero-Temperature Stars. *ApJ*, 134:683, November 1961. doi: 10.1086/147195.

T. H. Hankins. Pulsar Radio Emission Mechanisms: The Crab Enigmas. In W. Lewandowski, O. Maron, and J. Kijak, editors, *Electromagnetic Radiation from Pulsars and Magnetars*, volume 466 of *Astronomical Society of the Pacific Conference Series*, page 65, December 2012.

T. H. Hankins and J. M. Cordes. Interpulse emission from pulsar 0950+08 - How many poles. *ApJ*, 249:241–253, October 1981. doi: 10.1086/159281.

T. H. Hankins and J. A. Eilek. Radio Emission Signatures in the Crab Pulsar. *ApJ*, 670: 693–701, November 2007. doi: 10.1086/522362.

T. H. Hankins and B. J. Rickett. Pulsar signal processing. *Methods in Computational Physics*, 14:55–129, 1975.

T. H. Hankins, J. S. Kern, J. C. Weatherall, and J. A. Eilek. Nanosecond radio bursts from strong plasma turbulence in the Crab pulsar. *Nature*, 422:141–143, March 2003.

T. H. Hankins, J. M. Rankin, and J. A. Eilek. What is the Physics of Pulsar Radio Emission? In *astro2010: The Astronomy and Astrophysics Decadal Survey*, volume 2010 of *Astronomy*, page 112, 2009.

T. H. Hankins, G. Jones, and J. A. Eilek. The Crab Pulsar at Centimeter Wavelengths. I. Ensemble Characteristics. *ApJ*, 802:130, April 2015. doi: 10.1088/0004-637X/802/2/130.

A. K. Harding. The neutron star zoo. *Frontiers of Physics*, 8:679–692, December 2013. doi: 10.1007/s11467-013-0285-0.

A. Heger, C. L. Fryer, S. E. Woosley, N. Langer, and D. H. Hartmann. How Massive Single Stars End Their Life. *ApJ*, 591:288–300, July 2003. doi: 10.1086/375341.

C. Heiles and D. B. Campbell. Pulsar NP 0532: Properties and Systematic Polarization of Individual Strong Pulses at 430 MHz. *Nature*, 226:529–531, May 1970. doi: 10.1038/226529a0.

C. Heiles and J. M. Rankin. Pulsar NP 0532: Recent Results on Strong Pulses Obtained at Arecibo. In R. D. Davies and F. Graham-Smith, editors, *The Crab Nebula*, volume 46 of *IAU Symposium*, page 103, 1971a.

C. Heiles and J. M. Rankin. Frequency Structure in Individual Strong Pulses of NP 0532. *Nature Physical Science*, 231:97–99, May 1971b. doi: 10.1038/physci231097a0.

W. A. Heindl, R. E. Rothschild, W. Coburn, R. Staubert, J. Wilms, I. Kreykenbohm, and P. Kretschmar. Timing and Spectroscopy of Accreting X-ray Pulsars: the State of Cyclotron Line Studies. In P. Kaaret, F. K. Lamb, and J. H. Swank, editors, *X-ray Timing 2003: Rossi and Beyond*, volume 714 of *American Institute of Physics Conference Series*, pages 323–330, July 2004. doi: 10.1063/1.1781049.

J. L. Herfindal and J. M. Rankin. Periodic nulls in the pulsar B1133+16. *MNRAS*, 380:430–436, September 2007. doi: 10.1111/j.1365-2966.2007.12089.x.

K. H. Hesse and R. Wielebinski. Pulse Intensity Histograms of Pulsars. *A&A*, 31:409, April 1974.

J. J. Hester. The Crab Nebula: An Astrophysical Chimera. *ARA&A*, 46:127–155, September 2008. doi: 10.1146/annurev.astro.45.051806.110608.

A. Hewish. Pulsars and high density physics. *Science*, 188:1079–1083, June 1975. doi: 10.1126/science.188.4193.1079.

A. Hewish, S. J. Bell, J. D. H. Pilkington, P. F. Scott, and R. A. Collins. Observation of a Rapidly Pulsating Radio Source. *Nature*, 217:709–713, February 1968. doi: 10.1038/217709a0.

A. M. Hillas. Cerenkov light images of EAS produced by primary gamma. *International Cosmic Ray Conference*, 3:445–448, August 1985.

R. R. Hillier, W. R. Jackson, A. Murray, R. M. Redfern, and R. G. Sale. Low-Energy Gamma Rays from NP 0532. *ApJ*, 162:L177, December 1970. doi: 10.1086/180649.

K. Hirotani. Particle Accelerator in Pulsar Magnetospheres: Super-Goldreich-Julian Current with Ion Emission from the Neutron Star Surface. *ApJ*, 652:1475–1493, December 2006. doi: 10.1086/508317.

G. Hobbs, A. Lyne, and M. Kramer. Pulsar Timing Noise. *Chinese Journal of Astronomy and Astrophysics Supplement*, 6(2):169–175, December 2006a.

G. B. Hobbs, R. T. Edwards, and R. N. Manchester. TEMPO2, a new pulsar-timing package - I. An overview. *MNRAS*, 369:655–672, June 2006b. doi: 10.1111/j.1365-2966.2006.10302.x.

R. A. Hulse and J. H. Taylor. Discovery of a pulsar in a binary system. *ApJ*, 195:L51–L53, January 1975. doi: 10.1086/181708.

A. W. Irwin and T. Fukushima. A numerical time ephemeris of the Earth. *A&A*, 348:642–652, August 1999.

M. S. Jackson and J. P. Halpern. A Refined Ephemeris and Phase-resolved X-Ray Spectroscopy of the Geminga Pulsar. *ApJ*, 633:1114–1125, November 2005. doi: 10.1086/491615.

H.-T. Janka. Explosion Mechanisms of Core-Collapse Supernovae. *Annual Review of Nuclear and Particle Science*, 62:407–451, November 2012. doi: 10.1146/annurev-nucl-102711-094901.

A. Jessner, M. V. Popov, V. I. Kondratiev, Y. Y. Kovalev, D. Graham, A. Zensus, V. A. Soglasnov, A. V. Bilous, and O. A. Moshkina. Giant pulses with nanosecond time resolution detected from the Crab pulsar at 8.5 and 15.1 GHz. *A&A*, 524:A60, December 2010. doi: 10.1051/0004-6361/201014806.

T. Jogler. *Detailed study of the binary system LS I +63° 303 in VHE gamma-rays with the MAGIC telescope*. PhD thesis, Technische Universität München, dec 2009.

T. J. Johnson, L. Guillemot, M. Kerr, I. Cognard, P. S. Ray, M. T. Wolff, S. Bégin, G. H. Janssen, R. W. Romani, C. Venter, J. E. Grove, P. C. C. Freire, M. Wood, C. C. Cheung, J. M. Casandjian, I. H. Stairs, F. Camilo, C. M. Espinoza, E. C. Ferrara, A. K. Harding, S. Johnston, M. Kramer, A. G. Lyne, P. F. Michelson, S. M. Ransom, R. Shannon, D. A. Smith, B. W. Stappers, G. Theureau, and S. E. Thorsett. Broadband Pulsations from PSR B1821-24: Implications for Emission Models and the Pulsar Population of M28. *ApJ*, 778:106, December 2013. doi: 10.1088/0004-637X/778/2/106.

S. Johnston and R. W. Romani. Giant Pulses from PSR B0540-69 in the Large Magellanic Cloud. *ApJ*, 590:L95–L98, June 2003. doi: 10.1086/376826.

S. Johnston, W. van Straten, M. Kramer, and M. Bailes. High Time Resolution Observations of the Vela Pulsar. *ApJ*, 549:L101–L104, March 2001. doi: 10.1086/319154.

S. Johnston, R. W. Romani, F. E. Marshall, and W. Zhang. Radio and X-ray observations of PSR B0540-69. *MNRAS*, 355:31–36, November 2004. doi: 10.1111/j.1365-2966.2004.08286.x.

B. C. Joshi, M. Kramer, A. G. Lyne, M. A. McLaughlin, and I. H. Stairs. Giant Pulses in Millisecond Pulsars. In F. Camilo and B. M. Gaensler, editors, *Young Neutron Stars and Their Environments*, volume 218 of *IAU Symposium*, page 319, 2004.

A. Karastergiou, M. Kramer, S. Johnston, A. G. Lyne, N. D. R. Bhat, and Y. Gupta. Simultaneous single-pulse observations of radio pulsars. II. Orthogonal polarization modes in PSR B1133+16. *A&A*, 391:247–251, August 2002. doi: 10.1051/0004-6361:20020793.

O. Kargaltsev, G. G. Pavlov, and G. P. Garmire. X-Ray Emission from the Nearby PSR B1133+16 and Other Old Pulsars. *ApJ*, 636:406–410, January 2006. doi: 10.1086/497897.

R. Karuppusamy and B. W. Stappers. Giant Pulses in Crab and B1133+16. In C. Bassa, Z. Wang, A. Cumming, and V. M. Kaspi, editors, *40 Years of Pulsars: Millisecond Pulsars, Magnetars and More*, volume 983 of *American Institute of Physics Conference Series*, pages 121–123, February 2008. doi: 10.1063/1.2900121.

R. Karuppusamy, B. Stappers, and W. van Straten. PuMa-II: A Wide Band Pulsar Machine for the Westerbork Synthesis Radio Telescope. *PASP*, 120:191–202, February 2008. doi: 10.1086/528699.

R. Karuppusamy, B. W. Stappers, and W. van Straten. Giant pulses from the Crab pulsar. A wide-band study. *A&A*, 515:A36, June 2010. doi: 10.1051/0004-6361/200913729.

R. Karuppusamy, B. W. Stappers, and M. Serylak. A low frequency study of PSRs B1133+16, B1112+50, and B0031-07. *A&A*, 525:A55, January 2011. doi: 10.1051/0004-6361/201014507.

V. M. Kaspi. BOOK REVIEW: Rotation and Accretion Powered Pulsars. *Classical and Quantum Gravity*, 25(5):059001, March 2008. doi: 10.1088/0264-9381/25/5/059001.

V. M. Kaspi and D. J. Helfand. Constraining the Birth Events of Neutron Stars. In P. O. Slane and B. M. Gaensler, editors, *Neutron Stars in Supernova Remnants*, volume 271 of *Astronomical Society of the Pacific Conference Series*, page 3, 2002.

V. M. Kaspi, F. P. Gavriil, P. M. Woods, J. B. Jensen, M. S. E. Roberts, and D. Chakrabarty. A Major Soft Gamma Repeater-like Outburst and Rotation Glitch in the No-longer-so-anomalous X-Ray Pulsar 1E 2259+586. *ApJ*, 588:L93–L96, May 2003. doi: 10.1086/375683.

V. M. Kaspi, M. S. E. Roberts, and A. K. Harding. Isolated neutron stars. In W. H. G. Lewin and M. van der Klis, editors, *Compact stellar X-ray sources*, pages 279–339. Cambridge University Press, April 2006.

E. F. Keane and M. A. McLaughlin. Rotating radio transients. *Bulletin of the Astronomical Society of India*, 39:333–352, September 2011.

A. Kinkhabwala and S. E. Thorsett. Multifrequency Observations of Giant Radio Pulses from the Millisecond Pulsar B1937+21. *ApJ*, 535:365–372, May 2000. doi: 10.1086/308844.

H. S. Knight. A Parkes radio telescope study of giant pulses from PSR J1823-3021A. *MNRAS*, 378:723–729, June 2007. doi: 10.1111/j.1365-2966.2007.11810.x.

H. S. Knight, M. Bailes, R. N. Manchester, and S. M. Ord. A Study of Giant Pulses from PSR J1824-2452A. *ApJ*, 653:580–586, December 2006a. doi: 10.1086/508253.

H. S. Knight, M. Bailes, R. N. Manchester, S. M. Ord, and B. A. Jacoby. Green Bank Telescope Studies of Giant Pulses from Millisecond Pulsars. *ApJ*, 640:941–949, April 2006b. doi: 10.1086/500292.

M. Kramer, A. Karastergiou, Y. Gupta, S. Johnston, N. D. R. Bhat, and A. G. Lyne. Simultaneous single-pulse observations of radio pulsars. IV. Flux density spectra of individual pulses. *A&A*, 407:655–668, August 2003. doi: 10.1051/0004-6361:20030842.

I. Kreykenbohm, J. Wilms, P. Kretschmar, J. M. Torrejón, K. Pottschmidt, M. Hanke, A. Santangelo, C. Ferrigno, and R. Staubert. High variability in Vela X-1: giant flares and off states. *A&A*, 492:511–525, December 2008. doi: 10.1051/0004-6361:200809956.

K. Krzeszowski, O. Maron, A. Słowikowska, J. Dyks, and A. Jessner. Analysis of single pulse radio flux measurements of PSR B1133+16 at 4.85 and 8.35 GHz. *MNRAS*, 440:457–464, May 2014. doi: 10.1093/mnras/stu293.

L. Kuiper, W. Hermsen, G. Cusumano, R. Diehl, V. Schönfelder, A. Strong, K. Bennett, and M. L. McConnell. The Crab pulsar in the 0.75-30 MeV range as seen by CGRO COMPTEL. A coherent high-energy picture from soft X-rays up to high-energy gamma-rays. *A&A*, 378: 918–935, November 2001. doi: 10.1051/0004-6361:20011256.

L. Kuiper, W. Hermsen, R. Walter, and L. Foschini. Absolute timing with IBIS, SPI and JEM-X aboard INTEGRAL. Crab main-pulse arrival times in radio, X-rays and high-energy gamma -rays. *A&A*, 411:L31–L36, November 2003. doi: 10.1051/0004-6361:20031353.

A. D. Kuzmin and A. A. Ershov. Giant pulses in pulsar <ASTROBJ>PSR B0031-07</ASTROBJ>. *A&A*, 427:575–579, November 2004. doi: 10.1051/0004-6361:20035904.

A. D. Kuzmin, A. A. Ershov, and B. Y. Losovsky. Detection of Giant Pulses from the Pulsar PSR B0031-07. *Astronomy Letters*, 30:247–250, April 2004. doi: 10.1134/1.1695085.

L. Landau. Origin of Stellar Energy. *Nature*, 141:333–334, February 1938. doi: 10.1038/141333b0.

K. R. Lang. Interstellar Scintillations of Pulsar Radiation. *Science*, 166:1401–1403, December 1969. doi: 10.1126/science.166.3911.1401.

M. I. Large, A. E. Vaughan, and B. Y. Mills. A Pulsar Supernova Association? *Nature*, 220: 340–341, October 1968. doi: 10.1038/220340a0.

J. M. Lattimer and M. Prakash. Neutron Star Structure and the Equation of State. *ApJ*, 550: 426–442, March 2001. doi: 10.1086/319702.

T.-P. Li and Y.-Q. Ma. Analysis methods for results in gamma-ray astronomy. *ApJ*, 272: 317–324, September 1983. doi: 10.1086/161295.

B. Link, R. I. Epstein, and J. M. Lattimer. Pulsar Constraints on Neutron Star Structure and Equation of State. *Physical Review Letters*, 83:3362–3365, October 1999. doi: 10.1103/PhysRevLett.83.3362.

M. A. Livingstone, S. M. Ransom, F. Camilo, V. M. Kaspi, A. G. Lyne, M. Kramer, and I. H. Stairs. X-ray and Radio Timing of the Pulsar in 3C 58. *ApJ*, 706:1163–1173, December 2009. doi: 10.1088/0004-637X/706/2/1163.

D. R. Lorimer. Binary and Millisecond Pulsars. *Living Reviews in Relativity*, 11:8, November 2008. doi: 10.12942/lrr-2008-8.

D. R. Lorimer and M. Kramer. *Handbook of Pulsar Astronomy*. October 2012.

R. B. E. Lovelace, J. M. Sutton, and H. D. Craft. Pulsar NP 0532 Near Crab Nebula. *IAU Circ.*, 2113:1, 1968.

R. V. E. Lovelace and H. D. Craft. Intensity Variations of the Pulsar CP 1919. *Nature*, 220: 875–879, November 1968. doi: 10.1038/220875a0.

S. C. Lundgren, J. M. Cordes, R. Foster, T. Hankins, M. Ulmer, and C. Garasi. Crab pulsar giant pulses: Simultaneous radio and GRO observations. In C. R. Shrader, N. Gehrels, and B. Dennis, editors, *NASA Conference Publication*, volume 3137 of *NASA Conference Publication*, pages 260–266, February 1992.

S. C. Lundgren, J. M. Cordes, M. Ulmer, S. M. Matz, S. Lomatch, R. S. Foster, and T. Hankins. Giant Pulses from the Crab Pulsar: A Joint Radio and Gamma-Ray Study. *ApJ*, 453:433, November 1995. doi: 10.1086/176404.

A. Lyne. Glitches and Timing Noise. In Z. Arzoumanian, F. Van der Hooft, and E. P. J. van den Heuvel, editors, *Pulsar Timing, General Relativity and the Internal Structure of Neutron Stars*, page 141, 1999.

A. Lyne, F. Graham-Smith, P. Weltevrede, C. Jordan, B. Stappers, C. Bassa, and M. Kramer. Evolution of the Magnetic Field Structure of the Crab Pulsar. *Science*, 342:598–601, November 2013. doi: 10.1126/science.1243254.

A. G. Lyne. Mode changing in pulsar radiation. *MNRAS*, 153:27P, 1971.

A. G. Lyne and F. Graham-Smith. Pulsar astronomy. *Cambridge Astrophysics Series*, 16, 1990.

A. G. Lyne, A. Brinklow, J. Middleditch, S. R. Kulkarni, and D. C. Backer. The discovery of a millisecond pulsar in the globular cluster M28. *Nature*, 328:399–401, July 1987. doi: 10.1038/328399a0.

A. G. Lyne, R. S. Pritchard, and F. G. Smith. Crab pulsar timing 1982-87. *MNRAS*, 233: 667–676, August 1988.

A. G. Lyne, R. S. Pritchard, and F. Graham-Smith. Twenty-Three Years of Crab Pulsar Rotational History. *MNRAS*, 265:1003, December 1993.

A. G. Lyne, C. A. Jordan, F. Graham-Smith, C. M. Espinoza, B. W. Stappers, and P. Weltevrede. 45 years of rotation of the Crab pulsar. *MNRAS*, 446:857–864, January 2015. doi: 10.1093/mnras/stu2118.

M. Lyutikov. On generation of Crab giant pulses. *MNRAS*, 381:1190–1196, November 2007. doi: 10.1111/j.1365-2966.2007.12318.x.

MAGIC Collaboration, J. Aleksic, S. Ansoldi, L. A. Antonelli, P. Antoranz, A. Babic, P. Bangale, M. Barcelo, J. A. Barrio, J. Becerra Gonzalez, W. Bednarek, E. Bernardini, B. Biasuzzi, A. Biland, M. Bitossi, O. Blanch, S. Bonnefoy, G. Bonnoli, F. Borracci, T. Bretz, E. Carmona, A. Carosi, R. Cecchi, P. Colin, E. Colombo, J. L. Contreras, D. Corti, J. Cortina, S. Covino, P. Da Vela, F. Dazzi, A. De Angelis, G. De Caneva, B. De Lotto, E. de Ona Wilhelmi, C. Delgado Mendez, A. Dettlaff, D. Dominis Prester, D. Dorner, M. Doro, S. Einecke, D. Eisenacher, D. Elsaesser, D. Fidalgo, D. Fink, M. V. Fonseca, L. Font, K. Frantzen, C. Fruck, D. Galindo, R. J. Garcia Lopez, M. Garczarczyk, D. Garrido Terrats, M. Gaug, G. Giavitto, N. Godinovic, A. Gonzalez Munoz, S. R. Gozzini, W. Haberer, D. Hadasch, Y. Hanabata, M. Hayashida, J. Herrera, D. Hildebrand, J. Hose, D. Hrupec, W. Idec, J. M. Illa, V. Kadenius, H. Kellermann, M. L. Knoetig, K. Kodani, Y. Konno, J. Krause, H. Kubo, J. Kushida, A. La Barbera, D. Lelas, J. L. Lemus, N. Lewandowska, E. Lindfors, S. Lombardi, F. Longo, M. Lopez, R. Lopez-Coto, A. Lopez-Oramas, A. Lorca, E. Lorenz, I. Lozano,

M. Makariev, K. Mallot, G. Maneva, N. Mankuzhiyil, K. Mannheim, L. Maraschi, B. Marcote, M. Mariotti, M. Martinez, D. Mazin, U. Menzel, J. M. Miranda, R. Mirzoyan, A. Moralejo, P. Munar-Adrover, D. Nakajima, M. Negrello, V. Neustroev, A. Niedzwiecki, K. Nilsson, K. Nishijima, K. Noda, R. Orito, A. Overkemping, S. Paiano, M. Palatiello, D. Paneque, R. Paoletti, J. M. Paredes, X. Paredes-Fortuny, M. Persic, J. Poutanen, P. G. Prada Moroni, E. Prandini, I. Puljak, R. Reinthal, W. Rhode, M. Ribo, J. Rico, J. Rodriguez Garcia, S. Rugamer, T. Saito, K. Saito, K. Satalecka, V. Scalzotto, V. Scapin, C. Schultz, J. Schlammer, S. Schmidl, T. Schweizer, S. N. Shore, A. Sillanpaa, J. Sitarek, I. Snidaric, D. Sobczynska, F. Spanier, A. Stamerra, T. Steinbring, J. Storz, M. Strzys, L. Takalo, H. Takami, F. Tavecchio, L. A. Tejedor, P. Temnikov, T. Terzic, D. Tescaro, M. Teshima, J. Thaele, O. Tibolla, D. F. Torres, T. Toyama, A. Treves, P. Vogler, H. Wetteskind, M. Will, and R. Zanin. The major upgrade of the MAGIC telescopes, Part II: A performance study using observations of the Crab Nebula. *ArXiv e-prints*, September 2014.

O. I. Malov, V. M. Malofeev, D. A. Teplykh, and S. V. Logvinenko. The Geminga radio pulsar. New low-frequency results. *Astronomy Reports*, 59:183–190, March 2015. doi: 10.1134/S1063772915020055.

R. N. Manchester, G. R. Huguenin, and J. H. Taylor. Polarization of the Crab Pulsar Radiation at Low Radio Frequencies. *ApJ*, 174:L19, May 1972. doi: 10.1086/180940.

R. N. Manchester, D. P. Mar, A. G. Lyne, V. M. Kaspi, and S. Johnston. Radio detection of PSR B0540-69. *ApJ*, 403:L29–L31, January 1993a. doi: 10.1086/186714.

R. N. Manchester, L. Staveley-Smith, and M. J. Kesteven. The radio structure of supernova remnant 0540-693. *ApJ*, 411:756–760, July 1993b. doi: 10.1086/172877.

R. N. Manchester, G. B. Hobbs, A. Teoh, and M. Hobbs. The Australia Telescope National Facility Pulsar Catalogue. *AJ*, 129:1993–2006, April 2005. doi: 10.1086/428488.

O. Maron, J. Kijak, M. Kramer, and R. Wielebinski. Pulsar spectra of radio emission. *A&AS*, 147:195–203, December 2000. doi: 10.1051/aas:2000298.

G. J. Mathews and R. A. Ward. Neutron capture processes in astrophysics. *Reports on Progress in Physics*, 48:1371–1418, October 1985. doi: 10.1088/0034-4885/48/10/002.

D. N. Matsakis and R. S. Foster. Application of millisecond pulsar timing to the long-term stability of clock ensembles. In R. Y. Chiao, editor, *Amazing Light*, pages 445–462, 1996.

N. U. Mayall and J. H. Oort. Further Data Bearing on the Identification of the Crab Nebula with the Supernova of 1054 A.D. Part II. The Astronomical Aspects. *PASP*, 54:95–104, April 1942. doi: 10.1086/125410.

E. P. Mazets and S. V. Golenetskii. Recent results from the gamma-ray burst studies in the KONUS experiment. *Ap&SS*, 75:47–81, March 1981. doi: 10.1007/BF00651384.

E. P. Mazets, S. V. Golentskii, V. N. Ilinskii, R. L. Aptekar, and I. A. Guryan. Observations of a flaring X-ray pulsar in Dorado. *Nature*, 282:587–589, December 1979. doi: 10.1038/282587a0.

B. A. Mazin, S. R. Meeker, M. J. Strader, P. Szypryt, D. Marsden, J. C. van Eyken, G. E. Duggan, A. B. Walter, G. Ulbricht, M. Johnson, B. Bumble, K. O"Brien, and C. Stoughton.

ARCONS: A 2024 Pixel Optical through Near-IR Cryogenic Imaging Spectrophotometer. *PASP*, 125:1348–1361, November 2013. doi: 10.1086/674013.

P. A. Mazzali, F. K. Röpke, S. Benetti, and W. Hillebrandt. A Common Explosion Mechanism for Type Ia Supernovae. *Science*, 315:825–, February 2007. doi: 10.1126/science.1136259.

D. D. McCarthy and P. K. Seidelmann. *Time: From Earth Rotation to Atomic Physics*. 2009.

M. A. McLaughlin, A. G. Lyne, D. R. Lorimer, M. Kramer, A. J. Faulkner, R. N. Manchester, J. M. Cordes, F. Camilo, A. Possenti, I. H. Stairs, G. Hobbs, N. D'Amico, M. Burgay, and J. T. O'Brien. Transient radio bursts from rotating neutron stars. *Nature*, 439:817–820, February 2006. doi: 10.1038/nature04440.

D. Melrose. Pulse Emission Mechanisms. In F. Camilo and B. M. Gaensler, editors, *Young Neutron Stars and Their Environments*, volume 218 of *IAU Symposium*, page 349, 2004.

D. B. Melrose. Coherent Radio Emission from Pulsars. *Royal Society of London Philosophical Transactions Series A*, 341:105–115, October 1992. doi: 10.1098/rsta.1992.0087.

M. B. Mickaliger, M. A. McLaughlin, D. R. Lorimer, G. I. Langston, A. V. Bilous, V. I. Kondratiev, M. Lyutikov, S. M. Ransom, and N. Palliyaguru. A Giant Sample of Giant Pulses from the Crab Pulsar. *ApJ*, 760:64, November 2012. doi: 10.1088/0004-637X/760/1/64.

J. Middleditch and C. Pennypacker. Optical pulsations in the large Magellanic Cloud remnant 0540-69.3. *Nature*, 313:659–661, February 1985. doi: 10.1038/313659a0.

J. Middleditch, C. Pennypacker, and M. S. Burns. Infrared study of the Crab pulsar - The 'shoulder' pulse and the 3.45 micron pulse profile. *ApJ*, 273:261–266, October 1983. doi: 10.1086/161365.

J. Middleditch, C. R. Pennypacker, and M. S. Burns. Optical color, polarimetric, and timing measurements of the 50 MS Large Magellanic Cloud pulsar, PSR 0540-69. *ApJ*, 315:142–148, April 1987. doi: 10.1086/165119.

A. B. Migdal. Superfluidity and the moments of inertia of nuclei. *Nucl. Phys. A*, 13:655–674, November 1959. doi: 10.1016/0029-5582(59)90264-0.

R. P. Mignani, G. G. Pavlov, and O. Kargaltsev. Optical-Ultraviolet Spectrum and Proper Motion of the Middle-aged Pulsar B1055-52. *ApJ*, 720:1635–1643, September 2010a. doi: 10.1088/0004-637X/720/2/1635.

R. P. Mignani, A. Sartori, A. de Luca, B. Rudak, A. Słowikowska, G. Kanbach, and P. A. Caraveo. HST/WFPC2 observations of the LMC pulsar PSR B0540-69. *A&A*, 515:A110, June 2010b. doi: 10.1051/0004-6361/200913870.

R. P. Mignani, A. De Luca, W. Hummel, A. Zajczyk, B. Rudak, G. Kanbach, and A. Słowikowska. The near-infrared detection of PSR B0540-69 and its nebula. *A&A*, 544: A100, August 2012. doi: 10.1051/0004-6361/201219177.

R. Mikami, T. Terasawa, K. Takefuji, M. Sekido, H. Takeuchi, Y. Tanaka, S. Kisaka, K. Asano, N. Kawai, and K. Nagata. Search for correlation between giant radio pulses and hard X-ray pulses from the Crab pulsar. In J.-U. Ness, editor, *The Fast and the Furious: Energetic*

Phenomena in Isolated Neutron Stars, Pulsar Wind Nebulae and Supernova Remnants, May 2013.

R. Mikami, T. Terasawa, S. Kisaka, K. Asano, S. J. Tanaka, M. Sekido, K. Takefuji, H. Takeuchi, H. Odaka, T. Sato, Y. T. Tanaka, and N. Kawai. Hard X-ray observations with Suzaku HXD at the time of giant radio pulses from the Crab pulsar. In M. Ishida, R. Petre, and K. Mitsuda, editors, *Suzaku-MAXI 2014: Expanding the Frontiers of the X-ray Universe*, page 180, September 2014.

R. Mirzoyan, E. Lorenz, D. Petry, and C. Prosch. On the influence of afterpulsing in PMTs on the trigger threshold of multichannel light detectors in self-trigger mode. *Nuclear Instruments and Methods in Physics Research A*, 387:74–78, February 1997. doi: 10.1016/S0168-9002(96)00964-3.

D. A. Moffett and T. H. Hankins. Multifrequency Radio Observations of the Crab Pulsar. *ApJ*, 468:779, September 1996. doi: 10.1086/177734.

D. A. Moffett and T. H. Hankins. Polarimetric Properties of the Crab Pulsar between 1.4 and 8.4 GHZ. *ApJ*, 522:1046–1052, September 1999. doi: 10.1086/307654.

A. Moralejo, M. Gaug, E. Carmona, P. Colin, C. Delgado, S. Lombardi, D. Mazin, V. Scalzotto, J. Sitarek, D. Tescaro, and for the MAGIC collaboration. MARS, the MAGIC Analysis and Reconstruction Software. *ArXiv e-prints*, July 2009.

G. Naletto, C. Barbieri, T. Occhipinti, I. Capraro, A. di Paola, C. Facchinetti, E. Verroi, P. Zoccarato, G. Anzolin, M. Belluso, S. Billotta, P. Bolli, G. Bonanno, V. da Deppo, S. Fornasier, C. Germanà, E. Giro, S. Marchi, F. Messina, C. Pernechele, F. Tamburini, M. Zaccariotto, and L. Zampieri. Iqueye, a single photon-counting photometer applied to the ESO new technology telescope. *A&A*, 508:531–539, December 2009. doi: 10.1051/0004-6361/200912862.

R. E. Nather, B. Warner, and M. Macfarlane. Optical Pulsations in the Crab Nebula Pulsar. *Nature*, 221:527–529, February 1969. doi: 10.1038/221527a0.

G. Neugebauer, E. E. Becklin, J. Kristian, R. B. Leighton, G. Snellen, and J. A. Westphal. Infrared and Optical Measurements of the Crab Pulsar NP 0532. *ApJ*, 156:L115, June 1969. doi: 10.1086/180361.

L. Nicastro, G. Cusumano, L. Kuiper, W. Becker, W. Hermsen, and M. Kramer. The 2-10 keV emission properties of PSR B1937+21. In W. Becker, H. Lesch, and J. Trümper, editors, *Neutron Stars, Pulsars, and Supernova Remnants*, page 87, 2002.

P. L. Nolan, Z. Arzoumanian, D. L. Bertsch, J. Chiang, C. E. Fichtel, J. M. Fierro, R. C. Hartman, S. D. Hunter, G. Kanbach, D. A. Kniffen, P. W. Kwok, Y. C. Lin, J. R. Mattox, H. A. Mayer-Hasselwander, P. F. Michelson, C. von Montigny, H. I. Nel, D. Nice, K. Pinkau, H. Rothermel, E. Schneid, M. Sommer, P. Sreekumar, J. H. Taylor, and D. J. Thompson. Observations of the Crab pulsar and nebula by the EGRET telescope on the Compton Gamma-Ray Observatory. *ApJ*, 409:697–704, June 1993. doi: 10.1086/172699.

S. A. Olausen and V. M. Kaspi. The McGill Magnetar Catalog. *ApJS*, 212:6, May 2014. doi: 10.1088/0067-0049/212/1/6.

T. Oosterbroek, I. Cognard, A. Golden, P. Verhoeve, D. D. E. Martin, C. Erd, R. Schulz, J. A. Stüwe, A. Stankov, and T. Ho. Simultaneous absolute timing of the Crab pulsar at radio and optical wavelengths. *A&A*, 488:271–277, September 2008. doi: 10.1051/0004-6361:200809751.

J. R. Oppenheimer and G. M. Volkoff. On Massive Neutron Cores. *Physical Review*, 55:374–381, February 1939. doi: 10.1103/PhysRev.55.374.

F. Pacini. Energy Emission from a Neutron Star. *Nature*, 216:567–568, November 1967. doi: 10.1038/216567a0.

D. M. Palmer, S. Barthelmy, N. Gehrels, R. M. Kippen, T. Cayton, C. Kouveliotou, D. Eichler, R. A. M. J. Wijers, P. M. Woods, J. Granot, Y. E. Lyubarsky, E. Ramirez-Ruiz, L. Barbier, M. Chester, J. Cummings, E. E. Fenimore, M. H. Finger, B. M. Gaensler, D. Hullinger, H. Krimm, C. B. Markwardt, J. A. Nousek, A. Parsons, S. Patel, T. Sakamoto, G. Sato, M. Suzuki, and J. Tueller. A giant γ-ray flare from the magnetar SGR 1806 - 20. *Nature*, 434:1107–1109, April 2005. doi: 10.1038/nature03525.

R Paoletti, C Bigongiari, M Bitossi, R Cecchi, and R Pegna. The global trigger system of the magic telescope array. In *Nuclear Science Symposium Conference Record, 2008. NSS'08. IEEE*, pages 2781–2783. IEEE, 2008.

W. Pauli. Über den Zusammenhang des Abschlusses der Elektronengruppen im Atom mit der Komplexstruktur der Spektren. *Zeitschrift fur Physik*, 31:765–783, February 1925. doi: 10.1007/BF02980631.

A. Pellizzoni, M. Pilia, A. Possenti, F. Fornari, P. Caraveo, E. del Monte, S. Mereghetti, M. Tavani, A. Argan, A. Trois, M. Burgay, A. Chen, I. Cognard, E. Costa, N. D'Amico, P. Esposito, Y. Evangelista, M. Feroci, F. Fuschino, A. Giuliani, J. Halpern, G. Hobbs, A. Hotan, S. Johnston, M. Kramer, F. Longo, R. N. Manchester, M. Marisaldi, J. Palfreyman, P. Weltevrede, G. Barbiellini, F. Boffelli, A. Bulgarelli, P. W. Cattaneo, V. Cocco, F. D'Ammando, G. DeParis, G. Di Cocco, I. Donnarumma, M. Fiorini, T. Froysland, M. Galli, F. Gianotti, A. Harding, C. Labanti, I. Lapshov, F. Lazzarotto, P. Lipari, F. Mauri, A. Morselli, L. Pacciani, F. Perotti, P. Picozza, M. Prest, G. Pucella, M. Rapisarda, A. Rappoldi, P. Soffitta, M. Trifoglio, E. Vallazza, S. Vercellone, V. Vittorini, A. Zambra, D. Zanello, C. Pittori, F. Verrecchia, B. Preger, P. Santolamazza, P. Giommi, and L. Salotti. High-Resolution Timing Observations of Spin-Powered Pulsars with the AGILE Gamma-Ray Telescope. *ApJ*, 691:1618–1633, February 2009. doi: 10.1088/0004-637X/691/2/1618.

C. R. Pennypacker. Infrared studies of pulsars. *ApJ*, 244:286–289, February 1981. doi: 10.1086/158706.

S. A. Petrova. On the origin of giant pulses in radio pulsars. *A&A*, 424:227–236, September 2004. doi: 10.1051/0004-6361:20047171.

S. A. Petrova. Mechanism of giant pulses in radio pulsars. In T. Bulik, B. Rudak, and G. Madejski, editors, *Astrophysical Sources of High Energy Particles and Radiation*, volume 801 of *American Institute of Physics Conference Series*, pages 314–315, November 2005. doi: 10.1063/1.2141889.

S. A. Petrova. Nature of Giant Pulses in Radio Pulsars. *Chinese Journal of Astronomy and Astrophysics Supplement*, 6(2):113–119, December 2006.

A. A. Philippov and A. Spitkovsky. Ab Initio Pulsar Magnetosphere: Three-dimensional Particle-in-cell Simulations of Axisymmetric Pulsars. *ApJ*, 785:L33, April 2014. doi: 10.1088/2041-8205/785/2/L33.

J. D. H. Pilkington, A. Hewish, S. J. Bell, and T. W. Cole. Observations of some further Pulsed Radio Sources. *Nature*, 218:126–129, April 1968. doi: 10.1038/218126a0.

P. Podsiadlowski, S. Rappaport, and E. D. Pfahl. Evolutionary Sequences for Low- and Intermediate-Mass X-Ray Binaries. *ApJ*, 565:1107–1133, February 2002. doi: 10.1086/324686.

M. V. Popov and B. Stappers. Simultaneous Dual-Frequency Observations of Giant Radio Pulses from the Millisecond Pulsar B1937+21. *Astronomy Reports*, 47:660–669, August 2003. doi: 10.1134/1.1601634.

M. V. Popov and B. Stappers. Statistical properties of giant pulses from the Crab pulsar. *A&A*, 470:1003–1007, August 2007. doi: 10.1051/0004-6361:20066589.

M.V. Popov, A.D. Kuz'min, O.M. Ul'yanov, A.A. Deshpande, A.A. Ershov, V.V. Zakharenko, V.I. Kondrat'ev, S.V. Kostyuk, B.Ya. Losovskiĭ, and V.A. Soglasnov. Instantaneous radio spectra of giant pulses from the crab pulsar from decimeter to decameter wavelengths. *Astronomy Reports*, 50:562–568, July 2006. doi: 10.1134/S1063772906070067.

J. M. Rankin. Pulsar NP 0532: Polarization of Strong Pulses at 430 MHz as seen with 300 kHz Bandwidth. *Nature*, 227:1330–1331, September 1970. doi: 10.1038/2271330a0.

J. M. Rankin, J. M. Comella, H. D. Craft, Jr., D. W. Richards, D. B. Campbell, and C. C. Counselman, III. Radio Pulse Shapes, Flux Densities, and Dispersion of Pulsar NP 0532. *ApJ*, 162:707, December 1970. doi: 10.1086/150703.

J. M. Rankin, C. C. Counselman, III, and D. W. Richards. Crab Nebula Pulsar Radio Pulse Arrival Times at Arecibo Observatory. *AJ*, 76:686, October 1971a. doi: 10.1086/111185.

J. M. Rankin, C. C. Counselman, III, and D. W. Richards. Erratum: Crab Nebula Pulsar Radio Pulse Arrival Times at Arecibo Observatory. *AJ*, 76:1154, December 1971b. doi: 10.1086/111234.

J. M. Rankin, A. Wolszczan, and D. R. Stinebring. Mode changing and quasi-periodic modulation in pulsar 1737+13, a bright, five-componented pulsar. *ApJ*, 324:1048–1055, January 1988. doi: 10.1086/165961.

S. M. Ransom, G. G. Fazio, S. S. Eikenberry, J. Middleditch, J. Kristian, K. Hays, and C. R. Pennypacker. High time resolution infrared observations of the Crab Nebula pulsar. *ApJ*, 431:L43–L46, August 1994. doi: 10.1086/187468.

L. A. Rawley, J. H. Taylor, M. M. Davis, and D. W. Allan. Millisecond pulsar PSR 1937+21 - A highly stable clock. *Science*, 238:761–765, November 1987. doi: 10.1126/science.238.4828.761.

P. S. Ray, M. Kerr, and D. Parent. Pulsar Timing with the Fermi LAT. In M. Burgay, N. D'Amico, P. Esposito, A. Pellizzoni, and A. Possenti, editors, *American Institute of Physics Conference Series*, volume 1357 of *American Institute of Physics Conference Series*, pages 121–126, August 2011a. doi: 10.1063/1.3615094.

P. S. Ray, M. Kerr, D. Parent, A. A. Abdo, L. Guillemot, S. M. Ransom, N. Rea, M. T. Wolff, A. Makeev, M. S. E. Roberts, F. Camilo, M. Dormody, P. C. C. Freire, J. E. Grove, C. Gwon, A. K. Harding, S. Johnston, M. Keith, M. Kramer, P. F. Michelson, R. W. Romani, P. M. Saz Parkinson, D. J. Thompson, P. Weltevrede, K. S. Wood, and M. Ziegler. Precise γ-ray Timing and Radio Observations of 17 Fermi γ-ray Pulsars. *ApJS*, 194:17, June 2011b. doi: 10.1088/0067-0049/194/2/17.

S. L. Redman and J. M. Rankin. On the randomness of pulsar nulls. *MNRAS*, 395:1529–1532, May 2009. doi: 10.1111/j.1365-2966.2009.14632.x.

R. Reifarth, C. Lederer, and F. Käppeler. Neutron reactions in astrophysics. *Journal of Physics G Nuclear Physics*, 41(5):053101, May 2014. doi: 10.1088/0954-3899/41/5/053101.

D. W. Richards and J. M. Comella. The Period of Pulsar NP 0532. *Nature*, 222:551–552, May 1969. doi: 10.1038/222551a0.

M. Rissi, N. Otte, T. Schweizer, and M. Shayduk. A New Sum Trigger to Provide a Lower Energy Threshold for the MAGIC Telescope. *IEEE Transactions on Nuclear Science*, 56: 3840–3843, December 2009. doi: 10.1109/TNS.2009.2030802.

J. A. Roberts and D. W. Richards. Timing Observations of the Crab Nebula Pulsar at the Arecibo Observatory. *Nature Physical Science*, 231:25–28, May 1971. doi: 10.1038/physci231025a0.

R. W. Romani. Gamma-Ray Pulsars: Radiation Processes in the Outer Magnetosphere. *ApJ*, 470:469, October 1996. doi: 10.1086/177878.

R. W. Romani and S. Johnston. Giant Pulses from the Millisecond Pulsar B1821-24. *ApJ*, 557: L93–L96, August 2001. doi: 10.1086/323415.

R. W. Romani and I.-A. Yadigaroglu. Gamma-ray pulsars: Emission zones and viewing geometries. *ApJ*, 438:314–321, January 1995. doi: 10.1086/175076.

A. H. Rots, K. Jahoda, D. J. Macomb, N. Kawai, Y. Saito, V. M. Kaspi, A. G. Lyne, R. N. Manchester, D. C. Backer, A. L. Somer, D. Marsden, and R. E. Rothschild. Rossi X-Ray Timing Explorer Absolute Timing Results for the Pulsars B1821-24 and B1509-58. *ApJ*, 501: 749–757, July 1998. doi: 10.1086/305836.

A. H. Rots, K. Jahoda, and A. G. Lyne. Absolute Timing of the Crab Pulsar with the Rossi X-Ray Timing Explorer. *ApJ*, 605:L129–L132, April 2004. doi: 10.1086/420842.

M. A. Ruderman and P. G. Sutherland. Theory of pulsars - Polar caps, sparks, and coherent microwave radiation. *ApJ*, 196:51–72, February 1975. doi: 10.1086/153393.

O. Ryan, M. Redfern, and A. Shearer. An avalanche photodiode photon counting camera for high-resolution astronomy. *Experimental Astronomy*, 21:23–30, February 2006. doi: 10.1007/s10686-006-9056-z.

M. Ryle. The New Cambridge Radio Telescope. *Nature*, 194:517–518, May 1962. doi: 10.1038/194517a0.

M. Ryle and A. Hewish. The synthesis of large radio telescopes. *MNRAS*, 120:220, 1960.

Maurizio Salaris and Santi Cassisi. *Evolution of stars and stellar populations*. John Wiley & Sons, 2005.

S. Sallmen and D. C. Backer. Single Pulse Statistics for PSR 1534+12 and PSR 1937+21. In A. S. Fruchter, M. Tavani, and D. C. Backer, editors, *Millisecond Pulsars. A Decade of Surprise*, volume 72 of *Astronomical Society of the Pacific Conference Series*, page 340, 1995.

S. Sallmen, D. C. Backer, T. H. Hankins, D. Moffett, and S. Lundgren. Simultaneous Dual-Frequency Observations of Giant Pulses from the Crab Pulsar. *ApJ*, 517:460–471, May 1999. doi: 10.1086/307183.

E. E. Salpeter. Energy and Pressure of a Zero-Temperature Plasma. *ApJ*, 134:669, November 1961. doi: 10.1086/147194.

P. A. G. Scheuer. Amplitude Variations in Pulsed Radio Sources. *Nature*, 218:920–922, June 1968. doi: 10.1038/218920a0.

C.H.E. Schultz. *Development of New Composite Mirrors for Imaging Cherenkov Telescopesand Observations of the Two Blazar Objects 1ES 0806+524 and 1ES 1011+496 with MAGIC*. PhD thesis, Universita Degli Studi Di Padova, 2013.

F. D. Seward, F. R. Harnden, Jr., and D. J. Helfand. Discovery of a 50 millisecond pulsar in the Large Magellanic Cloud. *ApJ*, 287:L19–L22, December 1984. doi: 10.1086/184388.

I. I. Shapiro. Fourth Test of General Relativity. *Physical Review Letters*, 13:789–791, December 1964. doi: 10.1103/PhysRevLett.13.789.

Irwin Shapiro, Gordon Pettengill, Michael Ash, Melvin Stone, William Smith, Richard Ingalls, and Richard Brockelman. Fourth test of general relativity: Preliminary results. *Physical Review Letters*, 20, 5 1968. doi: 10.1103/PhysRevLett.20.1265. URL `http://gen.lib.rus.ec/scimag/index.php?s=10.1103/PhysRevLett.20.1265`.

S. L. Shapiro and S. A. Teukolsky. *Black holes, white dwarfs, and neutron stars: The physics of compact objects*. 1983.

M. Shayduk, T. Hengstebeck, O. Kalekin, N. A. Pavel, and T. Schweizer. A New Image Cleaning Method for the MAGIC Telescope. *International Cosmic Ray Conference*, 5:223, 2005.

A. Shearer and A. Golden. Why study pulsars optically? In W. Becker, H. Lesch, and J. Trümper, editors, *Neutron Stars, Pulsars, and Supernova Remnants*, page 44, 2002.

A. Shearer, B. Stappers, P. O'Connor, A. Golden, R. Strom, M. Redfern, and O. Ryan. Enhanced Optical Emission During Crab Giant Radio Pulses. *Science*, 301:493–495, July 2003. doi: 10.1126/science.1084919.

S. L. Shemar and A. G. Lyne. Observations of pulsar glitches. *MNRAS*, 282:677–690, September 1996.

Zbyněk Šidák. Rectangular confidence regions for the means of multivariate normal distributions. *Journal of the American Statistical Association*, 62(318):626–633, 1967.

J. Sitarek, E. Carmona, P. Colin, K. Frantzen, M. Gaug, M. Lopez, S. Lombardi, A. Moralejo, K. Satalecka, V. Scapin, V. Stamatescu, R. Zanin, D. Mazin, D. Tescaro, and for the MAGIC Collaboration. Physics performance of the upgraded MAGIC telescopes obtained with Crab Nebula data. *ArXiv e-prints*, August 2013.

J. Skilling. Oscillations of Hamada-Salpeter White Dwarfs including General Relativistic Effects. *Nature*, 218:923–924, June 1968. doi: 10.1038/218923a0.

A. Slowikowska, B. W. Stappers, A. K. Harding, S. L. O'Dell, R. F. Elsner, A. J. van der Horst, and M. C. Weisskopf. High-Time-Resolution Measurements of the Polarization of the Crab Pulsar at 1.38 GHz. *ArXiv e-prints*, February 2014.

C. Sobey, N. J. Young, J. W. T. Hessels, P. Weltevrede, A. Noutsos, B. W. Stappers, M. Kramer, C. Bassa, A. G. Lyne, V. I. Kondratiev, T. E. Hassall, E. F. Keane, A. V. Bilous, R. P. Breton, J.-M. Grießmeier, A. Karastergiou, M. Pilia, M. Serylak, S. t. Veen, J. van Leeuwen, A. Alexov, J. Anderson, A. Asgekar, I. M. Avruch, M. E. Bell, M. J. Bentum, G. Bernardi, P. Best, L. Bîrzan, A. Bonafede, F. Breitling, J. Broderick, M. Brüggen, A. Corstanje, D. Carbone, E. de Geus, M. de Vos, A. van Duin, S. Duscha, J. Eislöffel, H. Falcke, R. A. Fallows, R. Fender, C. Ferrari, W. Frieswijk, M. A. Garrett, A. W. Gunst, J. P. Hamaker, G. Heald, M. Hoeft, J. Hörandel, E. Jütte, G. Kuper, P. Maat, G. Mann, S. Markoff, R. McFadden, D. McKay-Bukowski, J. P. McKean, D. D. Mulcahy, H. Munk, A. Nelles, M. J. Norden, E. Orrù, H. Paas, M. Pandey-Pommier, V. N. Pandey, G. Pietka, R. Pizzo, A. G. Polatidis, D. Rafferty, A. Renting, H. Röttgering, A. Rowlinson, A. M. M. Scaife, D. Schwarz, J. Sluman, O. Smirnov, M. Steinmetz, A. Stewart, J. Swinbank, M. Tagger, Y. Tang, C. Tasse, S. Thoudam, C. Toribio, R. Vermeulen, C. Vocks, R. J. van Weeren, R. A. M. J. Wijers, M. W. Wise, O. Wucknitz, S. Yatawatta, and P. Zarka. LOFAR discovery of a quiet emission mode in PSR B0823+26. *MNRAS*, 451:2493–2506, August 2015. doi: 10.1093/mnras/stv1066.

V. A. Soglasnov, M. V. Popov, N. Bartel, W. Cannon, A. Y. Novikov, V. I. Kondratiev, and V. I. Altunin. Giant Pulses from PSR B1937+21 with Widths <=15 Nanoseconds and $T_b > 5\times10^{39}$ K, the Highest Brightness Temperature Observed in the Universe. *ApJ*, 616:439–451, November 2004. doi: 10.1086/424908.

D. H. Staelin. Observed Shapes of Crab Nebula Radio Pulses. *Nature*, 226:69–70, April 1970. doi: 10.1038/226069a0.

D. H. Staelin and E. C. Reifenstein, III. Pulsating Radio Sources near the Crab Nebula. *Science*, 162:1481–1483, December 1968. doi: 10.1126/science.162.3861.1481.

I. H. Stairs. Pulsars in Binary Systems: Probing Binary Stellar Evolution and General Relativity. *Science*, 304:547–552, April 2004. doi: 10.1126/science.1096986.

M. J. Strader, M. D. Johnson, B. A. Mazin, G. V. Spiro Jaeger, C. R. Gwinn, S. R. Meeker, P. Szypryt, J. C. van Eyken, D. Marsden, K. O'Brien, A. B. Walter, G. Ulbricht, C. Stoughton, and B. Bumble. Excess Optical Enhancement Observed with ARCONS for Early Crab Giant Pulses. *ApJ*, 779:L12, December 2013. doi: 10.1088/2041-8205/779/1/L12.

C. Straubmeier, G. Kanbach, and F. Schrey. OPTIMA: A Photon Counting High-Speed Photometer. *Experimental Astronomy*, 11:157–170, 2001. doi: 10.1023/A:1013117110998.

P. A. Sturrock. A Model of Pulsars. *ApJ*, 164:529, March 1971. doi: 10.1086/150865.

S. A. Suleimanova and V. D. Pugachev. Polarization of individual pulses of radio pulsars at the low frequencies 40, 60, and 103 MHz. *Astronomy Reports*, 46:309–326, April 2002. doi: 10.1134/1.1471396.

J. M. Sutton, D. H. Staelin, and R. M. Price. Individual Radio Pulses from NP 0531. In R. D. Davies and F. Graham-Smith, editors, *The Crab Nebula*, volume 46 of *IAU Symposium*, page 97, 1971.

M. Takahashi, S. Shibata, K. Torii, Y. Saito, N. Kawai, M. Hirayama, T. Dotani, S. Gunji, H. Sakurai, I. H. Stairs, and R. N. Manchester. Pulsed X-Ray Emission from the Fastest Millisecond Pulsar: PSR B1937+21 with ASCA. *ApJ*, 554:316–321, June 2001. doi: 10.1086/321330.

J. Takata and H.-K. Chang. Pulse Profiles, Spectra, and Polarization Characteristics of Non-thermal Emissions from the Crab-like Pulsars. *ApJ*, 670:677–692, November 2007. doi: 10.1086/521785.

G. H. Tan. The multi frequency front end - A new type of front end for the Westerbork Synthesis Radio Telescope. In T. J. Cornwell and R. A. Perley, editors, *IAU Colloq. 131: Radio Interferometry. Theory, Techniques, and Applications*, volume 19 of *Astronomical Society of the Pacific Conference Series*, pages 42–46, 1991.

D. J. Thompson. Gamma ray pulsars: Observations. In F. A. Aharonian and H. J. Völk, editors, *American Institute of Physics Conference Series*, volume 558 of *American Institute of Physics Conference Series*, pages 103–114, April 2001. doi: 10.1063/1.1370784.

S. E. Thorsett and D. Chakrabarty. Neutron Star Mass Measurements. I. Radio Pulsars. *ApJ*, 512:288–299, February 1999. doi: 10.1086/306742.

V. Trimble. Motions and Structure of the Filamentary Envelope of the Crab Nebula. *AJ*, 73: 535, September 1968. doi: 10.1086/110658.

M. Umizaki and S. Shibata. Method of the Particle-in-Cell Simulation for the Y-Point in the Pulsar Magnetosphere. *PASJ*, 62:131–, February 2010. doi: 10.1093/pasj/62.1.131.

M. van der Klis. Millisecond Oscillations in X-ray Binaries. *ARA&A*, 38:717–760, 2000. doi: 10.1146/annurev.astro.38.1.717.

W. van Straten and M. Bailes. DSPSR: Digital Signal Processing Software for Pulsar Astronomy. *Publications of the Astronomical Society of Australia*, 28:1–14, January 2011. doi: 10.1071/AS10021.

G. Vasisht and E. V. Gotthelf. The Discovery of an Anomalous X-Ray Pulsar in the Supernova Remnant Kes 73. *ApJ*, 486:L129–L132, September 1997. doi: 10.1086/310843.

J. Vasseur, J. Paul, B. Parlier, J. P. Leray, M. Forichon, and B. Agrinier. Possible Pulsed Gamma Ray Emission above 50 MeV from the Crab Pulsar. *Nature*, 226:534–535, May 1970. doi: 10.1038/226534a0.

VERITAS Collaboration, E. Aliu, T. Arlen, T. Aune, M. Beilicke, W. Benbow, A. Bouvier, S. M. Bradbury, J. H. Buckley, V. Bugaev, K. Byrum, A. Cannon, A. Cesarini, J. L. Christiansen, L. Ciupik, E. Collins-Hughes, M. P. Connolly, W. Cui, R. Dickherber, C. Duke, M. Errando, A. Falcone, J. P. Finley, G. Finnegan, L. Fortson, A. Furniss, N. Galante, D. Gall, K. Gibbs, G. H. Gillanders, S. Godambe, S. Griffin, J. Grube, R. Guenette, G. Gyuk, D. Hanna, J. Holder, H. Huan, G. Hughes, C. M. Hui, T. B. Humensky, A. Imran, P. Kaaret, N. Karlsson, M. Kertzman, D. Kieda, H. Krawczynski, F. Krennrich, M. J. Lang, M. Lyutikov, A. S. Madhavan, G. Maier, P. Majumdar, S. McArthur, A. McCann, M. McCutcheon, P. Moriarty, R. Mukherjee, P. Nuñez, R. A. Ong, M. Orr, A. N. Otte, N. Park, J. S. Perkins, F. Pizlo, M. Pohl, H. Prokoph, J. Quinn, K. Ragan, L. C. Reyes, P. T. Reynolds, E. Roache, H. J. Rose, J. Ruppel, D. B. Saxon, M. Schroedter, G. H. Sembroski, G. D. Şentürk, A. W. Smith, D. Staszak, G. Tešić, M. Theiling, S. Thibadeau, K. Tsurusaki, J. Tyler, A. Varlotta, V. V. Vassiliev, S. Vincent, M. Vivier, S. P. Wakely, J. E. Ward, T. C. Weekes, A. Weinstein, T. Weisgarber, D. A. Williams, and B. Zitzer. Detection of Pulsed Gamma Rays Above 100 GeV from the Crab Pulsar. *Science*, 334:69–, October 2011. doi: 10.1126/science.1208192.

M. Vivekanand. Giant radio pulses from the millisecond pulsar PSR B1937+21 at 327MHz. *MNRAS*, 332:55–58, May 2002. doi: 10.1046/j.1365-8711.2002.05275.x.

J. L. L. Voûte, M. L. A. Kouwenhoven, P. C. van Haren, J. J. Langerak, B. W. Stappers, D. Driesens, R. Ramachandran, and T. D. Beijaard. PuMa, a digital Pulsar Machine. *A&A*, 385:733–742, April 2002. doi: 10.1051/0004-6361:20020123.

J. V. Wall and C. R. Jenkins. *Practical Statistics for Astronomers*. April 2012.

J. C. Weatherall. Pulsar Radio Emission by Conversion of Plasma Wave Turbulence: Nanosecond Time Structure. *ApJ*, 506:341–346, October 1998. doi: 10.1086/306218.

T. C. Weekes. *Very high energy gamma-ray astronomy*. 2003.

T. C. Weekes, M. F. Cawley, D. J. Fegan, K. G. Gibbs, A. M. Hillas, P. W. Kowk, R. C. Lamb, D. A. Lewis, D. Macomb, N. A. Porter, P. T. Reynolds, and G. Vacanti. Observation of TeV gamma rays from the Crab nebula using the atmospheric Cerenkov imaging technique. *ApJ*, 342:379–395, July 1989. doi: 10.1086/167599.

A. Weigert and H. J. Wendker. *Astronomie und Astrophysik - ein Grundkurs*. VCH Verlagsgesellschaft, Weinheim, 3rd edition, 1996. ISBN 3-527-29394-9.

P. Weltevrede, R. T. Edwards, and B. W. Stappers. The subpulse modulation properties of pulsars at 21 cm. *A&A*, 445:243–272, January 2006. doi: 10.1051/0004-6361:20053088.

R. Wielebinski, N. Junkes, and B. H. Grahl. The Effelsberg 100-m Radio Telescope: Construction and Forty Years of Radio Astronomy. *Journal of Astronomical History and Heritage*, 14:3–21, March 2011.

Thomas L Wilson, Kristen Rohlfs, and Susanne Hüttemeister. *Tools of radio astronomy*, volume 86. Springer, 2009.

A. Wolszczan, J. Cordes, and D. Stinebring. a Single Pulse Study of the Millisecond Pulsar 1937+214 (Poster). In S. P. Reynolds and D. R. Stinebring, editors, *Birth and Evolution of Neutron Stars: Issues Raised by Millisecond Pulsars*, page 63, 1984.

A. Wongwathanarat, E. Müller, and H.-T. Janka. Three-dimensional simulations of core-collapse supernovae: from shock revival to shock breakout. *A&A*, 577:A48, May 2015. doi: 10.1051/0004-6361/201425025.

P. M. Woods and C. Thompson. Soft gamma repeaters and anomalous X-ray pulsars: magnetar candidates. In W. H. G. Lewin and M. van der Klis, editors, *Compact stellar X-ray sources*, pages 547–586. Cambridge University Press, April 2006.

S. Woosley and T. Janka. The physics of core-collapse supernovae. *Nature Physics*, 1:147–154, December 2005. doi: 10.1038/nphys172.

G. A. E. Wright, W. Sieber, and A. Wolszczan. Mode-switching, nulling and drifting subpulses in PSR 1112 + 50. *A&A*, 160:402–405, May 1986.

L. Zampieri, A. Čadež, C. Barbieri, G. Naletto, M. Calvani, M. Barbieri, E. Verroi, P. Zoccarato, and T. Occhipinti. Optical phase coherent timing of the Crab nebula pulsar with Iqueye at the ESO New Technology Telescope. *MNRAS*, 439:2813–2821, April 2014. doi: 10.1093/mnras/stu136.

R. Zanin. *Observations of the Crab pulsar wind nebula and microquasar candidates with MAGIC*. PhD thesis, Universitat Autonoma de Barcelona, 2013.

R. Zanin, J. Cortina, and for the MAGIC Collaboration. The Central Control of the MAGIC telescopes. *ArXiv e-prints*, July 2009.

V. E. Zavlin and G. G. Pavlov. Modeling Neutron Star Atmospheres. In W. Becker, H. Lesch, and J. Trümper, editors, *Neutron Stars, Pulsars, and Supernova Remnants*, page 263, 2002.

S. Zharikov and R. P. Mignani. On the PSR B1133+16 optical counterpart. *MNRAS*, 435:2227–2233, November 2013a. doi: 10.1093/mnras/stt1439.

S. Zharikov and R. P. Mignani. On the PSR B1133+16 optical counterpart. *MNRAS*, 435:2227–2233, November 2013b. doi: 10.1093/mnras/stt1439.

S. V. Zharikov, Y. A. Shibanov, R. E. Mennickent, and V. N. Komarova. Possible optical detection of a fast, nearby radio pulsar PSR B1133+16. *A&A*, 479:793–803, March 2008. doi: 10.1051/0004-6361:20077728.

V. I. Zhuravlev, M. V. Popov, V. A. Soglasnov, V. I. Kondrat'ev, Y. Y. Kovalev, N. Bartel, and F. Ghigo. Statistical and polarization properties of giant pulses of the millisecond pulsar B1937+21. *MNRAS*, 430:2815–2821, April 2013. doi: 10.1093/mnras/stt094.

Acknowledgements

Dear reader, your are almost done. This section is dedicated to the people who helped to get this multiwavelength study going. Numerous people have been included in this project and have contributed in their own specific way to its final outcome. I would like to adress all of them in this section.
First of all I would like to thank Prof. Dr. Karl Mannheim for giving me the opportunity to carry out this project which opened many paths to different topics of γ-ray and radio astronomy for me.
Many thanks to Prof. Dr. Felix Spanier for reading through the thesis and giving useful suggestions and remarks which helped me to improve it significantly.
At this point I would also like to thank Dominik Elsässer for supporting me in my decisions and the paths which I chose during this project.
Thanks to Daniela Dorner for her advice regarding the analysis of MAGIC data and her reading during thesis writing.
A big thanks to Robert Schulz for constantly stirring my fascination of radio telescopes and spending hours building paper models (the Parkes telescope, an ALMA antenna + the truck and a DS9 telescope). These meetings brought along lots of interesting discussions about their construction and radio astronomy from the VLBI point of view.
Many thanks to Till Steinbring for taking care of the simultaneous observations with the MAGIC telescopes in the long winter of 2012/13. Due the dedication of you and your shift crew we got nearer to the final aim of getting a large amount of coverage with the radio facilities.
Thanks to Aleksander Paravac for constant support with my very first software installations for the analysis of γ-ray and radio data.
Thanks to Katja Meier for having a good time at one of the MAGIC software schools, discussions about proper background discrimination procedures and simply for keeping asking me how I was doing even if in remote mode.
Thanks to Sonja Boyer, Sheetal Saxena and Jan Storz for accompanying me on the very first trip to the Effelsberg radio telescope and helping with numerous issues ranging from data taking to data analysis. All of you were a great help in gaining the very first experience with radio observations.

One key part of this project without which the radio observations could not have been carried out was the Effelsberg radio telescope group. At this point I would like to thank Alex Kraus for supporting our project and showing lots of patience when I needed to shift observation slots repeatedly. It was an exceptional opportunity for me to carry out the radio observations with the Effelsberg telescope myself. Many thanks to Ralf Kisky, Jörg Barthel and Thomas Wedel for introducing me into the various technical aspects of the Effelsberg radio telescope during my frequent stays at the observatory. I learned a lot about the properties of a telescope of that size.
A big thanks to Axel Jessner for advice and mentoring during various stages of data analysis and pulsar observations. Thanks for encouraging my attendance of the URSI meeting which

gave me a new insight into different branches of radio science.
Many thanks to Ramesh Karuppusamy for teaching me the very first steps of pulsar radio analysis and how to observe the Crab pulsar with the Effelsberg radio telescope. Thanks for taking care of the proper reduction of the data.
Thanks to Joris Verbiest for constantly answering my questions about Tempo2 and LOFAR. I can be somewhat persistent sometimes, but you patiently answered all my questions.
Thanks to Lucas Guillemot for various discussions about pulsars, the proper barycentering of radio and γ-ray data and for teaching me the analyis of pulsar Fermi LAT data.
A huge thanks to Charlotte Sobey for helping me with the analysis of pulsar radio data and the support with regard to my very first LOFAR proposal and the later proposals for the multifrequency study of giant pulse emitting pulsars.
Finally thanks to Michael Kramer who supported our project and also encouraged my contribution to the new SKA Science Book.

Another decisive role in this project was carried out by the WSRT and the ASTRON pulsar working group.
A big thanks to Vlad Kondratiev who guided me through the process of proposal writing and radio data analysis and showed patience when I repeatedly showed up with a whole bunch of new questions. Besides thanks for teaching me how to "build" a pulsar.
I would also like to thank Gyula Josza and Roy Smits for arranging and reducing the radio observations taken with the WSRT. You guys showed great endurance while meeting with all my concerns ranging from changes of observation slots to the process of data reduction.
A big thanks to Maura Pilia for introducing me to the world of famous scientists during our first Fermi Symposium. The trips to Groningen brought along lots of fun and laughter. I enjoyed each of them.
Many thanks to Gemma Janssen for her constant help and advice during my time as a Helena Kluyver fellow at the ASTRON institute (and beyond). Thanks for letting me take care of Aurora and Saros. I had lots of fun and they reminded me of past times to which I will certainly come back again.
Thanks to Cees Bassa for teaching me how to deal with the sometimes not so easy reduction of RFI and the discussions about LEAP.
Thanks to Dan Stinebring for numerous discussions about pulsars, radio astronomy and life in general.
Many thanks to Megan Argo for welcoming me warmly during my very first stay at ASTRON and for sharing her experiences about a life as a postdoc. I keep remembering our discussions looking forward to the time which lies ahead.
Thanks to Anne Archibald for various discussions about the functioning of the Tempo2 software and for giving suggestions about effective ways of testing it.
Apart from that I would like to thank Jason Hessels and Joeri van Leeuwen for welcoming me warmly in the ASTRON pulsar working group, Elisabeth Mahony, Ilse van Bemmel and Gyula Josza for being nice company while we shared an office together, Harm Munk for introducing me into measurements with the Dwingeloo radio telescope and CAMRAS and Fritz for showing up sometimes late in the evening when I was still working, miraculously equipped with a plate of food.

Thanks to Marta Burgay for helping me with my first baby steps with the Tempo2 software. I benefited quite a lot from the HTRA workshop on Sardinia.

Many thanks to Stefan Osłowski for constantly answering my questions about various aspects of the PSRCHIVE software. Yes, polish people are literally everywhere :-) .

The other essential branch for carrying out this study was carried out by the MAGIC telescopes maintained by the MAGIC Collaboration.
First of all thanks to Julian Śitarek for always answering my questions and for explaining to me the essentials of the calibration of MAGIC data (sometimes even till 2 am).
Speaking of which I would like to thank all shift leaders, Riho Reinthal, Andrea Boller and Cornelia Schulz, for helping me as an operator on my very first shift P112 on the Roque de los Muchachos. I gained lots of new knowledge and expertise in this one month up there. I fondly remember our trips during day time to other parts of the island. Those trips were lots of fun and enlarged my knowledge about the beautiful habitat on the island.
A big thanks also to my MAGIC P129 shift crew for one month on the Roque de los Muchachos in June 2013 which was full of surprise and fun. Thanks to Michele Pallatielo and Benito Marcote for creating a nice atmosphere and sometimes weird, but tasty combinations of breakfast after one night full of work. Till today Michele´s "C´mon!" is still sounding in my ears ;-) .
Thanks to Daniela Dorner for showing me the beauty of sunrise as seen from the top of the Roque de los Muchachos. La Palma is indeed a exceptionally beautiful place to which I will certainly return in near future even if not work related.
Thanks to Oscar Blanch for meeting up with almost all my requirements related to schedule changes for our multiwavelength study. I believe this was not always an easy task to fulfill.
A big thanks to Simon Bonnefoy, Riho Reinthal and their shift crews for taking special care of MAGIC observations taken simultaneously with radio observations. The "Lecker Burger" discussion via Skype was definitely one of the best I ever had sitting in the control room of the Effelsberg observatory at the same time.
Thanks to Gianluca Giavitto for encountering all my questions regarding the barycentering of MAGIC pulsar data.
Thanks to Emiliano Carmona for always answering my questions and for updating me on the MC issue. It helped me numerous times making a time table throughout the process of data analysis.
Thanks to David Carreto-Fidalgo and Roberta Zanin for their support related to the MAGIC pulsar analysis. The resulting discussions were a great help to me in understanding the essence of this kind of special part of the analysis of γ-ray data.

A big thanks to Malwina Uellenbek for helping me with the MAGIC data analysis, giving good advice and simply for cheering me up.

Many thanks to Jana Polednikova for encouragement and advice in difficult situations and always cheering me up. I fondly remember when we were sitting in a guest house in a remote place in Armenia without any contact to the outside world contemplating what would happen next.

A huge thanks to Inga Nielsen, my long time friend and former lab partner during physics studies who has been reading through all my texts patiently and without exception. You keep reminding me in stressful situations what a cool job I am carrying out.

A very warm thanks to Patrick Kilian for constantly supporting me in everything what I did even if it seemed a bit crazy at first. Thanks for supporting me with your opinion, advice, a common fascination of big telescopes (one of my happiest moments is indeed when I can move around many tons of steel in the form of a telescope) and incredibly huge amounts of coffee!

Najbardziej jednak dziekuję moim rodzicom którzy w każdy możliwy sposób mi pokazali jak można przetrwac i osiagnąc tego czego się pragnie. Ten moment w którym dostalam od Was swój pierwszy mały teleskop, rozbudził zainteresowanie i pasje która trwa do dzisiejszej chwili. Prowadziliscie mnie w dobrych i zlych czasach. I nawet jak nasz system juz nie jest kompletny, niemniej jednak cały czas jest.

This study is partly based on observations with the 100-m telescope of the MPIfR (Max-Planck-Institut für Radioastronomie) at Effelsberg.
Another part of this study was carried out with data taken with the Westerbork Synthesis Radio Telescope (WSRT). The Westerbork Synthesis Radio Telescope is operated by the ASTRON (Netherlands Institute for Radio Astronomy) with support from the Netherlands Foundation for Scientific Research (NWO).
NL would like to thank the Instituto de Astrofísica de Canarias for the excellent working conditions at the Observatorio del Roque de los Muchachos on La Palma.
Some of the figures shown in this thesis were constructed with data taken from the "The ATNF Pulsar Catalogue", R. N. Manchester, G. B. Hobbs, A. Teoh & M. Hobbs, Astronomical Journal, 129, 1993-2006 (2005), http://www.atnf.csiro.au/research/pulsar/psrcat .
Part of this research has made use of the database of published pulse profiles maintained by the European Pulsar Network, available at: http://www.jb.man.ac.uk/research/pulsar/Resources/epn/.
The timing analysis presented in this study was carried out with the software package TEMPO2 (Hobbs et al. [2006b]).
NL gratefully acknowledges the support of this study by the BMWF grant 05A11WW and funding from the ASTRON/JIVE Helena Kluyver female visitor programme.